

# Investigating and applying rock surface luminescence dating in archaeological and geomorphological contexts

Inaugural-Dissertation

zur

Erlangung des Doktorgrades

der Mathematisch-Naturwissenschaftlichen Fakultät

der Universität zu Köln

Köln (Cologne), 2024

vorgelegt von

Lucas Ageby

aus Råsunda, Schweden

Berichterstatte r/Gutachte r:

Prof. Dr. Helmut Brückner

Prof. Dr. Tony Reimann

Tag der mündlichen Prüfung:

18.10.2023

# Abstract

Rock surface luminescence dating is a developing geochronological method which utilises the zeroing of the dose-dependent, optically sensitive luminescence signal at rock surfaces. Extended exposure to daylight resets the signal from the rock surface deeper inwards. If the surface is subsequently covered from daylight, then the luminescence signal will increase due to ionising radiation, forming a luminescence signal-depth profile. This depth profile is demonstrative of sufficient signal resetting before a potential burial, and hence, the method is increasingly often used for burial dating of rock surfaces. Exposure dating of rock surfaces is also, in some cases, possible if the rate of signal zeroing with depth is known for a specific lithology and geographical location. This study focuses on investigating rock surface luminescence dating in archaeological environments or in environments of importance for archaeological research since significant methodological and practical limitations apply to this kind of research. This work specifically addresses (i) the application of rock surface luminescence to date various open-air sites; (ii) the direct dating of stone structures of varying states of degradation; as well as (iii) the methodological impact for successfully dating with regard to lithology. This study explores the possibility of dating rock surfaces at various locations, either directly connected to human activities in pre-history or in environments associated with archaeological research.

Open-air sites are notoriously difficult to date. Ages from covered rock surfaces from gneissic stones from archaeological horizons in Val di Sole, Italy, provide insights into site development and human use of the site from the Early Bronze Age until the Medieval period, including humans using fire. In contrast, exposed granite and vein quartz cobbles from desert pavements in the Eastern Desert, Egypt, proved difficult to date because of insufficient signal resetting resulting in too short signal-depth profiles in the granites, or due to bad signal characteristics with significant input of slow luminescence signal components in the quartz.

Work from the upland landscape of Val di Sole demonstrates that novel geochronological data can be obtained from gneissic rocks collected directly from rock structures.

Direct dating of these structures using buried rock surfaces dates construction and degradation cycles from the Bronze Age (1000 BC) until the Early Modern Period (19th century). It is unlikely that any other dating method could resolve such a complex record. Regrettably, the dating of exposed rock surfaces caused severe age underestimations due to shorter-than-expected signal-depth profiles.

A key result of this study is the importance of lithology for the successful application of rock surface luminescence dating. Dating of shorelines in the coastal Atacama Desert, Chile using cobbles of various lithologies demonstrates that despite good bleaching conditions, many samples suffered from insensitivity to luminescence stimulation, or the luminescence signal-depth profiles were affected by high dose rates and low signal saturation limits. Also, investigations into calcarenites rocks from the Mula Valley, Spain, demonstrated it is possible to date deposits which lack silica-rich rocks. The luminescence signal is sufficiently bright for the dating of at least two cobbles. However, the rock surface burial ages (10–15 ka) currently underestimate the chronological understanding of the site.

In summary, the research from this thesis further demonstrates the usefulness of rock surface luminescence dating for archaeological research. The chronological data related to site development and human activity that are accessible using this method are challenging to acquire with other methods for many settings. However, the chosen lithology for dating is consequential for a successful application, perhaps more so than other site-related factors such as bleaching conditions.



# Kurzzusammenfassung

Die Lumineszenzdatierung von Gesteinsoberflächen (rock surface luminescence dating) ist eine sich in der Entwicklung befindliche geochronologische Methode. Diese macht sich die Tatsache zunutze, dass das dosisabhängige, optisch empfindliche Lumineszenzsignal an Gesteinsoberflächen zurückgesetzt wird, wenn es dem Tageslicht ausgesetzt ist. Dabei gilt, je länger die Gesteinsoberfläche dem Tageslicht ausgesetzt wird, desto tiefer in den Stein wird das Signal zurückgesetzt. Wird die Gesteinsoberfläche nicht länger dem Tageslicht ausgesetzt – z.B. wenn die Oberfläche verschüttet wird, nimmt das Lumineszenzsignal aufgrund der ionisierenden Strahlung zu und bildet ein Lumineszenzsignal-Tiefenprofil. Aus diesem Tiefenprofil kann eine ausreichende Zurücksetzung des Signals vor einer möglichen Verschüttung ermittelt werden, weshalb die Methode immer häufiger zur Datierung der Verschüttung von Gesteinsoberflächen verwendet wird. Die Datierung von Gesteinsoberflächen durch Freilegung ist in einigen Fällen auch möglich, wenn die Rate der Zurücksetzung des Signals für eine bestimmte Lithologie und geografische Lage bekannt ist. Die vorliegende Dissertation konzentriert sich auf die Untersuchung der Lumineszenzdatierung von Gesteinsoberflächen im archäologischen Umfeld bzw. in Bereichen, die für die archäologische Forschung von Bedeutung sind, da hier erhebliche methodische und praktische Einschränkungen gelten. Sie befasst sich insbesondere mit (i) der Anwendung der Lumineszenzdatierung von Gesteinsoberflächen aus verschiedenen Freiluftstationen, (ii) der direkten Datierung von Steinstrukturen in unterschiedlichen Degradationszuständen sowie (iii) den methodischen Auswirkungen für eine erfolgreiche Datierung im Hinblick auf die Lithologie. Dabei wird die Möglichkeit der Datierung von Gesteinsoberflächen an verschiedenen Orten untersucht, die entweder in direktem Zusammenhang mit menschlichen Aktivitäten in der Vorgeschichte stehen oder in Umgebungen, die mit archäologischen Forschungen zusammenhängen.

Freilandstationen sind bekanntermaßen schwer zu datieren. Altersbestimmungen von verschütteten Gesteinsoberflächen aus Gneis aus archäologischen Schichten in Val di Sole, Italien, geben Aufschluss über die Entwicklung der Stätte und ihre Nutzung

durch den Menschen von der frühen Bronzezeit bis zum Mittelalter, einschließlich der Nutzung von Feuer durch den Menschen. Im Gegensatz dazu erwies sich die Datierung von freiliegenden Graniten und Quarzen aus Steinpflastern in der östlichen Wüste Ägyptens als schwierig: zum einen, weil die Signalmücksetzung (Granit) unzureichend war, was zu zu kurzen Signaltiefenprofilen führte, und zum anderen, weil die Charakteristiken des Signals aufgrund von langsameren Komponenten des Lumineszenzsignals schlecht waren (Quarz).

Die Untersuchungen in der Hochgebirgslandschaft des Val di Sole zeigen, dass neue geochronologische Daten aus Gneisgestein gewonnen werden können, das direkt von Gesteinsstrukturen stammt. Die direkte Datierung dieser Strukturen anhand der verschütteten Gesteinsoberfläche datiert Bau- und Abbauzyklen von der Bronzezeit (1000 v. Chr.) bis zur frühen Neuzeit (19. Jahrhundert). Es ist unwahrscheinlich, dass irgendeine andere Datierungsmethode einen so komplexen Datensatz entschlüsseln könnte. Bedauerlicherweise führte die Datierung von freiliegenden Gesteinsoberflächen zu erheblichen Unterschätzungen des Alters, da die Profile der Signaltiefe kürzer waren als erwartet.

Ein zentrales Ergebnis dieser Dissertation ist die Bedeutung der Lithologie für die erfolgreiche Anwendung der Lumineszenzdatierung von Gesteinsoberflächen. Die Datierung von Strandlinien und Terrassen in der küstennahen Atacama-Wüste, Chile, unter Verwendung von Schottern und Steinen verschiedener Lithologien zeigt, dass viele Proben trotz guter Bleichbedingungen unempfindlich gegenüber der Lumineszenzanregung waren oder dass die Lumineszenzsignaltiefenprofile durch hohe Dosisraten und niedrige Signalsättigungsgrenzen beeinträchtigt waren. Untersuchungen an Kalkareniten aus dem Mulatal, Spanien, haben außerdem gezeigt, dass es möglich ist, Sedimentschichten zu datieren, die keine siliziumdioxidreichen Gesteine enthalten. Das Lumineszenzsignal ist ausreichend intensiv für die Datierung von mindestens zwei Steinen. Das Alter der Verschüttung an der Gesteinsoberfläche (10-15 ka) unterschätzt jedoch das derzeitige chronologische Verständnis der archäologischen Stätte.

Zusammenfassend lässt sich sagen, dass die in dieser Dissertation durchgeführten Untersuchungen die Bedeutung der Lumineszenzdatierung von Gesteinsoberflächen für die archäologische Forschung weiter untermauern. Die mit dieser Methode erzielten chronologischen Daten über die Entwicklung der archäologischen Stätten und

die menschlichen Aktivitäten sind mit anderen Methoden in vielen Fällen nur schwer zu erreichen. Die für die Datierung gewählte Lithologie ist jedoch entscheidend für eine erfolgreiche Anwendung – vielleicht sogar wichtiger als andere standortbezogene Faktoren wie z. B. die Zurücksetzung des Signals.



## *Acknowledgements*

First, I would like to express my deepest appreciation to my supervisor, Prof. Dr. Helmut Brückner at the University of Cologne, for giving me the opportunity to come to Cologne for my doctoral studies. His feedback and guidance during my time in Cologne have greatly improved my abilities as a researcher, and I am forever grateful for his support. I am deeply indebted to my co-supervisors, PD Dr. Dominik Brill and Dr. Nicole Klasen at the University of Cologne, for advising me throughout my work with their extensive knowledge in the field of luminescence dating. Dominik's guidance has been crucial to the outcome of the research in this PhD thesis and has hugely improved my abilities as a scientist. Dominik's support was also essential in the final phase of the writing of my dissertation, as he has given great feedback and encouragement. Nicole developed the research project in which I worked. She also instructed me in the field and the laboratory and introduced me to new colleagues whose assistance proved essential for the work presented in this thesis. I want to recognise all the members of my doctoral committee: Prof. Dr. Tony Reimann, Prof. Dr. Tibor Dunai, Prof. Dr. Helmut Brückner, and PD Dr. Dominik Brill; I thank them very much for their time and effort.

I also extend my gratitude to other colleagues at the University of Cologne. I am very grateful to Dr. Simon Matthias May for providing invaluable feedback on my work and writing. Special thanks to Dr. Anja Zander, who instructed me in the laboratory, offered essential help with equipment such as the rock drill and performed the gamma spectrometry of my samples. The Val di Sole charcoal samples were radiocarbon dated by the Organic Geochemistry & Radiocarbon Group of Prof. Dr. Janet Rethemeyer.

During my PhD, I participated in the Integrated Research Graduate School and the Graduate School of Geosciences at the University of Cologne. My development has been greatly aided by these programmes and the hard work of the administrators. Here, I would like to give special thanks to Dr. Hannah Hartung and Dr. Karin Boessenkool from the graduate schools for helping me with the administrative aspects of the thesis, and Prof. Dr. Frank Schäbitz for his inspiring leadership. I really appreciate the working groups of Prof. Dr. Helmut Brückner and Prof. Dr. Tony

Reimann for the great camaraderie and good discussions and for making me feel welcome from the very first day.

During my PhD, I worked with many German and international colleagues who made my research possible. Prof. Dr. Diego E. Angelucci (University of Trento) has been essential to my work. I express my sincere gratitude to him for a thoroughly enjoyable collaboration in Val di Sole and Mula. His in-depth knowledge of geosciences and archaeology, his patience and his scientific curiosity have been crucial in applying the still-developing method of rock surface luminescence to challenging sites. I am also very grateful to Dr. Francesco Carrer (Newcastle University) for the great collaboration in Val di Sole and for helping me better understand the fascinating dynamics of upland archaeology. I wish to acknowledge the assistance of all other ALPES project participants in Val di Sole. Also in Val di Sole I appreciate the hospitality of Fabio and his family. I wish to thank to Prof. Dr. João Zilhão (University of Lisbon) and all other colleagues from the Mula excavations for their support during fieldwork. Fieldwork and sampling in Egypt were only possible due to the invaluable help of Dr. Karin Kindermann (University of Cologne) and Dr. Felix Henselowsky (University of Heidelberg), and I appreciate having had the opportunity to work with samples from the exciting Sodmein site. I had the great pleasure of working with Dr. Eike F. Rades, who invited me to the Nordic Luminescence Laboratory for micro-XRF measurements. I acknowledge the assistance of Dr. Benjamin Lehmann and Dr. Joanne Elkadi at the University of Lausanne for instructing me on processing rocks for luminescence dating, which greatly aided my research.

Throughout my doctoral studies, my fantastic wife, Frederieke, has been my greatest supporter, and I am forever grateful for having her in my life. I am also very appreciative of all my family members: Mamma Lotta and Pappa Mats, my siblings Linn and Linus, and Mormor Anita and Morfar Tony and Farmor Siv and Farfar Ray, and my Godmother Liselott, who all have supported me so much throughout my life. Without all their support, I would never have been able to find my way to Germany for the opportunity of a lifetime. Finally, I would like to thank Mr. Gabriel Norén for providing me with accommodation during my visit to Cologne when I was interviewed for the position that led to this PhD thesis, for helping me settle in a new country in 2018, and for always being a great friend.

During my PhD, I was funded by the German Research Foundation (DFG) as part of the Collaborative Research Centre (SFB) 806 “Our Way to Europe“ in the subproject F2 (Project number 57444011), which I gratefully acknowledge.





# Contents

<b>Abstract</b>	<b>iii</b>
<b>Kurzzusammenfassung</b>	<b>v</b>
<b>Acknowledgements</b>	<b>ix</b>
<b>Contents</b>	<b>xiii</b>
<b>List of Figures</b>	<b>xvii</b>
<b>List of Tables</b>	<b>xxi</b>
<b>1 Introduction</b>	<b>1</b>
1.1 Rationale for this thesis . . . . .	1
1.2 The Collaborative Research Centre 806 – <i>Our way to Europe</i> . . . . .	2
1.3 Rock surface luminescence dating – development, application, and state of the art . . . . .	4
1.3.1 Optical dating – a brief overview . . . . .	4
1.3.2 Rock surface luminescence dating . . . . .	8
1.4 Hypotheses and objectives of this thesis . . . . .	18
1.5 Research design and methodology . . . . .	22
1.5.1 Fieldwork . . . . .	22
1.5.2 Luminescence dating . . . . .	22
1.5.2.1 Equivalent dose and dose rate . . . . .	22
1.5.2.2 Rock surface luminescence dating . . . . .	25
1.5.2.3 Sediment dating with luminescence . . . . .	27
1.5.3 Radiocarbon dating . . . . .	29
1.5.4 $\mu$ -X-ray fluorescence analysis . . . . .	29

1.5.5	Thesis outline . . . . .	30
1.6	Overview of the study areas . . . . .	33
1.6.1	The upland pastures of Val di Sole, Italy – Chapters 2 & 3 . . .	33
1.6.2	Mula basin, Spain – Chapter 4 . . . . .	35
1.6.3	Wadi Sodmein, Egypt – Chapter 5 . . . . .	36
1.6.4	The coast of the Atacama Desert, Chile – Chapter 6 . . . . .	38
<b>2</b>	<b>Rock Surface IRSL Dating of Buried Cobbles from an Alpine Dry- Stone Structure in Val di Sole, Italy</b>	<b>41</b>
<b>3</b>	<b>Dating dry-stone walls with rock surface luminescence: A case study from the Italian Alps</b>	<b>59</b>
<b>4</b>	<b>Investigating optical dating of carbonate-rich cobbles from a river terrace: A pilot study from the Mula Valley, Spain</b>	<b>71</b>
<b>5</b>	<b>Towards luminescence rock surface dating of wadi terraces: signal characteristics and profiles from Sodmein, Egypt</b>	<b>83</b>
5.1	Introduction . . . . .	84
5.2	Methods and material . . . . .	85
5.2.1	Samples and preparation . . . . .	85
5.2.2	Measurements procedures . . . . .	86
5.2.3	Dose rate calculations, fitting and age calculations . . . . .	86
5.3	Luminescence characteristics . . . . .	87
5.3.1	Luminescence decay curves . . . . .	87
5.3.2	OSL signal sensitivity changes . . . . .	88
5.3.3	Dose recovery test for quartz sample QD4 . . . . .	90
5.3.4	Fading . . . . .	91
5.4	Luminescence-depth profiles . . . . .	92
5.5	Preliminary burial age estimates from sample QB4 . . . . .	94
5.6	Discussion . . . . .	96
5.6.1	Luminescence performance . . . . .	96
5.6.2	Age of cobble QD4 . . . . .	98
5.6.3	Dating of desert pavements using rock surface luminescence dating	99

<b>6</b>	<b>Investigating the resetting of IRSL signals in beach cobbles and their potential for rock surface dating of marine terraces in Northern Chile</b>	<b>101</b>
<b>7</b>	<b>Discussion</b>	<b>119</b>
7.1	Dating of man-made structures and natural deposits using rock surface luminescence . . . . .	119
7.1.1	The construction, degradation and burial of archaeological structures . . . . .	119
7.1.2	Rock surface luminescence dating as a tool for understanding geomorphological processes . . . . .	122
7.2	The effect of lithology on rock surface luminescence dating . . . . .	124
7.2.1	Luminescence characteristics . . . . .	124
7.2.2	Luminescence-depth profiles . . . . .	125
7.2.3	Dose rate and signal saturation . . . . .	128
7.2.4	Anomalous fading . . . . .	130
7.3	Dating of palaeolithic sites with rock surface luminescence dating – significance for future research on pre-historic migration into and within Europe . . . . .	131
<b>8</b>	<b>Conclusions and Outlook</b>	<b>137</b>
	<b>Bibliography</b>	<b>141</b>
<b>A</b>	<b>Supplementary material: Rock Surface IRSL Dating of Buried Cobbles from an Alpine Dry-Stone Structure in Val di Sole, Italy</b>	<b>179</b>
<b>B</b>	<b>Supplementary material: Dating dry-stone walls with rock surface luminescence: A case study from the Italian Alps</b>	<b>187</b>
<b>C</b>	<b>Supplementary material: Investigating optical dating of carbonate-rich cobbles from a river terrace: A pilot study from the Mula Valley, Spain</b>	<b>192</b>

<b>D</b>	<b>Supplementary material: Investigating the resetting of IRSL signals in beach cobbles and their potential for rock surface dating of marine terraces in Northern Chile</b>	<b>211</b>
<b>E</b>	<b>Paper contribution</b>	<b>232</b>
<b>F</b>	<b>Curriculum Vitae</b>	<b>234</b>
<b>G</b>	<b>Erklärung</b>	<b>237</b>

# List of Figures

- 1.1 Calculated depth-dependent dose rate throughout a 20 mm thick rock matrix using the approach of [Freiesleben et al. \(2015\)](#) (A) or by using the tool *calc\_CobbleDoseRate* from the *Luminescence* package ([Kreutzer et al., 2021](#)) in R version 4.1.1 ([Riedesel and Autzen, 2021](#)) (B). . . . . 13
- 1.2 Plotting of an exponentially fitted dose response curve used to determine  $D_e$  (in this example: 223 Gy) in one aliquot. Uncertainties in  $D_e$  estimation of each subsample arises from ratio between the brightness of the integrated signal and the background signal, the error of the fitting, and instrumental errors ([Galbraith and Roberts, 2012](#)). . . . . 24
- 1.3 Hypothetical luminescence-depth profiles: no bleaching before burial, the dose is saturated from the surface to the centre of the rock (A); lower signal at the surface compared to deeper into the rock, but no signal plateau is visible, it in this scenario unknown if the signal was fully bleached before burial (B); a signal plateau reaching 3 mm before increasing to saturation at the centre of the rock (C). Signal saturation is defined as  $L_n/T_n = 1$ . . . . . 27
- 1.4 Modeled luminescence-depth profiles ( $\overline{\sigma\varphi_0} = 2 \text{ a}^{-1}$ ;  $\mu = 1 \text{ mm}^{-1}$ ;  $L_0 = 1$ ) for a range of exposure durations (1 a–10 Ma) using eq. 1.1 (A) and eq. 1.2 (B), demonstrating the difference in shape that arises when  $\dot{D}$  ( $2 \text{ Gy ka}^{-1}$ ; assumed to be constant throughout the rock for simplicity) and  $D_0$  (500 Gy) are included (A), compared to when no trapping is assumed to occur (B). For these specific (and arbitrarily chosen) parameters, the exposed signal-depth profiles have reached equilibrium by  $t_e = 1 \text{ Ma}$  when  $\frac{\dot{D}}{D_0}$  is included. . . . . 28

1.5	Complex patterns of luminescence-depth profiles, modelled using the equations from table 1.2. These profiles show series of exposure and burial events, which can be quantified using the model developed by Freiesleben et al. (2015). Here, the parameters: $L_0$ , $\overline{\sigma\varphi_0}$ , $\dot{D}$ , and $D_0$ are the same as those used for the profiles in Fig. 1.4. The modelling in plot A shows that the rock surface was first exposed ( $L_1(x)$ ) for 500 years ( $t_{e1}$ ), followed by burial ( $L_2(x)$ ) at 50 ka ( $t_{b1}$ ). Plot B displays subsequent exposure $L_3(x)$ and burial events $L_4(x)$ , where the rock surface is exposed for 10 years ( $t_{e2}$ ) following $L_2(x)$ , before the final burial occurring at 10 ka ( $t_{b2}$ ). . . . .	28
1.6	Overview map of study sites. Base map was made with Natural Earth.	33
1.7	(A) An overview of Wadi Sodmein, showing the ridge of Jebel Duwi and the location of the Sodmein Cave. (B) The position of wadi terraces in Wadi Sodmein; the green point marks the location for the northeastern field-of-view, overlooking some of the wadi terraces (C). . . . .	39
5.1	Luminescence decay curves following beta irradiation (45–90 Gy) from pavement vein quartz (A–D), pavement granites (E), and modern granites (F–H). . . . .	89
5.2	Natural ( $L_n$ ) OSL decay curves from QD4 and QE3. . . . .	90
5.3	Changes in fast ratio in sample QD4 over cycles of OSL stimulation and beta dosing of 90 Gy (cycle 1 is the natural signal $L_n$ without any additional dose). The error bars represent $1\sigma$ . . . . .	91
5.4	Dose recovery test for seven fresh slices from QD4. The OSL protocol described in Table 5.1 was used for all measurements. . . . .	92
5.5	Luminescence signal-depth profiles for sample QD4. The natural luminescence signal ( $L_n$ ) was corrected with a test dose ( $T_n = 90$ Gy). . . .	93
5.6	IRSL and pIRIR signal-depth profiles of the granites exposed on the rooftop for $\sim 1$ year. The natural luminescence signal ( $L_n$ ) was corrected with a test dose ( $T_n = 32$ Gy). . . . .	94
5.7	Luminescence signal-depth profiles for sample QB4. The natural IRSL and pIRIR <sub>225</sub> signals ( $L_n$ ) were corrected with a test dose of 32 Gy. . .	95

5.8	Fitting of the $L_n/T_n$ IRSL data from bottom surface of QB4 using Eq. 1.7, assuming one exposure event followed by one burial event. The data were normalised using the average $L_n/T_n$ calculated from all slices for which $L_n/T_n$ ratio $>5$ from Fig 5.6, using this value as a proxy for the field saturated $L_n/T_n$ level. . . . .	96
7.1	Modelled IRSL-depth profiles (signal saturation = 1) from different lithologies using $\mu$ values from exposed or previously exposed surfaces. The profiles are fitted assuming $\overline{\sigma\phi_0} = 333 a^{-1}$ ; this value was estimated based on a bleaching experiment exposure on a rooftop in Cologne, Germany, for 32 days during summer (see Chapter 2 for more detail). . . . .	129
7.2	$2D_0$ /dose rate versus the effective dose rate (including environmental dose rate from the surrounding) at the outer 1 mm of rock, derived from the rock itself in samples from the different sites investigated in this thesis. . . . .	132
7.3	Fading (g-values) of IRSL measured from cobbles of eight different lithologies in this thesis. . . . .	132
7.4	Schematic of dateable features in an archaeological landscape using rock surface luminescence dating. . . . .	133





# List of Tables

1.1	Two adaptations of SAR protocols for measuring quartz using OSL (Murray and Wintle, 2003) and feldspar using pIRIR <sub>225</sub> (Buylaert et al., 2009).	23
1.2	The model for multiple exposure and burial events developed by Freiesleben et al. (2015).	27
5.1	The OSL and pIRIR SAR protocols applied to the Sodmein samples .	87
5.2	Summary of ages derived from the bottom surface from sample QB4. Depth is noted from the covered surface–substrate interface.	95



# Chapter 1

## Introduction

### 1.1 Rationale for this thesis

Chronology is crucial to understand archaeological development: it allows for temporal constraining of human or natural events affecting society, the quantification of rates of societal changes, and the assessment of relative and absolute temporal relationships between different archaeological deposits. The development of dating techniques during the latter half of the 20<sup>th</sup> century and the 21<sup>th</sup> century has enabled absolute age estimates of archaeological deposits and structures. The introduction (Libby, 1946; Arnold and Libby, 1949; Libby et al., 1949) and subsequent advancement of radiocarbon dating has provided archaeologists with a powerful chronological tool for dating organic material younger than 50.000 years. For its discovery, William F. Libby was awarded the Nobel Prize in chemistry in 1960. However, since organic materials – necessary for radiocarbon dating – are not always available or suitable for dating, and because research within the field of palaeolithic archaeology spans far too deep into the past to be covered solely by radiocarbon dating, other methods are frequently applied. The list of additional, commonly applied dating methods used in archaeological research includes potassium-argon and argon-argon dating (Gabunia and Vekua, 1995; McHenry and Stanistreet, 2018), uranium series dating (Sauvet et al., 2017; Hoffmann et al., 2018), dendrochronology (Bonde and Christensen, 1993; Hafner et al., 2021), and various methods of trapped charge dating (Grün et al., 1990; Klasen et al., 2017; Richter et al., 2017). This thesis focuses on optically stimulated luminescence (OSL) dating – a trapped charge dating technique – applied to rock surfaces, henceforth termed: *rock surface luminescence dating*. Below is a short description regarding the

motivation for why rock surface luminescence dating in geoarchaeological contexts warrants further investigation.

Rock surface luminescence dating is a potentially unique tool for dating in a geoarchaeological context. While conventional OSL dating (and related methods) of unconsolidated sediments are invaluable for dating the time of formation of sedimentary units in which archaeological horizons are formed, the method requires the presence of grains of the medium sand to silt fractions, and the dated grains were sufficiently exposed to daylight during sediments transport. Rock surface luminescence dating provides the opportunity to optically date larger clasts from stone structures or gravel deposits, and allows an assessment of whether the pre-burial signal resetting was sufficient to zero the luminescence clock, which can be of significant advantage in numerous archaeological contexts. However, further investigation regarding the application of rock surface luminescence dating is necessary since (i) it is a relatively young technique with challenges and (ii) so far, the method has only been applied sparsely to a handful of archaeological and geoscientific sites and settings. The overarching motivation for this thesis is to perform pilot studies in challenging archaeological and archaeologically relevant geological settings to test the method's potential and provide necessary methodological development, which, ultimately, may help provide chronologies for settings important to human spatio-temporal dispersal patterns that were previously undateable.

## 1.2 The Collaborative Research Centre 806 – *Our way to Europe*

The Collaborative Research Centre (CRC) 806 "*Our Way to Europe – Culture-Environment Interaction and Human Mobility in the Late Quaternary*" (<https://www.sfb806.uni-koeln.de>) is an interdisciplinary research centre based at the universities of Cologne, Aachen, and Bonn, which focuses on geoscientific and archaeological investigations in Africa and Western Eurasia. CRC 806 is funded by the German Research Foundation (Deutsche Forschungsgemeinschaft; DFG); the third funding phase of the CRC started in 2017 and finished in 2021. The overarching focus of CRC 806 is to spatially and temporally constrain the migration patterns of

anatomically modern humans (AMH) from the African continent into Eurasia and investigate the environmental and climatic conditions during which such emigration occurred.

The origin and migration patterns of AMH throughout the Pleistocene are crucial to understanding the development of our species. Higher genetic diversity within contemporary populations from Africa, compared to non-African populations (Cann et al., 1987; Prugnolle et al., 2005), places the emergence of AMH in Africa (Prugnolle et al., 2005; Skoglund and Mathieson, 2018). Recent discoveries of new fossils and improved chronological constraints have demonstrated that the development of AMH might be pan-African (e.g., Hublin et al., 2017; Richter et al., 2017), and the origin of AMH cannot thus necessarily be attributed to a single African region (Stringer, 2016; Scerri et al., 2018). Nevertheless, a single region model cannot be excluded based on the current fossil and genetic record (Bergström et al., 2021). The genetic heritage of all contemporary non-African humans is mainly derived from a population of AMH that migrated out of Africa at  $\sim 60$  ka (Skoglund and Mathieson, 2018; Bergström et al., 2021). This migration event does not represent the earliest dispersal of AMH out of Africa; this is established by several discoveries of older fossils outside of Africa: e.g., in Greece ( $>210$  ka; Harvati et al., 2019) and in Israel ( $\sim 180$  ka HersHKovitz et al., 2018) (86–95 ka Groucutt et al., 2018).

The dispersal events of AMH appear to coincide globally with orbitally-driven changes in the climate (Timmermann and Friedrich, 2016). Human dispersal towards Europe likely occurred through the Levant into the Balkans. Early human fossils in the Balkans were discovered in cave sites dating to up to  $\sim 46,000$ – $44,000$  cal BP (e.g., Fewlass et al., 2020; Hublin et al., 2020), and in Upper Palaeolithic sites in the Danube catchment (e.g., Chu, 2018). The timing for the transition between the Middle and Upper Palaeolithic in Europe is commonly dated to occur between 40–47 ka (e.g., Fewlass et al., 2020; Devièse et al., 2021), even though later persistence of Middle Palaeolithic technology south of Rio Ebro drainage in the Iberian Peninsula has been proposed (e.g., Zilhão et al., 2017).

The chronological work conducted as part of CRC 806 was concentrated in the *Timelines* cluster, which in the third phase of the CRC researched methodological development of luminescence (*F2*), radiocarbon (*F5*), and palaeomagnetic (*F6*) dating

in geoarchaeological settings. The work that comprises this thesis was produced as part of project *F2* since it aims at developing rock surface luminescence dating.

### 1.3 Rock surface luminescence dating – development, application, and state of the art

This section primarily covers the development of rock surface luminescence dating, a literature review of the application of the method, and the current state of the art. Theoretical considerations and methodology are covered in detail in section 1.5.2.2.

#### 1.3.1 Optical dating – a brief overview

Optical dating using luminescence, first proposed by [Huntley et al. \(1985\)](#), has become a widely applied dating method to date archaeological (e.g., [Jacobs et al., 2011](#); [Junge et al., 2016](#); [Klasen et al., 2017](#); [Porat et al., 2018](#)) and natural settings (e.g., [Fuchs and Lang, 2001](#); [Lauer et al., 2010](#); [Sohbati et al., 2016](#); [Brill and Cisternas, 2020](#)), covering decadal to Late Pleistocene time scales.

No matter which luminescence dosimeter is used, the principle is that a signal builds when electrons absorb energy in mineral grain lattices due to ionising radiation emitted from surrounding radionuclides and cosmic radiation. This signal is removed when the grain is sufficiently exposed to light or heat. A simple model for the commonly used dosimeter for dating purposes – quartz – is frequently described in publications reviewing luminescence models ([McKeever and Chen, 1997](#)) or luminescence dating in general (e.g., [Preusser et al., 2008](#); [Murray et al., 2021](#)). This model details how the luminescence signal accumulates because some electrons get trapped in lattice defects located between the conduction and valence band, following absorption of ionising radiation which causes some electrons to leave their ground state and move into an excited stage. The electrons remain trapped until they can recombine with electron holes located at lower energy levels within the band gap; this can occur when the electrons absorb sufficient energy from illumination or heating. Luminescence is emitted as photons during the recombination of electrons and electron holes. This process zeroes the luminescence signal. The number of emitted photons, i.e.,

the intensity of the luminescence signal, is proportional to the number of excited electrons; their numbers, in turn, are proportional to the amount of absorbed radiation. Hence, extended periods since the last zeroing event induce more intense luminescence emission during stimulation due to the higher amounts of trapped electrons that can recombine. The luminescence signal can be used for geochronological purposes if the relationship between the naturally accumulated, stimulated luminescence signal and absorbed ionising radiation is known, as well as the rate at which dosing occurs.

The most commonly used luminescence dosimeter is the light-sensitive signal from quartz grains, referred to as optically stimulated luminescence (OSL) (Huntley et al., 1985). The OSL signal possesses several desirable qualities for a Quaternary chronometer. Firstly, weathering-resistant quartz is an abundant mineral formed in felsic igneous rocks and hydrothermal veins, frequently found in sufficient amounts in archaeological and geological records. Secondly, the quartz signal quickly resets during daylight exposure and is therefore more likely to have been thoroughly reset before burial, compared to other luminescence signals (e.g., Murray et al., 2012). Thirdly, the signal remains stable over Quaternary time scales (Murray and Wintle, 2000). Lastly, the quartz signal rarely displays any anomalous signal loss during storage, a phenomenon that is well documented in the light-sensitive signals emitted from feldspar grains (e.g., Wintle, 1973; Auclair et al., 2003; King et al., 2018).

The OSL emission from quartz regularly used for dating is located in the ultraviolet spectrum (e.g. Huntley et al., 1991; Martini and Galli, 2007; Lomax et al., 2015) at around 365 nm. The emission wavelength appears to be independent of stimulation temperature (Lomax et al., 2015); the intensity of the OSL emission and the decay rate, however, are affected by the chosen stimulation temperature (Murray and Wintle, 1998). Early studies of the OSL emission of quartz showed the decay of OSL to consist of three components – fast, medium, and slow (Bailey et al., 1997; Smith and Rhodes, 1994), which originate from three traps with decreasing photoionising cross-sections. Applications of linear modulation OSL (LM-OSL, measurement of the OSL signal with increasing stimulation intensity) have affirmed the existence of up to seven components, including two additional slow components (Singarayer and Bailey, 2003) and an ultrafast component (Jain et al., 2008). For dating applications, samples whose emission is dominated by the fast component are preferable because

of their rapid depletion during light exposure (Li and Li, 2006) and the stability of the component well beyond archaeological and geological time scales of interest (Singarayer and Bailey, 2003). The OSL fast component can be measured using standard measurements and analysing procedures (Wintle and Murray, 2006). The inclusion of contaminating OSL signal components, however, can lead to  $D_e$  underestimation due to thermal instabilities (Li and Li, 2006; Jain et al., 2008; Steffen et al., 2009), or due to sensitivity changes between the measurement cycles (Singarayer et al., 2000). Since LM-OSL measurements are particularly time-consuming, different methods, such as prolonged IR stimulation (Jain et al., 2005) and early signal background subtraction (Cunningham and Wallinga, 2010), have been developed to isolate the fast component from continuous wave (CW) OSL decay curves. However, the major limitation affecting OSL dating of quartz is related to the saturation of the signal at relatively low doses (Wintle and Murray, 2006). Significant efforts have been directed to extend the dating range of quartz. Suggested approaches include thermally-transferred OSL (Wang et al., 2006; Pagonis et al., 2008; Stevens et al., 2009) and violet stimulated luminescence (Ankjærgaard et al., 2013; Colarossi et al., 2018; Ankjærgaard, 2019), and while experimental, both these luminescence signals appear to saturate at higher doses.

The potential of dating the optically sensitive feldspar signal was investigated by Godfrey-Smith et al. (1988), who showed that quartz and feldspar grains bleach up to 1 % of their initial luminescence intensities during exposure to sunlight after 10 seconds and 9 minutes, respectively. The first results of infrared stimulated luminescence (IRSL) from feldspar grains, presented by Hütt et al. (1988), provided ages with a better agreement to the geological interpretation compared to thermoluminescence (TL) dating. Further work on potassium-rich feldspar by Spooner et al. (1990) demonstrated that inexpensive infrared diodes could be used to stimulate sand-sized feldspar grains. The advantages of IRSL dating of feldspar over quartz are: higher saturation levels of the signal, which theoretically enables the dating of older samples (Preusser, 2001); the bright luminescence characteristics compared to quartz, especially quartz from some geographic areas that display low OSL sensitivity; and more reliable dose rate estimations due to the proportionally higher internal dose rate component compared to quartz, generated by the internal potassium content in



alkali feldspar. Despite these advantages, IRSL dating was less utilised as a dating method for Quaternary deposits due to anomalous fading, which causes age underestimation of IRSL ages compared to OSL ages unless fading is corrected. Several methods have been designed to correct for the signal loss over archaeological and geological time scales (Huntley and Lamothe, 2001; Auclair et al., 2003; Huntley and Lian, 2006; Kars et al., 2008), mainly using the measurements of fading during storage over laboratory time scales (g-value Aitken, 1985).

Significant efforts have also been aimed at isolating a non-fading feldspar signal. The most applied approach is to measure the second post-IRSL-IRSL signal (pIRIR) at an elevated temperature following an initial IRSL stimulation. Thomsen et al. (2008) investigated the rates of fading for different feldspar luminescence signals and reported that the pIRIR signal (stimulated at 225 °C) faded at ~60 % lower rates compared to the IRSL signal. Several subsequent studies (e.g. Buylaert et al., 2009; Thiel et al., 2011; Reimann and Tsukamoto, 2012; Klasen et al., 2017) have successfully used pIRIR signals to date numerous settings of different time scales. Various measurement protocols have been employed using different initial IRSL and pIRIR temperatures (Thiel et al., 2011; Kars et al., 2012; Li and Li, 2012a; Reimann and Tsukamoto, 2012, e.g.), along with multiple-elevated temperature (MET-pIRIR) pIRIR protocols (Li and Li, 2012a), where several pIRIR signals are measured in increasing temperature steps. In general, the higher the pIRIR temperature, the lower the observed fading rates (e.g. Thiel et al., 2011). However, these high-temperature pIRIR signals (e.g., 290 °C) also bleach slower (Kars et al., 2014; Smedley et al., 2015) and have larger residual doses (Buylaert et al., 2011); hence, Zhang and Li (2020) propose that high-temperature pIRIR protocols should primarily be used for samples >10 ka. Recently, a non-destructive measurement protocol was proposed by Prasad et al. (2017), termed infrared photoluminescence (IRPL), where electron traps are excited without the electrons returning to recombination centres. IRPL emission is centred at around 885 nm (Kumar et al., 2018) and 955 nm (Prasad et al., 2017). Encouragingly, single-grain IRPL measurements (955 nm) from an aeolian sand sample provided a burial age in unison with pIRIR data (Duller et al., 2020), and the signal is though not to fade (Prasad et al., 2017). Other feldspar dating methods, reported to not suffer from fading, include post-isothermal IRSL (Lamothe et al., 2020)

and infrared-radiofluorescence dating (Wagner et al., 2010).

### 1.3.2 Rock surface luminescence dating

Luminescence dating of rocks predates the introduction of optical dating by Huntley et al. (1985). Burned rocks are typically sensitive to TL stimulation (Wintle, 1980), and TL can hence be used to date the use of cooking stones as Huxtable et al. (1976) showed by dating sandstones collected from mounds of burned stones. TL dating of burned flint artefacts was introduced by Göksu et al. (1974), and the method remains relevant to the field of Palaeolithic archaeology, as was demonstrated by the dating of artefacts from Jebel Irhoud, Morocco by Richter et al. (2017). While the dating of heated rocks (heated flints and cherts in particular) has been practised since the 1970s, investigation of optical dating of rock surfaces started more recently. When using rocks for optical dating, it is essential that the signal sufficiently resets (bleaches) when the surface is exposed to daylight. Further use of TL dating of rocks was suggested by Liritzis (1994) who demonstrated that optical bleaching of carved limestone blocks was sufficient to reset the TL signal at the rock surface during exposure to daylight. Once the surface was shielded, the TL signal re-grew due to ionising radiation, and the measured TL could be used to date the construction of ancient buildings. Also, the TL signal in marble decreased during exposure to light in a solar simulator, especially at the surface (Liritzis and Galloway, 1999). The effect of exposure time on signal resetting was further investigated by Polikreti et al. (2002) who demonstrated that the TL signal in marble could be optically decreased to low levels at depth >10 mm from the exposed marble surface. By measuring TL by depth, Liritzis and Galloway (1999) and Polikreti et al. (2002) created a profile showing the TL signal versus depth into the marble. Such profiles – luminescence signal-depth profiles – can also be measured using optically sensitive luminescence signals in lithologies which contain quartz or feldspar grains.

An important experiment regarding OSL dating of rock surfaces was conducted by Habermann et al. (2000), investigating the bleaching of the IRSL signal in rock surfaces. Their experiment proved that IRSL in a granite surface was partly reset after 2 minutes of exposure in a solar machine, and 20 minutes of exposure fully removed the signal in the outer 0.5 mm of the rock surface. Vafiadou et al. (2007) showed that 14

days of exposure to winter daylight causes a decrease in the luminescence signal nearer the rock surface compared to the centre of the rock. Polikreti et al. (2002) proposed a model describing the relationship between TL intensity at various depths and the duration of exposure of the marble surface. The model used a double exponential equation, including an attenuation factor, to describe the decrease in the trap emptying with depth due to the decrease in photon flux with increasing depth. This model for signal bleaching was expanded on by Sohbati et al. (2011), based on their investigation into exposed rock surfaces from modern beach cobbles. Sohbati et al. (2011) measured the IRSL signal (sensitivity-corrected by the luminescence response to a given test dose:  $L_n/T_n$ ) with depth to investigate the depth of signal resetting in two rock surfaces from granitoid rocks with coarse-grained or metamorphosed structures. Assuming first-order electron de-trapping kinetics: i) electrons are not re-trapped due to e.g. tunnelling; ii) electron trapping due to ionising radiation being negligible in an exposed rock surface; iii) the population density of trapped electrons is initially identical at all depths; and iv) light penetrates into the rock occurs at the same rate throughout the solar wavelength spectrum, Sohbati et al. (2011) proposed that a luminescence signal-depth profile contains information regarding the exposure history of a rock surface including the residual dose before burial. The bleaching rate at the surface is defined by the photoionising cross-section and the local photon flux; this rate is attenuated with increasing depth due to the opaqueness of the rock matrix. The bleaching rate is not directly measurable and will be sample- and location-dependent; hence, it must be determined for each site and lithology. The attenuation of light penetration with depth appears to some degree to correspond to the lithology of the investigated sample. The investigation by Ou et al. (2018) into the attenuation of light in different lithologies exposed for up to 90 days demonstrated significant differences between sandstone and two granites and much lighter-coloured quartzite. Signal bleaching ranged between being barely bleached deeper than the surface slice in a dark greywacke specimen and deep bleaching in a quartzite specimen. The effect of light attenuation was then confirmed experimentally, with light penetrating significantly quicker in the lighter samples, compared to more opaque ones. The lithological influence on luminescence-depth profiles was further studied by Meyer et al. (2018) using X-ray powder diffractometer (XRD) and colour analysis of slices with image

processing. Their results suggest that variations in luminescence-depth profiles are to be expected in heterogeneous lithologies due to the presence of opaque minerals (in their samples: biotites) and, potentially, in apparent homogeneous lithologies, due to the presence of iron hydroxides.

To describe the shape of the luminescence-signal profiles exposed to daylight and to calculate the exposure duration, [Sohbati et al. \(2011\)](#) put forth the model:

$$L(x) = L_0 e^{-t_e \overline{\sigma \varphi_0} e^{-\mu x}} \quad (1.1)$$

where  $L$  is the luminescence signal at depth  $x$  (mm),  $L_0$  is the saturated luminescence signal,  $\sigma$  is the photoionising cross-section ( $\text{cm}^2$ ) and  $\phi$  is the photon flux at the rock surface ( $\text{cm}^{-2} \text{ s}^{-1}$ ) integrated over the solar light spectrum, and  $\mu$  is the attenuation factor ( $\text{mm}^{-1}$ ) assumed to be independent of wavelength. The final variable of the model,  $t_e$ , is the duration of exposure for the rock surface. It is necessary to determine the site-specific  $\overline{\sigma \varphi_0}$  to solve for  $t_e$  when fitting a luminescence-depth profile using eq. 1.1.

The model was validated experimentally by [Glignani et al. \(2019\)](#); quartzite surfaces were illuminated in a solar simulator for five different durations (1.035–1040 ks), a common  $\overline{\sigma \varphi_0}$  and  $\mu$  value for all cores was calculated using eq. 1.1 (since all cores are collected from the same lithology), and finally  $t_e$  was re-calculated from each core by fitting each core using the  $\overline{\sigma \varphi_0}$  and  $\mu$  derived from the initial fitting. The results showed good unity (except for one outlier) between the given and fitted  $t_e$ , indicating that the model can accurately be used to calculate exposure ages in rock surfaces of unknown exposure rates.

To describe luminescence-depth profiles from rock surfaces that have been buried following exposure to daylight, [\(Sohbati et al., 2012a\)](#) added the effect of ionising radiation to the shape of the profile:

$$L(x) = \frac{\overline{\sigma \varphi_0} e^{-\mu x} + e^{-t \left[ \overline{\sigma \varphi_0} e^{-\mu x} + \frac{\dot{D}}{D_0} \right]} + \frac{\dot{D}}{D_0}}{\overline{\sigma \varphi_0} e^{-\mu x} + \frac{\dot{D}}{D_0}} \quad (1.2)$$

where  $D_0$  (Gy) is the sample-specific characteristic dose derived from fitting signal-dose response curves, and  $\dot{D}(x)$  ( $\text{Gy ka}^{-1}$ ) is the depth-dependent dose rate.  $\dot{D}(x)$  is

the sum of all dose components:

$$\dot{D}(x) = \dot{D}_\gamma(x) + \dot{D}_\beta(x) + \dot{D}_\alpha + \text{internal dose} + \text{cosmic dose} \quad (1.3)$$

where  $\dot{D}_\gamma(x)$  and  $\dot{D}_\beta(x)$  are infinite-matrix dose rates,  $b$  is the attenuation factor of the beta dose (exchanged for attenuation of gamma for  $\dot{D}_\gamma(x)$ ), and  $h$  is the thickness of the rock. In practice, Eq. 1.2 considers that during the long exposure time, irradiation will affect the shape of the luminescence-depth profiles, and moreover, the bleaching front (for which the depth is usually defined as the point where the signal = 50 % of the saturated signal levels) cannot reach deeper into the rock when the equilibrium between trapping and de-trapping is reached (Sohbati et al., 2012a).

Further terms can be added to Eq. 1.2 to include additional exposure and burial events (Freiesleben et al., 2015; Sohbati et al., 2015). Also, other equations have been proposed to describe the luminescence-depth profiles including fitting the profiles assuming a log-normal distribution (Laskaris and Liritzis, 2011), and considering electron re-trapping during exposure and recombination density (Freiesleben et al., 2022). A recent development in fitting models is the use of a general-order model to fit profiles that do not follow first-order kinetics (Freiesleben et al., 2023), which is expected for feldspar signals (e.g., Jain et al., 2015).

Calculating the dose rate for rocks is challenging. Part of the challenge is variations in effective gamma and beta radiations, which will vary at different depths into the rock due to any heterogeneity in the radionuclide concentration between the rock and the surrounding matrix. The gamma and beta gradients are commonly scaled (e.g., Sohbati et al., 2012b; Freiesleben et al., 2015; Sohbati et al., 2015) using the principle of superposition (Aitken, 1985, Appendix H). Freiesleben et al. (2015) calculated beta dose gradients (and gamma gradients, using attenuation coefficient calculated for gamma instead of beta) in a granite cobble using the equation:

$$\dot{D}(x)_\beta = \dot{D}_{rock,\beta} [1 - 0.5(e^{-bx} + e^{-b(h-x)})] + \dot{D}_{sediment,\beta} 0.5(e^{-bx} + e^{-b(h-x)}) \quad (1.4)$$

deriving beta attenuation  $b$  ( $\text{mm}^{-1}$ ) from Aitken (1985). A recent investigation of beta and gamma attenuation rates in rocks and sediments (Riedesel and Autzen,

2020) resulted in a higher beta attenuation coefficient compared to Aitken (1985), improving the calculation of dose rates at the rock/sediment interface since the beta emitted from the surrounding sediments will contribute less to the total dose rate in the rock (Riedesel and Autzen, 2020). Eq. 1.4 assumes that the dose rate contribution from both the sediment and the rock at the rock/sediment interface is 50 % of their corresponding infinite matrix dose rates. To verify this, Riedesel and Autzen (2020) investigated the effect of the rock size on the ratio of the dose contribution by simulating the fraction of the infinite matrix dose rate at the rock centre and the rock/sediment interface for different rock sizes. Their results indicate that assuming symmetry might cause the dose rate to overestimate up to  $\sim 50\%$ .

The internal dose rate from the dated mineral grains provides an additional challenge for rock surface luminescence dating: no mineral separation and poorly constrained grain size ranges. The K concentration in alkali feldspars will affect the dose rate as the grain size increases. Hence, assuming high K concentrations such as  $10 \pm 2 \%$  (Smedley et al., 2012) or  $12.5 \pm 0.5 \%$  (Huntley and Baril, 1997) would lead to significant dose rate overestimation if the dated mineral grains actually are feldspar grains with lower K content. Separating alkali feldspars from quartz and plagioclases through the crushing of rock material and subsequent density separation is not possible since information regarding grain size is then lost; any retrieved size fraction would contain artificial grain sizes formed during crushing. Rades et al. (2018) suggested using micro-X-ray fluorescence ( $\mu$ -XRF; see section 1.5.4 for methodological details) on rock slices to determine the K concentration within the feldspars. They subsequently used element maps to determine the size of the feldspar grains by converting identified grains to ellipsoids, excluding aggregates of grains where determining the size of each individual grain was not possible.

The use of rock surface luminescence dating has been investigated in different studies from various archaeological settings. Dating of the construction or destruction of stone structures built from granitoid rocks was proposed by Greulich et al. (2005), using spatially resolved luminescence measured with a charge-coupled device camera (Greulich et al., 2002). The authors targeted quartz and feldspars to date a Medieval stone wall and Peruvian pre-Colombian geoglyphs and presented ages in agreement with historical and archaeological evidence from both settings. Further evidence for

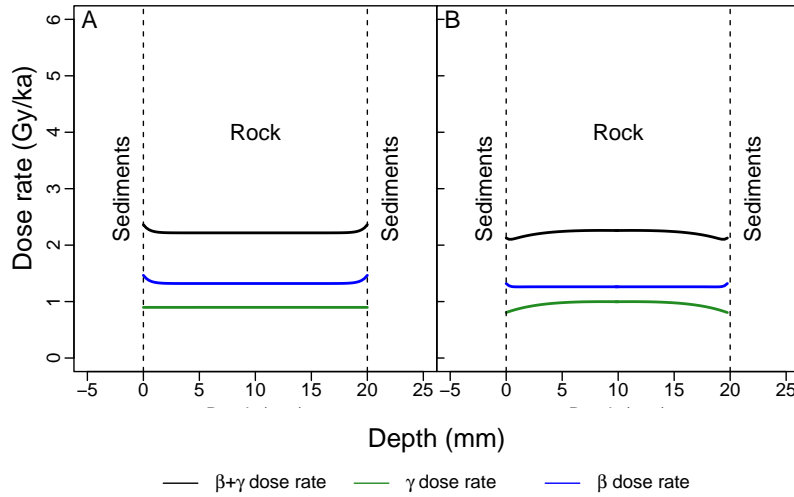


FIGURE 1.1: Calculated depth-dependent dose rate throughout a 20 mm thick rock matrix using the approach of [Freiesleben et al. \(2015\)](#) (A) or by using the tool *calc\_CobbleDoseRate* from the *Luminescence* package ([Kreutzer et al., 2021](#)) in R version 4.1.1 ([Riedesel and Autzen, 2021](#)) (B).

the usefulness of the method was presented by [Vafiadou et al. \(2007\)](#) as two cobbles from neolithic archaeological settings produced OSL ages approximately in agreement with sediment OSL and radiocarbon ages.

One unique application of the method is the dating of rock art. For example, rockfall deposits beneath the Great Gallery rock art panel, USA, contain colour pigments demonstrating that the rockfall occurred after the creation of the rock art. [Chapot et al. \(2012\)](#) determined that the luminescence signal was bleached 3 mm into the sandstone surface before the wall collapsed and the surface was covered at around 1100 AD; thus, providing a minimum age for the rock art. This date was confirmed by sediment luminescence ages and, crucially, by radiocarbon dating of a trapped leaf beneath the rockfall deposits. Rock surface luminescence dating was also used to constrain the maximum age of the rock art by determining the pre-burial exposure duration of the rock surface as part of the rock art panel by calculating the luminescence signal bleaching rate into the rock ([Sohbati et al., 2012c](#)). This bleaching rates were calculated based on resetting at a calibration rock surface with a known exposure age (80 a), collected from a road cut. By applying the model from [Sohbati et al. \(2011\)](#), [Sohbati et al. \(2012c\)](#) concluded that the rock panel had been exposed for 700 years before the burial. Rock surface luminescence dating, combined with

luminescence dating of local alluvial terraces, constrained the origin of the rock art to 1-1100 AD (Pederson et al., 2014). The approach of using surfaces of known exposure ages has since been used by other studies (Freiesleben et al., 2015; Gliganic et al., 2019; Lehmann et al., 2018; Luo et al., 2018; Brill et al., 2021) to calculate the duration of exposure for rock surfaces from different non-archaeological settings. Sohbati et al. (2012a) improved on the model by including electron trapping due to ionising radiation, co-occurring with trap emptying due to exposure, in a paper focusing on the hypothetical application of luminescence dating on other planets than Earth.

The exposure and burial histories of cobbles from archaeological surfaces can be complex, with several exposures and burial events affecting the surfaces. A cobble collected from a stone pavement from a Neolithic cult site in Israel displayed two exposure and burial events from the bottom surface in both IRSL and pIRIR signal-depth profiles (Sohbati et al., 2015). The mean age from surface slices from this cobble was in agreement with sediment grains collected from beneath the cobble ( $\sim 4$  ka) but underestimated the expected ages with 3–4 ka causing Sohbati et al. (2015) to conclude that the last burial might correspond to a later disturbance at the site. Another example was presented by Freiesleben et al. (2015), who reconstructed the history of whetstone by measuring the luminescence signal with depth. Their top surface profile was complex, displaying bleaching by exposure during archaeological excavations for several months, succeeding over a millennium of burial. The signal-depth profile further demonstrated that the burial was preceded by exposure for hundreds of years, likely during the period of use of the whetstone.

Additional archaeological applications of rock surface luminescence dating have been presented on time scales from decades (Gliganic et al., 2019) to the Early Holocene (al Khasawneh et al., 2019b). Megalithic structures have received some attention since the dating of the rock surfaces could directly date the construction of such structures. For example, Galli et al. (2020) dated stones from a ceremonial site in Italy. While the ages between some of the different stones varied considerably ( $\sim 1900$ – $5200$  BC), the retrieved ages were comparable between rock surfaces and corresponding underlying sediments, thus validating the hypothesis that different parts of the site were in use during different periods. Rock surface luminescence dating from megalithic structures in the Middle East also provided dates in agreement with



associated potsherds from a lengthy stone line (al Khasawneh et al., 2019a,  $400 \pm 100$  BC), and surprisingly old ages (Neolithic, rather than Chalcolithic/Bronze Age) from a desert hunting trap (al Khasawneh et al., 2019b).

Another exciting use of luminescence dating of rock surfaces is the direct optical dating of stone artefacts. Gliganic et al. (2021) presented optical ages from six quartzite flakes embedded in surface soil near a quartzite quarry on the Tibetan Plateau. Most flakes provided increasing luminescence ages with rock depth, and the luminescence-depth profile of one flake revealed that the flake had experienced not only one – but two burial events. The oldest age from such an event from the quarry flakes dated the quarry activity to earlier than 5 ka, and the younger burial event occurred  $\sim 2$  ka due to re-use of the flakes, or natural erosion and re-deposition of buried artefacts.

Besides archaeological contexts, rock surface luminescence dating can be used in different geomorphological settings. Luminescence dating of sediments in fluvial and alluvial environments is commonly applied (e.g., Fuchs and Lang, 2001; Lauer et al., 2010), even though insufficient bleaching of the luminescence signals is not uncommon (e.g., Olley et al., 1998; Colarossi et al., 2018). While statistical approaches can be used to deal with partially bleached sediments (e.g., Arnold et al., 2007; Cunningham and Wallinga, 2012; Medialdea et al., 2014), rock surface luminescence dating has been proposed as an alternative chronological tool in fluvial and alluvial settings (Smedley and Skirrow, 2020; Ishii et al., 2022). Sohbaty et al. (2012b) investigated the dating of quartzite cobbles collected from an alluvial layer at a Palaeolithic open-air site in Portugal. Their results showed that the cobbles had experienced a final burial between 14 and 45 ka and that the luminescence signal had been bleached in the centre of two cobbles at  $\sim 45$  ka. This observation demonstrated that cobbles can be sufficiently bleached in alluvial settings and that quartzites are susceptible to deep signal bleaching.

Most studies applying rock surfaces with luminescence dating techniques detected the luminescence emitted from intact slices using a photomultiplier tube (e.g., Sohbaty et al., 2012b; Freiesleben et al., 2015). An alternative technique of spatially resolving the luminescence with an electron-multiplying charge-coupled device (EMCCD) camera has been proposed to target mineral grains in rock slices (Greilich et al., 2002),

or to rapidly measure luminescence-depth profiles of the luminescence signal over different rock depths (Sellwood et al., 2019). Hence, Sellwood et al. (2019) pointed out how this approach of scanning samples (since the signal over the entire rock surface is measured simultaneously) increases the measurement speed considerably, plus it prevents the loss of material occurring during the slicing of rock cores. The approach of scanning rock surfaces for luminescence was further explored by Sellwood et al. (2022a), who developed an EMCDD system capable of spatially resolving the non-destructive infrared photoluminescence (IRPL) signal (e.g. Prasad et al., 2017; Kumar et al., 2018, 2021) or IRSL in larger samples of several centimetres in size. With this novel approach, IRSL and IRPL signal-depth profiles from granite samples showed that bleaching depths into rocks could be assessed without normalisation using a test dose (Sellwood et al., 2022b). Despite the recent progress in rock surface luminescence dating, the method has only been applied in a few archaeological or geoscientific settings, using a limited selection of rock types. So far, only the surface has been scratched when it comes to possible applications considering the diverse settings in nature or in human-made constructions where buried or exposed rock surfaces are present.

Within archaeology, various stone structures have been successfully targeted with burial dating (al Khasawneh et al., 2019a,b; Liritzis et al., 2019; Galli et al., 2020; Thompson et al., 2022), but variations in lithology and bleaching conditions between different environments mean that a good outcome is not guaranteed for other sites. Furthermore, the interpretation of the received ages is not always straightforward. For example, al Khasawneh et al. (2022) calculated significant variations between burial ages from the same rock surfaces, indicating that parts of the rock surface were either exposed more recently than others, or were irradiated at a different rate during burial. Further case studies are required to determine which kind of structures can be reliably dated and what novel chronological information can be extracted using rock surface luminescence dating. An underused application for rock surface luminescence dating is dating of open-air sites by targeting rocks from archaeological layers, which would be useful for settings lacking organic material for radiocarbon dating or heated flints for TL dating, or where insufficient bleaching conditions might make sediment luminescence dating impractical. However, uncertainties in bleaching conditions, difficult

depositional environments, and the effect of post-depositional processes mean that not all sites will be dateable, and further work is needed on sites with good age control.

Furthermore, since a good understanding of the depositional environment is crucial to interpret archaeological sites, projects studying Palaeolithic archaeology tend to involve geoscientific data, including geochronology. In theory, rock surface luminescence dating opens up new applications of dating within depositional environments important to ancient humans, such as cave and rock shelter sites, or various geomorphological features useful for understanding palaeoenvironments or climate development such as terraces landforms (Ishii et al., 2022) or beach ridges (Simms et al., 2011; Souza et al., 2019). However, similar to direct dating of archaeological sites, the interpretation of burial ages might not always be clear-cut in such (at least periodically) geomorphologically active settings. Considering that rock surfaces in erosive environments can be re-exposed and weathered and that different surfaces might yield different ages due to different exposure histories, the dating processes must include an analysis of potential processes inferred by the geomorphological situation when the ages are interpreted. These processes are likely varied from those encountered during dating of sediments with luminescence, such as the input of older grains into the dose population (e.g., Jacobs et al., 2011) or incomplete bleaching before burial (e.g., Thomsen et al., 2007), since the grains that form the rock matrix will not be as easily reorganised or lost.

An additional limitation when using rock surface luminescence dating in archaeological settings is a lack of suitable lithologies. While granites have consistently been shown to produce more rapid bleaching compared to sedimentary rocks (Ou et al., 2018; Liu et al., 2019) and to yield burial and exposure ages (Freiesleben et al., 2015; Lehmann et al., 2018; Thompson et al., 2022), nearby granitic outcrops are not always prevalent in areas of importance for archaeological research such as the Iberian Peninsula. It is, therefore, crucial to continue to investigate rock surface luminescence dating at sites with various lithologies to investigate if different rocks are bleached before burial, to determine if the luminescence characteristics make the rocks suitable for dating, and to resolve the dosimetric challenge of dating polymineral samples containing various feldspars. This thesis aims at addressing some of the knowledge gaps and underutilised applications mentioned above.

## 1.4 Hypotheses and objectives of this thesis

Since the focus of subproject F2 in the CRC 806 is the development of luminescence techniques, this thesis aims to constrain necessary factors for the successful dating of archaeological and geoarchaeological settings by dating rock surfaces with luminescence. As such, it contributes to several open questions in the rather new rock surface dating technique in the framework of several case studies from different geographical areas (see section 1.6).

**Hypothesis 1 – Rock surface luminescence dating techniques can be used to date the geoarchaeological development of archaeological open-air sites**

*Objective: Compare rock surface luminescence ages with open-air sites of known archaeological age and usage.*

It is often challenging to date the direct presence of human activity at archaeological open-air sites. One dating approach is applying TL to heated flint tools (e.g., Richter et al., 2007; Frouin et al., 2014); thus, providing direct chronological data regarding firing events. Another approach is to date the past use of fire with radiocarbon on charcoal fragments. However, charcoal or heated flint tools might not be present at the site or have been reworked and, therefore, lost the direct chronological relationship with the site. Considering this, the age of such sites is often constrained by typological comparisons (e.g., Bradley et al., 1995), or by combining geoarchaeological with radiocarbon of bones or plants or luminescence dating methods to constrain the archaeological data by understanding and dating the geomorphological development of the site (e.g., Fuchs and Owen, 2008; Henselowsky et al., 2023). However, methodological constraints still apply (too old for radiocarbon dating, partial resetting of luminescence signal, heterogeneity in the radiation field etc.) demonstrating that alternative approaches would be desirable. Considering that rocks are frequently found within deposits at open-air sites, using rocks from within or around open-air sites could be a useful chronological method. Importantly, information regarding the previous exposure of the rock surfaces can be preserved in

the luminescence-depth profiles, and the issue of residual signals would be reduced. Also, in some cases, previous exposure and burial events might remain visible in the profiles, indicating that the rocks have been reworked before being deposited at the site. Finally, it might also be possible to identify heated rocks (Pop et al., 2021) using rock surface luminescence, which directly dates human use of fire at the site. To further investigate the potential of rock surface luminescence dating from open-air sites, rocks spread out from archaeological layers in a chronologically well-constrained open-air site Val di Sole, Italy are dated.

*Objective: Investigate if rock surface luminescence dating can be used to chronologically constrain open-air sites in highly dynamic geomorphological environments.*

Archaeological open-air sites are frequently situated in highly dynamic sedimentary environments such as fluvial environments (Greenbaum et al., 2014; Terradillos-Bernal et al., 2017; Eixea et al., 2022), or shorelines (Broadbent and Bergqvist, 1986; Bulut et al., 2022). Such environments tend consist to a large extent of gravel deposits since finer grain size fractions tend to be washed away in these high-energy environment. Therefore, while sediment dating with luminescence of open-air sites within these environments can be difficult, rock surface dating of the coarser gravel could be an intriguing option. This objective is realised by investigating the dating of various geomorphological settings: an alluvial terrace in southeastern Spain, desert pavements in Egypt, and raised beaches in Chile.

#### **Hypothesis 2 – Rock surface luminescence dating can provide novel geochronological data from stone structures**

*Objective: Investigating rock surface luminescence dating of human-made stone structures.*

The dating of rock structures is generally challenging. Methods like terrestrial cosmogenic nuclide (TCN) dating and lichenometry can be applied to date the exposure period of stone structures, but there are many methodological considerations such as inheritance (TNC) or to reliably constrain the local growth rate of lichens.

Radiocarbon (e.g., Hajdas et al., 2021) or luminescence (e.g., Kemp et al., 2022) dating of mortar or material accidentally lodged between the rocks have also been used to constrain the time of construction of stone structures; however, such materials are not always available in dry-stone walls, and again, methodological limitations affects the interpretation of the age estimates. Rock surface luminescence dating has previously been applied to various human-made stone structures (e.g., Greulich et al., 2005; al Khasawneh et al., 2019a,b; Liritzis et al., 2019), demonstrating the value of the method within certain archaeological settings. These studies, however, targeted intact walls with the sole target of dating the time of construction. While valuable, many structures have collapsed since construction (e.g., Papanastassiou et al., 2005; Heising et al., 2020), or have been rebuilt during various phases (e.g., Mökkönen et al., 2007). This thesis aims at further investigating the potential of rock surface luminescence dating of stone structures, to date the construction, and potential collapse or rebuilding events, by targeting of intact and collapsed walls. Here, dry-stone structures from Val di Sole (Chapter 3), which have been extensively studied since 2010 (e.g., Carrer and Angelucci, 2013), provide a case study that can serve as a base for future research.

### **Hypothesis 3 – Successful application of rock surface luminescence dating as a geochronological tool is strongly correlated to the lithology of the dated material**

*Objective: Investigate the luminescence signal resetting in clasts of various lithologies.* Good resetting of the latent, optically sensitive signal is a prerequisite for reliable optical dating of any natural or archaeological archive. The pioneering study by Habermann et al. (2000) showed that in laboratory settings, the optical signal could be bleached to 2 millimetres of depth in granites in a matter of minutes. More recently, Ou et al. (2018) investigated the resetting in freshly exposed surfaces, showing severe variation between different lithologies. Also, high erosion rates, partly dependent on lithology, have been identified to affect the depth of the bleaching profiles (Sohbati et al., 2018; Lehmann et al., 2019a,b; Smedley et al., 2021). While

bleaching experiments in controlled settings are invaluable for understanding the signal resetting process in rock surfaces, only natural samples contain chronological information valuable in archaeological or geomorphological settings. The objective here is to understand further if lithology is a critical consideration for sample selection. Samples originate from all sites described in section 1.6.

*Objective: Examine luminescence properties of various lithologies.*

The sensitivity of the luminescence signal to optical stimulation varies significantly between different samples. For quartz, the sensitivity is often related to the geological history of the stimulated grains (e.g., Choi et al., 2006; Capaldi et al., 2022), and it has been reported that even in bright quartz samples, only 10–30 % of the grains provide a strong emission (Jacobs et al., 2003; Duller, 2006). For feldspars, grains from the same compositional phase can display variously strong responses to infrared stimulation (Fitzgerald et al., 2022). Since the luminescence sensitivity in certain rocks is not always sufficiently bright to be used for dating, further investigations are necessary to decipher which lithologies are suitable for rock surface luminescence dating. Thus, this thesis aims to investigate luminescence properties from lithologies from archaeologically important settings. Furthermore, signal characteristics from various lithologies from raised beaches in Chile are investigated.

## 1.5 Research design and methodology

### 1.5.1 Fieldwork

Fieldwork, from which the results complete this thesis, was conducted at three different sites (see Chapter 1.6) between 2017 and 2019. An initial field campaign in Val di Sole, Italy, took place in July, 2018, during which cobbles were collected from the walls of two exposed dry-stone enclosures and one buried hut, and from archaeological layers inside a buried enclosure. In-situ gamma radiation was measured, and soil samples were collected to analyse radionuclide concentrations. Fresh rock surfaces were also exposed by removing several centimetres of rock with a hammer and chisel. These surfaces were subsequently sampled during a second field campaign in 2019.

Two field campaigns were conducted in the Mula basin, Spain, in 2018 and 2019. The first campaign aimed to explore potential sampling localities. Eventually, cobbles, in-situ gamma measurements, and sediment samples were collected from four alluvial terraces. The second campaign targeted two of these terraces to collect additional samples.

Wadi Sodmein was visited twice: sampling took place in autumn 2017 and spring 2018. Cobbles were sampled from the top of the desert pavement and the wadi gravel.

### 1.5.2 Luminescence dating

#### 1.5.2.1 Equivalent dose and dose rate

Luminescence burial ages are calculated using the following equation:

$$age = \frac{absorbed\ dose}{dose\ rate} \quad (1.5)$$

Therefore, the amount of absorbed dose in gray (Gy; J kg<sup>-1</sup>) and the dose rate must be constrained before burial ages can be determined.

The amount of absorbed dose cannot be measured directly. However, the absorbed dose in buried mineral grains is proportional to the intensity of the natural luminescence emission ( $L_n$ ); this proportionality is also sample-dependent. Hence, the equivalent dose ( $D_e$ ) that produces an emission equal to  $L_n$  is assumed to represent the dose absorbed since the last burial.



TABLE 1.1: Two adaptations of SAR protocols for measuring quartz using OSL (Murray and Wintle, 2003) and feldspar using pIRIR<sub>225</sub> (Buylaert et al., 2009).

Step	Murray and Wintle (2003)		Buylaert et al. (2009)	
	Treatment	Observation	Treatment	Observation
1	Irradiation <sup>a</sup>		Irradiation <sup>a</sup>	
2	Preheat for 10 s at 160–300 °C		Preheat for 60 s at 250 °C	
3	OSL for 40 s at 125 °C	L <sub>x</sub> OSL	IRSL for 100 s at 50 °C	L <sub>x</sub> IRSL
4			IRSL for 100 s at 225 °C	L <sub>x</sub> pIRIR
5	Irradiation (fixed test dose)		Irradiation (fixed test dose)	
6	Cutheat to 160 °C			
7	OSL for 40 s at 125 °C	T <sub>x</sub> OSL	IRSL for 100 s at 50 °C	T <sub>x</sub> IRSL
8			IRSL for 100 s at 225 °C	T <sub>x</sub> pIRIR
9	OSL for 40 s at >preheat		IRSL for 40 s at 290 °C	
10	Return to step 1 for next SAR cycle		Return to step 1 for next SAR cycle	

<sup>a</sup>This step is not implemented in the first cycle when measuring L<sub>n</sub>

Several protocols have been designed to measure D<sub>e</sub>; various adaptations of the single aliquot regenerative (SAR) protocol (Murray and Wintle, 2000, 2003) have routinely been used as the standard approach to measure D<sub>e</sub> (e.g., Stokes et al., 2003; Murray et al., 2007; Thiel et al., 2011; Klasen et al., 2017; Fuchs and Lomax, 2019), including in this thesis. Table 1.1 demonstrates the SAR protocols used by Murray and Wintle (2003) for OSL, and by Buylaert et al. (2009) for pIRIR measurements. The specific SAR protocols used for the samples reported on in this thesis are described in the relevant chapters.

Both natural and regenerative luminescence (L<sub>x</sub>) after irradiation from the same aliquot is measured with the SAR protocol; these are normalised for by the net luminescence emitted after irradiation of a fixed test dose (T<sub>x</sub>; T<sub>n</sub> when sensitivity-correcting L<sub>n</sub>) to correct for any sensitivity changes (Stokes, 1994) arising during cycles of dosing and stimulation (Murray and Roberts, 1998; Murray and Wintle, 2000). The L<sub>x</sub>/T<sub>x</sub> ratios from the regenerative dose points are plotted (including a regenerative point for zero dose), the growth of the dose is fitted as a luminescence-dose response curve (Figure 1.2), and dose equivalent of L<sub>n</sub>/T<sub>n</sub> can be deduced.

All luminescence measurements were conducted using Risø TL/OSL-DA-20 readers in the Cologne Luminescence Laboratory (Bøtter-Jensen et al., 2010). The readers were equipped with blue/UV sensitive photo-multiplier tubes and <sup>90</sup>Sr/<sup>90</sup>Y beta sources. The light emitted from the blue or infrared stimulation sources was filtered through a 7.5 mm thick Hoya U340 (340 nm; OSL) or an interference filter (410 nm; IRSL/pIRIR).

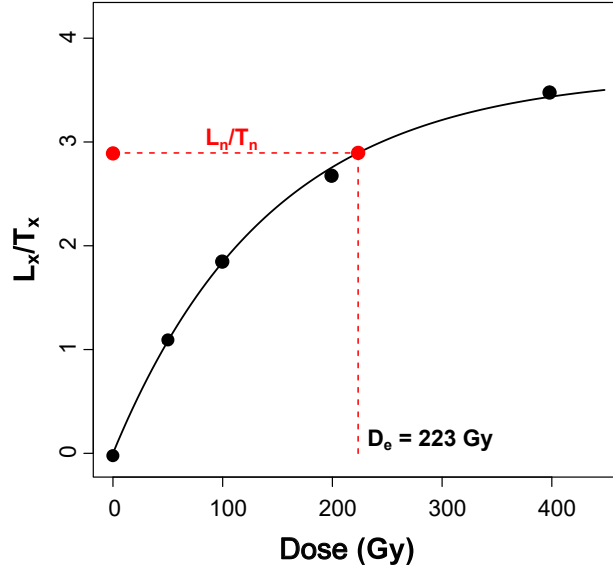


FIGURE 1.2: Plotting of an exponentially fitted dose response curve used to determine  $D_e$  (in this example: 223 Gy) in one aliquot. Uncertainties in  $D_e$  estimation of each subsample arises from ratio between the brightness of the integrated signal and the background signal, the error of the fitting, and instrumental errors (Galbraith and Roberts, 2012).

The dose rate ( $\dot{D}$ ) from Eq. 1.5 constitutes three components: external dose rate ( $\dot{D}_{external}$ ), internal dose rate  $\dot{D}_{internal}$ , and cosmic dose rate ( $\dot{D}_{cosmic}$ ) giving:

$$\dot{D} = \dot{D}_{external} + \dot{D}_{internal} + \dot{D}_{cosmic}. \quad (1.6)$$

$\dot{D}_{external}$  is the sum of gamma, beta, and alpha radiation arising from surrounding radionuclides, mainly:  $^{40}\text{K}$ , U, and Th. Any moisture attenuates the dosing from all surrounding radionuclides in the pores of surrounding sediments. Also, the restricted range of beta and, in particular, alpha particles causes significant attenuation in dose rate as the grain size increases.  $\dot{D}_{internal}$  arises from radionuclides from inside the mineral grains; the presence of  $^{40}\text{K}$  in alkali feldspars (Huntley and Baril, 1997; Smedley et al., 2012), for example, induces a significant contribution to the total dose rate as the grain size increases (e.g. Guérin et al., 2012).  $\dot{D}_{cosmic}$  is related to the burial depth of the grains and the altitude and latitude of the sampled site.

The environmental radionuclide concentrations reported in this thesis (including in rocks) were measured using high-resolution gamma spectrometry (Murray et al., 1987). All cosmogenic dose rates were modelled using the approach of Prescott and Hutton (1994). Internal radionuclide concentrations are discussed in sections 1.5.2.2

and 1.5.2.3. Specific methodological descriptions and considerations for luminescence dating of rock surfaces are presented in section 1.5.2.2) and for unconsolidated sediment samples in section 1.5.2.3.

### 1.5.2.2 Rock surface luminescence dating

It is crucial for rock surface luminescence dating to know from what depth the measured luminescence signal originates. The laboratory work on the collected rock samples was primarily conducted in red-light conditions not to disturb the luminescence signal. Cores (10 mm diameter) were extracted from the rocks using benchtop drill pressers equipped with diamond-tipped corers. The cores were sliced into  $\sim 0.7$  mm thin slices to facilitate this, using a diamond-tipped wafer blade. Cooling was applied to prevent heat build-up during coring (cold water) and slicing (cooling lubricant). The slices were washed in acetone to remove eventual cooling lubricant, debris, and loose grains. For the measurements: whole slices were positioned directly in the sample carousel with a minimum of one empty sample slot between each slice. The rock chips were placed inside a stainless steel cup for any broken slices. Some calcarenite slices were dissolved using hydrochloric acid (10 % concentration) for 24 h before; these extracted grains were mounted with silicon as 2 mm aliquots on stainless steel discs. The applied measurement protocols include pIRIR, IRSL, and pIR-OSL. The chosen protocol varied between different sites and samples; each protocol is described in detail in the respective chapters.

The degree of bleaching during exposure of the surface to daylight was investigated by measuring the luminescence intensity (commonly sensitivity-corrected by the luminescence response to a test dose) with depth into the rock. A straightforward approach to identifying well-bleached samples is to visually compare the signal intensity (representing the accumulated dose during burial) measured at the surface with the intensity measured deeper into the rock. A well-bleached sample is identified through the presence of a non-saturated (luminescence) signal plateau reaching from the surface, deeper into the rock (Fig. 1.3). However, since the intensity of the luminescence signal is dose-dependent, a flat luminescence plateau would only form if the dose rate remains constant with increasing rock depth. However, dose rate variations throughout the rock can cause variations in the appearance of luminescence plateaus

that are not related to bleaching. Modelling luminescence-depth profiles by fitting the measured luminescence-depth data is an alternative to visual inspection (e.g., [Sohbati et al., 2012b](#); [Freiesleben et al., 2015](#); [Sohbati et al., 2015](#)).

All fitting of signal depth profiles was achieved with the *R* programming language ([R Core Team, 2021](#)) by non-linear least square (NLS) regression analysis using the *nls()* package. NLS uses an iterative approach to predict best-fit parameters for a non-linear curve by minimising the residual  $\epsilon_i$  for each data point  $x_i, y_i$ . Exposed rock surfaces were fitted using Eq. 1.1 (Fig. 1.4) as suggested by [Sohbati et al. \(2012b\)](#), while buried surfaces were fitted using the equation:

$$L(x) = \underbrace{\left( \frac{\overbrace{L_0 e^{-t_e \overline{\sigma \varphi_0} - \mu x}}^{\text{Exposure event}}}{-1} \right)}_{\text{Burial event}} e^{D(x) \frac{t_b}{D_0}} + 1 \quad (1.7)$$

presented by [Freiesleben et al. \(2015\)](#) and [Sohbati et al. \(2015\)](#), which allows for calculating the burial time  $t_b$  (ka) using depth-dependent dose rates  $D(x)$ . Eq. 1.7 models the luminescence-depth profile for one exposure event and a subsequent burial event, but additional exposure and burial events (Fig. 1.5) can be modelled ([Freiesleben et al., 2015](#); [Sohbati et al., 2015](#)) following the models presented in table 1.2. The [Freiesleben et al. \(2015\)](#) model provides an alternative way (to  $D_e$  measurements) to calculate burial ages, by solving for  $t_b$  using a fitted luminescence-depth profile. Some studies (e.g. [Freiesleben et al., 2015](#)) have reported good agreement between fitted ages and  $D_e$  ages, but [al Khasawneh et al. \(2019b\)](#) have pointed out that  $D_e$  ages are more reliable since  $D_e$  measurements uses individual  $D_0$  values derived from SAR measurements of each aliquot, compared to a mean  $D_0$  used for fitting.

The effective beta and gamma dose rates in the cobbles in Chapters 2 and 6 were calculated using the approach suggested by [Freiesleben et al. \(2015\)](#) (Eq: 1.4), based on superposition ([Aitken, 1985](#)). The beta and gamma dose rates in Chapters 3 and 4 were calculated using the R function *calc\_CobbleDoseRate* (available with the *Luminescence* package), developed by [Riedesel and Autzen \(2021\)](#), based on the work by [Riedesel and Autzen \(2020\)](#). To estimate the contribution from the internal dose rate from the alkali feldspars, a similar approach presented by [Rades et al. \(2018\)](#) was used in Chapter 2: measuring the potassium content using  $\mu$ -XRF, combined

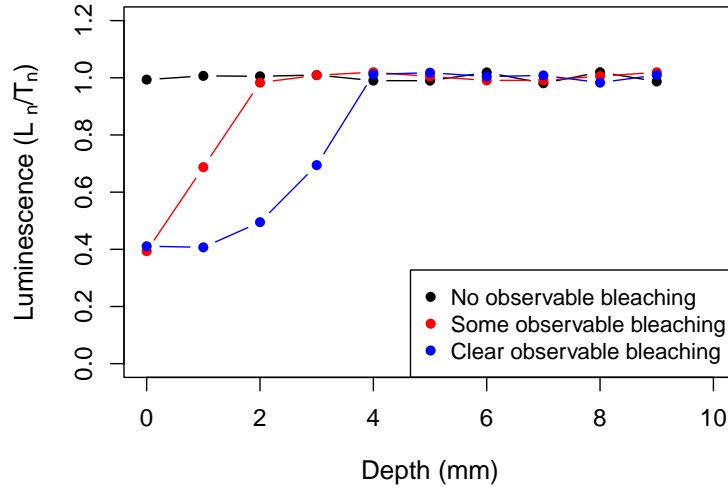


FIGURE 1.3: Hypothetical luminescence-depth profiles: no bleaching before burial, the dose is saturated from the surface to the centre of the rock (A); lower signal at the surface compared to deeper into the rock, but no signal plateau is visible, it in this scenario unknown if the signal was fully bleached before burial (B); a signal plateau reaching 3 mm before increasing to saturation at the centre of the rock (C).

Signal saturation is defined as  $L_n/T_n = 1$ .

TABLE 1.2: The model for multiple exposure and burial events developed by Freiesleben et al. (2015).

Event	Fitting model
Initial burial	$L_0(x) = 1$
First exposure E1	$L_1(x) = L_0(x)e^{-t_{e1}\sigma\varphi_0}e^{-\mu x}$
First burial B1	$L_2(x) = (L_1(x) - 1)e^{-F(x)t_{b1}} + 1$
Second exposure E2	$L_3(x) = L_2(x)e^{-t_{e2}\sigma\varphi_0}e^{-\mu x}$

with optical investigation in a petrographic thin section to estimate the grain size. An average of the results from Chapter 2 was assumed to represent the potassium content in the samples presented in Chapter 3 since they originate from the same geological unit. The feldspar grain sizes in the samples in Chapters 4 and 6 were estimated by petrographic analysis and the potassium content was assumed to be  $10 \pm 2$  % (Smedley et al., 2012).

### 1.5.2.3 Sediment dating with luminescence

The sediment sample in Chapter 4 was prepared for dating using routine laboratory preparations (e.g., Lang et al., 1996): extraction of the 100–200  $\mu\text{m}$  grain fraction through sieving; chemical treatment with 10 % HCl to remove carbonates, 10 %  $\text{H}_2\text{O}_2$  to remove organic matter. Alkali feldspar and quartz fractions were separated from the sediment by density separation using sodium polytungstate. The quartz fraction

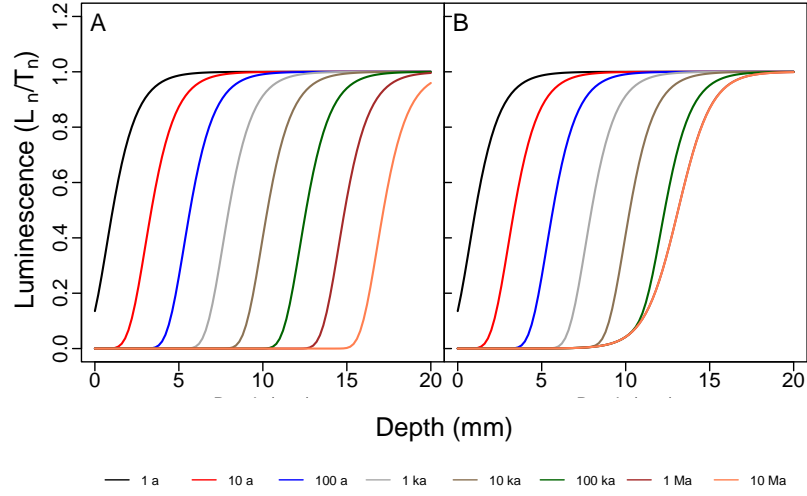


FIGURE 1.4: Modeled luminescence-depth profiles ( $\overline{\sigma\varphi_0} = 2 \text{ a}^{-1}$ ;  $\mu = 1 \text{ mm}^{-1}$ ;  $L_0 = 1$ ) for a range of exposure durations (1 a–10 Ma) using eq. 1.1 (A) and eq. 1.2 (B), demonstrating the difference in shape that arises when  $\dot{D}$  (2 Gy ka<sup>-1</sup>; assumed to be constant throughout the rock for simplicity) and  $D_0$  (500 Gy) are included (A), compared to when no trapping is assumed to occur (B). For these specific (and arbitrarily chosen) parameters, the exposed signal-depth profiles have reached equilibrium by  $t_e = 1 \text{ Ma}$  when  $\frac{\dot{D}}{D_0}$  is included.

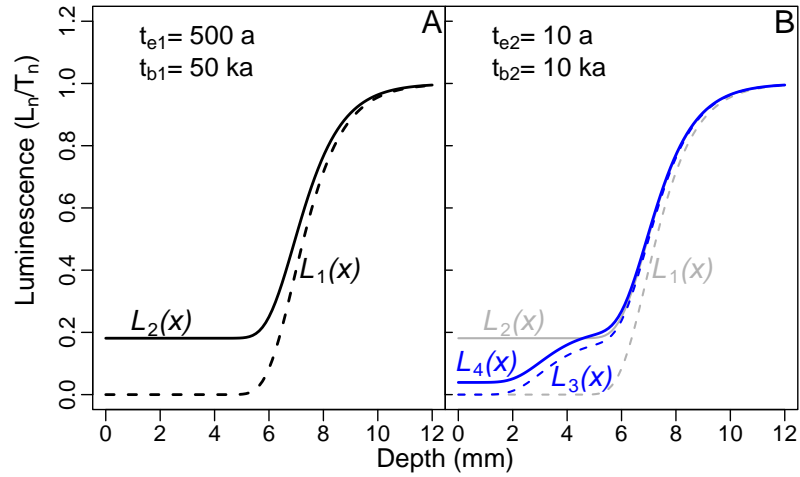
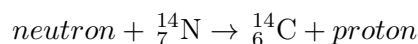


FIGURE 1.5: Complex patterns of luminescence-depth profiles, modelled using the equations from table 1.2. These profiles show series of exposure and burial events, which can be quantified using the model developed by [Freiesleben et al. \(2015\)](#). Here, the parameters:  $L_0$ ,  $\overline{\sigma\varphi_0}$ ,  $\dot{D}$ , and  $D_0$  are the same as those used for the profiles in Fig. 1.4. The modelling in plot A shows that the rock surface was first exposed ( $L_1(x)$ ) for 500 years ( $t_{e1}$ ), followed by burial ( $L_2(x)$ ) at 50 ka ( $t_{b1}$ ). Plot B displays subsequent exposure  $L_3(x)$  and burial events  $L_4(x)$ , where the rock surface is exposed for 10 years ( $t_{e2}$ ) following  $L_2(x)$ , before the final burial occurring at 10 ka ( $t_{b2}$ ).

was etched to remove the alpha irradiated rim of the grains. Dose rates and ages were calculated with the DRAC calculator (Durcan et al., 2015).

### 1.5.3 Radiocarbon dating

Radiocarbon dating (also known as  $^{14}\text{C}$  dating) is a well-established dating method (e.g., Libby, 1961; Ramsey, 2008; Hajdas et al., 2021), used to date organic material younger than 50–55 ka. Radiocarbon ( $^{14}\text{C}$ ) is a radioactive carbon isotope that forms in the upper layers of the atmosphere when neutrons, originating from cosmic rays, are absorbed by  $^{14}\text{N}$  according to:



where the rate of  $^{14}\text{C}$  production varies due to variations in the Earth’s magnetic field and the influx of cosmic rays. Radiocarbon decays (half-life:  $5,730 \pm 40$  years) back to  $^{14}\text{N}$  by emitting an electron ( $\beta$ -decay). The uptake of any  $^{14}\text{C}$  available in the carbon cycle by an organism ends after its death; therefore, the  $^{14}\text{C}/^{14}\text{N}$  ratio measured in the remains dates the death of the organism.

Radiocarbon dating was utilised in this thesis as independent age control in Chapter 2. Charcoal samples from soil layers containing archaeological material were submitted for Accelerator Mass Spectrometry (AMS) dating at the CologneAMS facilities at the University of Cologne under the supervision of Prof. Janet Rethemeyer, following the procedure presented in Rethemeyer et al. (2019). The IntCal20 calibration curve (Reimer et al., 2020) was used to correct for fluctuations in atmospheric  $^{14}\text{C}$  concentrations.

### 1.5.4 $\mu$ -X-ray fluorescence analysis

X-ray fluorescence (XRF) analysis is an analytical method to measure the chemical composition of various materials (Oyedotun, 2018). The method is based on the emission of fluorescent X-rays of element-specific energies occurring when an element is irradiated with high-energy X-rays. The element-specific emission is produced by the transfer of an electron from an outer electron shell to an inner shell following the expulsion of an electron by X-ray radiation. Since the energy state of the inner shells is

lower, the excess energy is emitted as X-ray radiation. The energy level is determined by the energy difference between the different electron shells, which is unique for each element. Consequently, by detecting at which energy levels the emission of a sample occurs, then relative element concentrations can be identified. XRF techniques are commonly applied within geoscientific and archaeological disciplines; for example, measuring elements as climate proxies in sediment cores (e.g., Foerster et al., 2022), determining the chemical composition of human-made objects (e.g., Liritzis et al., 2010), or using hand-held instruments to collect chemical data in the field (e.g., Steiner et al., 2017).

In this thesis, XRF analysis was used to investigate the element concentrations of feldspar grain in dated rock samples; specifically, the elements of interest were the main elements of feldspars: K, Si, Fe, Al, Na, and Ca. Since bulk measurements of the samples would not isolate the feldspar grains, micro-XRF ( $\mu$ -XRF) was used to spatially determine the distribution of the elements within the rocks at a high resolution. This was possible since developments in XRF technology has lead to the introduction of benchtop XRF units that provide high spot resolution ( $<100\ \mu\text{m}$ ), which enables measurements on intact rock samples at the  $\mu\text{m}$  scale using spot measurements (Flude et al., 2017). Hence, it is possible to spatially map the distribution of elements on the rock slices ( $<10\ \text{mm}$  in diameter) commonly used for rock surface luminescence dating. The  $\mu$ -XRF measurements in this thesis were measured using a Bruker M4 Tornado at the Technical University of Denmark in collaboration with Dr. Eike F. Rades.

### 1.5.5 Thesis outline

This thesis comprises of an introductory Chapter 1 followed by two sections: i) rock surface luminescence dating of archaeological settings (Chapters 2 and 3) and ii) investigations of luminescence signal characteristics, signal resetting, and methodological considerations from geochronologically challenging settings (Chapters 4, 5, and 6). This thesis was written with the general aim of developing rock surface luminescence dating as a geochronological tool in archaeological contexts. Chapter 2 focuses on the dating of gneissic cobbles from archaeological units excavated inside a livestock enclosure in Val di Sole, Italy. The resetting of the luminescence signal



is discussed, including the apparent resetting by heat observed in one cobble. The reported ages, combined with additional radiocarbon dates, provide novel chronological information regarding human activities at >2000 meters of elevation in Val di Sole. The results from Chapter 2 demonstrate that rock surface luminescence dating is a useable tool to date archaeological units, even in upland settings dominated by hillslope and periglacial processes. The chapter contributes to the development of rock surface luminescence dating by: i) proving that scattered cobbles from within archaeological structures can provide valuable chronological information regarding the geoarchaeological development of open-air sites, including information of occupational phases; ii) demonstrating that gneissic rocks can be useable for luminescence dating and that the orientation of the foliation of dark mica minerals does not affect the bleaching rate of IRSL signal; and iii) thorough resetting of the luminescence signal due to heating can be observed in samples from archaeological sites, even if they are not collected directly from hearths. This study is published in *Quaternary Geochronology* (Ageby et al., 2021).

Chapter 3 investigates direct exposure and burial dating of dry-stone structures from Val di Sole, Italy. Enclosures and huts with dry-stone walls were used during seasonal pastoral activities from the Middle Ages until the 20<sup>th</sup> century. The time of construction of such structures is challenging to date. Hence, developing a robust optical dating technique for such structures is hugely beneficial for future archaeological studies. The outcome of this study provides insights into past pastoral land use in Val di Sole and the post-glacial environmental development of the surrounding landscape. Also, Chapter 3 contributes to the development of rock surface luminescence dating by: i) different phases of construction and degradation can be dated with luminescence dating; ii) gneissic rocks can be used to date dry-stone structures despite relatively slow bleaching rate; and iii) demonstrating that exposure dating of dry-stone structures in high-erosive environments appears unrealistic. These results are published in *Archaeological Sciences* (Ageby et al., 2022).

Chapter 4 describes investigations of rock surface luminescence dating in an alluvial environment. Carbonate-rich cobbles were sampled from an alluvial terrace

in the Mula basin, Spain. The results were compared with new and previously published (Burow et al., 2015) optical ages. The results highlight: i) the need to carefully select lithologies during sampling, ii) display the short luminescence-depth profiles observed in a fluvial system, and iii) discuss dose rate calculations in environments with low radionuclide concentrations. These results are published in *Radiation Measurements* (Ageby et al., 2023).

Chapter 5 deals with clasts sampled from wadi terraces in the Eastern Desert, Egypt. A palimpsest of archaeological artefacts (Late Stone Age to Roman) superimposes the desert pavement covering these terraces. The desert pavement consists partly of vein quartz and granitoid clasts; these lithologies were sampled to investigate the applicability of exposure and burial dating of desert pavements. The results highlight that: i) vein quartz luminescence characteristics are significantly less suitable for dating compared to e.g., feldspars in granites, and the rapid signal resetting in such a translucent lithology makes vein quartz poor for exposure dating or for dating burial for the covered bottom surface; and ii) dating desert pavement formation with rock surface luminescence appears possible but would require knowledge regarding pavement formation processes to interpret the chronological data.

Chapter 6 covers a study from the Atacama Desert, Chile, which focused on the signal characteristics and resetting in cobbles of diverse lithologies from active and relict, Pleistocene shorelines. The study discusses the luminescence sensitivity in rocks, luminescence-depth profiles in exposed and buried cobbles, and age underestimation compared to independent age control. The results presented in this chapter are significant for rock surface dating in general and when targeting shorelines. Chapter 6 contributes to the development of rock surface luminescence dating by: i) the luminescence signal is bleaching in modern beach cobbles, and frequent flipping of the cobble will result in low dose at both the exposed and covered rock surface; ii) demonstrating that high residual doses can affect exposed rock surfaces and must be considered when dating Holocene samples; and, iii) showing how high dose rates, dim luminescence signals, and low signal saturation levels remain, just as with many sediment deposits, problematic when trying to date old samples, and lithological

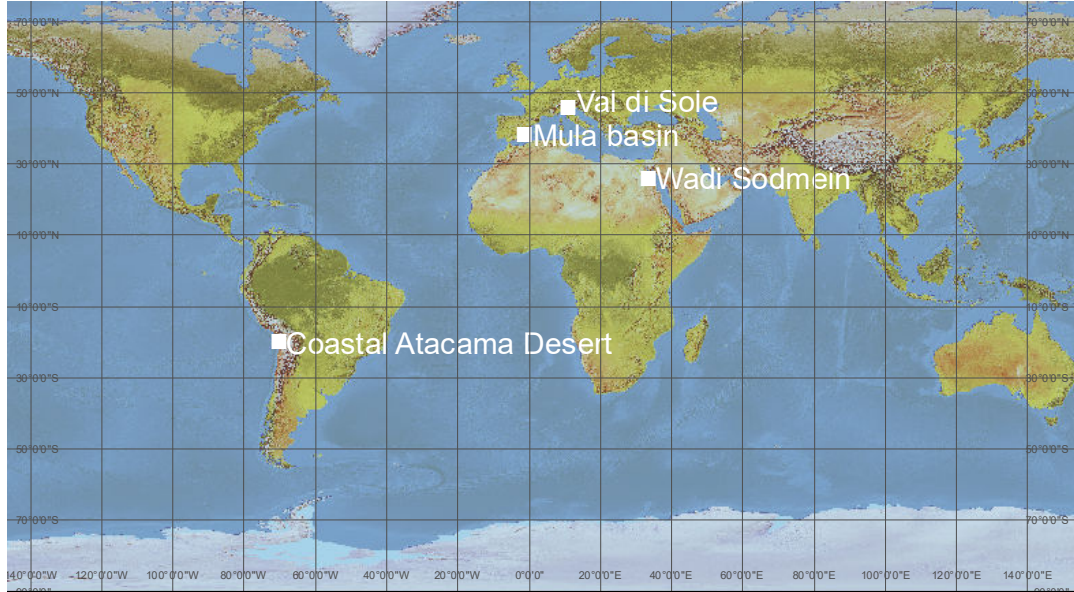


FIGURE 1.6: Overview map of study sites. Base map was made with Natural Earth.

observations are crucial during sample selection. These results are published in *Marine Geology* (Brill et al., 2022).

Chapter 7 discusses the results with regards to the working hypotheses listed in Chapter 1, and Chapter 8 concludes this thesis and provides an outlook for future work on rock surface luminescence dating.

## 1.6 Overview of the study areas

Here follows a presentation of the four study sites (Fig. 1.6) where rock surface luminescence dating was attempted.

### 1.6.1 The upland pastures of Val di Sole, Italy – Chapters 2 & 3

The Alpine Valley of Val di Sole is located in the Italian Alps in Trentino. The valley, which direction runs east to west, forms part of the Periadriatic Line: a large tectonic fault that separates the Adriatic and Eurasian tectonic plates. Geologically, the valley's north side belongs to the southern edge of the Austroalpine complex (mainly consisting of Variscan basement lithologies) in the Eastern Alps, while towards the south, Mesozoic sedimentary bedrock dominates. The region attended to in this thesis extends over two tributary valleys: Val Poré and Val Molinac (the municipality

of Mezzana), located on the northern slope of Val di Sole. The geology in these valleys consists of metamorphic siliceous lithologies, predominantly paragneiss, with outcrops of orthogneiss, quartzite, amphibolites and peridotites, all belonging to the Tonale and Ulmo geological units (Dal Piaz et al., 2007). The area of interest for this thesis is located at high altitudes (2000–2700 metres above sea level) in the upper reaches of Val Poré and Val Molinac. The geomorphology in both Val Poré and Val Molinac is influenced by glacial and paraglacial processes (Angelucci et al., 2014). The valley heads are shaped as glacial cirques filled with coarse sediment and talus, and rock glaciers (of various current activity) are prevalent in both valleys (Angelucci et al., 2014). Grasslands dominate the landscape downslope (2000–2400 m) of the exposed rock glaciers; these have formed on top of relict rock glaciers, glacial till, and directly on the bedrock. Slope processes of various scales shape the grasslands, including frost creep and deep-gravitational deformation (Angelucci et al., 2014). The higher elevations of Val di Sole are estimated to have been deglaciated by the mid-Holocene (Favilli et al., 2009), and the onset of soil formation has been radiocarbon dated in Val Molinac to the 6<sup>th</sup> Millennium BC (Angelucci and Carrer, 2015). Soils are mostly poorly developed at elevations >2350 m, in contrast to the pastures where podsol and cambisol horizons are around 25–40 cm thick (Angelucci et al., 2014). The present-day treeline in the flatter parts of the valley is located at ~1900–2000 m (at valley slopes, the trees grow up to almost 2300 m); trees likely grew at higher altitudes prior to anthropogenic wood clearings (Angelucci et al., 2014).

The present-day land use is primarily related to pastoralism; dairy livestock grazes (primarily used for cheese production) the pastures during the summer months, during which herders stay at high altitudes in seasonal huts (locally termed *malghe*) (Angelucci et al., 2014). Surveys in Val Molinac and Val Poré, conducted since 2010 as part of the research project *Alpine Landscapes: Pastoralism and Environment of Val di Sole* (ALPES), have uncovered a set of dry-stone structures of various sizes, mainly located between 2000–2400 m (Angelucci and Carrer, 2015). These structures are related to ephemeral land use in upland pastures, initiated in the Bronze Age (Angelucci et al., 2017, 2021), and continuing until modern times (Carrer and Angelucci, 2013). The smallest structures are rock shelters, usually located at higher elevations (>2400 m); larger structures are huts and enclosure complexes, many of which were

constructed near water sources. Many of these are surface structures that have so far not been excavated; hence, the age of most structures has not been established. Archaeological excavation and radiocarbon dating of an enclosure complex in Val Poré demonstrated occupation during the 15<sup>th</sup>–17<sup>th</sup> century (Carrer and Angelucci, 2013). An additional radiocarbon date (Carrer and Angelucci, 2013, 650–770 cal AD), together with a radiocarbon age from a nearby hut of similar age (Angelucci and Carrer, 2015, 680–880 cal AD), is the only data from the 1<sup>st</sup> millennium AD from either valley. Accordingly, little is known regarding land use during this historical period. Prehistorical evidence of the ephemeral human presence in Val Poré, related to pastoralism, has been discovered to have started in the Early Bronze Age at a buried dry-stone enclosure, based on radiocarbon dating ( $\sim$ 2000–1450 cal BC) of charcoal fragments and lithic and potsherd finds (Angelucci et al., 2021).

### 1.6.2 Mula basin, Spain – Chapter 4

The Mula basin is an intramontane tectonic basin in the region of Murcia, south-eastern Spain. Geologically, the basin is part of the eastern Baetic Cordillera – a mountain range formed during the Alpine Orogeny during the Middle Oligocene–Early Miocene. The Baetic Cordillera is divided into the External Zone (the northern parts) and the Internal Zone (the southern parts). The geology of the External Zone is commonly divided into the Pre-Baetic and sub-Baetic, both consisting of post-Palaeozoic marine sediments that were folded during the Miocene (for the Sub-Baetic, significant deformation also occurred during the Mesozoic). In the Internal Zone, Palaeozoic and Mesozoic marine sediments were heavily metamorphosed before the Miocene (Lonergan et al., 1994); locally, some post-deformation sediments were deposited (Rodríguez-Fernández et al., 2011). In the Baetic Cordillera, intramontane basins, including the Mula basin, are situated in the Internal Zone (Rodríguez-Fernández et al., 2011). These basins were formed during the Miocene, were filled by sediments (coarse-grained breccias, bioclastic limestones, limnic limestones) during the late Miocene, and were subsequently further covered by sediments from alluvial fan systems (Rodríguez-Fernández et al., 2011). Parts of the sedimentary record are missing here due to an unconformity, but increasing continental conditions caused a

change in the sedimentary environment from marine limestones and marls towards alluvial and lacustrine sediments and evaporites. The third and final main sedimentary deposition sequence consists of continental sediments (sandstones, conglomerates, and claystones) deposited during the Pliocene–Pleistocene. In the Mula basin specifically, the exposed bedrock outcrops include deformed Cretaceous–Miocene limestones and marls (with some conglomerates and sandstones), superimposed by undeformed Upper Miocene limestones and Marls (Martín-Martín and Martín-Algarra, 2002).

A prominent large-scale geomorphological feature in the Mula basin is the fluvial valley – the Mula valley – formed by fluvial dissection by the Mula river. The geomorphological development of the Mula valley has primarily occurred as cycles of river dissection and aggradation (Silva et al., 1996). Up to six Pleistocene terrace levels have been associated with River Mula (Angelucci et al., 2018), plus a recent seventh terrace level (+2 metre above modern thalweg) that occasionally is reactivated during high flood levels. Modern River Mula has been dammed at the La Cierva dam, creating a water reservoir; the section of the river upstream of the dam is of particular interest for Palaeolithic archaeology due to the presence of a rock shelter – Cueva Antón – in Eocene limestone (Zilhão et al., 2010; Angelucci et al., 2013; Zilhão et al., 2016). Alluvial sediments have been deposited inside the rock shelter; all sequences, except the youngest, have been dated with OSL (Burow et al., 2015) and palaeoclimatic proxies (Zilhão et al., 2016) to the MIS 5. Radiocarbon dating of the youngest alluvial sequence indicates deposition during MIS 3, after which river incision lowered the river level to beneath Cueva Antón, thus ending all alluvial deposition (Zilhão et al., 2016). The alluvial sequences in Cueva Antón are interpreted to be analogous to the +5–7 m River Mula terrace level found outside and upstream of the rock shelter (Angelucci et al., 2018).

### 1.6.3 Wadi Sodmein, Egypt – Chapter 5

Wadi Sodmein (Fig. 1.7A–B) is a desert valley located in a pull-apart basin in the Eastern Desert, Egypt, approximately 35 km northeast of the village Quseir. Tectonic activity throughout the Cenozoic has shaped the landscape through the onset of the Red Sea Rift during the Eocene (Swartz and Arden, 1960). The outset of the wadi is positioned in the western part of the basin (Henselowsky, 2019), at the edge of the

Precambrian basement rocks, consisting mainly of metavolcanic and metasedimentary rocks (Gaby et al., 1990). The wadi cuts towards the northeast through Jebel Duwi, a hogback formation made of Late Cretaceous sandstone and Late Cretaceous to Eocene limestone, marl, and shale deposits (Said, 1990; Khalil and McClay, 2002). The oldest sedimentary unit (Nubian unit) rests unconformably on the Precambrian basement (Said, 1990). East of Jebel Duwi, the wadi runs into the next basin, the Nakheil basin. The surface geology in the wadi mainly consists of alluvial gravels, which deposit in the wadi during ephemeral stream events. The lithology of clasts is varied and originates from the Precambrian basement (e.g. basalts, granite, quartzites) and the nearby sandstone bedrock outcrops.

The primary wadi incision into the pre-Pliocene bedrock likely occurred before the Quaternary since climate conditions during the Quaternary would generally have been too dry for such large-scale fluvial landforms to form (Henselowsky, 2019). Anyhow, wetter phases did develop during the Pleistocene; while the modern-day climate in Wadi Sodmein is hyper-arid, local speleothem growth demonstrates humid phases during MIS 5 (Henselowsky et al., 2021). Climate conditions were also significantly more humid than today during the Middle Holocene, as demonstrated by the presence of Holocene desert playa sediments wedged between the wadi and Cretaceous sandstone outcrops (Henselowsky, 2019). Further back in time, humid phases must have occurred, as is demonstrated by the prevalence of karstic landforms in the Miocene bedrock (Henselowsky, 2019). No definite local palaeoclimatic proxies exist for the period between MIS 5 and the Holocene; regional climatic proxies, derived from run-off and aeolian dust from Mediterranean Sea cores, suggest somewhat humid conditions during the early MIS 4 (Grant et al., 2017). Quaternary in-filling of the wadi basin, therefore, should have occurred in an already developed wadi system (Henselowsky, 2019). Remnants of old terrace surfaces (Fig. 1.7B-C) were discovered on the wadi floor. These surfaces are elevated up to 2 metres above the present-day wadi floor and can be distinguished from active surfaces by the vanish-covered desert pavements (Henselowsky, 2019). The desert pavement consists of a gravel monolayer at the surface and a up to 40 cm thick aeolian sand layer beneath. No absolute dating exists for the deposition of these terrace levels. Lithic artefacts of varying ages (Middle Stone Age to Neolithic) have been discovered on top of these surfaces (Kindermann et al.,



2018), which, in combination with the presence of desert varnish, suggests that the terraces are of Pleistocene age rather than Holocene (Henselowsky, 2019).

Due to the archaeological footprint and its location, Wadi Sodmein is an essential area for studying AMH dispersal out of Africa and is, hence, of interest for CRC 806. The most distinctive archaeological feature in the area is the Sodmein Cave: a limestone cave formed in the Eocene limestone of Jebel Duwi (Vermeersch et al., 1994; Moeyersons et al., 1996, 2002). The stratigraphy of the cave consists of a sequence of alternating layers of calcareous sands and limestone rockfall debris and layers rich in organic debris, disrupted by three disconformities (Moeyersons et al., 1996), all resting on limestone boulders from the collapsed cave roof. The archaeological finds in the lower layers are characterised by Nubian and Levallois stone artefacts. In contrast, the middle layers show more transitional technologies (Kindermann et al., 2021). The chronostratigraphy in the cave is defined with TL dating of heated flint artefacts from the lowermost Middle Palaeolithic layer to  $118 \pm 8$  ka (Mercier et al., 1999) and  $121 \pm 15$  ka to  $87 \pm 9$  ka (Schmidt et al., 2015), and with radiocarbon dating of the upper layers with the last recorded human occupation ending during the Middle Holocene (Moeyersons et al., 2002; Vermeersch and Van Neer, 2015). Re-excavations of the Sodmein cave were started in 2010 as part of the work conducted by CRC 806 toward understanding human dispersal throughout Northeastern Africa.

#### 1.6.4 The coast of the Atacama Desert, Chile – Chapter 6

The final study area where samples were collected for this thesis is located in the coastal Atacama Desert in Northern Chile. The Atacama desert is the driest known area on Earth with yearly average precipitation levels of  $0.15 \text{ mm a}^{-1}$  in its hyper-arid core (Houston and Hartley, 2003). Hyperarid conditions in the Atacama Desert have persisted during the entire last glacial period ( $\sim 12\text{--}115$  ka) and the Holocene, despite periods of increased precipitation that occurred during MIS 7 and MIS 5, as is demonstrated by increased fluvial input into basins in the Coastal Cordillera (Ritter et al., 2019). The hyperaridity is commonly attributed to i) the Atacama Desert's latitudinal position ( $15\text{--}30^\circ\text{S}$ ) in the subtropical high-pressure region, ii) the rain shadow at this geographical location due to the geographical situation of the area between the Andes and the Coastal Cordillera mountain ranges (Houston and Hartley,



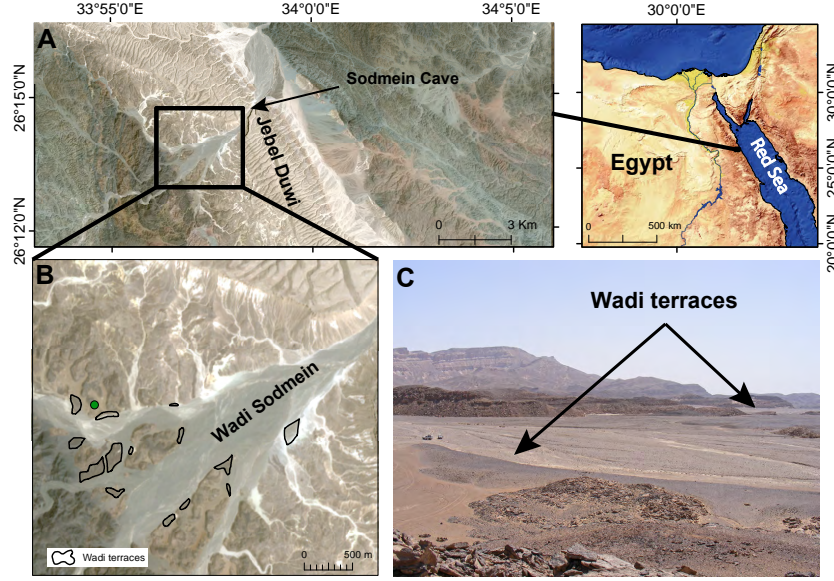


FIGURE 1.7: (A) An overview of Wadi Sodmein, showing the ridge of Jebel Duwi and the location of the Sodmein Cave. (B) The position of wadi terraces in Wadi Sodmein; the green point marks the location for the northeastern field-of-view, overlooking some of the wadi terraces (C).

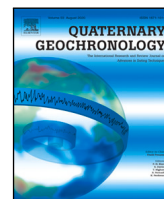
2003), and iii) upwelling of cold seawater at South American west coast that lead to moisture-poor onshore-blowing air masses (Houston and Hartley, 2003). The little precipitation in the Atacama Desert could be related to moisture transported from the Pacific Ocean by winds that regularly blow eastwards during the night and morning (Schween et al., 2020). The transported moisture frequently causes fog (Cáceres et al., 2007; Cereceda et al., 2008) that can extend from the coast up to 1000 m of elevation. Geologically, the most prominent process in the region is the still ongoing Andean orogeny, which was initiated during the Early Jurassic by the subduction of the oceanic Nazca Plate beneath the South American Plate (Ramos, 2009). Erosion rates are overall very low to non-existent ( $<10^{-3}$  mm a<sup>-1</sup>) (e.g. Dunai et al., 2005; Nishiizumi et al., 2005; Kober et al., 2007), likely due to the hyperarid conditions observed in the desert.

The coastal region of the Atacama Desert is confined by the Coastal Cordillera, an eroded volcanic arc with peaks reaching up to 3000 m.a.s.l., which runs north-south along the Chilean coastline. This mountain range was structurally separated from the Andes during the Paleogene due to the subsidence of the Chilean Central Valley (Carter and Aguirre le B, 1965). The coastline of Chile is defined by up to 3 km

wide coastal plains sandwiched between the modern coastline and the Coastal Cliff of Chile. These plains consist of alluvial fan complexes (Walk et al., 2019, 2020), deposited on top of a marine abrasion surface formed by the retreat of the Coastal Cliff (Marquardt et al., 2004) during phases in the Late Pleistocene and the Holocene (Bartz et al., 2020b). Neotectonic activities affect the coastline by raising the beaches, thus creating a series of marine terraces in the coastal region of Atacama (Marquardt et al., 2004). Chronologically, these terraces are dated to MIS 11 and younger (Radtke, 1988; Regard et al., 2010; Bartz et al., 2020a), with uplift rates between 0.1 and 0.6 m ka<sup>-1</sup> (Victor et al., 2011).

## Chapter 2

# Rock Surface IRSL Dating of Buried Cobbles from an Alpine Dry-Stone Structure in Val di Sole, Italy



## Research paper

# Rock surface IRSL dating of buried cobbles from an alpine dry-stone structure in Val di Sole, Italy

Lucas Ageby<sup>a,\*</sup>, Diego E. Angelucci<sup>b</sup>, Dominik Brill<sup>a</sup>, Francesco Carrer<sup>c</sup>, Eike F. Rades<sup>d,e</sup>, Janet Rethemeyer<sup>f</sup>, Helmut Brückner<sup>a</sup>, Nicole Klasen<sup>a</sup>

<sup>a</sup> Institute of Geography, University of Cologne, 50923 Cologne, Germany

<sup>b</sup> Dipartimento di Lettere e Filosofia, University of Trento, 38122 Trento, Italy

<sup>c</sup> School of History, Classics and Archaeology, Newcastle University, NE1 7RU Newcastle, UK

<sup>d</sup> Nordic Laboratory for Luminescence Dating, Department of Geoscience, Aarhus University, Risø Campus, Roskilde, DK, 4000, Denmark

<sup>e</sup> Radiation Physics Section, Department of Physics, Technical University of Denmark, DTU Risø Campus, Roskilde, DK, 4000, Denmark

<sup>f</sup> Institute of Geology and Mineralogy, University of Cologne, 50923 Cologne, Germany



## ARTICLE INFO

## Keywords:

Rock surface luminescence dating

Luminescence-depth profiles

IRSL

Dry-stone structures

Val di Sole

Pastoralism

## ABSTRACT

Here, we investigate the application of rock surface IRSL dating to chronology restrain archaeological structures related to upland pastoralism. We applied the method to cobbles collected from archaeological units in an excavation of a dry-stone structure in Val di Sole in the Italian Alps. At this site, archaeological finds and previous radiocarbon analyses have dated an initial human occupation of the site to the Early Bronze Age (ca. 2200–1600 BC), and a possible second occupation to the Middle Bronze Age (ca. 1600–1350 BC). These archaeological units have later been buried by colluvial sediments. Theoretically, the luminescence-depth profiles from rock surfaces from inside such structures could record the exposure and burial of these archaeological units. We collected buried gneiss cobbles from these archaeological units and measured rock slices and chips from 1 to 4 cm long cores with a low-temperature pIR-IRSL protocol to investigate the signal resetting in these cobbles. Only the IRSL<sub>50</sub> signal was deemed appropriate for dating. Measured luminescence-depth profiles demonstrate varying levels of signal resetting before burial. Dating of two paragneiss cobbles from the lower unit yielded corrected burial ages of ~1450–700 BC and ~19 ka. The older date is clearly not associated with human occupation; the younger date slightly underestimates the Early Bronze Age occupation, which was confirmed by new radiocarbon dating of charcoal (1731–1452 and 2124–1773 cal. BC). The burial of the upper archaeological unit was dated to ~AD 1000, based on ages derived from the bottom surface of an orthogneiss cobble and the top surface of a paragneiss cobble. This is slightly younger than two new radiocarbon ages (426–596 and 537–654 cal. AD) from charcoal fragments sampled from the same unit. This new chronological data show longer exposure of the upper archaeological unit than was previously known. Furthermore, the paragneiss cobble from the upper unit has been exposed to sufficient heat to reset the IRSL<sub>50</sub> and pIR-IRSL<sub>290</sub> signals throughout the cobble; an event which can be dated to ~AD 100–1500 BC. Comparisons between fading-corrected IRSL<sub>50</sub> ages and pIR-IRSL<sub>290</sub> ages from the heated cobble are in agreement, which suggests that the conventional g-value approach accurately corrects for signal loss during burial. Overall, our research suggests that rock surface IRSL dating can provide complementary chronological data for archaeological settings.

## 1. Introduction

The timing and strategies of prehistoric upland pastoralism in the European Alps remain largely uncertain. Although high-mountain pastures in the Alpine regions have historically had significant economic importance, known archaeological sites are still scarce (Carrer, 2012). Therefore, a thorough chronological understanding of site formation

and periods of human impact on the environment from currently known sites is essential to infer the nature of human occupation of upland areas in the past.

Soon after the last deglaciation, groups of late Upper Paleolithic and, later, Mesolithic hunter-gatherers started to exploit high altitude (>2000 m above sea level) areas in the Alps, presumably during the summers (Cavulli et al., 2011). Lithic assemblages and scat-

\* Corresponding author.

E-mail address: [lageby@uni-koeln.de](mailto:lageby@uni-koeln.de) (L. Ageby).

<https://doi.org/10.1016/j.quageo.2021.101212>

Received 23 December 2020; Received in revised form 30 April 2021; Accepted 6 June 2021

Available online 10 June 2021

1871-1014/© 2021 The Authors.

Published by Elsevier B.V. This is an open access article under the CC BY-NC-ND license

(<http://creativecommons.org/licenses/by-nc-nd/4.0/>).

tered finds which indicate upland hunting during the early Holocene have been recorded from several Alpine sectors, e.g., from the eastern Southern Alps (Cavulli et al., 2011), from the Silvretta Alps (Switzerland/Austria), dated to the mid-9th millennium BC (Kothieringer et al., 2015), and slightly later (8000–7000 BC) from the French Alps (Walsh et al. 2014). Palaeoecological and archaeological records (e.g., Hafner and Schwörer, 2018; Kothieringer et al., 2015) show that intense human land use, including grazing and forest clearing, may have locally occurred during the Neolithic and the Chalcolithic, while similar studies in other sectors of the Alps (e.g., Festi et al., 2014; Walsh et al., 2007) show a modest human impact on the upland environment in these early phases. During the Bronze Age (~2300–800 BC), grazing of upland pastures in the Alps became more established and widespread (Festi et al., 2014; Leveau and Walsh, 2005; Moe et al., 2007; Walsh et al., 2007). The oldest dry-stone structures (huts and enclosures) in the Alpine uplands date to this period, documenting a more intensive use of summer pastures (Angelucci et al., 2014; Reitmaier et al., 2018; Walsh and Mocci, 2011; Walsh et al., 2014), and possibly a transition toward more specialised dairy practices (Carrer et al., 2016).

Radiocarbon dating is the most frequently applied dating method for such structures (e.g., Angelucci et al., 2017), whereby, as a rule, the stratigraphically associated units are dated. Although radiocarbon dating is a well-established method that can provide reliable and high-precision ages, caution is advisable when choosing material for dating. Suitable materials such as wood, charcoal, and macrofossils are not always present in archaeological deposits. Furthermore, the stratigraphic relationship between sample depth and age is not always straightforward, e.g., due to the shallowness of upland soils (Angelucci and Anesin, 2012) or due to reworking (e.g., by bioturbation or freeze-thaw cycles), which Carcaillet (2001) reported for charcoal fragments from high altitude soils in the Alps. Also, radiocarbon ages derived from wood and charcoal might overestimate the true age, e.g., if the sampled material belongs to decay-resistant tree species, which may persist in the landscape long after the death of the tree (Schiffer, 1986). Traditional optical dating approaches (multi-grain and single-grain quartz and feldspar dating) are useful geochronological tools in some archaeological contexts (e.g., Junge et al., 2016). However, insufficient signal resetting causes significant challenges when these methods are applied to settings that are affected by slope processes (Fuchs and Lang, 2009), such as alpine dry-stone structures (e.g. Carrer and Angelucci, 2013).

Keeping these dating limitations in mind, rock surface luminescence has become a promising technique for dating archaeological contexts (e.g., Feathers et al., 2019; Galli et al., 2020; al Khasawneh et al., 2019; Sohbaty et al., 2012a, 2015). The time of burial of rock surfaces can be dated by utilising the dose-dependent, light-sensitive luminescence signal, which accumulates in feldspar and quartz grains during burial. Exposure to daylight bleaches the luminescence signal in the rock surface grains within minutes to hours (Habermann et al., 2000; Vafiadou et al., 2007), and longer periods of exposure bleach the luminescence signal further into the rock (Gliganic et al., 2019; Ou et al., 2018; Sohbaty et al., 2011, 2012b). Once the rock is buried, the dose in the bleached part of the rock (i.e., the bleaching front) increases due to radioactive decay. However, information regarding the depth of the bleaching front remains, even after burial. This is a significant advantage over conventional optical dating techniques in settings where bleaching conditions are less favourable since cobbles that were sufficiently exposed can be identified by the existence of luminescence signal-depth plateaus which are not saturated.

This study aims to investigate if rock surface luminescence dating is a viable dating method for chronologically constraining site formation of buried dry-stone structures in upland environments. To do so, we apply feldspar infrared stimulated luminescence (IRSL) dating to rock surfaces from cobbles collected from two archaeological units within a dry-stone structure from the Italian Alps. We compare our optical dating results to new and previously published radiocarbon ages. Furthermore, we offer new insight into the annealing of IRSL and post-infrared-IRSL (pIR-IRSL) signals in rocks.

## 2. Regional setting and site description

The study area is located in Val Poré, a tributary valley on the south-facing slope of the tectonic valley Val di Sole, Trentino, Italy (Fig. 1A). Local metamorphic rocks belong to the Ulten unit, which, together with the Tonale unit, forms the Tonale nappe in the Upper Austroalpine domain. The Tonale nappe is mainly made up of paragneiss, with intercalations of orthogneiss and mafic lithologies (Dal Piaz et al., 2007). The paragneiss (TUG in Fig. 1A) shows medium-high polycyclic metamorphism. The rock mainly features micas (both biotite and muscovite), quartz, sodium-rich feldspars, kyanites, and garnets. The paragneiss often displays compositional banding due to the alternation between micaceous layers and layers rich in quartz and feldspars. The orthogneiss (TUO in Fig. 1A) contains quartz, plagioclase, alkali feldspars, and micas (mostly biotite). The metamorphic overprinting of the Upper Austroalpine domain is polycyclic and covers a prolonged time interval, which includes a Palaeozoic phase (mostly Variscan) and an Eoalpine, Cretaceous phase. The orthogneiss intercalations, and the banding in the paragneiss, are parallel to regional schistosity and consistent with regional-scale foliation referring to the Variscan orogeny (Dal Piaz et al., 2007). The geomorphology of Val Poré is mainly dominated by glacial and periglacial processes (see Angelucci et al., 2014). The head of Val Poré is a glacial cirque filled with coarse talus and, on the eastern side, an active rock glacier that mainly consists of gneissic boulders. Downslope of the cirque, the rock glaciers appear mostly inactive. Gravitational and periglacial slope processes are also visible. Grasslands occur below the rock glaciers (~2300 metres of elevation), exploited as grazing areas during the summer. Here podzols and cambisols (25–40 cm thick) cover the bedrock, moraine ridges, and relict rock glaciers. The landscape is affected by slope processes, most notably frost creep and gravitational slope deformations.

The chosen site for this study, MZ051S (Fig. 1B), is located at ~2240 m above sea level in Val Poré. It is currently being investigated as part of the *Alpine Landscapes: Pastoralism and Environment of Val di Sole* (ALPES) project (e.g., Carrer and Angelucci, 2013; Angelucci et al., 2014; Carrer and Angelucci, 2018). This site is interpreted as a livestock enclosure, delimited by a collapsed dry-stone wall which is partly embedded in the topsoil (Fig. 1B). The dimensions of the enclosure are approximately 41 × 17 m, with the longer axis positioned with a north–south orientation. Fieldwork at the site has uncovered a ~40 cm thick deposit which includes two archaeological units: US4a and US5a (Fig. 1C), both consisting of thin, poorly developed, buried A horizons. These horizons were developed from yellowish-brown silty loam (usually containing clasts of local gneiss), and later buried by colluvium derived from the erosion and re-deposition of former surface sediments and soil horizons, re-deposited from upslope of the site. Unit US4a yielded only scarce archaeological finds; several lithic and ceramic finds (knapped artefacts obtained from chert and potsherds) have been recovered from layer US5a (Angelucci et al., 2017). The units have previously been <sup>14</sup>C dated (Table 1) to Middle and Early Bronze Age, respectively (Angelucci et al., 2017). New radiocarbon ages (COL6511.1.1–COL6514.1.1), measured at the CologneAMS facility of University of Cologne (Dewald et al., 2013), verify US5a as Early Bronze Age, while also establishing a more complex chronology for US4a with the surprisingly young <sup>14</sup>C ages of 537–654 and 426–596 cal. AD. Younger and better preserved dry-stone structures have been surveyed in Val Poré and neighbouring tributary valleys (Carrer and Angelucci, 2013; Angelucci et al., 2014; Carrer and Angelucci, 2018). The largest of such structures (e.g., MZ005S; located at ~2260 m above sea level in Val Poré) typically consist of a hut and four enclosures. These structures are associated with historic pastoral land use (Carrer and Angelucci, 2013) and have been constructed using local lithologies, mostly from paragneiss. The archaeological finds associated with MZ005S (Dell'Amore et al., 2017; Medici et al., 2014), and three <sup>14</sup>C samples (also from MZ005S) dated to the 7th, the 15th, and the 20th centuries AD (Angelucci and Carrer, 2015; Carrer and Angelucci, 2013), indicate that these still exposed structures were built between late Medieval to early Modern periods.



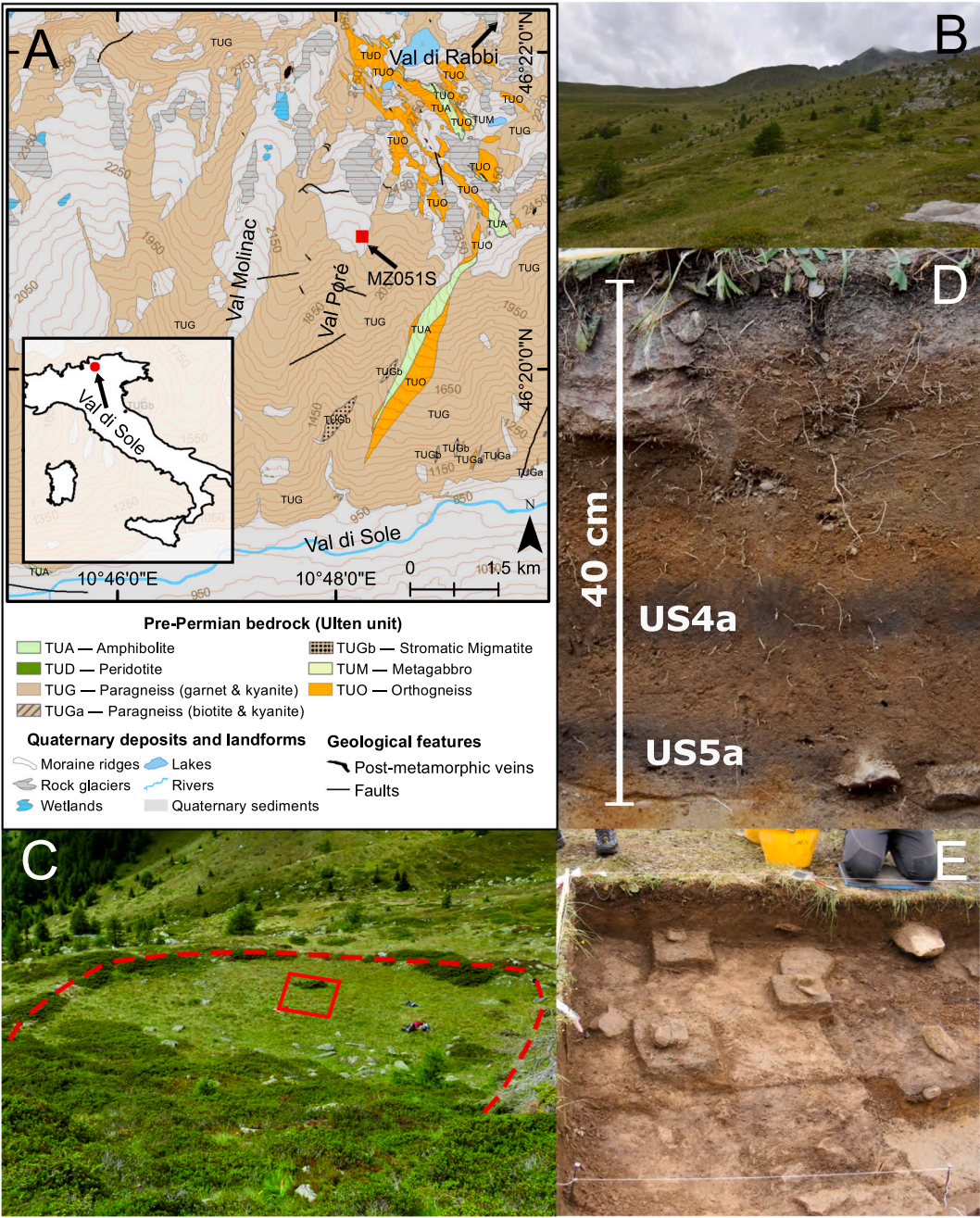


**Fig. 1.** (A) Geological mapping of the study area. Data visualisation: Geological Service of the Autonomous Province of Trento (Italy). (B) The landscape of Val Poré is dominated by grazed grasslands covering Quaternary sediments and gneissic bedrock. Gneissic boulders form a rock glacier, which southern snout is visible in the upper right corner. (C) Outline (dashed line) of MZ051S in Val Poré. The approximate location of the 2018 excavation is outlined (solid line) near the centre of the excavation. (D) The stratigraphic succession of MZ051S. Two archaeological units, US4a and US5a, have previously been described by Angelucci et al. (2017). C and D are modified after Angelucci et al. (2017). (E) Gneissic cobbles were excavated from the archaeological units inside MZ051S.

Table 1							
Results from radiocarbon dating of charcoal fragments from MZ051S (Fig. A.1, Appendix). All radiocarbon ages (including previously published ages) were (re-)calibrated using OxCal 4.4.2 (Bronk Ramsey, 2009) with the IntCal 20 curve from Reimer et al. (2020) and are reported as before present (BP, present = AD 1950). The calibrated ages (AD/BC) are reported with 95.4% probability. Samples COL6511.1.1, COL6512.1.1, COL6513.1.1, and COL6514.1.1 were prepared according to the procedure described by Rethemeyer et al. (2019). Lab. ID COL = CologneAMS, University of Cologne, Germany; DSH = CIRCE, INNOVA SCARL, Italy.							
Depth (m)	Lab. ID	Sample	Unit	$\delta^{13}\text{C}$ (‰)	Radiocarbon age (a BP)	cal. AD/BC	Previously published in:
0.20	COL6514.1.1	ID1216	US4a	−34	1476 ± 46	537-654 AD	
0.25	COL6511.1.1	RR68	US4a	−29	1550 ± 40	426-596 AD	
0.20	DSH6956	ID1145	US4a	−26	3225 ± 26	1532-1435 BC	Angelucci et al. (2017)
0.35	COL6512.1.1	RR100	US5a	−22	3296 ± 48	1731-1452 BC	
0.35	COL6513.1.1	ID1149	US5a	−24	3585 ± 46	2124-1773 BC	
0.25	DSH6955	ID1146	US5a	−20	3459 ± 23	1880-1691 BC	Angelucci et al. (2017)

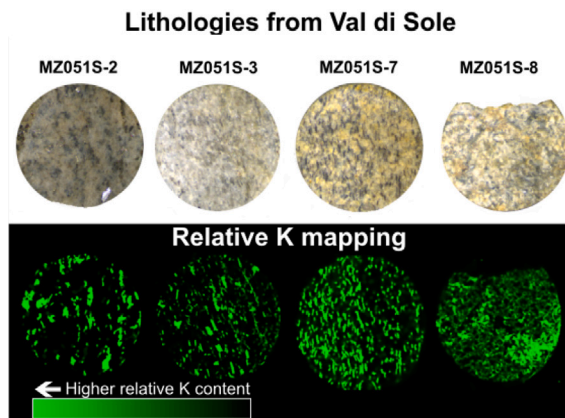


Fig. 2. Lithologies collected from the excavation of MZ051S in Val di Sole, Italy. The relative potassium concentrations within the slices were mapped with  $\mu$ XRF. Visual comparisons between the slices and the potassium maps show that areas of high relative potassium content mainly correlate with mica minerals (see also Fig. D.1, Appendix), not with potassium-rich feldspars. The slices are  $\sim 10$  mm in diameter.

Table 2

Overview of the cobbles dated in this study.

Lab code	Sample	Unit	Clast size (mm)	Lithology
C-L4626	MZ051S-2	US4a	100x80x70	Paragneiss (TUG)
C-L4627	MZ051S-3	US4a	100x60x30	Orthogneiss (TUO)
C-L4629	MZ051S-7	US5a	200x130x50	Paragneiss (TUG)
C-L4630	MZ051S-8	US5a	260x120x110	Paragneiss (TUG)

### 3. Methodology

#### 3.1. Samples and preparation

Cobble-sized rocks, embedded in a scattered distribution within the excavated archaeological units (Fig. 1E), were sampled during a fieldwork campaign in July 2018. The cobbles were collected from an area of approximately 4 m<sup>2</sup>. Due to the archaeological excavation, the top surfaces of some cobbles were exposed in the excavation for up to two days before sampling. After extraction, the cobbles were covered in aluminium foil and stored in opaque bags. Some cobbles were deemed inadequate for further preparation upon inspection in red-light condition due to their shape which would make extraction of intact cores difficult. We proceeded with two cobbles from each layer (Fig. B.1, Appendix): MZ051S-2 and MZ051S-3 from layer US4a, and MZ051S-7 and MZ051S-8 from layer US5a (Table 2). The cobbles originate from local outcrops of pre-Permian paragneiss (MZ051S-2, MZ051S-7, MZ051S-8) and orthogneiss (MZ051S-3). The cobbles demonstrate sub-angular morphology. MZ051S-2 is spherical, while MZ051S-3, MZ051S-7, and MZ051S-8 have elongated shapes. All sample preparation and measurements were carried out in the Cologne Luminescence Laboratory at the University of Cologne, Germany. The cobbles were cored parallel to their shortest axis (MZ051S-2  $\sim 70$  mm; MZ051S-3  $\sim 30$  mm; MZ051S-7  $\sim 50$  mm; MZ051S-8  $\sim 110$  mm) with a water-cooled Proxxon TBH 28124 diamond-tipped bench drill, or with a water-cooled WEKA DK17 diamond core drill mounted on a stand. All cores were extracted more than 10 mm from the edge of the cobble to minimise the effect of signal resetting, which might have occurred when the sides of the cobbles had been exposed in the past. The cores were sliced into  $\sim 0.7$  mm thin round slices or irregular chips with a cooled Buehler Isomet 1000 precision saw. Charcoal pieces were prepared for AMS radiocarbon analysis using acid and alkali extraction and conversion of the organic carbon to elemental carbon by combustion and graphitization (Rethemeyer et al., 2019).

#### 3.2. Measurements

All measurements were carried out with an automated Risø TL/OSL reader (model DA-20) (Bøtter-Jensen et al., 2010). For MZ051S-2 and MZ051S-3, whole slices were measured mounted directly in the sample carousel of the reader. This was not always possible for MZ051S-7 and MZ051S-8 since many slices broke during preparation, and thus, additional chips were measured in aluminium cups. A single aliquot regenerative (SAR) protocol (Murray and Wintle, 2000), modified for a low-temperature pIR-IRSL protocol with the post-infrared stimulation of 150 °C (e.g., Riedesel et al., 2018) (Table 3), was used to measure equivalent doses ( $D_e$ ). Measurement time could be reduced by restricting the protocol to only measure the normalised, natural signal emission ( $I_n/t_n$ ) for slices that were extracted from depths that were clearly in saturation. Dose-response curves (Fig. 3A–B) were fitted with exponential growth curves with the Luminescence Analyst v. 4.57 software (Duller, 2015). Beta irradiation was administered with a  $^{90}\text{Sr}/^{90}\text{Y}$  beta source ( $\sim 0.088$  Gy s<sup>-1</sup>). Preheat (180 °C) was administered with a heating rate of 2 °C/s for 100 s. The slices/chips were stimulated with infrared light-emitting diodes (LED) (peak emission = 870 nm) at 50 °C (pIR-IRSL<sub>150</sub>; step 4 and 9 in Table 3), followed by an additional infrared stimulation at 150 °C (pIR-IRSL<sub>150</sub>; step 5 and 10 in Table 3). Emissions (insets in Fig. 3A–B) were filtered through an interference filter (410 nm) and detected with an Electron Tube PDM 9107Q-APTTL-03 blue/UV sensitive photomultiplier tube. Sample-dependent test doses varied between  $\sim 2.5$  and 8.7 Gy. We aimed at keeping the test dose  $\leq 100\%$  of expected  $D_e$  (determined by a dose test). A significant reduction in test dose-response ( $>40\%$ ) has been reported by Colarossi et al. (2018) for pIR-IRSL single grain data when applying a hot bleach at the end of the test dose cycle; results which are similar to those observed for our slices (Fig. 3C) when measured with IRSL protocol with a hot bleach at the end of the test dose cycle. To lessen this sensitivity change, Colarossi et al. (2018) proposed the use of a long, elevated IR stimulation (500 s at 225 °C) at the end of both the natural and test dose cycles to remove recuperation. Here, we use the low-temperature pIR-IRSL<sub>150</sub> protocol to prevent the sensitivity change between the natural and first test dose cycle (Fig. 3C). We measured additional slices from cobble MZ051S-2 with a pIR-IRSL<sub>290</sub> protocol (Table 3). We wanted to investigate the intensity of the optically less sensitive, high-temperature pIR-IRSL<sub>290</sub> signal (Kars et al., 2014) in the centre of this cobble when preliminary luminescence-depth measurement showed that it might have experienced heating.

Dose recovery tests were administered to three slices/chips per sample (bleached for 24 h in a Höhle solar simulator) to examine the ability of the SAR protocols to recover known beta doses of  $\sim 2.6$  to 21.9 Gy. Arithmetic mean dose recovery ratios (Fig. C.1, Appendix) are reported with and without subtraction of the dose residuals (Fig. C.2, Appendix). Dose recovery ratios (measured/given dose) range between 0.97–1.06 for the IRSL<sub>50</sub> signal and are thus near unity after subtraction of the residual dose. Without the subtraction, recovered doses for the IRSL<sub>50</sub> signal slightly overestimate but are still within 10% of the given dose. We did not use the pIR-IRSL<sub>150</sub> signal to date our samples due to the mostly poor dose recovery, both with or without residual subtraction (ratio range with subtraction: 0.75–1.31; without subtraction: 1.10–1.37). IRSL<sub>50</sub> residual doses from bleached slices/chips were low ( $< 0.5$  Gy) except for MZ051S-7 ( $1.09 \pm 0.35$  Gy). The measured residuals range for the pIR-IRSL<sub>150</sub> signal is between  $1.1 \pm 0.1$  to  $3.8 \pm 0.3$  Gy. Dose recovery ratios for the pIR-IRSL<sub>290</sub> protocol were measured after 300 s of heating at 450 °C. The dose recovery ratio for this protocol is acceptable at  $1.09 \pm 0.19$ .

#### 3.3. Effective dose rate throughout the cobbles

The radionuclide concentrations (Table 4) in the cobbles and the surrounding sediments were measured with high-resolution gamma spectrometry with a germanium detector for  $\sim 42$  h. One dose rate



**Table 3**

Overview of the low-temperature pIR-IRSL<sub>150</sub> and the pIR-IRSL<sub>290</sub> SAR protocols. The pIR-IRSL<sub>150</sub> protocol was applied to all rocks. The pIR-IRSL<sub>290</sub> protocol was only applied to MZ051S-2 to investigate the depth of resetting for the harder-to-bleach pIR-IRSL<sub>290</sub> signal. The IRSL<sub>50</sub> signal in pIR-IRSL<sub>290</sub> protocol was not used for any analysis since high preheat temperatures have shown to cause underestimation in the IRSL<sub>50</sub> signal (Li and Li, 2011a).

Step	Action		Signal	
	pIR-IRSL <sub>150</sub>	pIR-IRSL <sub>290</sub>	pIR-IRSL <sub>150</sub>	pIR-IRSL <sub>290</sub>
1	Irradiation	Irradiation		
2	Preheat (180 °C for 100 s)	Preheat (320 °C for 100 s)		
3	Pause (30 s)	Pause (30 s)		
4	IRSL (50 °C for 300 s)	IRSL (50 °C for 300 s)	L <sub>x</sub> (IRSL <sub>50</sub> )	
5	IRSL (150 °C for 300 s)	IRSL (290 °C for 300 s)	L <sub>x</sub> (pIR-IRSL <sub>150</sub> )	L <sub>x</sub> (pIR-IRSL <sub>290</sub> )
6	Irradiation	Irradiation		
7	Preheat (180 °C for 100 s)	Preheat (320 °C for 100 s)		
8	Pause (30 s)	Pause (30 s)		
9	IRSL (50 °C for 300 s)	IRSL (50 °C for 300 s)	T <sub>x</sub> (IRSL <sub>50</sub> )	
10	IRSL (150 °C for 300 s)	IRSL (290 °C for 300 s)	T <sub>x</sub> (pIR-IRSL <sub>150</sub> )	T <sub>x</sub> (pIR-IRSL <sub>290</sub> )

**Table 4**

Summary of radionuclide concentrations in the cobbles and the surrounding sediments, and the attenuated infinite matrix dose rates.

Sample	Sample type	Water content (%)	Radionuclide concentration				Dose rate (Gy ka <sup>-1</sup> )				
			<sup>238</sup> U (ppm)	<sup>232</sup> Th (ppm)	<sup>40</sup> K (%)	InternalK (%)	Gamma	Beta	Alpha	Cosmic	Internal <sup>40</sup> K
MZ051S-2	Cobble	0	1.96 ± 0.11	6.46 ± 0.42	1.11 ± 0.01	0.49 ± 0.08	0.81 ± 0.02	1.34 ± 0.02	0.04 ± 0.02	0.34 ± 0.03	0.012 ± 0.004
MZ051S-3	Cobble	0	2.88 ± 0.16	12.25 ± 0.74	0.89 ± 0.01	1.30 ± 0.15	1.14 ± 0.03	1.42 ± 0.03	0.06 ± 0.03	0.34 ± 0.03	0.042 ± 0.011
MZ051S-7	Cobble	0	2.34 ± 0.13	10.76 ± 0.63	1.00 ± 0.01	0.57 ± 0.09	1.04 ± 0.02	1.40 ± 0.03	0.05 ± 0.02	0.32 ± 0.03	0.014 ± 0.004
MZ051S-8	Cobble	0	0.69 ± 0.04	2.05 ± 0.14	0.52 ± 0.01	1.63 ± 0.15	0.57 ± 0.01	0.31 ± 0.01	0.01 ± 0.01	0.32 ± 0.03	0.039 ± 0.010
MZ051S-4a	Sediment	68 ± 6	4.68 ± 0.25	11.88 ± 0.62	2.49 ± 0.03		0.97 ± 0.05	1.61 ± 0.08	0.10 ± 0.04		
MZ051S-5a	Sediment	68 ± 6	5.51 ± 0.29	10.39 ± 0.62	2.17 ± 0.03		0.94 ± 0.05	1.50 ± 0.07	0.10 ± 0.04		

sample per cobble (~200 grams each) was homogenised and allowed to rest for a minimum of three weeks to allow <sup>222</sup>Rn to reach equilibrium. For MZ051S-3, the majority of the cobble was crushed for dose rate measurements. For the other cobbles, cross-sections were cut to create representative subsamples. Radionuclide concentrations were converted to environmental dose rates with conversion factors reported by Cresswell et al. (2018). The average summer moisture content was calculated from moisture content upon sampling. The winter moisture content is assumed to be equal to the average saturated moisture content. We calculated the weighted average moisture content assuming three months of summer and nine months of winter, based on five soil samples. The moisture content in the cobbles is assumed to be negligible. We assume an average feldspar grain size of 400 µm for the cobbles. This is based on visual inspections of thin sections from previously collected rocks from the site. Depth-dependent, effective dose rates were calculated using the approach of Freiesleben et al. (2015), which uses the principle of superposition (Aitken, 1985) to scale the effective contribution of gamma and beta radiation to the cobbles based on infinite matrix dose rates derived from the sediments and the cobbles themselves. Attenuation factors of 1.89 and 0.01 for beta and gamma, respectively, were used to scale the attenuation of radiation (Aitken, 1985). The alpha radiation from the cobbles and surrounding sediments was not considered as the infinite matrix alpha dose rate was <4% of total dose rate in all samples, and thus, the effective alpha dose rate to 400 µm grains is considered to be negligible. The cosmic dose rate was assumed to be constant throughout the cobbles (Freiesleben et al., 2015) and was calculated using the *calc\_CosmicDoseRate* function from the R-package *Luminescence* (Burow, 2019). Due to the shallow deposition depth, the function used data from Prescott and Hutton (1988, their Fig. 1) to estimate the soft and hard components of cosmic ray flux, and Prescott and Stephan (1982, their Eq. 1) to correct the cosmic component for altitude and latitude.

The internal potassium content of the feldspar grains within the cobbles was estimated with micro-X-ray fluorescence (µ-XRF), with a Bruker M4 Tornado µ-XRF spectrometer; an approach previously utilised by Rades et al. (2018). Relative element concentrations (potassium, calcium, aluminium, sodium, and silicon) were mapped on five

slices per sample (Fig. D.1, Appendix). Visual comparison indicates that areas with relatively high concentrations of potassium align with the distribution of dark minerals (Fig. 2), which appear to have low concentrations of calcium and sodium. These darker grains are presumed to be micas, most likely biotites. We targeted feldspar grains by point measuring (spot size ~20 µm) the non-mica grains which showed high concentrations of potassium, aluminium, calcium or sodium; elements which are abundant in feldspar. The acquired XRF spectra were analysed using the Bruker M4 Tornado software. A combined approach of fundamental parameter analysis and type calibration (Flude et al., 2017) with a feldspar standard was used to quantify element concentration in the slices. The average potassium concentrations of the feldspar grains in all rocks (Table 4) indicate significantly lower concentrations than the commonly assumed 12.5 ± 0.5% (Huntley and Baril, 1997) for alkali feldspars.

#### 3.4. Fitting of luminescence-depth profiles

We fitted the luminescence-depth profiles in R v. 3.6.1 with the *nls* function from the *stats* package (R. Core Team, 2019). We applied the model (Table 5) developed by Freiesleben et al. (2015) to discern between exposure and burial events in our luminescence-depth profiles. The model uses the luminescence intensity (*L*), the saturated luminescence intensity (*L*<sub>0</sub>), and the light attenuation coefficient (*μ*). Also, the model includes the exposure time (*t*<sub>e</sub>) and the subsequent burial time (*t*<sub>b</sub>). The rate of electron trapping:  $F(x) = \frac{D}{D_0}$  is included in the model, in which *D* is the effective dose rate at depth *x*, and *D*<sub>0</sub> is the characteristic dose. Average IRSL<sub>50</sub> luminescence-depth profiles were calculated from the individual cores. Individual *μ* values were determined for each surface by fitting; this, to allow for spatial variations of mineralogy within each of the cobbles. The sample-dependent average *D*<sub>0</sub> was constrained by exponential fitting of growth curves (highest irradiated dose >2800 Gy) and is assumed to be constant for all cores. The parameter *σφ*<sub>0</sub> describes the rate of emptying of traps based on the product of the photon flux and the photoionisation cross-section for *x* = 0. Since no exposure age calculations were attempted through fitting, *σφ*<sub>0</sub> was combined with *t*<sub>e</sub>. No weights were applied during fitting. Fitting param are reported in Table 6 and fitting residuals are presented in Fig. C.3 (Appendix).



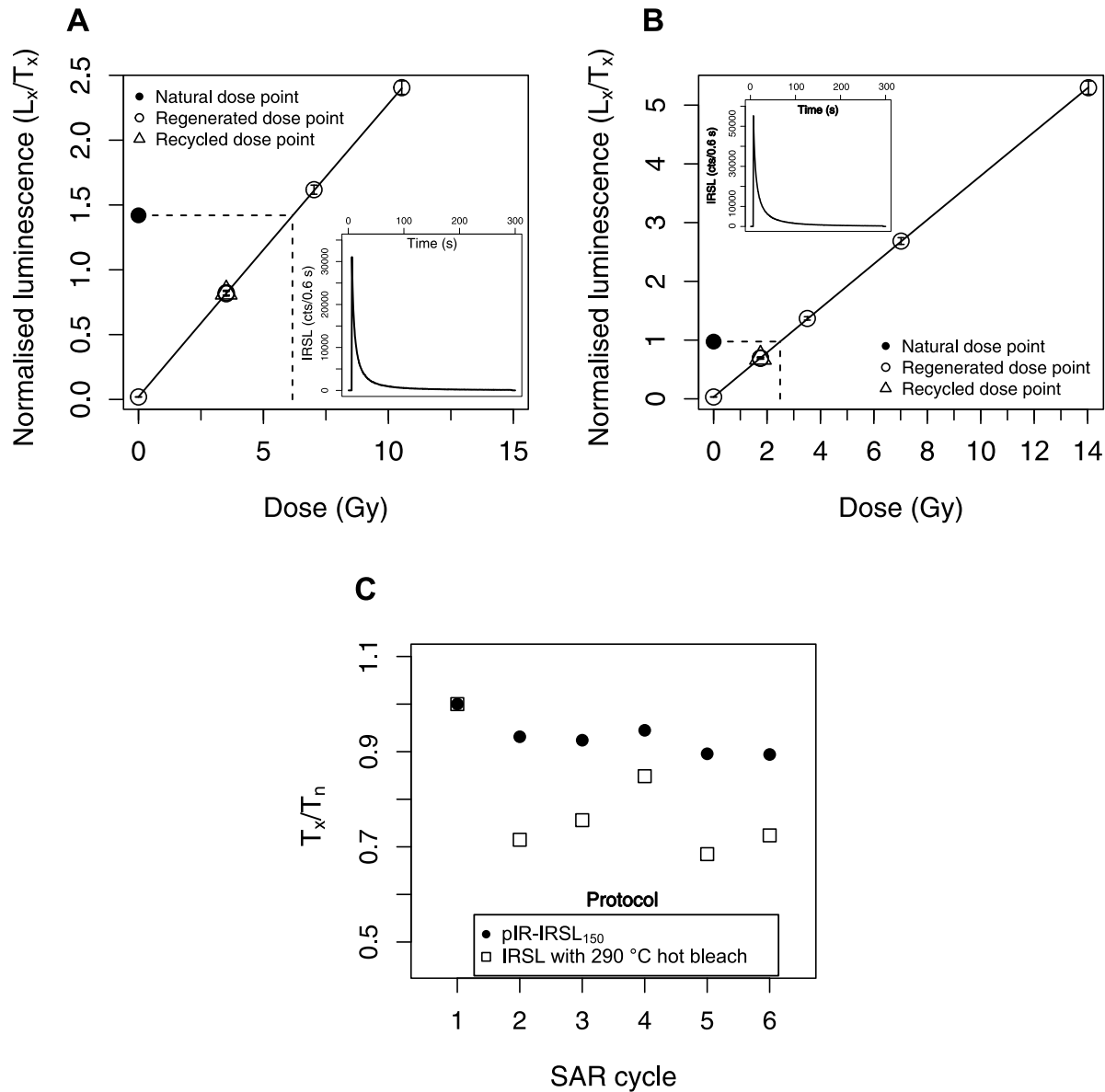


**Fig. 3.** Representative dose response curves for (A) MZ051S-2 (paragneiss) at ~12 mm depth from the top surface, and (B) MZ051S-3 (orthogneiss) at ~3 mm depth from the bottom surface. The insets show the natural IRSL<sub>50</sub> decay curve for the same slices. (C) Comparison of test dose response ( $T_x/T_n$ ) from a paragneiss rock from Val di Sole, measured over several SAR cycles. The low-temperature pIR-IRSL protocol show significantly less change in test dose sensitivity, compared to an IRSL protocol with a hot bleach at the end of each cycle.

**Table 5**

Model developed by Freiesleben et al. (2015), used to fit burial and exposure events in the cobbles.

Event	Fitting model
Initial burial	$L_0(x) = 1$
First exposure E1	$L_1(x) = L_0(x)e^{-t_{e1}\sigma\varphi_0e^{-\mu x}}$
First burial B1	$L_2(x) = (L_1(x) - 1)e^{-F(x)t_{b1}} + 1$
Second exposure E2	$L_3(x) = L_2(x)e^{-t_{e2}\sigma\varphi_0e^{-\mu x}}$

### 3.5. Age calculations

The burial age can be calculated by either deriving the  $t_b$  parameter from the modelled exposure history of each rock surface (e.g., Freiesleben et al., 2015; al Khasawneh et al., 2019) or by estimating the burial dose by measuring  $D_e$  in slices from depths in which the signal was reset prior to burial (e.g., al Khasawneh et al., 2019;

Rades et al., 2018; Sohbati et al., 2015). For our cobbles, we only consider the second approach reliable because we cannot detach the  $t_e$  and  $\sigma\varphi_0$  parameters, we have significant intra-core variations in our luminescence-depth profiles, and, as noted by al Khasawneh et al. (2019),  $t_b$  uses average  $D_0$  values rather than individual  $D_0$  values derived from dose–response curves from individual slices.

Instead, we calculated burial ages (ka before AD 2018) by dividing arithmetic mean  $D_e$  values derived from measuring slices/chips with depth-corrected dose rates. To identify which depths were suitable to use for  $D_e$  calculations (i.e. the slices had been sufficiently reset before burial), we applied the approach described by al Khasawneh et al. (2019). They proposed using the modelled luminescence-depth profiles to calculate a ratio between the pre-burial (E1; Table 5) and burial profiles (B1; Table 5). This ratio ( $E1/B1$ ) represents the proportion of the burial dose, which is a pre-burial dose residual. Significant proportions of pre-burial dose indicate insufficient bleaching, which is undesirable for dating. We consider depths for which pre-burial dose

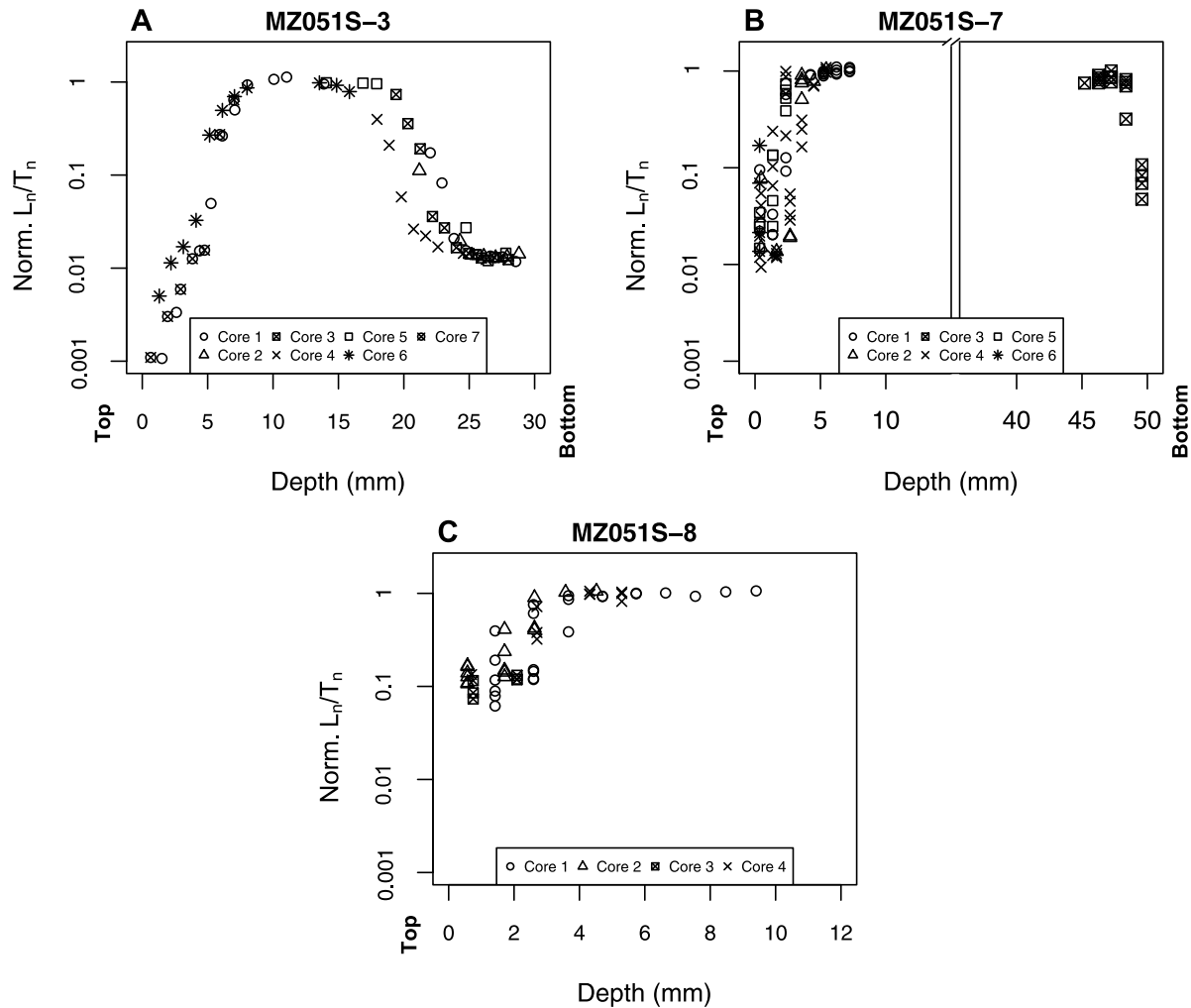


**Fig. 4.** IRSL<sub>50</sub> luminescence-depth profiles from individual cores from MZ051S-3 (A), MZ051S-7 (B), and MZ051S-8 (C). All data points represent one chip or slice. The IRSL<sub>50</sub> data are derived from IRSL stimulation at 50 °C in a pIR-IRSL<sub>150</sub> protocol. An overview of the measurement protocols is available in Table 3. The  $L_n/T_n$  data are normalised by the mean  $L_n/T_n$  data derived from the saturated dose plateau from the centre of the cobbles. The vertical axes of are plotted in logarithmic scale.

was modelled to constitute  $\leq 1\%$  ( $E1/B1 \leq 0.01$ ) of the burial dose to have been fully reset. Therefore, burial ages were calculated from slices that were extracted from such depths. All luminescence ages are reported with 1- $\sigma$  errors and measurement uncertainties.

### 3.6. Fading corrections

Anomalous fading (Wintle, 1977; Spooner, 1994) was measured using two different approaches. The first is the standard approach (Aucclair et al., 2003) for sediment dating of feldspars, during which samples are irradiated and preheated in the laboratory, and the signal intensities are measured after different storage periods. For each cycle, the slices were irradiated with  $\sim 8.9$  Gy and storage periods ranged between prompt (i.e. no pause) to  $\sim 17$ –33 h. For MZ051S-7, we added a measurement of signal loss after approximately 7 months of storage. Three slices per cobble were measured and cobble-specific, mean g-values were calculated from the results with the *analyseFadingMeasurement* function (Kreutzer and Burow, 2020) in R. The mean g-values<sub>2days</sub> were calculated to  $2.12 \pm 0.67$ ,  $2.74 \pm 0.57$ ,  $4.61 \pm 0.35$  and  $1.16 \pm 0.58$  %/decade for MZ051S-2, MZ051S-3, MZ051S-7 and MZ051S-8, respectively (Fig. C.4, Appendix). Also, we measured g-values for four slices (storage up to 8 months) for the pIR-IRSL<sub>290</sub> protocol applied to MZ051S-2 (fading =  $1.63 \pm 0.51\%$ /decade). Ages were subsequently corrected using the procedure of Huntley and Lamothe (2001) with the R function *calcFadingCorr* (Kreutzer, 2020).

The second approach uses the ratio between the intensity of the field saturation levels from the centre of the cobbles and the laboratory saturation level to correct for signal fading (Rades et al., 2018). The rationale behind this approach is that the field saturated signal should be in saturation; hence, the difference between the field saturated signal and the signal irradiated to saturation in the laboratory is assumed to arise from fading. The normalised natural signal ( $L_{nat}$ ) and the saturated laboratory doses ( $L_{sat}$ ) were measured for three slices per rock (doses  $>2800$  Gy), and the average ratios were used to correct ages. The fading ratios  $L_{nat}/L_{sat}$  are  $0.57 \pm 0.07$  for MZ051S-3,  $0.44 \pm 0.10$  for MZ051S-7, and  $0.52 \pm 0.09$  for MZ051S-8. This approach did not apply to MZ051S-2 since no slices were in saturation (see Section 4.1). Thus, for MZ051S-2, we were restricted to use only the conventional approach for fading correction since we lacked a field saturated signal to compare with.

## 4. Luminescence-depth profiles and burial ages

### 4.1. Luminescence-depth profiles

Here, we present IRSL<sub>50</sub>  $L_n/T_n$  data from individual cores as luminescence-depth profiles (Figs. 4 and 5). The depth of resetting of the IRSL<sub>50</sub> signal in the cobbles varies between different cobbles and surfaces. The luminescence-depth profiles from MZ051S-3 (Fig. 4A) demonstrate significantly larger  $L_n/T_n$  values at the centre, compared

**Table 6**

The parameters acquired from fitting luminescence-depth profiles.

Cobble	Surface	$D_0$ (Gy)	$\mu$ (mm <sup>-1</sup> )	$t_{e1}\sigma\varphi_0$	$t_{e2}\sigma\varphi_0$	$t_b$ (ka)
MZ051S-3	Top	430 ± 30	0.91 ± 0.16	250 ± 261	4 ± 24	2 ± 5
MZ051S-3	Bottom	430 ± 30	0.65 ± 0.07	872 ± 699		2 ± 2
MZ051S-7	Top	615 ± 23	0.86 ± 0.13	10 ± 4		7 ± 9
MZ051S-7	Bottom	615 ± 23	1.18 ± 0.30	4 ± 2		
MZ051S-8	Top	467 ± 19	0.93 ± 0.20	9 ± 5		35 ± 17

to the top or bottom surface. The signal in the outer millimetres at the top surface has been bleached to <1% of the level measured in the centre of the cobble (field saturation). At ~2 mm (core 6) or 3.5 mm (core 7) of depth,  $L_n/T_n$  is >1%.  $L_n/T_n$  increases deeper into the cobble until field saturation is reached at ~7.5 mm of depth. At the bottom surface of MZ051S-3, all cores demonstrate a  $L_n/T_n$  plateau at between 1%–2% of field saturation until ~5 mm (25–30 mm in Fig. 4A) of depth. Between ~5–10 mm of depth (20–25 mm in Fig. 4A)  $L_n/T_n$  rises towards field saturation. Here, the luminescence-profiles differ between some of the cores; most notably the deeper bleaching front of core 4 compared to the other cores, and the shallower bleaching front of cores 1 and 5 compared to cores 2 and 3. At the top surface, cores 6 and 7 also demonstrate some scatter at ~2–5 mm of depth. The luminescence-depth profiles (IRSL<sub>50</sub> data) from MZ051S-7 (Fig. 4B) demonstrate more shallow resetting compared to MZ051S-3. The luminescence-depth profiles for MZ051S-7 are mostly based on measurements of chips, not on whole slices, and these measurements demonstrate considerable intra-core variations between chips from the same depth within a single core. The bleaching front is shallow at the top surface since  $L_n/T_n$  is only below field saturation in the outer ~4 mm of the rock. At the bottom surface, field saturation is reached already in the second slice. The surface slice at the bottom has a  $L_n/T_n$  of ~8% of field saturation. In the top surface of MZ051S-8,  $L_n/T_n$  (Fig. 4C) increases from the surface, until ~4 mm of depth. Like for MZ051S-7, the luminescence-depth profiles of MZ051S-8 are mostly based on chips, which demonstrate similar intra-core variations. At the top surface of MZ051S-2,  $L_n/T_n$  (Fig. 5) from IRSL<sub>50</sub> measurements increases without any obvious plateau from the surface until ~5 mm of depth. Here,  $L_n/T_n$  plateaus, through the entire remaining depth of the cobble, until the bottom surface. The  $L_n/T_n$  values from this plateau are surprisingly low, considering the thickness (70 mm) of MZ051S-2. Despite using a test dose of only ~4.3 Gy, the maximum  $L_n/T_n$  for the IRSL<sub>50</sub> signal we observe in any slice at any depth is < 3.0. The arithmetic mean  $L_n/T_n$  from this plateau is ~1.3; assuming that field saturation  $L_n/T_n$  (measured with the same test dose) from the lithologically similar MZ051S-7 is applicable to MZ051S-2, then this is only ~4% of the expected  $L_n/T_n$  if MZ051S-2 had a saturated signal plateau. Due to the lack of a saturated signal level, Fig. 5 is plotted without any normalisation. We measured  $L_n/T_n$  for the optically more stable pIR-IRSL<sub>290</sub> signal in four slices from the bottom surface, and seven slices from the centre of MZ051S-7. Overall, these  $L_n/T_n$  values are comparable (Fig. 5) to those determined from IRSL<sub>50</sub> measurements.

#### 4.2. Fitting

Here, we present fitting of averaged luminescence-depth profiles (for the IRSL<sub>50</sub> signal) (Fig. 7) and their corresponding model parameters (Table 6). No fitting is attempted for MZ051S-2 since  $L_0(x)$  is not known for this cobble. The top surface for MZ051S-3 is best fitted with two exposure events ( $E1_{top}$  and  $E2_{top}$ ), separated by a burial event ( $B1_{top}$ ). The bleaching front of  $E1_{top}$  appears to have reached ~4 mm of depth before burial during  $B1_{top}$ . The second exposure event  $E2_{top}$  appear to be shorter than  $E1_{top}$ , and only the outer ~2.5 mm appear to have been affected. The fitting of the bottom surface is challenging due to the large inter-core variations in  $L_n/T_n$  at depths >5 mm. Visual inspections of the luminescence-depth profiles from the individual cores

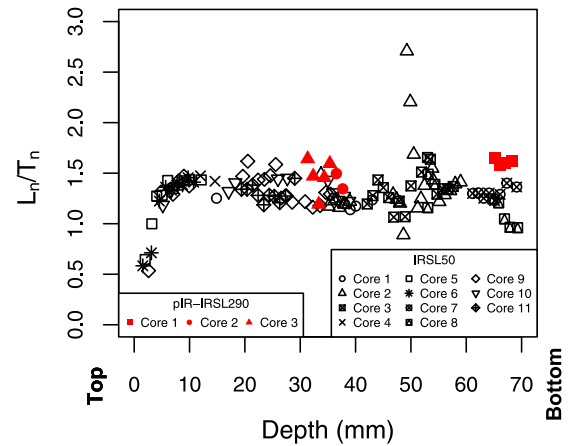


**Fig. 5.** IRSL<sub>50</sub> and pIR-IRSL<sub>290</sub> luminescence-depth profiles from individual cores from MZ051S-2. All data points represent one slice. The IRSL<sub>50</sub> data are derived from IRSL stimulation at 50 °C in a pIR-IRSL<sub>150</sub> protocol (Table 3). 97% of the slices from the plateau (5–70 mm of depth) are within 2σ of the mean. These  $L_n/T_n$  are not normalised (test dose ~4.3 Gy) and are plotted on a linear vertical axis. The pIR-IRSL<sub>290</sub> data are derived from additional slices, which were stimulated at 290 °C after an initial stimulation at 50 °C (Table 3).

clearly show a single exposure event, followed by a single burial event. Keeping this in mind, we fit the averaged luminescence-depth profile for the bottom surface for a single exposure event ( $E1_{bottom}$ ) and for a single burial event ( $B1_{bottom}$ ) despite the poor fit at depths >6 mm from either surface (Fig. C.3, Appendix). The bleaching front of  $E1_{bottom}$  reset the signal <1% of  $L_0(x)$  to ~7 mm of depth from the bottom surface. While there is no ambiguity regarding the thoroughness of resetting on the bottom surface of MZ051S-3, the ratio  $E1_{bottom}/B1_{bottom}$  (Fig. 7A2) show that  $B1_{bottom}$  contains no significant pre-burial dose at depths between ~23–30 mm. The severe resetting (<1%) of the IRSL<sub>50</sub> signal in the top surface of MZ051S-3 suggests that no burial age can be calculated from  $D_e$  values from slices located at <3 mm of depth. However, since the fitting indicates the presence of a weak burial plateau between 3 mm and 4 mm we will proceed to use  $D_e$  values from slices extracted from this depth to calculate a burial age for  $B1_{top}$ . The top surface of MZ051S-7 has been fitted for an exposure event ( $E1_{top}$ ), followed by a burial event ( $B1_{top}$ ). While the observed signal plateau at this surface is very short, the IRSL<sub>50</sub> signal appears to have been sufficiently reset during  $E1_{top}$  to create a bleaching front which reached >0.5 mm. The ratio  $E1_{top}/B1_{top}$  (Fig. 7B.2) shows that <1% of the observed dose was present before burial. Thus, despite the weak signal plateau of only 2 mm, we proceed to calculate a burial age from the top surface of MZ051S-7. The modelled pre-burial luminescence-depth profile from the bottom surface predicts that signal resetting was insufficient the last time this surface was exposed to create a bleaching front even at the very surface of the cobble. This suggests that no information regarding the last burial is available from the bottom surface of MZ051S-7. For MZ051S-8 (Fig. 7C.1), we fit the top surface for an exposure event ( $E1_{top}$ ) and a subsequent burial event ( $B1_{top}$ ). Sufficient bleaching appears to have occurred during  $E1_{top}$  to reset the IRSL<sub>50</sub> signal beneath the surface. The subsequent  $B1_{top}$  event should therefore date the last burial of this rock surface. The  $E1_{top}/B1_{top}$  ratio from the fitting (Fig. 7C.2) indicates that ~1% of the observed dose is

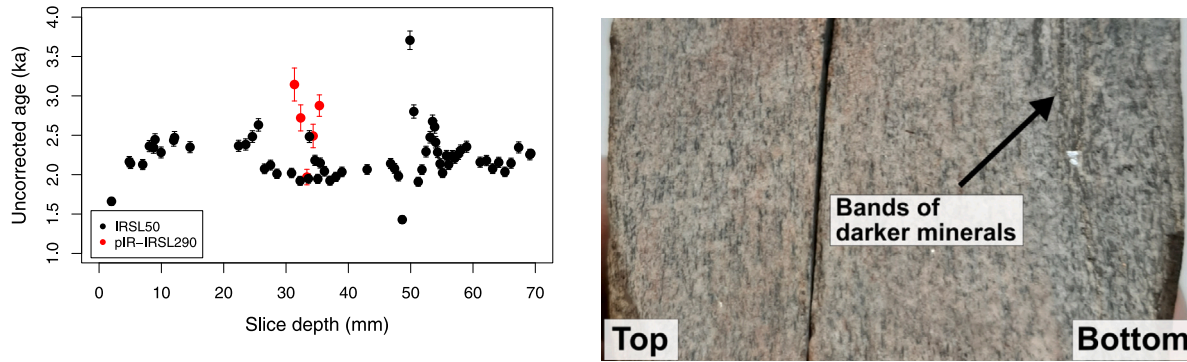


**Fig. 6.** (Left) IRSL<sub>50</sub> and pIR-IRSL<sub>290</sub> ages, calculated throughout cobble MZ051S-2 ( $n=1$ ). The ages have not been corrected for fading. The error bars represent uncertainties from  $D_e$  and dose rate measurements. (Right) cross-cut of MZ051S-2 along the cored axis. Approximately 0.5 mm of the rock is missing due to a previous cut across the cored axis. The scatter in the age data around 50 mm of depth appear to coincide with a band of dark minerals.

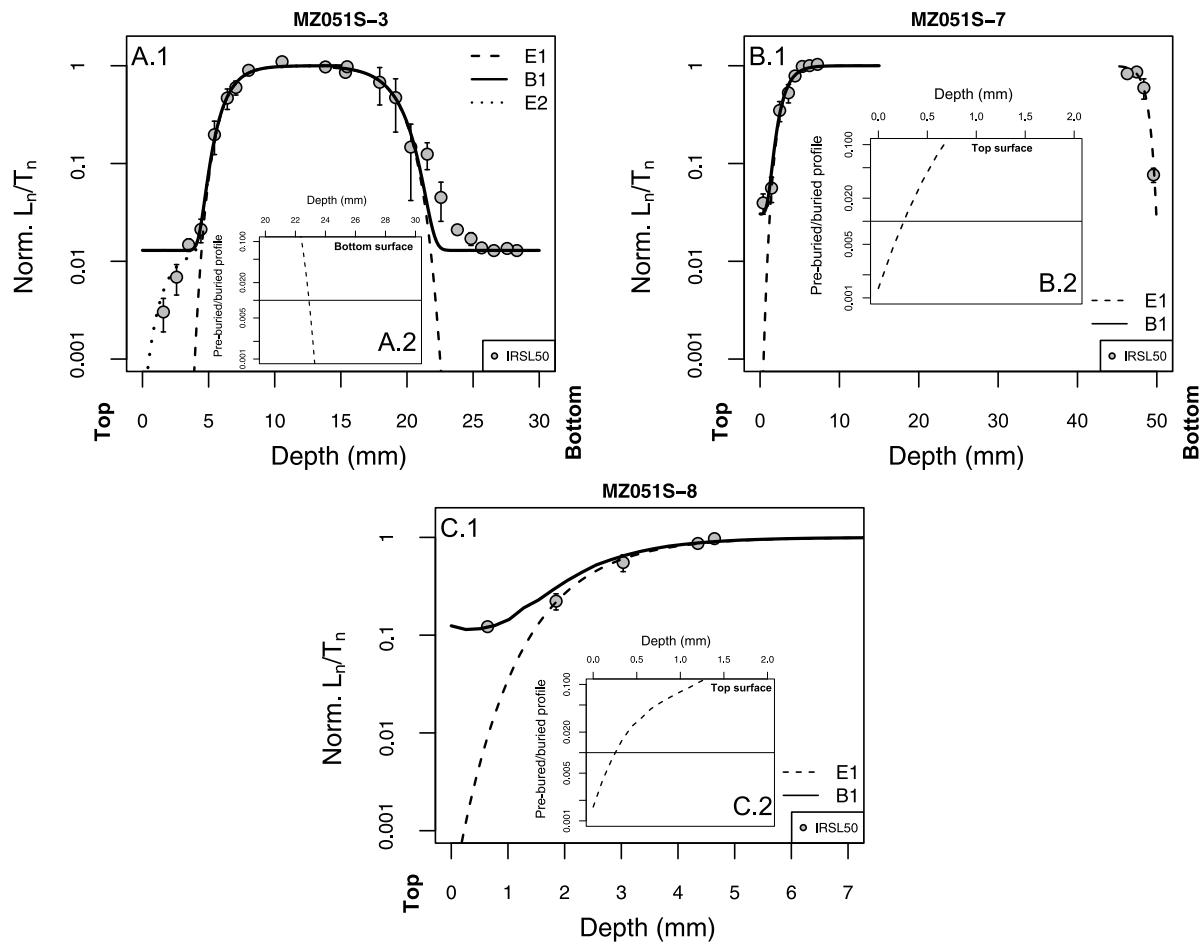


**Fig. 7.** Averaged ( $n \geq 2$ ) IRSL<sub>50</sub> luminescence-depth profiles and their corresponding fits with the Freiesleben et al. (2015) model from MZ051S-3 (A), MZ051S-7 (B), and MZ051S-8 (C). The normalised sensitivity-corrected luminescence signals ( $L_n/T_n$ ) are plotted in logarithmic scale. The dashed lines in the insets show the ratios (E/B) between modelled exposure events (E) and modelled burial event (B) with depth.

pre-burial in the surface slice. Therefore, a burial age from the surface slices should not be affected by inherited dose from a previous event.

#### 4.3. Burial ages

Burial ages for the four cobbles are presented in Table 7. Considering the similarity in  $L_n/T_n$  in the non-saturated plateau ( $\sim 5$ – $70$  mm) in MZ051S-2, we interpret this to represent an isochronous resetting event which can be dated using SAR protocols (Table 3). Since this plateau is manifested over significant depth-distances in the cobble ( $\sim 65$  mm),

we would expect the effective dose rate to vary between some of the slices. Therefore, we calculate the age for each slice individually before averaging the age over the entire plateau, instead of using the approach described in Section 3.5. For the IRSL<sub>50</sub> signal, we calculate an arithmetic mean age from 62 slices collected varying depths of the plateau (Fig. 6A). The same approach was used to calculate pIR-IRSL<sub>290</sub> ages from five additional slices (Fig. 6A). The IRSL<sub>50</sub> uncorrected ages throughout this signal plateau range between 1.4 and 4.6 ka, with an arithmetic mean age estimate of  $2.23 \pm 0.61$  ka. The uncorrected pIR-IRSL<sub>290</sub> ages range between 2.00 and 3.19 ka, with the arithmetic mean

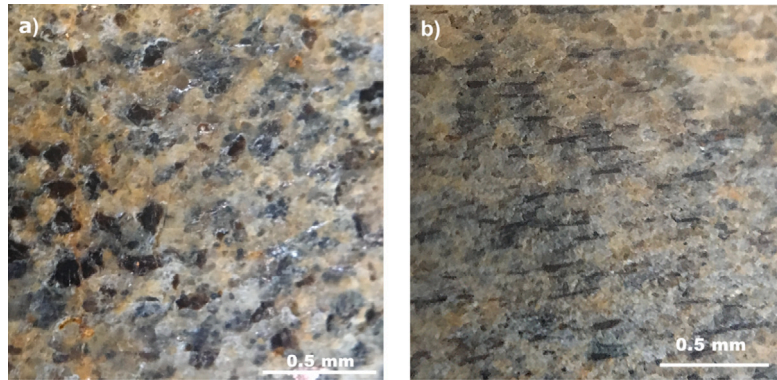


Fig. 8. The mica grains in the paragneisses in Val di Sole show distinct foliation. The readers view direction is perpendicular onto (a), and parallel to (b) the metamorphic foliation.

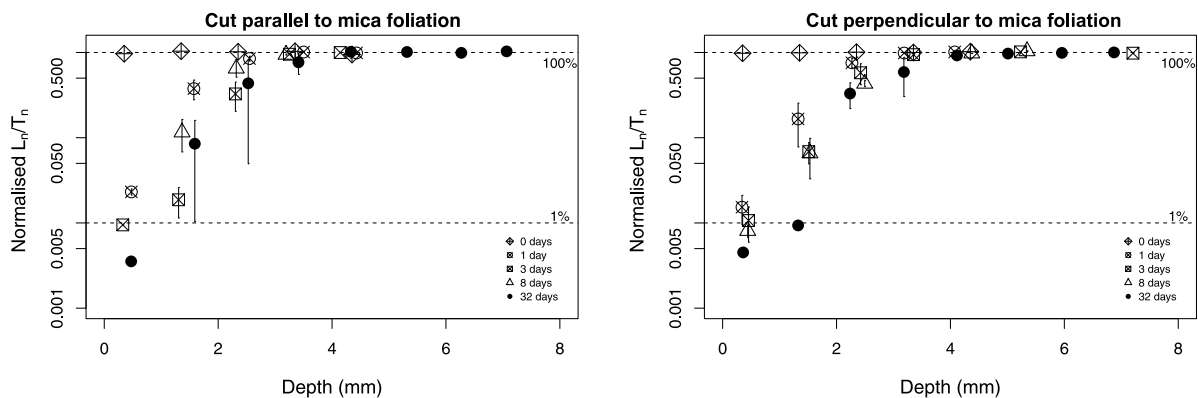


Fig. 9. The luminescence-depth profiles ( $n=2$ , except for 0 days for which  $n=1$ ) from MZ051S-7, measured in fresh rock surfaces which had been exposed on a rooftop in Cologne, Germany for: 0, 1, 3, 8, and 32 days. The cores were extracted from surfaces which were cut parallel (left) and perpendicular (right) to the mica foliation. The error bars represent  $1\sigma$ . The dashed lines represent 1% and 100% of the saturated  $\text{IRSL}_{50}$  intensity  $L_0$ , respectively.

age estimate of  $2.68 \pm 0.55$  ka. Fading correction with  $g$ -values (Auclair et al., 2003; Huntley and Lamothe, 2001), yield corrected ages of  $2.64 \pm 0.75$  ka (1370 BC–130 AD) and  $3.03 \pm 0.67$  ka (1680–340 BC) for the  $\text{IRSL}_{50}$  and  $\text{IRSL}_{290}$  protocols, respectively. The luminescence-depth profile from the outer  $\sim 4$  mm of the top surface of MZ051S-2 (Fig. 4A) indicates that some resetting of the signal has occurred after the previously described resetting event. We measured the  $D_e$  of one slice from  $\sim 2$  mm depth to date this event. The resulting  $\text{IRSL}_{50}$  age estimate for this slice yields an uncorrected burial age of  $0.85 \pm 0.10$  ka and a corrected burial age of  $1.00 \pm 0.13$  ka (890–1150 AD). We calculate the burial age from two slices (3–4 mm of depth) from the top surface of MZ051S-3 which yields an uncorrected arithmetic mean age of  $1.08 \pm 0.08$  ka. For the bottom surface, we calculate the arithmetic mean  $\text{IRSL}_{50}$  age of five slices from  $\sim 2$  mm of depth. The uncorrected mean age is  $0.86 \pm 0.05$  ka. When corrected with the measured  $g$ -value, the top surface dates to  $1.34 \pm 0.13$  ka (550–810 AD), and the bottom surface dates to slightly younger:  $1.05 \pm 0.09$  ka (880–1060 AD). Fading corrections with the  $L_{\text{nat}}/L_{\text{sat}}$  fading ratio yields older ages of  $1.90 \pm 0.24$  ka (120 BC–360 AD) for the top surface and  $1.51 \pm 0.18$  ka (330–690 AD) for the bottom surface. For MZ051S-7, we calculate a burial  $\text{IRSL}_{50}$  age by measuring  $D_e$  measurements on three intact surface slices. Age calculations yield an uncorrected burial age of  $2.19 \pm 0.24$  ka. Again, the fading-corrected ages vary depending on which fading correction method we apply. Fading correction with  $g$ -value yields an age of  $3.11 \pm 0.37$  ka (1460–720 BC), compared to the considerably older age of  $4.99 \pm 0.51$  ka (3480–2460 BC) with the  $L_{\text{nat}}/L_{\text{sat}}$  ratio correction method.  $D_e$  measurements from 12 surface chips from the top surface of MZ051S-8 yield an uncorrected arithmetic mean age of  $16.9 \pm 1.9$  ka; much older than the expected age. Fading correction with  $g$ -value increases the age estimate to  $18.7 \pm 2.3$  ka.

Correcting the age estimate with  $L_{\text{nat}}/L_{\text{sat}}$  ratio increases the age further to  $38.3 \pm 9.7$  ka.

## 5. Bleaching experiment

The results presented in Section 4 show that while at least some resetting has occurred in all cobbles, the bleaching fronts, especially for MZ051S-7 and MZ051S-8, are shallow. The  $E1_{\text{top}}/B1_{\text{top}}$  ratios for both these cobbles indicate that the pre-burial dose constitutes significant proportions of the buried dose already at 0.5 mm of depth (see insets in Fig. 7B–C). We would expect deeper bleaching in rock surfaces that should have experienced significant exposure. One possible explanation for these shallow bleaching fronts is erosion. While erosion of rock surfaces has been shown to affect the depth of the bleaching front (Sohbati et al., 2018; Lehmann et al., 2020), in the given case, we cannot quantify erosion rates since we lack independent dates for how long these surfaces were exposed before burial. An alternative explanation for shallow depth-profiles is strong attenuation of light due to lithological parameters (e.g., Ou et al., 2018). We investigate the effect of light penetration on the resetting of the  $\text{IRSL}_{50}$  signal in MZ051S-7 and which potential effect the mineral orientation may have on the rate of resetting. The paragneisses from Val Poré have a distinct orientation of mineral foliation (Fig. 8), and dark mica minerals are common. The occurrence of dark minerals has shown to block the bleaching of the luminescence signal in minerals beneath (Meyer et al., 2018). Visual inspection of a thin section from a paragneiss from the relevant geological unit clearly shows mica grains surrounding the more translucent quartz and feldspar grains (Fig. B.2, Appendix). If the attenuation of light penetration into the rock is weaker at surfaces with planes perpendicular to the foliation (with a lower surface area



Table 7

Summary of uncorrected and fading corrected IRSL<sub>50</sub> ages, number of slices used for age estimation (n), dose rate for surface slices, normalised g-values, and  $L_{nat}/L_{sat}$  ratios.

Sample	Protocol	Part of rock	Dose rate surface slice (Gy ka <sup>-1</sup> ) <sup>a</sup>	g-value <sub>2days</sub> (%/decade)	Fading ratio <sup>b</sup>	Mean D <sub>e</sub> (Gy) <sup>c</sup>	n	Uncorr. age (ka)	Corr. age <sup>d</sup> (ka)	Corr. age <sup>e</sup> (ka)	Corr. age <sup>d</sup> (AD/BC)	Corr. age <sup>e</sup> (AD/BC)
MZ051S-2	IRSL <sub>50</sub>	Top	2.74 ± 0.06	2.05 ± 0.55		2.28 ± 0.05	1	0.85 ± 0.10	1.00 ± 0.13		890–1150 AD	
MZ051S-2	IRSL <sub>50</sub>	Centre-bottom	2.74 ± 0.06	2.05 ± 0.55		5.93 ± 1.19	62	2.23 ± 0.61	2.64 ± 0.75		1370 BC–130 AD	
MZ051S-2	pIR-IRSL <sub>290</sub>	Centre	2.74 ± 0.06	1.63 ± 0.51		7.11 ± 1.38	5	2.68 ± 0.55	3.03 ± 0.67		AD	1680–340 BC
MZ051S-3	IRSL <sub>50</sub>	Top	2.85 ± 0.06	2.74 ± 0.57	0.57 ± 0.07	3.03 ± 0.21	2	1.08 ± 0.08	1.34 ± 0.13	1.90 ± 0.24	550–810 AD	120 BC–360 AD
MZ051S-3	IRSL <sub>50</sub>	Bottom	2.85 ± 0.06	2.74 ± 0.57	0.57 ± 0.07	2.41 ± 0.13	5	0.86 ± 0.05	1.05 ± 0.09	1.51 ± 0.18	880–1060 AD	330–690 AD
MZ051S-7	IRSL <sub>50</sub>	Top	2.73 ± 0.06	4.61 ± 0.34	0.44 ± 0.10	5.98 ± 0.54	3	2.19 ± 0.24	3.11 ± 0.37	4.99 ± 0.51	1460–720 BC	3480–2460 BC
MZ051S-8	IRSL <sub>50</sub>	Top	1.91 ± 0.06	1.16 ± 0.58	0.52 ± 0.09	27.67 ± 2.26	12	16.87 ± 1.90	18.66 ± 2.34	38.33 ± 9.72		

<sup>a</sup>Integrated over 0 to 0.7 mm of depth.<sup>b</sup>Fading ratio ( $L_{nat}/L_{sat}$ ).<sup>c</sup>Errors include standard error (1σ) and measurement uncertainties.<sup>d</sup>Fading correction with g-value (Huntley and Lamothe, 2001).<sup>e</sup>Fading correction calculated by dividing uncorrected age by fading ratio.

covered by mica minerals), then these surfaces should be targeted during sampling. Unbleached surfaces were exposed on a rooftop of the University of Cologne, Germany, during the summer of 2019. We sampled the exposed surfaces after 0, 1, 3, 8, and 32 days and subsequently measured the luminescence-depth intensity of two cores for each surface and each period of exposure (Fig. 9). The signal is, as predicted, in saturation throughout the cores that have not been exposed (0 days of exposure). The surface slices in all other cores have been bleached <5% of saturated IRSL.  $L_n/T_n$  is less than 1% in the surface slice after three days at the rooftop in optimal bleaching conditions (e.g., a fresh surface, many hours of daylight in sunny weather, and no coverage of sediments or lichen). After 32 days of exposure has  $L_n/T_n$  been reset to <0.5% of saturation at the surface. The IRSL<sub>50</sub> signal reaches 95% of field saturation between 3.2 mm (1 day of exposure) and 4.1 mm (32 days of exposure) of depth in the cores cut parallel to the foliation. This is similar to cores cut perpendicular to the foliation for which the signal reaches field saturation between 3.5 mm (1 day of exposure) and 4.3 mm (32 days of exposure). Our experiment shows that residual IRSL<sub>50</sub> signals in the surface slice in paragneiss rock surfaces from Val di Sole can be expected to be beneath 1% of field saturation after three days of exposure. Both surfaces did bleach during exposure; however, resetting appears to occur slightly quicker in the surface cut perpendicular to foliation. It is not possible, based on our experiment, to assert if the shallow bleaching profiles observed in the natural paragneisses are due to erosion or insufficient light penetration, but simulated profiles (Fig. 10) indicate that exposure periods longer than a decade would bleach the signal to 5 mm or more.

## 6. Discussion

### 6.1. Signal resetting in the cobbles

Rock surface luminescence dating of buried cobbles is only possible if the luminescence signals can be reset during exposure to light or heat. A previous study by Ou et al. (2018) demonstrated little or no depletion in IRSL<sub>50</sub> and pIR-IRSL signals in some lithologies during lengthy exposure. Three of the cobbles (MZ051S-3, MZ051S-7, MZ051S-8) presented in this paper demonstrate significantly lower (approximately one order of magnitude or more)  $L_n/T_n$  towards the edges of the cobbles, compared to their respective centres. This, together with the data presented in Fig. 9, shows that some resetting in the outer millimetres of our cobbles will occur if the surfaces are exposed for at least four weeks. The resetting appears to occur even quicker in MZ051S-3, based on the observed resetting ( $E2_{top}$ ) of the top surface, which we interpret to have occurred while the surface was exposed in the excavation; a reasonable assumption since the cobble was completely covered before being excavated. Overall, MZ051S-3 displays considerable inter-core variations for the depth of resetting. These variations become

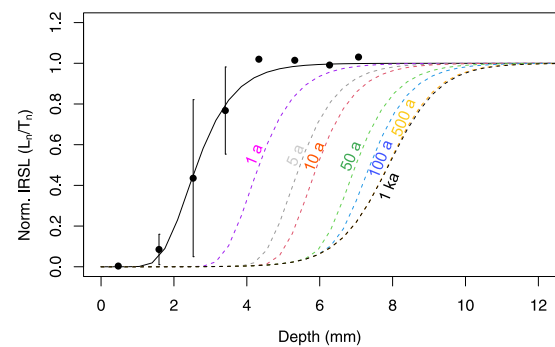


Fig. 10. Modelled luminescence-depth profiles, simulated (dashed lines) for different exposure durations for MZ051S-7. The parameters  $\mu$  ( $1.42 \pm 0.18 \text{ mm}^{-1}$ ) and  $\sigma\varphi_0$  ( $333 \pm 158 \text{ a}^{-1}$ ) were derived by fitting (solid line) the signal profile (non-weighted) from a surface exposed on the rooftop in Cologne (Fig. 9, 32 days of exposure of surface cut parallel to the mica foliation) with the model:  $L(x) = \frac{\sigma\varphi_0 e^{-\mu x} e^{-\frac{1}{\sigma\varphi_0} (\sigma\varphi_0 e^{-\mu x})^{1/2} + F(x)}}{\sigma\varphi_0 e^{-\mu x} + F(x)}$  developed by Sohbati et al. (2012c).  $F(x)$  was constrained as described in Section 3.4.

apparent when we fit the averaged luminescence-depth profiles with the Freiesleben et al. (2015) model. Fitting of an average luminescence-depth profile is challenging when fitted with average  $\mu$  and  $\sigma\varphi_0$  values since these parameters do not consider small-scale mineralogical variation or uneven spatial erosion of the rock surface. Spatially uneven light attenuation due to the presence of darker minerals is a problem in banded metamorphic rocks (Meyer et al., 2018); this is likely affecting our cobbles too.

The outer 0.5 mm from the top surface of MZ051S-7 appear to have been bleached before burial, which is demonstrated by the  $E1/B1$  ratio (Fig. 7B.2)  $\sim 0.01$ . This is a shallow luminescence-depth profile considering that simulated luminescence-depth profiles (Fig. 10) indicate that exposure periods longer than one year would bleach the signal 2 mm into the rock or more. While we cannot be certain regarding the length of exposure of the top surface from MZ051S-7, the formation of an A horizon (US5a) suggests extended exposure of this unit before being buried by colluvium. The luminescence-depth profile of MZ051S-8 displays a similar pattern with a short bleaching front. Erosion would likely have shortened the bleaching front of the luminescence-depth profile of these two cobbles if they were exposed for extended periods (e.g., one year or longer).

The measured chips from MZ051S-7 show significant intra-core variation for the luminescence intensity, for which the underlying reason is currently not understood. To circumvent the problem of intra-core variations, we exclusively derive the burial age of the top surface of MZ051S-7 from three intact surface slices. The bottom surface of

MZ051S-7 was insufficiently bleached or eroded before burial and thus, does not provide significant information regarding the cobble's history.

The lack of a saturated IRSL<sub>50</sub> (or pIR-IRSL) signal plateau throughout MZ051S-2 is an interesting and unexpected observation. The extensive period between the cooling of the minerals after the rock formation and sampling is well beyond the saturation limit for any luminescence signal, and thus, the electron traps in the mineral crystals in the centre of the rock must have been emptied during a later event. There is some scatter observed in the luminescence-depth profile, especially around 50 mm of depth (Fig. 4A). This area of scatter appears to coincide with a mineralogical change towards a more prominent foliation of dark minerals (Fig. 6). Possibly, these darker areas represent an area with a higher dose rate. It is unlikely that these outliers represent a different event than the other slices from the centre of MZ051S-2. None of them appears to be close to saturation, and they do not form a visible plateau. Hence, despite this scatter, we interpret the luminescence-depth profile presented in Fig. 4A as an isochronous dose plateau (excluding the top ~5 mm). Therefore, a resetting event must, at some point in the past, have depleted the luminescence signals throughout the entire cobble. Complete optical resetting of the luminescence signals throughout MZ051S-2 during light exposure is unlikely. When we model the rate of resetting of the IRSL signal in MZ051S-7 (i.e. a rock of similar lithology) with the model by [Sohbati et al. \(2012c\)](#), the simulated profiles indicate that optical resetting to the centre of the cobble is not possible (Fig. 10), even if the rock surface experienced no erosion during exposure. Furthermore, the resetting of the pIR-IRSL<sub>290</sub> signal within the centre of the cobble by optical resetting is even more unlikely, considering the hard-to-bleach character of the pIR-IRSL<sub>290</sub> signal demonstrated by laboratory bleaching experiments ([Kars et al., 2014](#)) and published pIR-IRSL<sub>290</sub>-depth profiles from cobbles ([Freiesleben et al., 2015](#)). In contrast, heat could effectively reset both the IRSL<sub>50</sub> and the pIR-IRSL<sub>290</sub> signals. Previous investigations of thermal stability of the IRSL<sub>50</sub> signal with pulse annealing ([Murray et al., 2009](#); [Li and Li, 2011b](#); [Thomsen et al., 2011](#)) have demonstrated that the IRSL<sub>50</sub> signal is thermally reset by short exposures (60 s or less) to temperatures >450 °C. Elevated temperature pIR-IRSL signals are more thermally stable ([Li and Li, 2011b](#); [Thomsen et al., 2011](#)), but do nevertheless deplete at temperatures >550 °C ([Thomsen et al., 2011](#)). A thermal reconstruction of a prehistoric hearth by [Brodard et al. \(2012\)](#) indicated that such a feature could reach temperatures >600 °C. No hearth has so far been discovered during excavations in Val Poré, but fire has likely been present at the site. This is demonstrated by the charcoal fragments and fire modified artefacts, collected from the archaeological units ([Angelucci et al., 2017](#)). While further investigations of the thermoluminescence characteristics of MZ051S-2 would be necessary to determine the duration and temperature of the heating events, the complete resetting throughout the cobbles would require extensive heat during longer periods, e.g., in a hearth, or, perhaps, during a forest fire. However, at our site, no other cobbles show any signs of resetting in the middle of the cobbles. The isolated observation of extreme resetting in MZ051S-2 indicates selective heating, unlikely to occur during a forest fire. Therefore, we find that the resetting of the centre-bottom part of MZ051S-2 is analogous to a heating event which most likely was induced by human activities at the site during the Late Bronze Age or during the Iron Age. We observe no signs of any subsequent resetting event on the bottom surface of the cobble, which indicates that the bottom surface did not see significant exposure following the heating. This interpretation implies lengthy exposure of the top surface of MZ051S-2 as part of the topsoil; such exposure should bleach to over 5 mm of depth as is indicated by the simulation exposure periods presented in Fig. 10. The bleached (and subsequently buried) profile at the top surface is, while deeper than the bleached profile of e.g., MZ051S-7, slightly shallower than expected for such a long exposure. Erosion is also here a likely but untested explanation.

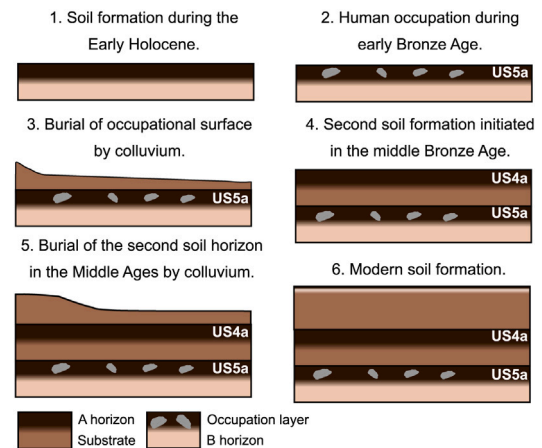


Fig. 11. Schematic illustration of the site formation of MZ051S, based on stratigraphy, radiocarbon dating (Table 1) and rock surface IRSL<sub>50</sub> dating (Table 7).

## 6.2. Fading estimates

For our cobbles, the application of g-value corrections ([Huntley and Lamothe, 2001](#)) yields significantly different ages compared to the  $L_{nat}/L_{sat}$  ratio ([Rades et al., 2018](#)). All conventional IRSL<sub>50</sub> g-values (~2–5%/decade) do not differ significantly to the average g-values reported by [Thomsen et al. \(2008\)](#) for potassium-rich ( $3.0 \pm 0.1\%$ /decade) and sodium-rich ( $3.1 \pm 0.2\%$ /decade) feldspar extracts from sediments of various geographical and sedimentological origins. The pIR-IRSL<sub>290</sub> signal from MZ051S-2 fades at a similar rate as is reported by [Sohbati et al. \(2013\)](#) for sodium-rich feldspars (~0.2–2.2%/decade) measured with a pIR-IRSL<sub>290</sub> protocol. The apparent thermal resetting of MZ051S-2 grants us the possibility to compare our g-value corrected IRSL<sub>50</sub> age with the uncorrected and corrected pIR-IRSL<sub>290</sub> ages. The IRSL<sub>50</sub> and pIR-IRSL<sub>290</sub> ages agree within uncertainties. This is encouraging, especially since our laboratory experiments with the pIR-IRSL<sub>290</sub> protocol show acceptable dose recovery. Previously, pIR-IRSL<sub>290</sub> dating of heated stones has been successfully compared to OSL dating of quartz ([al Khasawneh et al., 2015](#)), and pIR-IRSL<sub>290</sub> dating has repeatedly been demonstrated to be accurate when compared with other luminescence dating techniques or dating methods (e.g., [Buylaert et al., 2012](#); [Murray et al., 2014](#); [Klasen et al., 2018](#); [Zander et al., 2019](#)). Based on the agreement between the IRSL<sub>50</sub> and pIR-IRSL<sub>290</sub> in MZ051S-2 and previous successful applications of pIR-IRSL<sub>290</sub> dating, we propose that the g-value corrected ages in Table 7 are the preferred ages to use for chronostratigraphic interpretations. However, the extrapolation of this rationale to lithologies from other sites should be done with caution since [Rades et al. \(2018\)](#) have previously applied  $L_{nat}/L_{sat}$  ratio correction with success. When comparing both methods in their study, they received indistinguishable ages between g-value correction and  $L_{nat}/L_{sat}$  ratio for one boulder. For a second boulder, however, only the  $L_{nat}/L_{sat}$  ratio yielded a realistic age. The most appropriate fading correction approach could therefore vary between different lithologies, or be dependent on the size of the burial dose which is to be corrected; the latter since fading rates are expected to be higher for larger doses ([Huntley and Lian, 2006](#)). [Rades et al. \(2018\)](#) discussed that the  $L_{nat}/L_{sat}$  ratio represents an upper limit for fading estimates. If so, the  $L_{nat}/L_{sat}$  approach may be more suitable to older samples with luminescence intensities closer to saturation, compared to the [Huntley and Lamothe \(2001\)](#) approach which is more reliable in the lower dose range.

## 6.3. Chronostratigraphy

The burial age of ~19 ka derived from cobble MZ051S-8 is clearly not associated with the occupation of MZ051S, but rather dates a

burial event during the glaciation/deglaciation cycles in the Upper Pleistocene. Radiocarbon dating of soil organic matter and  $^{10}\text{Be}$  cosmogenic nuclide dating from the adjacent Val di Rabbi shows cycles of ice retreat and advances which started  $\sim 18$  ka cal. BP (Favilli et al., 2009). It is, therefore, possible that MZ051S-8 would have been exposed and subsequently buried during the early phase of deglaciation. More samples, preferably from primary depositions, are needed to verify such an event. We also cannot exclude that erosion has removed the more recent exposure history of the cobble. Charcoal fragments from Alpine soils (1800–2200 m above sea level) in Val di Sole have been dated to the early Holocene ( $\sim 8900$ – $8200$  BC), which is a clear indication that at this time, the area was deglaciated and post-glacial soil formation had begun (Favilli et al., 2010). Soil formation in the Early Holocene has been confirmed by radiocarbon dating of charcoal ( $\sim 6550$ – $6450$  cal. BC) from the adjacent tributary valley of Val Molinac, and slightly later ( $\sim 4600$ – $4500$  and  $\sim 4800$ – $4700$  cal. BC) also in Val Poré (Angelucci and Carrer, 2015). It is, therefore, well-established that the landscape in Val Poré remained relatively stable during the early and middle Holocene, which would have enabled soil formation (Fig. 11.1).

The previously reported, first known human occupation in Val Poré, dated to 1880–1691 BC (Angelucci et al., 2017), is confirmed by the new radiocarbon ages (COL6512.1.1:  $\sim 1750$ – $1450$  BC; COL6513.1.1:  $\sim 2100$ – $1750$  BC) from unit US5a at MZ051S (Fig. 11.2). These ages (together with radiocarbon age DSH6955 and the archaeological evidence) demonstrate that human groups occupied the Holocene topsoil during the Early Bronze Age. The occupied surface was subsequently buried by colluvium, deposited during a short period of reactivation of slope dynamics due to geomorphological instability (Fig. 11.3). The timing of such activities and the subsequent formation of US4a is currently not fully constrained. The previously published radiocarbon age DSH6956 ( $\sim 1550$ – $1450$  cal. BC) from US4a pinpoints the occurrence of human activities in the area during the Middle Bronze Age (Angelucci et al., 2017) and the possible reoccupation of MZ051S during this period. Logically, the top surface of cobble MZ051S-7 (collected from US5a) should represent the burial of US5a, i.e. the onset of deposition of colluvium, and should therefore pre-date US4a. However, the burial age (1460–720 BC) of MZ051S-7 is slightly younger than DSH6956 at  $1\sigma$ . This chronological inconsistency is not yet resolved. Although the reworking of sample DSH6956 from US5a is a possibility (which could result in age overestimation), the stratigraphic evidence suggests that the top surface of MZ051S-7 was exposed even after the deposition of the colluvium superimposing US5a. It is, therefore, our current interpretation that MZ051S-7 slightly underestimates the burial age of US5a. We consider the likeliest explanation for this to be the continued exposure of the top surface of MZ051S-7, even after the deposition of colluvium. The thinning of colluvium further away from the slope (where MZ051S-7 was collected) suggests that the explanation of a slightly protruding top surface of MZ051S-7 is quite likely. Additional age estimates from cobbles from US5a, combined with detailed observation of the vertical position of their top surface, could in the future help to establish the time of burial of US5a with more confidence; a re-interpretation of the onset of slope activities and the chronostratigraphic implication for MZ051S-7 might then be necessary.

Our dating efforts indicate that US4a remained exposed for a considerable time (Fig. 11.4), perhaps more than a millennium, before the reactivation of the nearby slope (Fig. 11.5). The heating event exhibited in MZ051S-2 provides a minimum age for the formation of unit US4a, together with the first date for human reoccupation at or near MZ051S. While the large dating uncertainty of this event prevents precise pinpointing for chronostratigraphic purposes, we now know, despite the scarcity of archaeological finds from US4a, that some human activity likely occurred at MZ051S during the Late Bronze Age or the Iron Age. Traces of human occupation (potsherds) in Val Poré from these periods have previously been discovered at the nearby dry-stone enclosure named MZ005S (Angelucci and Carrer, 2015). The new radiocarbon ages COL6511.1.1 and COL6514.1.1 from US4a show that

the surface of US4a remained exposed and stable, at least until the 5th–7th centuries AD. This observation is confirmed by burial ages from MZ051S-3 and the top of MZ051S-2, albeit that these cobble ages (except the top of MZ051S-3) suggest a slightly later time of burial at  $\sim$ AD 1000. These age disparities are small when dating uncertainties are considered, but an explanation for the observed scatter between the methods could be that they do not date the same event. While the radiocarbon ages date the death of trees from which wood was subsequently burned (both events could have occurred long before the final burial of US4a), the cobbles date the end of the last exposure of US4a. Therefore, our interpretation is that human activity occurred at or near MZ051S in the Early Middle Ages (dated by radiocarbon), which was followed by the initiation of the second period of slope instability (possibly due to human land use) towards the end of the 1st millennium AD/beginning of the 2nd millennium AD (constrained by cobble dating). Slope instability in Val Poré continued to occur during the 2nd millennium AD, as was previously confirmed during the excavation of MZ005S. At this site, at least two generations of colluvium are recorded. These have sealed an ephemeral surface dating from the 7th–8th centuries AD, and the early-Modern artefact-bearing topsoil (Carrer and Angelucci, 2013). At MZ051S, present soil formation was initiated following the deposition of colluvium (Fig. 11.6).

## 7. Conclusions

The investigated rock surfaces from MZ051S in Val di Sole display various levels of resetting before burial, a prerequisite for burial dating. The presented research aimed to examine the suitability of rock surface IRSL to date buried dry-stone structures linked to pastoralism in upland pastures. Our first results from Val di Sole show encouraging signs for the applicability of the method to such, from a dating point of view, challenging archaeological structures. We here provide new information on the chronostratigraphic development of the livestock enclosure MZ051S in the Italian Alps. Combined rock surface IRSL dating and radiocarbon dating show that the upper archaeological unit US4a was exposed from the Bronze Age until the Middle Ages, perhaps as late as at the shift between the 1st and 2nd millennia AD. The agreement shows the potential of rock surface IRSL dating as a chronological tool to date buried stone structures and to corroborate radiocarbon dating in contexts where such dating is challenging. For the lower archaeological unit US5a, the relationship between the cobble ages and the general chronostratigraphy is more complicated and requires further investigations.

One unexpected discovery from our research in Val di Sole is that one cobble demonstrates both optical bleaching and annealing by heat, which had occurred during different events in the past. The timing of such events is recorded within the luminescence-depth profiles; these events can be dated using both IRSL<sub>50</sub> and pIR-IRSL<sub>290</sub> dating techniques. A possible explanation for annealing is forest fires, which could occur naturally or induced by humans. None of the other cobbles from our site (including the smaller MZ051S-3) show any signs of resetting in the centre of the cobbles. Thus, we argue that in this case, we can directly date human activities with rock surface IRSL dating. The dating of the heating event demonstrates that the dry-stone structure MZ051S must have been occupied, at least ephemerally, even after the Early Bronze Age. The implication of our observations is that rock surface IRSL dating can be applied at archaeological sites to date heating events, even if no heated artefacts have been recovered. Furthermore, the archaeological implication is that rock surface luminescence dating may help to detect ephemeral events of human activity, which left no relevant archaeological record and could have remained undetected otherwise.

Questions on how to correct for fading of the feldspar signal in rocks remain. Here, we show that for the heated rock of MZ051S-2, the g-value corrected IRSL<sub>50</sub> age is in agreement with the more stable pIR-IRSL<sub>290</sub>. However, due to the lack of a naturally saturated signal,



we cannot directly compare such ages with  $L_{nat}/L_{sat}$  ratio corrected ages. We here favour the application of g-value corrected ages for the cobbles from Val di Sole, but encourage more research to explore the suitability of different fading correction approaches for rocks of different lithologies and with varying burial doses.

### Declaration of competing interest

The authors declare that they have no known competing financial interests or personal relationships that could have appeared to influence the work reported in this paper.

### Acknowledgements

Dr. Anja Zander, University of Cologne, is thanked for gamma spectrometry measurements. Laura Vezzoni, University of Trento, is thanked for visual inspections of petrographic thin sections. The authors are grateful to Dr. Fabio Cavulli, University of Trento, for helping during fieldwork and for providing photo-plans of the excavations. Lucas Ageby is funded by the Deutsche Forschungsgemeinschaft (DFG, German Research Foundation) — Project number 57444011 - SFB 806 as part of project F2 in CRC 806 — Our Way To Europe. Francesco Carrer's research is funded by the Newcastle University Academic Track programme (NUAcT), UK. Project ALPES is undertaken in the context of a specific agreement between the Department of Humanities of the University of Trento and the Soprintendenza per i Beni Culturali of the autonomous Province of Trento. The project is funded by the University of Trento, Italy and by the Terre Alte programme of the CAI (Italian Alpine Club) and is supported by the Municipality of Mezzana, Italy (Trento). The authors are indebted to the people from Ortisé and Menas for their help, and to all the students and researchers who have participated in fieldwork activities. The work by Eike F. Rades was funded by the German Research Foundation (DFG) in the framework of a Research Fellowship (RA 2836/1-1). Finally, we thank Dr. Michael Meyer and two anonymous reviewers for their helpful feedback and comments, which greatly improved the manuscript.

### Appendix A. Supplementary data

Supplementary material related to this article can be found online at <https://doi.org/10.1016/j.quageo.2021.101212>.

### References

- Aitken, M.J., 1985. *Thermoluminescence Dating*. Academic Press, London.
- al Khasawneh, S., Murray, A., Abudana, F., 2019. A first radiometric chronology for the Khatt Shebib megalithic structure in Jordan using the luminescence dating of rock surfaces. *Quat. Geochronol.* 49, 205–210. <http://dx.doi.org/10.1016/j.quageo.2018.02.007>.
- al Khasawneh, S., Murray, A., Bonatz, D., Freiesleben, T., 2015. Testing the application of post IR IRSF dating to Iron- and Viking-age ceramics and heated stones from Denmark. *Quat. Geochronol.* 30, 386–391. <http://dx.doi.org/10.1016/j.quageo.2015.05.014>.
- Angelucci, D.E., Anesin, D., 2012. Sedimenti e suoli, natura e cultura. Considerazioni geoarcheologiche sulla genesi delle stratificazioni archeologiche in ambiente montano. In: *APSAT 1. Teoria E Metodi Della Ricerca Sui Paesaggi D'Alta Quota*, Mantova. SAP Società Archeologica, Mantova, pp. 11–25.
- Angelucci, D.E., Carrer, F., 2015. *Paesaggi Pastoralis D'Alta Quota in Val di Sole (Trento): Le Ricerche Del Progetto ALPES, 2010-2014*. Università degli studi di Trento, Dipartimento di Lettere Filosofia.
- Angelucci, D.E., Carrer, F., Cavulli, F., 2014. Shaping a periglacial land into a pastoral landscape: a case study from Val di Sole (Trento, Italy). *Post-Class. Archaeol.* 4 (2014), 157–180.
- Angelucci, D.E., Carrer, F., Pedrotti, A., 2017. Due nuove datazioni dell'età del Bronzo da un Sito D'alta quota in Val Poré (Val di Sole). In: *Archeologia Delle Alpi*. Provincia autonoma di Trento, pp. 154–156.
- Auclair, M., Lamothe, M., Huot, S., 2003. Measurement of anomalous fading for feldspar IRSF using SAR. *Radiat. Meas.* 37 (4), 487–492. [http://dx.doi.org/10.1016/S1350-4487\(03\)00018-0](http://dx.doi.org/10.1016/S1350-4487(03)00018-0).
- Bøtter-Jensen, L., Thomsen, K., Jain, M., 2010. Review of optically stimulated luminescence (OSL) instrumental developments for retrospective dosimetry. *Radiat. Meas.* 45 (3), 253–257. <http://dx.doi.org/10.1016/j.radmeas.2009.11.030>.
- Brodard, A., Guibert, P., cois Lévêque, F., Mathé, V., Carozza, L., Burens, A., 2012. Thermal characterization of ancient hearths from the cave of Les Fraux (Dordogne, France) by thermoluminescence and magnetic susceptibility measurements. *Quat. Geochronol.* 10, 353–358. <http://dx.doi.org/10.1016/j.quageo.2012.04.013>.
- Bronk Ramsey, C., 2009. Bayesian Analysis of radiocarbon dates. *Radiocarbon* 51 (1), 337–360. <http://dx.doi.org/10.1017/S0033822200033865>.
- Burow, C., 2019. *calc\_CosmicDoseRate: Calculate the cosmic dose rate. function version 0.5.2*. In: Kreutzer, S., Burow, C., Dietze, M., Fuchs, M., Schmidt, C., Fischer, M., Friedrich, J. (Eds.), *Luminescence: Comprehensive Luminescence Dating Data Analysis. R Package Version 0.9.0.109*.
- Buylaert, J.-P., Jain, M., Murray, A.S., Thomsen, K.J., Thiel, C., Sohbati, R., 2012. A robust feldspar luminescence dating method for Middle and Late Pleistocene sediments. *Boreas* 41 (3), 435–451. <http://dx.doi.org/10.1111/j.1502-3885.2012.00248.x>.
- Carcaillet, C., 2001. Are Holocene wood-charcoal fragments stratified in alpine and subalpine soils? Evidence from the Alps based on AMS<sup>14</sup>C dates. *Holocene* 11 (2), 231–242. <http://dx.doi.org/10.1191/095968301674071040>.
- Carrer, F., 2012. Upland sites and pastoral landscapes. New perspectives into the archaeology of pastoralism in the Alps. In: Brogiolo, G., Angelucci, D., Colechia, A., Remondino, F. (Eds.), *APSAT 1. Teoria E Metodi Della Ricerca Sui Paesaggi D'Alta Quota*, Mantova. SAP Società Archeologica, Mantova, pp. 101–116.
- Carrer, F., Angelucci, D.E., 2013. First archaeological data from an Alpine pastoral enclosure at Val Poré (Val di Sole, Trentino, Italy). *Debates de Arqueología Medieval* 3 (2013), 149–165.
- Carrer, F., Angelucci, D.E., 2018. Continuity and discontinuity in the history of upland pastoral landscapes: the case study of Val Molinac and Val Poré (Val di Sole, Trentino, Eastern Italian Alps). *Landscape Res.* 43 (6), 862–877. <http://dx.doi.org/10.1080/01426397.2017.1390078>.
- Carrer, F., Colanese, A.C., Lucquin, A., Petersen Guedes, E., Thompson, A., Walsh, K., Reitmaier, T., Craig, O.E., 2016. Chemical analysis of pottery demonstrates pre-historic origin for high-altitude alpine dairying. *PLoS One* 11 (4), e0151442. <http://dx.doi.org/10.1371/journal.pone.0151442>.
- Cavulli, F., Grimaldi, S., Pedrotti, A., Angelucci, D.E., 2011. Toward an understanding of archaeological visibility: the case of the Trentino (southern Alps). In: van Leusen, M., Pizzolo, G., Sarti, L. (Eds.), *Hidden Landscapes of Mediterranean Europe. Cultural and Methodological Biases in Pre- and Protohistoric Landscape Studies. Proceedings of the International Meeting, Siena, Italy, May 25-27, 2007*. BAR International Series 2320, pp. 83–94.
- Colarossi, D., Duller, G., Roberts, H., 2018. Exploring the behaviour of luminescence signals from feldspars: Implications for the single aliquot regenerative dose protocol. *Radiat. Meas.* 109, 35–44. <http://dx.doi.org/10.1016/j.radmeas.2017.07.005>.
- Cresswell, A., Carter, J., Sanderson, D., 2018. Dose rate conversion parameters: Assessment of nuclear data. *Radiat. Meas.* 120, 195–201. <http://dx.doi.org/10.1016/j.radmeas.2018.02.007>.
- Dal Piaz, G., Castellarin, A., Martin, S., Selli, L., Carton, A., Pellegrini, G., Casolari, E., Damiano, F., Montresor, L., Picotti, V., Prosser, G., Santuliana, E., Cantelley, L., 2007. *Carta Geologica d'Italia alla scala 1:50.000. Foglio 042. Malé + Note illustrative della Carta Geologica d'Italia alla scala 1:50.000*. Trento-Roma.
- Dell'Amore, F., Carrer, F., Angelucci, D.E., 2017. Reperti archeologici dalla Val Molinac e dalla Val Poré (Val di Sole, Trento, Italia). *Atti Del Convegno Archeologia E Cultura in Val di Sole: Ricerche, Contesti, Prospettive*. pp. 131–143.
- Dewald, A., Heinze, S., Jolie, J., Zilges, A., Dunai, T., Rethemeyer, J., Melles, M., Staubwasser, M., Kuczewski, B., Richter, J., Radtke, U., von Blanckenburg, F., Klein, M., 2013. CologneAMS, a dedicated center for accelerator mass spectrometry in Germany. *Nucl. Instrum. Methods Phys. Res. B* 294, 18–23. <http://dx.doi.org/10.1016/j.nimb.2012.04.030>.
- Duller, G.A., 2015. The analyst software package for luminescence data: overview and recent improvements. *Ancient TL* 33 (1), 35–42.
- Favilli, F., Cherubini, P., Collenberg, M., Egli, M., Sartori, G., Schoch, W., Haeblerli, W., 2010. Charcoal fragments of Alpine soils as an indicator of landscape evolution during the Holocene in Val di Sole (Trentino, Italy). *Holocene* 20 (1), 67–79. <http://dx.doi.org/10.1177/0959683609348850>.
- Favilli, F., Egli, M., Brandova, D., Ivy-Ochs, S., Kubik, P.W., Maisch, M., Cherubini, P., Haeblerli, W., 2009. Combination of numerical dating techniques using <sup>10</sup>Be in rock boulders and <sup>14</sup>C of resilient soil organic matter for reconstructing the chronology of glacial and periglacial processes in a high Alpine catchment during the Late Pleistocene and Early Holocene. *Radiocarbon* 51 (2), 537–552. <http://dx.doi.org/10.1017/S0033822200055910>.
- Feathers, J., More, G.M., Quinteros, P.S., Burkholder, J.E., 2019. IRSF Dating of rocks and sediments from desert geoglyphs in coastal Peru. *Quat. Geochronol.* 49, 177–183. <http://dx.doi.org/10.1016/j.quageo.2018.07.009>.
- Festi, D., Putzer, A., Oegg, K., 2014. Mid and late Holocene land-use changes in the Ötztal Alps, territory of the Neolithic Iceman “Ötzi”. *Quat. Int.* 353, 17–33. <http://dx.doi.org/10.1016/j.quaint.2013.07.052>.
- Flude, S., Haschke, M., Storey, M., 2017. Application of benchtop micro-XRF to geological materials. *Mineral. Mag.* 81 (4), 923–948. <http://dx.doi.org/10.1180/minmag.2016.080.150>.

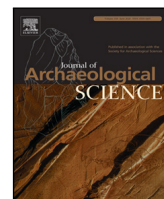
- Freiesleben, T., Sohbati, R., Murray, A., Jain, M., al Khasawneh, S., Hvidt, S., Jakobsen, B., 2015. Mathematical model quantifies multiple daylight exposure and burial events for rock surfaces using luminescence dating. *Radiat. Meas.* 81, 16–22. <http://dx.doi.org/10.1016/j.radmeas.2015.02.004>.
- Fuchs, M., Lang, A., 2009. Luminescence dating of hillslope deposits—A review. *Geomorphology* 109 (1), 17–26. <http://dx.doi.org/10.1016/j.geomorph.2008.08.025>.
- Galli, A., Panzeri, L., Rondini, P., Poggiani Keller, R., Martini, M., 2020. Luminescence dating of rock surface. The case of monoliths from the megalithic sanctuary of Ossimo-Pat (Valle Camonica, Italy). *Appl. Sci.* 10, 7403. <http://dx.doi.org/10.3390/app10217403>.
- Glignic, L., Meyer, M., Sohbati, R., Jain, M., Barrett, S., 2019. OSL Surface exposure dating of a lithic quarry in Tibet: Laboratory validation and application. *Quat. Geochronol.* 49, 199–204. <http://dx.doi.org/10.1016/j.quageo.2018.04.012>.
- Habermann, J., Schilles, T., Kalchgruber, R., Wagner, G.A., 2000. Steps towards surface dating using luminescence. *Radiat. Meas.* 32 (5), 847–851. [http://dx.doi.org/10.1016/S1350-4487\(00\)00066-4](http://dx.doi.org/10.1016/S1350-4487(00)00066-4).
- Hafner, A., Schwörer, C., 2018. Vertical mobility around the high-alpine Schnidejoch Pass. Indications of Neolithic and Bronze Age pastoralism in the Swiss Alps from paleoecological and archaeological sources. *Quat. Int.* 484, 3–18. <http://dx.doi.org/10.1016/j.quaint.2016.12.049>.
- Huntley, D.J., Baril, M., 1997. The K content of the K-feldspars being measured in optical dating or in thermoluminescence dating. *Ancient TL* 15 (1), 11–13.
- Huntley, D.J., Lamothe, M., 2001. Ubiquity of anomalous fading in K-feldspars and the measurement and correction for it in optical dating. *Can. J. Earth Sci.* 38 (7), 1093–1106. <http://dx.doi.org/10.1139/e01-013>.
- Huntley, D., Lian, O.B., 2006. Some observations on tunnelling of trapped electrons in feldspars and their implications for optical dating. *Quat. Sci. Rev.* 25 (19), 2503–2512. <http://dx.doi.org/10.1016/j.quascirev.2005.05.011>.
- Junge, A., Lomax, J., Shahack-Gross, R., Dunseth, Z.C., Finkelstein, I., Fuchs, M., 2016. OSL Age determination of archaeological stone structures using trapped aeolian sediments: A case study from the negev highlands, Israel. *Geoarchaeology* 31 (6), 550–563. <http://dx.doi.org/10.1002/gea.21578>.
- Kars, R.H., Reimann, T., Ankjærgaard, C., Wallinga, J., 2014. Bleaching of the post-IR IRSL signal: new insights for feldspar luminescence dating. *Boreas* 43 (4), 780–791. <http://dx.doi.org/10.1111/bor.12082>.
- Klasen, N., Kehl, M., Mikdad, A., Brückner, H., Weniger, G.-C., 2018. Chronology and formation processes of the Middle to Upper Palaeolithic deposits of Ifri n'Ammar using multi-method luminescence dating and micromorphology. *Quat. Int.* 485, 89–102. <http://dx.doi.org/10.1016/j.quaint.2017.10.043>.
- Kothieringer, K., Walser, C., Dietre, B., Reitmaier, T., Haas, J.N., Lambers, K., 2015. High impact: early pastoralism and environmental change during the Neolithic and Bronze Age in the Silvretta Alps (Switzerland/Austria) as evidenced by archaeological, palaeoecological and pedological proxies. *Z. Geomorphol. Suppl. Issue* 59 (2), 177–198. [http://dx.doi.org/10.1127/zfg\\_suppl/2015/S-59210](http://dx.doi.org/10.1127/zfg_suppl/2015/S-59210).
- Kreutzer, S., 2020. *calc\_FadingCorr: Apply a fading correction according to Huntley & Lamothe (2001) for a given g-value and a given tc. Function version 0.4.2.* In: Kreutzer, S., Burow, C., Dietze, M., Fuchs, M., Schmidt, C., Fischer, M., Friedrich, J., Riedesel, S., Autzen, M., Mittelstrass, D. (Eds.), *Luminescence: Comprehensive Luminescence Dating Data Analysis. R Package Version 0.9.0.10*.
- Kreutzer, S., Burow, C., 2020. *analyse\_FadingMeasurement: Calculate the cosmic dose rate. Function version 0.1.15.* In: Kreutzer, S., Burow, C., Dietze, M., Fuchs, M., Schmidt, C., Fischer, M., Friedrich, J., Riedesel, S., Autzen, M., Mittelstrass, D. (Eds.), *Luminescence: Comprehensive Luminescence Dating Data Analysis. R Package Version 0.9.0.10*.
- Lehmann, B., Herman, F., Valla, P.G., King, G.E., Biswas, R.H., Ivy-Ochs, S., Steinemann, O., Christl, M., 2020. Postglacial erosion of bedrock surfaces and deglaciation timing: New insights from the Mont Blanc massif (western Alps). *Geology* 48 (2), 139–144. <http://dx.doi.org/10.1130/G46585.1>.
- Leveau, P., Walsh, K., 2005. Population sequences in a high altitude alpine environment: Archaeological sites and historical and environmental time. *Int. J. Anthropol.* 20 (3), 155–171. <http://dx.doi.org/10.1007/BF02443056>.
- Li, B., Li, S.-H., 2011a. Luminescence dating of K-feldspar from sediments: A protocol without anomalous fading correction. *Quat. Geochronol.* 6 (5), 468–479. <http://dx.doi.org/10.1016/j.quageo.2011.05.001>.
- Li, B., Li, S.-H., 2011b. Thermal stability of infrared stimulated luminescence of sedimentary K-feldspar. *Radiat. Meas.* 46 (1), 29–36. <http://dx.doi.org/10.1016/j.radmeas.2010.10.002>.
- Medici, T., Foradori, G., Carrer, F., Dal Maschio, R., Gialanella, S., Montagna, M., Pedrotti, A., Angelucci, D.E., 2014. Una perla in vetro da un contesto pastorale alta quota della Val di Sole (Trento). In: Ciappi, S., Larese, A., Ubaldi, M. (Eds.), *Il Vetro in Età Protostorica in Italia, Atti Delle XVI Giornate Nazionali Di Studio Sul Vetro (Adria, 12-13 Maggio 2012). Comitato Nazionale Italiano AIHV (Association Internationale pour l'Histoire du Verre), Venezia*, pp. 115–121.
- Meyer, M., Glignic, L., Jain, M., Sohbati, R., Schmidmair, D., 2018. Lithological controls on light penetration into rock surfaces — Implications for OSL and IRSL surface exposure dating. *Radiat. Meas.* 120, 298–304. <http://dx.doi.org/10.1016/j.radmeas.2018.03.004>.
- Moe, D., Fedele, F.G., Maude, A.E., Kvamme, M., 2007. Vegetational changes and human presence in the low-alpine and subalpine zone in Val Febbraro, upper Valle di Spluga (Italian central Alps), from the Neolithic to the Roman period. *Veg. Hist. Archaeobot.* 16 (6), 431–451. <http://dx.doi.org/10.1007/s00334-006-0088-0>.
- Murray, A., Buylaert, J., Thomsen, K., Jain, M., 2009. The effect of preheating on the IRSL signal from feldspar. *Radiat. Meas.* 44 (5), 554–559. <http://dx.doi.org/10.1016/j.radmeas.2009.02.004>.
- Murray, A., Schmidt, E., Stevens, T., Buylaert, J.-P., Marković, S., Tsukamoto, S., Frechen, M., 2014. Dating Middle Pleistocene loess from Stari Slankamen (Vojvodina, Serbia) — limitations imposed by the saturation behaviour of an elevated temperature IRSL signal. *CATENA* 117, 34–42. <http://dx.doi.org/10.1016/j.catena.2013.06.029>.
- Murray, A., Wintle, A., 2000. Luminescence dating of quartz using an improved single-aliquot regenerative-dose protocol. *Radiat. Meas.* 32 (1), 57–73. [http://dx.doi.org/10.1016/S1350-4487\(99\)00253-X](http://dx.doi.org/10.1016/S1350-4487(99)00253-X).
- Ou, X., Roberts, H., Duller, G., Gunn, M., Perkins, W., 2018. Attenuation of light in different rock types and implications for rock surface luminescence dating. *Radiat. Meas.* 120, 305–311. <http://dx.doi.org/10.1016/j.radmeas.2018.06.027>.
- Prescott, J., Hutton, J., 1988. Cosmic ray and gamma ray dosimetry for TL and ESR. *Int. J. Radiat. Appl. Instrum. D* 14 (1), 223–227. [http://dx.doi.org/10.1016/1359-0189\(88\)90069-6](http://dx.doi.org/10.1016/1359-0189(88)90069-6).
- Prescott, J., Stephan, L., 1982. The contribution of cosmic radiation to the environmental dose for thermoluminescence dating. Latitude, altitude and depth dependences. *Pact* 6, 17–25.
- R. Core Team, 2019. *R: A Language and Environment for Statistical Computing. R Foundation for Statistical Computing, Vienna, Austria*.
- Rades, E., Sohbati, R., Lüthgens, C., Jain, M., Murray, A., 2018. First luminescence-depth profiles from boulders from moraine deposits: Insights into glaciation chronology and transport dynamics in Malta valley, Austria. *Radiat. Meas.* 120, 281–289. <http://dx.doi.org/10.1016/j.radmeas.2018.08.011>.
- Reimer, P.J., Austin, W.E.N., Bard, E., Bayliss, A., Blackwell, P.G., Bronk Ramsey, C., Butzin, M., Cheng, H., Edwards, R.L., Friedrich, M., et al., 2020. The IntCal20 northern hemisphere radiocarbon age calibration curve (0–55 cal BP). *Radiocarbon* 62 (4), 725–757. <http://dx.doi.org/10.1017/RDC.2020.41>.
- Reitmaier, T., Doppler, T., Pike, A.W., Deschler-Erb, S., Hajdas, I., Walser, C., Gerling, C., 2018. Alpine cattle management during the Bronze Age at Ramosch-Mottata, Switzerland. *Quat. Int.* 484, 19–31. <http://dx.doi.org/10.1016/j.quaint.2017.02.007>.
- Rethemeyer, J., Gierga, M., Heinze, S., Stolz, A., Wotte, A., Wischhöfer, P., Berg, S., Melchert, J., Dewald, A., 2019. Current sample preparation and analytical capabilities of the Radiocarbon Laboratory at CologneAMS. *Radiocarbon* 61 (5), 1449–1460. <http://dx.doi.org/10.1017/RDC.2019.16>.
- Riedesel, S., Brill, D., Roberts, H.M., Duller, G.A., Garrett, E., Zander, A.M., King, G.E., Tamura, T., Burow, C., Cunningham, A., Seeliger, M., Batist, M.D., Heyvaert, V.M., Fujiwara, O., Brückner, H., 2018. Single-grain feldspar luminescence chronology of historical extreme wave event deposits recorded in a coastal lowland, Pacific coast of central Japan. *Quat. Geochronol.* 45, 37–49. <http://dx.doi.org/10.1016/j.quageo.2018.01.006>.
- Schiffer, M.B., 1986. Radiocarbon dating and the “old wood” problem: The case of the Hohokam chronology. *J. Archaeol. Sci.* 13 (1), 13–30. [http://dx.doi.org/10.1016/0305-4403\(86\)90024-5](http://dx.doi.org/10.1016/0305-4403(86)90024-5).
- Sohbati, R., Jain, M., Murray, A., 2012c. Surface exposure dating of non-terrestrial bodies using optically stimulated luminescence: A new method. *Icarus* 221 (1), 160–166. <http://dx.doi.org/10.1016/j.icarus.2012.07.017>.
- Sohbati, R., Liu, J., Jain, M., Murray, A., Egholm, D., Paris, R., Guralnik, B., 2018. Centennial- to millennial-scale hard rock erosion rates deduced from luminescence-depth profiles. *Earth Planet. Sci. Lett.* 493, 218–230. <http://dx.doi.org/10.1016/j.epsl.2018.04.017>.
- Sohbati, R., Murray, A.S., Buylaert, J.-P., Almeida, N.A.C., Cunha, P.P., 2012a. Optically stimulated luminescence (OSL) dating of quartzite cobbles from the Tapada do Montinho archaeological site (east-central Portugal). *Boreas* 41 (3), 452–462. <http://dx.doi.org/10.1111/j.1502-3885.2012.00249.x>.
- Sohbati, R., Murray, A.S., Chapot, M.S., Jain, M., Pederson, J., 2012b. Optically stimulated luminescence (OSL) as a chronometer for surface exposure dating. *J. Geophys. Res.: Solid Earth* 117 (B9), <http://dx.doi.org/10.1029/2012JB009383>.
- Sohbati, R., Murray, A., Jain, M., Buylaert, J.-P., Thomsen, K., 2011. Investigating the resetting of OSL signals in rock surfaces. *Geochronometria* 38 (3), <http://dx.doi.org/10.2478/s13386-011-0029-2>.
- Sohbati, R., Murray, A., Jain, M., Thomsen, K., Hong, S.-C., Yi, K., Choi, J.-H., 2013. Na-rich feldspar as a luminescence dosimeter in infrared stimulated luminescence (IRSL) dating. *Radiat. Meas.* 51–52, 67–82. <http://dx.doi.org/10.1016/j.radmeas.2012.12.011>.
- Sohbati, R., Murray, A., Porat, N., Jain, M., Avner, U., 2015. Age of a prehistoric “Rodedian” cult site constrained by sediment and rock surface luminescence dating techniques. *Quat. Geochronol.* 30, 90–99. <http://dx.doi.org/10.1016/j.quageo.2015.09.002>.
- Spooner, N., 1994. The anomalous fading of infrared-stimulated luminescence from feldspars. *Radiat. Meas.* 23 (2), 625–632. [http://dx.doi.org/10.1016/1350-4487\(94\)90111-2](http://dx.doi.org/10.1016/1350-4487(94)90111-2).

- Thomsen, K., Murray, A., Jain, M., 2011. Stability of IRSL signals from sedimentary K-feldspar samples. *Geochronometrika* 38 (1), 1–13. <http://dx.doi.org/10.2478/s13386-011-0003-z>.
- Thomsen, K., Murray, A., Jain, M., Bøtter-Jensen, L., 2008. Laboratory fading rates of various luminescence signals from feldspar-rich sediment extracts. *Radiat. Meas.* 43 (9), 1474–1486. <http://dx.doi.org/10.1016/j.radmeas.2008.06.002>.
- Vafiadou, A., Murray, A., Liritzis, I., 2007. Optically stimulated luminescence (OSL) dating investigations of rock and underlying soil from three case studies. *J. Archaeol. Sci.* 34 (10), 1659–1669. <http://dx.doi.org/10.1016/j.jas.2006.12.004>.
- Walsh, K., Court-Picon, M., de Beaulieu, J.-L., Guiter, F., Mocci, F., Richer, S., Sinet, R., Talon, B., Tzortzis, S., 2014. A historical ecology of the ecrins (Southern French Alps): Archaeology and palaeoecology of the Mesolithic to the Medieval period. *Quat. Int.* 353, 52–73. <http://dx.doi.org/10.1016/j.quaint.2013.08.060>.
- Walsh, K., Mocci, F., 2011. Mobility in the mountains: Late third and second millennia alpine societies' engagements with the high-altitude zones in the Southern French Alps. *Eur. J. Archaeol.* 14 (1–2), 88–115. <http://dx.doi.org/10.1179/146195711798369427>.
- Walsh, K., Mocci, F., Palet-Martinez, J., 2007. Nine thousand years of human/landscape dynamics in a high altitude zone in the southern French Alps (Parc National des Ecrins, Hautes-Alpes). *Preistoria Alp.* 42, 9–22.
- Wintle, A., 1977. Detailed study of a thermoluminescent mineral exhibiting anomalous fading. *J. Lumin.* 15 (4), 385–393. [http://dx.doi.org/10.1016/0022-2313\(77\)90037-0](http://dx.doi.org/10.1016/0022-2313(77)90037-0).
- Zander, A., Strebler, D., Classen, E., Rethemeyer, J., Brückner, H., 2019. Roman traces in Germania magna: New thermoluminescence and pIRIR<sub>290</sub> data from a lime kiln at Bergisch Gladbach, Germany. *Archaeometry* 61 (2), 506–518. <http://dx.doi.org/10.1111/arcm.12435>.



## Chapter 3

# Dating dry-stone walls with rock surface luminescence: A case study from the Italian Alps



## Research papers

# Dating dry-stone walls with rock surface luminescence: A case study from the Italian Alps

Lucas Ageby<sup>a,\*</sup>, Diego E. Angelucci<sup>b</sup>, Dominik Brill<sup>a</sup>, Francesco Carrer<sup>c</sup>, Helmut Brückner<sup>a</sup>, Nicole Klasen<sup>a</sup>

<sup>a</sup> Institute of Geography, University of Cologne, 50923 Cologne, Germany

<sup>b</sup> Dipartimento di Lettere e Filosofia, University of Trento, 38122 Trento, Italy

<sup>c</sup> School of History, Classics and Archaeology, Newcastle University, NE1 7RU, Newcastle, UK



## ARTICLE INFO

## Keywords:

Rock surface luminescence dating

Luminescence-depth profiles

IRSL

Dry-stone walls

## ABSTRACT

Dating the construction of dry-stone walls is challenging since such structures are typically built without any mortar that can be used for dating. Rock surface luminescence dating is a developing dating method that could advance chronological insights from structures constructed using dry-stone techniques. This study explores rock surface luminescence dating by targeting dry-stone walls from two enclosure complexes and a hut located in the pastoral upland landscape in Val di Sole, Italy. Gneissic rocks were collected from the dry-stone walls, including surfaces that were either exposed or covered (buried) during the time of sampling. Their respective exposure and burial histories were investigated by measuring the luminescence intensity in feldspar minerals from polymineral rock slices. From covered rock surfaces from one enclosure complex, we calculated recent burial ages ( $\sim 200$  a) from one rock, and burial of  $\sim 500$  a (bottom surface) and  $3750 \pm 660$  a (top surface) from a second rock. The top surfaces of two additional rocks date the construction of an adjacent hut to the Early Middle Ages. The luminescence-depth profile from one such rock has a complex exposure and burial history, including events that predate the hut's construction. Fitted exposure ages from a second enclosure complex suggest with significant errors either a recent age ( $<10$  a) or construction during the 19th century AD. Burial dating using rock surface luminescence dating appears feasible for dry-stone walls provided that the rock surface was sufficiently exposed before being incorporated into the structure; here, the gneissic surfaces were bleached to depths of  $\sim 0.2$  mm before the last burial. Contrariwise, exposure dating generally underestimates the expected age. The variation in ages observed from our rock surfaces indicates that the degree of preservation of the wall, the position of the rock, erosion, and knowledge regarding the general archaeological setting are essential to interpreting the estimated ages. In this study, rock surface luminescence dating provides new, previously inaccessible chronological data with implications for interpreting human activities in the alpine areas of Val di Sole.

## 1. Introduction

The construction of dry-stone structures began early in the history of humankind. The most ancient dry-stone walls date from the Palaeolithic (e.g., Jaubert et al., 2016; Yar and Dubois, 1996). Since the Neolithic (e.g., Holl, 1998; Mazet, 2006), dry-stone structures were built to support functions related to animal husbandry. Later on, dry-stone masonry remained an established construction technique for dwellings (e.g., Ferrater et al., 2015; Manley, 1990), fences and enclosures (e.g., Colominas et al., 2020; Kremenčić et al., 2021; Walsh et al., 2014), as well as fortifications (e.g., Levine et al., 2019; Liszka, 2017) throughout history.

Due to the common historical use of dry-stone walls, methods to directly date the construction of dry-stone walls are critically important. Since dry-stone walls typically lack mortar, numerical dating of such structures is usually accomplished using radiocarbon dating of organic material recovered from associated archaeological layers (e.g., Ilves, 2018; Manley, 1990; Passariello et al., 2010; Walsh, 2005) once stratigraphic correlation has been assessed through the standard methods of archaeological stratigraphy (Harris, 1989). While essential in many archaeological settings, this approach does not directly date the actual construction of the structures. Also, not all such structures have associated archaeological horizons or assemblages, or the record might

\* Corresponding author.

E-mail address: [lageby@uni-koeln.de](mailto:lageby@uni-koeln.de) (L. Ageby).

<https://doi.org/10.1016/j.jas.2022.105625>

Received 17 February 2022; Received in revised form 16 May 2022; Accepted 17 May 2022

Available online 16 June 2022

0305-4403/© 2022 The Author(s). Published by Elsevier Ltd. This is an open access article under the CC BY-NC-ND license (<http://creativecommons.org/licenses/by-nc-nd/4.0/>).



not be stratigraphically associated with the time of construction. An additional method to date the age of dry-stone structures is luminescence dating of sediment grains trapped between the stones (Junge et al., 2016; Kemp et al., 2022), grains from the soil beneath the positioned stones (Sohbati et al., 2015; Vafiadou et al., 2007). However, alternative approaches are necessary for stone structures where trapped grains are not available.

Developments in luminescence dating – applied to rock surfaces – potentially provide a dating method that could be used for dry-stone walls. Rock surface luminescence dating is a dating technique (e.g., Habermann et al., 2000; Liritzis et al., 2019b,a; Sohbati et al., 2011, 2012a,b; Vafiadou et al., 2007), that enables dating of exposed (e.g., Brill et al., 2021; Gliganic et al., 2019; Lehmann et al., 2018; Polikreti et al., 2002; Sohbati et al., 2011, 2012b) and buried (e.g., Gliganic et al., 2021; Ishii et al., 2022; Rades et al., 2018; Sohbati et al., 2012a, 2015) rock surfaces. The basis of the method is that the luminescence signal intensity decreases into the rock during periods of exposure (bleaching) and increases during periods of burial. If the lithology is sufficiently translucent to allow for bleaching to occur (Ou et al., 2018), then minutes to hours of exposure can be enough to bleach the luminescence signal in the surface grains in some lithologies (Sohbati et al., 2011; Vafiadou et al., 2007), and prolonged exposure gradually resets the signal deeper into the rocks (e.g., Gliganic et al., 2019; Laskaris and Liritzis, 2011; Ou et al., 2018; Polikreti et al., 2002; Sohbati et al., 2011). The duration of exposure for a rock surface can be constrained if the bleaching rate of the signal is known (e.g., Sohbati et al., 2012b). The bleaching rate depends on the lithology, the photoionisation cross-section of the electron traps, and the photon flux at the rock surface (Sohbati et al., 2011) – parameters that vary between different samples and sites. Using locally sourced calibration samples with known exposure histories can constrain the mentioned parameters, after which the exposure time can be calculated for surfaces with unknown exposure histories for absolute dating (Brill et al., 2021; Gliganic et al., 2019; Lehmann et al., 2018; Sohbati et al., 2012b), or for artefact authentication (Polikreti et al., 2002). Burial ages can be extracted from rock surfaces if burial events can be identified by the presence of luminescence signal intensity plateaus that are not in field saturation (e.g., al Khasawneh et al., 2019a; Freiesleben et al., 2015; Gliganic et al., 2021; Jenkins et al., 2018; Liritzis et al., 2017; Rades et al., 2018; Sohbati et al., 2012a, 2015; Souza et al., 2019, 2021); hence, the signal must have been bleached at one time. The time of burial of rock surfaces is calculated by dividing the measured palaeodose with depth-dependent dose rates (e.g., Gliganic et al., 2021; Greilich et al., 2005; Liritzis, 2001; Liritzis et al., 2010; Rades et al., 2018; Sohbati et al., 2015; Souza et al., 2019), or, more experimentally, by fitting the signal-depth profiles from buried or covered rock surfaces (Freiesleben et al., 2015; Sohbati et al., 2015).

The advantage of burial dating dry-stone walls using rock surface luminescence dating is that if the rock surface was sufficiently exposed before being covered during construction, this surface should directly record the construction time, provided that no subsequent rearrangement at the structure further reset the signal. If rearrangement occurred, then it is conceivable that complex life histories of sites can be reconstructed using rock surface luminescence dating since multiple burial and exposure events can be recorded in the luminescence-depth profiles (Freiesleben et al., 2015; Rades et al., 2018). Previous attempts of burial dating of stone structures using the rock surface luminescence technique have been encouraging when applied to various lithologies, time spans, and archaeological settings (e.g., Galli et al., 2020; Greilich et al., 2005; Liritzis and Vafiadou, 2015; Liritzis et al., 2019b; al Khasawneh et al., 2019a,b). An application of exposure dating using rock surface luminescence has been the temporal constraining of rock art by dating adjacent rock falls (Chapot et al., 2012; Sohbati et al., 2012b; Liritzis et al., 2019a). Exposure dating of dry-stone structures using rock surface luminescence dating could provide minimum ages for the

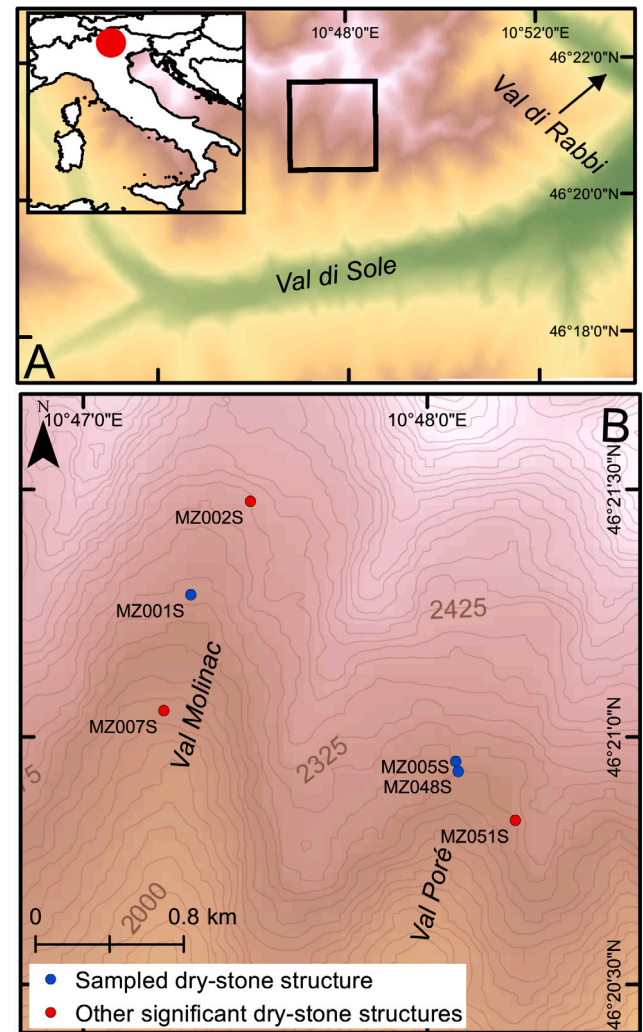


Fig. 1. Map of Val di Sole (A), where the black square outlines the study area in Val Molinac and Val Poré (B).

construction of such structures. The system is sensitive to millimetre-scale changes in luminescence-depth profiles and is suitable for dating decades to centuries-old dry-stone structures.

The specific objective of this study is to investigate the possibilities of using rock surface luminescence dating of stone structures to constrain the construction of three partly preserved dry-stone walls belonging to structures previously dated with radiocarbon and archaeological assemblages to the Middle Ages–Modern Period. We present novel chronological data collected from dry-stone structures. We investigate bleaching depths and burial and exposure ages of rock surfaces from intact and degraded walls by measuring the luminescence emission from feldspar grains from polymineral rock slices. The results are discussed regarding the chronological context of specific structures, including the interpretation of age scatter from presumably isochronous surfaces, along with general considerations for dating dry-stone structures.

## 2. Study site

### 2.1. Site context

The selected sites are located in Val Molinac and Val Poré (Fig. 1), south-facing, tributary valleys to the tectonic valley Val di Sole, located in the central-eastern Italian Alps. The valley is permanently settled up to ~1500 m above sea level, with only seasonal dwellings located at

higher altitudes. The geology is dominated by metamorphic, gneissic (mostly paragneisses with some orthogneisses) rocks from the Ulten unit (Dal Piaz et al., 2007). The environment in the upper parts of these tributary valleys predominantly shows glacial and periglacial features, with meadows covering the valley ends. While the current climatic conditions are insufficient to sustain glaciers, the valley heads of both Val Poré and Val Molinac had been shaped by cirque glaciers during the Pleistocene. Other prominent features are inactive rock glaciers, talus formations, gravitational slope deformation and other hillslope and gelifluction features (Angelucci et al., 2014).

## 2.2. Dry-stone structures in Val Poré and Val Molinac

The landscape in Val Poré and Val Molinac shows clear signs of long-term anthropogenic impact. Over eighty dry-stone structures (all located in an alpine environment above 2000 metres of elevation) have been identified during surveys by the project *Alpine Landscapes: Pastoralism and Environment of Val di Sole* (ALPES) (Angelucci and Carrer, 2015; Angelucci et al., 2017, 2021; Carrer and Angelucci, 2013, 2018). The structures mentioned in this work are marked in Fig. 1B. Stone structures are recorded at high altitudes in the Alps date from the late Neolithic and early Bronze Age to the modern period (e.g., Reitmaier et al., 2013; Walsh et al., 2014). In Val Poré and Val Molinac, such structures vary in size and character and have been subdivided by Carrer and Angelucci (2013) into three categories: enclosures, huts, and rock shelters. Most enclosures are compound structures consisting of several enclosures and a hut. The primary construction technique placed elongated gneissic boulders perpendicularly to the wall direction. Additional archaeological finds are scarce from the surveyed structures (Angelucci et al., 2014), but excavations from enclosures MZ005S and MZ051S in Val Poré have documented archaeological artefacts and provided insights into their occupation history (Angelucci et al., 2021; Carrer and Angelucci, 2013; Dell'Amore et al., 2017; Medici et al., 2014). Archaeological investigations revealed that, although evidence of human occupation in the area dates back to the Early Bronze Age (Angelucci et al., 2021), pastoral activities intensified from the late Middle Ages and the early modern period (Carrer and Angelucci, 2018). Our dating efforts here focus on three dry-stone structures (Fig. 2): two enclosure complexes (MZ001S and MZ005S) and a hut (MZ048S).

### 2.2.1. MZ001S — enclosure complex

MZ001S (Fig. 2A) is the largest structure so far discovered in the upland areas of Val di Sole. This site consists of three enclosures and a hut, located at 2293 m.a.s.l. in Val Molinac. The dry-stone walls are generally well-preserved, and the site's characteristics suggest its possible early Modern age. No excavations have so far been conducted at MZ001S, but a 19th century AD potsherd was discovered inside the hut during a survey of the structure (Dell'Amore et al., 2017).

### 2.2.2. MZ005S — enclosure complex

The enclosure complex MZ005S (Fig. 2B) was constructed in the Val Poré at 2257 m.a.s.l. The first results from excavations and structural analyses suggest that MZ005S consists of one hut and three enclosures, constructed and restored in five different phases (Carrer and Angelucci, 2013). The most recent enclosures are still well-defined, with mostly intact walls. The dry-stone walls forming the third, smaller and older enclosure have partly collapsed. Excavations in two test pits (one pit in the northernmost enclosure and one in the oldest enclosure) have unearthed two archaeological layers belonging to the current, and a buried A horizon. The artefact assemblage recovered from MZ005S consists of iron nails and rivets, an iron key, a coin and a glass bead, attributed to the Late Medieval and Early Modern period (Carrer and Angelucci, 2013; Medici et al., 2014). In particular, the coin and the glass bead were produced in Venice (Italy) in the mid-16th century AD. Additional flint and potsherd finds indicate an earlier occupation

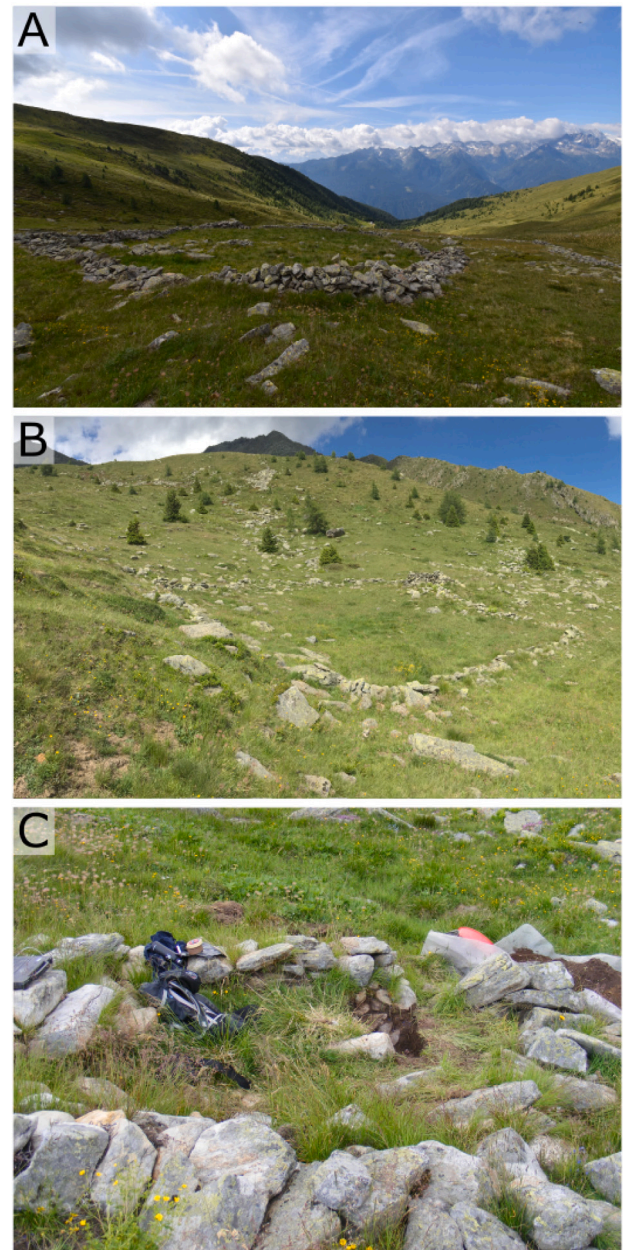


Fig. 2. The sampled dry-stone structures in Val Molinac (MZ001S; A) and Val Poré (MZ005S; B, MZ048S; C).

during prehistoric times. Charcoal fragments from the excavation gave radiocarbon ages of 1405–1438 cal AD, 1519–1645 cal AD, and the 20th century, while a charcoal fragment from a test-pit in the northern enclosure resulted in an age of 652–776 cal AD (Angelucci and Carrer, 2015; Carrer and Angelucci, 2013).

### 2.2.3. MZ048S — hut

The dry-stone structure MZ048S (Fig. 2C) is a hut located a few metres south of MZ005S. The structure appears affected by gravitational movement of the slope, and a section of a partly intact wall is buried. Only a single flint fragment was recovered from beneath the base of MZ048S, and its association with the hut is currently not fully understood (Dell'Amore et al., 2017). The radiocarbon age of 677–878 AD was obtained from a charcoal fragment collected inside the structure (Angelucci and Carrer, 2015). Two additional charcoal samples from silty sediments beneath the structure provided radiocarbon



**Table 1**  
List of collected samples from Val Molinac and Val Poré.

Lab. ID	Sample name	Structure/location	Sample type	Field context
C-L4632	MZ048S-1	MZ048S	Buried rock	Part of hut wall
C-L4633	MZ048S-2	MZ048S	Buried rock	Part of hut wall
C-L4634	MZ005S-1	MZ005S	Buried rock	Partly buried in degraded wall of the oldest enclosure
C-L4635	MZ005S-2	MZ005S	Buried rock	Wedged between larger rocks in the degraded wall of the oldest enclosure
C-L4637	MZ001S-1	MZ001S	Exposed rock	Wedged sample from intact part of wall, surface facing W.
C-L4638	MZ001S-2	MZ001S	Exposed rock	Wedged sample from intact part of wall, surface facing W.
C-L4962	MZ005S-CAL	Boulder near MZ005S	Calibration surface	Exposed for one year, surface facing E.
C-L4963	MZ001S-CAL-1	Boulder near MZ001S	Calibration surface	Exposed for one year, surface facing N.
C-L4965	MZ051S-CAL	Bedrock outcrop near MZ051S	Calibration surface	Exposed for one year, surface facing E.
C-L4966	MZ001S-3	MZ001S	Exposed rock	Positioned on top of partly collapsed complex wall, surface facing S.

ages from the early 5th millennium BC (Angelucci and Carrer, 2015), possibly dating mid-Holocene forest wildfires in Val Poré.

### 3. Materials and method

#### 3.1. Sampling, preparation, and luminescence measurements

Gneissic rocks were collected from the dry-stone structures during excavation campaigns in the summers of 2018 and 2019 (supplementary material: Fig. A.1 and A.2). The samples (Table 1; for photographs, see also supplementary material: Fig. A.3) were immediately covered in opaque plastic bags to protect the surfaces from exposure to daylight. The exposed surfaces (all from enclosure complex MZ001S) were marked on the samples at the time of collection. Samples MZ001S-1 and MZ001S-2 were wedged between other rocks, while sample MZ001S-3 was sampled from the top of the enclosure wall. The calibration surfaces were exposed by removing the outer part (~3 cm for sample MZ001S-CAL-1; more for other samples) of boulders and outcrops in 2018. They were subsequently collected after one year of exposure in 2019.

The top and bottom surfaces of the buried rocks were marked during sampling. The rocks from MZ048S had been placed into the wall stacked on top of each other during construction. MZ005S-1 was partly buried as part of the degraded enclosure wall from the oldest enclosure at MZ005S. MZ005S-2 was collected from the same wall but was positioned with its longest axis perpendicular to the ground in contrast to the other buried rocks. Hence, the terms “top” and “bottom” are, strictly speaking, arbitrary for MZ005S-2 and are used only to differentiate between the two surfaces.

The rocks were prepared for measurement following Sohbaty et al. (2011): cores were extracted with a bench drill and sliced into ~0.7 mm thin slices. Areas of the rock surfaces that might have been exposed to light before sampling were carefully avoided during coring.

All samples were measured in a RisøTL/OSL reader (model DA-20) (Bøtter-Jensen et al., 2010) in the Cologne Luminescence Laboratory, using intact slices mounted directly in the sample carousel. We used only infrared stimulated luminescence (IRSL) of feldspars since no separation between quartz and feldspars is possible during the preparation of intact slices. The sensitivity-corrected luminescence ( $L_n/T_n$ ) with depth was measured in the exposed samples using a IRSL protocol (e.g., Sohbaty et al., 2011) (50 °C stimulation for 300 s). For the buried samples, a post-infrared IRSL (pIRIR) protocol (e.g., Thomsen et al., 2008) (first IRSL, then pIRIR at 130 °C for 300 s) was applied to all slices. The equivalent doses ( $D_e$ ) in the outer slices were measured using cycles of increased regenerative dosing (see Murray and Wintle, 2000). Since the feldspar signal in IRSL and low-temperature pIRIR protocols are known to be subjected to anomalous fading, correcting for this signal loss is common practice when calculating burial ages (e.g., Brill and Cisternas, 2020; Reimann et al., 2011). We corrected for fading using the approach of Huntley and Lamothe (2001). The reproducibility of the measurement protocol used to date the buried samples was assessed with a dose recovery test (Fig. 3). The initial IRSL signal provides acceptable dose recovery for all samples following 2.6–6.0 Gy

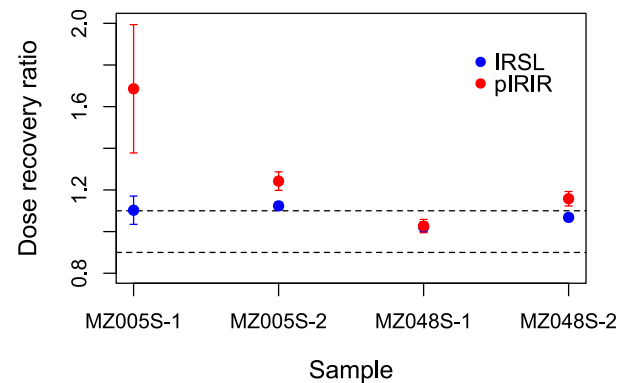


Fig. 3. Dose recovery ratios for IRSL and pIRIR signals from the buried rocks.

of beta radiation, while the pIRIR signal tends to overestimate the given dose. Therefore, we only proceeded with analysis by using the IRSL signal. Further details regarding the measurement protocols, fading corrections, and example dose–response curves (Fig. B.5) are presented in the supplementary material.

#### 3.2. Dose rate

Knowledge about the rate of environmental irradiation to the feldspar grains in the rocks is required to calculate burial ages from the rock surfaces. The dose rate depends on the radionuclide concentration in the rocks themselves and the surrounding sediments, the internal potassium content and the size of the feldspar grains, and the amount of cosmic radiation which reaches the rocks. We used high-resolution gamma spectrometry (Murray et al., 1987) to measure the concentrations of naturally occurring radionuclides in the sampled rocks from MZ005S and MZ048S (Table 2). The radionuclide content from the surrounding material was assumed to be the average of the four rocks sampled from MZ005S and MZ048S and the four rocks from the same geological unit (collected from archaeological layers in structure MZ051S) dated by Ageby et al. (2021). We converted the radionuclide concentrations into beta and gamma dose rate components using the conversion factors of Cresswell et al. (2018) and assumed that the moisture content in the rocks was insignificant. Infinite-matrix dose rates were calculated using R v. 4.1.1 (Team, 2021) with the *calcCobbleDoseRate()* package (Riedesel and Autzen, 2021) from the *Luminescence* package (Kreutzer et al., 2021), which uses attenuation factors for beta and gamma radiation from Riedesel and Autzen (2020) to calculate depth-dependent dose rates. The internal potassium concentration in feldspar grains from Val di Sole gneisses was measured with  $\mu$ -XRF by Ageby et al. (2021). We here estimated the internal potassium contribution from the feldspar in our rocks by using an average concentration from the data reported by Ageby et al. (2021). For internal potassium, the average feldspar grain size was assumed to be 400  $\mu$ m, based on visual inspections of thin sections of previously collected rocks from the same geological units in Val di Sole. Cosmic dose rate was calculated following Prescott and Hutton (1994).

**Table 2**

Summary of radionuclide concentrations and attenuated dose rates in the buried rocks and the average from eight gneissic rocks from Val Poré.

Sample	Radionuclide concentration				Dose rate (Gy ka <sup>-1</sup> )			
	<sup>238</sup> U (ppm)	<sup>232</sup> Th (ppm)	<sup>40</sup> K (%)	Internal K (%)	Gamma	Beta	Cosmic	Internal K
MZ048S-1	2.04 ± 0.11	7.67 ± 0.46	3.31 ± 0.04	1.00 ± 0.28	1.42 ± 0.02	2.80 ± 0.22	0.29 ± 0.03	0.13 ± 0.07
MZ048S-2	2.63 ± 0.14	14.34 ± 0.84	0.70 ± 0.01	1.00 ± 0.28	1.17 ± 0.02	1.10 ± 0.07	0.29 ± 0.03	0.13 ± 0.07
MZ005S-1	2.40 ± 0.13	8.04 ± 0.48	1.58 ± 0.02	1.00 ± 0.28	1.05 ± 0.02	1.58 ± 0.11	0.38 ± 0.04	0.13 ± 0.07
MZ005S-2	3.10 ± 0.16	15.40 ± 0.89	1.48 ± 0.02	1.00 ± 0.28	1.47 ± 0.03	1.74 ± 0.11	0.38 ± 0.04	0.13 ± 0.07
Average rock	2.25 ± 0.25	9.62 ± 1.47	1.43 ± 0.24					

### 3.3. Fitting of luminescence-depth profiles and exposure ages

Average luminescence-depth profiles (calculated from two or more cores from each surface) were fitted with R v. 4.1.1 (Team, 2021), using the *nls()* function. The calibration and exposed surfaces were fitted using the equation:

$$L = L_0 e^{-t_e \sigma \phi_0} e^{-\mu x} \quad (1)$$

following the model proposed by Sohbaty et al. (2011), where  $L$  is the luminescence intensity (i.e.,  $L_n/T_n$ ) measured in a specific slice,  $L_0$  is the saturated luminescence intensity,  $t_e$  is the exposure time,  $\sigma \phi_0$  is the bleaching rate at the rock surface based on the photoionising cross-section ( $\sigma$ ) and the photon flux ( $\phi_0$ ),  $\mu$  is the attenuation of light penetration with depth ( $x$ ). Following the approach first used by Sohbaty et al. (2012b), we constrained  $\sigma \phi_0$  by using the calibration surfaces with a known  $t_e$ , before calculating the  $t_e$  for the exposed surfaces. The buried surfaces were fitted following the model developed by Freiesleben et al. (2015), which allows for fitting of an exposure followed by a burial events:

$$L = (L_0 e^{-t_e \sigma \phi_0} e^{-\mu x} - 1) e^{-F(x)t_b} + 1 \quad (2)$$

where  $F(x)$  is the ratio between depth-dependent dose rate and the characteristic dose ( $D_0$ ) and  $t_b$  is the burial age. Additional exposure and burial events can be added to fit the shape of the luminescence-depth profiles (Freiesleben et al., 2015). All  $L_n/T_n$  values were normalised by the arithmetic mean  $L_n/T_n$  derived from saturated slices. All buried surfaces were fitted with a final burial event since these rocks were buried at the time of sampling. The pre-burial luminescence depth profiles were subsequently modelled (e.g., al Khasawneh et al., 2019a) using  $t_e \sigma \phi_0$  and  $\mu$  from the fit to assess depth of complete bleaching ( $L < 0.001$ ) before burial. The exposed rock surfaces were fitting using no weighting; the covered surfaces were fitted by weighting the profiles by the standard error; both using the *nls()* function.

## 4. Results

### 4.1. Calibration surfaces and exposed rock surfaces from MZ001S

A summary of the results from the exposure dating from structure MZ001S is presented in Table 3. Luminescence-depth profiles are presented from calibration and exposed surfaces from Val Molinac and Val Poré (Fig. 4). The depth of the bleaching front (<50% of field saturation) for the IRSL signal varies considerably between the different surfaces. This variation is especially notable for the exposed surfaces of unknown exposure ages (MZ001S-1–MZ001S-3), in which the depth of the bleaching front varies between 1.1 to 11.2 mm. The depth variation is lesser in the calibration surfaces, ranging between 1.5 to 3.2 mm. The site-specific bleaching rate ( $\sigma \phi_0$ ) at the rock surfaces for Val Molinac and Val Poré is fitted to be  $29.59 \pm 16.10 \text{ a}^{-1}$  based on three calibration surfaces. The fitted exposure ages ( $t_e$ ) from structure MZ001S using  $\sigma \phi_0$  ranges between 0.1 a (i.e., younger than the calibration surfaces) for MZ001S-2, to  $93 \pm 58$  a for MZ001S-3.

**Table 3**The results from fitting (Eq. (1)) of the calibration and exposed surfaces from Val Poré and Val Molinac. A  $\sigma \phi_0$  of  $29 \text{ a}^{-1}$  was used to calculate the exposure ages ( $t_e$ ) for the exposed surfaces.

Sample	$\mu \text{ mm}^{-1}$	Bleaching depth (mm) 50% of field saturation	$t_e$ (a)
MZ001S-CAL-1	1.18 ± 0.17	3.2	1
MZ005S-CAL	2.59 ± 0.38	1.5	1
MZ051S-CAL	1.38 ± 0.21	2.7	1
MZ001S-1	1.08 ± 0.12	5.5	15 ± 8
MZ001S-2	1.26 ± 0.36	1.1	0.1 ± 0.02
MZ001S-3	0.72 ± 0.04	11.2	93 ± 58

### 4.2. Burial dating of MZ048S and MZ005S

The luminescence-depth profiles (Fig. 5) show that  $L_n/T_n$  is significantly lower at the rock surfaces compared to saturated plateaus observed deeper into the rocks. The IRSL intensity has reached saturation at ~4 mm in all samples except MZ048S-1, in which saturation is reached at ~11 mm. All surfaces have at the minimum two slices with a  $L_n/T_n$  (normalised for field saturation) <0.2 except for the top surface of MZ005S-1. The parameters used for fitted profiles in Fig. 5 are reported in Table 4. The fitted profiles indicate that all surfaces, except the top surface of MZ005S-1, have experienced at least one burial event; MZ048S-1 is fitted for three burial events. The modelled pre-burial luminescence-depth profiles (for MZ048S-1; this is the profile before the final burial as part of the wall of MZ048S) indicate that the IRSL signal in the surface slices in all of the profiles was bleached before the last burial (see dotted line in Fig. 5). For structure MZ048S, the most recent fitted burial ages are estimated to be  $1.9 \pm 0.3 \text{ ka}$  (MZ048S-1) and  $4.1 \pm 0.1 \text{ ka}$  (MZ048S-2). The two previous burial events observed in MZ048S-1 are estimated to have occurred at  $8.1 \pm 1.1 \text{ ka}$  and  $19.0 \pm 5.7 \text{ ka}$ , respectively. The fitted burial ages ( $t_b$ ) from the rocks from MZ005S, which varies considerably between the different surfaces, are estimated to be: 0 a (MZ005S-1; top surface),  $0.7 \pm 0.3 \text{ ka}$  (MZ005S-1; bottom surface),  $1.2 \pm 0.1 \text{ ka}$  (MZ005S-2; top surface), and  $9.0 \pm 3.2 \text{ ka}$  (MZ005S-2; bottom surface).

The ages derived from  $D_e$  measurements are presented in Table 5. The calculated mean burial age from the surface slice from MZ048S-1 is  $1010 \pm 170 \text{ a}$ , yielding a fading corrected age of  $1030 \pm 180 \text{ a}$ . The surface slice of MZ048S-2 is dated to  $1450 \pm 100 \text{ a}$  (uncorrected age is  $1200 \pm 60 \text{ a}$ ). For MZ005S-1, the surface slice from the top surface yields a recent mean age of  $180 \pm 50 \text{ a}$ , fading corrected to  $220 \pm 60 \text{ a}$ . The surface slice for the bottom is estimated to be of similar age at  $160 \pm 70 \text{ a}$  (the uncorrected age is  $130 \pm 60 \text{ a}$ ). The surface slice from the top surface MZ005S-2 is dated to  $3750 \pm 660 \text{ a}$ , while the bottom surface is younger at  $500 \pm 60 \text{ a}$  (both ages are fading-corrected).

## 5. Discussion

### 5.1. Context for the luminescence ages

This study has measured the luminescence ages of three distinct dry-stone structures: MZ048S, MZ005S, and MZ001S. All fitting of luminescence-depth profiles in this study (Figs. 4–5) was attempted using a double exponential approach (e.g., Freiesleben et al., 2015;

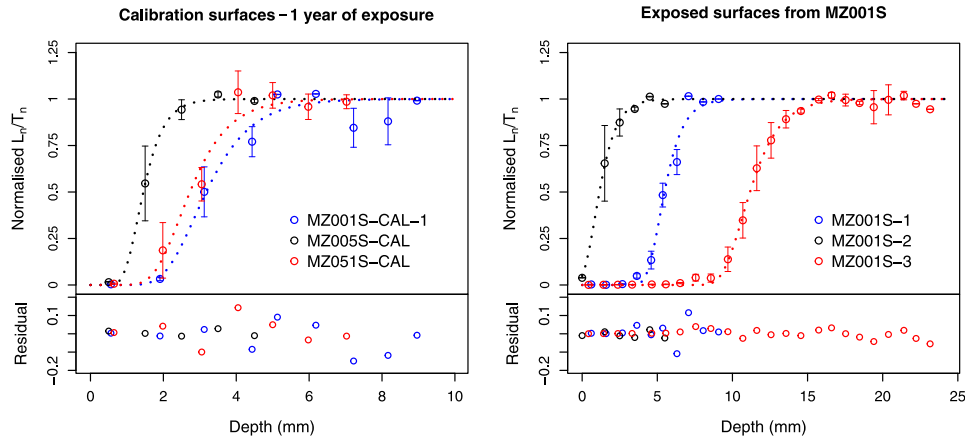


Fig. 4. Fitted luminescence-depth profiles for calibration surfaces exposed in Val di Sole for one year (left) and exposed surfaces from MZ001S-1 (right), fitted (dotted line) using the model  $L(x) = L_0 e^{-t_x \sigma \phi_0 e^{-\alpha x}}$  (Sohbati et al., 2011). The exposed surfaces were fitted using  $\sigma \phi_0$  derived from the calibration surfaces.

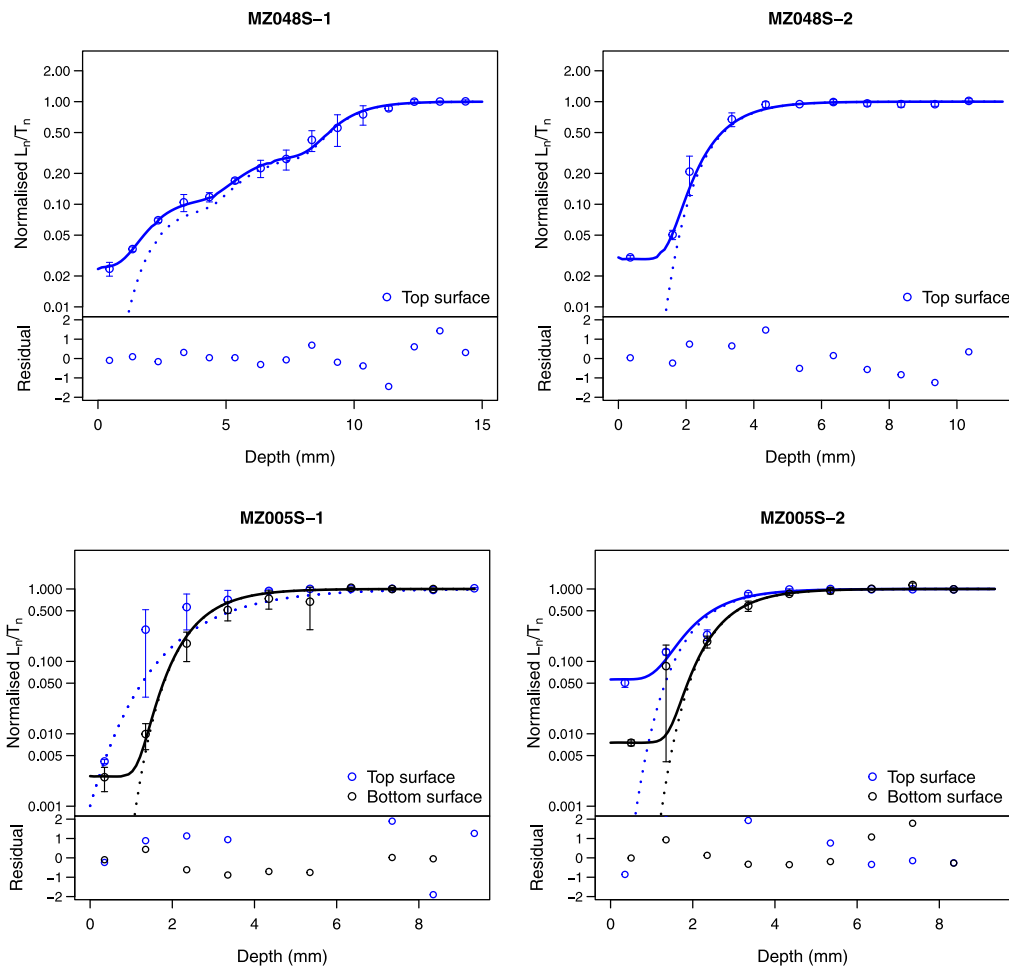


Fig. 5. Luminescence-depth profiles with  $1\sigma$  error bars from dry-stone structures MZ005S and MZ048S. Best-fit burial profiles (solid lines) are plotted with corresponding fitting residuals. Modelled exposure profiles (dotted lines) are plotted as well; these profiles represent the exposure event before the final burial, reset to 0.1% of the saturated signal between  $-0-2$  mm depending on surface and sample. The fitted and modelled profiles are identical for the top surface of MZ005S-1 ( $t_b = 0$ ); hence no solid line is plotted. No fitting is attempted for the bottom surfaces of MZ048S-1 and MZ048S-2 due to the unsuitable luminescence-depth profiles. Normalised  $L_n/T_n$  values are plotted on a logarithmic scale.

Sohbati et al., 2011). An alternative approach to fitting signal-depth profiles was proposed by (Laskaris and Liritzis, 2011); they instead suggested using cumulative log-normal fitting, demonstrating the relationship of the observed luminescence to the exposure time and the depth below the rock surface. Comparisons between simulated

signal-depth profiles have indicated a similarly good fit using either approach (Liritzis et al., 2017).

The spatial relationship between MZ048S-1 and MZ048S-2 (placed on top of each other) determines that they were likely positioned as part of the wall simultaneously; hence, the top surfaces of both rocks

**Table 4**Parameters used for fitting (Eq. (2)) luminescence-depth profiles in Fig. 5.  $D_0$  is assumed to be identical for both top and bottom surfaces.

Sample	Surface	Burial events	$D_0$ (Gy)	$\mu$ mm <sup>-1</sup>	$t_e \sigma \phi_0$	$t_{e2} \sigma \phi_0$	$t_{e3} \sigma \phi_0$	$t_b$ (a)	$t_{b2}$ (a)	$t_{b3}$ (a)
MZ005S-1	Top	0	818 ± 29	0.66 ± 0.13	7 ± 2			0		
MZ005S-1	Bottom	1		1.23 ± 0.22	27 ± 11			706 ± 315		
MZ005S-2	Top	1	508 ± 21	1.20 ± 0.20	15 ± 7			9027 ± 3188		
MZ005S-2	Bottom	1		1.26 ± 0.15	34 ± 13			1179 ± 108		
MZ048S-1	Top	3	334 ± 10	1.03 ± 0.13	8 ± 12	309 ± 483	13062 ± 6975	1923 ± 277	8124 ± 1133	18972 ± 5732
MZ048S-2	Top	1	348 ± 6	1.13 ± 0.04	23 ± 2			4062 ± 146		

**Table 5**Results from the buried rocks from structures MZ005S and MZ048S. Sample-dependent g-values (normalised for 2 days), depth-dependent slice dose rates,  $D_e$ , and uncorrected and fading-corrected IRSL ages.

Sample	Surface	g-value $_{2days}$ (%/decade)	Slice depth (mm)	Slice dose rate (Gy ka <sup>-1</sup> )	Mean $D_e$ (Gy)	n	Uncorr. age (ka)	Corr. age (ka)
MZ048S-1	Top	0.25 ± 0.54	0.0–0.7	4.16 ± 0.33	4.18 ± 0.70	4	1.01 ± 0.17	1.03 ± 0.18
MZ048S-2	Top	2.20 ± 0.49	0.0–0.7	2.64 ± 0.26	3.17 ± 0.13	2	1.20 ± 0.06	1.45 ± 0.10
MZ005S-1	Top	2.46 ± 0.69	0.0–0.7	3.02 ± 0.29	0.55 ± 0.11	4	0.18 ± 0.05	0.22 ± 0.06 <sup>a</sup>
MZ005S-1	Bottom	2.46 ± 0.69	0.0–0.7	3.02 ± 0.29	0.40 ± 0.17	3	0.13 ± 0.06	0.16 ± 0.07
MZ005S-2	Top	2.34 ± 0.50	0.0–0.7	3.27 ± 0.31	10.08 ± 1.67	3	3.08 ± 0.51	3.75 ± 0.66
MZ005S-2	Bottom	2.34 ± 0.50	0.0–0.7	3.27 ± 0.31	1.38 ± 0.15	2	0.42 ± 0.05	0.50 ± 0.06

<sup>a</sup>Upper limit age estimate.

should yield the same ages for their last burial event. Despite this expectation, the ages derived from the fitting show that  $t_b$  of MZ048S-1 (~1900 a) is ~50% younger as compared to MZ048S-2 (~4100 a). This suggests that our fitted ages are unreliable; a sentiment previously expressed by al Khasawneh et al. (2019a), who pointed out that fitted ages are less reliable due to the assumption of common  $D_0$ . Instead, we favour the ages calculated from average  $D_e$  values for dating the most recent burial event ( $t_b$ ). Since our main objective in this study is to investigate the application of rock surface dating to dry-stone structures, we did not measure individual  $D_e$  for the older burial events from MZ048S-1 since these events predate human occupation of the upland areas of Val di Sole as is currently understood (e.g., Angelucci et al., 2021). Instead, these ages seem to constrain geomorphological events occurring during the Late Pleistocene and the Holocene as part of the landscape evolution in Val Poré.

The original context of the burial events recorded in the luminescence-depth profile from MZ048S-1 is unknown since the rock was likely moved during exposure by natural processes or by humans. Accordingly, based on the fitted ages, we can only speculate on the processes that caused the exposure and burial events observed in the luminescence-depth profile. The oldest burial event ( $t_{b3}$  ~13–25 ka) is likely connected to glacial oscillation following the last glacial maximum, which would roughly fit with the timing of deglaciation in the adjacent (Favilli et al., 2009). The oldest known soil formation in Val Molinac and Val Poré was dated to the 7th millennium BC by Angelucci and Carrer (2015) and the second burial event ( $t_{b2}$ ) is dated to this period. Thus, following the re-exposure of MZ048S-1, the rock was re-buried, perhaps by slope or periglacial processes. Finally, the rock was exhumed before being buried a third and last time as part of the wall of MZ048S; it is this event ( $t_b$ ) we can date by measuring the palaeodose from slices. Since the fitting of MZ048S-1 indicates that the pre-last burial bleaching front reaches approximately the depth of the second slice at 2 mm depth (Fig. 5; dotted line), it is conceivable that the second slice of MZ048S-1 does record the correct burial age, with little pre-burial residual dose. If so, the burial age of the surface slice underestimates the burial age, perhaps due to bleaching during sampling, poorly constrained external beta dose rate at surface/surrounding material interface, light penetrating through gaps, or the top surface of MZ048S-1 was briefly re-exposed (even if the rock was never moved) at ~1000 AD during an otherwise undated restoration phase MZ048S-1.

The shape of the luminescence-depth profiles from MZ005S-1 and MZ005S-2 are mostly like MZ048S-2, i.e., a single burial event is represented by a short burial plateau ( $t_b$ ; Fig. 5; solid lines), succeeding

the pre-burial exposure events (Fig. 5; dotted lines). This is not the case at the top surface of MZ005S-1, where the signal-depth profile displays ambiguity in the fitting dependent on whether the signal was sufficiently bleached before burial. This, we cannot assess since the fitted profile shows no significant bleaching front. Further fitting uncertainty arises due to inter-core variations in the shape of the luminescence-depth profile, as is shown by the significant standard errors at depths ~1–4 mm. A significant error in luminescence is also observable to a lesser degree at the bottom surfaces of MZ005S-1 and MZ005S-2. Inter-core variations between luminescence-depth profiles from cores extracted from the same rock surface have been described by Meyer et al. (2018), who attributed it to spatial variation in the mineralogy when dark minerals could inhibit light from penetrating deeper into some areas of the rock surfaces. Such variations cause significant ambiguity in the fit, which must be adjusted by weighting for the luminescence error during fitting. A likely but untested explanation for some luminescence-depth variations in our samples since e.g., biotites are common in the Val di Sole gneisses (Ageby et al., 2021; Dal Piaz et al., 2007) see also supplementary material Fig A.4. Despite the uncertainty in the fitting (especially for the top surface of MZ005S-1 and the bottom surface of MZ005S-2), we can still calculate ages from  $D_e$  to estimate the upper age limit for when the surfaces were covered.

The ages from the top and bottom surfaces of MZ005S-1 agree at 1 $\sigma$  (1740–1860 AD and 1790–1930 AD for top and bottom surfaces, respectively) but are at least 180 years younger compared to the age derived from the bottom surface from MZ005S-2 (1460–1580 AD). While these ages are all chronologically consistent with the occupation at MZ005S from the Late Middle Ages until the mid-20th century (Carrer and Angelucci, 2013, 2018), the age difference between MZ005S-1 and MZ005S-2 could perhaps be explained by the recent history of the samples. Possibly, MZ005S-2 was not turned during the degradation of the wall; this would be consistent with how an older event (2400–1100 BC) remains recorded at the top surface. On the other hand, MZ005S-1 must have been turned recently since the surface slices at both surfaces have a small (~0.5 Gy) palaeodose. Possibly, the wedged position of MZ005S-2 in the wall protected the degradation of the wall; hence, the top surface could represent a repair of the wall during a time of intense occupation during the Late Medieval period and the Early Modern period, as demonstrated by the archaeological assemblage which strongly points to significant human activity at this time (Angelucci et al., 2014; Carrer and Angelucci, 2013; Medici et al., 2014). The burial event from the bottom surface of MZ005S-2 generally concurs with the dating of the buried enclosure MZ051S, where Angelucci et al. (2021) has identified human activity in the Early Bronze Age. The potsherds



recovered from MZ005S (Carrer and Angelucci, 2013) indicate human presence at the site during the Late Bronze Age to the Early Iron Age, which here appears to agree with rock-surface luminescence dating. Accordingly, we must now consider the possibility that the construction of MZ005S started at some point during the Bronze Age, just like at the nearby MZ051S.

Constraining the archaeological chronology of MZ001S to the 19th century AD is solely based on a single potsherd (Dell'Amore et al., 2017). Despite the weak age control, the young ages derived from the fitting of MZ001S-1 and MZ001S-2 are clearly too recent and do not contain any valid chronological information regarding the construction or use of MZ001S. The age from MZ001S-3 would fit the preliminary assessment that MZ001S was constructed at the latest in the 19th century. However, at this time, without a systematic sampling of all areas of the enclosure, we cannot determine if the age of MZ001S-3 represents the initial construction of MZ001S or a later building or repair phase occurring in the late 19th or early 20th century.

### 5.2. Rock surface luminescence dating of dry-stone walls

A plausible explanation for the age underestimation of MZ001S-1 and MZ001S-2 and short luminescence-depth profiles is that the luminescence-depth profiles were shortened by erosion. Since weathering and subsequent erosion of surface grains will shorten the bleaching profiles, the model (Eq. (1)) only estimates the minimum exposure age (Sohbati et al., 2012b). Post-glacial erosion rates at the Mount Blanc massif varied on scales between  $10^{-3}$  and  $10^0$  mm a<sup>-1</sup> at different natural rock surfaces (Lehmann et al., 2019b). While erosion rates of rock surfaces are beyond the scope of this study, such erosion rates, unless corrected for, will lead to severe age underestimations considering that Lehmann et al. (2019a) showed how steady-state erosion rates at  $10^{-4}$  mm a<sup>-1</sup> or higher would affect the luminescence-depth profiles. Friction due to rubbing between stone blocks of covered surfaces has also been proposed to cause shortening of luminescence-depth profiles (Liritzis et al., 2015, 2016). Considering how sensitive exposure dating is to erosion (Lehmann et al., 2019a), it appears reasonable that using such an approach to date dry-stone structures is only feasible in specific settings where erosion of exposed rock surfaces is limited. At the same time, good knowledge of geological context, geomorphological evolution, and past human impact is paramount for interpreting dating results. The new chronological data from MZ048S show that it is possible to provide direct ages from dry-stone walls with few associated archaeological artefacts using rock surface luminescence dating of buried surfaces. With rock surface luminescence dating, any structure with a sufficiently translucent lithology containing feldspars or quartz could be targeted. The possibility of providing such data is exciting since many dry-stone walls currently lack numerical dating of their construction. The scattered ages from MZ005S demonstrate that understanding the context of samples is necessary to interpret the ages. It appears that rocks collected from degraded walls could have disturbed luminescence-depth profiles concerning the initial construction of the wall. In the ideal case, such events could be preserved in luminescence depth profiles (as shown by the complex profile of MZ048S-1); then, ages could be derived for both the construction and the degradation of the wall. This is not the case for our MZ005S samples, for which all the luminescence-depth profiles showed a maximum of one exposure and burial event. Considering that erosion appears to be an issue at our alpine site, deep luminescence-depth profiles might be rare due to the shortening of the profiles as grains have been removed. Also, since lithology is essential for how deep the bleaching fronts reach during a given period, as was shown by bleaching experiments by Ou et al. (2018), other lithologies might more often show deeper bleaching fronts; this is usually preferable since each dose plateau becomes more distinct compared to plateaus from less translucent rocks. The luminescence-depth profiles in translucent samples, however, are likely more sensitive to bleaching if light can penetrate between the stones

when placed in the wall. Overall, it should be noted that the buried surfaces we sampled in Val Poré showed significant variations in the depth of the bleaching front, and for MZ005S-1 and MZ005S-2, variations in ages. Considering the quite degraded state of the sampled wall and the clear signs of multiple phases of construction at MZ005S (Carrer and Angelucci, 2013), variations between ages from different surfaces might be unavoidable for such a structure, and the variation might provide valuable information anyway. Scatter between ages is not always observed since previous dating attempts of stone structures using rock surface luminescence dating by al Khasawneh et al. (2019b) produced indistinguishable ages at ~10 ka, derived from a rock slab and two rocks. Future dating efforts of the Val Poré (and Val Molinac) dry-stone structures should include more surfaces to corroborate the ages presented here since increasing the number of samples should help more definitely resolve the history of the dry-stone enclosure complex MZ005S.

### 6. Conclusions

Using IRSL dating, our work from two dry-stone structures from Val Poré has provided new chronological data regarding the construction and life history of huts and enclosures used for purposes of pastoralism. Thus, we show that rock surface luminescence burial dating is a practical, albeit not a completely straightforward, tool for dating such structures. The depth of resetting varies between the different surfaces, meaning that in some cases, it is advisable to sample several specimens in case some surfaces were insufficiently bleached before the rocks were placed in the walls. The two rocks from MZ048S were collected from a mostly intact wall where the rocks likely remained in position since construction. These top surfaces show a similar final burial age, indicating that we can constrain the construction of this wall to the Early Middle Ages. One of these rocks also displayed a complex history of two older burial events. In our case, these events are associated with the landscape evolution in the uplands of Val di Sole, but recording a series of burial and exposure events could be helpful in archaeological settings, e.g., to constrain multiple construction phases or a series of construction and degradation events. The rocks from MZ005S were collected from a collapsed wall, and the corresponding ages varied between Bronze Age to ~200 a. It appears that dating in such a disturbed context provides ages that can be accredited to the initial construction or the subsequent wall degradation. Understanding the archaeological context then becomes invaluable when interpreting such data since rock surface luminescence ages alone cannot differentiate between the initial construction and re-burial during a restoration of the wall. Exposure dating proved less successful than burial dating, with ages being unrealistically young or inconclusive. While our calibration surfaces showed sufficient bleaching, we must conclude that dry-stone structures with luminescence dating might be challenging in alpine areas where rock surfaces are expected to erode. In summary, our work from Val di Sole demonstrates that rock surface luminescence dating of dry-stone walls appears to be a viable method to provide chronological data, which are hard to obtain using other methods.

### Declaration of competing interest

The authors declare that they have no known competing financial interests or personal relationships that could have appeared to influence the work reported in this paper.

### Acknowledgements

We thank Anja Zander for measuring the radionuclide concentration in our samples. Lucas Ageby is funded by the Deutsche Forschungsgemeinschaft, Germany (DFG, German Research Foundation) - Project number 57444011 - SFB 806 (Our Way to Europe). Francesco Carrer's research is funded by the Newcastle University, UK Academic Track

programme (NUAcT). Project ALPES is undertaken in the context of a specific agreement between the Department of Humanities of the University of Trento and the Soprintendenza per i Beni Culturali of the autonomous Province of Trento. The project is funded by the University of Trento, Italy and by the Terre Alte programme of the CAI, Italy (Italian Alpine Club) and is supported by the Municipality of Mezzana, Italy (Trento). The authors are indebted to the people from Ortisé and Menas for their help, and to all the students and researchers who have participated in fieldwork activities. Two reviewers are thanked for their comments, which helped improve the manuscript.

## Appendix A. Supplementary data

Supplementary material related to this article can be found online at <https://doi.org/10.1016/j.jas.2022.105625>.

## References

- Ageby, L., Angelucci, D.E., Brill, D., Carrer, F., Rades, E.F., Rethemeyer, J., Brückner, H., Klasen, N., 2021. Rock surface IRSI dating of buried cobbles from an alpine dry-stone structure in val di sole, Italy. *Quat. Geochronol.* 66, 101212. <http://dx.doi.org/10.1016/j.quageo.2021.101212>.
- al Khasawneh, S., Murray, A., Abudana, F., 2019a. A first radiometric chronology for the khatt shebib megalithic structure in Jordan using the luminescence dating of rock surfaces. *Quat. Geochronol.* 49, 205–210. <http://dx.doi.org/10.1016/j.quageo.2018.02.007>.
- al Khasawneh, S., Murray, A., Thomsen, K., AbuAziz, W., Tarawneh, M., 2019b. Dating a near eastern desert hunting trap (kite) using rock surface luminescence dating. *Archaeol. Anthropol. Sci.* 11 (5), 2109–2119. <http://dx.doi.org/10.1007/s12520-018-0661-3>.
- Angelucci, D., Carrer, F. (Eds.), 2015. *Paesaggi Pastoralisti d'alta Quota in Val Di Sole (Trento). Le Ricerche Del Progetto ALPES - 2010–2014*. Dipartimento di Lettere e Filosofia, Università di Trento, Trento.
- Angelucci, D.E., Carrer, F., Ageby, L., Castiglioni, E., Cavulli, F., Dell'Amore, F., Rethemeyer, J., Rottoli, M., Vezzoni, L., Pedrotti, A., 2021. Occupazione pastorale delle alte quote alpine Nell'età Del bronzo: Primi dati dal sito MZ051s (camp da Ortisé, val di sole, Trento). 71, pp. 1–30. <http://dx.doi.org/10.32097/1143>.
- Angelucci, D.E., Carrer, F., Cavulli, F., 2014. Shaping a periglacial land into a pastoral landscape: A case study from val di sole (Trento, Italy). *Eur. J. Post - Class. Archaeol.* 4, 157–180.
- Angelucci, D., Carrer, F., Pedrotti, A., 2017. Due nuove datazioni dell'età del bronzo da un sito d'alta quota in Val Poré (val di sole). *Archeologia Delle Alpi* 154–156.
- Bøtter-Jensen, L., Thomsen, K., Jain, M., 2010. Review of optically stimulated luminescence (OSL) instrumental developments for retrospective dosimetry. *Radiat. Meas.* 45 (3–6), 253–257. <http://dx.doi.org/10.1016/j.radmeas.2009.11.030>.
- Brill, D., Cisternas, M., 2020. Testing quartz and feldspar luminescence dating to determine earthquake and tsunami recurrence in the area of the giant 1960 Chile earthquake. *Quat. Geochronol.* 58, 101080. <http://dx.doi.org/10.1016/j.quageo.2020.101080>.
- Brill, D., May, S.M., Mhammedi, N., King, G., Lehmann, B., Burrow, C., Wolf, D., Zander, A., Brückner, H., 2021. Evaluating optically stimulated luminescence rock surface exposure dating as a novel approach for Reconstructing Coastal boulder movement on decadal to centennial timescales. *Earth Surf. Dyn.* 9 (2), 205–234. <http://dx.doi.org/10.5194/esurf-9-205-2021>.
- Carrer, F., Angelucci, D.E., 2013. First archaeological data from an alpine pastoral enclosure at val Poré (val di sole, trentino, Italy). *Debates Arqueología Medieval* 3, 149–165.
- Carrer, F., Angelucci, D.E., 2018. Continuity and discontinuity in the history of upland pastoral landscapes: The case study of val molinac and Val Poré (val di sole, Trentino, eastern Italian alps). *Landscape Res.* 43 (6), 862–877. <http://dx.doi.org/10.1080/01426397.2017.1390078>.
- Chapot, M.S., Sohbati, R., Murray, A.S., Pederson, J.L., Rittenour, T.M., 2012. Constraining the age of rock art by dating a rockfall event using sediment and rock-surface luminescence dating techniques. *Quat. Geochronol.* 13, 18–25. <http://dx.doi.org/10.1016/j.quageo.2012.08.005>.
- Colomina, L., Palet, J.M., Garcia-Molsosa, A., 2020. What happened in the highlands? characterising pyrenean livestock practices during the transition from the iron age to the roman period. *Archaeol. Anthropol. Sci.* 12 (3), 69. <http://dx.doi.org/10.1007/s12520-020-01023-3>.
- Cresswell, A.J., Carter, J., Sanderson, D.C.W., 2018. Dose rate conversion parameters: assessment of nuclear data. *Radiat. Meas.* 120, 195–201. <http://dx.doi.org/10.1016/j.radmeas.2018.02.007>.
- Dal Piaz, G., Castellari, A., Martin, S., Selli, L., Carton, A., Pellegrini, G., Casolari, E., Damiano, F., Picotti, V., Prosser, G., Santulana, E., Cantelli, L., 2007. Carta geologica d'Italia alla scala 1:50.000. foglio 042. Malé + note illustrative della carta geologica d'Italia alla scala 1:50.000.
- Dell'Amore, F., Carrer, F., Angelucci, D., 2017. *Reperti Archeologici Dalla Val Molinac E Dalla Val Poré (Val Di Sole, Trento, Italia)*.
- Favilli, F., Egli, M., Brandova, D., Ivy-Ochs, S., Kubik, P.W., Maisch, M., Cherubini, P., Haeblerli, W., 2009. Combination of numerical dating techniques using  $^{10}\text{Be}$  in rock boulders and  $^{14}\text{C}$  of resilient soil organic matter for reconstructing the chronology of glacial and periglacial processes in a high alpine catchment during the late pleistocene and early holocene. *Radiocarbon* 51 (2), 537–552. <http://dx.doi.org/10.1017/S0033822200055910>.
- Ferrater, M., Silva, P.G., Ortuño, M., Rodríguez-Pascua, M.A., Masana, E., 2015. Archaeoseismological analysis of a late bronze age site on the alhama de murcia fault, SE Spain. *Geoarchaeology* 30 (2), 151–164. <http://dx.doi.org/10.1002/gea.21505>.
- Freiesleben, T., Sohbati, R., Murray, A., Jain, M., al Khasawneh, S., Hvidt, S., Jakobsen, B., 2015. Mathematical model quantifies multiple daylight exposure and burial events for rock surfaces using luminescence dating. *Radiat. Meas.* 81, 16–22. <http://dx.doi.org/10.1016/j.radmeas.2015.02.004>.
- Galli, A., Panzeri, L., Rondini, P., Poggiani Keller, R., Martini, M., 2020. Luminescence dating of rock surface. the case of monoliths from the megalithic sanctuary of ossimo-pat (Valle Camonica, Italy). *Appl. Sci.* 10 (21), 7403. <http://dx.doi.org/10.3390/app10217403>.
- Glignani, L.A., Meyer, M.C., May, J.-H., Aldenderfer, M.S., Tropper, P., 2021. Direct dating of lithic surface artifacts using luminescence. *Sci. Adv.* 7 (23), eabb3424. <http://dx.doi.org/10.1126/sciadv.abb3424>.
- Glignani, L.A., Meyer, M.C., Sohbati, R., Jain, M., Barrett, S., 2019. OSL surface exposure dating of a lithic quarry in tibet: laboratory validation and application. *Quat. Geochronol.* 49, 199–204. <http://dx.doi.org/10.1016/j.quageo.2018.04.012>.
- Greilich, S., Glasmacher, U.A., Wagner, G.A., 2005. Optical dating of granitic stone surfaces. *Archaeometry* 47 (3), 645–665. <http://dx.doi.org/10.1111/j.1475-4754.2005.00224.x>.
- Habermann, J., Schilles, T., Kalchgruber, R., Wagner, G.A., 2000. Steps towards surface dating using luminescence. *Radiat. Meas.* 32 (5), 847–851. [http://dx.doi.org/10.1016/S1350-4487\(00\)00066-4](http://dx.doi.org/10.1016/S1350-4487(00)00066-4).
- Harris, E.C. (Ed.), 1989. *Principles of archaeological stratigraphy* (second edition). Academic Press, London. <http://dx.doi.org/10.1016/B978-0-12-326651-4.50001-8>.
- Holl, A.F.C., 1998. Livestock husbandry, pastoralisms, and territoriality: the west african record. *J. Anthropol. Archaeol.* 17 (2), 143–165. <http://dx.doi.org/10.1006/jaar.1998.0321>.
- Huntley, D.J., Lamothe, M., 2001. Ubiquity of anomalous fading in K-feldspars and the measurement and correction for it in optical dating. *Can. J. Earth Sci.* 38 (7), 1093–1106. <http://dx.doi.org/10.1139/e01-013>.
- Ives, K., 2018. Stone foundation houses of the late iron age and early medieval Å land and new C14-dates from the settlement of kulla. *Fennoscandia Archaeol.* XXXIV, 59–82.
- Ishii, Y., Takahashi, T., Ito, K., 2022. Luminescence dating of cobbles from pleistocene fluvial terrace deposits of the Ara River, Japan. *Quat. Geochronol.* 67, 101228. <http://dx.doi.org/10.1016/j.quageo.2021.101228>.
- Jaubert, J., Verheyden, S., Genty, D., Soulier, M., Cheng, H., Blamart, D., Burlet, C., Camus, H., Delaby, S., Deldicque, D., Edwards, R.L., Ferrier, C., Lacrampe-Cuyaubère, F., Lévêque, F., Maksud, F., Mora, P., Muth, X., Régnier, E., Rouzaud, J.-N., Santos, F., 2016. Early neanderthal constructions deep in bruniquel cave in southwestern France. *Nature* 534 (7605), 111–114. <http://dx.doi.org/10.1038/nature18291>.
- Jenkins, G.T.H., Duller, G.A.T., Roberts, H.M., Chiverrell, R.C., Glasser, N.F., 2018. A new approach for luminescence dating glaciofluvial deposits - high precision optical dating of cobbles. *Quat. Sci. Rev.* 192, 263–273. <http://dx.doi.org/10.1016/j.quascirev.2018.05.036>.
- Junge, A., Lomax, J., Shahack-Gross, R., Dunseth, Z.C., Finkelstein, I., Fuchs, M., 2016. OSL age determination of archaeological stone structures using trapped aeolian sediments: A case study from the negev highlands, Israel. *Geoarchaeology* 31 (6), 550–563. <http://dx.doi.org/10.1002/gea.21578>.
- Kemp, J., Olley, J., Stout, J., Pietsch, T., Corporation, M.A., 2022. Dating stone arrangements using optically stimulated luminescence and fallout radionuclides. *Geoarchaeology* n/a (n/a), 1–11. <http://dx.doi.org/10.1002/gea.21902>.
- Kremenić, T., Andlar, G., Varotto, M., 2021. How did sheep save the day? the role of dry stone wall heritage and agropastoralism in historical landscape preservation. A case-study of the town of cres olive grove. *Land* 10 (9), 978. <http://dx.doi.org/10.3390/land10090978>.
- Kreutzer, S., Burrow, C., Dietze, M., Fuchs, M.C., Schmidt, C., Fischer, M., Friedrich, J., Mercier, N., Smedley, R.K., Christophe, C., Zink, A., Durcan, J., King, G.E., Philippe, A., Guerin, G., Riedesel, S., Autzen, M., Guibert, P., Mittelstrass, D., Gray, H.J., Fuchs, M., 2021. Luminescence: comprehensive luminescence dating data analysis.
- Laskaris, N., Liritzis, I., 2011. A new mathematical approximation of sunlight attenuation in rocks for surface luminescence dating. *J. Lumin.* 131 (9), 1874–1884. <http://dx.doi.org/10.1016/j.jlumin.2011.04.052>.
- Lehmann, B., Herman, F., Valla, P.G., King, G.E., Biswas, R.H., 2019a. Evaluating post-glacial bedrock erosion and surface exposure duration by coupling in situ optically stimulated luminescence and  $^{10}\text{Be}$  dating. *Earth Surf. Dyn.* 7 (3), 633–662. <http://dx.doi.org/10.5194/esurf-7-633-2019>.

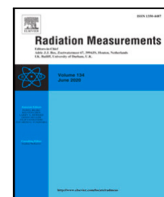
- Lehmann, B., Herman, F., Valla, P.G., King, G.E., Biswas, R.H., Ivy-Ochs, S., Steinemann, O., Christl, M., 2019b. Postglacial erosion of bedrock surfaces and deglaciation timing: new insights from the mont blanc massif (western alps). *Geology* 48 (2), 139–144. <http://dx.doi.org/10.1130/G46585.1>.
- Lehmann, B., Valla, P.G., King, G.E., Herman, F., 2018. Investigation of OSL surface exposure dating to reconstruct post-LIA glacier fluctuations in the French Alps (mer de glace, mont blanc massif). *Quat. Geochronol.* 44, 63–74. <http://dx.doi.org/10.1016/j.quageo.2017.12.002>.
- Levine, E.I., Rothenberg, M.A.W., Siegel, O., Knoblauch, C., Bestock, L., Klein, L., 2019. The uronarti regional archaeological project: second cataract fortresses and the western desert of Sudan. *Antiquity* 93 (372), <http://dx.doi.org/10.15184/aqy.2019.183>.
- Liritzis, I., 2001. Searching for precision of a new “luminescence clock” in dating calcitic rocks. *J. Radioanal. Nucl. Chem.* 247 (3), 727–730. <http://dx.doi.org/10.1023/A:1010696308875>.
- Liritzis, I., Aravantinos, V., Polymeris, G.S., Zacharias, N., Fappas, I., Agiamarniotis, G., Sfampa, I.K., Vafiadou, A., Kitis, G., 2015. Witnessing prehistoric delphi by luminescence dating. *C. R. Palevol* 14 (3), 219–232. <http://dx.doi.org/10.1016/j.crpv.2014.12.007>.
- Liritzis, I., Bednarik, R.G., Kumar, G., Polymeris, G., Iliopoulos, I., Xanthopoulou, V., Zacharias, N., Vafiadou, A., Bratitsi, M., 2019a. Daraki-chattan rock art constrained OSL chronology and multianalytical techniques: A first pilot investigation. *J. Cult. Herit.* 37, 29–43. <http://dx.doi.org/10.1016/j.culher.2018.09.018>.
- Liritzis, I., Panou, E., Exarhos, M., 2017. Novel Approaches In Surface Luminescence Dating Of Rock Art: A Brief Review. Zenodo, <http://dx.doi.org/10.5281/ZENODO.893194>.
- Liritzis, I., Polymeris, G.S., Vafiadou, A., Sideris, A., Levy, T.E., 2019b. Luminescence dating of stone wall, tomb and ceramics of kastroli (phokis, Greece) late helladic settlement: case study. *J. Cult. Herit.* 35, 76–85. <http://dx.doi.org/10.1016/j.culher.2018.07.009>.
- Liritzis, I., Vafiadou, A., 2015. Surface luminescence dating of some Egyptian monuments. *J. Cult. Herit.* 16 (2), 134–150. <http://dx.doi.org/10.1016/j.culher.2014.05.007>.
- Liritzis, I., Zacharias, N., Al-Otaibi, F., Iliopoulos, I., Katagas, C., Shaltout, M., 2016. Chronology of construction and occupational phases of nawamis tombs, sinai based on OSL dating. *Geochronometria* 43, <http://dx.doi.org/10.1515/geochr-2015-0041>.
- Liritzis, I., Zacharias, N., Polymeris, G.S., 2010. Surface luminescence dating of ‘dragon houses’ and armena gate at styra (euboea, Greece). *Mediterr. Archaeol. Archaeom.* 10 (3), 65–81.
- Liszka, K., 2017. Egyptian or nubian? dry-stone architecture at wadi el-hudi, wadi es-sebua, and the eastern desert. *J. Egypt. Archaeol.* 103 (1), 35–51. <http://dx.doi.org/10.1177/0307513317714407>.
- Manley, J., 1990. A late bronze age landscape on the denbigh moors, northeast Wales. *Antiquity* 64 (244), 514–526. <http://dx.doi.org/10.1017/S0003598X00078418>.
- Mazet, S., 2006. Habitat and stone enclosure of corsica: what is the function of the enclosed area during the neolithic and the bronze age? In: 2006 First International Symposium on Environment Identities and Mediterranean Area. <http://dx.doi.org/10.1109/ISEIMA.2006.345020>.
- Medici, T., Foradori, G., Carrer, F., Maschio, R., Gialanella, S., Montagna, M., Pedrotti, A., Angelucci, D., 2014. Una perla in vetro da un contesto pastorale d’altura della val di sole (trento). ISBN: 978-88-907297-3-7, pp. 115–123.
- Meyer, M., Gliganic, L., Jain, M., Sohbati, R., Schmidmair, D., 2018. Lithological controls on light penetration into rock surfaces – implications for OSL and IRSL surface exposure dating. *Radiat. Meas.* 120, 298–304. <http://dx.doi.org/10.1016/j.radmeas.2018.03.004>.
- Murray, A.S., Marten, R., Johnston, A., Martin, P., 1987. Analysis for naturally occurring radionuclides at environmental concentrations by Gamma spectrometry. *J. Radioanal. Nucl. Chem. Artic.* 115 (2), 263–288. <http://dx.doi.org/10.1007/BF02037443>.
- Murray, A., Wintle, A., 2000. Luminescence dating of quartz using an improved single-aliquot regenerative-dose protocol. *Radiat. Meas.* 32 (1), 57–73. [http://dx.doi.org/10.1016/S1350-4487\(99\)00253-X](http://dx.doi.org/10.1016/S1350-4487(99)00253-X).
- Ou, X., Roberts, H., Duller, G., Gunn, M., Perkins, W., 2018. Attenuation of light in different rock types and implications for rock surface luminescence dating. *Radiat. Meas.* 120, 305–311. <http://dx.doi.org/10.1016/j.radmeas.2018.06.027>.
- Passariello, I., Talamo, P., D’Onofrio, A., Barta, P., Lubritto, C., Terrasi, F., 2010. Contribution of radiocarbon dating to the chronology of eneolithic in campania (Italy). *GEOCHR* 35 (-1), 25–33. <http://dx.doi.org/10.2478/v10003-010-0008-2>.
- Polikreti, K., Michael, C., Maniatis, Y., 2002. Authenticating marble sculpture with thermoluminescence. *Ancient TL* 20, 11–18.
- Prescott, J.R., Hutton, J.T., 1994. Cosmic ray contributions to dose rates for luminescence and ESR dating: large depths and long-term time variations. *Radiat. Meas.* 23 (2), 497–500. [http://dx.doi.org/10.1016/1350-4487\(94\)90086-8](http://dx.doi.org/10.1016/1350-4487(94)90086-8).
- Rades, E., Sohbati, R., Lüthgens, C., Jain, M., Murray, A., 2018. First luminescence-depth profiles from boulders from moraine deposits: insights into glaciation chronology and transport dynamics in malta valley, Austria. *Radiat. Meas.* 120, 281–289. <http://dx.doi.org/10.1016/j.radmeas.2018.08.011>.
- Reimann, T., Tsukamoto, S., Naumann, M., Frechen, M., 2011. The potential of using K-rich feldspars for optical dating of Young coastal sediments – A test case from darss-zingst peninsula (southern baltic sea coast). *Quat. Geochronol.* 6 (2), 207–222. <http://dx.doi.org/10.1016/j.quageo.2010.10.001>.
- Reitmaier, T., Lambers, K., Walser, C., Zingman, I., Haas, J.N., Dietre, B., Reidl, D., Hajdas, I., Nicolussi, K., Kathrein, Y., Naef, L., Kaiser, T., 2013. Alpine Archäologie in der silvretta. *Archäologie Schweiz* 36 (1), 4–15.
- Riedesel, S., Autzen, M., 2020. Beta and Gamma dose rate attenuation in rocks and sediment. *Radiat. Meas.* 133, 106295. <http://dx.doi.org/10.1016/j.radmeas.2020.106295>.
- Riedesel, S., Autzen, M., 2021. Calc\_CobbleDoseRate: calculate dose rate of slices in a spherical cobble.
- Sohbati, R., Murray, A.S., Buylaert, J.P., Almeida, N.A.C., Cunha, P.P., 2012a. Optically stimulated luminescence (OSL) dating of quartzite cobbles from the tapada do montinho archaeological site (east-central Portugal): OSL dating of quartzite cobbles, tapada do montinho, Portugal. *Boreas* 41 (3), 452–462. <http://dx.doi.org/10.1111/j.1502-3885.2012.00249.x>.
- Sohbati, R., Murray, A.S., Chapot, M.S., Jain, M., Pederson, J., 2012b. Optically stimulated luminescence (OSL) as a chronometer for surface exposure dating. *J. Geophys. Res.: Solid Earth* 117 (B9), <http://dx.doi.org/10.1029/2012JB009383>.
- Sohbati, R., Murray, A.S., Jain, M., Buylaert, J.P., Thomsen, K.J., 2011. Investigating the resetting of OSL signals in rock surfaces. *Geochronometria* 38 (3), 249–258. <http://dx.doi.org/10.2478/s13386-011-0029-2>.
- Sohbati, R., Murray, A.S., Porat, N., Jain, M., Avner, U., 2015. Age of a prehistoric “Rodedian” cult site constrained by sediment and rock surface luminescence dating techniques. *Quat. Geochronol.* 30, 90–99. <http://dx.doi.org/10.1016/j.quageo.2015.09.002>.
- Souza, P.E., Sohbati, R., Murray, A.S., Clemmensen, L.B., Kroon, A., Nielsen, L., 2021. Optical dating of cobble surfaces determines the chronology of holocene beach ridges in Greenland. *Boreas* 50 (2), 606–618. <http://dx.doi.org/10.1111/bor.12507>.
- Souza, P.E., Sohbati, R., Murray, A.S., Kroon, A., Clemmensen, L.B., Hede, M.U., Nielsen, L., 2019. Luminescence dating of buried cobble surfaces from sandy beach ridges: A case study from Denmark. *Boreas* 48 (4), 841–855. <http://dx.doi.org/10.1111/bor.12402>.
- Team, R.C., 2021. R: A Language and Environment for Statistical Computing. R Foundation for Statistical Computing, Vienna, Austria, URL <https://www.R-project.org/>.
- Thomsen, K.J., Murray, A.S., Jain, M., Bøtter-Jensen, L., 2008. Laboratory fading rates of various luminescence signals from feldspar-rich sediment extracts. *Radiat. Meas.* 43 (9), 1474–1486. <http://dx.doi.org/10.1016/j.radmeas.2008.06.002>.
- Vafiadou, A., Murray, A., Liritzis, I., 2007. Optically stimulated luminescence (OSL) dating investigations of rock and underlying soil from three case studies. *J. Archaeol. Sci.* 34 (10), 1659–1669. <http://dx.doi.org/10.1016/j.jas.2006.12.004>.
- Walsh, K., 2005. Risk and marginality at high altitudes: new interpretations from fieldwork on the faravel plateau, hautes-alpes. *Antiquity* 79, <http://dx.doi.org/10.1017/S0003598X00114097>.
- Walsh, K., Court-Picon, M., de Beaulieu, J.-L., Guiter, F., Mocci, F., Richer, S., Sinet, R., Talon, B., Tzortzis, S., 2014. A historical ecology of the ecrons (southern french alps): archaeology and palaeoecology of the mesolithic to the medieval period. *Quat. Int.* 353, 52–73. <http://dx.doi.org/10.1016/j.quaint.2013.08.060>.
- Yar, B., Dubois, P., 1996. Les structures d’habitat au Paléolithique inférieur et moyen en France : entre réalité et imaginaire. *Bull. Société Préhistorique Française* 93 (2), 149–163. <http://dx.doi.org/10.3406/bspf.1996.10133>.





## Chapter 4

# Investigating optical dating of carbonate-rich cobbles from a river terrace: A pilot study from the Mula Valley, Spain



# Investigating optical dating of carbonate-rich cobbles from a river terrace: A pilot study from the Mula Valley, Spain

Lucas Ageby<sup>a,\*</sup>, Dominik Brill<sup>a</sup>, Diego E. Angelucci<sup>b</sup>, Helmut Brückner<sup>a</sup>, Nicole Klasen<sup>a</sup>

<sup>a</sup> Institute of Geography, University of Cologne, Albertus-Magnus-Platz, Cologne, 50937, Germany

<sup>b</sup> Department of Humanities, University of Trento, via T. Gar 14, Trento, 38122, Italy

## ARTICLE INFO

### Keywords:

Rock surface luminescence dating  
IRSL  
Feldspars  
River terrace  
Calcarenites

## ABSTRACT

Rock surface luminescence dating has emerged as a powerful geochronological tool; however, the method requires lithologies containing sufficient amounts of quartz or feldspar grains. The application of burial dating to fluvial cobbles, containing only sparse amounts of feldspars, is evaluated in calcarenite cobbles collected in the Mula valley, Spain. Two sampled cobbles demonstrated sufficient luminescence sensitivity. We extracted three or more drill cores from each cobble surface and subsequently measured the sensitivity-corrected luminescence signal with depth using an IRSL/pIRIR protocol to target feldspar grains in calcarenites. We observed significant luminescence-signal depth variations between the cores collected from the same rock surface, suggesting the value of measuring several cores. None of the top surfaces has been significantly bleached; therefore, they convey no relevant age data. Cores from the bottom surfaces show evidence of bleaching in the first 1 to 3 mm, but generally, only the surface slices can be used for dating. One core from each cobble displays a short, non-saturated dose plateau near the surfaces; the modelling demonstrates that the surface slices from these cores contained negligible doses before burial. The age estimate for the bottom surfaces mainly falls into two groups: 24–38 ka and 11–16 ka. The older age group is within the expected age range, previously dated with radiocarbon on another outcrop of the same terrace system. However, the signal-depth profiles indicate that the younger date is more reliable than the older date. Currently, no geomorphological explanation exists to explain the younger-than-expected ages.

## 1. Introduction

Since sufficient amounts of quartz and feldspar are a prerequisite for optical dating of rock surfaces, most studies using rock surface luminescence dating have involved cobbles of lithologies that are rich in those minerals, e.g., granites (Freiesleben et al., 2015; Jenkins et al., 2018), gneisses (Rades et al., 2018; Ageby et al., 2021), quartzites (Gliganic et al., 2019, 2021), and sandstones (Chapot et al., 2012; Sohbati et al., 2012b; al Khasawneh et al., 2019). However, lithologies that contain large amounts of quartz and feldspar are rare in some regions. For example, the southern Iberian Peninsula, an important region concerning the debate regarding late Neanderthal persistence (e.g. Finlayson et al., 2008; Zilhão et al., 2017; Zilhão, 2021), is dominated by sedimentary carbonate rocks, among them calcarenites, which contain only small amounts of quartz and feldspars.

Palaeolithic sites in the Iberian Peninsula are commonly located in fluvial valleys (e.g. Kehl et al., 2016, 2018; Alcaraz-Castaño et al., 2021), where alluvial processes dominate the landscape evolution. Such valleys are part of fluvial systems, many of which have evolved through

cycles of river incision and aggradation (e.g. Macklin et al., 2002; Santisteban and Schulte, 2007; Silva et al., 2017). Reliable geochronology is essential to understanding the timing of terrace formation, which has further implications regarding environmental changes (Gregory et al., 2006). Late Pleistocene and Holocene archaeological sites and terraces in such fluvial systems in the Iberian Peninsula are often dated by radiocarbon and OSL dating of sediments (e.g. Schulte et al., 2008; Geach et al., 2015; Kehl et al., 2018; Wolf et al., 2021). While indispensable, these techniques can be affected by methodological and environmental constraints. Radiocarbon dating, for example, requires suitable in-situ organic matter, and the Middle-Upper Palaeolithic transition is located at the upper age range (~40 ka) of the method. Luminescence dating of sediments is often used since the range of the technique often extends beyond this age range. Luminescence dating of alluvial and fluvial sediments can, however, be challenging since grains in such deposits may be affected by partial bleaching (e.g. Olley et al., 1999; Smedley and Skirrow, 2020), which requires the utilisation of advanced luminescence dating techniques such as single-grain dating (e.g., Duller

\* Corresponding author.

E-mail address: [lucas.ageby@hotmail.com](mailto:lucas.ageby@hotmail.com) (L. Ageby).

<https://doi.org/10.1016/j.radmeas.2023.106962>

Received 30 March 2022; Received in revised form 30 March 2023; Accepted 25 May 2023

Available online 30 May 2023

1350-4487/© 2023 Elsevier Ltd. All rights reserved.

et al., 1999; Olley et al., 1999; Duller et al., 2003), and appropriate age distribution modelling (e.g., Galbraith et al., 1999; Thomsen et al., 2007; Medialdea et al., 2014; Chamberlain et al., 2018). Successful single-grain luminescence dating of fluvial deposits is frequently reported (e.g., Trauerstein et al., 2014). Single-grain luminescence dating is, however, not always straightforward. For example, the dose distributions can be affected by sources other than partial bleaching, such as small-scale variations in microdosimetry (e.g., Mayya et al., 2006; Guérin et al., 2015; Jankowski and Jacobs, 2018; Smedley et al., 2020; Fu et al., 2022), making data interpretation harder. Carbonate-rock-dominated environments are susceptible to dosimetry variations due to lower overall potassium concentrations (Mayya et al., 2006). Also, coarse-grained fluvial deposits might not always be suitable for single-grain dating.

Rock surface luminescence dating is a geochronological tool that can date when a rock surface is buried. The method provides valuable information regarding how thoroughly the luminescence signal was reset by bleaching during exposures. Since the spatial relationships between mineral grains in rocks are consistent during cycles of transport and deposition, the grains are not mixed or lost (unless the rock is abraded during transport), luminescence signal-depth profiles (e.g. Habermann et al., 2000; Sohbati et al., 2011; Gliganic et al., 2019) store information regarding recent or past exposure and burial events (e.g., Freiesleben et al., 2015). Therefore, rock surface luminescence dating may be used to identify rock surfaces that were well-bleached before burial. The luminescence signal is reset with depth into the rock during exposure, and once a rock surface is again buried, the ionising radiation will increase the luminescence signal at the bleached surface to form a signal plateau. Previous investigations of burial dating with rock surface luminescence in fluvial settings have shown promising results regarding signal resetting (Sohbati et al., 2012a; Liu et al., 2019) and comparisons with independent age control (Ishii et al., 2022). No study, however, has investigated the application of rock surface luminescence dating of alluvial terraces in environments where only carbonate-rich rocks are available for sampling.

The Mula basin IGME (1972a,b) is dominated by carbonate deposits, and a valley has formed due to alluvial activity of the Mula river during the Quaternary. Cycles of incision and aggradation by the Mula river have produced a system of Pleistocene and Holocene terrace levels (Mather et al., 1995; Silva et al., 1996; Angelucci et al., 2018). Several Middle and Upper Palaeolithic sites are located within the Mula basin Zilhão et al. (2010), Angelucci et al. (2013), Zilhão et al. (2016, 2017), and thus, the area is of considerable archaeological importance concerning the still-debated topics regarding the Neanderthal-sapiens transition in the Iberian Peninsula (Zilhão, 2021). Here, we investigate the application of rock surface luminescence dating of feldspars in carbonate-rich rocks from the Mula basin, southeastern Spain, attempting to apply feldspar luminescence dating to a – from a mineralogical point of view – challenging lithology. This pilot study aims to describe signal characteristics and luminescence signal resetting in calcarenites from a fluvial setting; the results also provide insights into the application of burial dating of river-transported cobbles.

## 2. Material and methods

### 2.1. Site description and sampling

The sampled location (MULA1802) is situated in the Mula valley (Fig. 1A), upstream of the La Cierva reservoir and the El Corcovado gorge. The site is an outcrop of a terrace remnant (Fig. 1B–C), which is +5–7 m above the modern Mula river thalweg. A ~2 m thick stratigraphic section is exposed at the northeastern edge of MULA1802. This section contains a ~30 cm layer of matrix-supported gravels, which are visible at the lowermost exposed part of the outcrop and are buried by up to two metres of slope deposits. This gravel layer mainly

consists of rounded cobbles and pebbles of intrabasin lithologies: limestones and marlstones, with some calcarenite clasts. Selecting cobbles which contain sufficient silicate minerals (checked with a hand lens, magnification: 10x) was challenging since such minerals could only be observed in a few clasts. We collected 18 calcarenite clasts from the gravel layer (Table B.1; supplementary material). All samples are rounded and of varied sphericity. The orientation of the cobble was marked; the upward and downward-facing surfaces will here be termed “top” and “bottom” surfaces, respectively. The cobbles were extracted from the outcrop and quickly covered in opaque plastic bags to prevent signal bleaching during sampling. Any exposed surfaces were marked before sampling to be identified later in the laboratory (these areas were carefully avoided during further sample preparations). However, many of the selected clasts were too small for core extraction. The large clasts were screened for luminescence sensitivity by dosing a bleached slice with 26 Gy or more before measuring the luminescence count. Three of the eleven sampled screened for their luminescence properties (including samples from an adjacent valley to Mula) showed significant luminescence response. Two of these cobbles, MULA1802-2 (Fig. 1D) and MULA1802-7 (Fig. 1E), were large enough to permit the extraction of three or more intact cores from each cobble surface. These samples were buried horizontally approximately 1.5 metres apart. Additionally, a bulk sediment sample (MULA1802-DR) was collected from the gravel layer to measure the concentration of radionuclides surrounding the collected cobbles.

The terrace level of MULA1802 was previously observed as a series of alluvial sequences in the Middle Palaeolithic rock shelter Cueva Antón (Angelucci et al., 2013; Zilhão et al., 2016), located ~1 km downstream in the El Corcovado gorge (see supplementary material for additional regional description). The formation of the terrace level at Cueva Antón (Table A.1, supplementary material) occurred during cycles of fluvial activity in Marine Isotope Stages (MIS) 4 (lower sequence: OSL dating) and 3 (upper sequence: radiocarbon dating) (Burow et al., 2015; Zilhão et al., 2016).

A layer of fluvial sand exposed slightly upstream at MULA1802 dates to  $103 \pm 5$  ka (sample MULA1802-4; OSL-dating of quartz; see supplementary material for more detail). This date provides a minimum age for the dated cobbles and supports the model for the evolution of the Mula valley during the early Late Pleistocene as proposed by Angelucci et al. (2018).

A thin section from one sampled cobble (MULA1802-2; see Figure D.1 in the supplementary material for photomicrographs) allowed for the study of the mineralogical composition of this cobble on a microscopic scale. Accordingly, cobble MULA1802-2 mainly consists of fossils and sparry cement. Tectosilicates are only minor minerals, observable as less than 5% of the total grain volume. Some low birefringence detrital tectosilicate grains are observed, surrounded by sparite. A handful of these grains show wavy extinction, which indicates that they are most likely quartz; however, most grains show no twinning or are significantly weathered, making it hard to differentiate between quartz and feldspar. The apparent size of the quartz and feldspar grains in the thin section is <50 µm; most grains appear to be of subangular to angular shape.

### 2.2. Laboratory preparations and luminescence measurements

We extracted drill cores (~10 mm diameter) from both the upper and lower surface of the cobbles with a water-cooled, diamond-tipped drill, all in subdued red light conditions. A minimum of three cores from each cobble surface were prepared in this manner. We cut the cores into ~0.5–1.3 mm thin slices (see Table B.2 for the thickness of each individual slice), which were then cleaned in acetone to remove rock residue from the saw blade. Each slice was measured using a micrometre tool, calculating an average thickness of two perpendicular measurements. Surface slices were cut thicker due to their fragility.



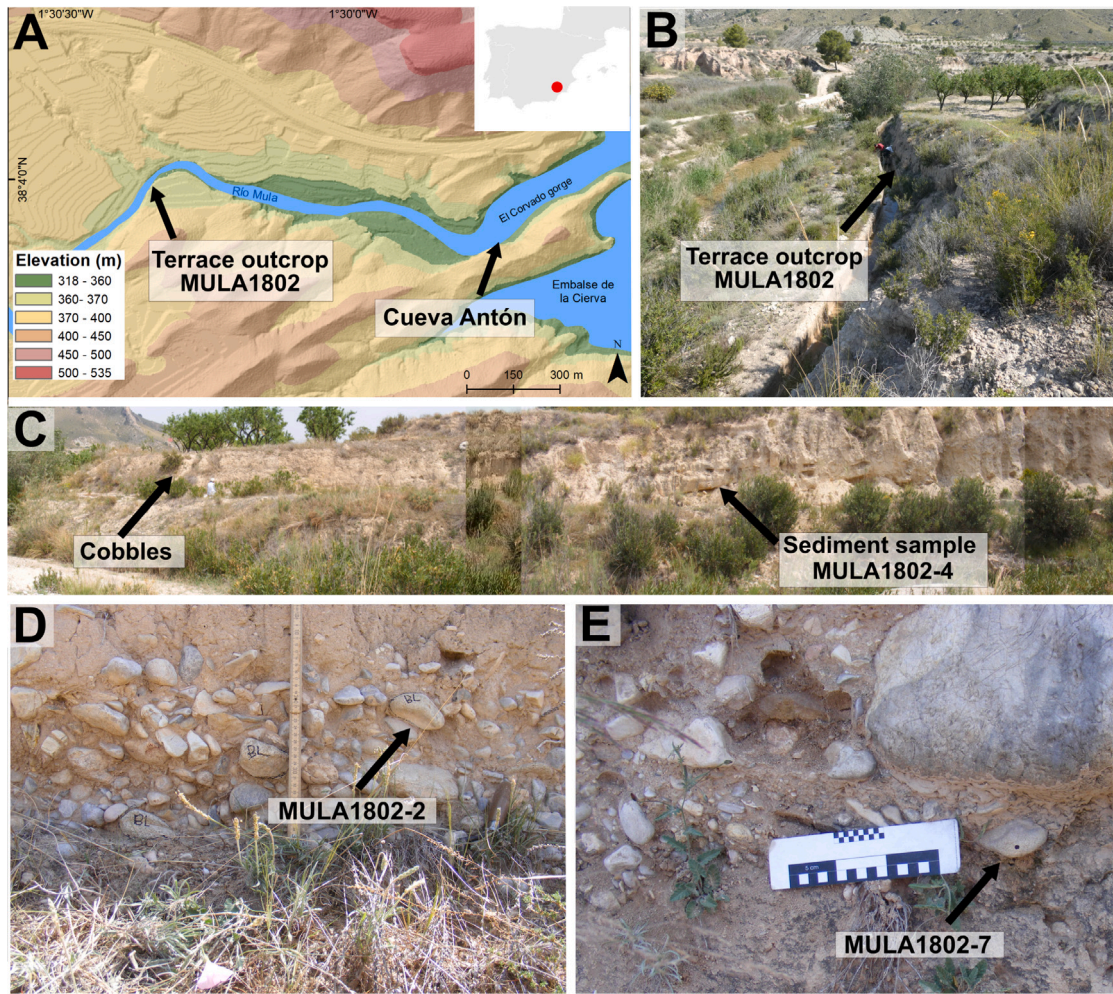


Fig. 1. Digital elevation model of the Mula valley (National Aerial Orthophoto Plan; <https://pnoa.ign.es/>). (B) View from the southwest of the +5–7 m terrace at the outcrop MULA1802, and (C) mosaic image of the entire MULA1802. (D–E) The position of the buried cobbles before sampling.

**Table 1**  
The measurement protocol for cobbles.

Step	Action	Observed signal
1	Beta irradiation	
2	Preheat (100 s at 250 °C)	
3	Pause (30 s)	
4	IRSL (300 s at 50 °C)	IRSL ( $L_x$ )
5	IRSL (300 s at 225 °C)	pIRIR <sub>225</sub> ( $L_x$ )
6	Beta irradiation	
7	Preheat (100 s at 250 °C)	
8	Pause (30 s)	
9	IRSL (300 s at 50 °C)	IRSL ( $T_x$ )
10	IRSL (300 s at 225 °C)	pIRIR <sub>225</sub> ( $T_x$ )

From one core per bottom surface and cobble, the outer 1 mm was dissolved in 10% hydrochloric acid to extract non-carbonate grains. All luminescence measurements were conducted at the Cologne Luminescence Laboratory at the University of Cologne, Germany, using a RisøTL/OSL reader (model DA-20) (Bøtter-Jensen et al., 2010). All IRSL and pIRIR signals were filtered through a blue light interference filter (D410 nm) and detected with a blue/UV sensitive 9235QB photomultiplier tube. Infrared diodes (870 nm; ~130 mW/cm<sup>2</sup>) were used for stimulation. The heating rate was 2 °C s<sup>-1</sup> for all heat treatments and measurements. The reader was equipped with a beta radiation source (~0.08 Gy s<sup>-1</sup>), calibrated using quartz grains (Hansen et al., 2015) (for grains from dissolved slices) and ~1.1 mm thick gamma irradiated quartz arenite rock slices (for slices). OSL dating of rocks using

blue-light stimulation is often impractical since polymineral aliquots (e.g. slices) from many lithologies will contain both quartz and feldspar grains. This is because the luminescence signals in quartz and some feldspars are sensitive to blue stimulation (Krbetschek et al., 1997), making it hard to distinguish from which mineral the luminescence emission originates. Thus, considering that our collected rocks contain both quartz and feldspar grains (albeit in small quantities), we instead used infrared (IR) stimulation to isolate the feldspar fraction using IRSL and pIRIR dating techniques (e.g. Wallinga et al., 2000; Preusser, 2003; Buylaert et al., 2009). We applied a pIRIR protocol to the rock samples using an initial IR stimulation at 50 °C for 300 s (IRSL), followed by a pIRIR stimulation at 225 °C for an additional 300 s (pIRIR<sub>225</sub>). This protocol is similar to others used previously for rock surface dating (Sohbati et al., 2015; Brill et al., 2022; Ishii et al., 2022). We measured the sensitivity corrected natural IRSL and pIRIR ( $L_n/T_n$ ) from the first cycle of a single aliquot regenerative (SAR) protocol (Murray and Wintle, 2000) (Table 1) on whole slices to create luminescence signal-depth profiles. A test dose of 25.6 Gy was used for sensitivity correction. Equivalent doses ( $D_e$ ) for surface slices and dissolved grains from surface chips were measured with a full SAR protocol, including cycles of increasing regenerative beta doses. Preheat was 250 °C, administered for 100 s. A 30 s pause was inserted between the preheat and the first IR stimulation. Slices were mounted directly into the sample carousel, while the grains were mounted as 1 mm aliquots on stainless steel discs; both types of samples fit into the sample carousel for standard discs without additional modifications.

**Table 2**

Radionuclide concentrations and effective dose rate. The cosmic dose rate for both cobbles is  $0.20 \pm 0.02$  Gy ka<sup>-1</sup>. Internal K is  $0.11 \pm 0.04$  Gy ka<sup>-1</sup>. Beta and gamma dose rates are reported for 0–1.5 mm rock depth.

Sample	Lab.ID	Sample type	Radionuclide concentration			Dose rate (Gy ka <sup>-1</sup> )		
			U (ppm)	Th (ppm)	K (%)	Alpha <sup>a</sup>	Beta <sup>a,b</sup>	Gamma
MULA1802-2	C-L4619	Cobble	1.12 ± 0.06	1.47 ± 0.13	0.30 ± 0.01	0.23 ± 0.07	0.44 ± 0.04	0.24 ± 0.02
MULA1802-7	C-L4643	Cobble	1.14 ± 0.07	1.44 ± 0.10	0.27 ± 0.01	0.24 ± 0.07	0.43 ± 0.03	0.27 ± 0.02
MULA1802-DR		Sediment	1.36 ± 0.08	2.26 ± 0.15	0.39 ± 0.01			

<sup>a</sup>Calculated for 20–40 µm grain diameter.

<sup>b</sup>Excluding internal K.

### 2.3. Dose rate

The radionuclide concentrations in the cobbles and sediments (Table 2) were measured with high-resolution gamma spectrometry on ~200 g of crushed samples. After crushing, the samples were stored for three weeks or more before being measured. The cosmic dose component was calculated following Prescott and Hutton (1994). Since moisture in rock samples is usually negligible (e.g., Sohbati et al., 2015; Jenkins et al., 2018), moisture is not considered when calculating the dose rate originating from radionuclides within the cobbles themselves. We assume a moisture content of  $20 \pm 5\%$  for the surrounding sediments based on observation of previous groundwater levels. The radionuclide concentrations from the cobbles and the surrounding sediments were converted using conversion factors from Cresswell et al. (2018). Depth-dependent attenuated beta and gamma dose rates were estimated with the *calc.CobbleDoseRate()* function (Riedesel and Autzen, 2021) supplied by the *Luminescence* package (Kreutzer et al., 2021) for R v. 4.1.0 (R Core Team, 2021). The function attenuates beta and gamma radiation with depth based on cobble diameter (~40 mm for both MULA1802-2 and MULA1802-7) and density (2.7 g/cm<sup>3</sup>) using attenuation factors modelled by Riedesel and Autzen (2020). The alpha dose component, corrected with an a-value of  $0.11 \pm 0.03$  (Balescu and Lamothe, 1993), was assumed to be independent of depth into cobbles.

Determining the internal potassium content of the feldspar grains in cobbles remains challenging. While values of  $10 \pm 2\%$  (Smedley et al., 2012) or  $12.5 \pm 0.5\%$  (Huntley and Baril, 1997) are most commonly used for sediment dating, investigations with µXRF of rock slices from Alpine gneisses indicate that lower internal potassium contents may be more suitable for some lithologies (Rades et al., 2018). Inspecting the thin section from MULA1802-2 did not allow us to draw conclusions about the most common feldspars in our lithologies. While grain size estimations derived from microscopic examination usually differ slightly from sieved grain sizes since the cutting plane might not intersect the grain in the middle (Baiyegunhi et al., 2020), which could cause an underestimation in the beta dosing deriving from any truncated grains (Bailiff, 2018). We did not observe any low birefringence grains >50 µm along their longest axis. Therefore, we estimate a feldspar grain diameter range of 20–40 µm to be realistic. The dose contribution from internal potassium is overall small (<10% of total dose rate) from silt-sized feldspar grains. Hence, the chosen potassium content will only slightly affect any reported ages. Finally, a potassium content of  $12.5 \pm 0.5\%$  and grain size of  $30 \pm 10$  µm were assumed for dose rate calculations.

### 2.4. Fitting and age determination

The bleaching fronts into the cobbles are modelled by fitting signal-depth profiles with the model presented in Freiesleben et al. (2015):

$$L(x) = \underbrace{\left( \frac{\text{Exposure event}}{L_0 e^{-t_e \bar{\sigma} \varphi_0 - \mu x}} - 1 \right)}_{\text{Burial event}} e^{\frac{D(x)}{D_0} t_b} + 1 \quad (1)$$

which models a pre-burial exposure event, followed by the burial of the rock surface. Although this study will not quantify exposure events,

the fitting of signal-depth profiles provides an objective way to identify burial events. The luminescence  $L$  at depth  $x$  (mm; calculated from the average thickness midpoint of each individual slice) is dependent on the luminescence signal in field saturation  $L_0$ , the attenuation of light ( $\mu$ ; mm<sup>-1</sup>) into the rock, the time in seconds ( $t_e$ ) for which the surface has been exposed, the rate at which the trapped charge decays  $\bar{\sigma} \varphi_0$  (s<sup>-1</sup>) based on the photoionising cross-section ( $\sigma$ ) and the light flux at the rock surface ( $\varphi_0$ ), the depth-dependent dose rate  $\dot{D}$ , the characteristic dose ( $D_0$ ), and the length of burial ( $t_b$ ).  $\bar{\sigma} \varphi_0$  is commonly quantified by using calibration surfaces with a known  $t_e$  (Sohbati et al., 2012b). We do not have access to such a surface (and our focus is on burial dating), so we instead fit our signal-depth profiles with a combined parameter  $t_e \bar{\sigma} \varphi_0$  (e.g., Freiesleben et al., 2015; Rades et al., 2018), and an unconstrained  $\mu$  (e.g., Cunningham et al., 2022).  $\frac{t_b}{D_0}$  were combined into a single fitted parameter since we calculated the burial ages from the measured  $D_e$ . We fitted the observed  $L_n/T_n$  data with the entire Eq. (1) using the *nls()* function in R (v 4.2).

The anomalous fading of the luminescence signal observed in feldspars (Wintle, 1973) was measured using the approach of Auclair et al. (2003). Fading rates on laboratory time scales were measured by irradiating (~24 Gy) and preheating the slices before storage. The storage periods ranged from prompt to ~2 days before the signal was measured (Figure E.2; supplementary material). The IRSL signals fade at  $1.7 \pm 0.62$  and  $1.2 \pm 0.67\%$  /decade for MULA1802-2 and MULA1802-7, respectively. Fading is negligible for the pIRIR<sub>225</sub> signal. Ages were calculated by dividing the  $D_e$  from the surface slice by the depth-dependent dose rate. The cobble ages and sediment IRSL and pIRIR ages were corrected for fading using the g-values following Huntley and Lamothe (2001). All fading analyses and age calculations were executed with the *Luminescence* package (Kreutzer et al., 2021) in R.

## 3. Results

### 3.1. Signal characteristics

The IRSL and pIRIR sensitivities vary considerably between different slices. Overall, the IRSL signal is sufficiently bright for dating, while the pIRIR<sub>225</sub> signal is dim in both MULA1802-2 and MULA1802-7 (Fig. 2). Dose recovery tests were performed on three fresh slices per cobble to test the ability of the measurement protocol to recover a known beta dose. The slices were bleached for 24 h in a Hönle Solar Simulator before the beta dose was administered. The results demonstrate good dose recovery for the IRSL signal for both samples, producing dose ratios of  $1.06 \pm 0.05$  and  $1.05 \pm 0.02$  for MULA1802-2 and MULA1802-7, respectively. However, for the pIRIR signal, the recovered doses overestimate the given dose (23 Gy) and are outside the acceptable ratio range (unity ± 10%) with  $1.13 \pm 0.08$  for MULA1802-2 and  $1.62 \pm 0.41$  for MULA1802-7. After 24 h of bleaching in the solar simulator, the residual dose was measured on three slices from MULA1802-7, providing residual doses of  $0.9 \pm 0.1$  Gy and  $5.4$  Gy ± 0.6 Gy for IRSL and pIRIR, respectively. Despite the significant residual dose for the pIRIR signal, this does not explain the severe overestimation of the dose recovery since subtracting the residual dose before calculating the dose recovery ratio still yields a pIRIR ratio of  $1.27 \pm 0.30$ .



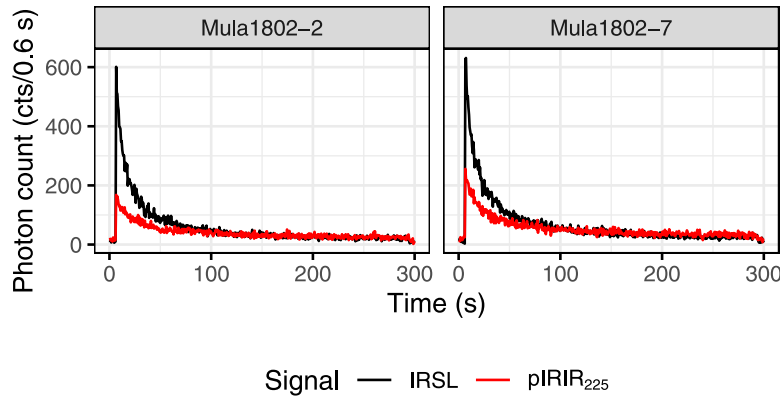


Fig. 2. Decay curves from surface slices following  $\sim 26$  Gy of beta irradiation.

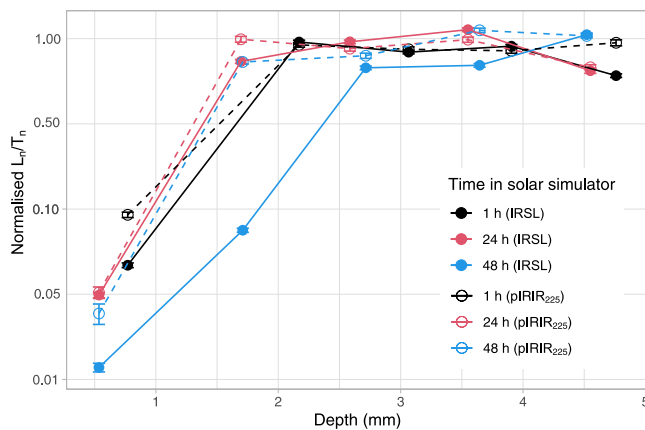


Fig. 3. Observed luminescence-depth profiles from a freshly exposed surface of MULA1802-2 following exposure in a solar simulator. The y-axis is plotted on a logarithmic scale. The slice depth is plotted as the mid-point of each slice.

### 3.2. Signal-depth profiles

We exposed a freshly cut surface of MULA1802-2 in a Hönle solar simulator for 1, 24, and 48 h (Fig. 3) to investigate if the IRSL and pIRIR<sub>225</sub> bleaching fronts would form if the surface is exposed to light. If no or little bleaching is observed, then insufficient bleaching and high residual signals would prevent the successful dating of our cobbles. Since the centre of MULA1802-2 is in field saturation, any observed bleaching should have occurred in the solar simulator. The surface was cored after increasing periods of exposure, the cores were sliced, and slices were measured using the protocol presented in Table 1. Both the IRSL and pIRIR<sub>225</sub> signals were reset to  $<10\%$  of saturation in the surface slice after one hour of exposure. Prolonged exposure bleaches both signals deeper into the artificial surface, and only a negligible IRSL residual remains in the surface slice after 48 h of exposure.

The shape of the natural signal-depth profiles (Fig. 4) differs significantly between the top and bottom surfaces of the buried cobbles MULA1802-2 and MULA1802-7. At the top surface of MULA1802-2, the signal-depth profiles show little or no signs of bleaching for either the IRSL or the pIRIR signals. Potentially, core 1 could display a weak bleaching front, but the large scatter in  $L_n/T_n$  displayed between saturated slices (19% and 15% relative standard deviation for the IRSL and pIRIR signals, respectively) means that this observation could also be related to scatter. The surface slices of the cores from the bottom surface show significantly more bleaching than at the top surface. All cores, except for cores 4 and 13, show that the IRSL signal is bleached to  $<25\%$  of the saturated signal in the surface slices. The bleaching fronts are overall short; the IRSL signal intensity rises significantly beyond

the first 1.5 mm in most cores. Only core 3 displays a short IRSL signal plateau (this plateau is not observed for the pIRIR data), where the normalised signal intensity increases from 0.07% in the surface slice to 12% in the second slice ( $\sim 2$  mm depth from the bottom surface).  $L_n/T_n$  is  $>50\%$  of the saturated IRSL level in the second slices for the other cores. For the pIRIR signal, only core 3 shows bleaching to  $<25\%$  of the saturated signal in the surface slice. All other cores show only some ( $>50\%$  of the saturated signal) or no resetting. Similar to the top surface, the saturated signal plateau shows significant scatter between different cores; core 5, for example, has a saturated IRSL  $\sim 20\%$  higher than the average level observed in MULA1802-2. We also observe significant variations in saturated  $L_n/T_n$  within individual cores.

The IRSL  $L_n/T_n$  at the outer millimetre of the top surface of MULA1802-7 is below saturation in cores 4 and 5; for core 8,  $L_n/T_n$  is within the  $2\sigma$  range for the average signal saturation. The pIRIR  $L_n/T_n$  is  $>70\%$  of the saturated signal in the surface slice for all three cores.

At the bottom surface, the IRSL signal is  $<30\%$  of saturation in all surface slices and  $<10\%$  for cores 3, 6, and 7. The IRSL intensity varies considerably between the second slices ( $\sim 1$ – $2$  mm of depth from the bottom surface) in the cores, with differently shaped profiles. Core 3 displays the deepest bleaching front with an apparent signal plateau in the surface and second slices. In contrast, in cores 7 and 9, IRSL  $L_n/T_n$  reaches  $>50\%$  of saturated levels already in their respective second slices ( $1$ – $2$  mm of depth from the surface). IRSL increases more slowly in core 6 but without a discernible signal plateau. The pIRIR  $L_n/T_n$  is lower than the saturated level saturation in all surface slices;  $L_n/T_n$  is between 10%–20% in cores 3, 7, and 9, compared to  $\sim 60\%$  in core 6.

Rades et al. (2018) and al Khasawneh et al. (2019) suggest estimating the impact of the pre-burial residual dose on any calculated burial ages. To this end, the signal-depth profiles from the deepest bleached cores (core 3; MULA1802-2, and core 3; MULA1802-7) were fitted with the entire Eq. (1) (curve N) using the parameters from Table F.1. Only the first part of Eq. (1) (exposure event) was used in the second step. This curve (M) predicts the shape of the pre-burial bleaching front (Fig. 5), which purpose is to assess if IRSL was fully reset in the surface slices before burial in these cores. The ratio M/N (insets; Fig. 5) estimates the contribution of the pre-burial residual dose to the observed luminescence-depth profiles. Slices are considered to be sufficiently bleached if the ratio M/N is  $<5\%$ . When comparing the fitted profiles in Fig. 5 with their respective modelled profiles, it appears that the IRSL signal was sufficiently bleached in the surface slices of these two cores (M/N  $<5\%$  in the outer 1.5 mm of rock nearest the surface).

### 3.3. Equivalent dose and ages

The calculated IRSL ages from MULA1802-2 and MULA1802-7 are presented in Table 3. No pIRIR<sub>225</sub> ages were calculated because of the unsatisfactory dose recovery results. In MULA1802-2, the  $D_e$  values in

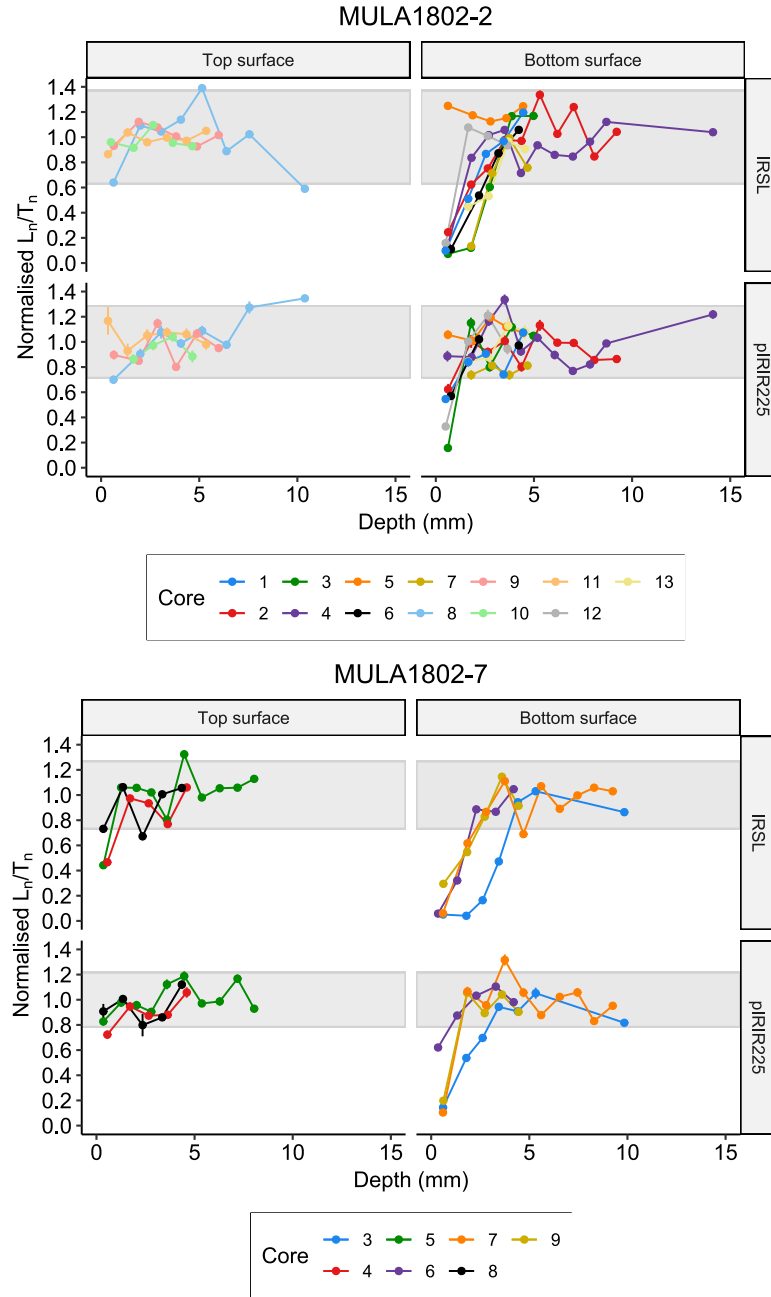


**Fig. 4.** Signal-depth profiles from the buried cobbles MULA1802-2 (top) and MULA1802-7 (bottom). Each data point represents the  $L_n/T_n$  from a single rock slice; error bars represent measurement error, normalised by averaged  $L_n/T_n$  from saturated slices ( $L_0$ ; Table F.1). The shaded areas represent the  $2\sigma$  distribution of saturated slices. The slice depth is plotted as the mid-point of each individual slice.

two surface slices range from  $194 \pm 7$  Gy (core 9) to  $258 \pm 13$  Gy (core 11), which is considerably larger than any  $D_e$  value observed in any of the surface slices from the bottom of the cobble ( $16 \pm 1$  to  $61 \pm 2$  Gy). The ages from the top surface are calculated to  $160 \pm 13$  ka and  $213 \pm 19$  ka for cores 9 and 11, considerably older than the expected ages, even before any fading correction is applied. In contrast, the fading-corrected ages from cores 1, 4, and 6 range between 23–29 ka, while core 12 is slightly older ( $38 \pm 6$  ka). Age outliers from the bottom surface are cores 2 and 3; for core 2, we calculate an old age of  $64 \pm 6$  ka age, while the age of core 3 is much younger at  $15 \pm 2$  ka. Finally, an average fading-corrected age of  $30 \pm 4$  ka is calculated for MULA1802-2, based on four discs with grains extracted from the surface slice of core 14.

The  $D_e$  values from the bottom surface are significantly lower than at the top surface, ranging from  $12 \pm 1$  to  $50 \pm 3$  Gy. For MULA1802-7,

a  $D_e$  value from the top surface is measured to  $128 \pm 4$  Gy, which, after fading correction, is calculated to  $119 \pm 13$  ka. The fading corrected ages from cores 3, 6, and 7 are:  $11 \pm 1$ ,  $13 \pm 2$ , and  $14 \pm 2$  ka; core 9 is considerably older ( $48 \pm 7$  ka). The mean fading-corrected age from the dissolved surface slice of core 2 (MULA1802-7) is  $11 \pm 2$  ka.

#### 4. Discussions

##### 4.1. Bleaching of the fluvial cobbles

Overall, the IRSL signal-depth profiles from the cobbles show short bleaching fronts where only outer  $\sim 1$  mm of rock appears to have been bleached before burial. This is in contrast to some deeper bleaching fronts reported from various archaeological settings (e.g. Freiesleben et al., 2015; Sohbati et al., 2015; Ageby et al., 2021), beach ridges (Souza

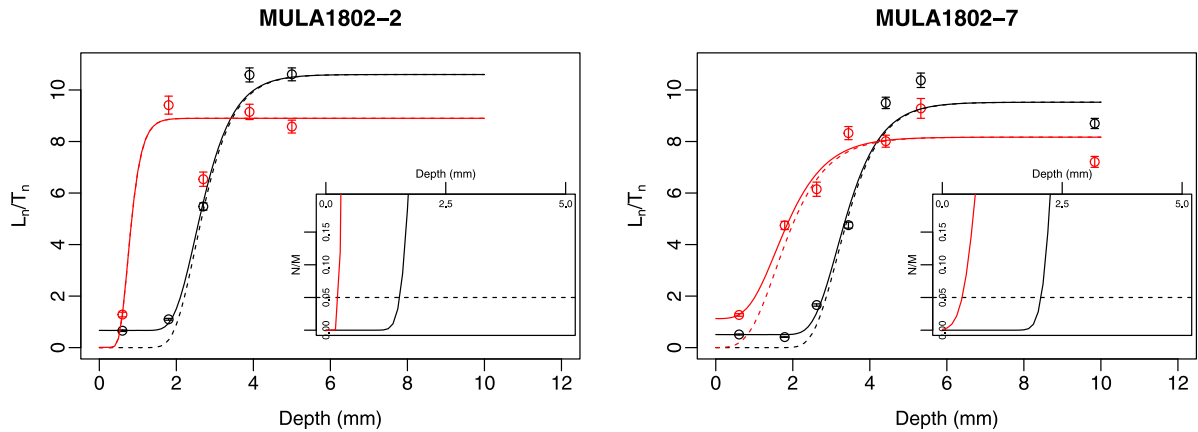


Fig. 5. Fitted signal-depth profiles for IRSL (black) and pIRIR<sub>225</sub> (red) data. The solid lines plot the fitted profiles (N) using Eq. (1); the dotted lines plot the modelled profiles (M), displaying the depth of bleaching before burial. The insets plot M/N, i.e., the ratio of luminescence in the fitted profile N remaining from the exposed profile M. The dashed horizontal lines in the insets represent the threshold where 5% of the observed luminescence was inherited from profile M. Fitting parameters are presented in Table F.1 in the supplementary material.

Table 3

IRSL data from individual slices and mean data from multiple-grain discs, derived from cobbles MULA1802-2 and MULA1802-7. n = numbers of discs (for slices: n = 1); Corr.age = age corrected for fading with g-value, following the approach by Huntley and Lamothe (2001).

Surface	Core	Slice/discs (n)	Slice depth (mm)	Dose rate (Gy ka <sup>-1</sup> )	De (Gy)	Age (ka)	Corr.age (ka)
MULA1802-2							
Bottom	1	Slice	0.0–1.0	1.21 ± 0.09	23.79 ± 1.22	19.7 ± 1.8	23.0 ± 2.6
Bottom	2	Slice	0.0–1.3	1.21 ± 0.09	61.33 ± 2.48	50.69 ± 4.3	59.9 ± 6.5
Bottom	3	Slice	0.0–1.2	1.21 ± 0.09	15.75 ± 1.11	13.02 ± 1.3	15.2 ± 1.8
Bottom	4	Slice	0.0–1.2	1.21 ± 0.09	30.21 ± 1.20	24.97 ± 2.1	29.3 ± 3.1
Bottom	6	Slice	0.0–1.5	1.21 ± 0.09	25.49 ± 0.85	21.07 ± 1.9	24.7 ± 2.8
Top	9	Slice	0.0–1.3	1.21 ± 0.09	194.09 ± 7.30	160.4 ± 13.4	191.5 ± 21.6
Top	11	Slice	0.0–1.0	1.21 ± 0.09	257.67 ± 13.08	213.0 ± 19.1	254.9 ± 30.1
Bottom	12	Slice	0.0–1.0	1.21 ± 0.09	37.52 ± 1.31	31.0 ± 2.6	36.5 ± 3.9
Bottom	14	discs (4)	0.0–1.0	1.21 ± 0.09	29.21 ± 2.59	24.1 ± 2.8	28.1 ± 2.7
MULA1802-7							
Bottom	2	discs (3)	0.0–1.0	1.22 ± 0.10	11.94 ± 1.44	9.8 ± 1.4	10.9 ± 1.8
Bottom	3	Slice	0.0–1.2	1.22 ± 0.10	12.57 ± 0.47	10.3 ± 0.9	11.4 ± 1.3
Top	5	Slice	0.0–1.1	1.22 ± 0.10	128.46 ± 4.44	105.3 ± 8.6	118.6 ± 13.0
Bottom	6	Slice	0.0–1.3	1.22 ± 0.10	14.70 ± 1.29	12.1 ± 1.5	13.4 ± 1.8
Bottom	7	Slice	0.0–1.2	1.22 ± 0.10	15.75 ± 1.11	12.9 ± 1.4	14.4 ± 1.8
Bottom	9	Slice	0.0–1.3	1.22 ± 0.10	50.00 ± 2.87	41.0 ± 4.1	45.9 ± 5.7

et al., 2019, 2021) or glaciofluvial deposits (Jenkins et al., 2018). As expected, the pIRIR<sub>225</sub> signal is overall less well-bleached than IRSL (e.g. Freiesleben et al., 2015; Sohbati et al., 2015; Ishii et al., 2022). Nevertheless, since the fitting of core 3 (MULA-1802-7) shows that the surface slice was bleached, it is conceivable that the pIRIR<sub>225</sub> could have been used for dating with a protocol with better dose recovery.

Investigations by Liu et al. (2019) of IRSL resetting in modern sandstone cobbles sampled in a fluvial system showed bleaching fronts reaching ~1 mm of depth comparable to the bleaching fronts observed in most of the cores from the bottom surfaces of our cobbles. Such short bleaching fronts are less than optimal since it is hard to distinguish any burial dose plateaus in the IRSL-depth profiles near the surface. Several reasons for the lack of deep bleaching fronts in a cobble are possible. For example, Brill et al. (2022) have commented that high dose rates (>6 Gy ka<sup>-1</sup>) could be a factor that explains their weak bleaching fronts in cobbles from uplifted last interglacial beaches on the coast of Chile. High dose rates, however, are unlikely to be an issue for the Mula cobbles since dose rates are much lower (~1 Gy ka<sup>-1</sup>). Also, the attenuation of light due to lithological factors has been demonstrated by Ou et al. (2018) to affect the rate of bleaching, where IRSL and pIRIR<sub>225</sub> signals bleached more rapidly in translucent crystalline rocks, compared to opaquer sedimentary rock such as sandstones and graywacke. Since the Mula cobbles are of sedimentary origin, we would expect bleaching rates more similar to sandstones. We cannot calculate

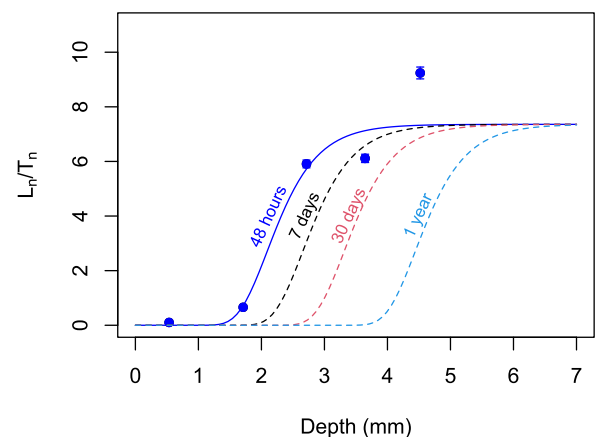


Fig. 6. Fitted (solid line) and simulated (dashed lines) IRSL-depth profiles, derived from the IRSL  $L_n/T_n$  data (points) measured after 48 h of exposure in a solar simulator. The fitted profile was calculated assuming a single exposure event for 48 h (Eq. (1)) using the model developed by Sohbati et al. (2011). Simulated profiles of various exposure duration were predicted using  $\mu = 2.2 \text{ mm}^{-1}$  and  $\sigma\phi_0 = 5.9 \times 10^{-4} \text{ mm}^{-1}$ ; the variables were derived from the fitting.

the bleaching rate during previous exposure events since we lack access to any natural surfaces of known exposure age.



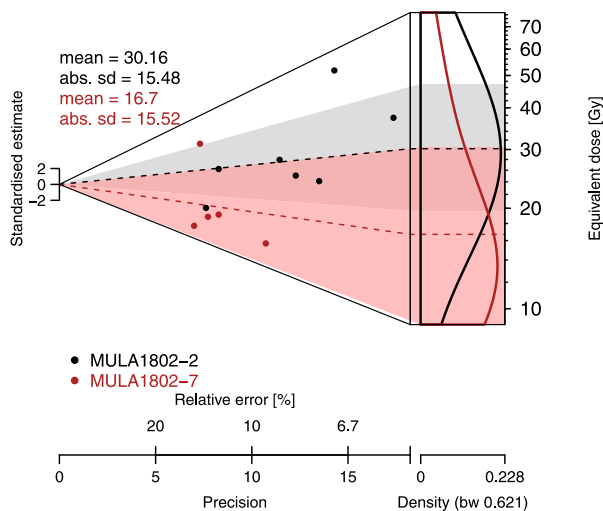


Fig. 7. Plotting of the distribution of ages calculated from the surface slices from the bottom surfaces of MULA1802-2 and MULA1802-7.

Nevertheless, our bleaching experiment in a solar simulator (Fig. 3) shows how bleaching of both the IRSL and pIRIR<sub>225</sub> signals occurs during exposure and that longer exposure bleaches the signal deeper into the rock. A rough estimate of the inwards development of the bleaching front by fitting the IRSL data from 48 h of bleaching in the solar simulator (Fig. 6) predicts that one year of exposure would bleach the signal to 4–5 mm of depth, enough to form deeper bleaching profiles than we observe in our natural surfaces. Perhaps, our cobble surfaces were not sufficiently exposed before or during transport, and therefore, no bleaching fronts could develop. However, abrasion, chipping, and fragmentation during fluvial transport (e.g. Schumm and Stevens, 1973; Novák-Szabó et al., 2018; Gale, 2021), will also cause attrition of such cobbles, reducing the length of any bleaching profiles that had developed before transport. Therefore, attrition of the cobble might not occur evenly across the cobble surfaces. Also, one previous study on fluvial cobbles showed intra-cobble variations in granodiorites for which at least one core from each cobble surface was insufficiently bleached before burial in their data set (Ishii et al., 2022). It might hence be advisable to measure more cores in fluvial settings to avoid to sample eroded parts of the surfaces.

We can here only speculate about the reason for the short and varied appearance of the IRSL-depth profiles observed in our cobbles. The roundness of the cobbles definitively determines that fluvial processes at one point (but not necessarily during the last transport phase) reshaped the cobbles, and we know that some signal bleaching has occurred. Overall, the bottom surface of both our cobbles at one point remained exposed long enough to reset the signal to a minimum of 2 mm in one core for each cobble. Considering that the observed  $L_n/T_n$  at ~2 mm depth in core 3 (MULA1802-2) is similar to the surface slices for several of the other cores, this could mean that the bleaching fronts of the other cores have been more shortened compared to core 3, perhaps due to uneven attrition at the millimetre scale. The lack of bleaching at the top surface of both cobbles indicates that neither cobble remained exposed in the landscape after having been transported.

#### 4.2. Luminescence ages

The variation in  $L_n/T_n$  between the different cores naturally results in scatter in the ages calculated from the  $D_e$  measurements. Since neither cobble top surface demonstrates any robust signs of bleaching, only ages from the respective bottom surface are considered (Fig. 7). One consideration which is not quantified here is the potential for beta

radiation hot spots such as K-feldspars having an unequal impact on the small-scale dosimetry, especially in low dose rate environments such as the Mula Valley (e.g., Guérin et al., 2015). Essentially, the ages from individual cores from MULA1802-2 indicate that the rock was either buried during MIS 4, the late MIS 3/early MIS 2 (ages ranging between 23–37 ka) or late MIS 2 ( $15 \pm 2$  ka); hence, providing several possible dates for when the terrace could have formed. For MULA1802-7, the ages from all cores except one indicate burial during late MIS 2/early MIS 1 ( $11 \pm 2$  to  $14 \pm 2$  ka), lacking ages ranging between 25–40 ka. Hence, either MULA1802-7 was exposed more recently than MULA1802-2 or most of the ages calculated from MULA1802-2 do not represent the true depositional age. Since we can be the most confident in the thoroughness of the bleaching in the cores with the deepest bleaching profiles, these cores must be considered to provide the most robust ages for when either surface was last exposed to daylight. This would have occurred during MIS 2, which is also the age provided by two additional cores (cores 6 and 7) from MULA1802-7, which, despite their shorter bleaching fronts, also dates to this period, i.e., MIS 2.

Previous studies from southeastern Spain have presented chronological data indicating that fluvial aggradation occurred during MIS 2 (Schulte et al., 2008; Geach et al., 2015), which is in agreement with our cobble ages from the Mula Valley during MIS 2. This interpretation is, however, inconsistent with the geomorphological development suggested for the Mula Valley (Angelucci et al., 2018), suggested by the robust dating provided by radiocarbon from the uppermost alluvial unit from Cueva Antón (Zilhão et al., 2016, see their Table 2). Those ages demonstrate instead that the final aggradation phase in the Mula valley occurred during MIS 3, much earlier than estimated from the cores with the deepest bleaching profiles. The chronological inconsistency between previous dating and our new cobble ages has not yet been resolved. Possible explanations for the younger-than-expected ages (besides aggradation during MIS 2) include the reactivation of the alluvial deposits at MULA1802 that is not visible in the Cueva Antón sequence, methodological inaccurately constrained dosimetry or signal fading, incorrect geomorphological assessment of the stratigraphical relationship between MULA1802 and the Cueva Antón alluvial deposits, or bleaching of the samples during collection. The two latter explanations appear especially unlikely since the surface levels above the river channel are approximately the same, and the bleaching experiment (Fig. 3) shows that an hour of exposure in the solar simulator is required to reset the IRSL signal to the same approximate levels as observed at the bottom surfaces of our cobbles. Also, the top surfaces appear not to be affected by bleaching, which we would expect if the signal was affected by exposure during sampling.

#### 5. Conclusions

The luminescence response in our samples is rather weak due to their carbonate-rich nature. Two calcarenite cobbles, however, still produced sufficiently bright emissions for satisfactory dose recovery when using a pIRIR protocol, at least for the IRSL signal, demonstrating that attempting to date the +5–7 m terrace with rock surface luminescence dating is worthwhile, despite the lack of silica-rich lithologies in the fluvial system.

Overall, we observed short natural bleaching fronts in the calcarenite cobbles. The apparent lack of signal resetting in the natural surfaces indicates that bleaching might be an issue for this lithology, short exposure duration, or cobble attrition during transport; likely, all these factors combine, which signify the methodological challenges when dating sedimentary rocks from fluvial settings. The significant variation in the bleaching depth between different cores and surfaces could be an issue for fluvially transported rocks, making it advisable to sample rock surfaces using multiple cores to avoid missing the most thoroughly reset parts of the surfaces. Otherwise, there is the risk that parts of the signal-depth profile that still contain a significant pre-burial dose are dated. Further investigations into the processes affecting the

shape of the signal-depth profiles could be valuable for future dating of fluvial deposits and could perhaps provide information regarding signal bleaching in fluvial settings. Hopefully, this approach will enable identifying more dateable samples from settings like the Mula valley, where quartz or feldspar-bearing rocks are rare.

The dating of the +5–7 m terrace in the Mula Valley is ambiguous due to the variation in absorbed dose observed for different cores. The cores with the deepest bleaching fronts represent the most reliable burial ages since we can be more confident that the IRSL signal was fully reset there. These cores also produce the youngest ages, ranging between 10–15 ka, which, however, do not conform with the current geochronological understanding of the evolution of the Mula Valley and are unlikely to correlate with an aggradation phase. They are also considerably younger than the minimum ages provided by one OSL date from a fluvial sand layer from the same terrace (see supplementary material). The rock surface luminescence ages do, therefore, not at this point provide better insight into the geomorphological development of the valley. Further work is required to understand if the challenges we have experienced in the Mula valley are methodological in nature or related to the geomorphological setting.

Nevertheless, despite the challenges presented by the calcarenites from Mula, we can conclude that rock surface luminescence dating should be considered an additional geochronological tool in fluvial systems, even if no quartz and feldspar-rich lithologies are present.

### Declaration of competing interest

The authors declare that they have no known competing financial interests or personal relationships that could have appeared to influence the work reported in this paper.

### Data availability

Data will be made available on request.

### Acknowledgements

We thank Anja Zander for gamma spectrometry measurements. We also thank João Zilhão for his support during fieldwork. Finally, we are grateful for the constructive comments and suggestions from three anonymous reviewers that greatly helped to improve the manuscript. Lucas Ageby was funded by the Deutsche Forschungsgemeinschaft (DFG, German Research Foundation) - Project number 57444011 - SFB 806.

### Appendix A. Supplementary data

Supplementary material related to this article can be found online at <https://doi.org/10.1016/j.radmeas.2023.106962>.

### References

- Ageby, L., Angelucci, D.E., Brill, D., Carrer, F., Rades, E.F., Rethemeyer, J., Brückner, H., Klasen, N., 2021. Rock surface IRSL dating of buried cobbles from an alpine dry-stone structure in Val Di Sole, Italy. *Quat. Geochronol.* 66, 101212. <https://doi.org/10.1016/j.quageo.2021.101212>.
- al Khasawneh, S., Murray, A., Abudanah, F., 2019. A first radiometric chronology for the Khatt Shebib megalithic structure in Jordan using the luminescence dating of rock surfaces. *Quat. Geochronol.* 49, 205–210. <https://doi.org/10.1016/j.quageo.2018.02.007>.
- Alcaraz-Castaño, M., Alcolea-González, J.J., de Andrés-Herrero, M., Castillo-Jiménez, S., Cuartero, F., Cuenca-Bescós, G., Kehl, M., López-Sáez, J.A., Luque, L., Pérez-Díaz, S., Piqué, R., Ruiz-Alonso, M., Weniger, G.-C., Yravedra, J., 2021. First modern human settlement recorded in the Iberian hinterland occurred during Heinrich Stadial 2 within Harsh environmental conditions. *Sci. Rep.* 11 (1), 15161. <https://doi.org/10.1038/s41598-021-94408-w>.
- Angelucci, D.E., Anesin, D., Susini, D., Villaverde, V., Zapata, J., Zilhão, J., 2013. Formation processes at a high resolution Middle Paleolithic site: Cueva Antón (Murcia, Spain). *Quat. Int.* 315, 24–41. <https://doi.org/10.1016/j.quaint.2013.03.014>.
- Angelucci, D.E., Anesin, D., Susini, D., Villaverde, V., Zapata, J., Zilhão, J., 2018. A tale of two Gorges: late quaternary site formation and surface dynamics in the Mula basin (Murcia, Spain). *Quat. Int.* 485, 4–22. <https://doi.org/10.1016/j.quaint.2017.04.006>.
- Auclair, M., Lamothe, M., Huot, S., 2003. Measurement of anomalous fading for Feldspar IRSL using SAR. *Radiat. Meas.* 37 (4), 487–492. [https://doi.org/10.1016/S1350-4487\(03\)00018-0](https://doi.org/10.1016/S1350-4487(03)00018-0).
- Bailliff, I.K., 2018. An examination of beta dose attenuation effects in coarse grains located in sliced samples. *Radiat. Meas.* 120, 188–194. <https://doi.org/10.1016/j.radmeas.2018.07.015>.
- Baiyegunhi, T.L., Liu, K., Gwavava, O., Baiyegunhi, C., 2020. Textural characteristics, mode of transportation and depositional environment of the cretaceous sandstone in the bredasdorp basin, off the South Coast of South Africa: evidence from grain size analysis. *Open Geosci.* 12 (1), 1512–1532. <https://doi.org/10.1515/geo-2020-0135>.
- Balescu, S., Lamothe, M., 1993. Thermoluminescence dating of the Holsteinian marine formation of Herzelee, northern France. *J. Quat. Sci.* 8 (2), 117–124. <https://doi.org/10.1002/jqs.3390080204>.
- Bøtter-Jensen, L., Thomsen, K.J., Jain, M., 2010. Review of optically stimulated luminescence (OSL) instrumental developments for retrospective dosimetry. *Radiat. Meas.* 45 (3), 253–257. <https://doi.org/10.1016/j.radmeas.2009.11.030>.
- Brill, D., Ageby, L., Obert, C., Hollerbach, R., Duval, M., Kolb, T., Bartz, M., 2022. Investigating the resetting of IRSL signals in beach cobbles and their potential for rock surface dating of marine terraces in Northern Chile. *Mar. Geol.* 443, 106692. <https://doi.org/10.1016/j.margeo.2021.106692>.
- Burrow, C., Kehl, M., Hilgers, A., Weniger, G.-C., Angelucci, D.E., Villaverde, V., Zapata, J., Zilhão, J., 2015. Luminescence dating of fluvial deposits in the rock shelter of Cueva Antón, Spain. *Geochronometria* 42 (1), 107–125. <https://doi.org/10.1515/geochr-2015-0010>.
- Buylaert, J.P., Murray, A.S., Thomsen, K.J., Jain, M., 2009. Testing the potential of an elevated temperature IRSL signal from K-feldspar. *Radiat. Meas.* 44 (5), 560–565. <https://doi.org/10.1016/j.radmeas.2009.02.007>.
- Chamberlain, E.L., Wallinga, J., Shen, Z., 2018. Luminescence age modeling of variably-bleached sediment: Model selection and input. *Radiat. Meas.* 120, 221–227. <https://doi.org/10.1016/j.radmeas.2018.06.007>.
- Chapot, M.S., Sohbati, R., Murray, A.S., Pederson, J.L., Rittenour, T.M., 2012. Constraining the age of rock art by dating a rockfall event using sediment and rock-surface luminescence dating techniques. *Quat. Geochronol.* 13, 18–25. <https://doi.org/10.1016/j.quageo.2012.08.005>.
- Cresswell, A.J., Carter, J., Sanderson, D.C.W., 2018. Dose rate conversion parameters: Assessment of nuclear data. *Radiat. Meas.* 120, 195–201. <https://doi.org/10.1016/j.radmeas.2018.02.007>.
- Cunningham, A.C., Khashchevskaya, D., Semikolennykh, D., Kurbanov, R., Murray, A.S., 2022. Luminescence dating of mass-transport sediment using rock-surface burial methods: A test case from the Baksan valley in the Caucasus Mountains. *Quat. Geochronol.* 68, 101253. <https://doi.org/10.1016/j.quageo.2022.101253>.
- Duller, G., Bøtter-Jensen, L., Kohsiek, P., Murray, A., 1999. A high-sensitivity optically stimulated luminescence scanning system for measurement of single sand-sized grains. *Radiat. Prot. Dosim.* 84 (1–4), 325–330. <https://doi.org/10.1093/oxfordjournals.rpd.a032748>.
- Duller, G.A.T., Bøtter-Jensen, L., Murray, A.S., 2003. Combining infrared- and green-laser stimulation sources in single-grain luminescence measurements of feldspar and quartz. *Radiat. Meas.* 37 (4), 543–550. [https://doi.org/10.1016/S1350-4487\(03\)00050-7](https://doi.org/10.1016/S1350-4487(03)00050-7).
- Finlayson, C., Fa, D.A., Jiménez Espejo, F., Carrión, J.S., Finlayson, G., Giles Pacheco, F., Rodríguez Vidal, J., Stringer, C., Martínez Ruiz, F., 2008. Gorham's Cave, Gibraltar—The persistence of a Neanderthal population. *Quat. Int.* 181 (1), 64–71. <https://doi.org/10.1016/j.quaint.2007.11.016>.
- Freiesleben, T., Sohbati, R., Murray, A., Jain, M., al Khasawneh, S., Hvidt, S., Jakobsen, B., 2015. Mathematical model quantifies multiple daylight exposure and burial events for rock surfaces using luminescence dating. *Radiat. Meas.* 81, 16–22. <https://doi.org/10.1016/j.radmeas.2015.02.004>.
- Fu, X., Romanyukha, A.A., Li, B., Jankowski, N.R., Lachlan, T.J., Jacobs, Z., George, S.P., Rosenfeld, A.B., Roberts, R.G., 2022. Beta dose heterogeneity in sediment samples measured using a Timepix pixelated detector and its implications for optical dating of individual mineral grains. *Quat. Geochronol.* 68, 101254. <https://doi.org/10.1016/j.quageo.2022.101254>.
- Galbraith, R.F., Roberts, R.G., Laslett, G.M., Yoshida, H., Olley, J.M., 1999. Optical dating of single and multiple grains of quartz from jinnium rock shelter, Northern Australia: Part I, experimental design and statistical models\*. *Archaeometry* 41 (2), 339–364. <https://doi.org/10.1111/j.1475-4754.1999.tb00987.x>.
- Gale, S.J., 2021. The shape of fluvial gravels: insights from Fiji's Sabeto River. *Geosciences* 11 (4), 161. <https://doi.org/10.3390/geosciences11040161>.
- Geach, M.R., Thomsen, K.J., Buylaert, J.P., Murray, A.S., Mather, A.E., Telfer, M.W., Stokes, M., 2015. Single-grain and multi-grain OSL dating of river terrace sediments in the Tabernas Basin, SE Spain. *Quat. Geochronol.* 30, 213–218. <https://doi.org/10.1016/j.quageo.2015.05.021>.
- Gliganic, L.A., Meyer, M.C., May, J.-H., Aldenderfer, M.S., Tropper, P., 2021. Direct dating of lithic surface artifacts using luminescence. *Sci. Adv.* 7 (23), eabb3424. <https://doi.org/10.1126/sciadv.abb3424>.

- Glignic, L.A., Meyer, M.C., Sohbati, R., Jain, M., Barrett, S., 2019. OSL surface exposure dating of a lithic quarry in Tibet: Laboratory validation and application. *Quat. Geochronol.* 49, 199–204. <http://dx.doi.org/10.1016/j.quageo.2018.04.012>.
- Gregory, K.J., Benito, G., Dikau, R., Golosov, V., Johnstone, E.C., Jones, J.A.A., Macklin, M.G., Parsons, A.J., Passmore, D.G., Poesen, J., Soja, R., Starkel, L., Thorndycraft, V.R., Walling, D.E., 2006. Past hydrological events and global change. *Hydrol. Process.* 20 (1), 199–204. <http://dx.doi.org/10.1002/hyp.6105>.
- Guérin, G., Jain, M., Thomsen, K.J., Murray, A.S., Mercier, N., 2015. Modelling dose rate to single grains of quartz in well-sorted sand samples: The dispersion arising from the presence of potassium feldspars and implications for single grain OSL dating. *Quat. Geochronol.* 27, 52–65. <http://dx.doi.org/10.1016/j.quageo.2014.12.006>.
- Habermann, J., Schilles, T., Kalchgruber, R., Wagner, G.A., 2000. Steps towards surface dating using luminescence. *Radiat. Meas.* 32 (5), 847–851. [http://dx.doi.org/10.1016/S1350-4487\(00\)00066-4](http://dx.doi.org/10.1016/S1350-4487(00)00066-4).
- Hansen, V., Murray, A., Buylaert, J.-P., Yeo, E.-Y., Thomsen, K., 2015. A new irradiated quartz for beta source calibration. *Radiat. Meas.* 81, 123–127. <http://dx.doi.org/10.1016/j.radmeas.2015.02.017>.
- Huntley, D.J., Baril, M., 1997. The K content of the K-feldspars being measured in optical dating or in thermoluminescence dating. *Ancient TL* 15 (1), 11–13.
- Huntley, D.J., Lamothe, M., 2001. Ubiquity of anomalous fading in K-feldspars and the measurement and correction for it in optical dating. *Can. J. Earth Sci.* 38 (7), 1093–1106. <http://dx.doi.org/10.1139/e01-013>.
- IGME, 1972a. Mapa Geológica de España E. 1:50 00. In: Hoja 911 - Cehegín, Instituto Geológico y Minero de España, Madrid.
- IGME, 1972b. Mapa Geológica de España E. 1:50 000. In: Hoja 912 - Mula, Instituto Geológico y Minero de España, Madrid.
- Ishii, Y., Takahashi, T., Ito, K., 2022. Luminescence dating of cobbles from Pleistocene fluvial terrace deposits of the Ara River, Japan. *Quat. Geochronol.* 67, 101228. <http://dx.doi.org/10.1016/j.quageo.2021.101228>.
- Jankowski, N.R., Jacobs, Z., 2018. Beta dose variability and its spatial contextualisation in samples used for optical dating: An empirical approach to examining beta microdosimetry. *Quat. Geochronol.* 44, 23–37. <http://dx.doi.org/10.1016/j.quageo.2017.08.005>.
- Jenkins, G.T.H., Duller, G.A.T., Roberts, H.M., Chiverrell, R.C., Glasser, N.F., 2018. A new approach for luminescence dating glaciofluvial deposits - high precision optical dating of cobbles. *Quat. Sci. Rev.* 192, 263–273. <http://dx.doi.org/10.1016/j.quascirev.2018.05.036>.
- Kehl, M., Álvarez-Alonso, D., de Andrés-Herrero, M., Díez-Herrero, A., Klasen, N., Rethemeyer, J., Weniger, G.-C., 2018. The rock shelter Abrigo del Molino (Segovia, Spain) and the timing of the late middle paleolithic in Central Iberia. *Quat. Res.* 90 (1), 180–200. <http://dx.doi.org/10.1017/qua.2018.13>.
- Kehl, M., Burrow, C., Cantalejo, P., Domínguez-Bella, S., Durán, J.J., Henselowsky, F., Klasen, N., Linstädter, J., Medianero, J., Pastoors, A., Ramos, J., Reicherter, K., Schmidt, C., Weniger, G.-C., 2016. Site formation and chronology of the new paleolithic site sima de Las Palomas de Teba, Southern Spain. *Quat. Res.* 85 (2), 313–331. <http://dx.doi.org/10.1016/j.jyqres.2016.01.007>.
- Krbetschek, M.R., Götze, J., Dietrich, A., Trautmann, T., 1997. Spectral information from minerals relevant for luminescence dating. *Radiat. Meas.* 27 (5), 695–748. [http://dx.doi.org/10.1016/S1350-4487\(97\)00223-0](http://dx.doi.org/10.1016/S1350-4487(97)00223-0).
- Kreutzer, S., Burrow, C., Dietze, M., Fuchs, M.C., Schmidt, C., Fischer, M., Friedrich, J., Mercier, N., Smedley, R.K., Christophe, C., Zink, A., Durcan, J., King, G.E., Philippe, A., Guerin, G., Riedesel, S., Autzen, M., Guibert, P., Mittelstrass, D., Gray, H.J., Fuchs, M., 2021. Luminescence: comprehensive luminescence dating data analysis.
- Liu, J., Cui, F., Murray, A.S., Sohbati, R., Jain, M., Gao, H., Li, W., Li, C., Li, P., Zhou, T., Chen, J., 2019. Resetting of the luminescence signal in modern riverbed cobbles along the course of the Shiyang River, China. *Quat. Geochronol.* 49, 184–190. <http://dx.doi.org/10.1016/j.quageo.2018.04.004>.
- Macklin, M.G., Fuller, I.C., Lewin, J., Maas, G.S., Passmore, D.G., Rose, J., Woodward, J.C., Black, S., Hamlin, R.H.B., Rowan, J.S., 2002. Correlation of fluvial sequences in the Mediterranean basin over the last 200ka and their relationship to climate change. *Quat. Sci. Rev.* 21 (14), 1633–1641. [http://dx.doi.org/10.1016/S0277-3791\(01\)00147-0](http://dx.doi.org/10.1016/S0277-3791(01)00147-0).
- Mather, A.E., Silva, P.G., Goy, J.L., Harvey, A.M., Zazo, C., 1995. Tectonics versus Climate: An Example from Late Quaternary Aggradational and Dissectional Sequences of the Mula Basin, Southeast Spain. *Balkema, A. A.*
- Mayya, Y.S., Mortheikai, P., Murari, M.K., Singhvi, A.K., 2006. Towards quantifying beta microdosimetric effects in single-grain quartz dose distribution. *Radiat. Meas.* 41 (7), 1032–1039. <http://dx.doi.org/10.1016/j.radmeas.2006.08.004>.
- Medialdea, A., Thomsen, K.J., Murray, A.S., Benito, G., 2014. Reliability of equivalent-dose determination and age-models in the OSL dating of historical and modern palaeoflood sediments. *Quat. Geochronol.* 22, 11–24. <http://dx.doi.org/10.1016/j.quageo.2014.01.004>.
- Murray, A.S., Wintle, A.G., 2000. Luminescence dating of quartz using an improved single-aliquot regenerative-dose protocol. *Radiat. Meas.* 32 (1), 57–73. [http://dx.doi.org/10.1016/S1350-4487\(99\)00253-X](http://dx.doi.org/10.1016/S1350-4487(99)00253-X).
- Novák-Szabó, T., Sipos, A.Á., Shaw, S., Bertoni, D., Pozzebon, A., Grottoli, E., Sarti, G., Ciavola, P., Domokos, G., Jerolmack, D.J., 2018. Universal characteristics of particle shape evolution by bed-load chipping. *Sci. Adv.* 4 (3), ea04946. <http://dx.doi.org/10.1126/sciadv.a04946>.
- Olley, J.M., Caitcheon, G.G., Roberts, R.G., 1999. The origin of dose distributions in fluvial sediments, and the prospect of dating single grains from fluvial deposits using optically stimulated luminescence. *Radiat. Meas.* 30 (2), 207–217. [http://dx.doi.org/10.1016/S1350-4487\(99\)00040-2](http://dx.doi.org/10.1016/S1350-4487(99)00040-2).
- Ou, X.J., Roberts, H.M., Duller, G.A.T., Gunn, M.D., Perkins, W.T., 2018. Attenuation of light in different rock types and implications for rock surface luminescence dating. *Radiat. Meas.* 120, 305–311. <http://dx.doi.org/10.1016/j.radmeas.2018.06.027>.
- Prescott, J.R., Hutton, J.T., 1994. Cosmic ray contributions to dose rates for luminescence and ESR dating: Large depths and long-term time variations. *Radiat. Meas.* 23 (2), 497–500. [http://dx.doi.org/10.1016/1350-4487\(94\)90086-8](http://dx.doi.org/10.1016/1350-4487(94)90086-8).
- Preusser, F., 2003. IRSL Dating of K-rich Feldspars Using the SAR Protocol: Comparison with Independent Age Control. Laboratoire de Physique Corpusculaire, <http://dx.doi.org/10.7892/BORIS.86653>.
- R. Core Team, 2021. R: A Language and Environment for Statistical Computing. R Foundation for Statistical Computing, Vienna, Austria, URL <https://www.R-project.org/>.
- Rades, E.F., Sohbati, R., Lüthgens, C., Jain, M., Murray, A.S., 2018. First luminescence-depth profiles from boulders from moraine deposits: insights into glaciation chronology and transport dynamics in Malta valley, Austria. *Radiat. Meas.* 120, 281–289. <http://dx.doi.org/10.1016/j.radmeas.2018.08.011>.
- Riedesel, S., Autzen, M., 2020. Beta and Gamma dose rate attenuation in rocks and sediment. *Radiat. Meas.* 133, 106295. <http://dx.doi.org/10.1016/j.radmeas.2020.106295>.
- Riedesel, S., Autzen, M., 2021. Calc\_CobbleDoseRate: Calculate dose rate of slices in a spherical cobble.
- Santesteban, J.I., Schulte, L., 2007. Fluvial networks of the Iberian Peninsula: A chronological framework. *Quat. Sci. Rev.* 26 (22), 2738–2757. <http://dx.doi.org/10.1016/j.quascirev.2006.12.019>.
- Schulte, L., Julià, R., Burjachs, F., Hilgers, A., 2008. Middle Pleistocene to Holocene geochronology of the River Aguas terrace sequence (Iberian Peninsula): Fluvial response to Mediterranean environmental change. *Geomorphology* 98 (1), 13–33. <http://dx.doi.org/10.1016/j.geomorph.2007.03.018>.
- Schumm, S.A., Stevens, M.A., 1973. Abrasion in place: A mechanism for rounding and size reduction of coarse sediments in rivers. *Geology* 1 (1), 37–40. [http://dx.doi.org/10.1130/0091-7613\(1973\)1<37:AIPAMF>2.0.CO;2](http://dx.doi.org/10.1130/0091-7613(1973)1<37:AIPAMF>2.0.CO;2).
- Silva, P.G., Mather, A.E., Goy, J.L., Zazo, C., 1996. Controles en el Desarrollo y Evolución del Drenaje en Zonas Tectónicamente Activas: el Caso del Río Mula (Región de Murcia, SE España). p. 16.
- Silva, P.G., Roquero, E., López-Recio, M., Huerta, P., Martínez-Graña, A.M., 2017. Chronology of fluvial terrace sequences for large Atlantic rivers in the Iberian Peninsula (Upper Tagus and Duero drainage basins, Central Spain). *Quat. Sci. Rev.* 166, 188–203. <http://dx.doi.org/10.1016/j.quascirev.2016.05.027>.
- Smedley, R.K., Duller, G.A.T., Pearce, N.J.G., Roberts, H.M., 2012. Determining the K-content of single-grains of feldspar for luminescence dating. *Radiat. Meas.* 47 (9), 790–796. <http://dx.doi.org/10.1016/j.radmeas.2012.01.014>.
- Smedley, R.K., Duller, G.A.T., Rufer, D., Utley, J.E.P., 2020. Empirical assessment of beta dose heterogeneity in sediments: Implications for luminescence dating. *Quat. Geochronol.* 56, 101052. <http://dx.doi.org/10.1016/j.quageo.2020.101052>.
- Smedley, R.K., Skirrow, G.K.A., 2020. Luminescence dating in fluvial settings: Overcoming the challenge of partial bleaching. In: Herget, J., Fontana, A. (Eds.), *Palaeohydrology: Traces, Tracks and Trails of Extreme Events*. In: Geography of the Physical Environment, Springer International Publishing, Cham, pp. 155–168. [http://dx.doi.org/10.1007/978-3-030-23315-0\\_8](http://dx.doi.org/10.1007/978-3-030-23315-0_8).
- Sohbati, R., Murray, A.S., Buylaert, J.-P., Almeida, N.A.C., Cunha, P.P., 2012a. Optically stimulated luminescence (OSL) dating of quartzite cobbles from the Tapada do Montinho archaeological site (east-central Portugal). *Boreas* 41 (3), 452–462. <http://dx.doi.org/10.1111/j.1502-3885.2012.00249.x>.
- Sohbati, R., Murray, A.S., Chapot, M.S., Jain, M., Pederson, J., 2012b. Optically stimulated luminescence (OSL) as a chronometer for surface exposure dating. *J. Geophys. Res. Solid Earth* 117 (B9), <http://dx.doi.org/10.1029/2012JB009383>.
- Sohbati, R., Murray, A.S., Jain, M., Buylaert, J.-P., Thomsen, K.J., 2011. Investigating the resetting of OSL signals in rock surfaces. *Geochronometria* 38 (3), 249–258. <http://dx.doi.org/10.2478/s13386-011-0029-2>.
- Sohbati, R., Murray, A.S., Porat, N., Jain, M., Avner, U., 2015. Age of a prehistoric “Rodedian” cult site constrained by sediment and rock surface luminescence dating techniques. *Quat. Geochronol.* 30, 90–99. <http://dx.doi.org/10.1016/j.quageo.2015.09.002>.
- Souza, P.E., Sohbati, R., Murray, A.S., Clemmensen, L.B., Kroon, A., Nielsen, L., 2021. Optical dating of cobble surfaces determines the chronology of Holocene beach ridges in Greenland. *Boreas* 50 (2), 606–618. <http://dx.doi.org/10.1111/bor.12507>.
- Souza, P.E., Sohbati, R., Murray, A.S., Kroon, A., Clemmensen, L.B., Hede, M.U., Nielsen, L., 2019. Luminescence dating of buried cobble surfaces from sandy beach ridges: A case study from Denmark. *Boreas* 48 (4), 841–855. <http://dx.doi.org/10.1111/bor.12402>.
- Thomsen, K.J., Murray, A.S., Bøtter-Jensen, L., Kinahan, J., 2007. Determination of burial dose in incompletely bleached fluvial samples using single grains of quartz. *Radiat. Meas.* 42 (3), 370–379. <http://dx.doi.org/10.1016/j.radmeas.2007.01.041>.
- Trauerstein, M., Lowick, S.E., Preusser, F., Schlunegger, F., 2014. Small aliquot and single grain IRSL and post-IR IRSL dating of fluvial and alluvial sediments from

- the Pativilca valley, Peru. *Quat. Geochronol.* 22, 163–174. <http://dx.doi.org/10.1016/j.quageo.2013.12.004>.
- Wallinga, J., Murray, A., Wintle, A., 2000. The single-aliquot regenerative-dose (SAR) protocol applied to coarse-grain feldspar. *Radiat. Meas.* 32 (5), 529–533. [http://dx.doi.org/10.1016/S1350-4487\(00\)00091-3](http://dx.doi.org/10.1016/S1350-4487(00)00091-3).
- Wintle, A.G., 1973. Anomalous Fading of Thermo-luminescence in Mineral Samples. *Nature* 245 (5421), 143–144. <http://dx.doi.org/10.1038/245143a0>.
- Wolf, D., García-Tortosa, F.J., Richter, C., Dabkowski, J., Roettig, C.B., Faust, D., 2021. Holocene landscape evolution in the Baza Basin (SE-Spain) as indicated by fluvial dynamics of the Galera River. *Quat. Sci. Adv.* 4, 100030. <http://dx.doi.org/10.1016/j.qsa.2021.100030>.
- Zilhão, J., 2021. The late persistence of the middle palaeolithic and neandertals in Iberia: A review of the evidence for and against the “Ebro Frontier” model. *Quat. Sci. Rev.* 270, 107098. <http://dx.doi.org/10.1016/j.quascirev.2021.107098>.
- Zilhão, J., Ajas, A., Badal, E., Burow, C., Kehl, M., López-Sáez, J.A., Pimenta, C., Preece, R.C., Sanchis, A., Sanz, M., Weniger, G.-C., White, D., Wood, R., Angelucci, D.E., Villaverde, V., Zapata, J., 2016. Cueva Antón: A multi-proxy MIS 3 to MIS 5a paleoenvironmental record for SE Iberia. *Quat. Sci. Rev.* 146, 251–273. <http://dx.doi.org/10.1016/j.quascirev.2016.05.038>.
- Zilhão, J., Anesin, D., Aubry, T., Badal, E., Cabanes, D., Kehl, M., Klasen, N., Lucena, A., Martín-Lerma, I., Martínez, S., Matias, H., Susini, D., Steier, P., Wild, E.M., Angelucci, D.E., Villaverde, V., Zapata, J., 2017. Precise dating of the middle-to-upper paleolithic transition in Murcia (Spain) supports late neandertal persistence in Iberia. *Heliyon* 3 (11), e00435. <http://dx.doi.org/10.1016/j.heliyon.2017.e00435>.
- Zilhão, J., Angelucci, D.E., Badal-García, E., d’Errico, F., Daniel, F., Dayet, L., Douka, K., Higham, T.F.G., Martínez-Sánchez, M.J., Montes-Bernárdez, R., Murcia-Mascarós, S., Pérez-Sirvent, C., Roldán-García, C., Vanhaeren, M., Villaverde, V., Wood, R., Zapata, J., 2010. Symbolic use of marine shells and mineral pigments by Iberian Neandertals. *Proc. Natl. Acad. Sci.* 107 (3), 1023–1028. <http://dx.doi.org/10.1073/pnas.0914088107>.

## Chapter 5

Towards luminescence rock surface  
dating of wadi terraces: signal  
characteristics and profiles from  
Sodmein, Egypt



## 5.1 Introduction

Dating of wadi deposits can be accomplished using conventional luminescence dating of unconsolidated sediments (e.g., Klasen et al., 2013; Bartz et al., 2015). Dating desert pavements, however, is more challenging due to the lack of unconsolidated sediments that can be dated using luminescence. Desert pavements – (mono)layers of gravel, often laying on top of aeolian sediments – are common in many deserts (e.g., Cooke, 1970; Adelsberger and Smith, 2009), and their presence can provide significant environmental (Dietze et al., 2016) or archaeological information (Adelsberger and Smith, 2009). Dating the formation of desert pavements is commonly accomplished by i) dating the near-surface exposure of the clastic monolayer that constitutes the actual pavement using cosmogenic nuclides (Wells et al., 1995; Matmon et al., 2009; Guralnik et al., 2010), or by ii) dating the underlying accretion layer of finer-grained sediments using luminescence (Matmon et al., 2009; Fuchs et al., 2015; Dietze et al., 2016; Fuchs and Lomax, 2019). None of these approaches is necessarily straightforward since exposure dating with cosmogenic nuclides is susceptible to both over- and underestimation of the true exposure age (Ivy-Ochs and Kober, 2008) because of reworking or erosion, respectively, and luminescence dating of accretion layer show significant overdispersion in the measured dose populations and age variation between different grain fractions (Fuchs et al., 2015; Fuchs and Lomax, 2019). Also, dating the aeolian sediments beneath the monolayer with OSL does not necessarily date the age of the actual pavement surface since some desert pavements may form by finer sediments lifting part of the gravel deposits from the previous surface level (McFadden et al., 1987), making such sediments younger than the actual gravel surface.

Instead, rock surface luminescence dating is an additional potential method to date the antiquity of desert pavements since the method targets the non-aeolian gravel that forms the pavement surface; landforms that are relevant for both archaeological (Ahlstrom and Roberts, 2001; Ugalde et al., 2020) and climatological and geomorphological (Adelsberger and Smith, 2009; Knight and Zerboni, 2018) research. Optically stimulated luminescence (OSL) and infrared stimulated (IRSL) luminescence dating of buried (e.g., Sohbaty et al., 2015; al Khasawneh et al., 2019a) and exposed (e.g., Sohbaty et al., 2012b; Lehmann et al., 2018) rock surfaces is a recently developed

geochronological tool that can be applied to different geological and archaeological settings (see 1.3 for a summary of applications). This chapter examines the potential application of rock surface luminescence dating to desert pavements in Wadi Sodmein, Egypt, focusing on luminescence signal characteristics and signal resetting in hydrothermal quartz and granite cobbles.

The age of the wadi terraces and desert pavements in Wadi Sodmein, Egyptian Eastern Desert, is of particular archaeological interest since the surfaces the pavement covers constitute a Middle Stone Age (MSA) open-air site (Kindermann et al., 2018). Here, the desert pavement has formed on top of remnants of Quaternary gravel terraces (Henselowsky, 2019; Kindermann et al., 2021). A palimpsest of archaeological artefacts (MSA until the Neolithic) have been discovered on top of these remnant surfaces – presumably in their in-situ position – indicating that these surfaces are part of a relict Pleistocene landscape (Kindermann et al., 2018). Providing ages of the surface clasts from desert pavement covering the surface remnants would help chronologically constrain the development of the Pleistocene landscape in Wadi Sodmein and would provide a *terminus post quem* for the deposition of the MSA artefacts and age for an open-air site; settings that have been deemed crucial for understanding the MSA in the mountainous landscape of the Eastern Desert, Egypt.

## 5.2 Methods and material

### 5.2.1 Samples and preparation

The lithology of the collected samples was either metamorphosed granites or hydrothermal quartz. The samples were divided into two groups: "pavement samples" and "rooftop samples". All pavement samples were interbedded into the desert pavement at the top of the wadi terraces. The top surface of the pavement samples has been naturally exposed to daylight for an unknown period; the bottom surface has been facing downwards, remaining covered for an unknown period. The rooftop samples were excavated from the gravel of the terraces, and one surface (henceforward referred to as the "top surface") was subsequently exposed on the rooftop for  $\sim 1.5$  years. The bottom surfaces of the rooftop samples lightly experienced some exposure to daylight during and when being placed on the rooftop.



Cores were extracted with a water-cooled WEKA DK17 diamond core drill. The cores were cut into  $\sim 0.7$  mm slices (except the surface slices, which were cut to  $\sim 1.2$  mm to prevent breakage) with a cooled Buhler Isomet 1000 precision saw.

### 5.2.2 Measurements procedures

All samples were measured in the Cologne Luminescence Laboratory with an automated Risø TL/OSL reader (model DA-20) (Bøtter-Jensen et al., 2010). Whole slices were placed directly onto the reader sample carousel, and broken slices were placed into cups. Dose estimations and dose recovery tests were performed with a full SAR protocol (Murray and Wintle, 2000) (Table 5.1), while luminescence intensity with depth ( $L_n/T_n$ ) into the rock was measured using only the first cycle of the SAR protocol. The samples were irradiated with an internal  $^{90}\text{Sr}/^{90}\text{Y}$  beta source (providing  $\sim 0.09 \text{ Gy s}^{-1}$ ). The rock slices were stimulated with infrared light-emitting diodes (LED) (peak emission = 870 nm) or with blue LEDs (peak emission = 470 nm). The heating rate during all heating and stimulation steps was  $2 \text{ }^\circ\text{C/s}$ . All SAR steps at a temperature  $>200 \text{ }^\circ\text{C}$  were performed in a nitrogen atmosphere. An OSL protocol with a  $280 \text{ }^\circ\text{C}$  blue light hot bleach was used to measure the quartz samples. An IR stimulation at  $50 \text{ }^\circ\text{C}$  was introduced before the OSL stimulation to isolate a potential feldspar signal (Lehmann et al., 2018; Brill and Cisternas, 2020) and to reduce the effect of feldspars on the quartz signal (e.g., Roberts, 2007). Two pIRIR protocols were applied to the granites (Table 5.1): a low-temperature pIRIR protocol using an IR stimulation at  $50 \text{ }^\circ$ , followed by a pIR stimulation at  $150 \text{ }^\circ\text{C}$  (e.g., Reimann and Tsukamoto, 2012); and, a higher temperature protocol with the pIR stimulation at  $225 \text{ }^\circ\text{C}$  (e.g., Thomsen et al., 2008; Buylaert et al., 2009).

### 5.2.3 Dose rate calculations, fitting and age calculations

Radionuclide concentrations in sample QB4 were measured using high-resolution gamma spectrometry. The measured concentrations were converted to beta and gamma dose rates using the *calc\_CobbleDoseRate* R function (Riedesel and Autzen, 2021). The function scales the dose rate with depth into the rock, following beta and gamma attenuation factors reported by Riedesel and Autzen (2020). The grain size was assumed to be  $150\text{--}350 \text{ }\mu\text{m}$ . The alpha dose rate was calculated using attenuation

TABLE 5.1: The OSL and pIRIR SAR protocols applied to the Sodmein samples

Step	Treatment		
	OSL (quartz)	pIRIR <sub>150</sub>	pIRIR <sub>225</sub>
1	Beta irradiation	Beta irradiation	Beta irradiation
2	Preheat 220 °C for 100 s	Preheat 180 °C for 100 s	Preheat 250 °C for 100 s
3	Paus 30 s	Paus 30 s	Paus 30 s
4	IRSL 50 °for 100 s	IRSL 50 °for 300 s	IRSL 50 °for 200–300 s
5	OSL 125 °C for 100 s	IRSL 150 °for 300 s	IRSL 225 °for 200–300 s
6	Beta irradiation	Beta irradiation	Beta irradiation
7	Preheat 220 °C for 100 s	Preheat 180 °C for 100 s	Preheat 250 °C for 100 s
8	Paus 30 s	Paus 30 s	Paus 30 s
9	IRSL 50 °for 100 s	IRSL 50 °for 300 s	IRSL 50 °for 200–300 s
10	OSL 125 °C for 100 s	IRSL 150 °for 300 s	IRSL 225 °for 200–300 s
11	OSL 280 °C for 100 s		

factors provided by [Brennan et al. \(1991\)](#). The internal K content was set to  $10 \pm 2$  % ([Smedley et al., 2012](#)), and cosmic radiation was calculated according to [Prescott and Hutton \(1994\)](#). The fitting for the covered bottom surface was done assuming one exposure event, followed by one burial event according to the model from [Freiesleben et al. \(2015\)](#) (more details on fitting and the model are provided in chapter 1). Depth-specific dose rates were used to calculate the apparent burial age for rock depths up to 5 mm from the surface-sediment interface. Ages are either calculated from one  $D_e$  measurement per slice per rock depth (pIRIR<sub>150</sub> protocol) or as a mean age from several chips from one sliced rock fragment per depth.

## 5.3 Luminescence characteristics

### 5.3.1 Luminescence decay curves

Luminescence-decay curves following  $\sim 45$ – $90$  Gy of beta radiation are presented in Fig. 5.1. The IRSL decay is generally weak in all hydrothermal quartz samples, especially in QD4, where the IRSL decay following irradiation is barely stronger than background irradiation. The pIR OSL decay varies between the different samples, but overall, the decay is rapid in the initial part of the signal ( $< 1$  s), followed by a slower decay. No natural OSL decay occurs near the bottom surface of the hydrothermal quartz, as is demonstrated by the decay curves of QD4 and QE3 (Fig. 5.2). Some, primarily weak, OSL decay occurred during stimulation of slices extracted from the

centre of these samples (Fig. 5.2). The pavement granite QB4 demonstrates significant IRSL and pIRIR signal decay with a moderately weak signal (decay starts at  $\sim 1100$  photons per 0.6 s). However, it is crucial to consider that the signals from QB4 were measured from small chips in cups due to the sample friability. The IRSL and pIRIR signals from the modern samples are bright; however, the shorter stimulation time (200 s) for pIRIR appears insignificant to fully reset the signal to background levels.

### 5.3.2 OSL signal sensitivity changes

There are severe sensitivity changes to beta dosing observed between the initial test dosing ( $T_n$ ) during the first SAR cycle and subsequent cycles. This could result from changes in the ratio from which trap the OSL emission originates. The decaying OSL signal, emitted from quartz, is formed by several exponential curves, originating from different signal components (e.g., [Smith and Rhodes, 1994](#); [Bailey et al., 1997](#); [Jain et al., 2003](#); [Singarayer and Bailey, 2003](#); [Jain et al., 2008](#)). The "fast" component is the most readily used for dating due to its rapid bleaching ([Bailey et al., 1997](#); [Li and Li, 2006](#)) in combination with stability over geological time scales ([Singarayer and Bailey, 2003](#)). A strong influence of the thermally unstable "medium" component could lead to underestimation of equivalent doses (e.g. [Li and Li, 2006](#); [Steffen et al., 2009](#)), and, therefore, samples dominated by the fast component should be targeted for dating ([Wintle and Murray, 2006](#)).

An approach using infrared stimulation to isolate the fast component in bright quartz samples was developed by [Bailey \(2010\)](#); such an approach is clearly not suitable for our dim vein quartz. Alternatively, the fast ratio is a quantitative tool developed by [Durcan and Duller \(2011\)](#) to assess the proportion of the fast component in a sample from continuous-wave OSL decay curves using:

$$\frac{L_1 - L_3}{L_2 - L_3} \quad (5.1)$$

by dividing the difference of the photon count from the fast component ( $L_1$ ; defined as the first channel when LEDs are activated) subtracted by the photon count from the background ( $L_3 = \text{mean of channels between } 1 \% \text{ of } L_2 \text{ and } 0.1 \% \text{ of } L_2$ ), with the difference of the photon count from the medium component ( $L_2 = 1 \% \text{ of } L_1$ ) again

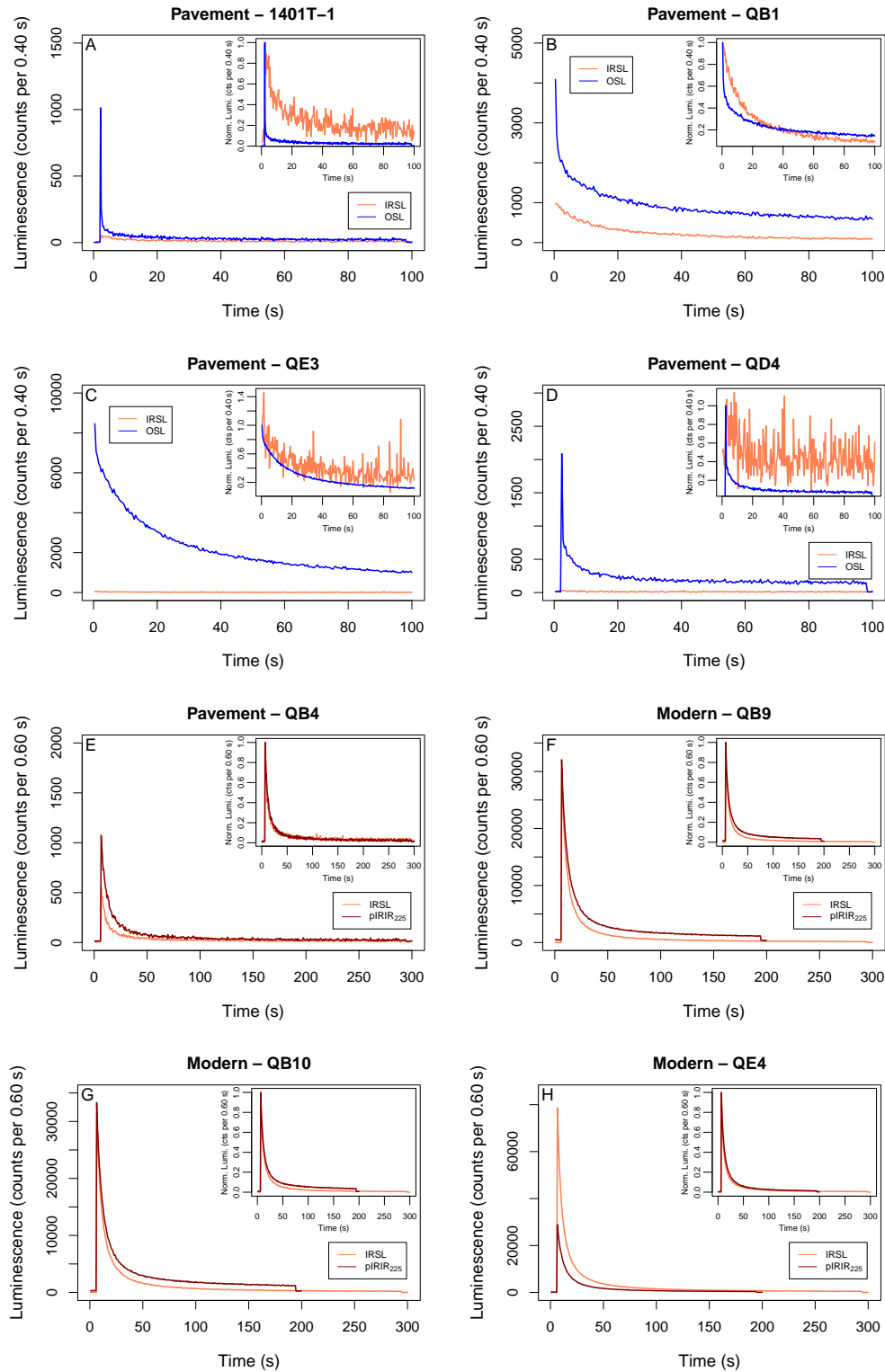


FIGURE 5.1: Luminescence decay curves following beta irradiation (45–90 Gy) from pavement vein quartz (A–D), pavement granites (E), and modern granites (F–H).

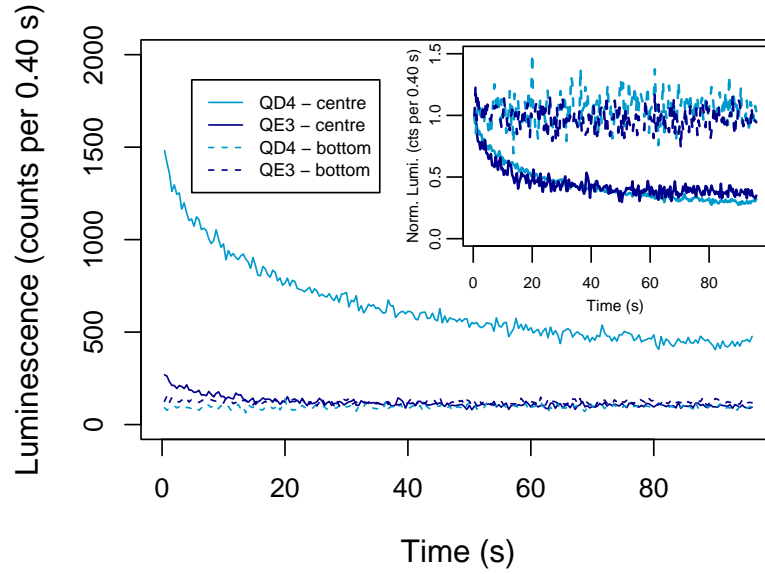


FIGURE 5.2: Natural ( $L_n$ ) OSL decay curves from QD4 and QE3.

subtracted by the background. The signal decay rate is dependent on the photoionising cross-section of the electron trap and the light intensity of the stimulation source (Bulur, 2000); these parameters are necessary to define the channels for  $L_2$  and  $L_3$  (see Durcan and Duller, 2011).

The fast ratio was calculated (Fig 5.3) using the `calc_FastRatio` function of the R Luminescence package, using the photoionising cross-section values for the fast and medium components reported in Durcan and Duller (2011), and a stimulation irradiance of  $27.2 \text{ W/cm}^2$ . The results demonstrate that while some variation is observable between the different slices, the general trend is a significant increase in the proportion of the signal originating from the fast component for each cycle of stimulation and irradiation. The increase is especially noticeable between cycles 2 and 3 and then plateaus after cycle 4.

### 5.3.3 Dose recovery test for quartz sample QD4

The ability of the double SAR protocol to recover a laboratory beta dose was tested on seven slices. Following 400 s of bleaching with blue LEDs in the OSL reader, each slice was irradiated with 155 Gy. The OSL decay curves were analysed using two approaches. For the first approach, the OSL signal was integrated over the first 0.4 seconds of the stimulation period, and the background integral was set to the

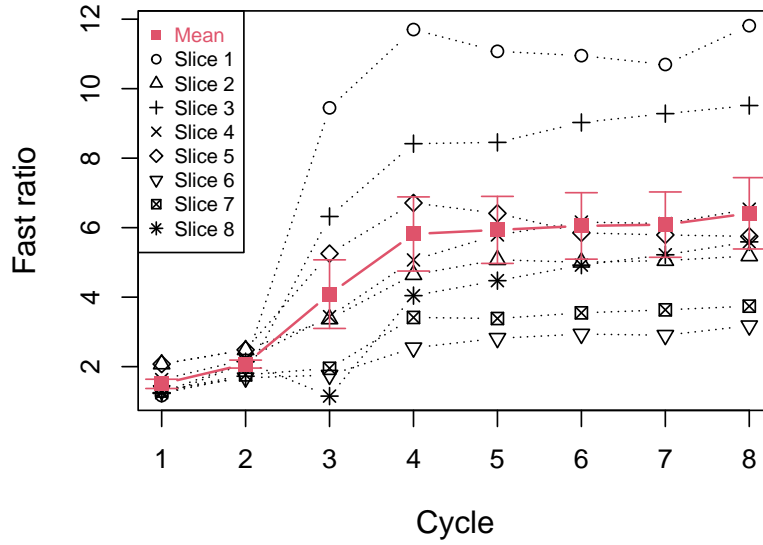


FIGURE 5.3: Changes in fast ratio in sample QD4 over cycles of OSL stimulation and beta dosing of 90 Gy (cycle 1 is the natural signal  $L_n$  without any additional dose). The error bars represent  $1\sigma$ .

last 0.4-2.4 seconds. The second approach aimed at isolating the fast component in the OSL decay curves by using an early background subtraction (Cunningham and Wallinga, 2010), where the first 0.4 s was used for signal, and the subsequent 2 s was used as background. The results from the dose recovery test (Fig. 5.4) show a wide spread in the ability between the different slices to recover a known dose, independent whether late or early background subtraction was used. The mean recovered doses were  $1.02 \pm 0.18$  for late background subtraction and  $0.99 \pm 0.23$  for early background subtraction. The dose recovery of the IRSL signal systematically overestimates the given dose, providing a mean recovery of  $1.33 \pm 0.12$ .

#### 5.3.4 Fading

Fading for the pIRIR<sub>225</sub> protocol was measured in two slices per sample in granites QB9 and QE4 using the approach of Auclair et al. (2003). Fading rates for the IRSL signal are  $6.9 \pm 0.8$  and  $5.4 \pm 0.9$  % per decade for QB9 and QE4, respectively. The pIRIR<sub>225</sub> signals fade less, where QB9 appears to fade at  $0.8 \pm 0.9$  % per decade, and QE4 fades at  $0.9 \pm 1.1$  % per decade.

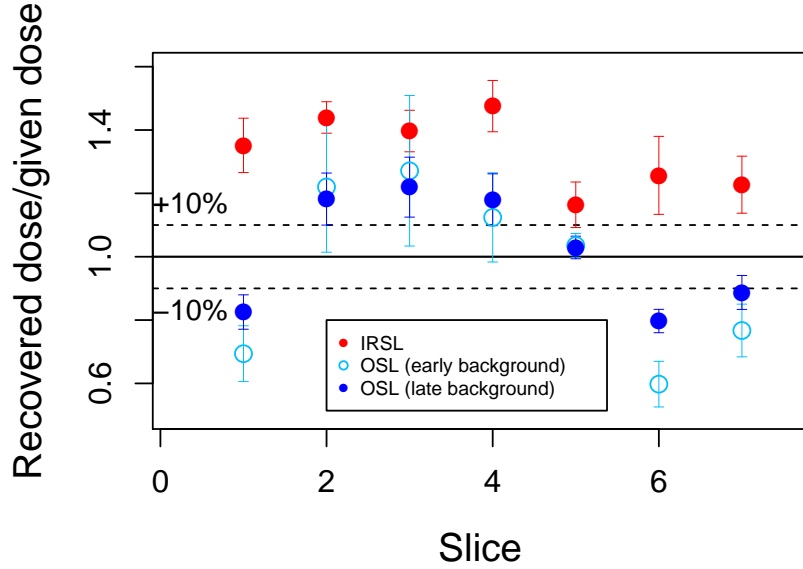


FIGURE 5.4: Dose recovery test for seven fresh slices from QD4. The OSL protocol described in Table 5.1 was used for all measurements.

## 5.4 Luminescence-depth profiles

The luminescence signal-depth profile for the vein quartz sample QD4 (Fig. 5.5) demonstrates significant bleaching (essentially no signal remains) of the OSL signal at the exposed top surface down to  $\sim 30$  mm of depth. Between 30 to 40 mm, the OSL signal increases and forms an apparent signal plateau at the centre of the sample. This intensity of this plateau is lesser if an early BG is used, compared to a late BG; there is significant scatter observed in this plateau regardless of the BG approach. The IRSL signal is severely scattered at all depths but is slightly more intense at the bottom surface.

The depth of signal bleaching in the modern granites varies between the IRSL and the pIRIR<sub>225</sub> signals (Fig. 5.6), with the IRSL signal systematically being bleached the deepest. The IRSL signal at the exposed top surfaces reaches field saturation at around 10 mm of depth for QB9 (Fig. 5.6B), QB10 (Fig. 5.6C), and QE4 (Fig. 5.6D). For QA4, a saturated IRSL level is not defined in the deepest extracted slice ( $\sim 8$  mm of depth). The IRSL signal is essentially reset at the surface slice (0–1 mm of depth) in all samples:  $< 5\%$  of the field saturation signal level remains in the surface slices for QB9, QB10, and QE4; for QA4,  $\sim 5\%$  of IRSL remains in the surface slice, compared to the innermost slice. The pIRIR<sub>225</sub> signal increases rapidly towards field saturation at depths  $< 5$  mm of depths in all samples, except for QB9,



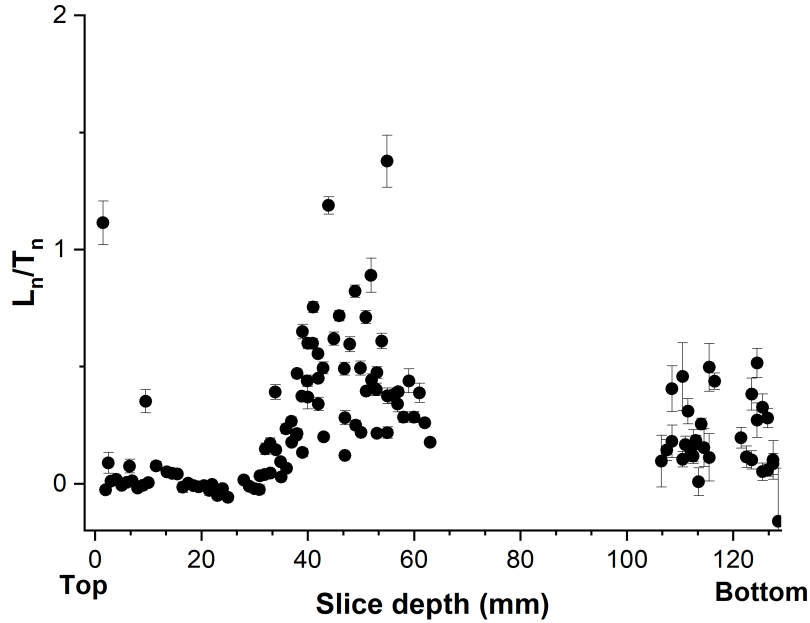


FIGURE 5.5: Luminescence signal-depth profiles for sample QD4. The natural luminescence signal ( $L_n$ ) was corrected with a test dose ( $T_n = 90$  Gy).

where the increase is gentler, and field saturation is not reached until between 7 and 10 mm of depths. At the surfaces (0–1 mm of depth),  $\sim 20$ –25 % residual pIRIR<sub>225</sub> signal remains in QA4 and QB9, compared to  $\sim 1$  % signal residual in QB10 and QE4. The residual IRSL and pIRIR<sub>225</sub> signals with depth at the covered bottom surface were measured in QB10 and QE4 (Fig. 5.6C–D). The IRSL-depth profiles from the bottom surfaces are shallower (saturation is reached at  $\sim 5$  mm of depth) compared to the corresponding top surfaces. The surface slices are similarly bleached at the top surface. The pIRIR<sub>225</sub> signal is near saturation at the bottom surface of QB10; at QE4, bleaching at the surface has been thorough ( $\sim 4$  % residual signal), but the signal increases rapidly towards saturation beneath the rock surface.

The signal resetting at the top and bottom surfaces of the friable pavement granite QB4 is presented in Fig. 5.7. The IRSL signal is bleached to 2 % of field saturation at the uppermost 3 mm of the top surface; thereafter, the signal increases and reaches an apparent saturation plateau at  $\sim 7$  mm. The pIRIR<sub>225</sub> signal increases rapidly and reaches saturation at depths  $< 5$  mm. Based on the shape of the profile, the IRSL signal at the bottom surface appears to have been fully bleached to a minimum of

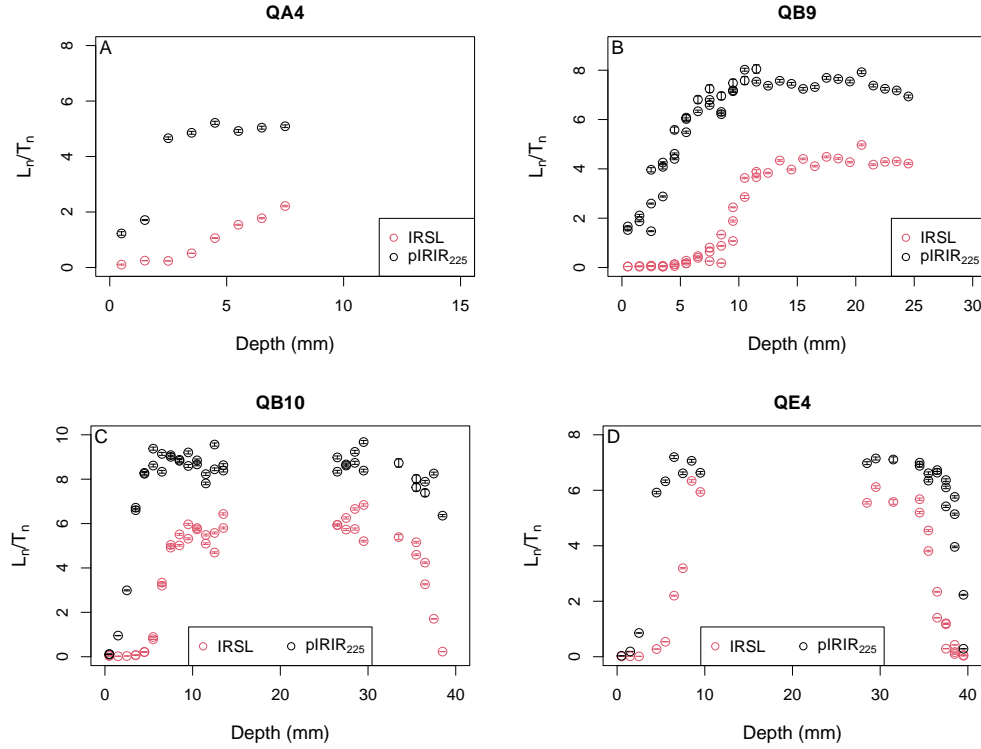


FIGURE 5.6: IRSL and pIRIR signal-depth profiles of the granites exposed on the rooftop for  $\sim 1$  year. The natural luminescence signal ( $L_n$ ) was corrected with a test dose ( $T_n = 32$  Gy).

5 mm at some point in time. A 6 % signal, relative to the field saturated signal level, remains at the outermost slice. An IRSL plateau is present at 2–5 mm from the surface, where 14 and 17 % of the signal remain (Figure 5.8). The outermost slice demonstrates pIRIR<sub>225</sub> signals of similar size while the signal increases rapidly towards saturation at  $\sim 5$  mm of depth from the bottom surface. The preliminary fitting of the IRSL profile from the bottom surface confirms that a burial plateau is present at depths up to almost 4.5 mm (55.5 mm in Fig. 5.8) from the surface.

## 5.5 Preliminary burial age estimates from sample QB4

The luminescence ages from the covered bottom surface of QB4 are presented from depths  $\sim 0$ –5 mm from the surface–substrate interface (Table 5.2. Equivalent doses were measured using two pIRIR protocols at 150 (slices) and 225 (cups) °C, respectively. The initial IR stimulation was measured at 50 °C for both protocols. Equivalent doses range between 21 to 29 Gy for the IRSL (pIRIR<sub>150</sub>) measurements. This is similar to the mean  $D_e$  estimated measured using the IRSL (pIRIR<sub>225</sub>) protocol

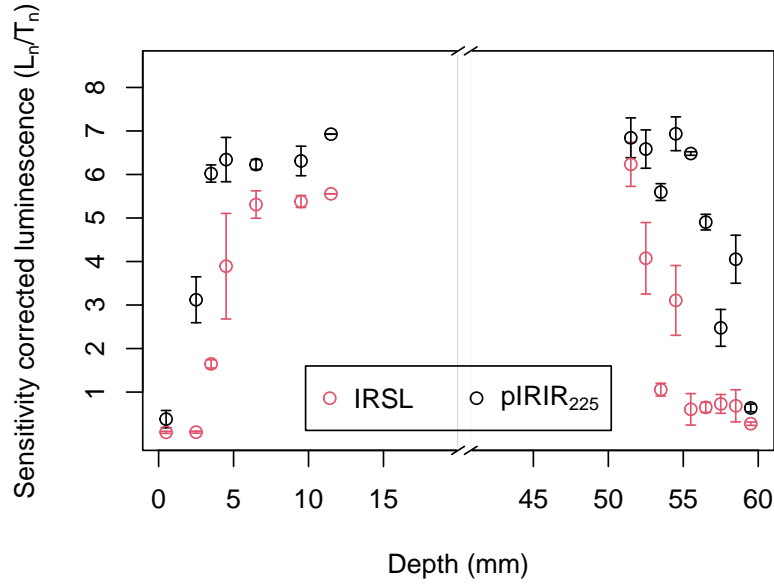


FIGURE 5.7: Luminescence signal-depth profiles for sample QB4. The natural IRSL and pIRIR<sub>225</sub> signals ( $L_n$ ) were corrected with a test dose of 32 Gy.

TABLE 5.2: Summary of ages derived from the bottom surface from sample QB4. Depth is noted from the covered surface–substrate interface.

Depth (mm)	Total dose rate	pIRIR <sub>150</sub> protocol (slices placed in the sample carousel)					pIRIR <sub>225</sub> protocol (chips mounted in steel discs)				
		IRSL (pIRIR <sub>150</sub> )			pIRIR <sub>150</sub>		IRSL (pIRIR <sub>225</sub> )			pIRIR <sub>225</sub>	
		n	De (Gy)	Age (ka)	De (Gy)	Age (ka)	n	Mean De (Gy)	Mean age (ka)	Mean De (Gy)	Mean age (ka)
0–0.7	6.2 ± 0.6	1	29.3 ± 1.0	4.7 ± 0.5	42.7 ± 2.5	6.9 ± 0.8	2	9.1 ± 2.9	1.5 ± 0.5	25.9 ± 1.4	4.2 ± 0.3
1–1.7	7.0 ± 0.6	1	20.6 ± 0.3	2.9 ± 0.3	31.6 ± 1.0	4.5 ± 0.4					
2–2.7	7.0 ± 0.6	1	26.9 ± 1.7	3.8 ± 0.4	55.8 ± 4.4	8.0 ± 0.9	4	26.8 ± 6.2	3.8 ± 0.9		
3–3.7	7.0 ± 0.6	1	23.7 ± 0.5	3.4 ± 0.3	31.6 ± 1.0	4.5 ± 0.4	4	21.5 ± 4.1	3.1 ± 0.9		
4–4.7	7.0 ± 0.6	1	27.4 ± 0.6	3.9 ± 0.3	51.2 ± 2.3	7.3 ± 0.7	2	19.5 ± 13.1	2.8 ± 1.9		

at depths 2–4.7 mm (20–27 Gy). The mean IRSL (pIRIR<sub>225</sub>)  $D_e$  from the outermost slice is considerably lower at  $9 \pm 3$  Gy. Ages calculated for the IRSL signals using the depth-specific dose rate ranges between  $1.5 \pm 0.5$  ka to  $4.7 \pm 0.5$  ka. pIRIR<sub>150</sub> ages are overall older than the corresponding IRSL ages due to the larger  $D_e$  values (32–56 Gy), resulting in ages between  $4.5 \pm 0.4$  and  $8.0 \pm 0.9$  ka. The  $D_e$  value (26 Gy) measured from the surface slice using pIRIR<sub>225</sub> signal yielded a burial age of  $4.2 \pm 0.3$  ka.

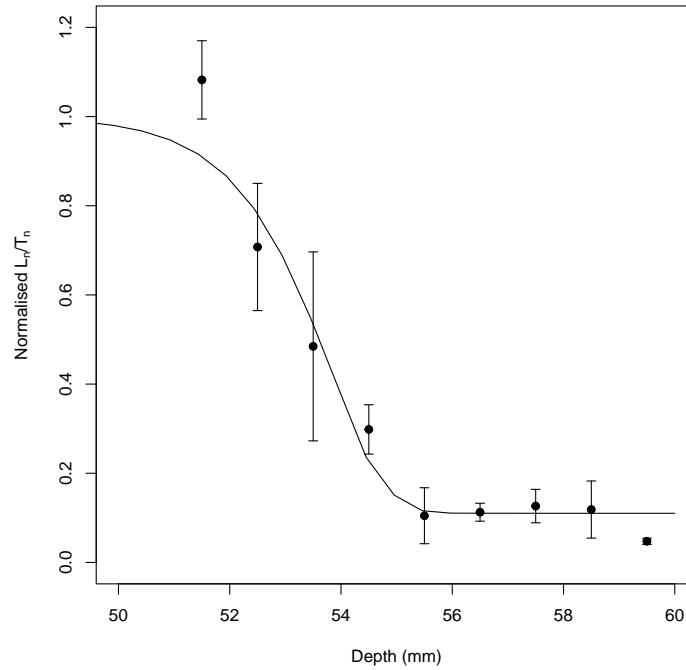


FIGURE 5.8: Fitting of the  $L_n/T_n$  IRSL data from bottom surface of QB4 using Eq. 1.7, assuming one exposure event followed by one burial event. The data were normalised using the average  $L_n/T_n$  calculated from all slices for which  $L_n/T_n$  ratio  $>5$  from Fig 5.6, using this value as a proxy for the field saturated  $L_n/T_n$  level.

## 5.6 Discussion

### 5.6.1 Luminescence performance

While the IRSL and pIRIR signals in the granites are bright (especially when measured on whole slices), the luminescence characteristics of the quartz from Wadi Sodmein appear unsuitable for dating. The low IRSL intensities are explainable by a negligible presence of feldspars. For the quartz signal, the primary issue is the slow OSL decay observed in the natural signal due to the apparent lack of a strong, fast component. Low OSL intensities have previously been attributed to the lack of a strong, fast component in a vein quartz sample from South America (Mineli et al., 2021). Cycles of irradiation and stimulation, on average, triple the fast-medium component ratio in the Sodmein quartz, indicating that natural cycles of exposure and burial could improve signal properties for dating; such improvements are frequently reported for sediment quartz (e.g., Pietsch et al., 2008; Sawakuchi et al., 2011; Mineli et al., 2021).

It is also clear from optical observation of decay curves from irradiated slices (Fig. 5.1) that a fast decaying component arises following laboratory irradiation. However, there is still a considerable contribution of slower signal components in most of the samples. The dose recovery data demonstrate a significant spread in the ability to recover known doses between different slices, no matter if a late or early background subtraction is used. This indicates that any equivalent doses calculated from the Sodmein quartz using the standard SAR protocol will not necessarily represent the palaeodose and the correct burial ages.

Overall, OSL dating of quartz from rocks is challenging. While some quartzite and some sandstones have previously demonstrated sufficiently good quartz signals to be used for dating (e.g., [Sohbati et al., 2012c](#); [al Khasawneh et al., 2019a](#); [Gliganic et al., 2021](#)), poor quartz signal characteristics appear common in many rocks, including hydrothermal quartz ([Jenkins et al., 2018](#); [Mineli et al., 2021](#)), igneous rocks ([Sohbati et al., 2011](#); [Mineli et al., 2021](#)), flints ([Poolton et al., 1995](#)), and quartz-poor sandstones ([Brill and Cisternas, 2020](#)). This poor signal performance is regrettable since the translucent matrix of quartz-dominated rocks translates into rapid and deep bleaching once the rocks are exposed to daylight. It is clear from sample QD4 that the OSL signal has been zeroed 3 cm into the small boulder, which confirms previous observations where deep bleaching was reported in translucent quartzites ([Sohbati et al., 2012c](#); [Ou et al., 2018](#); [Gliganic et al., 2019, 2021](#)). For the dating of wadi pavement, the deep bleaching appears unfavourable since the natural signal at the bottom of samples QE3 and QD4 are indistinguishable from background noise. This indicates that the signal might have penetrated so deep, from the top and the side of the cobbles, that all signal has been removed. Hence, the sample set of quartz from Wadi Sodmein investigated in this study has failed to produce any ages, and further efforts could likewise fail. However, the increase in the fast component observed after cycles of bleaching and irradiation does suggest that cycles further downstream in the system could demonstrate better signal performances. While dating might still not be possible, comparisons in signal characteristics between different samples from within a fluvial system could provide information regarding fluvial dynamics, similar to what [Pietsch et al. \(2008\)](#) suggested for unconsolidated quartz grains, where samples with higher OSL sensitivity have been transported and deposited more frequently

compared to dimmer samples.

### 5.6.2 Age of cobble QB4

The burial age from sample QB4 indicates that the bottom surface of the cobble was covered in the latter half of the Holocene. However, due to the few cores that could be extracted from QB4 due to the fragility of the sample and lack of fading estimates, the burial age provided in this chapter for the bottom surface of the single sample QB4 should be considered preliminary estimates for when a single rock surface was covered, rather than comprehensive dating of the development of desert pavement in Wadi Sodmein. Firstly, the youngest IRSL age (1.5 ka) measured from chips from one surface slice is approximately 50 % younger compared to the other IRSL ages calculated from the other slices. The lower signal levels in this particular slice could be due to a secondary exposure, followed by re-burial at around 1.5 ka. However, the signal depth profile does not contain sufficient depth resolution (i.e., thinner slices) to resolve such an event. Due to the extremely friable nature of the sample, it is possible that the part of the signal-depth profile that recorded this event was lost during sample preparation. Hence, whether the youngest-most age represents spread in the IRSL data or a separate event remains an open question. The current best estimate is that the bottom surface of QB4 was covered during the mid-Holocene, with a possible more recent burial event occurring at least at 0–1000 AD. Secondly, error estimates derived from the slices are here of limited value due to the lack of multiple-dose measurements. Therefore, the error estimates in the dose measurements are solely based on counting statistics (Duller, 2018) and do not consider any additional sources of uncertainty. Finally, the age estimate of the desert pavement is based on a single age estimate. While only samples embedded into the substrate were collected, it is likely impossible to optically determine if a cobble had been turned thousands of years before sampling if subsequent aeolian dust has partly recovered parts of the cobble.

### 5.6.3 Dating of desert pavements using rock surface luminescence dating

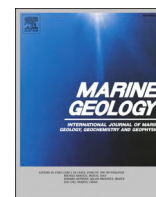
Rock surface luminescence dating appears to be a limited method to date the desert pavements in Wadi Sodmein. For the quartz cobbles, the challenge is mainly lithological and would, therefore, not necessarily transpose to other sites. The rooftop granite cobbles, extracted from the wadi gravel, demonstrate good bleaching and luminescence properties, but such a deep bleaching profile is not present at the top surface of pavement sample QB4. Any exposed surface of most lithologies would likely erode during long-term exposure to the pavement. Exposure dating using rock surface luminescence will severely underestimate any ages in such conditions unless known erosion rates are included in the age model (Sohbati et al., 2018; Lehmann et al., 2019a). For burial dating, the formation process of the desert pavement will affect the application of rock surface dating. Pre-burial exposure is necessary to bleach the signal; for the fluvial wadi deposits in Wadi Sodmein, this would most likely occur during the transport of the cobbles before deposition. Ideally, the uppermost gravel layer will be undisturbed so that the dose can accumulate at the covered bottom surfaces until sampling. Fuchs and Lomax (2019) identified several reasons for overdispersion in sediment luminescence doses: input of young grains through desiccation cracks or old grains due to weathering adjacent rocks and soil mixing due to swelling and shrinkage of fine sediments. Rock surface ages will not be much affected by the input of new grains, especially since the effect from radiation heterogeneity is diminished since most of the beta (Riedesel and Autzen, 2020) and a significant portion of the gamma radiation arises from the rock itself independent of the surrounding. However, the physical movement of a cobble by peloturbation or bioturbation could disturb the covered surfaces and disconnect the chronological link between surface formation and the dated age of the cobble. In general, the presence of a previous burial event at the top surface, combined with a younger-than-expected age at the bottom surface, would indicate that the cobble had been flipped and cannot be used to date the age of the surface. Since there is no indication of a burial event at the now exposed top surface of QB4, it cannot be determined if the cobble ever was flipped. While it is clear from the signal-depth profile from QB4 that some chronological information has been



recorded, be it the age of the pavement surface or just a data point indicating when a single cobble was flipped, it is clear that one age from a single cobble is insufficient to date a desert pavement surface.

## Chapter 6

Investigating the resetting of IRSL signals in beach cobbles and their potential for rock surface dating of marine terraces in Northern Chile



# Investigating the resetting of IRSL signals in beach cobbles and their potential for rock surface dating of marine terraces in Northern Chile

Dominik Brill<sup>a,\*</sup>, Lucas Ageby<sup>a</sup>, Christina Obert<sup>b</sup>, Rolf Hollerbach<sup>b</sup>, Mathieu Duval<sup>c,d</sup>, Thomas Kolb<sup>e</sup>, Melanie Bartz<sup>f,a</sup>

<sup>a</sup> Institute of Geography, University of Cologne, Germany

<sup>b</sup> Institute of Geology and Mineralogy, University of Cologne, Germany

<sup>c</sup> Centro Nacional de Investigación sobre la Evolución Humana (CENIEH), Burgos 09002, Spain

<sup>d</sup> Australian Research Centre for Human Evolution (ARCHE), Environmental Futures Research Institute, Griffith University, Nathan, QLD 4111, Australia

<sup>e</sup> Institute of Geography, Justus-Liebig-University, Gießen, Germany

<sup>f</sup> Institute of Earth Surface Dynamics, University of Lausanne, Switzerland

## ARTICLE INFO

### Keywords:

Luminescence dating  
Rock surface dating  
Post-infrared-infrared  
Lithology  
Marine terrace  
Beach cobble  
Modern analogue  
Atacama

## ABSTRACT

Inactive shorelines represent valuable records for sea level change, shoreline variations and tectonics if we can constrain the timing of their formation. Where the associated beaches are cobble dominated, luminescence rock surface dating is a promising alternative to established dating approaches, since unlike other techniques it offers the potential to identify clasts unaffected by inherited ages. While luminescence rock surface dating has successfully been used on Holocene and Late Pleistocene beach ridges previously, in this study the potential of IRSL rock surface dating is evaluated for the magmatic cobbles of uplifted Pleistocene terraces along the tectonically active coast of northern Chile. Cobbles from an active beach were used to investigate the influence of cobble lithology on IRSL signal properties and the effectiveness of IRSL signal resetting in the rock. While alkaline and andesitic cobbles yield low IRSL intensities and limited signal resetting due to strong light attenuation, more favourable characteristics for dating were observed for some diorite and granite cobbles. Their IRSL signals were well reset in the uppermost few mm without any systematic difference between upper and lower surface. Some of them revealed bleaching plateaus with inherited ages close to zero after correction for laboratory residuals. For dating, cobbles from three Pleistocene marine terraces, for which new uranium-thorium and ESR control ages on molluscs provide age control, were targeted. None of the associated IRSL rock surface burial ages agrees with the MIS 5 control ages of the terraces. Most of the selected cobbles are either too dark to allow for effective signal resetting or yield IRSL properties unsuitable for dating. Only one of the targeted cobbles shows both signs of signal resetting at its surface and sensitive IRSL signals, but its signal was already in field saturation due to dose rates >6 Gy/ka. In conclusion, our data indicate that beach cobbles with granitic to dioritic lithology combine appropriate IRSL properties and sufficient IRSL signal resetting for dating Holocene landforms. Last interglacial terraces may already be beyond the limit of IRSL dating for most cobbles of this lithology since they show large dose rates compared to IRSL sediment dating.

## 1. Introduction

While luminescence dating is typically used to determine the depositional age of sand- or silt-sized sediments, recent developments have extended its applicability to the dating of rock surfaces. Based on the observation of time- and depth-dependent luminescence signal resetting in the uppermost millimetres to centimetres of light-exposed rock surfaces (Habermann et al., 2000; Sohbati et al., 2011), luminescence rock

surface dating has shown potential for quantifying both burial and exposure durations of rock surfaces (see King et al., 2019b for a review). This approach offers the potential to apply luminescence dating to new substrates and research questions, including the formation of moraines (Jenkins et al., 2018; Rades et al., 2018), rock falls (Sohbati et al., 2012), archaeological structures and artefacts (Freiesleben et al., 2015; Sohbati et al., 2015; Ageby et al., 2021; Gliganic et al., 2021) and coastal boulders (Brill et al., 2021), as well as the reconstruction of deglaciation

\* Corresponding author.

E-mail address: [brilld@uni-koeln.de](mailto:brilld@uni-koeln.de) (D. Brill).

<https://doi.org/10.1016/j.margeo.2021.106692>

Received 27 July 2021; Received in revised form 29 September 2021; Accepted 28 October 2021

Available online 3 November 2021

0025-3227/© 2021 Elsevier B.V. All rights reserved.

histories (Lehmann et al., 2018, 2020) and erosion rates (Sohbati et al., 2018; Lehmann et al., 2019).

Luminescence rock surface dating may also inform about the depositional history of wave-transported beach cobbles (Sohbati et al., 2011). When forming raised beaches or marine terraces, beach cobbles can mark the position of former shorelines and, thus, may serve as indicators for sea-level variations (e.g. Garrett et al., 2020), rates of tectonic uplift or subsidence (e.g. Merritts and Bull, 1989), and shoreline

displacements (e.g. Brill et al., 2015). Chronologies based on radiocarbon, electron spin resonance (ESR), U-series or amino acid racemization dating of calcareous organisms incorporated in beach deposits are relatively common (e.g. Ortlieb et al., 1996; Schellmann and Radtke, 2000), but may be biased if the dated organisms have been reworked from older deposits, or behaved as open systems for U-series elements, and especially if they have experienced uranium leaching. In absence of sandy sediment suitable for conventional luminescence dating,

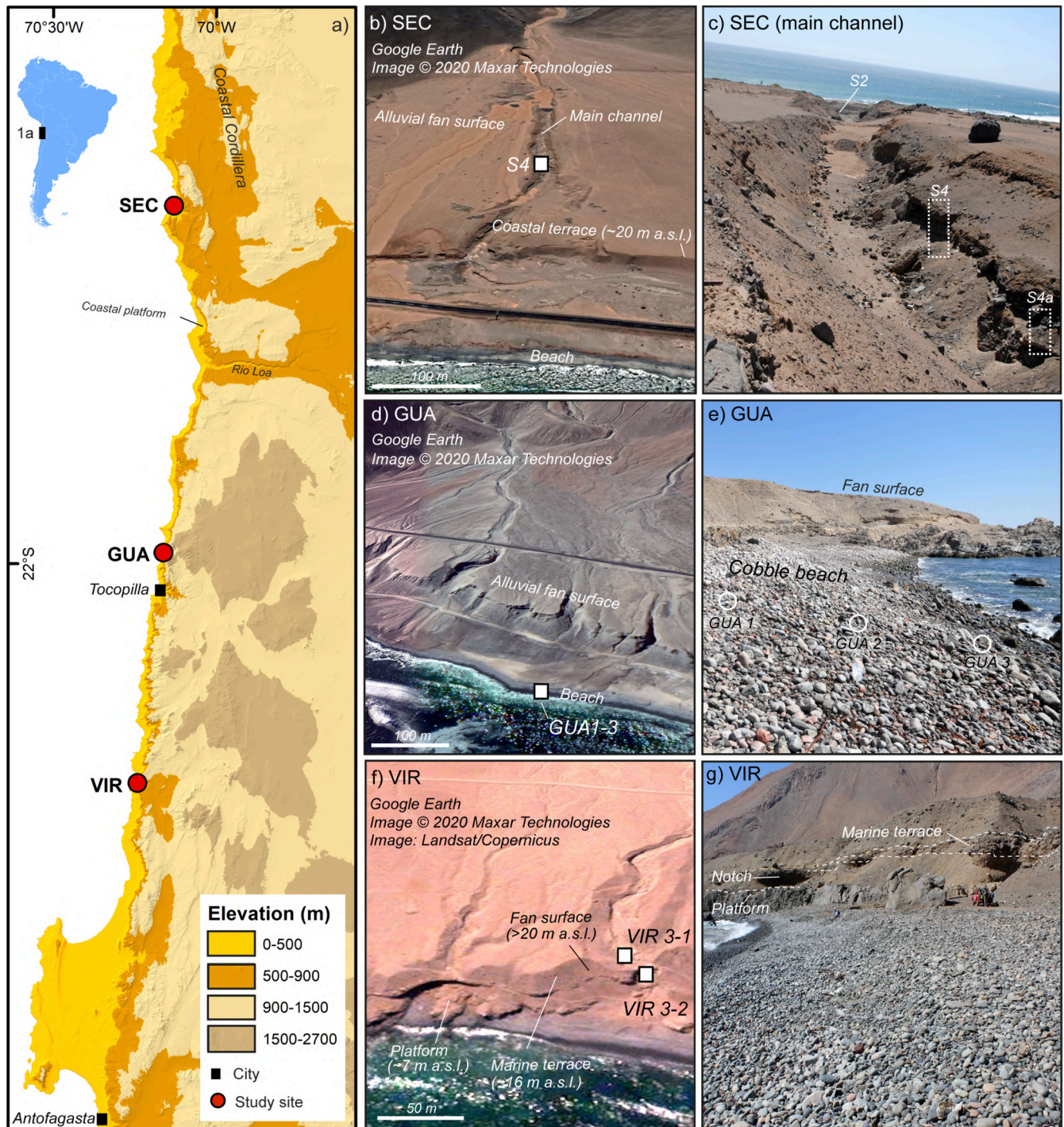


**Fig. 1.** Geomorphological setting of the sampling locations. a) Topographical map of the study area with locations of the sampling sites SEC, GUA and VIR (DEM based on SRTM data). Geomorphological settings and sampling locations of sites SEC (b, c), GUA (d, e) and VIR (f, g) (satellite images in b, d and f © Google Earth 2020).



terrestrial cosmogenic nuclide dating is the most common approach for determining the formation of marine terraces like wave-cut platforms or cobble deposits (e.g. Saillard et al., 2009). As first successful applications have indicated (Simms et al., 2011, 2012; Simkins et al., 2013; Souza et al., 2019, 2021), luminescence rock surface dating can provide complimentary chronological constraints for cobble beaches over at least Holocene and Late Pleistocene time scales; for specific lithologies such as pure quartz clasts, the approach may even date back to MIS 12 (Bailliff et al., 2021). Luminescence rock surface dating may also be advantageous compared to conventional luminescence dating where sandy strata are available since depth-resolved luminescence data offer the opportunity to unambiguously identify completely bleached deposits and dose rates virtually unaffected by temporal changes of water contents (Jenkins et al., 2018).

The aim of this study is to systematically evaluate luminescence rock surface dating applied to raised beaches and Pleistocene marine terraces along the tectonically active coast of Chile, which serve as valuable indicators for regional tectonics and relative sea-level fluctuations. Since quartz luminescence properties of magmatic rocks, as they dominate the lithology of the Andean Cordillera, are typically inadequate for dating (e.g. Tsukamoto et al., 2011; Simkins et al., 2016), we applied feldspar infrared stimulated luminescence (IRSL) and post-infrared-infrared stimulated luminescence (post-IR-IRSL) rock surface dating to cobbles from a modern beach and three Pleistocene marine terrace levels along the coast of northern Chile. Firstly, we studied the influence of different cobble lithologies on the associated IRSL and post-IR-IRSL signal properties. Secondly, the effectiveness of IRSL and post-IR-IRSL signal resetting at cobble beaches was investigated by using cobbles from a modern beach. And thirdly, cobbles from two Pleistocene marine terraces, for which chronological control is available from conventional post-IR-IRSL sediment ages (Bartz et al., 2020a), were targeted with IRSL and post-IR-IRSL rock surface burial dating. As additional age cross-check, we provide new U-series and combined U-series/ESR ages of three mollusc shells from the same sediment sections. The benefits of this study are not restricted to marine terraces along the coast of northern Chile, they are assumed to provide valuable insights into the potential of luminescence rock surface dating techniques to date marine terraces and raised cobble beaches in general.

## 2. Study area

Our study area is located at the coastal Atacama Desert (N Chile) between Iquique and the Mejillones Peninsula (Fig. 1a). The main geomorphological structures are the Coastal Cordillera and the Coastal Plain. The former is an eroded volcanic arc formed in the Mesozoic, mostly 1000–2000 m high and on average ~ 30 km wide (González et al., 2003). Its western margin is characterised by the Coastal Cliff. Regard et al. (2010) estimated the elevation and timing of the cliff foot to ~110 m a.s.l (above sea level) and ~ 400 ka, respectively. The up to 3-km wide Coastal Plain between the modern coastline and the Coastal Cliff exhibits hundreds of alluvial fan sequences (Walk et al., 2020) overlying and intersecting with uplifted marine terrace deposits (e.g. Radtke, 1989; Bartz et al., 2020b). In the tectonically active setting of the Andean subduction zone, marine terraces provide excellent indicators for tectonic uplift and the regional relative sea-level history (e.g. Ortlieb et al., 1996; Regard et al., 2010). A significant number of studies have conducted numerical dating to chronologically constrain the marine terrace deposits, including luminescence and ESR dating of sediments, ESR in combination with U-series dating of marine shells, as well as amino acid racemization and radiocarbon dating of shells and terrace material (Bartz et al., 2020a, 2020b; González-Alfaro et al., 2018; Labonne and Hillaire-Marcel, 2000; Leonard and Wehmiller, 1991; Ortlieb et al., 1996; Radtke, 1989; Ratusny and Radtke, 1988). These studies resulted in an almost complete chronology of palaeo-shorelines from the Holocene to MIS 11 (Regard et al., 2010). Quaternary uplift rates in the area are between 0.1 and 0.6 m/ka (Victor et al.,

2011), but have likely varied spatially and temporally during the Quaternary (e.g., Binnie et al., 2016; Saillard et al., 2009). This is indicated, for example, by varying elevation levels between 10 and 60 m a.s.l. for MIS 5 marine terrace surfaces (Radtke, 1989).

The sediments forming alluvial fans and marine terraces are mainly derived from fluvial systems that cut back into the Coastal Cordillera (Walk et al., 2020). The catchments feeding the fan-terrace complexes studied here are mainly characterised by (i) Mesozoic plutonic rocks with granitic to dioritic composition (specifically the Cerro Carrasco complex, the Gatico complex and the Tocopilla complex), and (ii) volcanic rocks of the Jurassic La Negra formation mainly composed of andesites and basalts, and only to a minor part of (iii) unconsolidated Late Tertiary sediments (e.g. the Alto Hospicio gravels) (Medina et al., 2012; Quezada et al., 2012; Sepúlveda, 2012; Vásquez and Sepúlveda, 2012; Mpodozis et al., 2015). Due to the long-term hyper-aridity of the region with currently less than 5 mm of annual rainfall on average, which was intersected only by short periods with slightly more humid conditions during the Pleistocene (e.g. Ritter et al., 2019), preservation conditions for raised coastal deposits and landforms in the study area are generally good.

## 3. Material and methods

### 3.1. Site stratigraphy and sample selection

Beach cobbles for luminescence rock surface dating were collected at three locations along the Atacama coastline, namely Río Seco (SEC), Guanillos (GUA) and Caleta El Fierro (VIR – “Virgen del Camino”) (Fig. 1a, Table S1). The geomorphological settings of all three sites have previously been described in Bartz et al. (2020a, 2020b) and Walk et al. (2019, 2020).

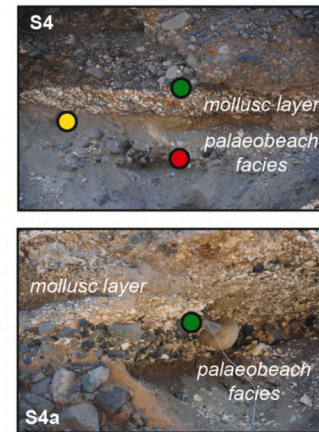
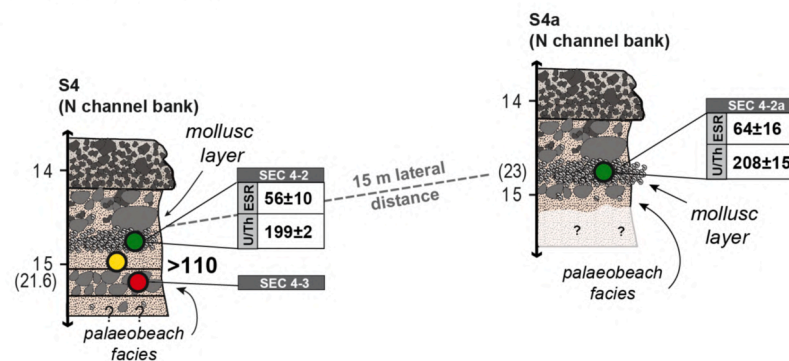
#### 3.1.1. Río Seco (SEC)

The Río Seco site is characterised by an alluvial fan complex that intercalates with at least one level of marine terrace deposits (Fig. 1b,c; Bartz et al., 2020a, 2020b). The marine sediments are composed of a succession of sandy units, layers with well-rounded cobbles and shell layers (Fig. 2a). At an elevation of ~21 m a.s.l. (section S4), a palaeo-beach composed of cobbles in sandy matrix was sampled for luminescence rock surface dating (SEC 4–3). Sandy beach deposits directly above this cobble layer were dated to older than 110 ka based on post-IR-IRSL<sub>225</sub> dating of potassium feldspar (Bartz et al., 2020a). For additional cross-check, two well-preserved, closed bivalves (SEC 4–2 and SEC 4-2a) from an up to 2-m thick mollusc layer directly above the sandy beach facies were sampled for ESR and U-series dating (Fig. 2a). Due to its heterogeneous composition of well-preserved bivalves of different species, shell fragments, rounded beach cobbles and angular alluvial fan clasts, as well as its lateral continuity over more than 200 m, the mollusc layer might be related to flooding by a high-energy event such as a tsunami rather than beach processes (layers with similar characteristics were interpreted as Holocene tsunami deposits in the South of the Atacama by León et al., 2019). Approximately 150 m seaward of section S4, beach deposits at an elevation of ~12 m a.s.l. (section S2 in Fig. 1c) were dated to the MIS 5c (95–110 ka) based on a combination of potassium feldspar post-IR-IRSL and quartz ESR dating (Bartz et al., 2020a). Based on the existing geochronological framework (Bartz et al., 2020a), as well as on observations by Radtke (1989) from marine terrace deposits close to Iquique, the marine deposits of S2 and S4 likely correspond to different MIS 5 sea levels (S2 was formed during MIS 5c and S4 during MIS 5e or older).

#### 3.1.2. Guanillos (GUA)

The Guanillos alluvial fan complex is fed by two fluvial catchments. Marine terrace deposits have not been observed at this location, most likely due to superposition or erosion by the Late Pleistocene alluvial fan activity (Bartz et al., 2020b). Cobbles for luminescence rock surface

## a) SEC (20°59'S 70°09'W)



## b) VIR (22°38'S 70°15'W)

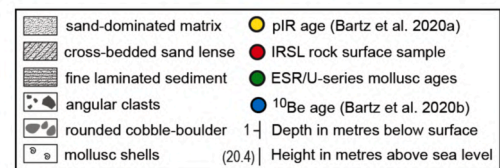
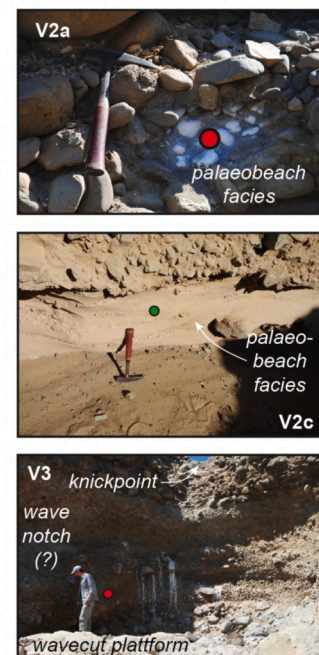
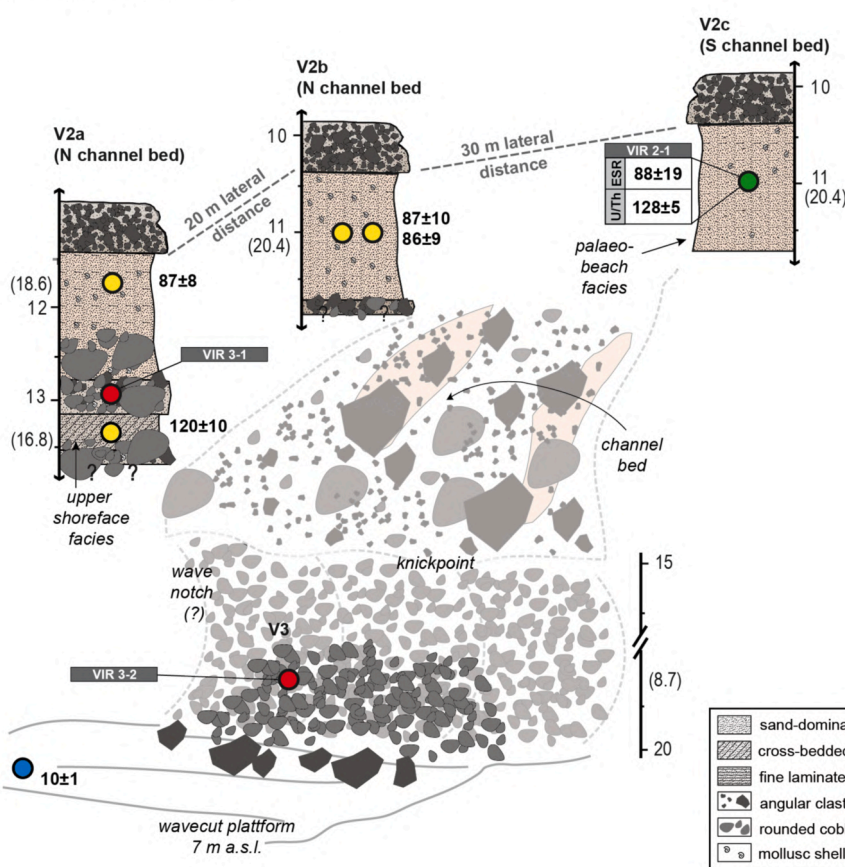


**Fig. 2.** Stratigraphy of sampled marine terraces at SEC (a) and VIR (b) including the positions of samples for luminescence rock surface dating of cobbles (red, this study), combines U-series/ESR and U-series dating of molluscs (green, this study) and conventional post-IR-IRSL<sub>225</sub> dating of sand grains (yellow, Bartz et al., 2020a). (For interpretation of the references to colour in this figure legend, the reader is referred to the web version of this article.)

dating were collected from the modern beach profile south of the main alluvial fan outlet (Fig. 1d,e). All cobbles originate from the seaward side of the present beach berm. Surface samples were collected in elevations of ~1 m a.s.l. (GUA 3), ~1.5 m a.s.l. (GUA 2) and ~2 m a.s.l. (GUA 1).

### 3.1.3. Virgen del Camino (VIR)

At the alluvial fan complex at Virgen del Camino (VIR, also called Caleta El Fierro), a succession of palaeo-beach deposits composed of well-rounded cobbles and homogeneous fine- to medium-sand with

abundant shell fragments and few mollusc shells is exposed along the outlet of the main channel (Bartz et al., 2020a, 2020b; Figs. 1f,g, 2b). Cobbles for luminescence rock surface dating were extracted from a beach-cobble layer at ~17 m a.s.l. (VIR 3-1) that was exposed at the northern channel section (V2a in Fig. 2b). Bartz et al. (2020a) post-IR-IRSL dated sandy upper shoreface deposits below (~16 m a.s.l.) and sandy beach deposits above the cobble layer (18–20 m a.s.l.) to the MIS 5e (120 ± 10 ka) and MIS 5a/c (~90 ka), respectively (Fig. 2b). For their interpretation it is important to highlight that the MIS 5e deposits were deposited under shallow marine conditions, so the contemporaneous



palaeo-beach deposits might be buried further inland at higher elevations (Leonard and Wehmiller, 1991; Bartz et al., 2020b). As a further crosscheck, a shell (VIR 2–1) from the sandy beach deposits above the cobble layer was collected for ESR and U-series dating at the southern channel section (V2c in Fig. 2b), where its location is laterally concordant to the post-IR-IRSL<sub>225</sub> dated sand horizon (Bartz et al., 2020a).

A second cobble sample for luminescence rock surface dating (VIR 3–2) was collected from the landward cliff of a wave-cut platform at ~7 m a.s.l. (section V3, Figs. 1f,g, 2b). The ~10 m high cliff at the alluvial fan toe and the associated wave-cut platform were formed during the Holocene, as indicated by <sup>10</sup>Be cosmogenic nuclide ages of ~10 ka (Bartz et al., 2020b; Fig. 2b). The cobbles collected for dating originate from a wave-cut notch at the cliff foot. Deposition of these cobbles could be both synchronous to the formation of the Holocene wave-cut platform, or to the formation of the MIS 5 marine strata exposed at the 8-m high knick-point of the alluvial channel outlet.

### 3.2. IRSL rock surface burial dating

Cobbles from the modern beach (GUA) were collected directly at the surface of the beach profile, while those from the marine terraces (VIR, SEC) were sampled at natural outcrops after removing the outermost ~30 cm of cobbles (Fig. 3a). After marking shielded and exposed cobble surfaces at the time of sample collection, cobbles were sealed in light-proof plastic bags for laboratory analyses.

Further processing of the cobbles was performed under subdued red light conditions in the Cologne Luminescence Laboratory (CLL) to avoid any bleaching of luminescence signals after sample collection. For each of the six samples, two cobbles were prepared (Table S1). Rock cores of ~1 cm diameter and 2–4 cm length were extracted from the cobbles using a water-cooled bench drill (WEKA DK17) with diamond core bits. In case of the modern beach samples (GUA), one core was extracted from the surface exposed during sampling and a second one from the shielded bottom surface. Only cores from the surface shielded during sample collection were taken from the marine terrace cobbles at VIR and SEC (Fig. 3b). All cores were cut into ~0.7 mm thick slices (in intervals of 1 mm) using a water-cooled low speed saw (Bühler Isomet 1000) with 0.3 mm thick diamond blades (Fig. 3c).

Luminescence measurements with a Risø TL/OSL DA 20 reader (Bøtter-Jensen et al., 2010) were performed on the complete rock slices or, for broken slices, on fragments put in aluminium cups without any previous chemical treatment or mineral separation. Since the measurement of polymineralic rock slices and fragments with significant feldspar contents does not permit robust instrumental isolation of quartz luminescence signals (Aitken, 1998), and since previous studies indicated inadequate luminescence properties for quartz from magmatic rocks in general (Sohbati et al., 2011; Souza et al., 2019) and quartz from Chile in

particular (del Rio et al., 2019; Brill and Cisternas, 2020), we focused on feldspar luminescence signals in all our measurements. All measurements followed the post-IR-IRSL<sub>225</sub> protocol (cf. Buylaert et al., 2009) outlined in Table S2 using infrared LEDs for signal stimulation and a photomultiplier plus a LOT interference filter with peak transmission at 410 nm for signal detection. All signals are based on integrating the first 10 s of each signal curve and subtracting the last 20 s. It is one of the standard protocols for Pleistocene sediments in general, which was already used successfully in numerous conventional luminescence dating studies on silty to sandy sediments from the study area (e.g. Bartz et al., 2020a, 2020b; May et al., 2020; Medialdea et al., 2020).

The measurement strategy outlined in Fig. 3c started with the determination of luminescence signal-depth profiles by measuring  $L_n/T_n$  ratios for the uppermost 10–20 slices of each core. Dose recovery experiments with given doses of ~30 Gy and the quantification of laboratory residual doses were performed on 24 h solar simulator (Hoenle Sol2) bleached slices from the inner part of each cobble using the full post-IR-IRSL<sub>225</sub> protocol. Rock slices for equivalent dose ( $D_e$ ) determination were selected from those parts of the cobbles that were indicated as bleached by the associated signal-depth profiles (typically from the uppermost 1–3 slices, see sections 4.3 and 4.4) and measured using the full post-IR-IRSL<sub>225</sub> protocol (Table S2). Successive data analysis was performed separately for both luminescence signals measured within our protocol, the IRSL signal and the post-IR-IRSL<sub>225</sub> signal.

For dosimetry, the combined dose rates of the feldspar crystals (internal dose rate), the cobbles and the surrounding sediments (external dose rates), as well as cosmic radiation (cosmic dose rate) were considered (Fig. 3b, c). Internal dose rates were calculated on the basis of assumed potassium concentrations of  $10 \pm 2\%$  in potassium feldspar (Smedley et al., 2012) and  $3 \pm 2\%$  in plagioclase (Sohbati et al., 2013), as well as average crystal sizes deduced from visual inspection of rock slices under a microscope. Cosmic dose rates were based on the geographic location and burial depth (Prescott and Hutton, 1994). Infinite matrix dose rates of the dated cobbles and the surrounding fine sediment were based on uranium, thorium and potassium contents determined with high-resolution gamma spectrometry. For the cobble matrix surrounding all dated cobbles, we assumed homogeneous lithology calculated by averaging the dose rates of all dated cobbles from a section, as well as pore volumes of 30% that were filled with sand at VIR 3–1 and SEC (the associated sand dose rates were reported by Bartz et al., 2020a) and filled with air at GUA and VIR 3–2. We did not consider differences between the buried bottom side and the exposed top side of the cobbles at the modern beach (GUA), since we assume constant movement of the cobbles within the beach berm by wave action; instead constant burial of all cobble sides was assumed for dose rate calculation. All infinite matrix dose rates were calculated with the DRAC software version 1.2 (Durcan et al., 2015).

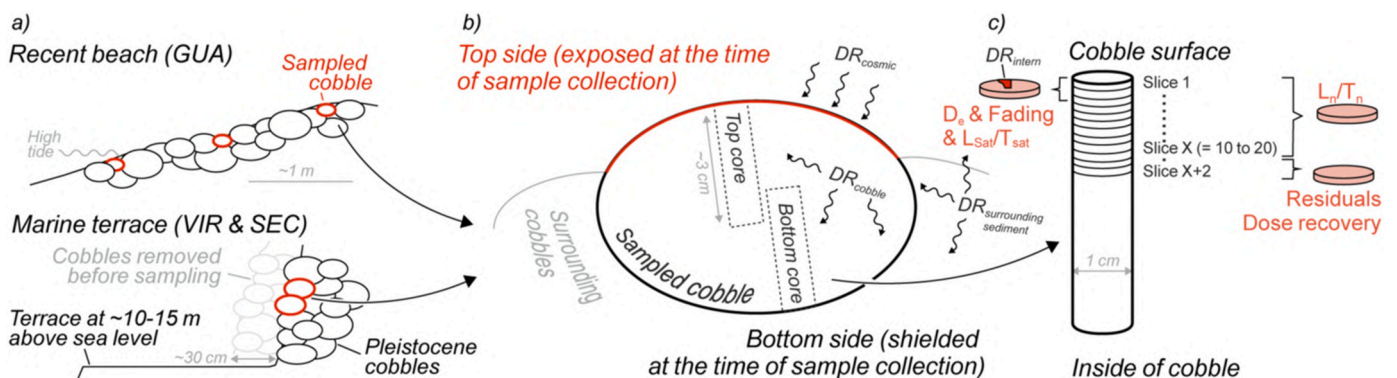


**Fig. 3.** Sampling and measurement strategy applied in this study to date beach cobbles with luminescence rock surface dating. a) Schematic cross-sections of a sampled beach profile (GUA) and marine terraces (VIR and SEC). b) Schematic cobble cross-section with the positions of drill cores and indication of dose-rate contributions. c) Schematic drill core cross-section with measurement strategy for the associated rock slices.



The contribution of beta radiation from each cobble and its surrounding sediment to the total beta dose rate of individual rock slices used for  $D_e$  determination ( $\dot{D}\beta_{total}$ ) were modelled using the approach presented by Freiesleben et al. (2015):

$$\dot{D}\beta_{total} = \dot{D}\beta_{cobble} [1 - 0.5(e^{-bx} + e^{-b(h-x)})] + \dot{D}\beta_{sed} 0.5(e^{-bx} + e^{-b(h-x)}) \quad (1)$$

where  $\dot{D}\beta_{cobble}$  (Gy/ka) and  $\dot{D}\beta_{sed}$  (Gy/ka) are the infinite-matrix beta dose rates of the cobble and the surrounding sediment,  $x$  (mm) is the depth of the slice from the cobble surface,  $h$  (mm) is the thickness of the cobble, and  $b$  ( $1.89 \text{ mm}^{-1}$ ) is the beta linear attenuation coefficient in the cobble. A similar approach was used to model the gamma dose rate, changing the attenuation coefficient  $b$  for  $c$  ( $0.01 \text{ mm}^{-1}$ ). Modelled beta and gamma dose rates for individual rock slices are summarized in Table S4.

The luminescence signal-depth data of all cores were normalized to their individual field-saturation plateau represented by the innermost slices, and fitted with the model of Freiesleben et al. (2015), which can model a sequence of exposure and burial events:

$$L_0(x) \xrightarrow{\text{exposure}} L_1(x) \xrightarrow{\text{burial}} L_2(x) \xrightarrow{\text{exposure}} L_3(x) \quad (2)$$

Where  $L_0$  is the luminescence signal at depth  $x$  (mm) below the rock surface at complete dosing after rock formation,  $L_1$  the luminescence signal after sunlight exposure of the cobble at the beach,  $L_2$  the luminescence signal after burial of the cobble in a raised beach or marine terrace, and  $L_3$  the signal in a previously buried and reactivated cobble. The depth-dependent luminescence signals measured in the collected samples, i.e.  $L_2(x)$  for buried surfaces and  $L_1(x)$  or  $L_3(x)$  for exposed surfaces, can be expressed by the equations:

$$L_1(x) = L_0(x) e^{-\overline{\sigma\phi_0} t_e e^{-\mu x}} \quad (3)$$

$$L_2(x) = (L_1(x) - 1) * e^{-F(x)t_b} + 1 \quad (4)$$

$$L_3(x) = L_2(x) e^{-\overline{\sigma\phi_0} t_e e^{-\mu x}} \quad (5)$$

where  $t_e$  (s) is the exposure time at the active beach,  $\overline{\sigma\phi_0}$  ( $\text{s}^{-1}$ ) the effective bleaching rate of the luminescence signal at the rock surface (i.e. the product of photo-ionisation cross section,  $\sigma$ , and the light flux at the rock surface,  $\phi_0$ ),  $\mu$  ( $\text{mm}^{-1}$ ) the light attenuation coefficient of the rock,  $F$  the ratio between total dose rate and the sample-dependent electron trap filling rate constant ( $D_0$ ), and  $t_b$  (s) the burial time in the raised beach or marine terrace.

Analytical determination of the exposure time ( $t_e$ ) was not possible due to missing data on the local effective bleaching rate,  $\overline{\sigma\phi_0}$ , which requires known-age surfaces for calibration (e.g. Sohbaty et al., 2012). Likewise, determining the time of burial in inactive landforms ( $t_b$ ) on the basis of model fitting (this can be achieved when combining  $t_e$  and  $\overline{\sigma\phi_0}$  to a single variable, cf. Sohbaty et al., 2015) is affected by significant fitting uncertainties. However, fitting of signal-depth data with Eq. (4) was used for evaluating the completeness of signal resetting.

Calculation of cobble burial ages in this study was based on measured equivalent doses of rock slices that were identified as bleached by the model, divided by their depth-specific dose rates. All ages were corrected for fading using  $g$ -values determined according to Auclair et al. (2003) and the approach of Huntley and Lamothe (2001) for samples from the modern beach, or the model of Huntley (2006) in combination with the approach of Kars et al. (2008) for the Pleistocene terrace samples. In addition, fading correction for all cobbles was determined using the field-to-laboratory-saturation ratio ( $[L_{nat}/T_{nat}]/[L_{sat}/T_{sat}]$ , cf. Rades et al., 2018). For this, signals in response to  $\sim 3000$  Gy laboratory doses were normalized with test doses of  $\sim 500$  Gy ( $L_{sat}/T_{sat}$ ) and compared to the natural saturation plateau ( $L_{nat}/T_{nat}$ ) of the luminescence-depth profiles.

### 3.3. ESR and U-series dating of marine molluscs

Prior to any analyses, X-ray powder diffraction (XRD) measurements were performed at the Laboratory for Physical Geography (University of Cologne) on bulk samples from each of the three mollusc shells (VIR 2–1, SEC 4–2, SEC 4-2a) to check their mineral composition and to evaluate their suitability for combined U-series/ESR dating.

ESR equivalent dose ( $D_E$ ) values were evaluated using the multiple aliquot additive dose (MAAD) method. ESR measurements were carried out at room temperature at the Institute of Geography (University of Cologne) using an ELEXSYS E500 Bruker X-band ESR spectrometer with a high-sensitivity cavity. All aliquots of a given sample were carefully weighted before ESR measurement to the same mass and centred in the cavity using a teflon sample tube holder. The following acquisition parameters were used for each aliquot: 10 scans, 25.3 mW microwave power, 1024 points resolution, 50 G sweep width, 100 kHz modulation frequency, 0.485 G modulation amplitude measurements, 20.48 ms conversion time and 163.84 ms time constant. Measurements were repeated on two different days. ESR intensities were extracted from peak-to-peak amplitude from the ESR signal at  $g = 2.0006$  (Grün et al., 1988; Bahain et al., 1994; Schellmann and Radtke, 1997, 1999).

U-series analyses of the shells were carried out at the Institute of Geology and Mineralogy (University of Cologne). Three to five sub-samples were collected from each mollusc shell to evaluate the spatial homogeneity of the U-series data. These samples were taken from the shells, not from the powder collected for ESR dating. Isotope ratios and concentrations were measured using a Thermo Scientific Neptune MC-ICPMS with a central SEM. We used an Aridus II desolvator system following a standard-sample bracketing procedure. For U, CRM112A reference material was used and for Th, IRMM35 and IRMM36 standards doped with CRM112A were used. Measured U isotope ratios are corrected for mass bias using the known ratio of the  $^{233}\text{U}$ - $^{236}\text{U}$  double spike. Thorium samples were doped with the CRM112A U standard, using the known  $^{238}\text{U}/^{235}\text{U}$  ratio for mass bias correction. The 'Faraday Cup-SEM' yield was corrected using the known  $^{234}\text{U}/^{238}\text{U}$  or  $^{230}\text{Th}/^{232}\text{Th}$  ratio of the respective bracketing standard. More details can be found in Obert et al. (in prep) and the Supplementary Information.

ESR and U-series data were combined through USESR, a Matlab-based program (Shao et al., 2014) using the US and AU models defined by Grün et al. (1988) and Shao et al. (2012), respectively. Details about sample preparation, equivalent dose and dose rate evaluation, as well as age calculation can be found in the Supplementary Information.

## 4. Results and interpretation

### 4.1. Cobble lithology and feldspar crystal size

For each targeted cobble, polished cutting surfaces of cobble fragments or slices (Fig. 4) were used for petrographic analyses at the Institute of Geology and Mineralogy, University of Cologne. Classification of the cobble lithology and determination of the mineral composition was based on visual inspection under a microscope. All cobbles were composed of a variety of different plutonic, volcanic and sub-volcanic rocks (Table S3, Fig. 4). Most cobbles with a dark (black to dark grey) colour were alkaline to intermediate volcanic (GUA 1–2, VIR 3–1 P1 and P2, VIR 3–2 P1) or alkaline plutonic rocks (SEC 4–3 P2) that were dominated by pyroxene, biotite and plagioclase. These rocks lacked potassium feldspar or quartz. Cobbles with lighter colours (light grey to pink) represented acidic to intermediate plutonic rocks such as granites (GUA 2–2, GUA 3–1, GUA 3–2), diorites (GUA 1–1, GUA 2–1, VIR 3–2 P2) and monzonites (SEC 4–3 P1) that contained varying amounts of potassium feldspar paired with quartz, plagioclase, biotite and sometimes amphibole.

Visual microscope analysis was also used to estimate average crystal sizes of potassium feldspar minerals used for luminescence dating. The

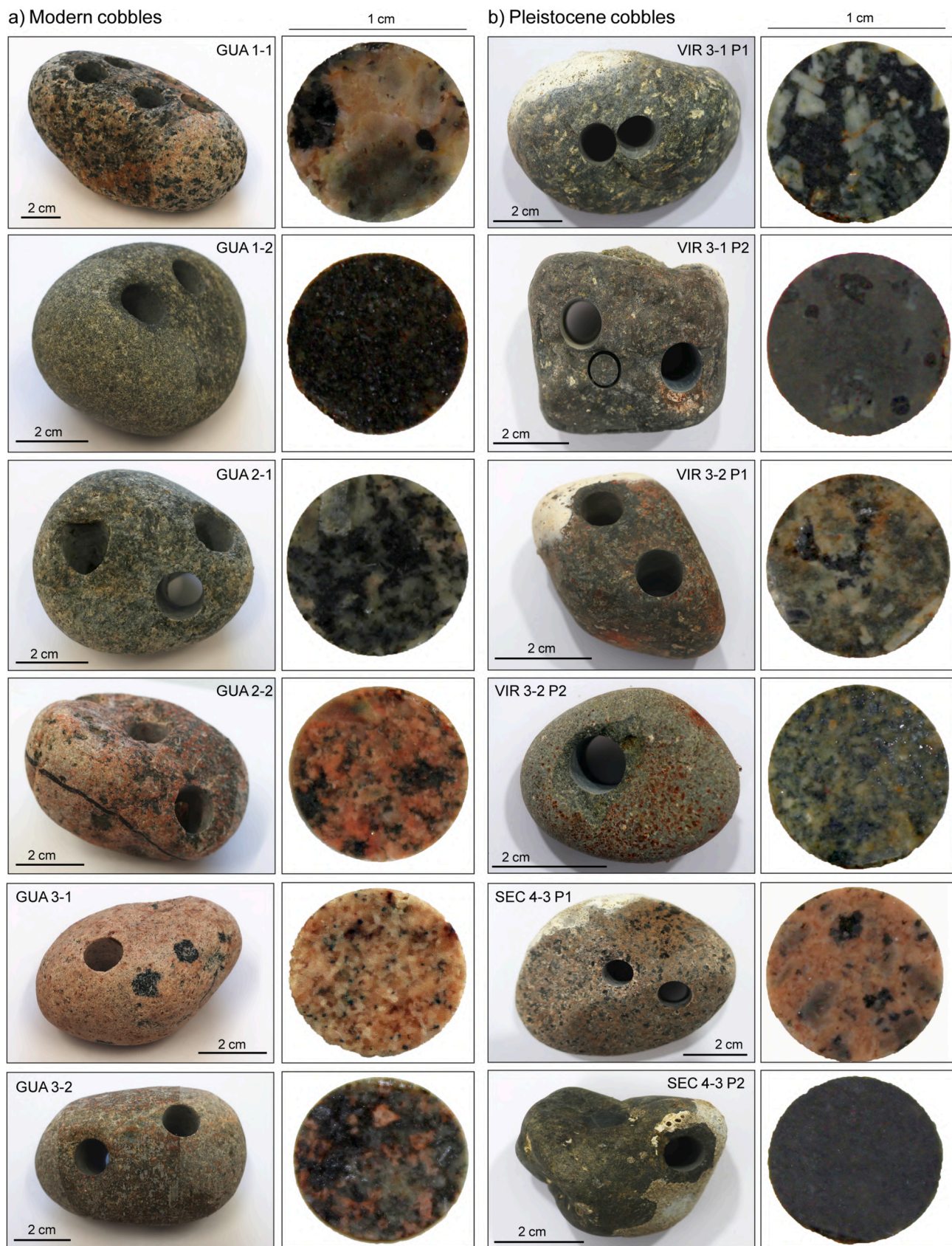


**Fig. 4.** Lithology of the targeted cobbles. In addition to the entire cobbles, one representative rock slice (1 cm diameter) is shown for each cobble.



average diameter of feldspar crystals in the granites, diorites and the monzonite was estimated to values between  $800 \pm 200 \mu\text{m}$  (GUA 3–2),  $600 \pm 200 \mu\text{m}$  (GUA 1–1, GUA 2–1, VIR 3–2 P2), and  $400 \pm 100 \mu\text{m}$  (GUA 2–2, GUA 3–1, SEC 4–3 P1) (Table S3). The estimated crystal size of plagioclase in basaltic and andesitic rocks was  $200 \pm 100 \mu\text{m}$  (GUA 1–2, VIR 3–1 P2, SEC 4–3 P2), and  $800 \pm 200 \mu\text{m}$  (VIR 3–1 P1, VIR 3–2 P1) (Table S3).

#### 4.2. Luminescence properties of the targeted cobbles

Both IRSL signal (Fig. 5a) and post-IR-IRSL<sub>225</sub> signal (Fig. 5b) shine-down curves in response to ~30 Gy laboratory doses documented very different sensitivities of the dated cobbles. Cobbles with bright IRSL and post-IR-IRSL<sub>225</sub> signals (i.e. several 1000 counts per 0.8 s) included GUA 1–1, GUA 2–1, GUA 3–2 and SEC 4–3 P1 (shown as blue lines in Fig. 5a, b). Cobble GUA 1–2 had IRSL signals that significantly differed from its background level (~1000 counts per 0.8 s), but no recognisable post-IR-IRSL<sub>225</sub> signal. With less than 200 counts per 0.8 s, all other cobbles had relatively insensitive IRSL and post-IR-IRSL<sub>225</sub> signals (shown as reddish curves in the insets of Fig. 5a,b).

Laboratory residual doses after 24 h of solar simulator bleaching (Fig. 5c) were between 0.16 Gy and 2.4 Gy for the IRSL signals of all cobbles. The corresponding post-IR-IRSL<sub>225</sub> residual doses remained at significantly larger levels between 1.6 Gy and 40 Gy. Dose recovery experiments indicated adequate reproducibility of laboratory-induced

IRSL signals for all cobbles with and without residual dose correction (those not corrected for residuals are shown as blue squares in Fig. 5d). The only exception was cobble VIR 3–2 P1, for which extremely dim IRSL signals did not allow for the construction of a dose response curve (Fig. S1). In contrast, the reproducibility of laboratory doses based on post-IR-IRSL<sub>225</sub> signals was comparatively poor (circles in Fig. 5d). Since residual doses were significant compared to the laboratory doses of ~30 Gy used in the dose recovery experiment, they were subtracted from the recovered doses (triangles in Fig. 5d). However, most samples still yielded inadequate dose recovery ratios. Exceptions were cobbles GUA 1–1, GUA 1–2, GUA 2–1, GUA 3–2 and SEC 4–3 P1, which provided satisfactory dose recovery ratios between 0.9 and 1.1 (blue circles and triangles in Fig. 5d).

Indicators for anomalous fading of feldspar luminescence signals in form of g-values and ratios between signals in field saturation and laboratory saturation ( $[L_{\text{nat}}/T_{\text{nat}}]/[L_{\text{sat}}/T_{\text{sat}}]$ ) are shown in Fig. S2. Due to comparably dim IRSL and post-IR-IRSL<sub>225</sub> signals, the g-values of half of the cobbles showed extremely large uncertainties. Only cobbles GUA 1–1, GUA 2–1, GUA 2–2, GUA 3–2, VIR 3–1 P2 and SEC 4–3 P1 (blue symbols in Fig. S2a) yielded g-values with adequate precision in the range of 2.1–4.3%/decade for IRSL signals (Table 1) and 0.4–2.1%/decade for post-IR-IRSL<sub>225</sub> signals (Table S6). These values are comparable to those reported by Bartz et al. (2020a) for surrounding sand samples using the same measurement protocol. Due to dim luminescence signals in some cobbles the  $(L_{\text{nat}}/T_{\text{nat}})/(L_{\text{sat}}/T_{\text{sat}})$  ratios varied

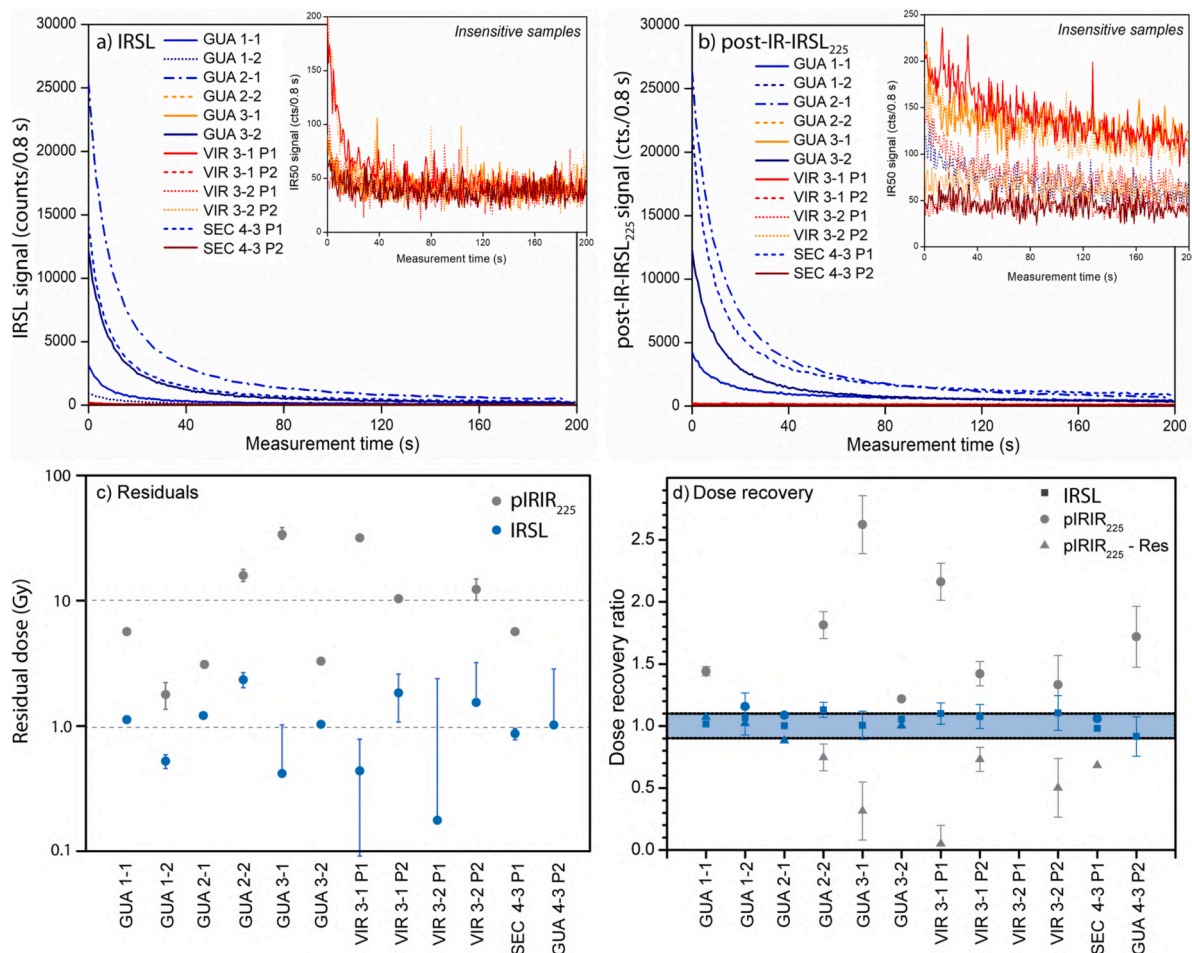


**Fig. 5.** Luminescence properties of the dated cobbles. Shine-down curves of (a) IRSL signals and (b) post-IR-IRSL<sub>225</sub> signals in response to test doses of ~30 Gy. Samples with signals significantly different from the background are shown as blue curves, those with dim signals in red (see insets for a close up). c) IRSL and post-IR-IRSL<sub>225</sub> residual doses after 24 h of solar simulator bleaching. d) IRSL and post-IR-IRSL<sub>225</sub> dose recovery ratios of all samples. Adequate ratios, i.e. matching  $1.0 \pm 0.1$  within their uncertainties, are shown in blue. (For interpretation of the references to colour in this figure legend, the reader is referred to the web version of this article.)

**Table 1**  
IRSL burial dating parameters of all targeted cobbles. Cobbles that provide robust ages are marked by shading.

Lab-ID	Cobble	Core	Depth (mm)	Dose rate (Gy/ka)	D <sub>0</sub> (Gy)	Burial Dose (Gy)	Age <sub>unad</sub> (ka)	g-value (%/dec)	g-value <sub>mean</sub> (%/dec)	Age <sub>cor1</sub> (ka)	Age <sub>cor1</sub> - Res (ka)	L <sub>nat</sub> /L <sub>sat</sub>	L <sub>nat</sub> /L <sub>sat</sub> mean	Age <sub>cor2</sub> (ka)	Age <sub>cor2</sub> - Res (ka)
C-L4989	GUA 1-1	GUA 1-1 Top	0-1	6.91 ± 0.73	160	14.2 ± 0.3	2.1 ± 0.2	3.8 ± 1.3	4.3 ± 0.2	3.0 ± 0.4	2.9 ± 0.4	0.44 ± 0.02	0.40 ± 0.02	5.2 ± 0.6	5.0 ± 0.6
			1-2	7.27 ± 0.73		1.4 ± 0.1	0.2 ± 0	4.7 ± 1.3		0.2 ± 0.1	0.1 ± 0.1	0.34 ± 0.02		0.4 ± 0.1	0.2 ± 0.1
		GUA 1-1 Base	1-2	7.27 ± 0.73		2.2 ± 0.1	0.3 ± 0.1	4.5 ± 1.4		0.5 ± 0.1	0.3 ± 0.1	0.40 ± 0.02		0.8 ± 0.2	0.6 ± 0.2
			2-3	7.33 ± 0.73		4.8 ± 0.3	0.6 ± 0.1	4.4 ± 1.5		0.9 ± 0.2	0.7 ± 0.2	0.43 ± 0.03		1.6 ± 0.2	1.4 ± 0.2
			4-5	7.33 ± 0.73		12.3 ± 0.3	1.7 ± 0.2	4.3 ± 1.2		2.4 ± 0.3	2.2 ± 0.3	-		4.2 ± 0.6	4.1 ± 0.6
	GUA 1-2	GUA 1-2 Top	0-1	2.85 ± 0.34	90	10.2 ± 0.5	3.6 ± 0.6	1.4 ± 1.6	2.7 ± 1.3	4.6 ± 1.0	4.3 ± 1.1	0.54 ± 0.03	0.49 ± 0.05	7.4 ± 1.1	7.1 ± 1.1
			0-1	2.85 ± 0.34		18 ± 0.7	6.3 ± 1	4.1 ± 1.7		8.0 ± 1.9	7.8 ± 1.9	0.44 ± 0.03		12.9 ± 2.2	12.6 ± 2.2
		GUA 2-1 Top	0-1	4.56 ± 0.34		3 ± 0.1	0.6 ± 0.1	1.8 ± 1.1		0.7 ± 0.1	0.5 ± 0.1	0.59 ± 0.02		1.1 ± 0.2	0.8 ± 0.2
	GUA 2-1	GUA 2-1 Top	1-2	4.79 ± 0.33	115	1.2 ± 0.1	0.2 ± 0.1	2.1 ± 1.1	2.1 ± 0.2	0.2 ± 0.1	0 ± 0.1	0.56 ± 0.02	0.60 ± 0.02	0.4 ± 0.1	0.2 ± 0.1
			0-1	4.56 ± 0.34		1.1 ± 0.1	0.2 ± 0.1	2.4 ± 1.1		0.2 ± 0.1	0 ± 0.1	0.64 ± 0.03		0.4 ± 0.1	0.2 ± 0.1

(continued on next page)

Table 1 (continued)

Lab-ID	Cobble	Core	Depth (mm)	Dose rate (Gy/ka)	D <sub>0</sub> (Gy)	Burial Dose (Gy)	Age <sub>radiat</sub> (ka)	g-value (%/dec)	g-value <sub>mean</sub> (%/dec)	Age <sub>cor1</sub> (ka)	Age <sub>cor1</sub> - Res (ka)	I <sub>nat</sub> /I <sub>sat</sub>	I <sub>nat</sub> /I <sub>sat</sub> mean	Age <sub>cor2</sub> (ka)	Age <sub>cor2</sub> - Res (ka)
C-L4367	VIR 3-2 P1	Base	1-2	1.80 ± 0.50	-	-	72.7 ± 11.2	-	-	-	-	0.12 ± 0.18	-	-	-
			1-2	2.55 ± 0.68	110	98.4 ± 32	38.6 ± 22.8	3.1 ± 13.4	-	-	-	0.45 ± 0.07	-	>69*	-
	VIR 3-2 P2	Base	1-2	6.32 ± 0.61	210	193.6 ± 8.8	30.6 ± 4.3	8.0 ± 8.0	-	-	-	0.76 ± 0.03	-	40 ± 5.6	-
			1-2	6.77 ± 0.49	230	>340*	>56*	2.9 ± 0.3	2.9 ± 0.3	>56*	-	0.03	-	>56*	-
C-L4368	SEC 4-3 P2	Base	1-2	2.21 ± 0.17	230	72 ± 7.2	32.6 ± 5.8	3.0 ± 1.2	-	59 ± 51	-	0.13 ± 0.08	-	>160*	-
			1-2	2.21 ± 0.17	230	72 ± 7.2	32.6 ± 5.8	5.5 ± 2.4	-	-	-	-	-	-	-

Age<sub>cor1</sub> - fading corrected age using g-values, Age<sub>cor1</sub>-Res - associated age with residual age subtraction, Age<sub>cor2</sub> - fading corrected age using ratios between field and laboratory saturation, Age<sub>cor2</sub>-Res - associated age with residual age subtraction. \*Minimum age estimates based on palaeodoses equal to 2 x D<sub>0</sub>.

between less than 0.1 and 0.8 for both the IRSL and the post-IR-IRSL<sub>225</sub> signal (Fig. S2b). This variability was reduced to ratios of 0.3–0.8 when focussing on cobbles with bright feldspar signals (blue symbols in Fig. S2b), but the ratios still showed no systematic relationship between IRSL and the typically less fading post-IR-IRSL<sub>225</sub> signals. While ages corrected for fading using g-values and the ratio between field and laboratory saturation differ particularly for cobbles with poor luminescence properties, they agree reasonably well for cobbles with bright signals (Table 1, Table S6).

#### 4.3. Model fitting of signal-depth profiles

The IRSL and post-IR-IRSL<sub>225</sub> signal-depth data of cobbles from the modern beach at GUA are presented in Fig. 6, those of cobbles from the marine terraces at VIR and SEC in Fig. 7. While only data from the shielded surfaces are presented for cobbles from the marine terraces, one core each from the exposed top and the shielded bottom surface were combined to a composite profile in case of the modern beach cobbles. Despite merging both cores in the figure, the signal-depth profiles from each cobble side were fitted individually with Eqs. (3) or (5). Also,  $\mu$  values were fitted independently for each surface to allow for small-scale lithological variations within the cobbles. Depth-dependent dose rates were retrieved from Eq. (1) by using the dose rate input data summarized in Table S4. Constant D<sub>0</sub> values for each cobble (Table 1, Table S6) were estimated by fitting the dose response curves of slices used for conventional equivalent dose determination with a single saturating exponential function. Since the cobbles from the active beach were overturned regularly by waves until sampled for dating, the last event recorded at each surface was assumed to be an exposure event. Remaining signals in the outermost slices, which at the top surface of GUA 2-2 even form a plateau, were interpreted to reflect remnant signals of the ultimate exposure period. For the shielded surfaces of cobbles collected from marine terraces, instead, signal-depth profiles are assumed to end with a burial event. The fitted signal-depth curves of all cobbles are presented in Figs. 6 and 7. The associated best-fit model parameters are summarized in Table S5.

Apart from cobble GUA 3-1, for which weak luminescence signals with significant scatter disabled proper fitting of the IRSL signal-depth data, the model fits of all cobbles from the active beach at GUA revealed clear, though varying signs of bleaching at their top and bottom surfaces (Fig. 6). Bleaching of both the IRSL and the post-IR-IRSL<sub>225</sub> signal similarly affected both sides of the cobbles, without a clear tendency of stronger signal resetting at the bottom or the top surface. However, the IRSL signal was always depleted further into the cobbles compared to the post-IR-IRSL<sub>225</sub> signal. The latter reflects a single exposure event at the top and bottom surface of all cobbles. The associated bleaching fronts, i.e. the position where signal resetting reaches 50% of the field saturation plateau in the core of the cobble (cf. Sellwood et al., 2019), remain at shallow depths of 0.1–2.6 mm at both top and bottom surface. Likewise, the measured post-IR-IRSL<sub>225</sub> remnant signals in the outermost slices of the cobbles remain at high levels of 27–77% of field saturation at the top and bottom sides of most cobbles (Fig. 6b,d,e,f). Only at the top surfaces of GUA 1-1 and GUA 2-1 post-IR-IRSL<sub>225</sub> signals have been reset to levels below 5% of field saturation (Fig. 6a,c).

Bleaching is generally more effective for the IRSL signal. This is reflected by deeper bleaching front depths of the last exposure event between 0.5 mm (GUA 1-2, bottom surface) and 4.8 mm (GUA 1-1, top surface), as well as smaller remnant signals measured in the outermost slices of 0.7–33% of field saturation at all cobble surfaces (Fig. 6). Minimum remnant signals of 0.7–1.9% of field saturation were reached at both the top and bottom side of GUA 1-1 and GUA 2-1. The smaller remnant signals and deeper bleaching fronts also allow the detection of more complex exposure and burial histories for the IRSL signal. According to the fitting, the bottom surface of GUA 1-1 records two exposure events separated by a period of burial (Fig. 6a). The same can be observed at the top surface of GUA 3-2 (Fig. 6f). If the older exposure

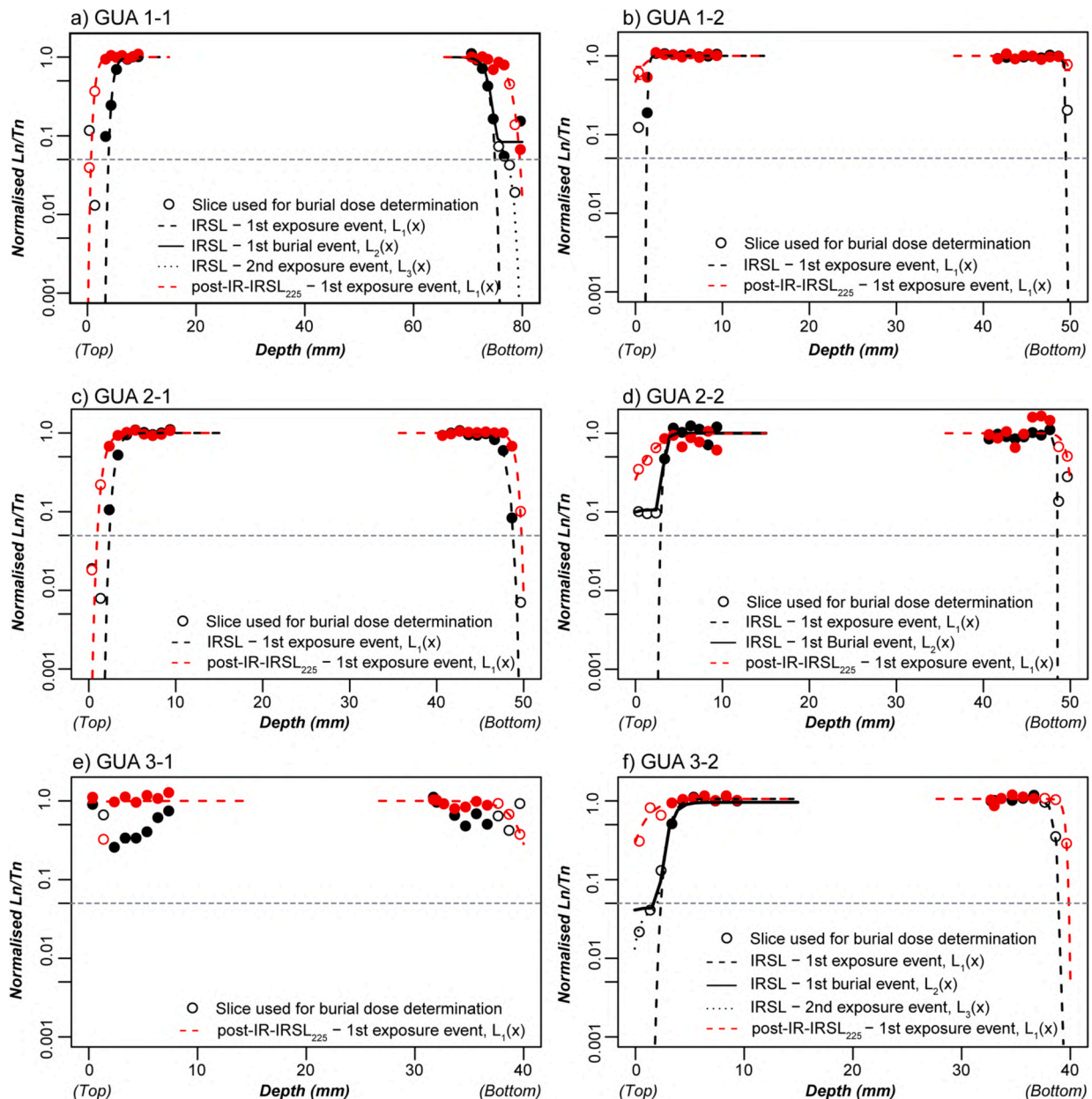


Fig. 6. Signal-depth profiles with fitting curves of the bleaching model for cobbles from the active beach. Black and red dots indicate IRSL and post-IR-IRSL<sub>225</sub> measurement data, respectively. (For interpretation of the references to colour in this figure legend, the reader is referred to the web version of this article.)

events recorded in these cobbles are considered, IRSL signal resetting can be proved in even larger depths of up to 6.5 mm, as indicated by the bleaching front of the older exposure event at the bottom surface of GUA 1-1 (Fig. 6a).

In contrast, none of the cobbles collected from marine terraces at VIR and SEC showed unambiguous signs of bleaching and subsequent burial for either the IRSL or post-IR-IRSL<sub>225</sub> signals (Fig. 7). Although all cobbles except from VIR 3-2 P1 revealed well-defined signal-depth profiles without too much scatter, most of them did not show any indication of bleaching and subsequent dosing and, thus, no fitting was attempted. Only the shielded surface of cobble SEC 4-3 P1 showed slight signs of depleted IRSL and post-IR-IRSL<sub>225</sub> signals to levels of 57% and 85% of field saturation, respectively, in its outermost slice (Fig. 7e). However, fitting of the data did indicate only a single bleaching event and no subsequent burial event.

#### 4.4. Burial dating of cobble surfaces

Extraction of burial ages for Pleistocene terrace cobbles by fitting with Eq. (4) was not possible due to the absence of pronounced bleaching fronts. Thus, just as for the remnant ages remaining in the surfaces of cobbles exposed to sunlight at the active beach (GUA), burial ages recorded in the surfaces of shielded marine terrace cobbles were determined using conventional post-IR-IRSL<sub>225</sub> burial dose measurements combined with modelled dose rates for each slice. The rock slices used for dating are indicated in Figs. 6 and 7, the associated burial doses, dose rates, as well as uncorrected and fading-corrected ages are summarized in Table 1 (IRSL) and Table S6 (post-IR-IRSL<sub>225</sub>).

Bleached sections of the modern beach cobbles yield natural remnant doses as low as 1.2 to 5.0 Gy for IRSL and 2.3 to 18 Gy for post-IR-IRSL<sub>225</sub>, which reduce to 0.1–1.8 Gy (IRSL) and – 0.9 to 15 Gy (post-IR-IRSL<sub>225</sub>) after subtraction of laboratory residual doses. Fading-corrected remnant ages were then calculated by subtracting fading corrected



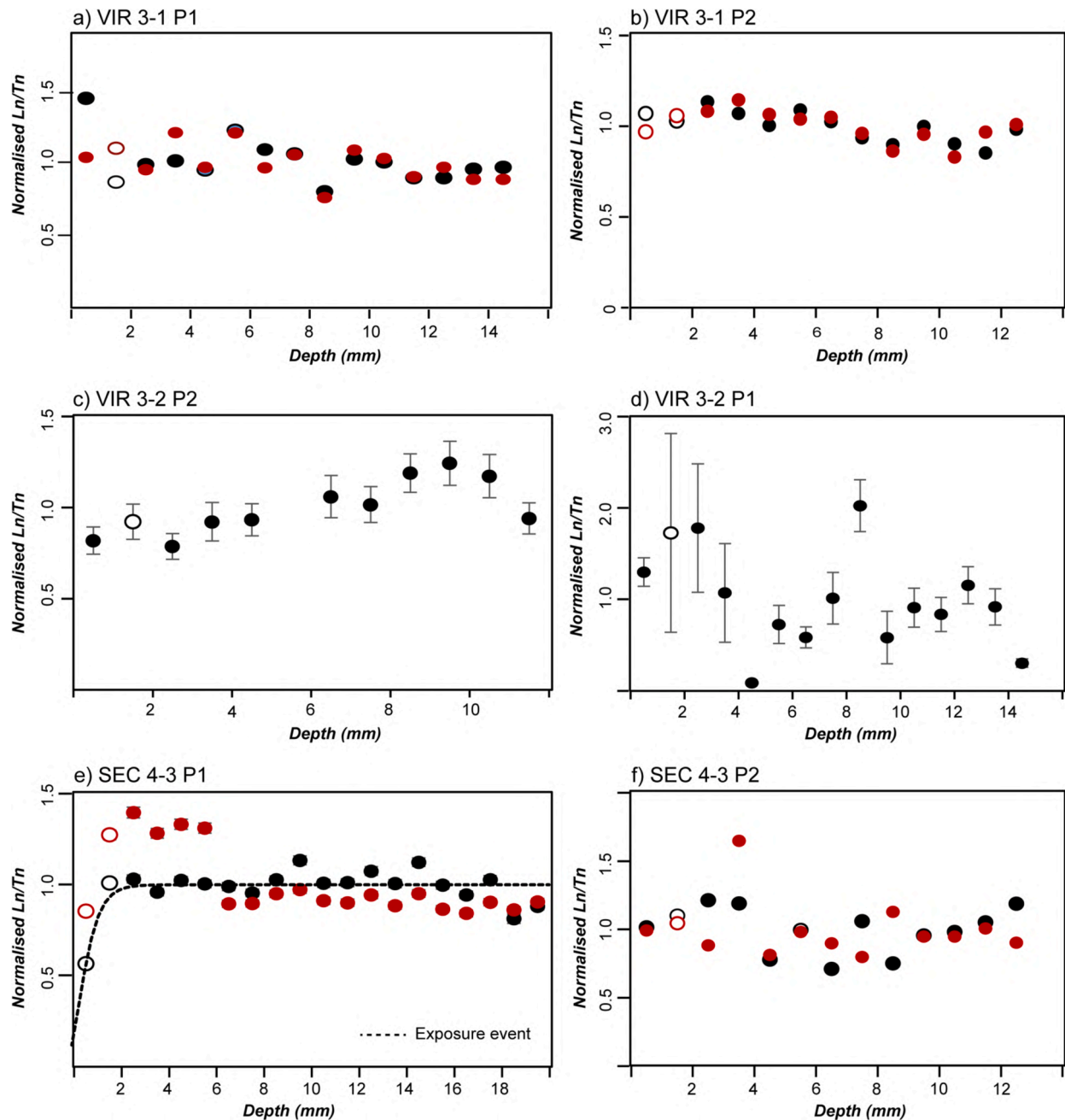


Fig. 7. Signal-depth profiles for cobbles from Pleistocene marine terraces. Black and red dots indicate IRSL and post-IR-IRSL<sub>225</sub> measurement data, respectively. Fitting of the bleaching model was only possible for cobble SEC 4-3 P1. Open circles indicate slices used for burial dose determination. (For interpretation of the references to colour in this figure legend, the reader is referred to the web version of this article.)

residual ages from the fading corrected ages of the same sample. This results in fading-corrected remnant ages of 0–800 years for IRSL and –160 to 2600 years for post-IR-IRSL<sub>225</sub> using g-values and 160–1600 years (IRSL) and 0–7100 years (post-IR-IRSL<sub>225</sub>) using the ratios between field and laboratory saturation (Fig. 8a, Table 1, Table S6).

The burial doses for surface slices of cobbles from the marine terraces range between 72 and 256 Gy (IRSL) and 96 to >340 Gy (post-IR-IRSL<sub>225</sub>). This equals fading corrected IRSL ages of 36–144 ka using g-values and 40–230 ka using the ratios between field and laboratory saturation. The fading corrected post-IR-IRSL<sub>225</sub> ages are in field saturation for all cobbles, providing minimum ages between >48 ka and >120 ka (Fig. 8b, Table 1, Table S6). For the marine terrace cobbles, laboratory residual ages are insignificant compared to their burial ages and were not subtracted. The burial events identified in the IRSL signal-

depth profiles of modern beach cobbles GUA 1–1 (bottom) and GUA 3–2 (top) yield residual and fading corrected ages (using g-values) of 1900–2500 years (slice 5) and 700–900 years (slice 2), respectively.

#### 4.5. New ESR and uranium-thorium control ages for marine terrace formation

The three mollusc shells are composed of aragonite, recrystallization to calcite has neither been observed by XRD nor ESR (i.e. no Mn<sup>2+</sup> signal; Low and Zeira, 1972; Inoue et al., 2000), which suggests that all samples are suitable for ESR and U-series dating.

The U concentration in the shells ranges from 0.34–0.65 ppm (Table S7), which is consistent with observations on marine shells from northern Chile by Radtke (1989). Multiple sub-sampling provides an

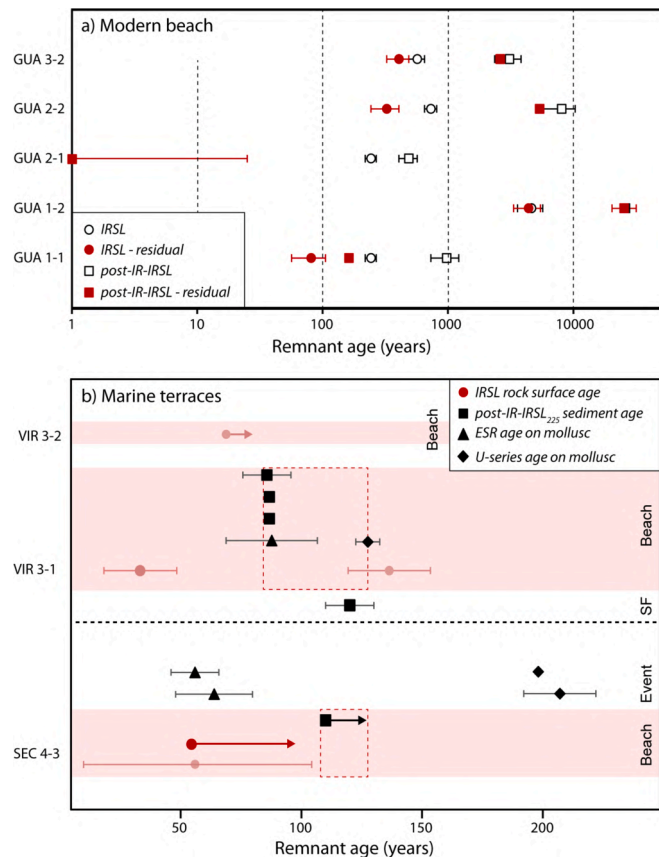


**Fig. 8.** IRSL rock surface remnant ages of modern beach cobbles (a) and IRSL burial ages of Pleistocene terrace cobbles compared to control ages presented in this study (U-series and combined U-series/ESR on molluscs) and previous work (post-IR-IRSL<sub>225</sub> on sediment, Bartz et al., 2020a). Shaded IRSL rock surface ages in (b) indicate cobbles with unfavourable feldspar luminescence properties. SF – Shore face.

idea of the spatial heterogeneity of the U-series data within each shell. While uranium concentrations vary between 3.9% (VIR 2–1) and 9.1% (SEC 4–2), the variability of apparent U-series ages ranges from 0.8% (SEC 4–2) to 7.1% (SEC 4–2a). These results show a non-negligible spatial variability. All  $^{230}\text{Th}/^{232}\text{Th}$  ratios are  $>16,000$  (Table S7), indicating that there is no detrital thorium contamination in the samples. All analyses return finite U-series age estimates, which suggests that there is no extensive uranium leaching (this was also supported by the combined ESR and U-series data). VIR 2–1 yields a mean U-series age of  $128 \pm 5$  ka, whereas the other two samples provide significantly older ages of  $199 \pm 1.5$  ka and  $208 \pm 15$  ka. All samples yielded initial  $^{234}\text{U}/^{238}\text{U}$  activity ratios (Table S7) that exceed the marine value (1.15), indicating open-system behaviour. Consequently, apparent U-series ages should be regarded as minimum age constraints in first instance, provided that the combination of ESR and U-series data confirms the absence of uranium leaching.

Typical ESR spectra are shown in Fig. S3. ESR measurement precision achieved for the three ESR samples is excellent, with a variation of the ESR intensities  $<2\%$ . The  $D_e$  repeatability over the two different days of measurement resulted in 9.2% (VIR 2–1), 0.3% (SEC 4–2), and 5.0% (SEC 4–2a) (Table S8). A detailed description of the ESR fitting results is provided in the Supplementary Information. Combined U-series/ESR age calculations using the US model do not return any finite age results. Instead, for all samples EU-ESR (EU = Early Uptake; this model is based on the closed-system assumption) estimates are younger than the corresponding U-series ages (Table S9). This demonstrates that the three molluscs experienced uranium leaching (e.g. Grün et al., 1988; Rink

et al., 2001). Consequently, only the Accelerating Uptake (AU) model by Shao et al. (2012) could be used. Sample VIR 2–1 returns an extrapolated AU-ESR age of  $88 \pm 19$  ka. The large age uncertainty results from the massive uranium leaching (ca. 800%) that has been modelled in order to obtain a finite age result. Samples SEC 4–2 and SEC 4–2a yield younger but consistent AU-ESR age estimates of  $56 \pm 10$  ka and  $64 \pm 16$  ka, respectively. Similarly, the large age uncertainties result from the uranium loss that has been modelled, although much lower compared to that of sample VIR 2–1 ( $<300\%$ ). Given the non-negligible uncertainty around the modelled uranium leaching, these AU-ESR ages should only be considered as rough approximations. Moreover, although U-series analyses could provide finite age estimates for the three samples, their combination with ESR data shows that the apparent U-series estimates are most likely overestimated as the result of uranium leaching. Therefore, they cannot not be even regarded as minimum age constraints for the molluscs.

## 5. Discussion

### 5.1. The significance of cobble lithology for IRSL rock surface dating

As for luminescence dating of sandy deposits, lithology has a crucial influence on the intensity and reproducibility of rock surface luminescence signals. Six out of twelve cobbles in this study revealed dim luminescence signals. Apart from two samples (GUA 3–1, VIR 3–2 P1), residual doses and equivalent doses did provide reproducible equivalent doses and signal-depth profiles without significant scatter, although all these cobbles were affected by large uncertainties on their g-values. They could be used to calculate burial ages, which should, however, be interpreted with great care.

Feldspar crystals completely insensitive to IRSL stimulation were also observed by Sohbati et al. (2011) for one out of five magmatic and metamorphic beach cobbles from Denmark, but without further details regarding their specific lithology. In this study, cobbles with dim signals are mostly dark coloured (VIR 3–1 P1 and P2, VIR 3–2 P1, SEC 4–3 P2) and their rather poor behaviour might have been expected due to a lack of significant amounts of potassium feldspar, which is the dosimeter of choice in the post-IR-IRSL<sub>225</sub> protocol applied in this study. However, also a granite (GUA 3–1) and a diorite cobble (VIR 3–2 P2), both light coloured and containing macroscopic potassium feldspar crystals, revealed dim luminescence signals unfavourable for dating. Cobbles with bright IRSL signals and properties more favourable for luminescence dating in this study are mainly restricted to dioritic cobbles (diorites of GUA 1–1 and 2–1) and granitic rocks (granite of GUA 3–2 and Monzonite of SEC 4–3 P1). With GUA 1–2, a basaltic pegmatite, only one of the intermediate to alkaline magmatic rocks yielded sensitive feldspar.

These more favourable properties for luminescence dating apply to both the IRSL and the post-IR-IRSL<sub>225</sub> signal. However, for all cobbles, independent of their luminescence characteristics, IRSL signals are at an advantage compared to post-IR-IRSL<sub>225</sub> signals in terms of intensity, reproducibility and the size of laboratory residual doses. Inadequate post-IR-IRSL<sub>180</sub> signals for rock samples with IRSL signals suitable for dating were already reported by Souza et al. (2019). The authors suggest that rising signals with illumination time due to isothermal thermoluminescence may be an indicator, and for some samples with inadequate post-IR-IRSL<sub>225</sub> properties in this study (e.g. VIR 3–1 P1 or VIR 3–2 P2) the same behaviour was observed during isothermal holding prior to stimulation.

Besides controlling the luminescence properties, lithology has a known influence on luminescence signal resetting at rock surfaces (e.g. Ou et al., 2018). Due to different bleaching sensitivities, the resetting of post-IR-IRSL<sub>225</sub> signals in the cobbles is generally reduced compared to that of IRSL signals. Also, light penetration and signal resetting are much less effective in dark basaltic and gabbroid cobbles (e.g. GUA 1–2), compared to the bright lithologies of some granites and diorites (e.g.

GUA 1–1). These differences in IRSL and post-IR-IRSL<sub>225</sub> signal resetting between light and dark rocks were already described for fluvial cobbles with varying transport distances (Liu et al., 2019) and during laboratory bleaching experiments (Ou et al., 2018).

### 5.2. IRSL signal resetting in modern beach cobbles

In accordance with observations by Sohbaty et al. (2011) and Souza et al. (2019), pronounced bleaching fronts of the IRSL signal were identified in all modern beach cobbles with adequate signal properties (i.e. cobbles with signal-depth profiles not blurred by scatter). The IRSL bleaching front reached maximum depths of 6.5 mm into the rock surface in case of cobbles with light lithology, while darker cobbles reveal less developed bleaching fronts that reach depths of less than 2 mm for approximately the same exposure duration. These bleaching fronts do not show systematic differences between the top and bottom sides of the cobbles at the time of sample collection, which indicates frequent overturning of the cobbles by wave swash and regular changes of the exposed and shielded surfaces. While this was also observed for cobbles from an active beach in Denmark (Souza et al., 2019), cobbles in fluvial systems show a trend towards better bleaching of their upper sides (Liu et al., 2019).

In cobbles with comparably shallow bleaching fronts, surface slices reveal natural IRSL remnants exceeding 8 Gy or 4.8 ka (Fig. 8a). Despite much more pronounced IRSL bleaching fronts that indicate complete signal resetting (e.g. bottom surface of GUA 1–1 or top surface of GUA 2–2, Fig. 6a,d), minimum remnant doses of 1.1 to 5.0 Gy, which are equal to ages of 240–1000 years, were measured in their outermost slices (Fig. 8a). This discrepancy may be explained by laboratory residual doses of up to ~2.4 Gy. Subtraction of these laboratory residual doses reduced the inheritance of the surface slices to less than 1.8 Gy or less than 800 years, and to values close to zero for the surface slices of some cobbles. Sohbaty et al. (2011) reported similar IRSL laboratory residuals of 2–4 Gy depending on the preheat temperature, but natural remnant doses of only  $0.17 \pm 0.02$  Gy or ~40 years in cobbles from an active beach. Likewise, Souza et al. (2019) reported small IRSL remnant ages of only 130 years for the surface slices of their beach cobbles. The quartz luminescence signals in surface slices of modern beach cobbles from Antarctica even appeared to be completely zeroed (Simms et al., 2011). These discrepancies are likely due to different measurement protocols applied in these studies. As shown by the data of Sohbaty et al. (2011), lower preheat and measurement temperatures compared to our post-IR-IRSL<sub>225</sub> protocol (which was selected since assumed to be more suitable for cobbles with MIS 5 ages) are expected to result in smaller remnant doses.

Comparable to the results of Sohbaty et al. (2015) and Ou et al. (2018), the post-IR-IRSL signals of the beach cobbles in this study are reset to a lesser extent than the IRSL signals. The associated bleaching fronts only reach depths of 2.6 mm or less. In consequence, the remnant doses and ages for the most bleached parts of the cobbles are significantly larger. Although laboratory residual doses are larger, as well, and subtraction can reduce the natural remnant doses and ages to less than 0.1 Gy or 160 years for some cobbles, the post-IR-IRSL remnants in the surface slices of most modern cobbles still exceed ~12 Gy or 2400 years after residual subtraction.

### 5.3. IRSL rock surface dating of raised beaches and marine terraces

Most of the Pleistocene terrace cobbles used in this study revealed unfavourable luminescence properties for dating. Five out of six cobbles have either weak signals, are relatively dark and therefore assumed to allow limited light penetration or both. The granitic cobble SEC 4–3 P1 shows much better luminescence characteristics, which is also the only cobble with IRSL and post-IR-IRSL<sub>225</sub> signal-depth profiles indicating signal resetting prior to burial (Fig. 7). Fitting is only possible with a single exposure event and, thus, evaluation of signal resetting prior to

burial in the terrace body (i.e. through their  $L_1/L_2$  ratios; cf. al Khasawneh et al., 2019) is not possible. The well-developed bleaching fronts identified in modern beach cobbles, however, suggest that in the outermost millimetres at least the IRSL signal was likely reset when the cobble was part of active littoral dynamics. The corresponding residual corrected IRSL remnant doses and ages identified in modern cobbles are insignificant for Pleistocene terrace cobbles from VIR and SEC with burial doses >72 Gy. Resetting of the post-IR-IRSL<sub>225</sub> signal to sufficiently low levels prior to burial, on the other hand, remains questionable since bleaching to sufficiently low levels (i.e. <5% of field saturation) is missing in most of our modern analogue samples. Residual corrected remnant doses of 12–32 Gy in the best bleached parts of most modern cobbles are significant even for the presumably MIS 5 marine terrace cobbles investigated here, yielding up to 30% of the burial dose. Therefore, only IRSL ages that have been corrected for fading using g-values are discussed from here on.

The uppermost slice of SEC 4–3 P1 provides a fading corrected IRSL age of >56 ka years (g-values) and  $40 \pm 6$  ka (ratio between field and laboratory saturation). Disregarding the significant differences between both fading correction approaches – this has been observed in other studies as well, and it remains unclear which approach provides the more robust results for different lithologies (Rades et al., 2018; Ageby et al., 2021) – these cobble ages cannot reproduce the at least MIS 5e age indicated by the post-IR-IRSL minimum age of 110 ka from the sandy beach unit above (Bartz et al., 2020a). An age older than the 40–60 ka cobble ages is also supported by the new ESR/U-series ages on molluscs from the overlying shell layer that were dated to  $56 \pm 10$  and  $64 \pm 16$  ka. The much older U-series age estimates of these molluscs compared to those of ESR dating are regarded unreliable due to uranium leaching (Table S9). This age pattern has also been reported in other ESR dating studies of molluscs from the Chilean coast (Radtke, 1989; Schellmann and Radtke, 1997), and is likely caused by uncertainties due to the open-system behaviour of the molluscs (Radtke, 1989) with associated uranium leaching. As the associated high-energy event deposits can also be found on top of the lower marine terrace at ~12 m a.s.l., which was post-IR-IRSL<sub>225</sub> dated to MIS 5c and covered by alluvial fan deposits with post-IR-IRSL and quartz ESR ages of ~60 ka (Bartz et al., 2020a), it was likely deposited during MIS 5a and provides a minimum age for the SEC4–3 cobbles (Fig. 8b).

The explanation for the apparent mismatch between cobble ages and age control is most likely field saturation of the IRSL signal. Based on the two times  $D_0$  criterion of the unfaded dose response curve (King et al., 2019a), the IRSL signal of SEC 4–3 P1 has a cobble-specific dating limit of ~340 Gy or 56 ka. Thus, the fading corrected ages of the outermost slice are already in or at least very close to field saturation and can only be interpreted as minimum ages. In addition to that, assuming homogeneous lithology for all cobbles despite partly very different compositions may lead to over- or underestimated dose rates for the surrounding sediments. Although the dose rate of cobble SEC 4–3 P1 is dominated by the high dose rate of the cobble itself (the sediment dose rate contributes only 12–23% to the total dose rate), inaccurate dose rates for the surrounding sediments may contribute to age underestimation as well. The surface age of the second cobble from this unit, SEC 4–3 P2 ( $74 \pm 64$  ka), is assumed to be unreliable due to its poor luminescence properties, as also indicated by its extremely large dating uncertainties.

At VIR, fading corrected IRSL ages of cobble surface slices point to ages of >69 ka (VIR 3–2 P2), 24–48 ka (VIR 3–1 P1), and 120–160 ka (VIR 3–1 P2). Similar to those at SEC, these ages cannot confirm the MIS 5c/e age implied by the control ages that indicate deposition between ~90 ka (new ESR/U-series ages and post-IR-IRSL sediment ages from overlying beach sand) and 120–130 ka (post-IR-IRSL sediment age from shoreface sand below) (Fig. 8b). While poor luminescence properties limit the reliability of the rock surface ages for all three cobbles, an additional reason for the overestimated ages of VIR 3–1 P2 may be its dark colour. VIR 3–2 P2 is apparently in field saturation and only provides a minimum age.



Although cobble dating of Pleistocene marine terraces in this study was limited due to inadequate luminescence signals, dark cobble lithologies and/or saturated IRSL signals, good agreement between age control and rock surface ages of Holocene to late Pleistocene beach cobbles were reported from Antarctica using quartz (Simms et al., 2011; Simkins et al., 2013) and from Denmark and Greenland using the IRSL signal of feldspar (Souza et al., 2019, 2021). These studies suggest that the approach has potential for dating littoral cobbles at least on Holocene and late Pleistocene time scales. This is also supported by the burial events identified in two reactivated cobbles from the active beach at GUA. Late Holocene ages of 1900–2500 years and 700–900 years (Table 1) agree with relative sea level regression during the past 4000 years following the Holocene maximum (Garrett et al., 2020).

## 6. Conclusions

Investigation of cobbles from an active beach with ongoing signal resetting by wave motion indicates that IRSL rock surface dating is a promising dating tool for inactive shorelines in Northern Chile. Signals on all sides of the cobbles may be bleached to levels close to zero and feldspar luminescence properties allow for dating Late Holocene burial events. A particular advantage for dating precision is the high cobble dose rates compared to sediment dating, which reduces uncertainties due to water content variations and heterogeneous gamma dosimetry.

However, careful selection of cobble lithology is essential for its successful application. In this study, suitable properties in terms of signal resetting and signal intensity were only associated with granitic and dioritic cobbles with large percentages of bright minerals and significant amounts of macroscopic feldspar crystals. While dark rocks with basaltic and andesitic lithologies that appeared to be unsuitable for dating can easily be excluded during sample collection in the field, our results show that also bright rocks with similar lithology and macroscopic appearance as those suitable for dating, and therefore hard to exclude based on visual inspection, often yield luminescence characteristics inadequate for dating. Additional sources for inaccurate cobble ages are the determination of internal dose rates and fading correction. Both the diameter and potassium content of signal-emitting feldspar crystals in the cobbles were only estimated and previous studies have shown that both parameters may vary significantly between rock types. The approaches applied for fading correction provide partly very different fading rates, while it is still not well understood how to find out the more reliable approach for individual samples. For cobbles from last interglacial terraces, the relatively large cobble dose rates observed in this study imply that IRSL rock surface dating is affected by signal saturation. Dating of such old deposits requires either lower dose rates or higher saturation levels than the cobbles measured in this study, which unfortunately limits the applicability of luminescence rock surface dating to pre-Holocene coastlines to specific lithologies.

## Data availability

The complete dataset of  $L_x/T_x$  values of all samples that were used for the fitting of luminescence depth data in this study is available on the database of the collaborative research centre 1211 (DOI: <https://doi.org/10.5880/CRC1211DB.42>).

## Declaration of Competing Interest

None.

## Acknowledgements

This study was funded by the Deutsche Forschungsgemeinschaft (DFG, German Research Foundation) – Projektnummer 268236062 – SFB 1211. Lucas Ageby is funded by the Deutsche Forschungsgemeinschaft (DFG, German Research Foundation) - Project

number 57444011 - SFB 806. Mathieu Duval's research is currently funded by the Spanish Ramón y Cajal Fellowship RYC2018-025221-I. We thank María Jesús Alonso Escarza, CENIEH, for technical support with the gamma irradiations. Stefan Opitz (University of Cologne) is gratefully acknowledged for the XRD measurements. We thank Janek Walk (RWTH Aachen University) for his support during field work.

## Appendix A. Supplementary data

Supplementary data to this article can be found online at <https://doi.org/10.1016/j.margeo.2021.106692>.

## References

- Ageby, L., Angelucci, D.E., Brill, D., Carrer, F., Rades, E.F., Rethemeyer, J., Brückner, H., Klasen, N., 2021. Rock surface IRSL dating of buried cobbles from an alpine dry-stone structure in Val di Sole, Italy. *Quat. Geochronol.* 66, 101212. <https://doi.org/10.1016/j.quageo.2021.101212>.
- Aitken, M.J., 1998. *An Introduction to Optical Dating: The Dating of Quaternary Sediments by the Use of Photon-Stimulated Luminescence*. Oxford University Press, Oxford, New York, Tokyo.
- al Khasawneh, S., Murray, A., Abudanan, F., 2019. A first radiometric chronology for the Khatt Shebib megalithic structure in Jordan using the luminescence dating of rock surfaces. *Quat. Geochronol.* 49, 205–210. <https://doi.org/10.1016/j.quageo.2018.02.007>.
- Auclair, M., Lamothe, M., Huot, S., 2003. Measurement of anomalous fading for feldspar IRSL using SAR. *Radiat. Meas.* 37, 487–492. [https://doi.org/10.1016/S1350-4487\(03\)00018-0](https://doi.org/10.1016/S1350-4487(03)00018-0).
- Bahain, J.-J., Yokoyama, Y., Masaoudi, H., Falguères, C., Laurent, M., 1994. Thermal behaviour of ESR signals observed in various natural carbonates. *Quat. Sci. Rev.* 13, 671–674. [https://doi.org/10.1016/0277-3791\(94\)90096-5](https://doi.org/10.1016/0277-3791(94)90096-5).
- Bailiff, I.K., Bridgland, D., Cunha, P.P., 2021. Extending the range of optically stimulated luminescence dating using vein-quartz and quartzite sedimentary pebbles. *Quat. Geochronol.* 65. <https://doi.org/10.1016/j.quageo.2021.101180>.
- Bartz, M., Duval, M., Brill, D., Zander, A., King, G., Rhein, A., Walk, J., Stauch, G., Lehmkuhl, F., Brückner, H., 2020a. Testing the potential of K-feldspar pIR-IRSL and quartz ESR for dating coastal alluvial fan complexes in arid environments. *Quat. Int.* <https://doi.org/10.1016/j.quaint.2020.03.037>.
- Bartz, M., Walk, J., Binnie, S.A., Brill, D., Stauch, G., Lehmkuhl, F., Hoffmeister, D., Brückner, H., 2020b. Late Pleistocene alluvial fan evolution along the coastal Atacama Desert (N Chile). *Glob. Planet. Chang.* 190 <https://doi.org/10.1016/j.gloplacha.2019.103091>. ARTN 103091.
- Bøtter-Jensen, L., Thomsen, K.J., Jain, M., 2010. Review of optically stimulated luminescence (OSL) instrumental developments for retrospective dosimetry. *Radiat. Meas.* 45, 253–257. <https://doi.org/10.1016/j.radmeas.2009.11.030>.
- Binnie, A., Dunai, T., Binnie, S., Victor, P., Gonzalez, G., Bolten, A., 2016. Accelerated late quaternary uplift revealed by  $^{10}\text{Be}$  exposure dating of marine terraces, Mejillones Peninsula, northern Chile. *Quaternary Geochronology* 36, 12–27.
- Brill, D., Cisternas, M., 2020. Testing quartz and feldspar luminescence dating to determine earthquake and tsunami recurrence in the area of the giant 1960 Chile earthquake. *Quaternary Geochronology* 58, 101080. <https://doi.org/10.1016/j.quageo.2020.101080>.
- Brill, D., Jankaew, K., Brückner, H., 2015. Holocene evolution of Phra Thong's beach-ridge plain (Thailand) - Chronology, processes and driving factors. *Geomorphology* 245, 117–134. <https://doi.org/10.1016/j.geomorph.2015.05.035>.
- Brill, D., May, S.M., Mhammedi, N., King, G., Lehmann, B., Burrow, C., Wolf, D., Zander, A., Brückner, H., 2021. Evaluating optically stimulated luminescence rock surface exposure dating as a novel approach for reconstructing coastal boulder movement on decadal to centennial timescales. *Earth Surf. Dyn.* 9, 205–234.
- Buylaert, J.P., Murray, A.S., Thomsen, K.J., Jain, M., 2009. Testing the potential of an elevated temperature IRSL signal from K-feldspar. *Radiat. Meas.* 44, 560–565. <https://doi.org/10.1016/j.radmeas.2009.02.007>.
- del Rio, I., Sawakuchi, A.O., Gonzalez, G., 2019. Luminescence dating of sediments from central Atacama Desert, northern Chile. *Quat. Geochronol.* 53 <https://doi.org/10.1016/j.quageo.2019.05.001>. ARTN 101002.
- Durcan, J.A., King, G.E., Duller, G.A.T., 2015. DRAC: Dose Rate and Age Calculator for trapped charge dating. *Quat. Geochronol.* 28, 54–61. <https://doi.org/10.1016/j.quageo.2015.03.012>.
- Freiesleben, T., Sohbati, R., Murray, A., Jain, M., al Khasawneh, S., Hvidt, S., Jakobsen, B., 2015. Mathematical model quantifies multiple daylight exposure and burial events for rock surfaces using luminescence dating. *Radiat. Meas.* 81, 16–22. <https://doi.org/10.1016/j.radmeas.2015.02.004>.
- Garrett, E., Melnick, D., Dura, T., Cisternas, M., Ely, L.L., Wesson, R.L., Jara-Munoz, J., Whitehouse, P.L., 2020. Holocene relative sea-level change along the tectonically active Chilean coast. *Quat. Sci. Rev.* 236 <https://doi.org/10.1016/j.quascirev.2020.106281>. ARTN 106281.
- Glignic, L.A., Meyer, M.C., May, J.-H., Aldenderfer, M.S., Tropper, P., 2021. Direct dating of lithic surface artifacts using luminescence. *Sci. Adv.* 7 <https://doi.org/10.1126/sciadv.abb3424>.
- González, G., Cembrano, J., Carrizo, D., Macci, A., Schneider, H., 2003. The link between forearc tectonics and Pliocene-Quaternary deformation of the Coastal Cordillera,

- northern Chile. *J. S. Am. Earth Sci.* [https://doi.org/10.1016/S0895-9811\(03\)00100-7](https://doi.org/10.1016/S0895-9811(03)00100-7).
- González-Alfaro, J., Vargas, G., Ortlieb, L., González, G., Ruiz, S., Báez, J.C., Mandeng-Yogo, M., Caquineau, S., Álvarez, G., del Campo, F., del Río, I., 2018. Abrupt increase in the coastal uplift and earthquake rate since ~40 ka at the northern Chile seismic gap in the Central Andes. *Earth Planet. Sci. Lett.* 502, 32–45. <https://doi.org/10.1016/j.epsl.2018.08.043>.
- Grün, R., Schwarcz, H.P., Chadam, J., 1988. ESR dating of tooth enamel: coupled correction for U-uptake and U-series disequilibrium. *Int. J. Radiat. Appl. Instrument. Part D. Nucl. Tracks Radiat. Meas.* 14, 237–241. [https://doi.org/10.1016/1359-0189\(88\)90071-4](https://doi.org/10.1016/1359-0189(88)90071-4).
- Habermann, J., Schilles, T., Kalchgruber, R., Wagner, G.A., 2000. Steps towards surface dating using luminescence. *Radiat. Meas.* 32, 847–851. [https://doi.org/10.1016/S1350-4487\(00\)00066-4](https://doi.org/10.1016/S1350-4487(00)00066-4).
- Huntley, D.J., 2006. An explanation of the power-law decay of luminescence. *J. Phys. Condens. Mat.* 18, 1359–1365. <https://doi.org/10.1088/0953-8984/18/4/020>.
- Huntley, D.J., Lamothe, M., 2001. Ubiquity of anomalous fading in K-feldspars and the measurement and correction for it in optical dating. *Canadian Journal of Earth Sciences* 38 (7), 1093–1106.
- Inoue, K., Hirai, M., Ikeya, M., Yim, W., 2000. Calibration method for ESR signal intensity of calcitic shells. *Appl. Magn. Reson.* 19, 255–269.
- Jenkins, G.T.H., Duller, G.A.T., Roberts, H.M., Chiverrell, R.C., Glasser, N.F., 2018. A new approach for luminescence dating glaciofluvial deposits - High precision optical dating of cobbles. *Quat. Sci. Rev.* 192, 263–273. <https://doi.org/10.1016/j.quascirev.2018.05.036>.
- Kars, R.H., Wallinga, J., Cohen, K.M., 2008. A new approach towards anomalous fading correction for feldspar IRSL dating - tests on samples in field saturation. *Radiat. Meas.* 43, 786–790. <https://doi.org/10.1016/j.radmeas.2008.01.021>.
- King, G.E., Burrow, C., Roberts, H.M., Pearce, N.J.G., 2019a. Age determination using feldspar: evaluating fading-correction model performance. *Radiat. Meas.* 119, 58–73. <https://doi.org/10.1016/j.radmeas.2018.07.013>.
- King, G.E., Valla, P.G., Lehmann, B., 2019b. Rock surface burial and exposure dating. In: Bateman, M. (Ed.), *Handbook of Luminescence Dating*, pp. 350–372.
- Labonne, M., Hillaire-Marcel, C., 2000. Geochemical gradients within modern and fossil shells of *Concholepas concholepas* from Northern Chile: an insight into U-Th systematics and diagenetic/ authigenic isotopic imprints in mollusk shells. *Geochim. Cosmochim. Acta* 64, 1523–1534. [https://doi.org/10.1016/S0016-7037\(99\)00367-1](https://doi.org/10.1016/S0016-7037(99)00367-1).
- Lehmann, B., Valla, P.G., King, G.E., Herman, F., 2018. Investigation of OSL surface exposure dating to reconstruct post-LIA glacier fluctuations in the French Alps (Mer de Glace, Mont Blanc massif). *Quat. Geochronol.* 44, 63–72. <https://doi.org/10.1016/j.quageo.2017.12.002>.
- Lehmann, B., Herman, F., Valla, P.G., King, G.E., Biswas, R.H., 2019. Evaluating post-glacial bedrock erosion and surface exposure duration by coupling in situ optically stimulated luminescence and Be-10 dating. *Earth Surf. Dyn.* 7, 633–662. <https://doi.org/10.5194/esurf-7-633-2019>.
- Lehmann, B., Herman, F., Valla, P.G., King, G.E., Biswas, R.H., Ivy-Ochs, S., Steinemann, O., Christl, M., 2020. Postglacial erosion of bedrock surfaces and deglaciation timing: New insights from the Mont Blanc massif (western Alps). *Geology* 48, 139–144. <https://doi.org/10.1130/G46585.1>.
- León, T., Vargas, G., Salazar, D., Goff, J., Guendon, J.L., Andrade, P., Alvarez, G., 2019. Geo-archaeological records of large Holocene tsunamis along the hyperarid coastal Atacama Desert in the major northern Chile seismic gap. *Quat. Sci. Rev.* 220, 335–358.
- Leonard, E.M., Wehmiller, J.F., 1991. Geochronology of marine terraces at Caleta Michilla, northern Chile; implications for late Pleistocene and Holocene uplift. *Rev. Geol. Chile* 18, 81–86.
- Liu, J.F., Cui, F.R., Murray, A.S., Sohbati, R., Jain, M., Gao, H.S., Li, W.P., Li, C.P., Li, P., Zhou, T.G., Chen, J., 2019. Resetting of the luminescence signal in modern riverbed cobbles along the course of the Shiyang River, China. *Quat. Geochronol.* 49, 184–190. <https://doi.org/10.1016/j.quageo.2018.04.004>.
- Low, W., Zeira, S., 1972. ESR spectra of Mn<sup>2+</sup> in heat-treated aragonite. *Am. Mineral.* 57, 1115–1124.
- May, S.M., Meine, L., Hoffmeister, D., Brill, D., Medialdea, A., Wennrich, V., Grobner, M., Schulte, P., Steininger, F., Deprez, M., de Kock, T., Bubenzer, O., 2020. Origin and timing of past hillslope activity in the hyper-arid core of the Atacama Desert the formation of fine sediment lobes along the Chuculay Fault System, Northern Chile. *Glob. Planet. Chang.* 184 <https://doi.org/10.1016/j.gloplacha.2019.103057>. ARTN 103057.
- Medialdea, A., May, S.M., Brill, D., King, G., Ritter, B., Wennrich, V., Bartz, M., Zander, A., Kuiper, K., Hurtado, S., Hoffmeister, D., Schulte, P., Grobner, M., Opitz, S., Bruckner, H., Bubenzer, O., 2020. Identification of humid periods in the Atacama Desert through hillslope activity established by infrared stimulated luminescence (IRSL) dating. *Glob. Planet. Chang.* 185 <https://doi.org/10.1016/j.gloplacha.2019.103086>. ARTN 103086.
- Medina, E., Jensen, A., Niemeyer, H., Wilke, H.-G., Cembrano, J., García, M., Riquelme, R., Espinoza, S., Chong, G., 2012. Cartas Tocopilla y María Elena, Región de Antofagasta, Serie Geología Básica 141-142, 59 p., 1 mapa escala 1:100.000. Servicio Nacional de Geología y Minería, Santiago.
- Merritts, D., Bull, W.B., 1989. Interpreting quaternary uplift rates at the mendocino triple junction, Northern California, from uplifted marine terraces. *Geology* 17, 1020–1024.
- Mpodozois, C.M., Cornejo, P.P., Mora, R.C., 2015. Mapa Geológico de la Cordillera de la Costa entre Tocopilla y Antofagasta, Escala 1:250.000. Antofagasta Minerals, Unpublished Internal Report.
- Ortlieb, L., Zazo, C., Goy, J.L., Hillaire-Marcel, C., Ghaleb, B., Cournoyer, L., 1996. Coastal deformation and sea-level changes in the northern Chile subduction area (23 degrees S) during the last 330 ky. *Quat. Sci. Rev.* 15, 819–831. [https://doi.org/10.1016/S0277-3791\(96\)00066-2](https://doi.org/10.1016/S0277-3791(96)00066-2).
- Ou, X.J., Roberts, H.M., Duller, G.A.T., Gunn, M.D., Perkins, W.T., 2018. Attenuation of light in different rock types and implications for rock surface luminescence dating. *Radiat. Meas.* 120, 305–311. <https://doi.org/10.1016/j.radmeas.2018.06.027>.
- Prescott, J.R., Hutton, J.T., 1994. Cosmic ray contributions to dose rates for luminescence and ESR dating: large depths and long-term time variations. *Radiat. Meas.* 23, 497–500. [https://doi.org/10.1016/1350-4487\(94\)90086-8](https://doi.org/10.1016/1350-4487(94)90086-8).
- Quezada, A., Vásquez, P., Sepúlveda, F.A., Blanco, N., Tomlinson, A.J., 2012. Mapa compilación geológica área Quillagua - Salar Grande, Región de Tarapacá. In: Blanco, N., Vásquez, P., Sepúlveda, F., Tomlinson, A.J., Quezada, A., Ladino, M. (Eds.), *Levantamiento Geológico Para El Fomento de La Exploración de Recursos Minerales e Hídricos de La Cordillera de La Costa, Depresión Central y Precordillera de La Región de Tarapacá (20°S-21°S)*, Informe Registrado IR- 12-50, 246 p., 7 Mapas Escala 1:100.000. Servicio Nacional de Geología y Minería, Santiago.
- Rades, E.F., Sohbati, R., Lüthgens, C., Jain, M., Murray, A.S., 2018. First luminescence-depth profiles from boulders from moraine deposits: Insights into glaciation chronology and transport dynamics in Malta valley, Austria. *Radiat. Meas.* 120, 281–289. <https://doi.org/10.1016/j.radmeas.2018.08.011>.
- Radtke, U., 1989. Marine Terrassen und Korallenriffe – das Problem der quartären Meeresspiegelschwankungen erläutert an Fallstudien aus Chile, Argentinien und Barbados. *Düsseldorfer Geographische Schriften* 27.
- Ratusny, A., Radtke, U., 1988. Jüngere Ergebnisse küstenmorphologischer Untersuchungen im “Grossen Norden” Chiles. *Hamburg. Geogr. Stud.* 44, 31–46.
- Regard, V., Saillard, M., Martinod, J., Audin, L., Carretier, S., Podoja, K., Riquelme, R., Paredes, P., Hérail, G., 2010. Renewed uplift of the Central Andes Forearc revealed by coastal evolution during the Quaternary. *Earth Planet. Sci. Lett.* 297, 199–210. <https://doi.org/10.1016/j.epsl.2010.06.020>.
- Rink, W.J., Schwarcz, H.P., Lee, H.K., Rees-Jones, J., Rabinovich, R., Hovers, E., 2001. Electron spin resonance (ESR) and thermal ionization mass spectrometric (TIMS) 230Th/234U dating of teeth in Middle Paleolithic layers at Amud Cave, Israel. *Geochronology* 16, 701–717. <https://doi.org/10.1002/gea.1017>.
- Ritter, B., Wennrich, V., Medialdea, A., Brill, D., King, G., Schneiderwind, S., Niemann, K., Fernandez-Galego, E., Diederich, J., Rolf, C., Bao, R., Melles, M., Duna, T.J., 2019. Climatic fluctuations in the hyperarid core of the Atacama Desert during the past 215 ka. *Sci. Rep.* 9 <https://doi.org/10.1038/s41598-019-41743-8>. ARTN 5270.
- Saillard, M., Hall, S.R., Audin, L., Farber, D.L., Herail, G., Martinod, J., Regard, V., Finkel, R.C., Bondoux, F., 2009. Non-steady long-term uplift rates and Pleistocene marine terrace development along the Andean margin of Chile (31 degrees S) inferred from Be-10 dating. *Earth Planet. Sci. Lett.* 277, 50–63. <https://doi.org/10.1016/j.epsl.2008.09.039>.
- Schellmann, G., Radtke, U., 1997. Electron spin resonance (ESR) techniques applied to mollusc shells from South America (Chile, Argentina) and implications for palaeo sea-level curve. *Quat. Sci. Rev.* 16, 465–475. [https://doi.org/10.1016/S0277-3791\(96\)00104-7](https://doi.org/10.1016/S0277-3791(96)00104-7).
- Schellmann, G., Radtke, U., 1999. Problems encountered in the determination of dose and dose rate in ESR dating of mollusc shells. *Quat. Sci. Rev.* 18, 1515–1527. [https://doi.org/10.1016/S0277-3791\(99\)00043-8](https://doi.org/10.1016/S0277-3791(99)00043-8).
- Schellmann, G., Radtke, U., 2000. ESR dating stratigraphically well-constrained marine terraces along the Patagonian Atlantic coast (Argentina). *Quat. Int.* 68, 261–273. [https://doi.org/10.1016/S1040-6182\(00\)00049-5](https://doi.org/10.1016/S1040-6182(00)00049-5).
- Sellwood, E.L., Guralnik, B., Kook, M., Prasad, A.K., Sohbati, R., Hippe, K., Wallinga, J., Jain, M., 2019. Optical bleaching front in bedrock revealed by spatially-resolved infrared photoluminescence. *Scientific Reports* 9, 2611. <https://doi.org/10.1038/s41598-019-38815-0>.
- Vásquez, P., 2012. Mapa geológico de Iquique, Región de Tarapacá. In: Sepúlveda, F.A., Blanco, N., Vásquez, P., Sepúlveda, F., Tomlinson, A.J., Quezada, A., Ladino, M. (Eds.), *Levantamiento Geológico Para El Fomento de La Exploración de Recursos Minerales e Hídricos de La Cordillera de La Costa, Depresión Central y Precordillera de La Región de Tarapacá (20°S-21°S)*, Informe Registrado IR-12-50, 246 p., 7 Mapas Escala 1:100.000. Servicio Nacional de Geología y Minería, Santiago.
- Shao, Q., Bahain, J.-J., Falguères, C., Dolo, J.-M., García, T., 2012. A new U-uptake model for combined ESR/U-series dating of tooth enamel. *Quat. Geochronol.* 10, 406–411. <https://doi.org/10.1016/j.quageo.2012.02.009>.
- Shao, Q., Bahain, J.-J., Dolo, J.-M., Falguères, C., 2014. Monte Carlo approach to calculate US-ESR age and age uncertainty for tooth enamel. *Quat. Geochronol.* 22, 99–106. <https://doi.org/10.1016/j.quageo.2014.03.003>.
- Simkins, L.M., Simms, A.R., DeWitt, R., 2013. Relative Sea-level history of Marguerite Bay, Antarctic Peninsula derived from optically stimulated luminescence-dated beach cobbles. *Quat. Sci. Rev.* 77, 141–155. <https://doi.org/10.1016/j.quascirev.2013.07.027>.
- Simkins, L.M., DeWitt, R., Simms, A.R., Briggs, S., Shapiro, R.S., 2016. Investigation of optically stimulated luminescence behavior of quartz from crystalline rock surfaces: A look forward. *Quat. Geochronol.* 36, 161–173. <https://doi.org/10.1016/j.quageo.2016.09.002>.
- Simms, A.R., DeWitt, R., Kouremenos, P., Drewry, A.M., 2011. A new approach to reconstructing sea levels in Antarctica using optically stimulated luminescence of cobble surfaces. *Quat. Geochronol.* 6, 50–60. <https://doi.org/10.1016/j.quageo.2010.06.004>.
- Simms, A.R., Ivins, E.R., DeWitt, R., Kouremenos, P., Simkins, L.M., 2012. Timing of the most recent Neoglacial advance and retreat in the South Shetland Islands, Antarctic Peninsula: insights from raised beaches and Holocene uplift rates. *Quat. Sci. Rev.* 47, 41–55. <https://doi.org/10.1016/j.quascirev.2012.05.013>.

- Smedley, R.K., Duller, G.A.T., Pearce, N.J.G., Roberts, H.M., 2012. Determining the K-content of single-grains of feldspar for luminescence dating. *Radiat. Meas.* 47, 790–796. <https://doi.org/10.1016/j.radmeas.2012.01.014>.
- Sohbati, R., Murray, A.S., Jain, M., Buylaert, J.P., Thomsen, K.J., 2011. Investigating the resetting of OSL signals in rock surfaces. *Geochronometria* 38, 249–258. <https://doi.org/10.2478/s13386-011-0029-2>.
- Sohbati, R., Murray, A.S., Chapot, M.S., Jain, M., Pederson, J., 2012. Optically stimulated luminescence (OSL) as a chronometer for surface exposure dating. *J. Geophys. Res.-Solid Earth* 117, 7. <https://doi.org/10.1029/2012jb009383>.
- Sohbati, R., Murray, A., Jain, M., Thomsen, K., Hong, S.-C., Yi, K., Choi, J.-H., 2013. Na-rich feldspar as a luminescence dosimeter in infrared stimulated luminescence (IRSL) dating. *Radiation Measurements* 51–52, 67–82.
- Sohbati, R., Murray, A.S., Porat, N., Jain, M., Avner, U., 2015. Age of a prehistoric “Rododian” cult site constrained by sediment and rock surface luminescence dating techniques. *Quat. Geochronol.* 30, 90–99. <https://doi.org/10.1016/j.quageo.2015.09.002>.
- Sohbati, R., Liu, J.F., Jain, M., Murray, A., Egholm, D., Paris, R., Guralnik, B., 2018. Centennial- to millennial-scale hard rock erosion rates deduced from luminescence-depth profiles. *Earth Planet. Sci. Lett.* 493, 218–230. <https://doi.org/10.1016/j.epsl.2018.04.017>.
- Souza, P.E., Sohbati, R., Murray, A.S., Kroon, A., Clemmensen, L.B., Hede, M.U., Nielsen, L., 2019. Luminescence dating of buried cobble surfaces from sandy beach ridges: a case study from Denmark. *Boreas* 48, 841–855. <https://doi.org/10.1111/bor.12402>.
- Souza, P.E., Sohbati, R., Murray, A.S., Clemmensen, L.B., Kroon, A., Nielsen, L., 2021. Optical Dating of Cobble Surfaces Determines the Chronology of Holocene Beach Ridges in Greenland. *Boreas* n/a. <https://doi.org/10.1111/bor.12507>.
- Tsukamoto, S., Duller, G.A.T., Wintle, A.G., Muhs, D., 2011. Assessing the potential for luminescence dating of basalts. *Quat. Geochronol.* 6, 61–70. <https://doi.org/10.1016/j.quageo.2010.04.002>.
- Vásquez, P., Sepúlveda, F.A., 2012. Mapa geológico de Pozo Almonte, Región de Tarapacá. In: Blanco, N., Vásquez, P., Sepúlveda, F., Tomlinson, A.J., Quezada, A., Ladino, M. (Eds.), *Levantamiento Geológico Para El Fomento de La Exploración de Recursos Minerales e Hídricos de La Cordillera de La Costa, Depresión Central y Precordillera de La Región de Tarapacá (20°S-21°S)*, Informe Registrado IR-12-50, 246 p., 7 Mapas Escala 1:100.000. Servicio Nacional de Geología y Minería, Santiago.
- Victor, P., Sobiesiak, M., Glodny, J., Nielsen, S.N., Oncken, O., 2011. Long-term persistence of subduction earthquake segment boundaries: evidence from Mejillones Peninsula, northern Chile. *J. Geophys. Res. Solid Earth*. <https://doi.org/10.1029/2010JB007771>.
- Walk, J., Stauch, G., Bartz, M., Brückner, H., Lehmkuhl, F., 2019. Geomorphology of the coastal alluvial fan complex Guanillos, northern Chile. *J. Maps* 15, 436–447. <https://doi.org/10.1080/17445647.2019.1611499>.
- Walk, J., Stauch, G., Reyers, M., Vásquez, P., Sepúlveda, F.A., Bartz, M., Hoffmeister, D., Brückner, H., Lehmkuhl, F., 2020. Gradients in climate, geology, and topography affecting coastal alluvial fan morphodynamics in hyperarid regions – the Atacama perspective. *Glob. Planet. Chang.* 185, 102994. <https://doi.org/10.1016/j.gloplacha.2019.102994>.



## Chapter 7

# Discussion

### 7.1 Dating of man-made structures and natural deposits using rock surface luminescence

#### 7.1.1 The construction, degradation and burial of archaeological structures

The dating of archaeological structures with rock surface luminescence is one of the earliest and most widely studied applications of the method (e.g., Polikreti et al., 2002; Greilich et al., 2005; Sohbati et al., 2012c; Freiesleben et al., 2015; Liritzis and Vafiadou, 2015; al Khasawneh et al., 2019a,b; Liritzis et al., 2019; Galli et al., 2020; al Khasawneh et al., 2022). For some structures with intact walls (Chapter 3), the burial dating approach appears straightforward. The luminescence is i) bleached during exposure of natural rocks or quarried stones to daylight prior to or during construction; ii) the rock is placed in the wall, which ends the bleaching process; and iii) luminescence increases until sampling due to ionising radiation. The age of the dated surface, providing that the signal was sufficiently zeroed at the rock surface during exposure, will chronologically correspond to the transition from step ii to iii, i.e., the time of construction of the wall. The construction event should be represented by the presence of a dose plateau at the sampled rock surface.

Chronological accuracy is paramount when applying any dating method since only accurate ages provide valuable chronological information for the archaeological structures dated. Good independent age control is not always available; hence, it is crucial to evaluate if rock surface luminescence dating, in general, can provide reliable chronologies. In Chapter 3, the most recent construction event of a largely intact

dry-stone wall from a hut, dated with rock surface luminescence from two rocks, is in agreement (within uncertainty) with a radiocarbon date collected from within the structure. In combination with previous efforts of dating archaeological structures with rock surface luminescence where the resulting ages are in agreement with historical data (Greilich et al., 2005) or other dating methods (Freiesleben et al., 2015), it appears that the method is promising, albeit only sparsely used so far. The two ages from the hut wall are internally consistent at  $2\sigma$ , which was also reported from some other sites where multiple samples from intact walls were dated (al Khasawneh et al., 2019a,b). However, some other studies have demonstrated some variation within the final ages (Thompson et al., 2022), indicating that different surfaces have recorded different construction events.

Variations in the age estimate from rock surfaces become more apparent when the targeted wall has degraded or collapsed. In Chapter 3 a large scatter of ages (recent to 3.75 ka) was recorded from surfaces from a collapsed dry-stone wall, where only one age ( $500 \pm 60$  a) was in agreement with the solid chronological evidence provided by archaeological artefacts (Carrer and Angelucci, 2013; Medici et al., 2014). al Khasawneh et al. (2022) reported intra-sample variations in ages derived from two rocks from a collapsed wall. The authors hypothesised that this variation could be due to a partial burial event of the samples, followed by a final burial  $\sim 1600$  years later. Hence, it appears that the dating of collapsed rock walls requires the dating of several samples to provide dating on the various phases of construction of such walls to decrease the risk that the most recent such event is missed. Alternatively, the appearance of multiple burial events might be observable in a single surface (Chapter 3; Thompson et al. (2022)), but it is presumably challenging to determine if older events indeed are associated with construction work instead of natural processes. Partial burial or re-exposure is probably to be expected when dating stone walls since such features will degrade over time (Preti et al., 2018) and, therefore, have to be repaired. Since these degradation and repair events could possibly be preserved in the luminescence-depth profile of individual samples as multiple cycles of burial and exposure or as scatter in ages between different surfaces from the same structures, clearly rock surface luminescence dating appears to be a most useful dating method for dating walls. However,

in such settings, additional chronological data will be crucial to interpret the archaeological significance of each age and to assess if the rock surface luminescence age represents the initial construction of the structure, the degradation, and repair of the structure, or is unrelated to human activity at the site. Analysis of several surfaces and thorough recording of the sample position and the state of the sampled structure is also essential to evaluate if the sample has been disturbed since the initial construction (or completely rebuilt). Finally, new scanning techniques with spatially resolved luminescence (Sellwood et al., 2022a,b) could increase the speed of luminescence-depth measurements, enabling systematic analysis of stone walls and similar features with rock surface luminescence using more than just a handful of samples.

As expected, sites with increased geoarchaeological complexity appear to provide increased variation in the luminescence ages (e.g., Galli et al., 2020). In Chapter 2, two archaeological horizons within a dry-stone enclosure with robust age control from radiocarbon dating and artefact typology demonstrated significant scatter between two rocks at the lower level: either severely overestimated or slightly underestimated the expected burial age. For the uppermost level, the ages are mostly slightly younger than expected from the radiocarbon dating. This site is affected by slope processes (Angelucci et al., 2021), meaning that various parts of the levels in structure might have been covered at different times. Also, since both radiocarbon and rock surface luminescence dating demonstrate that the structure was used for several thousands of years, the character of the human use of the structure likely changed over time (c.f. Carrer and Angelucci, 2018). Hence, rock surface luminescence dating of such a site is likely to provide ages from various processes – e.g., overland flows, constructions, collapses, even fire events – all of interest for understanding the development of an open-air site.

With regard to the dating of the use of fire: heat exposure (due to human use of fire) has been identified to have reset the pIRIR<sub>290</sub> signal in feldspar grains at the innermost parts of various igneous and metamorphic rocks collected from a palaeolithic horizon (Pop et al., 2021). A similar observation was presented for a sample in Chapter 2, where the pIRIR<sub>290</sub> signal too was significantly below saturation. The top surface of this sample was subsequently re-exposed before the final burial at ~1000 AD by colluvium. Hence, a single rock sample can contain information regarding both

anthropogenic and natural processes and exposure to heat and light.

### 7.1.2 Rock surface luminescence dating as a tool for understanding geomorphological processes

Since natural events such as lake damming (Vermeersch and Van Neer, 2015), river incision (Angelucci et al., 2018), and shoreline displacement (Benjamin et al., 2017; Hansson et al., 2018) considerably influenced human activities during prehistory, the ability to constrain such processes chronologically enables to decipher landscape evolution and palaeoenvironments of importance to palaeolithic, neolithic, and historical populations.

The work from Chapter 4 demonstrates the challenge of dating alluvial settings using rock surface luminescence. A previous study by Ishii et al. (2022) on alluvial cobbles demonstrated significant variations in the luminescence-depth profiles from different rock cores extracted from the same rock. This observation is similar to what was detected from the alluvial calcarenites from the Mula Valley.

The most accessible geomorphological process in an alluvial system to date with rock surface luminescence dates should be the deposition of the river-transported cobbles. Suppose the luminescence signal was bleached sufficiently deep into the rock matrix during pre-erosion exposure or transport. In that case, the bottom surface of such cobbles should record the deposition time as a dose plateau. Eroding cobble-sized particles requires significant flow velocities for the sheer force to exceed the threshold to move such large particles. In one data set of four modern river cobbles, IRSL was fully bleached at both top and bottom surfaces, albeit more often deeper at the top surface (Liu et al., 2019). Better bleaching at top surfaces has also been reported from glaciofluvial cobbles by Jenkins et al. (2018). It is quite conceivable that such a pattern results from post-depositional bleaching before superimposed sediments bury the surfaces. Therefore, if sufficient time transpires between the erosion, transport, and deposition events, differences in the accumulated  $D_e$  at the different surfaces could facilitate the dating of i) the initial erosion event at the bottom surface and ii) the subsequent coverage of the top surface. The two cobbles from the Mula Valley (Chapter 4) do not demonstrate this pattern. Here, the top surfaces were barely bleached, compared to better (albeit never particularly deep) bleaching at the bottom

surfaces. The lack of deep bleaching fronts could be due to abrasion of the river bedload during transport, followed by rapid burial where no post-transport bleaching profiles could develop. If the bleaching fronts (or dose plateaus corresponding to old burial events) are abraded during transport, then the geochronological information stored in signal-depth profiles is lost. Sampling the uppermost section of glaciofluvial gravel units was suggested by [Jenkins et al. \(2018\)](#) as the best strategy for acquiring zeroed samples; such approaches could also be applied for gravel bar formation in alluvial settings.

Compared to the radiocarbon dating of shells or reworked organic materials from shorelines, non-reworked rock surface luminescence ages from buried shoreline clasts directly date ridge formation ([Souza et al., 2021](#)) since signal build-up starts when the surfaces get covered. In some coastal settings, burial dating with rock surface luminescence yields satisfactory results, providing novel data regarding sea-level regression ([Simms et al., 2011](#); [Simkins et al., 2013](#); [Souza et al., 2021](#)). In the coastal region of the Atacama Desert, dating of uplifted palaeobeaches proved challenging, likely due to a combination of unsatisfactory luminescence characteristics, opaque lithologies preventing signal bleaching, and saturation of the IRSL signal, all factors that are related to this specific site and samples. Cobbles at a modern beach in the coastal Atacama Desert (Chapter 6) displayed similar signal-depth profiles from both the top and bottom surface, indicating the overturning of the clasts by extreme waves. No attempts were made to calculate the exposure durations of the Atacama cobbles due to a lack of calibration surfaces. However, if attempted, a lack of observed burial events would likely indicate frequent overturning events where fitted exposure ages would represent cumulative exposure durations rather than only the duration for the last exposure event. Burial events were identified in some modern beach cobbles, even at the top surfaces, indicating that overturning might have occurred recently in such cobbles. Such burial events were chronologically constrained when the surface was last covered. This does not provide information regarding processes moving the cobbles as an individual data point. However, patterns of overturning can be discerned using multiple samples, such as the work of [Brill et al. \(2021\)](#), demonstrating how large variability in rock surface ages signifies that more frequent storm events turned large coastal boulders rather than rarer tsunami events.

## 7.2 The effect of lithology on rock surface luminescence dating

### 7.2.1 Luminescence characteristics

Suitable luminescence characteristics in the dated material are a limiting factor for successful luminescence dating; i.e., the luminescence signal must be sufficiently sensitive to luminescence stimulation and be rapidly zeroed during exposure to daylight or heat and remain stable over geological periods.

The sensitivity of quartz OSL in unconsolidated sediments can vary considerably depending on the geological source of the quartz grains (Tsukamoto et al., 2011; Alexanderson, 2022; Capaldi et al., 2022), and on the number of cycles of erosion and deposition occurring before sampling (Sawakuchi et al., 2011; Gliganic et al., 2017). The OSL signal in consolidated rocks appears to show similar patterns. Sohbati et al. (2011) observed little luminescence response to blue stimulation of quartz grains from two crystalline rocks, and other studies have reported insensitive or unsuitable OSL characteristics in quartz from various rocks (e.g., Souza et al., 2019; Mineli et al., 2021). In contrast, sedimentary rocks such as various sandstones have demonstrated more acceptable levels of OSL sensitivity (e.g., Jeong and Choi, 2012; Alexanderson and Bernhardson, 2016; al Khasawneh et al., 2019a; Brill et al., 2021; al Khasawneh et al., 2022). Quartz-rich metasedimentary rocks appear to have suitable OSL characteristics; in particular, quartzites, which have been used for dating of alluvial cobbles (Sohbati et al., 2012b) and archaeological artefacts (Gliganic et al., 2021). The luminescence characteristics from the hydrothermal quartz from Wadi Sodmein are unsuitable since the fast ratio (Durcan and Duller, 2011) in response to cycles of irradiation fixed test dose increases up to  $\sim 12$  times from the natural signal. The increased sensitivity of the fast component has been correlated with a decrease in the characteristic dose (Mineli et al., 2021). A previous study using hydrothermal quartz by Bailiff et al. (2021) also reported on weak natural luminescence signal, observing maximum signal emission between one to seven times the background emission. Hence, hydrothermal quartz appears to demonstrate general unsuitable luminescence characteristics. The lack of fading observed in the OSL signal would make OSL dating



with rock surface luminescence advantageous, but the application so far appears to be limited to quartz-rich sedimentary rocks, preferably combined with density separation to remove any contamination in the UV emission from feldspars.

Directly targeting feldspars as the chronometer is a common approach for rock surface dating (e.g., [Sohbati et al., 2015](#)) since the OSL signal is often unsuitable or affected by feldspar contamination. A sensitive IRSL signal has been reported in feldspar-bearing rocks of different geological origins (e.g., [Sohbati et al., 2011](#); [Freiesleben et al., 2015](#); [Sohbati et al., 2015](#); [Rades et al., 2018](#)). In this thesis, we observe bright IRSL signals in alpine gneisses from Italy and in meta-granites from Egypt. In contrast, the carbonate-dominated sedimentary rocks from southeastern Spain have weaker signals, likely related to the sparse presence of feldspars observed in these rocks. The presence of feldspars does, however, not necessarily compel the presence of a sensitive IRSL signal. The Chilean coastal cobbles are a lithologically diverse group of alkaline, felsic, and intermediate volcanic and plutonic rocks, all containing plagioclases. The alkaline rocks, all lacking K-feldspars, displayed weak IRSL emission when stimulated with IR diodes. More surprising was the weak IRSL response in some coastal granites since other studies have reported on bright IRSL emission in granites (e.g., [Sohbati et al., 2011](#); [Freiesleben et al., 2015](#); [Jenkins et al., 2018](#)). While comparing spatially resolved IRSL and pIRIR with element mapping, [Thomsen et al. \(2018\)](#) demonstrated that IRSL in their granitic samples was emitted from both alkali and plagioclase feldspars (for pIRIR, the potassium-rich regions contributed more to the emission). Hence, the lack of IRSL sensitivity is even more curious since the dim granites contained both feldspar types. Previous studies of feldspars, however, have shown the complex patterns of IRSL sensitivity. For example, [Fitzgerald et al. \(2022\)](#) reported strong variations in IRSL response between samples within different feldspar groups.

### 7.2.2 Luminescence-depth profiles

The relationship between lithology and bleaching rate (for IRSL and pIRIR<sub>225</sub> signals) was established by [Ou et al. \(2018\)](#) based on their bleaching experiments on different lithologies, demonstrating that translucent rocks bleaches deeper quicker compared to opaquer rocks. During 91 days of exposure, [Ou et al. \(2018\)](#) showed that the IRSL

in dark greywacke did not bleach beyond the outer mm; in contrast, a translucent quartzite sample appeared to have been bleached even before the experiment was initiated, indicating fast bleaching to rock depths  $>15$  mm. For natural samples, the rock surface exposure histories are usually unknown; hence, it would be difficult to assess the suitable lithology for sampling when in the field. The suitable lithology has to partly be determined based on the applied dating method and the archaeological or geomorphological setting.

For exposure dating, sufficiently rapid bleaching is necessary to resolve changes in luminescence-depth profiles when slices of rock cores are  $\sim 0.7$  mm thin. Thinner slices are usually hard to consistently produce using wafer-blade saws, a common sample preparation technique (e.g., [Sohbati et al., 2011](#); [Lehmann et al., 2018](#)). Too fast bleaching, on the other hand, could completely bleach the signal throughout the entire clast (this is not an issue when bedrock outcrops are sampled). For burial dating, rapid bleaching is likely a significant advantage for most applications since it would ensure that luminescence was thoroughly zeroed before burial. This will be especially important for samples transported in low-light conditions such as glacial, hillslope, or fluvial sediments. However, rapid bleaching could remove previous exposure histories preserved in the rock surfaces, meaning that only information regarding the last burial event remains. High bleaching rates appear to be a potential advantage or limitation with quartz-dominated lithologies. [Sohbati et al. \(2012b\)](#) reported on quartzite pebbles that had been completely bleached through before burial, and the natural quartz sample QD4 from Sodmein, for example, displayed complete bleaching to  $>25$  mm of depth. Another advantage of quartz-rich rocks is that they are very weathering-resistant (e.g., [Pettijohn et al., 1987](#)), which was also observed in Wadi Sodmein where the granitic samples containing both quartz and feldspars, among other minerals, were much more affected by weathering compared to the vein quartz. Signal-depth profiles will, therefore, be better preserved in quartz-rich rocks. However, as discussed in Section 7.2.1 and other publications (e.g., [Sohbati et al., 2011](#)), the quartz OSL signal is not always usable for dating.

Due to issues with the OSL signal in several lithologies, feldspars will be the most targeted chronometer within rocks. The most used feldspar signal is IRSL, which bleaches quicker compared to pIRIR (e.g., [Buylaert et al., 2012](#); [Kars et al., 2014](#)) or

IRPL signals (Sellwood et al., 2022a). Simulated IRSL-depth profiles from naturally exposed rock surfaces of various lithologies using  $\mu$  values reported in this thesis are plotted, assuming a setting with excellent bleaching conditions (Fig. 7.1). These simulated profiles show that a brief exposure event (1 day) would leave a significant residual IRSL signal ( $\sim 40$  % of field saturation) at the outer 0.5 mm in all investigated samples. Based on such results, no matter the lithology, brief exposure, e.g., clast transport during erosional events or short-distance moving of stones during dry-stone construction occurring during a single day, would not zero the relatively bleachable IRSL signal sufficiently. Previous empirical work has demonstrated that hours are sufficient to bleach luminescence in rock slices to near-zero when exposed in a solar simulator (Vafiadou et al., 2007); the doses in the surface slices from the same samples showed similar results following longer exposure of 9-14 days to daylight. Illumination of a calcarenite cobble in a solar simulator (Chapter 4) showed bleaching to well beneath 10 % of field-saturated IRSL despite short bleaching fronts in the natural IRSL calcarenite profiles, indicating that, as expected, naturally exposed surfaces of most lithologies will require more than one day of exposure for the residual IRSL to reach near-zero levels. Hence, in settings where surfaces are expected to be exposed only for brief periods, a higher sample volume, no matter the lithology, is required to find surfaces exposed for longer periods before the erosion or construction event occurs.

As the exposure duration increases, variations in  $\mu$  cause more divergence between the top and bottom surfaces (Fig. 7.1). The modelled bleaching fronts (50 % of saturated IRSL) after one year of exposure to German daylight conditions during the summer period reach  $>2$  mm in all modelled rock samples except for a dark volcanic sample (GUA 1-2) and a reddish granite with subpar luminescence characteristics (GUA 2-2). The IRSL in the outer 0.5 mm of rock appears to bleach below  $<2$  % of saturation in all lithologies following one year of exposure. Bleaching was hence sufficient to determine the time of the last burial event but insufficient for developing dose plateaus that confirm that little residual dose remained when the surface was covered. For deeper bleaching fronts, the IRSL in the gneiss clasts from Val di Sole (with one exception: MZ005S-1) all bleached fully to  $>3$  mm, where a dose plateau, sufficient to extract several rock slices for measurements, could form. Considering

the bleaching fronts observed in naturally exposed samples, it appears that exposure dating of translucent, quartz-rich rocks would be ideal for exposure dating of younger surfaces e.g., related to Holocene geomorphology or Neolithic or younger archaeology. Significant additional methodological issues remain with exposure dating, however, especially related to constraining the local bleaching rates at the rock surfaces using calibration samples (Freiesleben et al., 2022).

### 7.2.3 Dose rate and signal saturation

As expected, the reported effective dose rates vary considerably between the samples and sites. While the environmental dose rates originating from surrounding sediments and cosmic rays will vary between different sites, the chemical composition of different lithologies could affect the rate of dosing. The effective dose rate originating from internal radionuclide in the rocks, including  $^{40}\text{K}$  beta decay from alkali feldspars, is the highest in felsic and intermediate igneous rocks compared to alkaline rocks, gneisses, or calcarenites. High dose rates do not constitute a limitation for samples dating from Holocene or the Upper Palaeolithic, but saturation could present a challenge for older samples if dose rates are too high. A first demonstration of using rock surface luminescence dating to extend the dating range (Bailiff et al., 2021) has demonstrated that quartz pebbles with low dose rates ( $<0.6 \text{ Gy ka}^{-1}$ ) did successfully capture OSL ages up to 500 ka. The saturation of quartz is usually 200 Gy or lower (Murray et al., 2021), considerably lower than saturation limits usually reported for feldspar IRSL (e.g., Buylaert et al., 2012). Luminescence ages based on palaeodoses higher than two times the characteristic dose threshold ( $2D_0$ ) are often considered to be infinite (Wintle and Murray, 2006). This is not necessarily true for feldspar since the signal fades, causing saturated samples to display natural IRSL intensity beneath the  $2D_0$  threshold, thus mistaking infinite dates to be finite unless the dose-response curves are corrected for anomalous fading (King et al., 2018). Fig. 7.2 demonstrates the maximum finite ages possible to date with samples collected for this thesis, assuming no fading in the dose-response curve (fading would decrease the maximum ages). When plotted against the effective dose rate component arising solely from the rock, there is a weak correlation between the maximum finite ages and the dose arising from the rock. Hence, lithologies such as quartz and quartzites (Bailiff et al., 2021), arkose

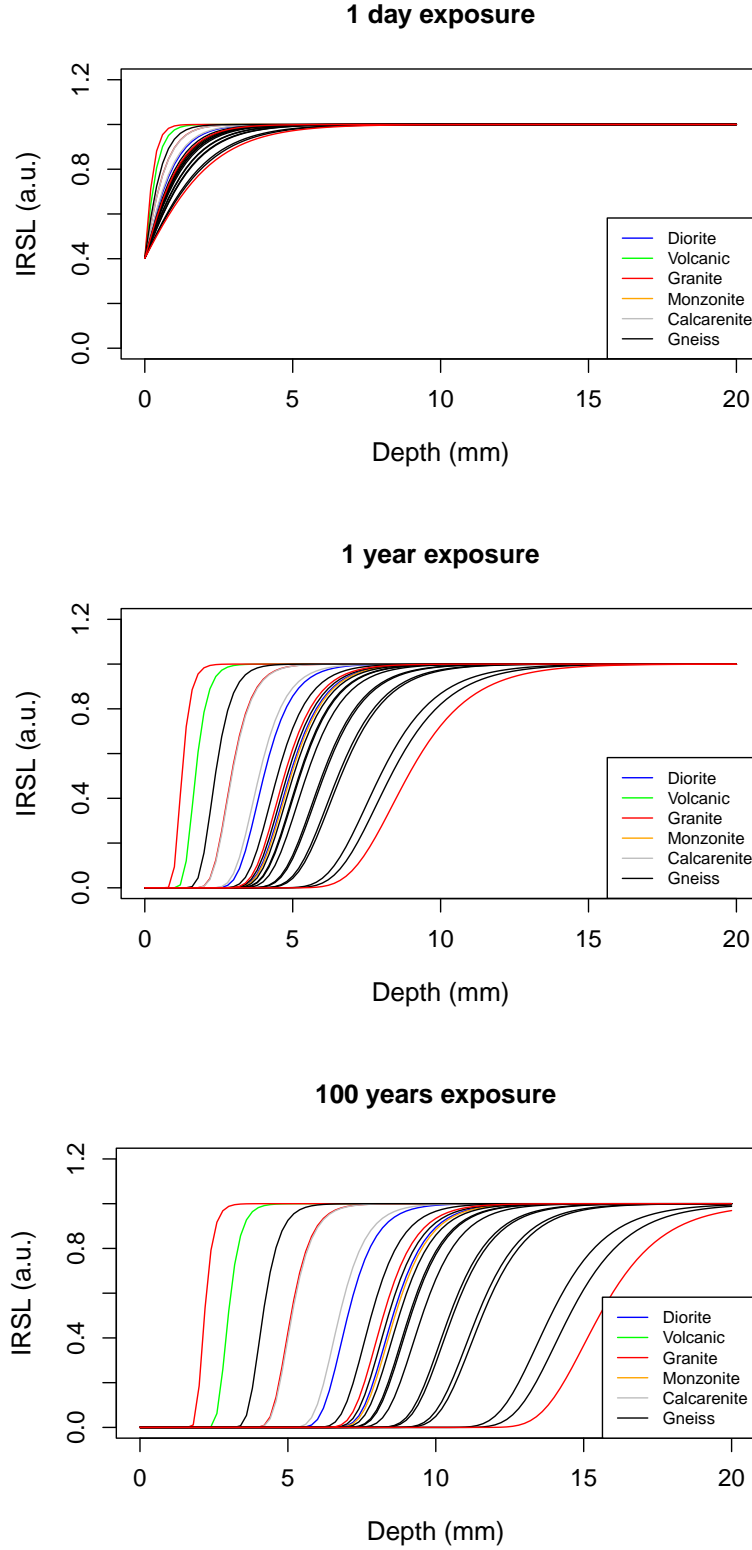


FIGURE 7.1: Modelled IRSL-depth profiles (signal saturation = 1) from different lithologies using  $\mu$  values from exposed or previously exposed surfaces. The profiles are fitted assuming  $\overline{\sigma\phi_0} = 333 \text{ a}^{-1}$ ; this value was estimated based on a bleaching experiment exposure on a rooftop in Cologne, Germany, for 32 days during summer (see Chapter 2 for more detail).

sandstones, calcarenites and gneisses are preferable to felsic and intermediate igneous rocks when expected ages are older than 100 ka.

#### 7.2.4 Anomalous fading

Anomalous fading (Wintle, 1973) in rock samples has been reported from different lithologies. Overall, fading values for the IRSL vary significantly between different studies; for example, Freiesleben et al. (2015) reported low fading (g-value =  $0.66 \pm 0.20$  % per decade) in a granitic sample, Rades et al. (2018) reported g-values ranging between  $3.9 \pm 2.6$  to  $15.1 \pm 0.9$  % per decade, and the samples of Souza et al. (2019) ranged between  $1.8 \pm 1.4$  to  $13.9 \pm 1.6$  % per decade. The IRSL anomalous fading observed in this thesis (Fig. 7.3) is moderate within gneisses (mean =  $2.2 \pm 0.4$  % per decade), and the two calcarenite samples ( $\sim 3.2$ – $3.4$  % per decade), but greater than 5 % per decade for some granites and intermediate/mafic lithologies. The range of g-values observed in rocks, including high values  $>10$  %, and, so far, less-fading feldspar signals tend not to bleach deep into rocks (e.g., Freiesleben et al., 2015; Sellwood et al., 2022b, and chapter 4), indicating that i) fading should be expected for rock samples, which necessitates fading correction approaches, and ii) different correction methods might be necessary for different samples.

Since the centre of most rocks will be in saturation due to dosing occurring over geological time scales (with no subsequent bleaching), the ratio between the field-saturated centre of the rock and laboratory saturation derived from saturated dose-response curves has been suggested to represent an estimate for fading (Rades et al., 2018), providing a correction approach to g-value corrections. The natural-laboratory fading ratio has been successfully applied when dating Swedish granites from an archaeological setting (Thompson et al., 2022). The results from comparisons between the different approaches vary. Rades et al. (2018) derived more realistic burial ages for LGP moraine boulders when using the ratio compared to unrealistically high fading rates when measuring laboratory fading with g-values. On the other hand, when dating crosscutting relationship of rock art from the Iberian Peninsula, both methods provided indistinguishable ages at around  $\sim 3$  ka (Moayed et al., 2022). In contrast, in Chapter 2, the natural-laboratory ratio-corrected ages overestimated the g-value corrected with 40-100 %. Eventually, g-value corrected ages were favoured due to the



agreement between g-value corrected IRSL and pIRIR<sub>290</sub> ages from sample MZ051S-2, in which both signals had been zeroed throughout the cobble by heat. No systematic comparison between the methods – including between known-age samples – has been presented so far. While the issues regarding g-value corrections are well-known, especially in the non-linear part of the growth curve (King et al. (2018) for comparison between different correction methods for fading in sediments), the parameters that produce the natural/laboratory ratio are less understood. For example, the ability to simulate natural dose growth in laboratory settings is crucial; for quartz, laboratory dose-response curves have been shown not to replicate natural dosing (e.g., Timar-Gabor et al., 2015). For feldspar IRSL, fading will affect the dose-response curves, which makes the evaluation of natural versus laboratory dose growth challenging. Li and Li (2012b) demonstrated that natural dose growth curves underestimate laboratory dose curves for IRSL in Chinese loess when measured as part of a MET-pIRIR protocol; there, the effect increased as the dose increased. Since the natural/laboratory saturation ratio per definition measures fading in the high dose range, these results indicate that the ratio approach is suitable for older samples. In contrast, the agreement between corrected IRSL and low-fading pIR ages presented in Chapter 2 demonstrated that ages corrected using a g-value can still be reliable, especially for younger samples, since the natural/laboratory saturation ratio risks overestimating the amount of fading.

### 7.3 Dating of palaeolithic sites with rock surface luminescence dating – significance for future research on pre-historic migration into and within Europe

Rock surface luminescence dating is increasingly established as a valuable dating method in archaeological contexts, which can be used to date many features of archaeological value in a landscape (Figure 7.4). Hence, the usefulness of the method is that some methodological limitations with other dating methods are diminished, and new archaeological and geoarchaeological archives are made available for dating.

Lack of signal bleaching is a common limitation when dating palaeolithic sites

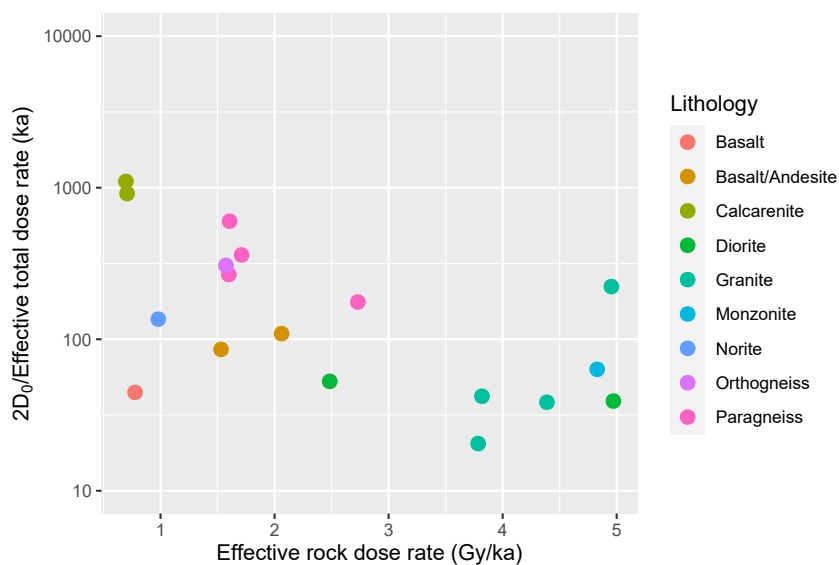


FIGURE 7.2:  $2D_0/\text{dose rate}$  versus the effective dose rate (including environmental dose rate from the surrounding) at the outer 1 mm of rock, derived from the rock itself in samples from the different sites investigated in this thesis.

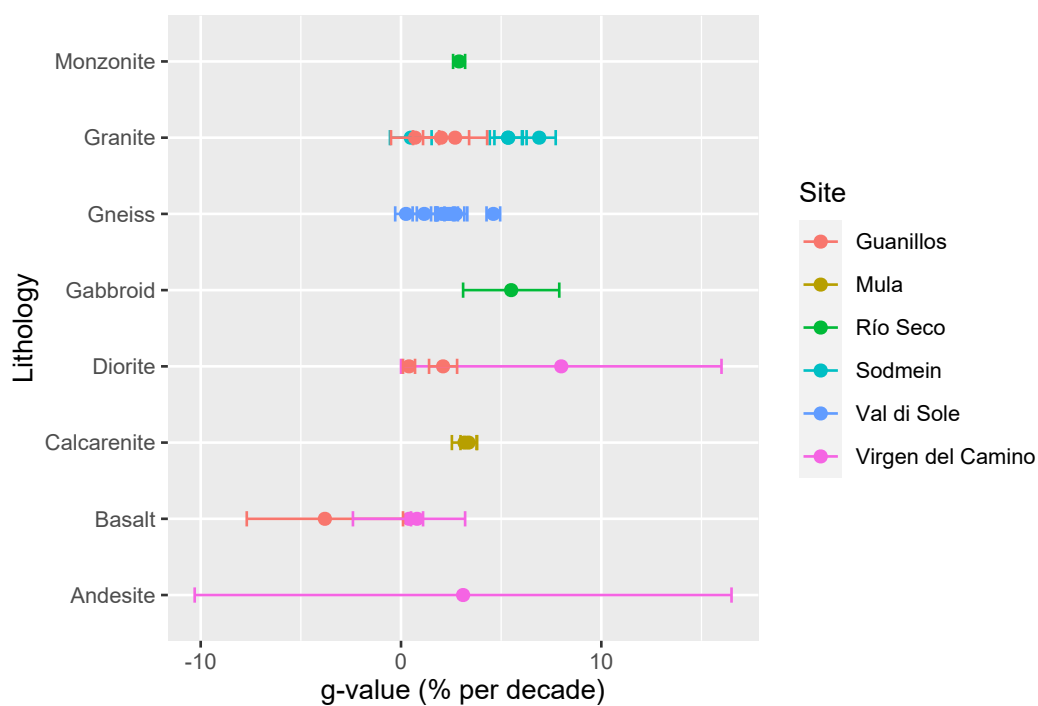


FIGURE 7.3: Fading (g-values) of IRSL measured from cobbles of eight different lithologies in this thesis.

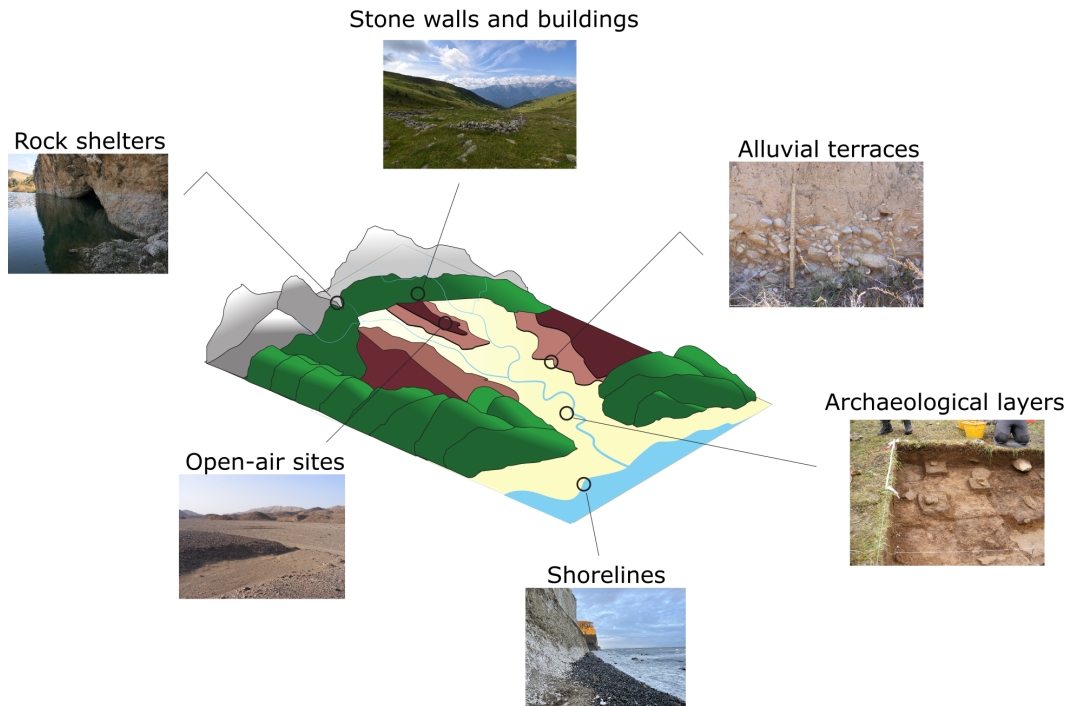


FIGURE 7.4: Schematic of dateable features in an archaeological landscape using rock surface luminescence dating.

with luminescence (Mercier et al., 2003; Arnold et al., 2013). Due to this, single-grain dating is commonly used to date such sites, using statistical procedures to identify the well-bleached grain population within a sample (Galbraith et al., 1999). While rock surface luminescence dating does not avoid the bleaching issue, the ability to determine when the sample was last sufficiently exposed to daylight is a major advantage. Some of the work from Chapters 2 and 3 in this thesis has demonstrated that rock surface luminescence dating can be used to date archaeological structures and horizons which have developed throughout the Bronze Age up until the Medieval Period. From a Palaeolithic point of view: extending the dating range into the Upper and late Middle Palaeolithic is, for the most cases, no issue, even though high dose rates and low  $D_0$  values caused saturation issues in some cobbles in Chapter 6, which could limit the dating range as is discussed in Chapter 7.2.3. Hence, when targeting old samples, it might be advisable to choose rocks with less specific activity, such as sandstones, since many granitic samples suffer from higher self-dosing due to high amounts of internal potassium. While sampling quartz pebbles is an option to avoid high dose rates, vein quartz should be avoided as is discussed in Chapter 5.

Site selection will be crucial for utilising rock surface luminescence dating to pre-historic contexts. The key strengths of the method are identifying bleached samples and dating coarse clasts to unlock previously challenging archives for dating. If a site contains dateable feldspar- or quartz-bearing rocks, then a multitude of varied sites could be targeted; some, where radiometric dating is otherwise challenging, especially as the ages nears the upper age limit for radiocarbon dating ( $\sim 50$  ka).

Direct dating of archaeological sites could include caves and rock shelters and human-made structures or the dating of open-air sites with rock surface luminescence (Gliganic et al., 2021). Open-air site stratigraphies frequently contain coarse clasts (e.g., Marder et al., 2011; Méndez-Quintas et al., 2022), especially in fluvial settings. Dating in these environments might be limited to a typological comparison of lithic technologies (e.g., Hess and Riede, 2021), but could then instead be dated with rock surface dating where it is possible to determine the pre-burial bleaching of the fluvial clasts. Since direct dating of artefacts is usually challenging due to the poor luminescence characteristics of materials such as flint (e.g., Poolton et al., 1995), which these tools are commonly made from, targeting cobbles from open-air sites with luminescence would improve the ability to date such sites. Furthermore, since not all sediments from open-air sites provide good luminescence characteristics (e.g., Klasen et al., 2013), luminescence dating of rocks would provide an alternative approach. Also, since some surfaces remain exposed for long periods (e.g., Kindermann et al., 2018) dating i.e., buried organic materials might not reflect the age of the archaeology (e.g., Crombé et al., 2013). Rock surface dating in such settings could provide the *terminus post quem* for the archaeological material since buried rock surfaces would date the deposition of the surface provided that the clast has been undisturbed. The attempt to date a wadi terrace surface in Chapter 5 indicates that post-depositional processes, such as the formation of desert pavement, complicate the dating of such surfaces.

The dating of caves and rock shelters would be possible in cases where clasts are transported into deposition by geomorphological or anthropogenic processes or where rockfalls from the cave walls create cross-cutting relationships of cave art (Moayed et al., 2022). Alluvial input into cave stratigraphies can contain layers dominated by gravels (e.g., Zilhão et al., 2016), which are challenging to date using luminescence in

sediments but could be dated using rock surfaces. Also, the effect of the water content on the calculated ages is diminished in rocks since the beta radiation is mostly emitted from within the rock itself, which removes some of the chronological uncertainty previously reported from e.g., rock shelters when using sediment dating (Zilhão et al., 2016).

A final setting in which rock surface dating could be useful for Palaeolithic research is stone structures. These structures might be rare, and their association with the Palaeolithic might be subject to discussion (e.g., Klíma, 1954); however, some early Neolithic sites have been discovered where rock surface dating could provide absolute dates (e.g., Craig et al., 2015; Scheib et al., 2019; Haklay and Gopher, 2020). The advantage of the method here is the ability to date the timing of construction directly rather than dating associated layers, e.g., sediment luminescence or radiocarbon dating. One limitation of rock surface dating in such settings, however, is the destructible nature of the method since stones have to be removed for analysis.





## Chapter 8

# Conclusions and Outlook

In this thesis, ages are determined from archaeological horizons (Chapter 2), dry-stone structures (3), alluvial gravels (Chapter 4), desert pavements (Chapter 5), and palaeobeaches (Chapter 6).

Overall, dating using rock surface luminescence proved successful at the archaeological site in Italy where the method (Chapters 2 and 3) provides new and valuable chronological data on time scales from the Bronze Age to the Early Modern Period. At the site, located on the Alpine slopes of Val di Sole, good age agreement between rock surface luminescence dating and radiocarbon dating is provided from one archaeological horizon. Ages from an older horizon are either underestimated slightly or severely overestimated when compared to the archaeological development of the site. These age discrepancies are understandable when site context is considered since too old ages indicate insufficient pre-burial bleaching in the glacial sediments from which the rocks originate, and the slope at the site could facilitate longer than expected exposure in some rock surfaces. The conclusion from the chronological work presented in this thesis is that rock surface luminescence dating provides additional chronological information compared to other dating methods but must be interpreted while keeping in mind site context and geomorphological and anthropogenic processes.

Furthermore, in the geoarchaeological context of Val di Sole, Italy, the work (Chapter 2) provided direct dating of fire use by humans. Here, the rock surface dating technique (i.e., measuring the luminescence signal versus depth into the rock) is crucial when interpreting the chronological information since the heated samples provided few visual clues that heating had occurred. Instead, the lack of a saturated signal plateau, not attributable to optical bleaching, provided evidence for heating. Also,

the presence of saturation plateaus in the other samples proved that heating had been selective and could not be attributed to natural fire events. The heating event dates to the Iron Age, a period with little other chronological or archaeological information from Val di Sole. Hence, the dating now provides the first evidence that human activities did occur in Val di Sole during the Iron Age despite the lack of widespread conventional archaeological traces. While heated rocks have recently been targeted using optical dating techniques (Pop et al., 2021), further work should aim to date rocks with known heating histories. Since fire would have been an essential part of any pre-historic settlement, heated samples might not be too scarce but could provide additional archaeological information regarding site use.

Another important human activity that is dateable using rock surface luminescence dating is the construction of stone structures. Val di Sole provided a setting with variously intact or collapsed dry-stone walls (Chapter 3). The variation in ages derived from the rock surfaces is considerable at the collapsed wall (Bronze Age to Early Modern Period). In such a setting, complementary archaeological data, as well as field observatories regarding the condition of the wall and the position of the samples and adjacent rocks, was crucial when interpreting the ages. A geoarchaeological understanding of the site proved extensively important since ages from such structures may represent different events in its lifetime: the original construction of the wall, a repair event following a collapse, or a collapse followed by re-burial due to subsequent collapses or sedimentation. Nevertheless, all such information is of archaeological value, and it is demonstrated that rock surface luminescence dating can chronologically constrain processes that other dating methods might not resolve. The construction event directly dates human activities and provides chronological constraints for the sites and dating technological prowess. Dating the time of repair of a wall also includes essential information on human activity at the site at specific periods and, in contrast, the collapse of a wall without subsequent repair indicates abandonment of the site or that human activity or the environmental situation had changed sufficiently that repair was considered futile. The data from dry-stone walls in this thesis consists of a few samples due to the considerable effort behind the dating of each sample. However, each sample consists of several rock surfaces that might have been subjected to different exposure histories, meaning that different surfaces

from each sample might provide corresponding or complementary chronological information. In the future, larger data sets would be desirable to identify different age groupings from collapsed walls. Scanning methods using spatially-resolved luminescence (e.g., [Sellwood et al., 2022b](#)) would enable quicker assessment of the suitability of samples for dating. The burial ages from the intact wall dated in this study were less spread, indicating that they were placed in the wall during the same construction event. However, different age groupings could exist in rock surfaces collected from intact walls at other sites, which would demonstrate that the wall had, at one point, been repaired. Such events might be visible in a single rock surface signal profile as multiple burial and exposure events.

Using rock surface luminescence dating at sites with high-energy depositional environments appears to be more complex than the upland setting of Val di Sole. While pre-historic humans have frequented terraces and shorelines, making dating these landforms meaningful, several methodological limitations might apply when using rock surface luminescence. Rock surface luminescence ages from both Mula, Spain (Chapter 4) and the Atacama Desert (Chapter 6) underestimate the expected ages. This underestimation could be the result of fading of the feldspar signal (which was insufficiently corrected for), field-saturation of the signal, or the ages were calculated with a too high dose rate. Otherwise, it could be due to a more recent exposure of the rock surface; hence, understanding the geomorphological or geoarchaeological processes that affect the dated site will be crucial when interpreting the ages. Inversely, rock surface luminescence techniques could be a valuable tool for understanding geomorphological processes such as reworking or erosion of sediments in high-energy depositional environments since the re-exposure of the rock surface can be identified in the luminescence signal-depth profile. However, exposure events might not always remain recorded in profiles from the sampled surfaces. Some rock surfaces from Mula and Atacama lacked any indication that the surface had been bleached before burial. Insufficient exposure is one possible explanation, but high dose rates, low signal saturation limits or erosion of the rock surfaces truncating the profiles, cannot be ignored as causes. Investigating samples from different lithologies, more samples of the same lithology, and more than one surface from each sample could further illuminate whether the site can be dated using rock surface luminescence.

Hence, prudent sample selection is crucial, but yet not straight-forward, since poor luminescence properties such as weak signal intensity, low saturation limits, high fading rates, etc., were observed in several lithologies, including granite and diorite cobbles (Chapter 6) containing feldspars. In contrast, para- and orthogneisses and granitic rocks appear to be best suitable for rock surface luminescence dating. While such lithologies should be targeted if possible, it must be considered that: i) many settings will not contain these lithologies, and it nevertheless appears worthwhile to sample less-than-ideal sedimentary rocks since rock surface luminescence dating provides chronological information not necessarily available using other dating methods; and ii) lithologies such as gneisses, quartzites, and sandstones have been successfully dated from other sites. In the future, methodological studies of the luminescence properties in rocks from archaeologically interesting regions will likely facilitate the dating of sites and processes by targeting specific lithologies depending on the depositional setting (bleaching rate of the signal), expected age (signal saturation and dose rate), or post-depositional weathering (mineral composition).

# Bibliography

- Adelsberger, K.A., Smith, J.R., 2009. Desert pavement development and landscape stability on the Eastern Libyan Plateau, Egypt. *Geomorphology* 107, 178–194. doi:10.1016/j.geomorph.2008.12.005.
- Ageby, L., Angelucci, D.E., Brill, D., Carrer, F., Brückner, H., Klasen, N., 2022. Dating dry-stone walls with rock surface luminescence: A case study from the Italian Alps. *Journal of Archaeological Science* 144, 105625. doi:10.1016/j.jas.2022.105625.
- Ageby, L., Angelucci, D.E., Brill, D., Carrer, F., Rades, E.F., Rethemeyer, J., Brückner, H., Klasen, N., 2021. Rock surface IRSL dating of buried cobbles from an alpine dry-stone structure in Val di Sole, Italy. *Quaternary Geochronology* 66, 101212. doi:10.1016/j.quageo.2021.101212.
- Ageby, L., Brill, D., Angelucci, D.E., Brückner, H., Klasen, N., 2023. Investigating optical dating of carbonate-rich cobbles from a river terrace: A pilot study from the Mula Valley, Spain. *Radiation Measurements* 166, 106962. doi:10.1016/j.radmeas.2023.106962.
- Ahlstrom, R.V.N., Roberts, H., 2001. Desert Pavement and Buried Archaeological Features in the Arid West: A Case Study from Southern Arizona. *Journal of California and Great Basin Anthropology* 23, 1–26. arXiv:27825749.
- Aitken, M.J., 1985. Thermoluminescence Dating. *Studies in Archaeological Science*. u.s. ed ed., Academic Press, London ; Orlando.
- al Khasawneh, S., Abu-Jaber, N., Hamarneh, C., Murray, A., 2022. Age determination of runoff terrace systems in Petra, Jordan, using rock surface luminescence dating. *Archaeological and Anthropological Sciences* 14, 48. doi:10.1007/s12520-022-01510-9.

- al Khasawneh, S., Murray, A., Abudanah, F., 2019a. A first radiometric chronology for the Khatt Shebib megalithic structure in Jordan using the luminescence dating of rock surfaces. *Quaternary Geochronology* 49, 205–210. doi:10.1016/j.quageo.2018.02.007.
- al Khasawneh, S., Murray, A., Thomsen, K., AbuAzizeh, W., Tarawneh, M., 2019b. Dating a near eastern desert hunting trap (kite) using rock surface luminescence dating. *Archaeological and Anthropological Sciences* 11, 2109–2119. doi:10.1007/s12520-018-0661-3.
- Alexanderson, H., 2022. Luminescence characteristics of Scandinavian quartz, their connection to bedrock provenance and influence on dating results. *Quaternary Geochronology* 69, 101272. doi:10.1016/j.quageo.2022.101272.
- Alexanderson, H., Bernhardson, M., 2016. OSL dating and luminescence characteristics of aeolian deposits and their source material in Dalarna, central Sweden. *Boreas* 45, 876–893. doi:10.1111/bor.12197.
- Angelucci, D., Carrer, F. (Eds.), 2015. *Paesaggi Pastorali d’alta Quota in Val Di Sole (Trento). Le Ricerche Del Progetto ALPES - 2010-2014.* Dipartimento di Lettere e Filosofia, Università di Trento, Trento.
- Angelucci, D., Carrer, F., Pedrotti, A., 2017. Due nuove datazioni dell’età del Bronzo da un sito d’alta quota in Val Poré (Val di Sole). *Archeologia delle Alpi* , 154–156.
- Angelucci, D.E., Anesin, D., Susini, D., Villaverde, V., Zapata, J., Zilhão, J., 2013. Formation processes at a high resolution Middle Paleolithic site: Cueva Antón (Murcia, Spain). *Quaternary International* 315, 24–41. doi:10.1016/j.quaint.2013.03.014.
- Angelucci, D.E., Anesin, D., Susini, D., Villaverde, V., Zapata, J., Zilhão, J., 2018. A tale of two gorges: Late Quaternary site formation and surface dynamics in the Mula basin (Murcia, Spain). *Quaternary International* 485, 4–22. doi:10.1016/j.quaint.2017.04.006.
- Angelucci, D.E., Carrer, F., Ageby, L., Castiglioni, E., Cavulli, F., Dell’Amore, F., Rethemeyer, J., Rottoli, M., Vezzoni, L., Pedrotti, A., 2021. Occupazione pastorale



- delle alte quote alpine nell'età del Bronzo: Primi dati dal sito MZ051S (Camp da Ortisé, Val di Sole, Trento) 71, 1–30. doi:10.32097/1143.
- Angelucci, D.E., Carrer, F., Cavulli, F., 2014. Shaping a periglacial land into a pastoral landscape: A case study from Val di Sole (Trento, Italy). *European Journal of Post - Classical Archaeologies* 4, 157–180.
- Ankjærsgaard, C., 2019. Exploring multiple-aliquot methods for quartz violet stimulated luminescence dating. *Quaternary Geochronology* 51, 99–109. doi:10.1016/j.quageo.2019.02.001.
- Ankjærsgaard, C., Jain, M., Wallinga, J., 2013. Towards dating Quaternary sediments using the quartz Violet Stimulated Luminescence (VSL) signal. *Quaternary Geochronology* 18, 99–109. doi:10.1016/j.quageo.2013.06.001.
- Arnold, J.R., Libby, W.F., 1949. Age Determinations by Radiocarbon Content: Checks with Samples of Known Age. *Science* doi:10.1126/science.110.2869.678.
- Arnold, L.J., Bailey, R.M., Tucker, G.E., 2007. Statistical treatment of fluvial dose distributions from southern Colorado arroyo deposits. *Quaternary Geochronology* 2, 162–167. doi:10.1016/j.quageo.2006.05.003.
- Arnold, L.J., Demuro, M., Navazo, M., Benito-Calvo, A., Pérez-González, A., 2013. OSL dating of the Middle Palaeolithic Hotel California site, Sierra de Atapuerca, north-central Spain. *Boreas* 42, 285–305. doi:10.1111/j.1502-3885.2012.00262.x.
- Auclair, M., Lamothe, M., Huot, S., 2003. Measurement of anomalous fading for feldspar IRSL using SAR. *Radiation Measurements* 37, 487–492. doi:10.1016/S1350-4487(03)00018-0.
- Bailey, R.M., 2010. Direct measurement of the fast component of quartz optically stimulated luminescence and implications for the accuracy of optical dating. *Quaternary Geochronology* 5, 559–568. doi:10.1016/j.quageo.2009.10.003.
- Bailey, R.M., Smith, B.W., Rhodes, E.J., 1997. Partial bleaching and the decay form characteristics of quartz OSL. *Radiation Measurements* 27, 123–136. doi:10.1016/S1350-4487(96)00157-6.

- Bailiff, I.K., Bridgland, D., Cunha, P.P., 2021. Extending the range of optically stimulated luminescence dating using vein-quartz and quartzite sedimentary pebbles. *Quaternary Geochronology* 65, 101180. doi:10.1016/j.quageo.2021.101180.
- Bartz, M., Duval, M., Brill, D., Zander, A., King, G.E., Rhein, A., Walk, J., Stauch, G., Lehmkuhl, F., Brückner, H., 2020a. Testing the potential of K-feldspar pIR-IRSL and quartz ESR for dating coastal alluvial fan complexes in arid environments. *Quaternary International* 556, 124–143. doi:10.1016/j.quaint.2020.03.037.
- Bartz, M., Klasen, N., Zander, A., Brill, D., Rixhon, G., Seeliger, M., Eiwanger, J., Weniger, G.C., Mikdad, A., Brückner, H., 2015. Luminescence dating of ephemeral stream deposits around the Palaeolithic site of Ifri n’Ammar (Morocco). *Quaternary Geochronology* 30, 460–465. doi:10.1016/j.quageo.2015.02.012.
- Bartz, M., Walk, J., Binnie, S.A., Brill, D., Stauch, G., Lehmkuhl, F., Hoffmeister, D., Brückner, H., 2020b. Late Pleistocene alluvial fan evolution along the coastal Atacama Desert (N Chile). *Global and Planetary Change* 190, 103091. doi:10.1016/j.gloplacha.2019.103091.
- Benjamin, J., Rovere, A., Fontana, A., Furlani, S., Vacchi, M., Inglis, R.H., Galili, E., Antonioli, F., Sivan, D., Miko, S., Mourtzas, N., Felja, I., Meredith-Williams, M., Goodman-Tchernov, B., Kolaiti, E., Anzidei, M., Gehrels, R., 2017. Late Quaternary sea-level changes and early human societies in the central and eastern Mediterranean Basin: An interdisciplinary review. *Quaternary International* 449, 29–57. doi:10.1016/j.quaint.2017.06.025.
- Bergström, A., Stringer, C., Hajdinjak, M., Scerri, E.M.L., Skoglund, P., 2021. Origins of modern human ancestry. *Nature* 590, 229–237. doi:10.1038/s41586-021-03244-5.
- Bonde, N., Christensen, A.E., 1993. Dendrochronological dating of the Viking Age ship burials at Oseberg, Gokstad and Tune, Norway. *Antiquity* 67, 575–583. doi:10.1017/S0003598X00045774.

- Bøtter-Jensen, L., Thomsen, K.J., Jain, M., 2010. Review of optically stimulated luminescence (OSL) instrumental developments for retrospective dosimetry. *Radiation Measurements* 45, 253–257. doi:10.1016/j.radmeas.2009.11.030.
- Bradley, B.A., Anikovich, M., Giria, E., 1995. Early Upper Palaeolithic in the Russian Plain: Streletskayan flaked stone artefacts and technology. *Antiquity* 69, 989–998. doi:10.1017/S0003598X00082521.
- Brennan, B.J., Lyons, R.G., Phillips, S.W., 1991. Attenuation of alpha particle track dose for spherical grains. *International Journal of Radiation Applications and Instrumentation. Part D. Nuclear Tracks and Radiation Measurements* 18, 249–253. doi:10.1016/1359-0189(91)90119-3.
- Brill, D., Ageby, L., Obert, C., Hollerbach, R., Duval, M., Kolb, T., Bartz, M., 2022. Investigating the resetting of IRSL signals in beach cobbles and their potential for rock surface dating of marine terraces in Northern Chile. *Marine Geology* 443, 106692. doi:10.1016/j.margeo.2021.106692.
- Brill, D., Cisternas, M., 2020. Testing quartz and feldspar luminescence dating to determine earthquake and tsunami recurrence in the area of the giant 1960 Chile earthquake. *Quaternary Geochronology* 58, 101080. doi:10.1016/j.quageo.2020.101080.
- Brill, D., May, S.M., Mhammdi, N., King, G., Lehmann, B., Burow, C., Wolf, D., Zander, A., Brückner, H., 2021. Evaluating optically stimulated luminescence rock surface exposure dating as a novel approach for reconstructing coastal boulder movement on decadal to centennial timescales. *Earth Surface Dynamics* 9, 205–234. doi:10.5194/esurf-9-205-2021.
- Broadbent, N.D., Bergqvist, K.I., 1986. Lichenometric Chronology and Archaeological Features on Raised Beaches: Preliminary Results from the Swedish North Bothnian Coastal Region. *Arctic and Alpine Research* 18, 297–306. doi:10.1080/00040851.1986.12004091.

- Bulur, E., 2000. A simple transformation for converting CW-OSL curves to LM-OSL curves. *Radiation Measurements* 32, 141–145. doi:10.1016/S1350-4487(99)00247-4.
- Bulut, H., Taşkıran, H., Özçelik, K., Karahan, G., 2022. Lower and Middle Palaeolithic evidence from the North Aegean coastline of Çanakkale, Turkey. *Antiquity* 96, 981–988. doi:10.15184/aqy.2022.59.
- Burow, C., Kehl, M., Hilgers, A., Weniger, G.C., Angelucci, D.E., Villaverde, V., Zapata, J., Zilhão, J., 2015. Luminescence Dating of Fluvial Deposits in the Rock Shelter of Cueva Antón, Spain. *Geochronometria* , 107–125doi:10.1515/geochr-2015-0010.
- Buylaert, J.P., Jain, M., Murray, A.S., Thomsen, K.J., Lapp, T., 2012. IR-RF dating of sand-sized K-feldspar extracts: A test of accuracy. *Radiation Measurements* 47, 759–765. doi:10.1016/j.radmeas.2012.06.021.
- Buylaert, J.P., Murray, A.S., Thomsen, K.J., Jain, M., 2009. Testing the potential of an elevated temperature IRSL signal from K-feldspar. *Radiation Measurements* 44, 560–565. doi:10.1016/j.radmeas.2009.02.007.
- Buylaert, J.P., Thiel, C., Murray, A.S., Vandenberghe, D.A., Yi, S., Lu, H., 2011. IRSL and post-IR IRSL residual doses recorded in modern dust samples from the Chinese Loess Plateau. *Geochronometria* 38, 432. doi:10.2478/s13386-011-0047-0.
- Cáceres, L., Gómez-Silva, B., Garró, X., Rodríguez, V., Monardes, V., McKay, C.P., 2007. Relative humidity patterns and fog water precipitation in the Atacama Desert and biological implications. *Journal of Geophysical Research: Biogeosciences* 112. doi:10.1029/2006JG000344.
- Cann, R.L., Stoneking, M., Wilson, A.C., 1987. Mitochondrial DNA and human evolution. *Nature* 325, 31–36. doi:10.1038/325031a0.
- Capaldi, T.N., Rittenour, T.M., Nelson, M.S., 2022. Downstream changes in quartz OSL sensitivity in modern river sand reflects sediment source variability: Case

- studies from Rocky Mountain and Andean rivers. *Quaternary Geochronology* 71, 101317. doi:10.1016/j.quageo.2022.101317.
- Carrer, F., Angelucci, D.E., 2013. First Archaeological Data From An Alpine Pastoral Enclosure At Val Poré (Val di Sole, Trentino, Italy). *Debates de Arqueología Medieval* 3, 149–165.
- Carrer, F., Angelucci, D.E., 2018. Continuity and discontinuity in the history of upland pastoral landscapes: The case study of Val Molinac and Val Poré (Val di Sole, Trentino, Eastern Italian Alps). *Landscape Research* 43, 862–877. doi:10.1080/01426397.2017.1390078.
- Carter, W.D., Aguirre le B, L., 1965. Structural Geology of Aconcagua Province and Its Relationship to the Central Valley Graben, Chile. *GSA Bulletin* 76, 651–664. doi:10.1130/0016-7606(1965)76[651:SGOAPA]2.0.CO;2.
- Cereceda, P., Larrain, H., Osses, P., Farías, M., Egaña, I., 2008. The climate of the coast and fog zone in the Tarapacá Region, Atacama Desert, Chile. *Atmospheric Research* 87, 301–311. doi:10.1016/j.atmosres.2007.11.011.
- Chapot, M.S., Sohbaty, R., Murray, A.S., Pederson, J.L., Rittenour, T.M., 2012. Constraining the age of rock art by dating a rockfall event using sediment and rock-surface luminescence dating techniques. *Quaternary Geochronology* 13, 18–25. doi:10.1016/j.quageo.2012.08.005.
- Choi, J.H., Duller, G.A.T., Wintle, A.G., Cheong, C.S., 2006. Luminescence characteristics of quartz from the Southern Kenyan Rift Valley: Dose estimation using LM-OSL SAR. *Radiation Measurements* 41, 847–854. doi:10.1016/j.radmeas.2006.05.003.
- Chu, W., 2018. The Danube Corridor Hypothesis and the Carpathian Basin: Geological, Environmental and Archaeological Approaches to Characterizing Auriagnacian Dynamics. *Journal of World Prehistory* 31, 117–178. doi:10.1007/s10963-018-9115-1.

- Colarossi, D., Chapot, M.S., Duller, G.A.T., Roberts, H.M., 2018. Testing single aliquot regenerative dose (SAR) protocols for violet stimulated luminescence. *Radiation Measurements* 120, 104–109. doi:10.1016/j.radmeas.2018.02.005.
- Cooke, R.U., 1970. Stone Pavements in Deserts. *Annals of the Association of American Geographers* 60, 560–577. doi:10.1111/j.1467-8306.1970.tb00741.x.
- Craig, O.E., Shillito, L.M., Albarella, U., Viner-Daniels, S., Chan, B., Cleal, R., Ixer, R., Jay, M., Marshall, P., Simmons, E., Wright, E., Pearson, M.P., 2015. Feeding Stonehenge: Cuisine and consumption at the Late Neolithic site of Durrington Walls. *Antiquity* 89, 1096–1109. doi:10.15184/aqy.2015.110.
- Crombé, Ph., Robinson, E., Van Strydonck, M., Boudin, M., 2013. Radiocarbon Dating of Mesolithic Open-Air Sites in the Coversand Area of the North-West European Plain: Problems and Prospects. *Archaeometry* 55, 545–562. doi:10.1111/j.1475-4754.2012.00693.x.
- Cunningham, A.C., Wallinga, J., 2010. Selection of integration time intervals for quartz OSL decay curves. *Quaternary Geochronology* 5, 657–666. doi:10.1016/j.quageo.2010.08.004.
- Cunningham, A.C., Wallinga, J., 2012. Realizing the potential of fluvial archives using robust OSL chronologies. *Quaternary Geochronology* 12, 98–106. doi:10.1016/j.quageo.2012.05.007.
- Dal Piaz, G., Castellarin, A., Martin, S., Selli, L., Carton, A., Pellegrini, G., Casolari, E., Daminato, F., Picotti, V., Prosser, G., Santulana, E., Cantelly, L., 2007. Carta Geologica d'Italia alla scala 1:50.000. Foglio 042. Malé + Note illustrative della Carta Geologica d'Italia alla scala 1:50.000.
- Devièse, T., Abrams, G., Hajdinjak, M., Pirson, S., De Groote, I., Di Modica, K., Toussaint, M., Fischer, V., Comeskey, D., Spindler, L., Meyer, M., Semal, P., Higham, T., 2021. Reevaluating the timing of Neanderthal disappearance in North-west Europe. *Proceedings of the National Academy of Sciences* 118, e2022466118. doi:10.1073/pnas.2022466118.



- Dietze, M., Dietze, E., Lomax, J., Fuchs, M., Kleber, A., Wells, S.G., 2016. Environmental history recorded in aeolian deposits under stone pavements, Mojave Desert, USA. *Quaternary Research* 85, 4–16. doi:10.1016/j.yqres.2015.11.007.
- Duller, G.A.T., 2006. Single grain optical dating of glaciogenic deposits. *Quaternary Geochronology* 1, 296–304. doi:10.1016/j.quageo.2006.05.018.
- Duller, G.A.T., 2018. Analyst User Manual v4.57. Technical Report. Aberystwyth University.
- Duller, G.A.T., Gunn, M., Roberts, H.M., 2020. Single grain infrared photoluminescence (IRPL) measurements of feldspars for dating. *Radiation Measurements* 133, 106313. doi:10.1016/j.radmeas.2020.106313.
- Dunai, T.J., López, G.A.G., Juez-Larré, J., 2005. Oligocene–Miocene age of aridity in the Atacama Desert revealed by exposure dating of erosion-sensitive landforms. *Geology* 33, 321–324. doi:10.1130/G21184.1.
- Durcan, J.A., Duller, G.A.T., 2011. The fast ratio: A rapid measure for testing the dominance of the fast component in the initial OSL signal from quartz. *Radiation Measurements* 46, 1065–1072. doi:10.1016/j.radmeas.2011.07.016.
- Durcan, J.A., King, G.E., Duller, G.A.T., 2015. DRAC: Dose Rate and Age Calculator for trapped charge dating. *Quaternary Geochronology* 28, 54–61. doi:10.1016/j.quageo.2015.03.012.
- Eixea, A., Cuevas-González, J., Díez-Canseco, D., Bel, M.Á., Bonnet, A., Carrión, Y., Martínez-Alfaro, Á., Martínez-Rubio, V., Martínez-Varea, C.M., Pardo, R., Rios-Garaizar, J., 2022. Los Aljezares archaeological site (Alicante, Spain) and the MIS 6/5 open-air settlement in the Iberian Peninsula. *Journal of Quaternary Science* 37, 1091–1111. doi:10.1002/jqs.3424.
- Favilli, F., Egli, M., Brandova, D., Ivy-Ochs, S., Kubik, P.W., Maisch, M., Cherubini, P., Haeberli, W., 2009. Combination of Numerical Dating Techniques Using  $^{10}\text{Be}$  in Rock Boulders and  $^{14}\text{C}$  of Resilient Soil Organic Matter for Reconstructing the Chronology of Glacial and Periglacial Processes

- in a High Alpine Catchment during the Late Pleistocene and Early Holocene. *Radiocarbon* 51, 537–552. doi:10.1017/S0033822200055910.
- Fewlass, H., Talamo, S., Wacker, L., Kromer, B., Tuna, T., Fagault, Y., Bard, E., McPherron, S.P., Aldeias, V., Maria, R., Martisius, N.L., Paskulin, L., Rezek, Z., Sinet-Mathiot, V., Sirakova, S., Smith, G.M., Spasov, R., Welker, F., Sirakov, N., Tsanova, T., Hublin, J.J., 2020. A  $^{14}\text{C}$  chronology for the Middle to Upper Palaeolithic transition at Bacho Kiro Cave, Bulgaria. *Nature Ecology & Evolution* 4, 794–801. doi:10.1038/s41559-020-1136-3.
- Fitzgerald, S.K., Sanderson, D.C.W., Cresswell, A.J., Martin, L., 2022. Using Infra-red stimulated luminescence and phototransferred thermoluminescence to investigate electron trapping and charge transport in feldspars. *Radiation Measurements* 156, 106817. doi:10.1016/j.radmeas.2022.106817.
- Flude, S., Haschke, M., Storey, M., 2017. Application of benchtop micro-XRF to geological materials. *Mineralogical Magazine* 81, 923–948. doi:10.1180/minmag.2016.080.150.
- Foerster, V., Asrat, A., Bronk Ramsey, C., Brown, E.T., Chapot, M.S., Deino, A., Duesing, W., Grove, M., Hahn, A., Junginger, A., Kaboth-Bahr, S., Lane, C.S., Opitz, S., Noren, A., Roberts, H.M., Stockhecke, M., Tiedemann, R., Vidal, C.M., Vogelsang, R., Cohen, A.S., Lamb, H.F., Schaebitz, F., Trauth, M.H., 2022. Pleistocene climate variability in eastern Africa influenced hominin evolution. *Nature Geoscience* 15, 805–811. doi:10.1038/s41561-022-01032-y.
- Freiesleben, T., Sohbati, R., Murray, A., Jain, M., al Khasawneh, S., Hvidt, S., Jakobsen, B., 2015. Mathematical model quantifies multiple daylight exposure and burial events for rock surfaces using luminescence dating. *Radiation Measurements* 81, 16–22. doi:10.1016/j.radmeas.2015.02.004.
- Freiesleben, T.H., Thomsen, K.J., Jain, M., 2023. Novel luminescence kinetic models for rock surface exposure dating. *Radiation Measurements* 160, 106877. doi:10.1016/j.radmeas.2022.106877.

- Freiesleben, T.H., Thomsen, K.J., Murray, A.S., Sohbati, R., Jain, M., Hvidt, S., Jakobsen, B., Aubry, T., 2022. Rock surface and sand-sized sediment quartz dating using optically stimulated luminescence of a Middle-to-Upper Palaeolithic sequence at the Bordes-Fitte rock shelter (Les Roches d'Abilly, Central France). *Quaternary Geochronology* 73, 101406. doi:10.1016/j.quageo.2022.101406.
- Frouin, M., Lahaye, C., Hernandez, M., Mercier, N., Guibert, P., Brenet, M., Folgado-Lopez, M., Bertran, P., 2014. Chronology of the Middle Palaeolithic open-air site of Combe Brune 2 (Dordogne, France): A multi luminescence dating approach. *Journal of Archaeological Science* 52, 524–534. doi:10.1016/j.jas.2014.09.012.
- Fuchs, M., Dietze, M., Al-Qudah, K., Lomax, J., 2015. Dating desert pavements – First results from a challenging environmental archive. *Quaternary Geochronology* 30, 342–349. doi:10.1016/j.quageo.2015.01.001.
- Fuchs, M., Lang, A., 2001. OSL dating of coarse-grain fluvial quartz using single-aliquot protocols on sediments from NE Peloponnese, Greece. *Quaternary Science Reviews* 20, 783–787. doi:10.1016/S0277-3791(00)00040-8.
- Fuchs, M., Lomax, J., 2019. Stone pavements in arid environments: Reasons for De overdispersion and grain-size dependent OSL ages. *Quaternary Geochronology* 49, 191–198. doi:10.1016/j.quageo.2018.05.013.
- Fuchs, M., Owen, L.A., 2008. Luminescence dating of glacial and associated sediments: Review, recommendations and future directions. *Boreas* 37, 636–659. doi:10.1111/j.1502-3885.2008.00052.x.
- Gabunia, L., Vekua, A., 1995. A Plio-Pleistocene hominid from Dmanisi, East Georgia, Caucasus. *Nature* 373, 509–512. doi:10.1038/373509a0.
- Gaby, S.E., List, F.K., Tehrani, R., 1990. The basement complex of the Eastern Desert and Sinai, in: *The Geology of Egypt*. Routledge.
- Galbraith, R.F., Roberts, R.G., 2012. Statistical aspects of equivalent dose and error calculation and display in OSL dating: An overview and some recommendations. *Quaternary Geochronology* 11, 1–27. doi:10.1016/j.quageo.2012.04.020.

- Galbraith, R.F., Roberts, R.G., Laslett, G.M., Yoshida, H., Olley, J.M., 1999. Optical Dating of Single and Multiple Grains of Quartz from Jinmium Rock Shelter, Northern Australia: Part I, Experimental Design and Statistical Models\*. *Archaeometry* 41, 339–364. doi:10.1111/j.1475-4754.1999.tb00987.x.
- Galli, A., Panzeri, L., Rondini, P., Poggiani Keller, R., Martini, M., 2020. Luminescence Dating of Rock Surface. The Case of Monoliths from the Megalithic Sanctuary of Ossimo-Pat (Valle Camonica, Italy). *Applied Sciences* 10, 7403. doi:10.3390/app10217403.
- Gliganic, L.A., Cohen, T.J., Meyer, M., Molenaar, A., 2017. Variations in luminescence properties of quartz and feldspar from modern fluvial sediments in three rivers. *Quaternary Geochronology* 41, 70–82. doi:10.1016/j.quageo.2017.06.005.
- Gliganic, L.A., Meyer, M.C., May, J.H., Aldenderfer, M.S., Tropper, P., 2021. Direct dating of lithic surface artifacts using luminescence. *Science Advances* doi:10.1126/sciadv.abb3424.
- Gliganic, L.A., Meyer, M.C., Sohbati, R., Jain, M., Barrett, S., 2019. OSL surface exposure dating of a lithic quarry in Tibet: Laboratory validation and application. *Quaternary Geochronology* 49, 199–204. doi:10.1016/j.quageo.2018.04.012.
- Godfrey-Smith, D., Huntley, D.J., Chen, W.H., 1988. Optical dating studies of quartz and feldspar sediment extracts doi:10.1016/0277-3791(88)90032-7.
- Göksu, H.Y., Fremlin, J.H., Irwin, H.T., Fryxell, R., 1974. Age determination of burned flint by a thermoluminescent method. *Science (New York, N.Y.)* 183, 651–654. doi:10.1126/science.183.4125.651.
- Grant, K.M., Rohling, E.J., Westerhold, T., Zabel, M., Heslop, D., Konijnendijk, T., Lourens, L., 2017. A 3 million year index for North African humidity/aridity and the implication of potential pan-African Humid periods. *Quaternary Science Reviews* 171, 100–118. doi:10.1016/j.quascirev.2017.07.005.
- Greenbaum, N., Ekshtain, R., Malinsky-Buller, A., Porat, N., Hovers, E., 2014. The stratigraphy and paleogeography of the Middle Paleolithic open-air site of ‘Ein

- Qashish, Northern Israel. *Quaternary International* 331, 203–215. doi:10.1016/j.quaint.2013.10.037.
- Greilich, S., Glasmacher, U.A., Wagner, G.A., 2002. Spatially resolved detection of luminescence: A unique tool for archaeochronometry. *Naturwissenschaften* 89, 371–375. doi:10.1007/s00114-002-0341-z.
- Greilich, S., Glasmacher, U.A., Wagner, G.A., 2005. Optical Dating of Granitic Stone Surfaces. *Archaeometry* 47, 645–665. doi:10.1111/j.1475-4754.2005.00224.x.
- Groucutt, H.S., Grün, R., Zalmout, I.A.S., Drake, N.A., Armitage, S.J., Candy, I., Clark-Wilson, R., Louys, J., Breeze, P.S., Duval, M., Buck, L.T., Kivell, T.L., Pomeroy, E., Stephens, N.B., Stock, J.T., Stewart, M., Price, G.J., Kinsley, L., Sung, W.W., Alsharekh, A., Al-Omari, A., Zahir, M., Memesh, A.M., Abdulshakoor, A.J., Al-Masari, A.M., Bahameem, A.A., Al Murayyi, K.M.S., Zahrani, B., Scerri, E.L.M., Petraglia, M.D., 2018. Homo sapiens in Arabia by 85,000 years ago. *Nature Ecology & Evolution* 2, 800–809. doi:10.1038/s41559-018-0518-2.
- Grün, R., Beaumont, P.B., Stringer, C.B., 1990. ESR dating evidence for early modern humans at Border Cave in South Africa. *Nature* 344, 537–539. doi:10.1038/344537a0.
- Guérin, G., Mercier, N., Nathan, R., Adamiec, G., Lefrais, Y., 2012. On the use of the infinite matrix assumption and associated concepts: A critical review. *Radiation Measurements* 47, 778–785. doi:10.1016/j.radmeas.2012.04.004.
- Guralnik, B., Matmon, A., Avni, Y., Fink, D., 2010. <sup>10</sup>Be exposure ages of ancient desert pavements reveal Quaternary evolution of the Dead Sea drainage basin and rift margin tilting. *Earth and Planetary Science Letters* 290, 132–141. doi:10.1016/j.epsl.2009.12.012.
- Habermann, J., Schilles, T., Kalchgruber, R., Wagner, G.A., 2000. Steps towards surface dating using luminescence. *Radiation Measurements* 32, 847–851. doi:10.1016/S1350-4487(00)00066-4.
- Hafner, A., Reich, J., Ballmer, A., Bolliger, M., Antolín, F., Charles, M., Emmenegger, L., Fandré, J., Francuz, J., Gobet, E., Hostettler, M., Lotter, A.F., Maczkowski, A.,

- Morales-Molino, C., Naumov, G., Stäheli, C., Szidat, S., Taneski, B., Todoroska, V., Bogaard, A., Kotsakis, K., Tinner, W., 2021. First absolute chronologies of neolithic and bronze age settlements at Lake Ohrid based on dendrochronology and radiocarbon dating. *Journal of Archaeological Science: Reports* 38, 103107. doi:10.1016/j.jasrep.2021.103107.
- Hajdas, I., Ascough, P., Garnett, M.H., Fallon, S.J., Pearson, C.L., Quarta, G., Spalding, K.L., Yamaguchi, H., Yoneda, M., 2021. Radiocarbon dating. *Nature Reviews Methods Primers* 1, 1–26. doi:10.1038/s43586-021-00058-7.
- Haklay, G., Gopher, A., 2020. Geometry and Architectural Planning at Göbekli Tepe, Turkey. *Cambridge Archaeological Journal* 30, 343–357. doi:10.1017/S0959774319000660.
- Hansson, A., Björck, S., Heger, K., Holmgren, S., Linderson, H., Magnell, O., Nilsson, B., Rundgren, M., Sjöström, A., Hammarlund, D., 2018. Shoreline displacement and human resource utilization in the southern Baltic Basin coastal zone during the early Holocene: New insights from a submerged Mesolithic landscape in south-eastern Sweden. *The Holocene* 28, 721–737. doi:10.1177/0959683617744262.
- Harvati, K., Röding, C., Bosman, A.M., Karakostis, F.A., Grün, R., Stringer, C., Karkanas, P., Thompson, N.C., Koutoulidis, V., Moulopoulos, L.A., Gorgoulis, V.G., Kouloukoussa, M., 2019. Apidima Cave fossils provide earliest evidence of *Homo sapiens* in Eurasia. *Nature* 571, 500–504. doi:10.1038/s41586-019-1376-z.
- Heising, A., Heuermann, M., Langenhoff, T., Roth, S., Schoenemann, L., 2020. An Ancillary Building with Collapsed Wall in the villa rustica Binger Wald (Gem. Weiler, Lkr. Mainz-Bingen/D). *Archaeol. Korrespondenzbl.* 50, S. 35–57.
- Henselowsky, F., 2019. Early Late Pleistocene environments in Northeast Africa and their relevance for Anatomically Modern Human dispersal. text.thesis.doctoral. Universität zu Köln.
- Henselowsky, F., Eichstädter, R., Schröder-Ritzrau, A., Herwartz, D., Almoazamy, A., Frank, N., Kindermann, K., Bubenz, O., 2021. Speleothem growth phases in



- the central Eastern Desert of Egypt reveal enhanced humidity throughout MIS 5. *Quaternary International* doi:10.1016/j.quaint.2021.05.006.
- Henselowsky, F., Klasen, N., Timms, R., White, D., Lincoln, P., Blockley, S., Kindermann, K., Bubbenzer, O., 2023. Rare Holocene sediment deposits from Sodmein Playa (Eastern Desert, Egypt)—Stratigraphic assessment and environmental setting. *Geoarchaeology* 38, 186–198. doi:10.1002/gea.21946.
- Hershkovitz, I., Weber, G.W., Quam, R., Duval, M., Grün, R., Kinsley, L., Ayalon, A., Bar-Matthews, M., Valladas, H., Mercier, N., Arsuaga, J.L., Martín-Torres, M., Bermúdez de Castro, J.M., Fornai, C., Martín-Francés, L., Sarig, R., May, H., Krenn, V.A., Slon, V., Rodríguez, L., García, R., Lorenzo, C., Carretero, J.M., Frumkin, A., Shahack-Gross, R., Bar-Yosef Mayer, D.E., Cui, Y., Wu, X., Peled, N., Groman-Yaroslavski, I., Weissbrod, L., Yeshurun, R., Tsatskin, A., Zaidner, Y., Weinstein-Evron, M., 2018. The earliest modern humans outside Africa. *Science* 359, 456–459. doi:10.1126/science.aap8369.
- Hess, T., Riede, F., 2021. The use of lithic raw materials at the Early Mesolithic open-air site Feuersteinacker (Vogelsbergkreis, Germany). *Geoarchaeology* 36, 252–265. doi:10.1002/gea.21828.
- Hoffmann, D.L., Standish, C.D., García-Diez, M., Pettitt, P.B., Milton, J.A., Zilhão, J., Alcolea-González, J.J., Cantalejo-Duarte, P., Collado, H., de Balbín, R., Lorblanchet, M., Ramos-Muñoz, J., Weniger, G.C., Pike, A.W.G., 2018. U-Th dating of carbonate crusts reveals Neandertal origin of Iberian cave art. *Science* 359, 912–915. doi:10.1126/science.aap7778.
- Houston, J., Hartley, A.J., 2003. The central Andean west-slope rainshadow and its potential contribution to the origin of hyper-aridity in the Atacama Desert. *International Journal of Climatology* 23, 1453–1464. doi:10.1002/joc.938.
- Hublin, J.J., Ben-Ncer, A., Bailey, S.E., Freidline, S.E., Neubauer, S., Skinner, M.M., Bergmann, I., Le Cabec, A., Benazzi, S., Harvati, K., Gunz, P., 2017. New fossils from Jebel Irhoud, Morocco and the pan-African origin of *Homo sapiens*. *Nature* 546, 289–292. doi:10.1038/nature22336.

- Hublin, J.J., Sirakov, N., Aldeias, V., Bailey, S., Bard, E., Delvigne, V., Endarova, E., Fagault, Y., Fewlass, H., Hajdinjak, M., Kromer, B., Krumov, I., Marreiros, J., Martisius, N.L., Paskulin, L., Sinet-Mathiot, V., Meyer, M., Pääbo, S., Popov, V., Rezek, Z., Sirakova, S., Skinner, M.M., Smith, G.M., Spasov, R., Talamo, S., Tuna, T., Wacker, L., Welker, F., Wilcke, A., Zahariev, N., McPherron, S.P., Tsanova, T., 2020. Initial Upper Palaeolithic Homo sapiens from Bacho Kiro Cave, Bulgaria. *Nature* 581, 299–302. doi:10.1038/s41586-020-2259-z.
- Huntley, D., Lian, O.B., 2006. Some observations on tunnelling of trapped electrons in feldspars and their implications for optical dating. *Quaternary Science Reviews* 25, 2503–2512. doi:10.1016/j.quascirev.2005.05.011.
- Huntley, D.J., Baril, M., 1997. The K content of the K-feldspars being measured in optical dating or in thermoluminescence dating. *Ancient TL* 15, 11–13.
- Huntley, D.J., Godfrey-Smith, D.I., Haskell, E.H., 1991. Light-induced emission spectra from some quartz and feldspars. *International Journal of Radiation Applications and Instrumentation. Part D. Nuclear Tracks and Radiation Measurements* 18, 127–131. doi:10.1016/1359-0189(91)90104-P.
- Huntley, D.J., Godfrey-Smith, D.I., Thewalt, M.L.W., 1985. Optical dating of sediments. *Nature* 313, 105–107. doi:10.1038/313105a0.
- Huntley, D.J., Lamothe, M., 2001. Ubiquity of anomalous fading in K-feldspars and the measurement and correction for it in optical dating. *Canadian Journal of Earth Sciences* 38, 1093–1106. doi:10.1139/e01-013.
- Hütt, G., Jaek, I., Tchonka, J., 1988. Optical dating: K-feldspars optical response stimulation spectra. *Quaternary Science Reviews* 7, 381–385. doi:10.1016/0277-3791(88)90033-9.
- Huxtable, J., Aitken, M.J., Hedges, J.W., Renfrew, A.C., 1976. Dating a settlement pattern by thermoluminescence: the burnt mounds of Orkney. *Archaeometry* 18, 5–17.

- Ishii, Y., Takahashi, T., Ito, K., 2022. Luminescence dating of cobbles from Pleistocene fluvial terrace deposits of the Ara River, Japan. *Quaternary Geochronology* 67, 101228. doi:10.1016/j.quageo.2021.101228.
- Ivy-Ochs, S., Kober, F., 2008. Surface exposure dating with cosmogenic nuclides. *E&G Quaternary Science Journal* 57, 179–209. doi:10.3285/eg.57.1-2.7.
- Jacobs, Z., Meyer, M.C., Roberts, R.G., Aldeias, V., Dibble, H., El Hajraoui, M.A., 2011. Single-grain OSL dating at La Grotte des Contrebandiers (‘Smugglers’ Cave’), Morocco: Improved age constraints for the Middle Paleolithic levels. *Journal of Archaeological Science* 38, 3631–3643. doi:10.1016/j.jas.2011.08.033.
- Jacobs, Z., Wintle, A.G., Duller, G.A.T., 2003. Optical dating of dune sand from Blombos Cave, South Africa: I—multiple grain data. *Journal of Human Evolution* 44, 599–612. doi:10.1016/S0047-2484(03)00048-4.
- Jain, M., Choi, J.H., Thomas, P.J., 2008. The ultrafast OSL component in quartz: Origins and implications. *Radiation Measurements* 43, 709–714. doi:10.1016/j.radmeas.2008.01.005.
- Jain, M., Murray, A.S., Bøtter-Jensen, L., 2003. Characterisation of blue-light stimulated luminescence components in different quartz samples: Implications for dose measurement. *Radiation Measurements* 37, 441–449. doi:10.1016/S1350-4487(03)00052-0.
- Jain, M., Murray, A.S., Bøtter-Jensen, L., Wintle, A.G., 2005. A single-aliquot regenerative-dose method based on IR (1.49eV) bleaching of the fast OSL component in quartz. *Radiation Measurements* 39, 309–318. doi:10.1016/j.radmeas.2004.05.004.
- Jain, M., Sohbati, R., Guralnik, B., Murray, A.S., Kook, M., Lapp, T., Prasad, A.K., Thomsen, K.J., Buylaert, J.P., 2015. Kinetics of infrared stimulated luminescence from feldspars. *Radiation Measurements* 81, 242–250. doi:10.1016/j.radmeas.2015.02.006.
- Jenkins, G.T.H., Duller, G.A.T., Roberts, H.M., Chiverrell, R.C., Glasser, N.F., 2018. A new approach for luminescence dating glaciofluvial deposits - High

- precision optical dating of cobbles. *Quaternary Science Reviews* 192, 263–273. doi:10.1016/j.quascirev.2018.05.036.
- Jeong, G.Y., Choi, J.H., 2012. Variations in quartz OSL components with lithology, weathering and transportation. *Quaternary Geochronology* 10, 320–326. doi:10.1016/j.quageo.2012.02.023.
- Junge, A., Lomax, J., Shahack-Gross, R., Dunseth, Z.C., Finkelstein, I., Fuchs, M., 2016. OSL Age Determination of Archaeological Stone Structures Using Trapped Aeolian Sediments: A Case Study from the Negev Highlands, Israel. *Geoarchaeology* 31, 550–563. doi:10.1002/gea.21578.
- Kars, R.H., Busschers, F.S., Wallinga, J., 2012. Validating post IR-IRSL dating on K-feldspars through comparison with quartz OSL ages. *Quaternary Geochronology* 12, 74–86. doi:10.1016/j.quageo.2012.05.001.
- Kars, R.H., Reimann, T., Ankjærgaard, C., Wallinga, J., 2014. Bleaching of the post-IR IRSL signal: New insights for feldspar luminescence dating. *Boreas* 43, 780–791. doi:10.1111/bor.12082.
- Kars, R.H., Wallinga, J., Cohen, K.M., 2008. A new approach towards anomalous fading correction for feldspar IRSL dating — tests on samples in field saturation. *Radiation Measurements* 43, 786–790. doi:10.1016/j.radmeas.2008.01.021.
- Kemp, J., Olley, J., Stout, J., Pietsch, T., Corporation, M.A., 2022. Dating stone arrangements using optically stimulated luminescence and fallout radionuclides. *Geoarchaeology* 37, 439–449. doi:10.1002/gea.21902.
- Khalil, S., McClay, K., 2002. Extensional fault-related folding, northwestern Red Sea, Egypt. *Journal of Structural Geology* 24, 743–762. doi:10.1016/S0191-8141(01)00118-3.
- Kindermann, K., Kuper, J., Bubenzer, O., Henselowsky, F., 2021. Ephemeral but not remote – Insights into the late Pleistocene of Northeast Africa, in: Litt, T., Richter, J., Schäbitz, F. (Eds.), *The Journey of Modern Humans from Africa to Europe: Culture-Environmental Interaction and Mobility*. Schweizerbart, Stuttgart, pp. 31–40.

- Kindermann, K., Peer, P., Henselowsky, F., 2018. At the lakeshore – An Early Nubian Complex site linked with lacustrine sediments (Eastern Desert, Egypt). *Quaternary International* 485, 131–139. doi:10.1016/j.quaint.2017.11.006.
- King, G.E., Burow, C., Roberts, H.M., Pearce, N.J.G., 2018. Age determination using feldspar: Evaluating fading-correction model performance. *Radiation Measurements* 119, 58–73. doi:10.1016/j.radmeas.2018.07.013.
- Klasen, N., Hilgers, A., Schmidt, C., Bertrams, M., Schyle, D., Lehmkuhl, F., Richter, J., Radtke, U., 2013. Optical dating of sediments in Wadi Sabra (SW Jordan). *Quaternary Geochronology* 18, 9–16. doi:10.1016/j.quageo.2013.08.002.
- Klasen, N., Loibl, C., Rethemeyer, J., Lehmkuhl, F., 2017. Testing feldspar and quartz luminescence dating of sandy loess sediments from the Doroshivtsy site (Ukraine) against radiocarbon dating. *Quaternary International* 432, 13–19. doi:10.1016/j.quaint.2015.05.036.
- Klíma, B., 1954. Palaeolithic Huts at Dolní Věstonice, Czechoslovakia\*. *Antiquity* 28, 4–14. doi:10.1017/S0003598X00021384.
- Knight, J., Zerboni, A., 2018. Formation of desert pavements and the interpretation of lithic-strewn landscapes of the central Sahara. *Journal of Arid Environments* 153, 39–51. doi:10.1016/j.jaridenv.2018.01.007.
- Kober, F., Ivy-Ochs, S., Schlunegger, F., Baur, H., Kubik, P.W., Wieler, R., 2007. Denudation rates and a topography-driven rainfall threshold in northern Chile: Multiple cosmogenic nuclide data and sediment yield budgets. *Geomorphology* 83, 97–120. doi:10.1016/j.geomorph.2006.06.029.
- Kreutzer, S., Burow, C., Dietze, M., Fuchs, M.C., Schmidt, C., Fischer, M., Friedrich, J., Mercier, N., Smedley, R.K., Christophe, C., Zink, A., Durcan, J., King, G.E., Philippe, A., Guerin, G., Riedesel, S., Autzen, M., Guibert, P., Mittelstrass, D., Gray, H.J., Fuchs, M., 2021. *Luminescence: Comprehensive Luminescence Dating Data Analysis*.

- Kumar, R., Kook, M., Jain, M., 2021. Sediment dating using Infrared Photoluminescence. *Quaternary Geochronology* 62, 101147. doi:10.1016/j.quageo.2020.101147.
- Kumar, R., Kook, M., Murray, A.S., Jain, M., 2018. Towards direct measurement of electrons in metastable states in K-feldspar: Do infrared-photoluminescence and radioluminescence probe the same trap? *Radiation Measurements* 120, 7–13. doi:10.1016/j.radmeas.2018.06.018.
- Lamothe, M., Forget Brisson, L., Hardy, F., 2020. Circumvention of anomalous fading in feldspar luminescence dating using Post-Isothermal IRSL. *Quaternary Geochronology* 57, 101062. doi:10.1016/j.quageo.2020.101062.
- Lang, A., Lindlauer, S., Kuhn, R., Wagner, G.A., 1996. Procedures used for optically and Infrared Stimulated Luminescence Dating of Sediments in Heidelberg. *Ancient TL* 14, 7–11.
- Laskaris, N., Liritzis, I., 2011. A new mathematical approximation of sunlight attenuation in rocks for surface luminescence dating. *Journal of Luminescence* 131, 1874–1884. doi:10.1016/j.jlumin.2011.04.052.
- Lauer, T., Frechen, M., Hoselmann, C., Tsukamoto, S., 2010. Fluvial aggradation phases in the Upper Rhine Graben—new insights by quartz OSL dating. *Proceedings of the Geologists' Association* 121, 154–161. doi:10.1016/j.pgeola.2009.10.006.
- Lehmann, B., Herman, F., Valla, P.G., King, G.E., Biswas, R.H., 2019a. Evaluating post-glacial bedrock erosion and surface exposure duration by coupling in situ optically stimulated luminescence and  $^{10}\text{Be}$  dating. *Earth Surface Dynamics* 7, 633–662. doi:10.5194/esurf-7-633-2019.
- Lehmann, B., Herman, F., Valla, P.G., King, G.E., Biswas, R.H., Ivy-Ochs, S., Steinemann, O., Christl, M., 2019b. Postglacial erosion of bedrock surfaces and deglaciation timing: New insights from the Mont Blanc massif (western Alps). *Geology* 48, 139–144. doi:10.1130/G46585.1.

- Lehmann, B., Valla, P.G., King, G.E., Herman, F., 2018. Investigation of OSL surface exposure dating to reconstruct post-LIA glacier fluctuations in the French Alps (Mer de Glace, Mont Blanc massif). *Quaternary Geochronology* 44, 63–74. doi:10.1016/j.quageo.2017.12.002.
- Li, B., Li, S.H., 2006. Comparison of De estimates using the fast component and the medium component of quartz OSL. *Radiation Measurements* 41, 125–136. doi:10.1016/j.radmeas.2005.06.037.
- Li, B., Li, S.H., 2012a. Luminescence dating of Chinese loess beyond 130 ka using the non-fading signal from K-feldspar. *Quaternary Geochronology* 10, 24–31. doi:10.1016/j.quageo.2011.12.005.
- Li, B., Li, S.H., 2012b. Luminescence dating of Chinese loess beyond 130 ka using the non-fading signal from K-feldspar. *Quaternary Geochronology* 10, 24–31. doi:10.1016/j.quageo.2011.12.005.
- Libby, W.F., 1946. Atmospheric Helium Three and Radiocarbon from Cosmic Radiation. *Physical Review* 69, 671–672. doi:10.1103/PhysRev.69.671.2.
- Libby, W.F., 1961. Radiocarbon Dating. *Science* doi:10.1126/science.133.3453.621.
- Libby, W.F., Anderson, E.C., Arnold, J.R., 1949. Age Determination by Radiocarbon Content: World-Wide Assay of Natural Radiocarbon. *Science* doi:10.1126/science.109.2827.227.
- Liritzis, I., 1994. A new dating method by thermoluminescence of carved megalithic stone building. *Comptes Rendus - Academie des Sciences, Serie II: Sciences de la Terre et des Planetes* 319, 603–610.
- Liritzis, I., Drivaliari, N., Polymeris, G.S., Katagas, C., 2010. NEW QUARTZ TECHNIQUE FOR OSL DATING OF LIMESTONES. *Mediterranean Archaeology and Archaeometry* 10, 81–87.
- Liritzis, I., Galloway, R.B., 1999. Dating implications from solar bleaching of thermoluminescence of ancient marble. *Journal of Radioanalytical and Nuclear Chemistry* 241, 361–368. doi:10.1007/BF02347476.



- Liritzis, I., Polymeris, G.S., Vafiadou, A., Sideris, A., Levy, T.E., 2019. Luminescence dating of stone wall, tomb and ceramics of Kastrouli (Phokis, Greece) Late Helladic settlement: Case study. *Journal of Cultural Heritage* 35, 76–85. doi:10.1016/j.culher.2018.07.009.
- Liritzis, I., Vafiadou, A., 2015. Surface luminescence dating of some Egyptian monuments. *Journal of Cultural Heritage* 16, 134–150. doi:10.1016/j.culher.2014.05.007.
- Liu, J., Cui, F., Murray, A.S., Sohbati, R., Jain, M., Gao, H., Li, W., Li, C., Li, P., Zhou, T., Chen, J., 2019. Resetting of the luminescence signal in modern riverbed cobbles along the course of the Shiyang River, China. *Quaternary Geochronology* 49, 184–190. doi:10.1016/j.quageo.2018.04.004.
- Lomax, J., Mittelstraß, D., Kreutzer, S., Fuchs, M., 2015. OSL, TL and IRSL emission spectra of sedimentary quartz and feldspar samples. *Radiation Measurements* 81, 251–256. doi:10.1016/j.radmeas.2015.02.018.
- Lonergan, L., Platt, J.P., Gallagher, L., 1994. The internal-external zone boundary in the eastern Betic Cordillera, SE Spain. *Journal of Structural Geology* 16, 175–188. doi:10.1016/0191-8141(94)90103-1.
- Luo, M., Chen, J., Liu, J., Qin, J., Owen, L.A., Han, F., Yang, H., Wang, H., Zhang, B., Yin, J., Li, Y., 2018. A test of rock surface luminescence dating using glaciofluvial boulders from the Chinese Pamir. *Radiation Measurements* 120, 290–297. doi:10.1016/j.radmeas.2018.07.017.
- Marder, O., Malinsky-Buller, A., Shahack-Gross, R., Ackermann, O., Ayalon, A., Bar-Matthews, M., Goldsmith, Y., Inbar, M., Rabinovich, R., Hovers, E., 2011. Archaeological horizons and fluvial processes at the Lower Paleolithic open-air site of Revadim (Israel). *Journal of Human Evolution* 60, 508–522. doi:10.1016/j.jhevol.2010.01.007.
- Marquardt, C., Lavenu, A., Ortlieb, L., Godoy, E., Comte, D., 2004. Coastal neotectonics in Southern Central Andes: Uplift and deformation of marine terraces in

- Northern Chile (27S). *Tectonophysics* 394, 193–219. doi:10.1016/j.tecto.2004.07.059.
- Martín-Martín, M., Martín-Algarra, A., 2002. Thrust sequence and syntectonic sedimentation in a piggy-back basin: The Oligo-Aquitania Mula–Pliego Basin (Internal Betic Zone, SE Spain). *Comptes Rendus Geoscience* 334, 363–370. doi:10.1016/S1631-0713(02)01757-1.
- Martini, M., Galli, A., 2007. Ionic mechanisms in the Optically Stimulated Luminescence of quartz. *physica status solidi (c)* 4, 1000–1003. doi:10.1002/pssc.200673862.
- Matmon, A., Simhai, O., Amit, R., Haviv, I., Porat, N., McDonald, E., Benedetti, L., Finkel, R., 2009. Desert pavement-coated surfaces in extreme deserts present the longest-lived landforms on Earth. *GSA Bulletin* 121, 688–697. doi:10.1130/B26422.1.
- McFadden, L.D., Wells, S.G., Jercinovich, M.J., 1987. Influences of eolian and pedogenic processes on the origin and evolution of desert pavements. *Geology* 15, 504–508. doi:10.1130/0091-7613(1987)15{<\$}504:IOEAPP{>\$}2.0.CO;2.
- McHenry, L.J., Stanistreet, I.G., 2018. Tephrochronology of Bed II, Olduvai Gorge, Tanzania, and placement of the Oldowan–Acheulean transition. *Journal of Human Evolution* 120, 7–18. doi:10.1016/j.jhevol.2017.12.006.
- McKeever, S.W.S., Chen, R., 1997. Luminescence models. *Radiation Measurements* 27, 625–661. doi:10.1016/S1350-4487(97)00203-5.
- Medialdea, A., Thomsen, K.J., Murray, A.S., Benito, G., 2014. Reliability of equivalent-dose determination and age-models in the OSL dating of historical and modern palaeoflood sediments. *Quaternary Geochronology* 22, 11–24. doi:10.1016/j.quageo.2014.01.004.
- Medici, T., Foradori, G., Carrer, F., Maschio, R., Gialanella, S., Montagna, M., Pedrotti, A., Angelucci, D., 2014. Una perla in vetro da un contesto pastorale d'altura della Val di Sole (Trento), pp. 115–123.

- Méndez-Quintas, E., Santonja, M., Pérez-González, A., Díaz-Rodríguez, M., Sero-dio Domínguez, A., 2022. Exploring the formation processes on open-air palaeolithic sites: A late Middle Pleistocene Acheulean assemblage at Arbo site (Miño River basin, Spain). *Journal of Archaeological Science: Reports* 43, 103453. doi:10.1016/j.jasrep.2022.103453.
- Mercier, N., Valladas, H., Froget, L., Joron, J.L., Reyss, J.L., Balescu, S., Escutenaire, C., Kozłowski, J., Sitlivy, V., Sobczyk, K., Zieba, A., 2003. Luminescence dates for the palaeolithic site of Piekary IIa (Poland): Comparison between TL of burnt flints and OSL of a loess-like deposit. *Quaternary Science Reviews* 22, 1245–1249. doi:10.1016/S0277-3791(03)00025-8.
- Mercier, N., Valladas, H., Froget, L., Joron, J.L., Vermeersch, P.M., Van Peer, P., Moeyersons, J., 1999. Thermoluminescence Dating of a Middle Palaeolithic Occupation at Sodmein Cave, Red Sea Mountains (Egypt). *Journal of Archaeological Science* 26, 1339–1345. doi:10.1006/jasc.1998.0369.
- Meyer, M., Gliganic, L., Jain, M., Sohbaty, R., Schmidmair, D., 2018. Lithological controls on light penetration into rock surfaces – Implications for OSL and IRSL surface exposure dating. *Radiation Measurements* 120, 298–304. doi:10.1016/j.radmeas.2018.03.004.
- Mineli, T.D., Sawakuchi, A.O., Guralnik, B., Lambert, R., Jain, M., Pupim, F.N., del Rio, I., Guedes, C.C.F., Nogueira, L., 2021. Variation of luminescence sensitivity, characteristic dose and trap parameters of quartz from rocks and sediments. *Radiation Measurements* 144, 106583. doi:10.1016/j.radmeas.2021.106583.
- Moayed, N.K., Sohbaty, R., Murray, A.S., Rades, E.F., Fattahi, M., Ruiz López, J.F., 2022. Rock Surface Luminescence Dating of Prehistoric Rock Art from Central Iberia. *Archaeometry* n/a. doi:10.1111/arcm.12826.
- Moeyersons, J., Vermeersch, P., Neer, V., Connck, D., 1996. Sodmein Cave Site, Red Sea Mountains, Egypt: Development, stratigraphy and palaeoenvironment, in: Pwiti, G., Soper, R. (Eds.), *Aspects of African Archaeology*. University of Zimbabwe Publications, pp. 53–62.

- Moeyersons, J., Vermeersch, P., Van Peer, P., 2002. Dry cave deposits and their palaeoenvironmental significance during the last 115ka, Sodmein Cave, Red Sea Mountains, Egypt. *Quaternary Science Reviews* 21, 837–851. doi:10.1016/S0277-3791(01)00132-9.
- Mökkönen, T., Nordqvist, K., Bel'skij, S., 2007. The Rupunkangas 1a site in the archipelago of ancient Lake Ladoga: A housepit with several rebuilding phases. *Fennoscandia archaeologica* XXIV .
- Murray, A., Arnold, L.J., Buylaert, J.P., Guérin, G., Qin, J., Singhvi, A.K., Smedley, R., Thomsen, K.J., 2021. Optically stimulated luminescence dating using quartz. *Nature Reviews Methods Primers* 1, 1–31. doi:10.1038/s43586-021-00068-5.
- Murray, A., Roberts, R., 1998. Measurement of the equivalent dose in quartz using a regenerative-dose single-aliquot protocol. *Radiation Measurements* 29, 503–515. doi:10.1016/S1350-4487(98)00044-4.
- Murray, A.S., Marten, R., Johnston, A., Martin, P., 1987. Analysis for naturally occurring radionuclides at environmental concentrations by gamma spectrometry. *Journal of Radioanalytical and Nuclear Chemistry* 115, 263–288. doi:10.1007/BF02037443.
- Murray, A.S., Svendsen, J.I., Mangerud, J., Astakhov, V.I., 2007. Testing the accuracy of quartz OSL dating using a known-age Eemian site on the river Sula, northern Russia. *Quaternary Geochronology* 2, 102–109. doi:10.1016/j.quageo.2006.04.004.
- Murray, A.S., Thomsen, K.J., Masuda, N., Buylaert, J.P., Jain, M., 2012. Identifying well-bleached quartz using the different bleaching rates of quartz and feldspar luminescence signals. *Radiation Measurements* 47, 688–695. doi:10.1016/j.radmeas.2012.05.006.
- Murray, A.S., Wintle, A.G., 1998. Factors controlling the shape of the OSL decay curve in quartz. *Radiation Measurements* 29, 65–79. doi:10.1016/S1350-4487(97)00207-2.

- Murray, A.S., Wintle, A.G., 2000. Luminescence dating of quartz using an improved single-aliquot regenerative-dose protocol. *Radiation Measurements* 32, 57–73. doi:10.1016/S1350-4487(99)00253-X.
- Murray, A.S., Wintle, A.G., 2003. The single aliquot regenerative dose protocol: Potential for improvements in reliability. *Radiation Measurements* 37, 377–381. doi:10.1016/S1350-4487(03)00053-2.
- Nishiizumi, K., Caffee, M.W., Finkel, R.C., Brimhall, G., Mote, T., 2005. Remnants of a fossil alluvial fan landscape of Miocene age in the Atacama Desert of northern Chile using cosmogenic nuclide exposure age dating. *Earth and Planetary Science Letters* 237, 499–507. doi:10.1016/j.epsl.2005.05.032.
- Olley, J., Caitcheon, G., Murray, A., 1998. The distribution of apparent dose as determined by Optically Stimulated Luminescence in small aliquots of fluvial quartz: Implications for dating young sediments. *Quaternary Science Reviews* 17, 1033–1040. doi:10.1016/S0277-3791(97)00090-5.
- Ou, X., Roberts, H., Duller, G., Gunn, M., Perkins, W., 2018. Attenuation of light in different rock types and implications for rock surface luminescence dating. *Radiation Measurements* 120, 305–311. doi:10.1016/j.radmeas.2018.06.027.
- Oyedotun, T.D.T., 2018. X-ray fluorescence (XRF) in the investigation of the composition of earth materials: A review and an overview. *Geology, Ecology, and Landscapes* 2, 148–154. doi:10.1080/24749508.2018.1452459.
- Pagonis, V., Wintle, A., Chen, R., Wang, X., 2008. A theoretical model for a new dating protocol for quartz based on thermally transferred OSL (TT-OSL). *Radiation Measurements* 43, 704–708. doi:10.1016/j.radmeas.2008.01.025.
- Papanastassiou, D., Gaki-Papanastassiou, K., Maroukian, H., 2005. Recognition of past earthquakes along the Sparta fault (Peloponnesus, southern Greece) during the Holocene, by combining results of different dating techniques. *Journal of Geodynamics* 40, 189–199. doi:10.1016/j.jog.2005.07.015.

- Pederson, J.L., Chapot, M.S., Simms, S.R., Sohbati, R., Rittenour, T.M., Murray, A.S., Cox, G., 2014. Age of Barrier Canyon-style rock art constrained by cross-cutting relations and luminescence dating techniques. *Proceedings of the National Academy of Sciences* 111, 12986–12991. doi:10.1073/pnas.1405402111.
- Pettijohn, F.J., Potter, P.E., Siever, R., 1987. *Sand and Sandstone*. 2nd ed., Springer.
- Pietsch, T.J., Olley, J.M., Nanson, G.C., 2008. Fluvial transport as a natural luminescence sensitiser of quartz. *Quaternary Geochronology* 3, 365–376. doi:10.1016/j.quageo.2007.12.005.
- Polikreti, K., Michael, C., Maniatis, Y., 2002. Authenticating marble sculpture with thermoluminescence. *Ancient TL* 20, 11–18.
- Poolton, N.R.J., Bøtter-Jensen, L., Rink, W.J., 1995. An optically stimulated luminescence study of flint related to radiation dosimetry. *Radiation Measurements* 24, 551–555. doi:10.1016/1350-4487(94)00115-H.
- Pop, E., Reidsma, F.H., Reimann, T., Sier, M.J., Arps, C.E.S., Gaudzinski-Windheuser, S., Roebroeks, W., 2021. Identifying Heated Rocks Through Feldspar Luminescence Analysis (pIRIR290) and a Critical Evaluation of Macroscopic Assessment. *Journal of Paleolithic Archaeology* 4, 13. doi:10.1007/s41982-021-00094-5.
- Porat, N., Davidovich, U., Avni, Y., Avni, G., Gadot, Y., 2018. Using OSL Measurements to Decipher Soil History in Archaeological Terraces, Judean Highlands, Israel. *Land Degradation & Development* 29, 643–650. doi:10.1002/ldr.2729.
- Prasad, A.K., Poolton, N.R.J., Kook, M., Jain, M., 2017. Optical dating in a new light: A direct, non-destructive probe of trapped electrons. *Scientific Reports* 7, 12097. doi:10.1038/s41598-017-10174-8.
- Prescott, J.R., Hutton, J.T., 1994. Cosmic ray contributions to dose rates for luminescence and ESR dating: Large depths and long-term time variations. *Radiation Measurements* 23, 497–500. doi:10.1016/1350-4487(94)90086-8.
- Preti, F., Errico, A., Caruso, M., Dani, A., Guastini, E., 2018. Dry-stone wall terrace monitoring and modelling. *Land Degradation & Development* 29, 1806–1818. doi:10.1002/ldr.2926.

- Preusser, F., 2001. IRSL dating of K-rich feldspars using the SAR protocol: Comparison with independent age control. *Ancient TL* 21, 17–23.
- Preusser, F., Degering, D., Fuchs, M., Hilgers, A., Kadereit, A., Klasen, N., Krbetschek, M., Richter, D., Spencer, J.Q.G., 2008. Luminescence dating: Basics, methods and applications. *E&G Quaternary Science Journal* 57, 95–149. doi:10.3285/eg.57.1-2.5.
- Prugnolle, F., Manica, A., Balloux, F., 2005. Geography predicts neutral genetic diversity of human populations. *Current biology : CB* 15, R159–R160. doi:10.1016/j.cub.2005.02.038.
- R Core Team, 2021. R: A Language and Environment for Statistical Computing. R Foundation for Statistical Computing. Vienna, Austria. URL: <https://www.R-project.org/>.
- Rades, E.F., Sohbati, R., Lüthgens, C., Jain, M., Murray, A.S., 2018. First luminescence-depth profiles from boulders from moraine deposits: Insights into glaciation chronology and transport dynamics in Malta valley, Austria. *Radiation Measurements* 120, 281–289. doi:10.1016/j.radmeas.2018.08.011.
- Radtke, U., 1988. Marine terraces in Chile (22–32S) — Geomorphology, chronostratigraphy and neotectonics : Preliminary results II, in: *Quaternary of South America and Antarctic Peninsula*. CRC Press.
- Ramos, V.A., 2009. Anatomy and global context of the Andes: Main geologic features and the Andean orogenic cycle. *Memoir of the Geological Society of America* 204, 31–65. doi:10.1130/2009.1204(02).
- Ramsey, C.B., 2008. Radiocarbon Dating: Revolutions in Understanding. *Archaeometry* 50, 249–275. doi:10.1111/j.1475-4754.2008.00394.x.
- Regard, V., Saillard, M., Martinod, J., Audin, L., Carretier, S., Pedoja, K., Riquelme, R., Paredes, P., Hérail, G., 2010. Renewed uplift of the Central Andes Forearc revealed by coastal evolution during the Quaternary. *Earth and Planetary Science Letters* 297, 199–210. doi:10.1016/j.epsl.2010.06.020.



- Reimann, T., Tsukamoto, S., 2012. Dating the recent past (<500 years) by post-IR IRSL feldspar – Examples from the North Sea and Baltic Sea coast. *Quaternary Geochronology* 10, 180–187. doi:10.1016/j.quageo.2012.04.011.
- Reimer, P.J., Austin, W.E.N., Bard, E., Bayliss, A., Blackwell, P.G., Ramsey, C.B., Butzin, M., Cheng, H., Edwards, R.L., Friedrich, M., Grootes, P.M., Guilderson, T.P., Hajdas, I., Heaton, T.J., Hogg, A.G., Hughen, K.A., Kromer, B., Manning, S.W., Muscheler, R., Palmer, J.G., Pearson, C., van der Plicht, J., Reimer, R.W., Richards, D.A., Scott, E.M., Southon, J.R., Turney, C.S.M., Wacker, L., Adolphi, F., Büntgen, U., Capano, M., Fahrni, S.M., Fogtmann-Schulz, A., Friedrich, R., Köhler, P., Kudsk, S., Miyake, F., Olsen, J., Reinig, F., Sakamoto, M., Sookdeo, A., Talamo, S., 2020. The IntCal20 Northern Hemisphere Radiocarbon Age Calibration Curve (0–55 cal kBP). *Radiocarbon* 62, 725–757. doi:10.1017/RDC.2020.41.
- Rethemeyer, J., Gierga, M., Heinze, S., Stolz, A., Wotte, A., Wischhöfer, P., Berg, S., Melchert, J.O., Dewald, A., 2019. Current Sample Preparation and Analytical Capabilities of the Radiocarbon Laboratory at CologneAMS. *Radiocarbon* 61, 1449–1460. doi:10.1017/RDC.2019.16.
- Richter, D., Grün, R., Joannes-Boyau, R., Steele, T.E., Amani, F., Rué, M., Fernandes, P., Raynal, J.P., Geraads, D., Ben-Ncer, A., Hublin, J.J., McPherron, S.P., 2017. The age of the hominin fossils from Jebel Irhoud, Morocco, and the origins of the Middle Stone Age. *Nature* 546, 293–296. doi:10.1038/nature22335.
- Richter, D., Mercier, N., Valladas, H., Jaubert, J., Texier, P.J., Brugal, J.P., Kervazo, B., Reyss, J.L., Joron, J.L., Wagner, G.A., 2007. Thermoluminescence dating of heated flint from the Mousterian site of Bérigoule, Murs, Vaucluse, France. *Journal of Archaeological Science* 34, 532–539. doi:10.1016/j.jas.2006.06.006.
- Riedesel, S., Autzen, M., 2020. Beta and gamma dose rate attenuation in rocks and sediment. *Radiation Measurements* 133, 106295. doi:10.1016/j.radmeas.2020.106295.
- Riedesel, S., Autzen, M., 2021. `calc_CobbleDoseRate()`: Calculate dose rate of slices in a spherical cobble.

- Ritter, B., Wennrich, V., Medialdea, A., Brill, D., King, G., Schneiderwind, S., Niemann, K., Fernández-Galego, E., Diederich, J., Rolf, C., Bao, R., Melles, M., Dunai, T.J., 2019. “Climatic fluctuations in the hyperarid core of the Atacama Desert during the past 215 ka”. *Scientific Reports* 9, 5270. doi:10.1038/s41598-019-41743-8.
- Roberts, H.M., 2007. Assessing the effectiveness of the double-SAR protocol in isolating a luminescence signal dominated by quartz. *Radiation Measurements* 42, 1627–1636. doi:10.1016/j.radmeas.2007.09.010.
- Rodríguez-Fernández, J., Azor, A., Azañón, J.M., 2011. The Betic Intramontane Basins (SE Spain): Stratigraphy, Subsidence, and Tectonic History, in: *Tectonics of Sedimentary Basins*. John Wiley & Sons, Ltd. chapter 23, pp. 461–479. doi:10.1002/9781444347166.ch23.
- Said, R., 1990. Red Sea coastal plain, in: *The Geology of Egypt*. Routledge.
- Sauvet, G., Bourrillon, R., Conkey, M., Fritz, C., Gárate-Maidagan, D., Rivero Vilá, O., Tosello, G., White, R., 2017. Uranium–thorium dating method and Palaeolithic rock art. *Quaternary International* 432, 86–92. doi:10.1016/j.quaint.2015.03.053.
- Sawakuchi, A.O., Blair, M.W., DeWitt, R., Faleiros, F.M., Hyppolito, T., Guedes, C.C.F., 2011. Thermal history versus sedimentary history: OSL sensitivity of quartz grains extracted from rocks and sediments. *Quaternary Geochronology* 6, 261–272. doi:10.1016/j.quageo.2010.11.002.
- Scerri, E.M.L., Thomas, M.G., Manica, A., Gunz, P., Stock, J.T., Stringer, C., Grove, M., Groucutt, H.S., Timmermann, A., Rightmire, G.P., d’Errico, F., Tryon, C.A., Drake, N.A., Brooks, A.S., Dennell, R.W., Durbin, R., Henn, B.M., Lee-Thorp, J., deMenocal, P., Petraglia, M.D., Thompson, J.C., Scally, A., Chikhi, L., 2018. Did Our Species Evolve in Subdivided Populations across Africa, and Why Does It Matter? *Trends in Ecology & Evolution* 33, 582–594. doi:10.1016/j.tree.2018.05.005.
- Scheib, C.L., Hui, R., D’Atanasio, E., Wohns, A.W., Inskip, S.A., Rose, A., Cessford, C., O’Connell, T.C., Robb, J.E., Evans, C., Patten, R., Kivisild, T., 2019. East

- Anglian early Neolithic monument burial linked to contemporary Megaliths. *Annals of Human Biology* 46, 145–149. doi:10.1080/03014460.2019.1623912.
- Schmidt, C., Kindermann, K., van Peer, P., Bubenzer, O., 2015. Multi-emission luminescence dating of heated chert from the Middle Stone Age sequence at Sodmein Cave (Red Sea Mountains, Egypt). *Journal of Archaeological Science* 63, 94–103. doi:10.1016/j.jas.2015.08.016.
- Schween, J.H., Hoffmeister, D., Löhnert, U., 2020. Filling the observational gap in the Atacama Desert with a new network of climate stations. *Global and Planetary Change* 184, 103034. doi:10.1016/j.gloplacha.2019.103034.
- Sellwood, E.L., Guralnik, B., Kook, M., Prasad, A.K., Sohbaty, R., Hippe, K., Wallinga, J., Jain, M., 2019. Optical bleaching front in bedrock revealed by spatially-resolved infrared photoluminescence. *Scientific Reports* 9, 2611. doi:10.1038/s41598-019-38815-0.
- Sellwood, E.L., Kook, M., Jain, M., 2022a. A 2D imaging system for mapping luminescence-depth profiles for rock surface dating. *Radiation Measurements* 150, 106697. doi:10.1016/j.radmeas.2021.106697.
- Sellwood, E.L., Kook, M., Jain, M., 2022b. Rapid in situ assessment of luminescence-bleaching depths for deriving burial and exposure chronologies of rock surfaces. *Quaternary Geochronology* 67, 101227. doi:10.1016/j.quageo.2021.101227.
- Silva, P.G., Mather, A.E., Goy, J.L., Zazo, C., 1996. Controles en el Desarrollo y Evolución del Drenaje en Zonas Tectónicamente Activas: el Caso del Río Mula (Región de Murcia, SE España) , 16.
- Simkins, L.M., Simms, A.R., DeWitt, R., 2013. Relative sea-level history of Marguerite Bay, Antarctic Peninsula derived from optically stimulated luminescence-dated beach cobbles. *Quaternary Science Reviews* 77, 141–155. doi:10.1016/j.quascirev.2013.07.027.
- Simms, A.R., DeWitt, R., Kouremenos, P., Drewry, A.M., 2011. A new approach to reconstructing sea levels in Antarctica using optically stimulated luminescence

- of cobble surfaces. *Quaternary Geochronology* 6, 50–60. doi:10.1016/j.quageo.2010.06.004.
- Singarayer, J.S., Bailey, R.M., 2003. Further investigations of the quartz optically stimulated luminescence components using linear modulation. *Radiation Measurements* 37, 451–458. doi:10.1016/S1350-4487(03)00062-3.
- Singarayer, J.S., Bailey, R.M., Rhodes, E.J., 2000. Potential of the slow component of quartz OSL for age determination of sedimentary samples. *Radiation Measurements* 32, 873–880. doi:10.1016/S1350-4487(00)00074-3.
- Skoglund, P., Mathieson, I., 2018. Ancient Genomics of Modern Humans: The First Decade. *Annual Review of Genomics and Human Genetics* 19, 381–404. doi:10.1146/annurev-genom-083117-021749.
- Smedley, R.K., Duller, G.A.T., Pearce, N.J.G., Roberts, H.M., 2012. Determining the K-content of single-grains of feldspar for luminescence dating. *Radiation Measurements* 47, 790–796. doi:10.1016/j.radmeas.2012.01.014.
- Smedley, R.K., Duller, G.A.T., Roberts, H.M., 2015. Bleaching of the post-IR IRSL signal from individual grains of K-feldspar: Implications for single-grain dating. *Radiation Measurements* 79, 33–42. doi:10.1016/j.radmeas.2015.06.003.
- Smedley, R.K., Skirrow, G.K.A., 2020. Luminescence Dating in Fluvial Settings: Overcoming the Challenge of Partial Bleaching, in: Herget, J., Fontana, A. (Eds.), *Palaeohydrology: Traces, Tracks and Trails of Extreme Events*. Springer International Publishing, Cham. *Geography of the Physical Environment*, pp. 155–168. doi:10.1007/978-3-030-23315-0\\_8.
- Smedley, R.K., Small, D., Jones, R.S., Brough, S., Bradley, J., Jenkins, G.T.H., 2021. Erosion rates in a wet, temperate climate derived from rock luminescence techniques. *Geochronology* 3, 525–543. doi:10.5194/gchron-3-525-2021.
- Smith, B.W., Rhodes, E.J., 1994. Charge movements in quartz and their relevance to optical dating. *Radiation Measurements* 23, 329–333. doi:10.1016/1350-4487(94)90060-4.

- Sohbati, R., Borella, J., Murray, A., Quigley, M., Buylaert, J.P., 2016. Optical dating of loessic hillslope sediments constrains timing of prehistoric rockfalls, Christchurch, New Zealand. *Journal of Quaternary Science* 31, 678–690. doi:10.1002/jqs.2895.
- Sohbati, R., Jain, M., Murray, A., 2012a. Surface exposure dating of non-terrestrial bodies using optically stimulated luminescence: A new method. *Icarus* 221, 160–166. doi:10.1016/j.icarus.2012.07.017.
- Sohbati, R., Liu, J., Jain, M., Murray, A., Egholm, D., Paris, R., Guralnik, B., 2018. Centennial- to millennial-scale hard rock erosion rates deduced from luminescence-depth profiles. *Earth and Planetary Science Letters* 493, 218–230. doi:10.1016/j.epsl.2018.04.017.
- Sohbati, R., Murray, A., Jain, M., Buylaert, J.P., Thomsen, K., 2011. Investigating the resetting of OSL signals in rock surfaces. *Geochronometria* 38, 249–258. doi:10.2478/s13386-011-0029-2.
- Sohbati, R., Murray, A.S., Buylaert, J.P., Almeida, N.A.C., Cunha, P.P., 2012b. Optically stimulated luminescence (OSL) dating of quartzite cobbles from the Tapada do Montinho archaeological site (east-central Portugal): OSL dating of quartzite cobbles, Tapada do Montinho, Portugal. *Boreas* 41, 452–462. doi:10.1111/j.1502-3885.2012.00249.x.
- Sohbati, R., Murray, A.S., Chapot, M.S., Jain, M., Pederson, J., 2012c. Optically stimulated luminescence (OSL) as a chronometer for surface exposure dating. *Journal of Geophysical Research: Solid Earth* 117. doi:10.1029/2012JB009383.
- Sohbati, R., Murray, A.S., Porat, N., Jain, M., Avner, U., 2015. Age of a prehistoric “Rodedian” cult site constrained by sediment and rock surface luminescence dating techniques. *Quaternary Geochronology* 30, 90–99. doi:10.1016/j.quageo.2015.09.002.
- Souza, P.E., Sohbati, R., Murray, A.S., Clemmensen, L.B., Kroon, A., Nielsen, L., 2021. Optical dating of cobble surfaces determines the chronology of Holocene beach ridges in Greenland. *Boreas* 50, 606–618. doi:10.1111/bor.12507.

- Souza, P.E., Sohbati, R., Murray, A.S., Kroon, A., Clemmensen, L.B., Hede, M.U., Nielsen, L., 2019. Luminescence dating of buried cobble surfaces from sandy beach ridges: A case study from Denmark. *Boreas* 48, 841–855. doi:10.1111/bor.12402.
- Spooner, N., Aitken, M., Smith, B., Franks, M., McElroy, C., 1990. Archaeological Dating by Infrared-Stimulated Luminescence Using a Diode Array. *Radiation Protection Dosimetry* 34, 83–86. doi:10.1093/oxfordjournals.rpd.a080853.
- Steffen, D., Preusser, F., Schlunegger, F., 2009. OSL quartz age underestimation due to unstable signal components. *Quaternary Geochronology* 4, 353–362. doi:10.1016/j.quageo.2009.05.015.
- Steiner, A.E., Conrey, R.M., Wolff, J.A., 2017. PXRF calibrations for volcanic rocks and the application of in-field analysis to the geosciences. *Chemical Geology* 453, 35–54. doi:10.1016/j.chemgeo.2017.01.023.
- Stevens, T., Buylaert, J.P., Murray, A.S., 2009. Towards development of a broadly-applicable SAR TT-OSL dating protocol for quartz. *Radiation Measurements* 44, 639–645. doi:10.1016/j.radmeas.2009.02.015.
- Stokes, S., 1994. The timing of OSL sensitivity changes in a natural quartz. *Radiation Measurements* 23, 601–605. doi:10.1016/1350-4487(94)90106-6.
- Stokes, S., Hetzel, R., Bailey, R.M., Mingxin, T., 2003. Combined IRSL-OSL single aliquot regeneration (SAR) equivalent dose (De) estimates from source proximal Chinese loess. *Quaternary Science Reviews* 22, 975–983. doi:10.1016/S0277-3791(03)00044-1.
- Stringer, C., 2016. The origin and evolution of *Homo sapiens*. *Philosophical Transactions of the Royal Society B: Biological Sciences* 371, 20150237. doi:10.1098/rstb.2015.0237.
- Swartz, D.H., Arden, Jr., D.D., 1960. Geologic History of Red Sea Area1. *AAPG Bulletin* 44, 1621–1637. doi:10.1306/0BDA6224-16BD-11D7-8645000102C1865D.
- Terradillos-Bernal, M., Díez Fernández-Lomana, J.C., Jordá Pardo, J.F., Benito-Calvo, A., Clemente, I., Marcos-Sáiz, F.J., 2017. San Quirce (Palencia, Spain).

- A Neanderthal open air campsite with short term-occupation patterns. *Quaternary International* 435, 115–128. doi:10.1016/j.quaint.2015.09.082.
- Thiel, C., Buylaert, J.P., Murray, A.S., Terhorst, B., Tsukamoto, S., Frechen, M., Sprafke, T., 2011. Investigating the chronostratigraphy of prominent palaeosols in Lower Austria using post-IR IRSL dating. *E&G Quaternary Science Journal* 60, 137–152. doi:10.3285/eg.60.1.10.
- Thompson, W.K., Arvidsson, D., Murray, A.S., Blidberg, A., Hansen, V., 2022. Rock and sediment luminescence dating of an ancient circular stone-walled enclosure at Sønnebøe, northern Scania, Sweden. *Quaternary Geochronology* 72, 101340. doi:10.1016/j.quageo.2022.101340.
- Thomsen, K., Murray, A., Jain, M., Bøtter-Jensen, L., 2008. Laboratory fading rates of various luminescence signals from feldspar-rich sediment extracts. *Radiation Measurements - RADIAT MEAS* 43, 1474–1486. doi:10.1016/j.radmeas.2008.06.002.
- Thomsen, K.J., Kook, M., Murray, A.S., Jain, M., 2018. Resolving luminescence in spatial and compositional domains. *Radiation Measurements* 120, 260–266. doi:10.1016/j.radmeas.2018.06.002.
- Thomsen, K.J., Murray, A.S., Bøtter-Jensen, L., Kinahan, J., 2007. Determination of burial dose in incompletely bleached fluvial samples using single grains of quartz. *Radiation Measurements* 42, 370–379. doi:10.1016/j.radmeas.2007.01.041.
- Timar-Gabor, A., Constantin, D., Buylaert, J.P., Jain, M., Murray, A.S., Wintle, A.G., 2015. Fundamental investigations of natural and laboratory generated SAR dose response curves for quartz OSL in the high dose range. *Radiation Measurements* 81, 150–156. doi:10.1016/j.radmeas.2015.01.013.
- Timmermann, A., Friedrich, T., 2016. Late Pleistocene climate drivers of early human migration. *Nature* 538, 92–95. doi:10.1038/nature19365.
- Tsukamoto, S., Nagashima, K., Murray, A.S., Tada, R., 2011. Variations in OSL components from quartz from Japan sea sediments and the possibility of reconstructing



- provenance. *Quaternary International* 234, 182–189. doi:10.1016/j.quaint.2010.09.003.
- Ugalde, P.C., Quade, J., Santoro, C.M., Holliday, V.T., 2020. Processes of Paleoindian site and desert pavement formation in the Atacama Desert, Chile. *Quaternary Research* 98, 58–80. doi:10.1017/qua.2020.39.
- Vafiadou, A., Murray, A.S., Liritzis, I., 2007. Optically stimulated luminescence (OSL) dating investigations of rock and underlying soil from three case studies. *Journal of Archaeological Science* 34, 1659–1669. doi:10.1016/j.jas.2006.12.004.
- Vermeersch, P., Peer, P., Moeyersons, J., Van Neer, W., 1994. Sodmein Cave site, Red Sea Mountains (Egypt). *Sahara* 6 6.
- Vermeersch, P.M., Van Neer, W., 2015. Nile behaviour and Late Palaeolithic humans in Upper Egypt during the Late Pleistocene. *Quaternary Science Reviews* 130, 155–167. doi:10.1016/j.quascirev.2015.03.025.
- Victor, P., Sobiesiak, M., Glodny, J., Nielsen, S.N., Oncken, O., 2011. Long-term persistence of subduction earthquake segment boundaries: Evidence from Mejillones Peninsula, northern Chile. *Journal of Geophysical Research: Solid Earth* 116. doi:10.1029/2010JB007771.
- Wagner, G.A., Krbetschek, M., Degering, D., Bahain, J.J., Shao, Q., Falguères, C., Voinchet, P., Dolo, J.M., Garcia, T., Rightmire, G.P., 2010. Radiometric dating of the type-site for *Homo heidelbergensis* at Mauer, Germany. *Proceedings of the National Academy of Sciences* 107, 19726–19730. doi:10.1073/pnas.1012722107.
- Walk, J., Stauch, G., Bartz, M., Brückner, H., Lehmkuhl, F., 2019. Geomorphology of the coastal alluvial fan complex Guanillos, northern Chile. *Journal of Maps* 15, 436–447. doi:10.1080/17445647.2019.1611499.
- Walk, J., Stauch, G., Reyers, M., Vásquez, P., Sepúlveda, F.A., Bartz, M., Hoffmeister, D., Brückner, H., Lehmkuhl, F., 2020. Gradients in climate, geology, and topography affecting coastal alluvial fan morphodynamics in hyperarid regions – The Atacama perspective. *Global and Planetary Change* 185, 102994. doi:10.1016/j.gloplacha.2019.102994.

- Wang, X., Lu, Y., Wintle, A., 2006. Recuperated OSL dating of fine-grained quartz in Chinese loess. *Quaternary Geochronology* 1, 89–100. doi:10.1016/j.quageo.2006.05.020.
- Wells, S.G., McFadden, L.D., Poths, J., Olinger, C.T., 1995. Cosmogenic  $^3\text{He}$  surface-exposure dating of stone pavements: Implications for landscape evolution in deserts. *Geology* 23, 613–616. doi:10.1130/0091-7613(1995)023<0613:CHSEDO>2.3.CO;2.
- Wintle, A.G., 1973. Anomalous Fading of Thermo-luminescence in Mineral Samples. *Nature* 245, 143–144. doi:10.1038/245143a0.
- Wintle, A.G., 1980. Thermoluminescence Dating: A Review of Recent Applications to Non-Pottery Materials. *Archaeometry* 22, 113–122. doi:10.1111/j.1475-4754.1980.tb00936.x.
- Wintle, A.G., Murray, A.S., 2006. A review of quartz optically stimulated luminescence characteristics and their relevance in single-aliquot regeneration dating protocols. *Radiation Measurements* 41, 369–391. doi:10.1016/j.radmeas.2005.11.001.
- Zhang, J., Li, S.H., 2020. Review of the Post-IR IRSL Dating Protocols of K-Feldspar. *Methods and Protocols* 3, 7. doi:10.3390/mps3010007.
- Zilhão, J., Ajas, A., Badal, E., Burow, C., Kehl, M., López-Sáez, J.A., Pimenta, C., Preece, R.C., Sanchis, A., Sanz, M., Weniger, G.C., White, D., Wood, R., Angelucci, D.E., Villaverde, V., Zapata, J., 2016. Cueva Antón: A multi-proxy MIS 3 to MIS 5a paleoenvironmental record for SE Iberia. *Quaternary Science Reviews* 146, 251–273. doi:10.1016/j.quascirev.2016.05.038.
- Zilhão, J., Anesin, D., Aubry, T., Badal, E., Cabanes, D., Kehl, M., Klasen, N., Lucena, A., Martín-Lerma, I., Martínez, S., Matias, H., Susini, D., Steier, P., Wild, E.M., Angelucci, D.E., Villaverde, V., Zapata, J., 2017. Precise dating of the Middle-to-Upper Paleolithic transition in Murcia (Spain) supports late Neandertal persistence in Iberia. *Heliyon* 3, e00435. doi:10.1016/j.heliyon.2017.e00435.
- Zilhão, J., Angelucci, D.E., Badal-García, E., d’Errico, F., Daniel, F., Dayet, L., Douka, K., Higham, T.F.G., Martínez-Sánchez, M.J., Montes-Bernárdez,

R., Murcia-Mascarós, S., Pérez-Sirvent, C., Roldán-García, C., Vanhaeren, M., Villaverde, V., Wood, R., Zapata, J., 2010. Symbolic use of marine shells and mineral pigments by Iberian Neandertals. *Proceedings of the National Academy of Sciences* 107, 1023–1028. doi:10.1073/pnas.0914088107.

## Appendix A

# Supplementary material: Rock Surface IRSL Dating of Buried Cobbles from an Alpine Dry-Stone Structure in Val di Sole, Italy

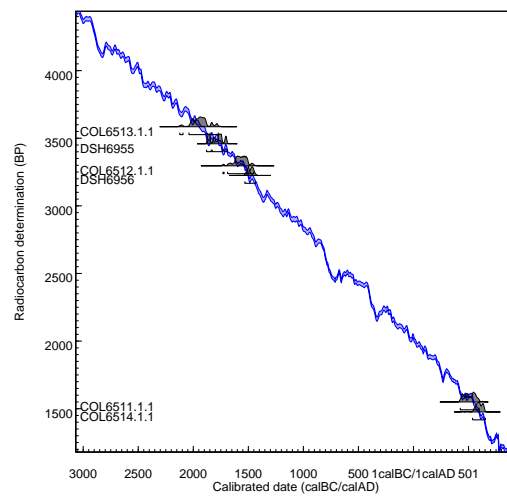


Fig. A.1: Radiocarbon ages and calibration curve (Reimer et al., 2020), calibrated and plotted with OxCal 4.4.2 (Bronk Ramsey, 2009).



Fig. B.2: The dated cobbles from MZ051S. MZ051S-2, MZ051S-7 and MZ051S-8 are paragneisses; MZ051S-3 is an orthogneiss. The pictures are taken after material (approximately 200 grams) has been removed for dose rate measurements (gamma spectrometry).

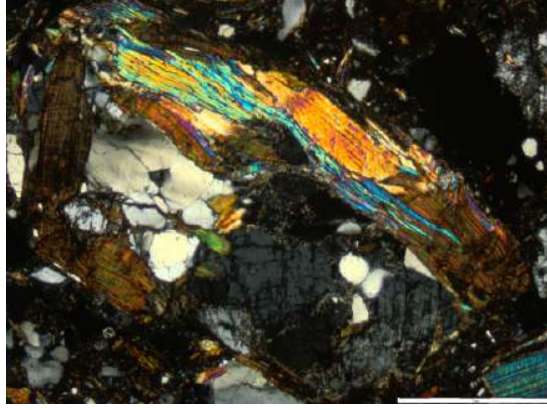


Fig. B.3: Photomicrograph of a thin section of a paragneiss (TUG) from Val di Sole, viewed in cross-polarized light. Quartz and feldspar grains are surrounded by biotite and muscovite. Photomicrograph: Laura Vezzoni.

## 825 Appendix C. Dose recovery test, residual doses, fading measurements, and fitting residuals

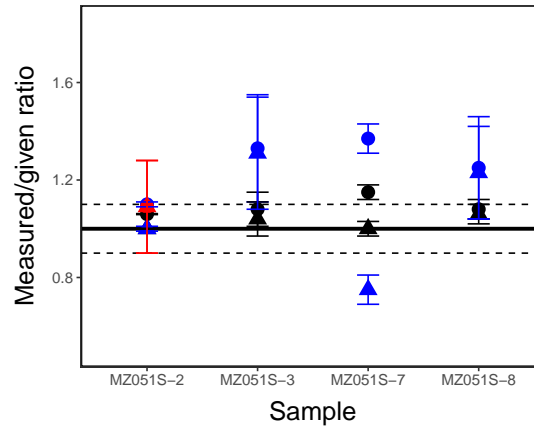


Fig. C.1: Results from dose recovery tests for IRSL<sub>50</sub> (black), pIR-IRSL<sub>150</sub> (blue) and pIR-IRSL<sub>290</sub> (red) signals. The points represent mean values from three or more slices and the error bars represent the 1 sigma confidence interval. Dose recovery is plotted with residual subtraction (triangles) and without (circles). The dashed lines represent  $\pm 10\%$  from unity. The slices were either bleached in a solar simulator for 24 hours (IRSL<sub>50</sub> or pIR-IRSL<sub>150</sub>), or heated at 450 °C for 300 seconds (pIR-IRSL<sub>290</sub>), before measurements.



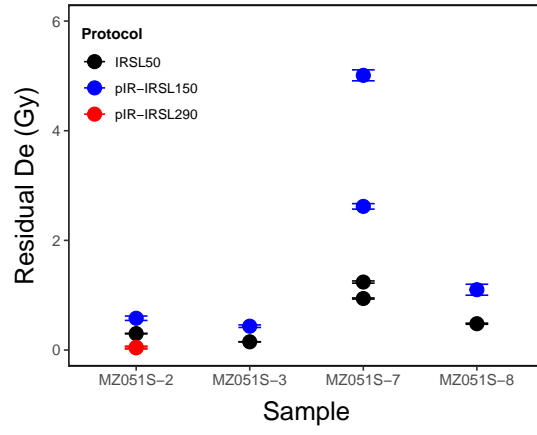


Fig. C.2: Results from residual measurements of the  $\text{IRSL}_{50}$ ,  $\text{pIR-IRSL}_{150}$  and  $\text{pIR-IRSL}_{290}$  signals. The points represent individual slices and the error bars represent measurement uncertainties. The slices were bleached in a solar simulator for 24 hours prior to measurements (except for those measured with the  $\text{pIR}_{290}$ , which were annealed for 300 seconds at 450 °C)

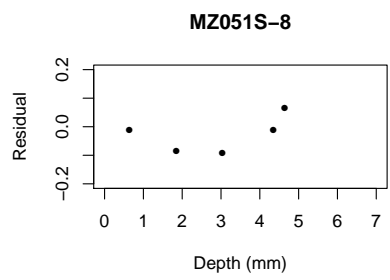
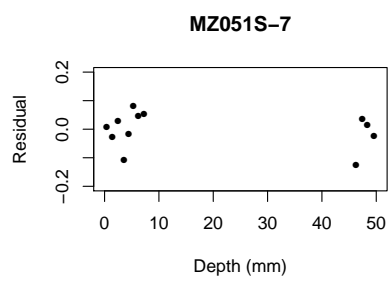
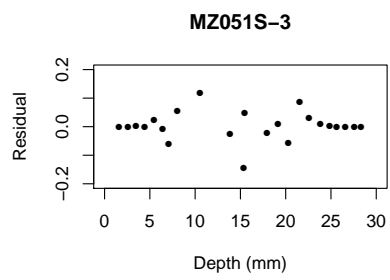


Fig. C.3: Residuals from nonlinear least-squares fitting in R (R Core Team, 2019).

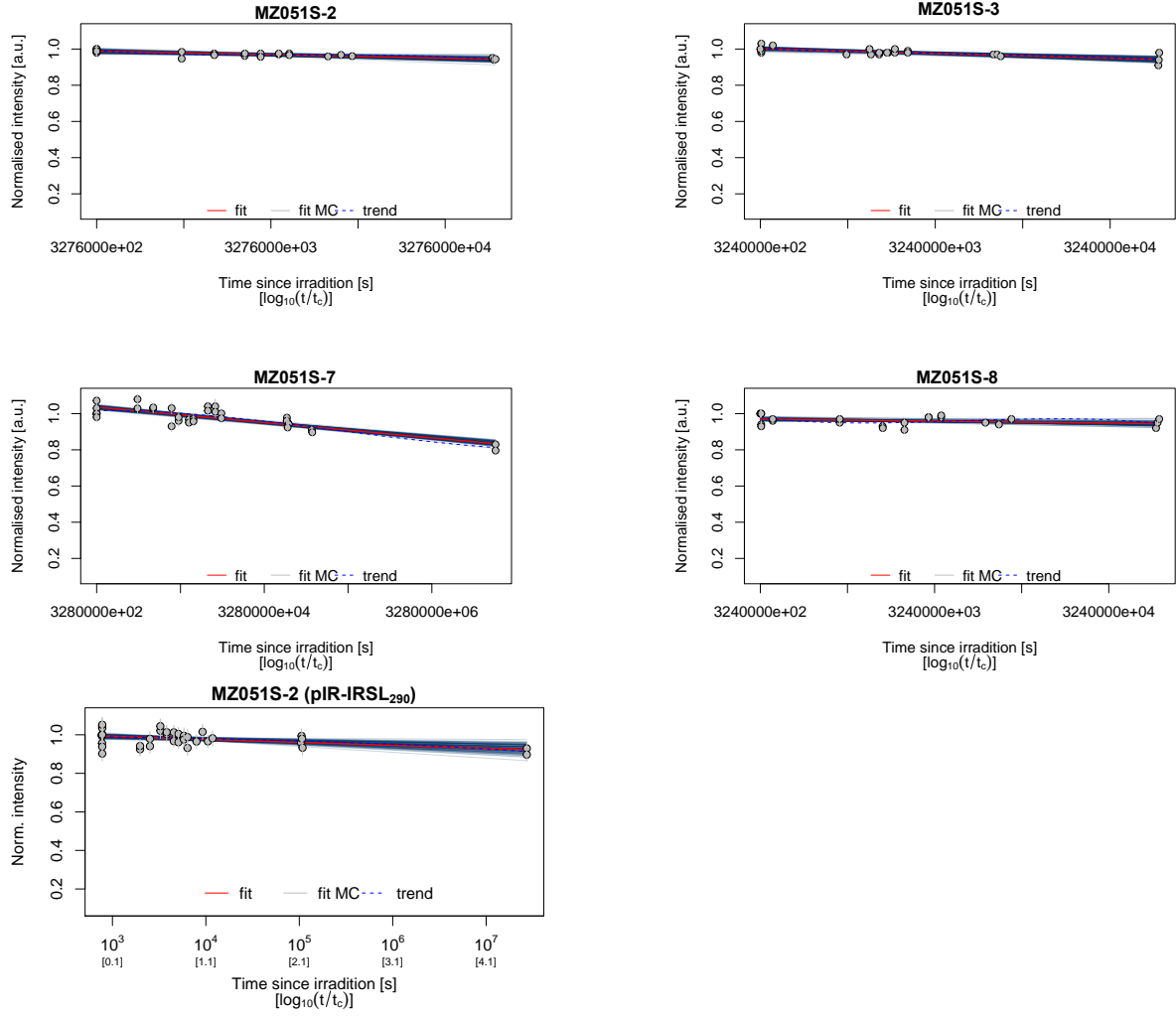


Fig. C.4: Fading measurements.

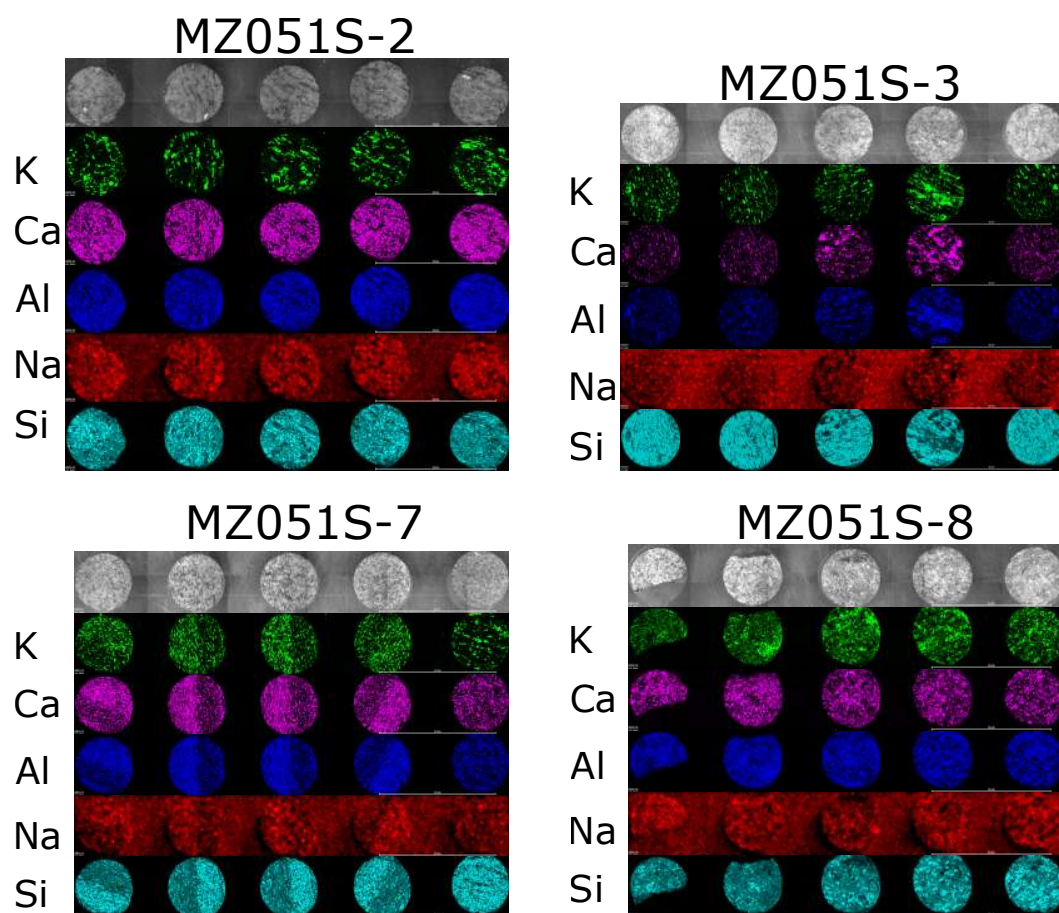


Fig. D.1:  $\mu$ -XRF maps showing the relative element contents in 5 slices from each cobble.

## Appendix B

# Supplementary material: Dating dry-stone walls with rock surface luminescence: A case study from the Italian Alps

## Appendix A. Photographs of the samples

Photographs of samples are presented in Fig. A.1 and A.2.

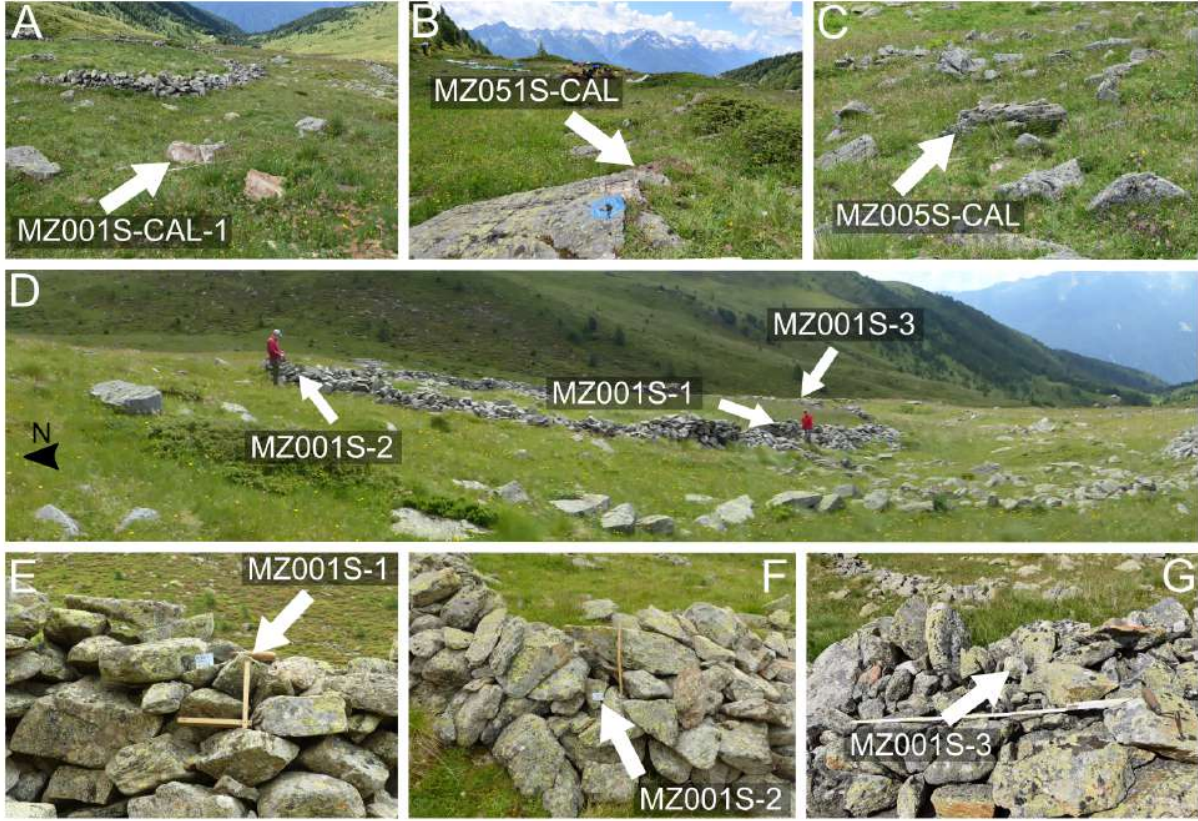


Fig. A.1: Calibration and exposed samples from Val Molinac and Val Poré. A–C) The positions in the valleys where the calibration surfaces were exposed. D) The positions of exposed samples at MZ001S. E–G) Position of the exposed samples collected from the enclosure MZ001S.

## Appendix B. Luminescence measurements and dose rate calculations

All samples were measured in a Risø TL/OSL reader (model DA-20) in the Cologne Luminescence Laboratory. The samples were irradiated with beta radiation using the internal  $^{90}\text{Sr}/^{90}\text{Y}$  source of the reader ( $\sim 0.08 \text{ Gy s}^{-1}$ ). A heating rate of  $2^\circ\text{C/s}$  was applied during all heating steps. All stimulation was performed using infrared diodes ( $\sim 875 \text{ nm}$ ). The luminescence emission was filtered through a  $410 \text{ nm}$  interference filter before being measured with an Electron Tubes 9107Q blue/UV sensitive photomultiplier tube. The natural luminescence ( $L_n$ ) with depth at the exposed rock surfaces were measured using a  $100 \text{ s}$  preheat at  $180^\circ\text{C}$ , then a  $30 \text{ s}$  pause, followed by  $300 \text{ s}$  of infrared stimulation at  $50^\circ\text{C}$ . The luminescence response to a test dose ( $T_n$ ) of  $\sim 17.2 \text{ Gy}$  was subsequently measured using the same protocol, which provides



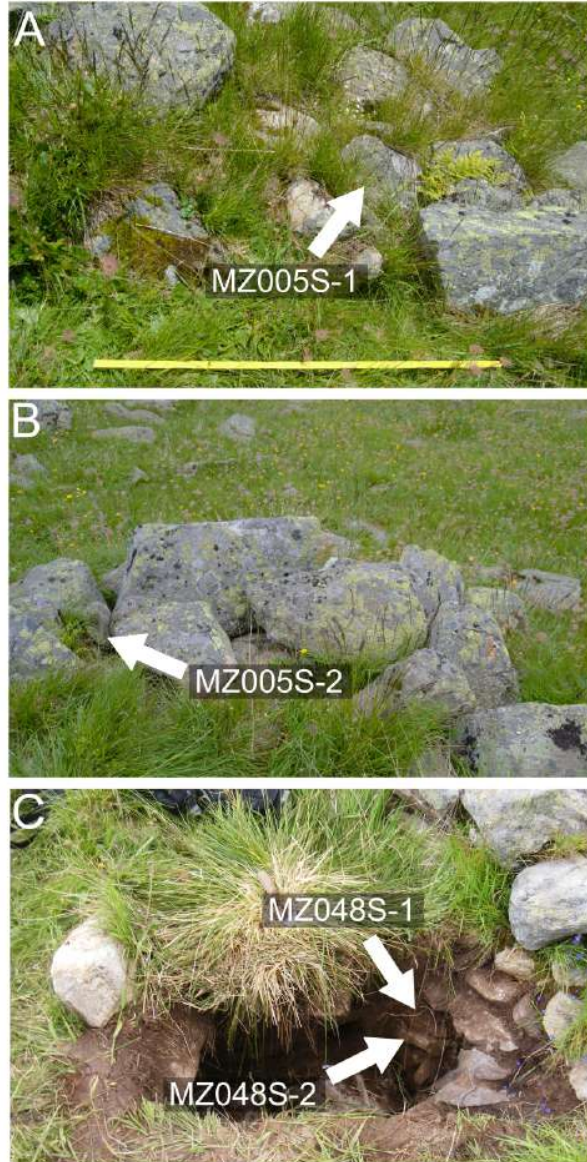


Fig. A.2: Position of samples collected from dry-stone structures MZ005S (A–B) and MZ048S (C) in Val Poré.

the sensitivity-corrected luminescence ( $L_n/T_n$ ). The buried rock surfaces were measured using a post-infrared IRSL (pIRIR) protocol where the samples are stimulated for 300 s at 50 °C (IRSL) and 130 °C (pIRIR), respectively.  $L_n/T_n$  was measured in all rock slices (test dose  $\sim 1.6$  Gy); equivalent doses ( $D_e$ ) were measured in the surface slices using cycles of increased regenerative dosing.  $D_e$  was analysed using the Analyst software.

Regarding fading measurements: storage after irradiation ranged from prompt measurements to  $\sim 17$  h of storage. Fading was measured on three slices per sample, and fading corrections were performed using the R Luminescence package.





Fig. A.3: Photographs of some of the collected rocks.

Radionuclide concentrations were measured using high-resolution gamma spectrometry. 200 g from each sample was homogenised and stored for a minimum of three weeks to allow for  $^{222}\text{Rn}$  to reach equilibrium prior to measurements.

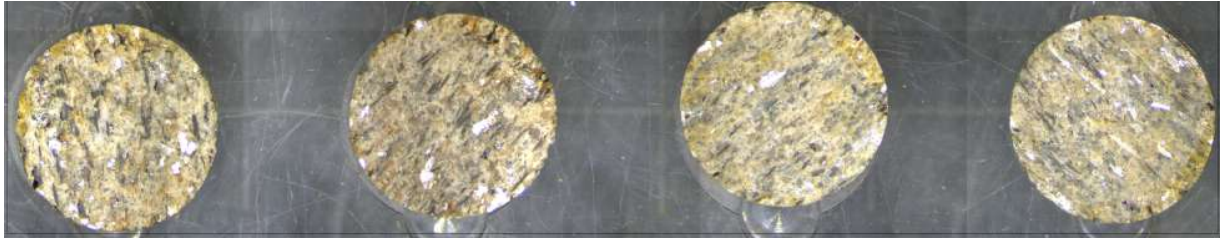


Fig. A.4: Slices from sample MZ005S-1, displaying the mineralogy and texture of the Val di Sole lithologies.

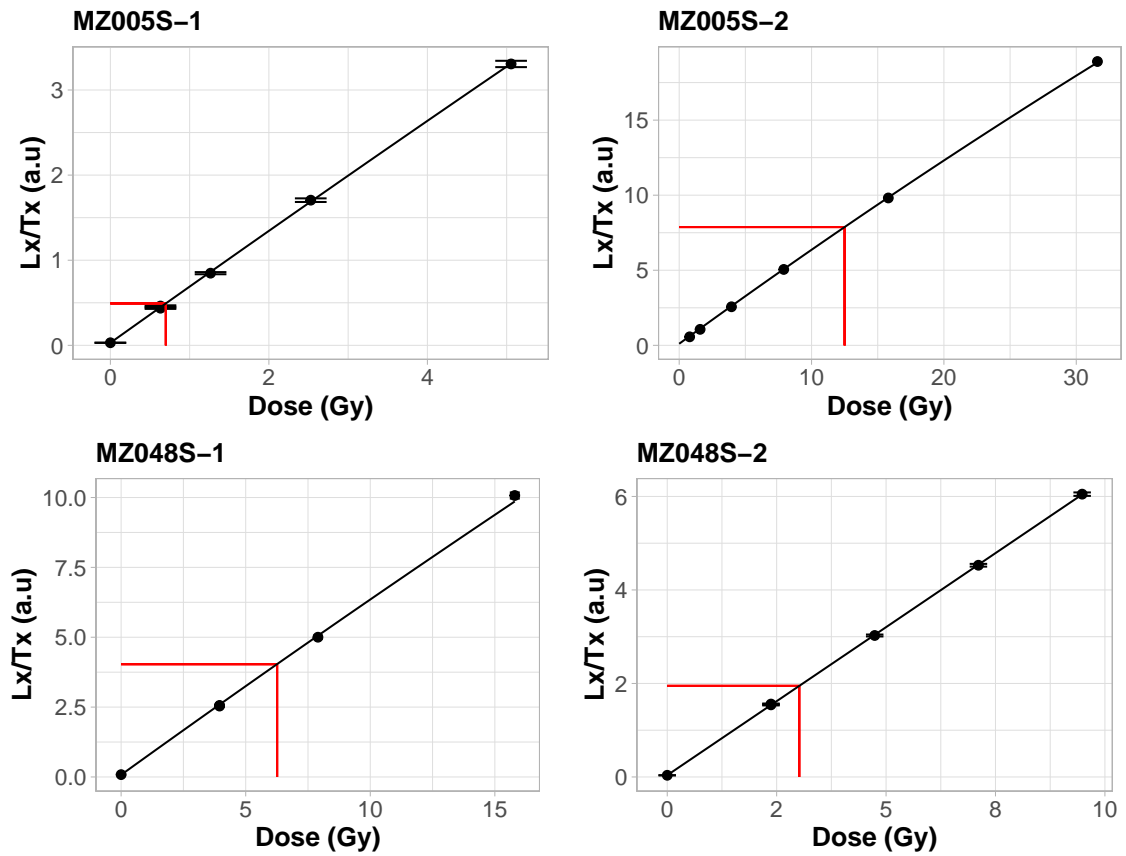


Fig. B.5: Example IRSL dose-response curves from surface slices from the buried rocks.

## Appendix C

### Supplementary material:

Investigating optical dating of  
carbonate-rich cobbles from a river  
terrace: A pilot study from the  
Mula Valley, Spain

## 612 Appendix A. Site

Table A.1: Table of age control for the +5-7 terrace from Cueva Antón. ABA = acid-base-acid treatment of charcoal; ABOx-SC = acid-base-oxidation-stepped combustion treatment of charcoal. Sample C-L4621 was collected from 4 m of depth from the terrace outcrop MULA1802, slightly upstream from the cobbles MULA1802-2 and MULA1802-7.

Sample ID	Site	Layer	Method	Protocol	Material	Age
K19-5	Cueva Antón	I-k	Radiocarbon dating	ABA	Pinus nigra	34603–35360 cal BP <sup>a</sup>
I20-3	Cueva Antón	I-k top	Radiocarbon dating	ABOx-SC	Conifer	35067–36245 cal BP <sup>a</sup>
G21-4	Cueva Antón	I-k base	Radiocarbon dating	ABOx-SC	Juniperus sp.	35627–36826 cal BP <sup>a</sup>
E21-11	Cueva Antón	II-a	Radiocarbon dating	ABOx-SC	Juniperus sp.	35594–37055 cal BP <sup>a</sup>
J19-7	Cueva Antón	II-b	Radiocarbon dating	ABOx-SC	Pinus sp.	36314–37714 cal BP <sup>a</sup>
N20-2	Cueva Antón	II-h/i	Radiocarbon dating	ABA	Juniperus sp.	39650 ± 550 BP <sup>a*</sup>
C-L2941	Cueva Antón	II-e	Luminescence dating	Multi-grain OSL	Quartz	71 ± 8 ka <sup>b</sup>
C-L2941	Cueva Antón	II-e	Luminescence dating	Single-grain OSL	Quartz	73 ± 8 ka <sup>b</sup>
C-L3137	Cueva Antón	II-e	Luminescence dating	Multi-grain OSL	Quartz	69 ± 8 ka <sup>b</sup>
C-L3375	Cueva Antón	II-ø	Luminescence dating	Multi-grain OSL	Quartz	82 ± 8 ka <sup>b</sup>
C-L2942	Cueva Antón	II-y	Luminescence dating	Multi-grain OSL	Quartz	69 ± 7 ka <sup>b</sup>
C-L2943	Cueva Antón	III-f	Luminescence dating	Multi-grain OSL	Quartz	70 ± 8 ka <sup>b</sup>
C-L2943	Cueva Antón	III-f	Luminescence dating	Single-grain OSL	Quartz	69 ± 7 ka <sup>b</sup>
C-L2943	Cueva Antón	III-f	Luminescence dating	Multi-grain OSL	Quartz	72 ± 8 ka <sup>b</sup>
C-L3377	Cueva Antón	III-k/l	Luminescence dating	Multi-grain OSL	Quartz	74 ± 8 ka <sup>b</sup>
C-L3138	Cueva Antón	III-m	Luminescence dating	Multi-grain OSL	Quartz	78 ± 10 ka <sup>b</sup>
C-L3378	Cueva Antón	III-m	Luminescence dating	Multi-grain OSL	Quartz	69 ± 7 ka <sup>b</sup>
C-L4621	MULA1802		Luminescence dating	Multi-grain OSL	Quartz	103 ± 5 ka <sup>c</sup>
C-L4621	MULA1802		Luminescence dating	Multi-grain IRSL	K-feldspar	98 ± 29 ka <sup>c</sup>
C-L4621	MULA1802		Luminescence dating	Multi-grain pIRIR <sub>225</sub>	K-feldspar	152 ± 26 ka <sup>c</sup>

<sup>a</sup>Published in Zilhão et al. (2016)

<sup>b</sup>Published in Burow et al. (2015)

<sup>c</sup>Method and results presented in the supplementary material of this study

\*Uncalibrated minimum age

613 The study area is located in the Mula valley, a fluvial valley in the Mula basin in the region of Murcia,  
614 southeastern Spain. The Mula basin, in which the Mula valley is situated, is one of several intramontane  
615 basins situated in the eastern Betic Cordillera, formed by crustal thinning initiated by extensional tectonic  
616 activity during the Late Neogene-Quaternary (Rodríguez-Fernández et al., 2011). The Mula basin is sur-  
617 rounded by the mountain ranges of Sierra Ricote (north), Sierra Espuña (south), and Cambrón (west). The  
618 deposits in the basin are mainly from the Mula unit (IGME, 1972a,b), which consists of carbonate sediments  
619 (limestones, marls, and calcarenites) deposited during the Cretaceous until the Miocene, and most of the  
620 sediments have been deformed by the Alpine orogeny. Post-orogeny sedimentary formations, mostly Upper  
621 Miocene in age, lie in unconformity on the older succession and are almost undeformed. The structural

formations within the basin control the path of the Mula river – the main watercourse draining the Mula basin – via the Segura River, eastwards into the Mediterranean Sea. Today, the fluvial discharge in the Mula river is affected by a large negative mean annual water balance ( $-600$  mm/y), despite occasional heavy rain events during the winter months, which can cause highly erosive flash floods. The river runs through the El Corcovado gorge, cutting through Eocene carbonate deposits. The Mula river was dammed in 1929, which flooded the downstream part of the gorge to create the La Cierva reservoir. A Middle Palaeolithic cave site, Cueva Antón, was discovered just upstream of the gorge (Martínez-Sánchez, 1997). The cave was formed by karstic processes, lateral erosion by the river, and wall degradation (Angelucci et al., 2013). Inside the cave, alluvial sediments are deposited as distinct sedimentary facies, corresponding to periods of fluvial activity for the Mula river. Five such sequences (AS1–AS5) have been excavated in Cueva Antón, each containing intercalations of limestone breccia and fluvial facies represented by layers of silt, sand, and gravel (Angelucci et al., 2013). Middle Palaeolithic stone tools have been recovered from AS5. The alluvial sequences in the cave (AS2, AS4, and AS5) have been dated (Table A.1, supplementary material) with single-grain and 1–2 mm multiple-grain OSL techniques (Burow et al., 2015). The OSL ages range between  $71 \pm 8$  and  $73 \pm 8$  ka (AS2) to  $78 \pm 10$  and  $69 \pm 7$  ka (AS5) and show relatively rapid fluvial accumulation of sediments during the marine isotope stage (MIS) 4. The uppermost sequence AS1 has been dated (Table A.1, supplementary material) with radiocarbon (six charcoal samples) to 34.6–37.7 ka (Zilhão et al., 2016).

Previous studies (Silva et al., 1996; Angelucci et al., 2018) from the Mula basin have reported a fluvial terrace system containing seven terrace levels (reported in metres above the present river bed). These terrace levels represent the dissection-aggradation history of the Mula system during the Pleistocene–Holocene (Silva et al., 1996). The two oldest terrace levels (+65/80 m and +40 m) are only present downstream of the La Cierva reservoir. The +65/80 m level was interpreted as remnants of Early Pleistocene alluvial sediments, eroded (along with the limestone substrate) by fluvial incision to form a palaeovalley. The +40 m terrace represents an aggradation phase during which up to six metres of alluvial sediments filled the palaeovalley floor. Following further incision, an up to  $\sim 18$  metres thick sequence of fluvio-lacustrine sediments was deposited during aggradation to form the +32–36 m terrace level (visible both downstream and upstream of the La Cierva reservoir). This infilling phase of the palaeovalley has been biostratigraphically linked to a pre-glacial warm period during the late Pleistocene (Agusti et al., 1990) and was triggered by tectonic movements in the lower Mula valley, which disconnected the Mula river from the Segura river, which a lacustrine environment in the palaeovalley due to the local shift in base level (Silva et al., 1996). According to Silva et al. (1996), headward erosion eventually reconnected the two river systems, which dramatically lowered the base layer and started an incision phase that formed the current Mula valley. However, intermediate cycles of dissection and aggradation have formed additional terrace levels: the +20–22 m terrace, discovered upstream of the La Cierva reservoir (Angelucci et al., 2013); the +15 m terrace; the +5–7 m terrace, which

656 has been observed near Cueva Antón and upstream (Angelucci et al., 2013); and the +2 m terrace. The  
657 latter has been reactivated during flash floods. Up to three metres of fluvial sediments (mostly gravels) have  
658 been reported from the +5–7 m terrace. For example, a 1.5 m thick outcrop of cemented gravels and sand  
659 lenses is visible just outside of Cueva Antón (Angelucci et al., 2018). Also, since the alluvial sequence in  
660 Cueva Antón reaches +8 m above the current Mula river thalweg, Angelucci et al. (2013) concluded that  
661 facies AS1-AS5 in the cave also correlate to the +5–7 m terrace. Therefore, based on the dating by Burow  
662 et al. (2015) and Zilhão et al. (2016), the aggradation phases which deposited the +5-7 m level occurred  
663 during the MIS 5–4 boundary (AS2–AS5) and during MIS 3 (AS 1) (Angelucci et al., 2018).





Table B.1: List of buried cobbles collected during the 2018 and 2019 field campaigns in the Mula valley and Rambla Perea.

Sample	Site	Description	Sampling – comments	Signal?
0701-1	Rambla Perea – +5m terrace	Reddish	Embedded in gravel layer	Moderate IRSL (600 cts/0.4s after 80 Gy dose)
0701-2	Rambla Perea – +5m terrace	Medium-grained and reddish	Embedded in gravel layer	Moderate IRSL (<270 cts/0.4s after 30 Gy dose)
0701-3	Rambla Perea – +5m terrace	Appears weathered, reddish	Embedded in gravel layer	Broke during coring
0717-1	Rambla Perea – +12m terrace	Cobble sized, angular	Embedded in gravel layer	Weak IRSL (<200 cts/0.4 s after 80 Gy dose)
0717-2	Rambla Perea – +12m terrace	Cobble sized, angular	Embedded in gravel layer	Weak IRSL (<400 cts/0.4 s after 80 Gy dose)
1802-1	Mula valley – +5-7m terrace	Gray	Embedded in gravel layer, only one surface exposed	Weak IRSL (<200 cts/0.4 s after 80 Gy dose)
1802-2	Mula valley – +5-7m terrace	Gray; some fossils and quartz visible; large cobble	Embedded in gravel layer, only one surface exposed	Acceptable IRSL response (>600 cts/0.6 s after 26 Gy of dose)
1802-3	Mula valley – +5-7m terrace	Gray	Embedded in gravel layer	Weak IRSL (>100 cts/0.4 s after 30 Gy of dose)
1802-5	Mula valley – +5-7m terrace	Small cobble	Exposed in the outcrop.	Not measured – cobble is too small
1802-6	Mula valley – +5-7m terrace	Gray, coarse-grained, weathered flat cobble	Completely buried	IRSL response (>450 cts/0.6 s after 26 Gy of dose)
1802-7	Mula valley – +5-7m terrace	Gray, fine-grained sandstone	Buried beneath a limestone boulder; part of the cobble was exposed in the outcrop	Acceptable IRSL response (>600 cts/0.6 s after 26 Gy of dose)
1802-8	Mula valley – +5-7m terrace	Rounded, light-grey cobble	One surface was briefly exposed in the outcrop during sampling	Broke during coring
1802-9	Mula valley – +5-7m terrace	Small, rounded cobble	Completely buried before burial; exposed during sampling	Not measured – cobble is too small
1802-11	Mula valley – +5-7m terrace	Small pebble-sized	Completely buried before burial; exposed during sampling	Not measured – too small
1802-12	Mula valley – +5-7m terrace	Gray, fine-grained, angular cobble	One side was briefly exposed during sampling;	Not measured
1802-13	Mula valley – +5-7m terrace	Small, flat, and rounded pebble	Completely buried; exposed during sampling.	Not measured – too small
1802-14	Mula valley – +5-7m terrace	Small, brittle, and dark cobble	Briefly exposed during sampling	Not measured – broke during coring.
1802-15	Mula valley – +5-7m terrace	Severely weathered, small, flat, and semi-rounded pebble	Completely buried; exposed during sampling	Not measured – too small
1802-16	Mula valley – +5-7m terrace	Pebble	Completely buried; exposed during sampling	Not measured – too small
1802-17	Mula valley – +5-7m terrace	Pebble	Completely buried; exposed during sampling.	Not measured – too small
1802-18	Mula valley – +5-7m terrace	Severely weathered, semi-rounded cobble	Completely buried; exposed during sampling	Not measured – too small
1802-19	Mula valley – +5-7m terrace	Pebble	Exposed in the outcrop	Not measured – too small
1803-1	Mula valley – +21m terrace	Gray, coarse-grained with carbonate minerals	Embedded in gravel; one surface partly exposed	Weak IRSL (<200 cts/0.4 s after 35 Gy dose)
1803-2	Mula valley – +21m terrace	Gray, coarse grained with carbonate minerals	Embedded in gravel; one surface partly exposed	Moderate IRSL (> 300 cts/0.4 s after 35 Gy dose)
1803-3	Mula valley – +21m terrace	Gray, coarse-grained with carbonate minerals	Embedded in gravel; one surface partly exposed	Weak IRSL (<100 cts/0.4 s after 35 Gy dose)
1901-1	Rambla Perea – +5m terrace	Small cobble	Exposed in the outcrop.	Not measured
1901-2	Rambla Perea – +5m terrace	Light limestone without visible grains	To be used to investigate an eventual TL signal.	Not measured
1901-3	Rambla Perea – +5m terrace	Small cobble	Exposed in the outcrop.	Not measured

Table B.2: The thickness of the measured slices.

MULA1802-2 – top surface			MULA1802-2 – bottom surface			MULA1802-7 – top surface			MULA1802-7 – bottom surface		
Core	Slice	Thickness (mm)	Core	Slice	Thickness (mm)	Core	Slice	Thickness (mm)	Core	Slice	Thickness (mm)
8	1	1.26	1	1	1	4	1	1.1	3	1	1.2
8	2	0.87	1	2	0.7	4	2	0.6	3	2	0.6
8	3	0.66	1	3	0.5	4	3	0.7	3	3	0.5
8	4	0.75	1	4	0.7	4	4	0.6	3	4	0.6
8	5	0.81	1	5	0.7	4	5	0.7	3	5	0.8
8	6	1.08	2	1	1.25	5	1	0.7	3	6	0.5
8	7	0.65	2	2	0.5	5	2	0.5	3	7	1.0
8	10	0.5	2	3	0.6	5	3	0.5	3	8	0.7
9	1	1.3	2	4	0.53	5	4	0.5	3	9	1.1
9	2	0.64	2	5	0.57	5	5	0.6	3	10	0.7
9	3	0.67	2	6	0.7	5	6	0.6	6	1	0.7
9	4	0.62	2	7	0.48	5	7	0.6	6	2	0.7
9	5	0.91	2	8	0.59	5	8	0.6	6	3	0.7
9	6	0.7	2	9	0.91	5	9	0.6	6	4	0.7
10	1	1	2	10	0.77	5	10	0.5	6	5	0.5
10	2	0.7	3	1	1.23	8	1	1.0	7	1	1.2
10	3	0.7	3	2	0.52	8	2	0.7	7	2	0.7
10	4	0.7	3	3	0.79	8	3	0.7	7	3	0.6
10	5	0.7	3	4	0.85	8	4	0.6	7	4	0.7
			3	5	0.77	8	5	0.7	7	5	0.6
			4	1	1.18				7	6	0.6
			4	2	0.67				7	7	0.7
			4	3	0.5				7	8	0.5
			4	4	0.51				7	9	0.6
			4	5	0.55				7	10	0.7
			4	6	0.54				9	1	1.2
			4	7	0.61				9	2	0.6
			4	8	0.64				9	3	0.6
			4	9	0.51				9	4	0.6
			4	10	0.56				9	5	0.5
			4	11	0.5						
			5	1	1.23						
			5	2	0.69						
			5	3	0.53						
			5	4	0.49						
			5	5	0.61						
			6	1	1.54						
			6	2	0.72						
			6	3	0.66						
			6	4	0.81						
			7	2	1						
			7	3	0.54						
			7	4	0.61						
			7	5	0.64						
			11	1	1						
			11	2	0.7						
			11	3	0.7						
			11	4	0.7						
			11	5	0.7						
			11	6	0.7						
			12	1	1						
			12	2	0.7						
			12	3	0.7						
			12	4	0.7						
			13	2	0.7						
			13	3	0.79						
			13	4	0.6						
			13	5	0.5						

## Appendix C. Sediment dating of fluvial sands from MULA1802

### Appendix C.1. Methodology

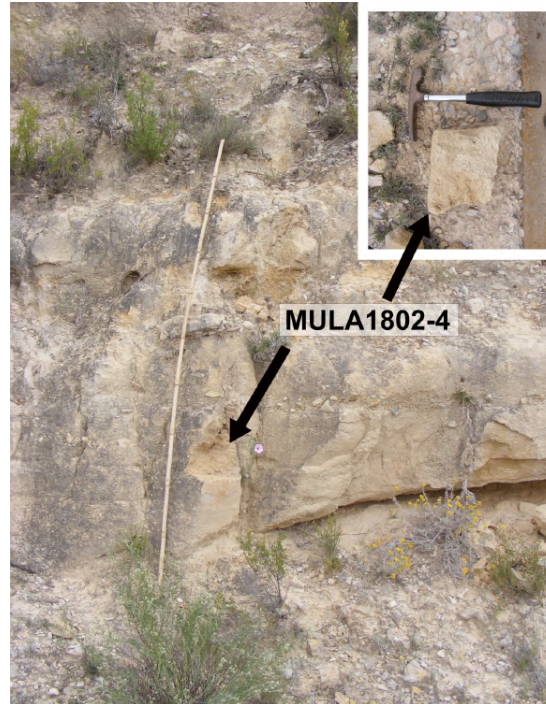


Figure C.1: Location of sediment sample MULA1802-4. The inset shows the sampled sediment slab.

The sediment sample MULA1802-4 was collected at 4 m below the terrace surface from a layer of fluvial sand (Figure C.1). The sample was collected as a slab of sediments, slightly consolidated by a cemented of calcium carbonate. The material used for dating was extracted from the centre of the monolith to avoid grains that could have been exposed to light. We prepared the sediment sample using conventional sample preparation for the very fine–fine sand fractions (e.g. Lang et al., 1996) with an additional, initial step where the sediments were washed in hydrochloric acid (HCL, 10 %) to separate the sand grains from the cement. The sediment was then dry-sieved, followed by a second treatment with HCL to dissolve any remaining carbonate minerals or cement, followed by hydrogen peroxide (H<sub>2</sub>O<sub>2</sub>, 10 %) to remove any organic material. Quartz and potassium-rich feldspars (K-feldspar) fractions were isolated using density separation (quartz separate: 2.62-2.68 g/cm<sup>3</sup>; K-feldspar: separate <2.58 g/cm<sup>3</sup>). The quartz was etched with hydrofluoric acid (HF, 40 %) to remove the alpha-radiated outer rim, followed by a final HCL treatment. All fractions were finally re-sieved before measurements. Blue light OSL emission (diodes; ~470 nm) was filtered through a Hoya U340 filter, and IRSL and pIRIR emissions (stimulation with infrared diodes at ~875 nm) were filtered through a blue light interference filter.

The heating rate during measurements was  $2\text{ }^{\circ}\text{C s}^{-1}$ . Discs were accepted if recycling, recuperation as well as palaeodose error were each below 10 %. The ability of the measurement protocol to determine an accurate natural dose is tested by dosing bleached discs with a known beta dose. All measurements were conducted using 1 mm aliquots mounted on stainless steel discs. Quartz OSL equivalent doses from MULA-1802-4 was measured at  $125\text{ }^{\circ}\text{C}$  with a SAR protocol for 40 s (Murray and Wintle, 2000) on the 100–150  $\mu\text{m}$  grain size fraction. A preheat of  $260\text{ }^{\circ}\text{C}$  for 10 seconds was chosen following a preheat plateau test (Figure C.2), which showed if  $D_e$  values are independent of the applied preheat temperatures between 220 and  $280\text{ }^{\circ}\text{C}$ . K-feldspars (grain size: 100–200  $\mu\text{m}$ ) of MULA-1802-4 was dated with a pIRIR protocol. Stimulation was performed with infrared diodes for 300 seconds at  $50\text{ }^{\circ}\text{C}$  (first stimulation) and  $225\text{ }^{\circ}\text{C}$  (pIRIR stimulation). A preheat at  $250\text{ }^{\circ}\text{C}$  for 100 seconds was employed before stimulation.

The radionuclide concentration in the sediments was measured with high-resolution gamma spectrometry on  $\sim 200\text{ g}$  of crushed samples (the samples were allowed to rest for three weeks or more before measurement). The cosmic dose component was calculated following Prescott and Hutton (1994). The measured moisture content in the collected sediment samples was negligible, but we assume a moisture content of  $20 \pm 5\%$  based on observation of previous groundwater levels. The radionuclide concentrations were converted using conversion factors from Cresswell et al. (2018). The environmental dose rate for MULA1802-4 was calculated using DRAC (Durcan et al., 2015).

## Appendix C.2. Results

The quality report from the OSL and pIRIR<sub>225</sub> protocols is presented in Table C.1 and the luminescence ages from sediment sample MULA1802-4 is presented in Table C.2. The OSL emission of 1 mm quartz aliquots is overall sufficiently bright and dominated by the fast component (Figure C.3). The dose recovery is within the accepted 10 % of unity for all signals (Table C.2). For the OSL, the recuperation ratio is  $<5\%$  for all discs; thus, all discs passed this rejection criterion. The mean recycling ratio for OSL is  $1.01 \pm 0.01$ , with a 90% acceptance rate. Also, 26 % of all quartz discs were rejected due to large relative errors. For the pIRIR<sub>225</sub> protocol measured on 1 mm K-feldspar aliquots, the mean recycling ratios are  $1.02 \pm 0.01$  and  $1.01 \pm 0.01$  for the IRSL and the pIRIR signals, respectively. Some recuperation of the IRSL signal occurred during measurements, and 17 % of the discs were rejected based on this criterion, compared to no rejected discs for the pIRIR or the OSL measurements. Relative palaeodose error was no significant problem for the K-feldspar measurements. In total,  $\sim 70\%$  of the quartz discs, as well as 74 % (IRSL) and 91 % (pIRIR) of the K-feldspar discs, passed the rejection criteria.

Plotting  $D_e$  as a function of illumination time ( $t$ ) for the integration of the signal has been suggested by (Bailey et al., 2003) as a check for partial bleaching since the different OSL components bleach at different rates (Bailey et al., 1997). When the time intervals at which the signal is integrated are shifted from earlier to later, this should cause an increase in the average  $D_e$  since the proportion of signal emission arising from

Table C.1: Quality report for SAR measurements of MULA1802-4.

Mineral	Protocol	Accepted/measured discs	Avg. recuperation (%)	Avg. recycling ratio	Rel. palaeodose error range	Acceptance rate (%)			
						Recuperation	Recycling	Palaeodose error	Total
K-feldspar	IRSL <sub>50</sub> (pIRIR <sub>225</sub> )	17/23	5.7±1.5	1.02±0.01	0.02-0.15	83	87	96	74
K-feldspar	pIRIR <sub>225</sub>	21/23	4.5±0.0	1.01±0.01	0.02-0.09	100	91	100	91
Quartz	OSL	38/55	0.7±0.1	1.01±0.01	0.01-0.25	100	91	76	70

Table C.2: Results from sediment sample MULA1802-4. Radionuclide concentrations: U =  $1.16 \pm 0.07$  ppm; Th =  $1.96 \pm 0.14$  ppm; K =  $0.31 \pm 0.01$  %. Ages were calculated using the central age model (Galbraith et al., 1999). K-feldspar ages were corrected using g-values following the approach of Huntley and Lamothe (2001).

Mineral	Protocol	Dose recovery	D <sub>e</sub> (Gy)	Avg. D <sub>0</sub> (Gy)	Overdispersion (%)	Dose rate (Gy/ka)	g <sub>2days</sub> (%/decade)	Age (ka)
K-feldspar	IRSL (pIRIR <sub>225</sub> )	0.90 ± 0.02	87.71 ± 6.97	519 ± 22	38 ± 6	1.46 ± 0.20	4.89 ± 1.30	97.6 ± 29.3
K-feldspar	pIRIR <sub>225</sub>	0.96 ± 0.01	171.22 ± 7.89	440 ± 11	19 ± 3	1.46 ± 0.20	2.64 ± 0.74	151.5 ± 25.6
Quartz	OSL	0.93 ± 0.03	83.19 ± 2.72	68 ± 3	20 ± 2	0.82 ± 0.02		102.8 ± 4.5

the harder-to-bleach medium component increases. For MULA1802-4, we do not see any increase in D<sub>e</sub>(t) as the integration interval is shifted backwards on the OSL decay curve (Figure C.4). Overdispersion in the data accounts for  $20 \pm 2$  % of the spread in the OSL data,  $38 \pm 6$  % for the spread in the IRSL data, and  $19 \pm 3$  % of the spread in the pIRIR<sub>225</sub> data (Table C.2). Neither dose distributions from the quartz nor the K-feldspars (Figure C.5) show a presence of different dose populations among our measured discs; therefore, we use the central age model (CAM) (Galbraith et al., 1999) to calculate equivalent doses of  $83.19 \pm 2.72$  Gy for the quartz,  $87.71 \pm 6.97$  Gy for the IRSL, and  $171.22 \pm 7.89$  Gy for the pIRIR<sub>225</sub>. The deposition of the quartz fraction of MULA1802-4 is estimated to have occurred at  $105 \pm 5$  ka during the early Last Glacial Period (LGP). The corrected IRSL age using the fading correction approach of Huntley and Lamothe (2001) is  $98 \pm 29$  ka, which also corresponds to the early LGP. The uncorrected pIRIR<sub>225</sub> age is  $118 \pm 17$  ka. However, the fading corrected age is older at  $152 \pm 26$  ka due to the substantial fading observed for the pIRIR<sub>225</sub> signal at  $2.64 \pm 0.74$  % /decade.

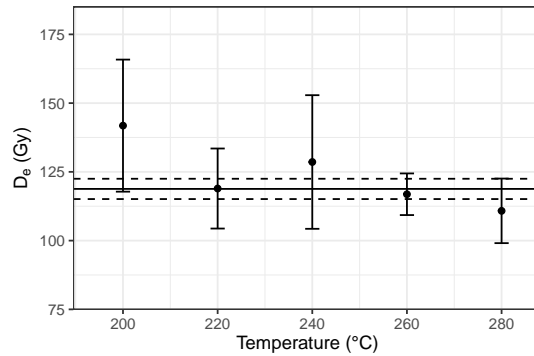


Figure C.2: Preheat plateau test for quartz OSL from MULA1802-4. The solid line represents the mean D<sub>e</sub> for preheat temperatures 220-280 °C, and the dashed lines mark the standard error.

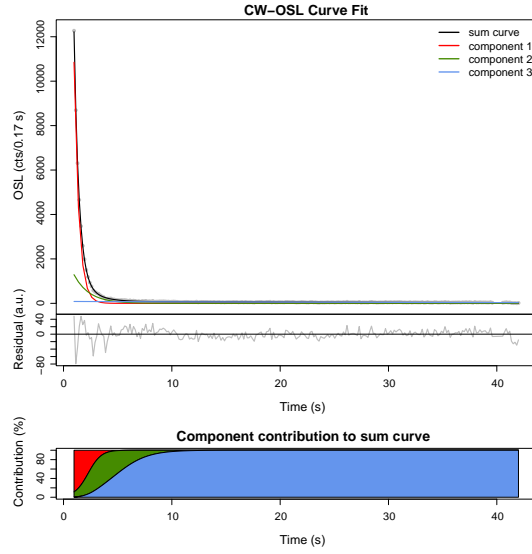


Figure C.3: Deconvolution of a quartz OSL decay curve from MULA1802-4, produced using the R Luminescence package (Kreutzer et al., 2021).

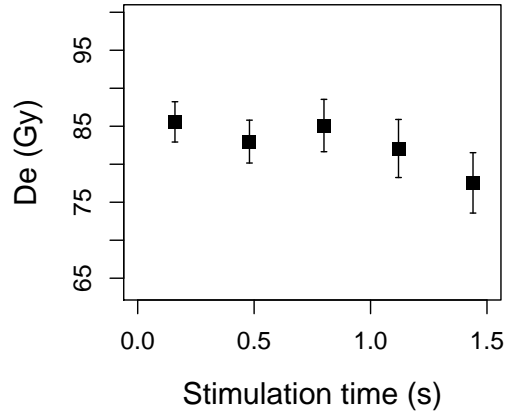


Figure C.4:  $D_e(t)$  results from OSL measurements of MULA1802-4.  $D_e(t)$  was analysed for all 54 measured aliquots, but only the aliquots which passed the rejection criteria from the SAR protocol (evaluated independently for each integration range) were used to calculate mean  $D_e$  and their corresponding standard error (points and error bars). The channel width is 0.16 s, and each point represents three channels.

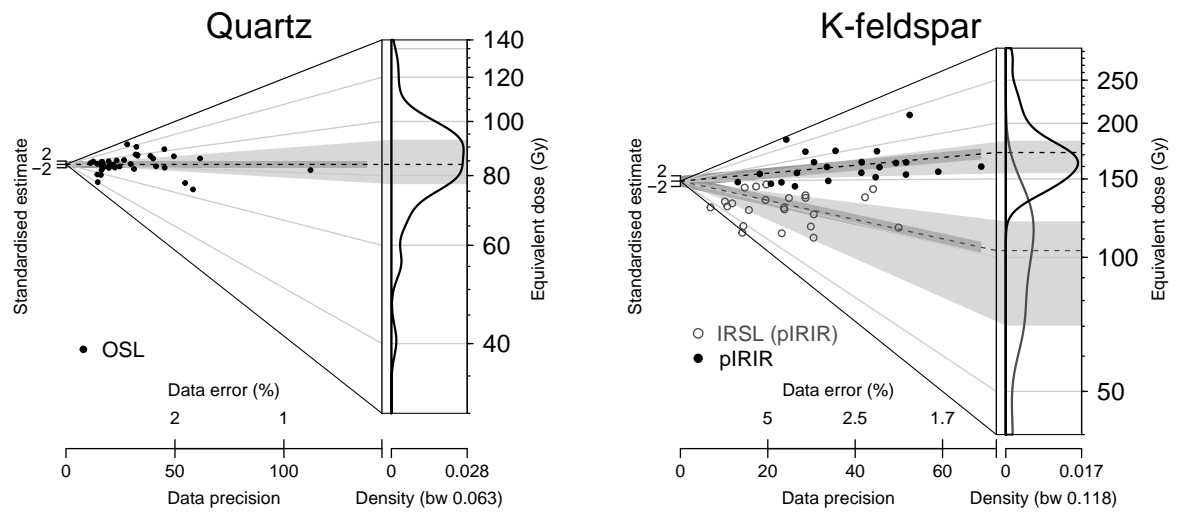


Figure C.5:  $D_e$  measurements of 1 mm quartz (left) and K-feldspar discs (right) for sample MULA1802-4. For K-feldspar, both IRSL and pIRIR<sub>225</sub> data are plotted.



## Appendix D. Petrographic microscopy

In the field, the cobbles were classified as calcarenites containing carbonate grains, fossils, quartz, and lithic fragments. All cobbles are rounded, cobble-sized and of varied sphericity. The thin section was observed in plane-polarised (PPL) and cross-polarised (XPL) light, and images were captured using a digital camera mounted on the petrographic microscope. Microscopic observation revealed, as expected, that MULA1802-2 consists mainly of carbonate material. The matrix consists primarily of sparry cement, which surrounds intrabasin allochems. Other sedimentary minerals include glauconite and chalcedony. For luminescence dating, we are interested in the presence of feldspars and quartz.

Low birefringence detrital tectosilicate grains can be observed in the thin section (Figure D.1A-D), surrounded by sparite. Some of these grains show undulose extinction (Figure D.1A), which indicates that they are likely quartz. Only a handful of low birefringence grains display twinning signs, making it hard to differentiate between quartz and feldspar grains. However, feldspar appears to be present in the MULA1802-2. One low birefringence grain appears to display cross-hatched twinning (Figure D.1B); potentially, this is a microcline. One plagioclase grain is identified by its lamellar twinning (Figure D.1C); some of the weathered low birefringence grains (Figure D.1D) are likely feldspars. Overall, it is hard to distinguish if the feldspars are potassium-rich or sodium-rich due to weathering and lack of twinning. The apparent size of the quartz and feldspar grains in the thin section is  $<50\text{ }\mu\text{m}$ . Most of the grains appear to be subangular to angular. Lithic fragments are also visible throughout the thin sections, mostly from metamorphic lithologies like quartzites or gneisses. Overall, tectosilicate grains are all minor minerals, making up 5 % or less of the volume of the thin section.

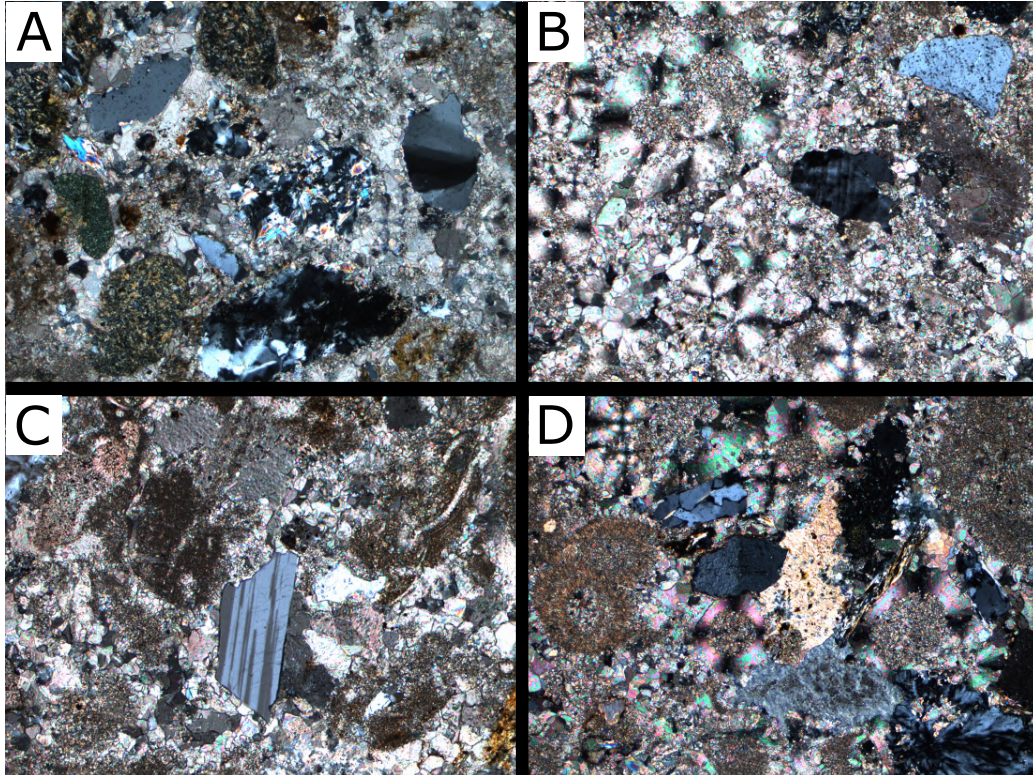


Figure D.1: XPL photomicrographs from MULA1802-2 of tectosilicate minerals. Allochems are present throughout the thin section, mostly as fossils. A) Silicate grains, which are likely quartz and lithic fragments based on the extinction pattern, are all surrounded by sparry cement and glauconite grains. B) Potential feldspar grains, surrounded by sparite and fibrous chalcedony. C) Twinned feldspar grain, surrounded by sparite and micrite. D) Rock fragments and weathered tectosilicates in the cement of sparry calcite. Each field of view = 140  $\mu\text{m}$ .



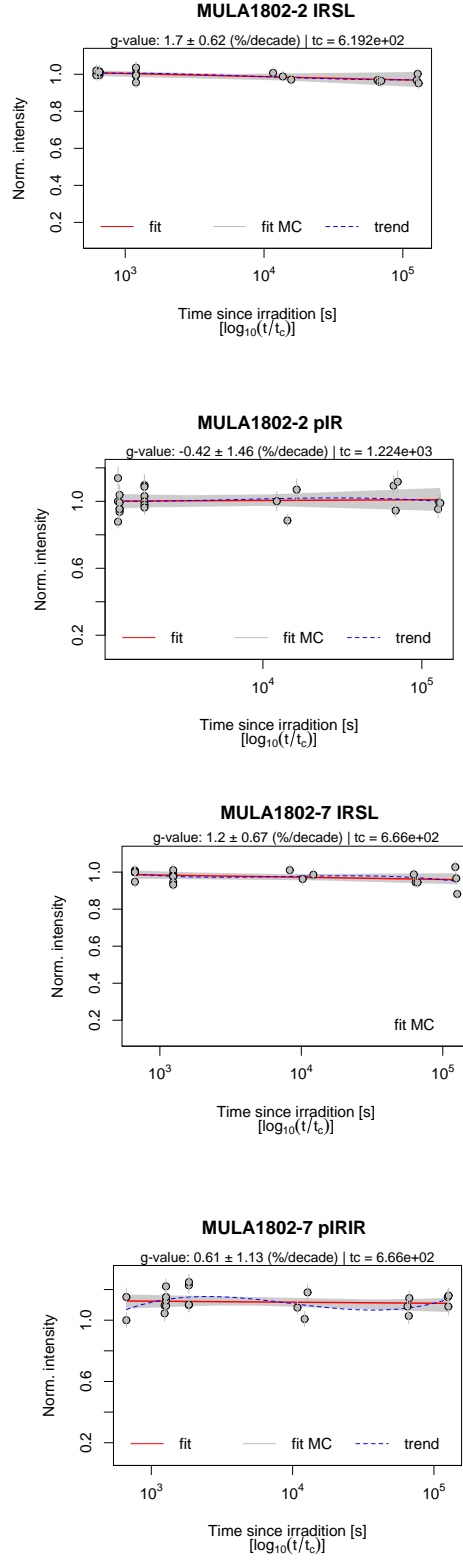


Figure E.2: Fading measurements from cobbles MULA1802-2 and MULA1802-7.

Table F.1: Best-fit parameters for fitting presented in Figure 5.

Cobble	Protocol	$L_0$	$\mu \text{ (mm}^{-1}\text{)}$	$t_e \overline{\sigma \varphi_0}$	$t_b/D_0$
MULA1802-2	IRSL	10.6	$1.8 \pm 0.3$	$95 \pm 74$	$0.05 \pm 0.01$
MULA1802-2	pIRIR225	8.9	$3 \pm 71$	$12 \pm 2000$	0
MULA1802-7	IRSL	9.5	$1.6 \pm 0.3$	$167 \pm 185$	$0.05 \pm 0.01$
MULA1802-7	pIRIR225	8.2	$1.4 \pm 0.8$	$9 \pm 16$	$0.13 \pm 0.15$

## References – supplementary material

- Agusti, J., Freudenthal, M., Lacomba, J., Martín Suárez, E., Nägeli, C., 1990. Primeros micromamíferos del Pleistoceno superior de la cuenca de Mula (Murcia, España). *Rev. Soc. Geol. España* 3, 289–293.
- Angelucci, D.E., Anesin, D., Susini, D., Villaverde, V., Zapata, J., Zilhão, J., 2013. Formation processes at a high resolution Middle Paleolithic site: Cueva Antón (Murcia, Spain). *Quaternary International* 315, 24–41. doi:10.1016/j.quaint.2013.03.014.
- Angelucci, D.E., Anesin, D., Susini, D., Villaverde, V., Zapata, J., Zilhão, J., 2018. A tale of two gorges: Late Quaternary site formation and surface dynamics in the Mula basin (Murcia, Spain). *Quaternary International* 485, 4–22. doi:10.1016/j.quaint.2017.04.006.
- Bailey, R.M., Singarayer, J.S., Ward, S., Stokes, S., 2003. Identification of partial resetting using De as a function of illumination time. *Radiation Measurements* 37, 511–518. doi:10.1016/S1350-4487(03)00063-5.
- Bailey, R.M., Smith, B.W., Rhodes, E.J., 1997. Partial bleaching and the decay form characteristics of quartz OSL. *Radiation Measurements* 27, 123–136. doi:10.1016/S1350-4487(96)00157-6.
- Burow, C., Kehl, M., Hilgers, A., Weniger, G.C., Angelucci, D.E., Villaverde, V., Zapata, J., Zilhão, J., 2015. Luminescence Dating of Fluvial Deposits in the Rock Shelter of Cueva Antón, Spain. *Geochronometria* , 107–125doi:10.1515/geochr-2015-0010.
- Cresswell, A.J., Carter, J., Sanderson, D.C.W., 2018. Dose rate conversion parameters: Assessment of nuclear data. *Radiation Measurements* 120, 195–201. doi:10.1016/j.radmeas.2018.02.007.
- Durcan, J.A., King, G.E., Duller, G.A.T., 2015. DRAC: Dose Rate and Age Calculator for trapped charge dating. *Quaternary Geochronology* 28, 54–61. doi:10.1016/j.quageo.2015.03.012.
- Galbraith, R.F., Roberts, R.G., Laslett, G.M., Yoshida, H., Olley, J.M., 1999. Optical Dating of Single and Multiple Grains of Quartz from Jinmium Rock Shelter, Northern Australia: Part I, Experimental Design and Statistical Models\*. *Archaeometry* 41, 339–364. doi:10.1111/j.1475-4754.1999.tb00987.x.
- Huntley, D.J., Lamothe, M., 2001. Ubiquity of anomalous fading in K-feldspars and the measurement and correction for it in optical dating. *Canadian Journal of Earth Sciences* 38, 1093–1106. doi:10.1139/e01-013.
- IGME, 1972a. Mapa Geológica de España E. 1:50 00, Instituto Geológico y Minero de España, Madrid. Hoja 911 - Cehegín.

- 778 IGME, 1972b. Mapa Geológica de España E. 1:50 000, Instituto Geológico y Minero de España, Madrid.  
779 Hoja 912 - Mula.
- 780 Kreutzer, S., Burow, C., Dietze, M., Fuchs, M.C., Schmidt, C., Fischer, M., Friedrich, J., Mercier, N.,  
781 Smedley, R.K., Christophe, C., Zink, A., Durcan, J., King, G.E., Philippe, A., Guerin, G., Riedesel, S.,  
782 Autzen, M., Guibert, P., Mittelstrass, D., Gray, H.J., Fuchs, M., 2021. Luminescence: Comprehensive  
783 Luminescence Dating Data Analysis.
- 784 Lang, A., Lindlauer, S., Kuhn, R., Wagner, G.A., 1996. Procedures used for optically and Infrared Stimulated  
785 Luminescence Dating of Sediments in Heidelberg. *Ancient TL* 14, 7–11.
- 786 Martínez-Sánchez, C., 1997. El yacimiento musteriense de Cueva Antón (Mula, Murcia). *Memorias Arqueol.*  
787 *Región Murcia* 6, 31.
- 788 Murray, A.S., Wintle, A.G., 2000. Luminescence dating of quartz using an improved single-aliquot  
789 regenerative-dose protocol. *Radiation Measurements* 32, 57–73. doi:10.1016/S1350-4487(99)00253-X.
- 790 Prescott, J.R., Hutton, J.T., 1994. Cosmic ray contributions to dose rates for luminescence and ESR  
791 dating: Large depths and long-term time variations. *Radiation Measurements* 23, 497–500. doi:10.1016/  
792 1350-4487(94)90086-8.
- 793 Rodríguez-Fernández, J., Azor, A., Azañón, J.M., 2011. The Betic Intramontane Basins (SE Spain): Stratig-  
794 raphy, Subsidence, and Tectonic History, in: *Tectonics of Sedimentary Basins*. John Wiley & Sons, Ltd.  
795 chapter 23, pp. 461–479. doi:10.1002/9781444347166.ch23.
- 796 Silva, P.G., Mather, A.E., Goy, J.L., Zazo, C., 1996. Controles en el Desarrollo y Evolución del Drenaje en  
797 Zonas Tectónicamente Activas: el Caso del Río Mula (Región de Murcia, SE España) , 16.
- 798 Zilhão, J., Ajas, A., Badal, E., Burow, C., Kehl, M., López-Sáez, J.A., Pimenta, C., Preece, R.C., Sanchis,  
799 A., Sanz, M., Weniger, G.C., White, D., Wood, R., Angelucci, D.E., Villaverde, V., Zapata, J., 2016.  
800 Cueva Antón: A multi-proxy MIS 3 to MIS 5a paleoenvironmental record for SE Iberia. *Quaternary*  
801 *Science Reviews* 146, 251–273. doi:10.1016/j.quascirev.2016.05.038.



## Appendix D

### Supplementary material:

Investigating the resetting of IRSL signals in beach cobbles and their potential for rock surface dating of marine terraces in Northern Chile

1    **SUPPLEMENTARY INFORMATION**

2    **Investigating the resetting of IRSL signals in beach cobbles and their potential for rock surface**  
3    **dating of marine terraces in Northern Chile**

4    Dominik Brill<sup>1</sup>, Lucas Ageby<sup>1</sup>, Christina Obert<sup>2</sup>, Rolf Hollerbach<sup>2</sup>, Mathieu Duval<sup>3,4</sup>, Thomas Kolb<sup>5</sup>,  
5    Melanie Bartz<sup>6,1</sup>

6    <sup>1</sup>Institute of Geography, University of Cologne, Germany

7    <sup>2</sup>Institute of Geology and Mineralogy, University of Cologne, Germany

8    <sup>3</sup>Centro Nacional de Investigación sobre la Evolución Humana (CENIEH), Burgos, 09002, Spain.

9    <sup>4</sup>Australian Research Centre for Human Evolution (ARCHE), Environmental Futures Research Institute, Griffith  
10    University, Nathan, QLD 4111, Australia.

11    <sup>5</sup>Institute of Geography, Justus-Liebig-University Gießen, Germany

12    <sup>6</sup>Institute of Earth Surface Dynamics, University of Lausanne, Switzerland

13    *Corresponding author: Dominik Brill ([brilld@uni-koeln.de](mailto:brilld@uni-koeln.de))*

14

15

16

17

18

19

20

21

22

23

24

25

26

27

28

29

30

# 1. Luminescence rock surface dating

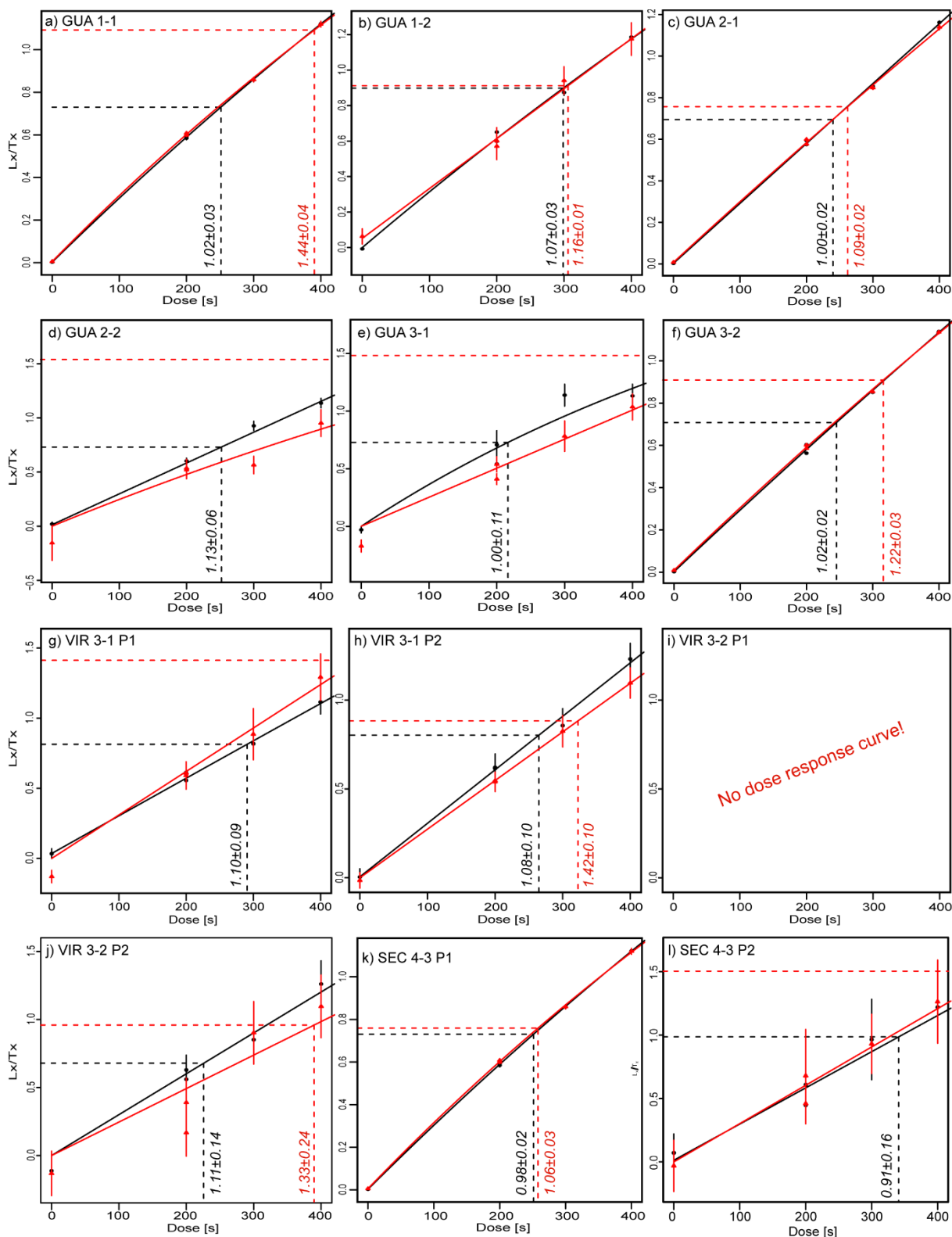
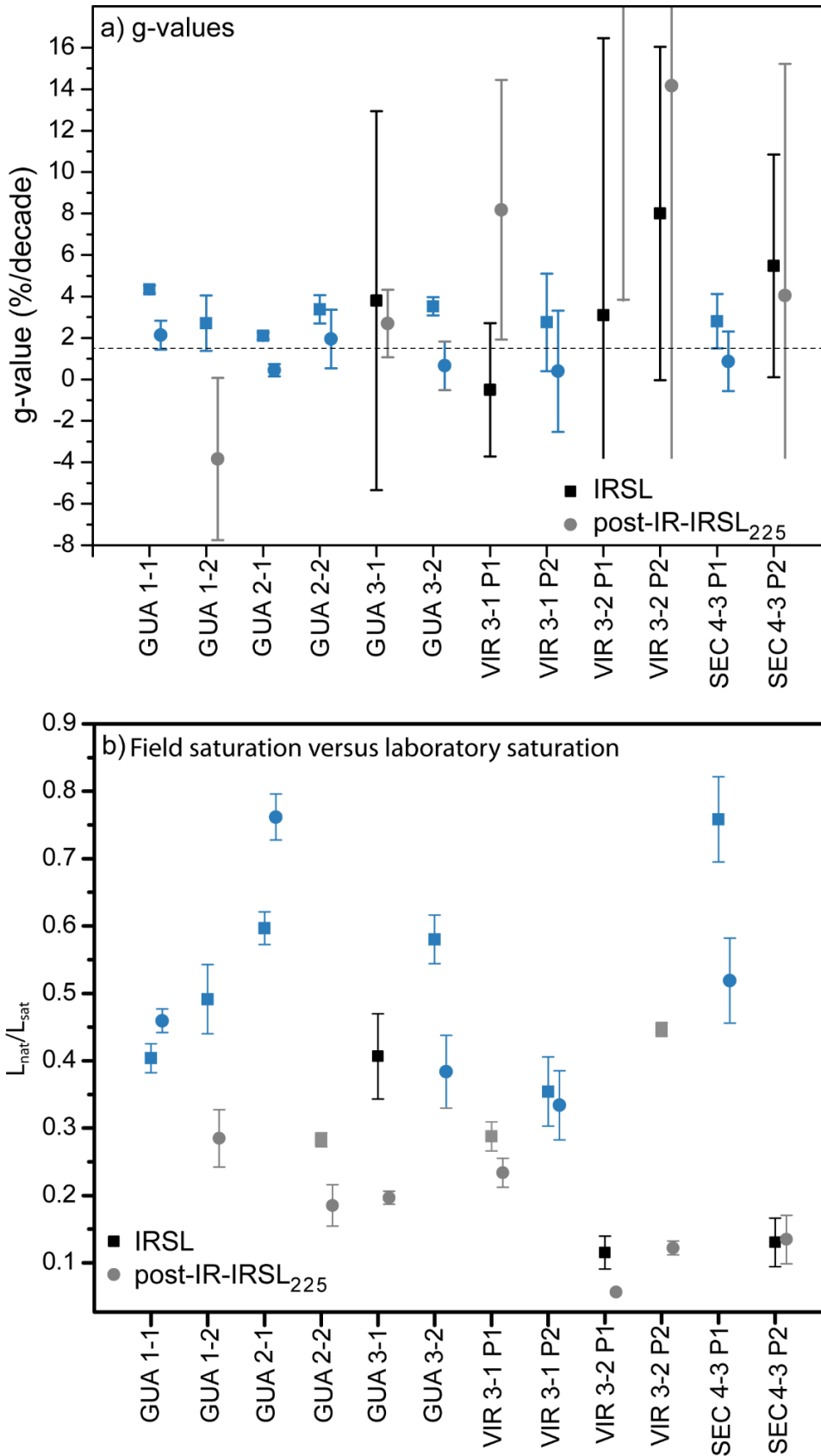


**Fig. S1.** Representative IRSL (black) and post-IR-IRSL<sub>225</sub> (red) dose-response curves of all samples constructed during dose-recovery tests. In case of sample VIR 3-2 P1 (i) the poor signal quality did not allow for reconstructing dose response curves for both signals.



37

38 **Fig. S2.** Determination of signal loss due to anomalous fading. a) g-values measured according to  
 39 Auclair et al. (2003). Each value represents the arithmetic mean of three aliquots. g-values with  
 40 reasonable reproducibility are marked in blue. b) Ratio between field saturation and laboratory  
 41 saturation according to Rades et al. (2018). Ratios originating from feldspar signals with adequate  
 42 brightness are marked in blue.

43 **Tab. S1.** Geographical location of cobble samples and position of drill cores within each cobble.  
 44 a.s.l. = above sea level; b.s. = below surface.

Site	Sample	Latitude	Longitude	Elevation	Cobble	Core
GUA	GUA 1	21.971396° S	70.181584 W	2 m a.s.l.	GUA 1-1	GUA 1-1 Top GUA 1-1 Base
					GUA 1-2	GUA 1-2 Top GUA 1-2 Base
	GUA 2	21.971395° S	70.181612° W	1.5 m a.s.l.	GUA 2-1	GUA 2-1 Top GUA 2-1 Base
					GUA 2-2	GUA 2-2 Top GUA 2-2 Base
	GUA 3	21.971393° S	70.181642° W	1 m a.s.l.	GUA 3-1	GUA 3-1 Top GUA 3-1 Base
					GUA 3-2	GUA 3-2 Top GUA 3-2 Base
	VIR 3-1	22.6369 S	70.2618 W	17 m a.s.l. (13 m b.s.)	VIR 3-1 P1	VIR 3-1 P1 Base
					VIR 3-1 P2	VIR 3-1 P2 Base
	VIR 3-2	22.6369 S	70.2618 W	8.7 m a.s.l. (19 m b.s.)	VIR 3-2 P1 VIR 3-2 P2	VIR 3-2 P1 Base VIR 3-2 P2 Base
SEC	SEC 4-3	20.9885 S	70.1523 W	21.2 m a.s.l. (15.3 m b.s.)	SEC 4-3 P1 SEC 4-3 P2	SEC 4-3 P1 Base SEC 4-3 P2 Base

45  
 46  
 47 **Tab. S2.** Post-IR-IRSL<sub>225</sub> measurement protocol used for luminescence rock surface dating. R1-R4  
 48 = regenerative doses; R0 = Zero dose; RR = Recycling ratio.

Step	L <sub>n</sub> /T <sub>n</sub>	Full protocol	Treatment	Signal
1			Preheat (250 °C for 60 s)	L <sub>n/x</sub> (IRSL) L <sub>n/x</sub> (post-IR-IRSL <sub>225</sub> )
2			IR LEDs (200 s @ 50 °C)	
3			IR LEDs (200 s @ 225 °C)	
4			Test dose (~25 Gy)	T <sub>n/x</sub> (IRSL) T <sub>n/x</sub> (post-IR-IRSL <sub>225</sub> )
5			Preheat (250 °C for 60 s)	
6			IR LEDs (200 s @ 50 °C)	
7			IR LEDs (200 s @ 225 °C)	
8			IR LEDs (100 s @ 270 °C)	
9			Dose (R1-R4, R0, RR)	
10			Return to step 1	

54

55 **Tab. S3.** Lithology and estimated feldspar crystal size of all cobbles targeted in this study.

Cobble	Rock type	K-feldspar	Feldspar size (µm)	Other minerals
GUA 1-1	Quartz diorite	Yes	600±200	Quartz, plagioclase, biotite, amphibole
GUA 1-2	Basaltic dyke rock	-	200±100	Pyroxene, amphibole, plagioclase, biotite, olivin
GUA 2-1	Diorite	Yes	600±200	Plagioclase, biotite
GUA 2-2	Granite	Yes	400±100	Quartz, plagioclase, biotite, fragments of metamorphic rocks
GUA 3-1	Granite (pegmatitic)	Yes	400±100	Quartz, biotite, haematite
GUA 3-2	Granite	Yes	800±200	Quartz, plagioclase, biotite
VIR 3-1 P1	Basalt/Andesite (porphyric)	-	800±200	Pyroxene, idiomorphic plagioclase
VIR 3-1 P2	Basalt (few idiomorphic crystals)	-	200±100	Pyroxene, plagioclase
VIR 3-2 P1	Andesite/Basalt (porphyric)	-	800±200	Pyroxene, plagioclase, ilmenite
VIR 3-2 P2	Diorite	Yes	600±200	Plagioclase, biotite, ilmenite
SEC 4-3 P1	Quartz monzonite (granitoidic rock)	Yes	400±100	Quartz, plagioclase (idiomorphic), biotite, amphibole
SEC 4-3 P2	Norite (gabbroidic rock)	-	200±100	Pyroxene, biotite, plagioclase (idiomorphic)

56

57

58

**Tab. S4.** Dose rates of cobbles and surrounding sediments.  $DR_{cos}$  – cosmic dose rate,  $DR_{int}$  – internal feldspar dose rate,  $DR_{cobble (IM Beta)}$  – infinite matrix beta dose rate of cobble,  $DR_{cobble (IM Gamma)}$  – infinite matrix gamma dose rate of cobble,  $DR_{sediment (IM Beta)}$  – infinite matrix beta dose rate of surrounding sediment,  $DR_{sediment (IM Gamma)}$  – infinite matrix gamma dose rate of surrounding sediment.

Cobble	Diameter (cm)	Uranium (ppm)	Thorium (ppm)	Potassium (%)	$DR_{cos}$ (Gy/ka)	$DR_{int}$ (Gy/ka)	$DR_{cobble (IM Beta)}$ (Gy/ka)	$DR_{cobble (IM Gamma)}$ (Gy/ka)	$DR_{sediment (IM Beta)}$ (Gy/ka)	$DR_{sediment (IM Gamma)}$ (Gy/ka)
GUA 1-1	8	6.57±0.34	33.6±1.77	2.51±0.03	0.26±0.03	1.89±0.68	3.14±0.01	2.97±0.09	1.61±0.24*	1.70±0.37*
GUA 1-2	5	1.15±0.07	2.84±0.18	0.72±0.01	0.26±0.03	0.20±0.15	0.68±0.01	0.44±0.01	1.61±0.24*	1.70±0.37*
GUA 2-1	5	5.60±0.29	15.51±0.91	2.45±0.03	0.26±0.03	1.89±0.68	2.62±0.01	1.98±0.06	1.61±0.24*	1.70±0.37*
GUA 2-2	5	8.66±0.45	29.35±1.57	1.63±0.02	0.26±0.03	1.29±0.38	2.89±0.01	2.78±0.09	1.61±0.24*	1.70±0.37*
GUA 3-1	4	9.04±0.47	69.15±3.96	0.12±0.01	0.26±0.03	1.29±0.38	2.50±0.01	4.35±0.2	1.61±0.24*	1.70±0.37*
GUA 3-2	4	6.37±0.33	18.8±1.01	1.63±0.02	0.26±0.03	2.45±0.72	2.22±0.01	2.02±0.06	1.61±0.24*	1.70±0.37*
VIR 3-1 P1	6	1.04±0.06	3.01±0.20	1.17±0.01	0.05±0.01	0.73±0.49	0.98±0.01	0.55±0.01	1.36±0.55**	0.87±0.40**
VIR 3-1 P2	4	2.92±0.16	11.8±0.72	2.44±0.03		0.20±0.15	2.24±0.01	1.5±0.04	1.36±0.55**	0.87±0.40**
VIR 3-2 P1	3	1.72 ± 0.23	6.11 ± 0.40	0.57±0.04	0.03±0.01	0.73±0.49	0.71±0.01	0.63±0.03	0.37±0.12*	0.30±0.14*
VIR 3-2 P2	3	0.30 ± 0.09	1.80 ± 0.13	0.41±0.03		1.89±0.68	0.35±0.01	0.22±0.01	0.37±0.12*	0.30±0.14*
SEC 4-3 P1	5	6.52±0.34	25.4±1.35	4.14±0.04	0.04±0.01	1.29±0.38	4.08±0.01	2.98±0.08	2.20±1.30**	1.49±1.05**
SEC 4-3 P2	4	0.70±0.05	1.71±0.13	1.26±0.02		0.20±0.15	0.97±0.01	0.47±0.01	2.20±1.30**	1.49±1.05**

\* Based on volume percentages of 70% cobbles (dose rate estimated by mean cobble gamma/beta dose rate of each sampling site) and 30% air-filled pore volume (zero dose rate)

\*\*Based on volume percentages of 70% cobbles (dose rate estimated by mean cobble gamma/beta dose rate of each sampling site) and 30% fine-grained sediment (dose rate estimated from dose rate data provided by Bartz et al., 2020)

59

60

61

62

63

64

65 **Tab. S5.** Parameters provided by the model of Freiesleben et al. (2015) for all fitted cobbles. BF – Depth of bleaching front below cobble surface.

Cobble	Side	IRSL					post-IR-IRSL			
		BF <sub>IRSL</sub> (mm)	$\mu$ (mm <sup>-1</sup> )	$t_{e1} * \sigma \varphi_0$	$t_b$ (ka)	$t_{e2} * \sigma \varphi_0$	BF <sub>post-IRSL</sub> (mm)	$\mu$ (mm <sup>-1</sup> )	$t_{e1} * \sigma \varphi_0$	$t_b$ (ka)
GUA 1-1	Top	4.8	1.53±0.31	1131±1696	-	-	2.6	1.61±0.68	8.9±8.8	-
	Bottom	6.5	0.99±0.21	412±558	1.6±0.6	8.0±14.2	2.6	0.70±0.13	4.1±1.5	-
GUA 1-2	Top	1.5	1.70±0.38	167±210	-	-	0.1	1.10±0.67	0.8±0.3	-
	Bottom	0.5	5.52±8.13	10.9±31.3	-	-	-	2.00±1.86	0.5±0.4	-
GUA 2-1	Top	3.2	1.70±0.38	167±210	-	-	1.9	1.54±0.34	13.5±10.3	-
	Bottom	2.2	1.37±0.18	14.1±5.7	-	-	1	1.93±0.23	4.8±1.3	-
GUA 2-2	Top	3.4	3.06±5.69	20000±382690	-	-	1.4	0.50±0.20	1.35±0.71	-
	Bottom	1.5	6.82±6.2	20000±178812	-	-	0.4	1.87±3.75	1.43±2.77	-
GUA 3-1	Top	-	-	-	-	-	-	0.61±7.03	0.05±0.35	-
	Bottom	-	-	-	-	-	-	0.86±0.26	1.26±0.40	-
GUA 3-2	Top	3.3	1.58±0.34	124±142	0.8±0.8	1.1±5.1	0.8	0.76±0.27	1.3±0.6	-
	Bottom	1.5	2.64±0.82	39±45	-	-	0.5	4.00±3.77	5.3±7.2	-
SEC 4-3 P1	Bottom	0.2	2.00±1.20	1.04±0.63	-	-	-	-	-	-

66  
67  
68



69 **Tab. S6.** Post-IR-IRSL<sub>225</sub> parameters for burial dating of all targeted cobbles. Age<sub>cor1</sub> – fading corrected age using g-values, Age<sub>cor1</sub>-Res - fading corrected  
70 age using g-values with residual age subtraction, Age<sub>cor2</sub> – fading corrected age using ratios between field and laboratory saturation, Age<sub>cor2</sub>-Res - fading  
71 corrected age using ratios between field and laboratory saturation with residual age subtraction. \*minimum age estimates based on palaeodoses equal to  
72 2 x D<sub>0</sub>. Grey shading indicates cobbles with luminescence properties adequate to provide robust burial ages.

Lab-ID	Cobble	Core	Depth (mm)	Dose rate (Gy/ka)	D <sub>0</sub> (Gy)	Dose (Gy)	Age <sub>faded</sub> (ka)	g-value (%/dec)	g-value <sub>mean</sub> (%/dec)	Age <sub>cor1</sub> (ka)	Age <sub>cor1</sub> - Res (ka)	L <sub>nat</sub> /L <sub>sat</sub>	L <sub>nat</sub> /L <sub>sat</sub> mean	Age <sub>cor2</sub> (ka)	Age <sub>cor2</sub> - Res (ka)
C-L4989	GUA 1-1	GUA 1-1 Top	0-1	6.91±0.73	135	5.6±0.2	0.8±0.2	3.1±1.7	2.1±0.7	1.0±0.2	0.2±0.2	0.50±0.02	0.46±0.02	1.8±0.3	1±0.3
			1-2	7.27±0.73		67±2.0	9.3±1.2	1.7±1.5		11.2±1.7	10.4±1.7	0.46±0.02		20±2.6	19±2.6
		GUA 1-1 Base	1-2	7.27±0.73		21±0.6	2.9±0.4	0.4±1.5		3.4±0.6	2.6±0.6	0.41±0.03		6.2±0.9	5.4±0.9
			2-3	7.33±0.73		89±3.0	12.2±1.6	3.4±1.6		14.8±2.2	14±2.2	0.47±0.04		27±3.4	26±3.4
	GUA 1-2	GUA 1-2 Top	0-1	2.85±0.34	55	73±7.4	25.5±5.6	-7.8±5.5	-3.8±3.9	25.5±5.6	24.9±5.6	0.24±0.14	0.28±0.04	>32*	>32*
		GUA 1-2 Base	0-1	2.85±0.34		80±16	28.1±9.0	0.1±6.1		28.1±9.0	27.4±9	0.33±0.14		>32*	>32*
C-L4990	GUA 2-1	GUA 2-1 Top	0-1	4.56±0.34	110	2.2±0.1	0.5±0.1	-0.1±1.2	0.4±0.3	0.5±0.1	-0.2±0.1	0.72±0.03	0.76±0.03	0.6±0.1	0±0.1
			1-2	4.79±0.33		34±0.8	7.2±0.6	0.6±1.2		7.4±0.6	6.8±0.6	0.74±0.03		9.4±0.9	8.8±0.9
		GUA 2-1 Base	0-1	4.56±0.34		14.9±0.3	3.3±0.3	0.9±1.2		3.4±0.3	2.7±0.3	0.83±0.03		4.3±0.4	3.7±0.4
			0-1	5.86±0.49		39±5.7	6.6±1.5	2.1±4.1		7.9±2.2	5.3±2.2	0.10±0.05		>20*	>20*
	GUA 2-2	GUA 2-2 Top	1-2	6.11±0.49	60	44±3.1	7.2±1.1	-1.4±2.9	2.0±1.4	8.6±1.9	5.9±1.9	0.16±0.04	0.19±0.03	>20*	>20*
			2-3	6.15±0.49		59±3.0	9.6±1.3	1.4±4.1		11.5±2.3	8.9±2.3	0.16±0.06		>20*	>20*
		GUA 2-2 Base	0-1	5.86±0.49		40±3.1	6.9±1.1	7.1±3.6		8.2±1.9	5.6±1.9	0.26±0.08		>20*	>20*
			1-2	6.11±0.49		56±4.6	9.2±1.5	0.7±3.2		11±2.5	8.4±2.5	0.25±0.07		>20*	>20*
C-L4991	GUA 3-1	GUA 3-1 Top	1-2	6.15±0.49	125	25±2.1	4.0±0.6	-1.6±6.8	2.7±1.6	5.0±1.3	-0.6±1.3	0.21±0.17	0.20±0.01	20±3.2	14±3.2
			0-1	5.94±0.49		37±5.1	6.2±1.4	3.5±5.7		7.8±2.3	2.2±2.3	0.17±0.09		31±6.8	25±6.8
		GUA 3-1 Base	1-2	6.15±0.49		75±8.0	12.2±2.2	2.7±6.2		15.6±4.6	10±4.6	0.21±0.13		>32*	>32*
			2-3	6.19±0.49		122±7	19.8±2.7	6.2±7.3		25.5±7.0	19.9±7	0.19±0.15		>32*	>32*
	GUA 3-2	GUA 3-2 Top	0-1	6.51±0.78	125	37±1.1	5.8±0.9	1.3±1.3	0.7±1.2	6.1±1.2	5.6±1.2	0.55±0.03	0.38±0.05	15±2.3	15±2.3
			1-2	6.65±0.78		171±10	26±4.6	1.2±1.2		27.4±6.1	26.9±6.1	0.47±0.02		>32*	>32*
		GUA 3-2 Base	2-3	6.67±0.78		76±1.8	11.4±1.6	0.8±1.3		12.1±2.2	11.6±2.2	0.48±0.02		30±4.2	29±4.2
			0-1	6.51±0.78		19±1.3	2.9±0.6	1.7±3.0		3.0±0.7	2.6±0.7	0.22±0.06		7.6±1.4	7.1±1.4
		GUA 3-2 Base	1-2	6.65±0.78		102±7	15.4±2.9	3.7±5.2		16.3±3.7	15.8±3.7	0.28±0.09		>32*	>32*
			2-3	6.67±0.78		84±4.8	12.6±2.2	-4.8±4.9		13.4±2.9	12.9±2.9	0.30±0.07		>32*	>32*
C-L4366	VIR 3-1	VIR 3-1 P1	1-2	2.59±0.59	115	176±64	68±29	8.2±6.3	-	>70*	-	0.23±0.06	-	>70*	-
	VIR 3-1	VIR 3-1 P2	0-1	3.21±0.39	175	>280*	>88*	0.4±2.8	0.4±2.8	>88*	-	0.33±0.04	0.33±0.04	>88*	-
	P2	Base	1-2	3.42±0.36		>280*	>82*	-		>82*	-	-		>82*	-
C-L4367	VIR 3-2	VIR 3-2 P1	1-2	1.80±0.50	-	-	-	24.3±22.3	-	-	-	0.06±0.21	-	-	-
	VIR 3-2	VIR 3-2 P2	1-2	2.55±0.68	-	-	-	14.2±18.5	-	-	-	0.12±0.06	-	-	-
C-L4368	SEC 4-3	SEC 4-3 P1	0-1	6.32±0.61	200	249±16	40±6.3	0.9±1.4	0.8±0.3	>50*	-	0.52±0.02	0.52±0.02	>50*	-
	P1	Base	1-2	6.77±0.49	-	>320*	>49*	0.7±1.3	-	>49*	-	-		>49*	-
	SEC 4-3	SEC 4-3 P2	1-2	2.21±0.17	170	98±13	44±9.5	4.0±11.2	-	-	-	0.13±0.12		>120*	-

## 75 2. ESR and U-series dating

### 76 Methods

#### 77 *Sample preparation for ESR and U-series dating*

78 The ESR samples were firstly washed in deionised water in an ultrasonic basin to remove clay minerals. The  
79 initial thickness of the shells was measured using a digital calliper. Etching was performed with 5% HCl for 3  
80 min to remove the alpha-irradiated outer layer. The dried shells were re-measured for thickness and then gently  
81 ground with an agate mortar and pestle. The 150-250  $\mu\text{m}$  fraction was used for ESR dating. ESR dose values  
82 were evaluated using the multiple aliquot additive dose method. For each sample, the shell powder was divided  
83 into 19 aliquots. While one aliquot was kept as natural reference, 18 aliquots were irradiated with a Gammacell  
84 1000  $^{137}\text{Cs}$  gamma source (dose rate =  $6.8 \pm 0.2$  Gy/min) at the Centro Nacional de Investigación sobre la  
85 Evolución Humana (CENIEH, Spain) with doses ranging from 10 to 1250 Gy.

86 For U-series dating, subsamples of around 500 mg were extracted using a small band saw. Potential  
87 contamination by sawing as well as surface contamination were removed by etching with strongly diluted  
88  $\text{HNO}_3$  for about 10 minutes. After etching the samples were rinsed with MilliQ water, dried, weighted and  
89 dissolved in 7M  $\text{HNO}_3$ . A mixed Th-U spike ( $^{229}\text{Th}$ - $^{233}\text{U}$ - $^{236}\text{U}$ ) was added to the dissolved samples. More  
90 information on the spike material and calibration can be found in Obert et al. (in prep). Sample-spike  
91 equilibration was achieved by cooking the samples over night at 120  $^\circ\text{C}$ . The samples were then dried down  
92 and treated with conc.  $\text{HNO}_3$ , conc. HCl and  $\text{H}_2\text{O}_2$  to dissolve organic matter. Samples were dried down again  
93 and taken up in 1 ml of 7M  $\text{HNO}_3$  ready for column chemistry. Chemical separation was performed using  
94 BioRad AG1-X8 anion exchange resin in  $\text{HNO}_3$  media. The majority of the matrix was not retained on the  
95 resin and rinsed off with 7M  $\text{HNO}_3$ , Th was eluted with 6M HCl and U was eluted with 1M HBr. Thorium  
96 was purified on the same column using a shortened version of the same protocol. Both Th and U were treated  
97 with  $\text{H}_2\text{O}_2$  in order to destroy potential organic residue of the resin and taken up for measurement.

98 Ages were calculated in an iterative approach using the decay constants of Cheng et al. (2013) and Jaffey et  
99 al. (1971). The corresponding uncertainties were determined by a Monte Carlo simulation.

#### 100 *ESR equivalent dose ( $D_e$ ) analyses*

101 Fitting was performed with Microcal OriginPro 8.5 software based on a Levenberg-Marquardt algorithm by  
102 chi-square minimisation. The goodness-of-fit is assessed through the adjusted r-square ( $r^2$ ) value, which  
103 accounts for the degree of freedom of the system. According to previous studies on ESR dating of mollusc  
104 shells (e.g. Schellmann and Radtke, 1997),  $D_e$  values were obtained by fitting a single saturating exponential  
105 (SSE) through the mean ESR intensities derived from the repeated measurements without data weighting  
106 (equal weights; EW). An additional fitting procedure was applied to our data set using a double saturating  
107 exponential (DSE). With the DSE function, we tested different weighting options: data weighting by the  
108 inverse of the squared ESR intensity ( $1/I^2$ ) and EW. The SSE and DSE fitting options were then used with the  
109  $D_e$ - $D_{\text{max}}$  plot (DDP) procedure for  $D_e$  determination (Schellmann and Radtke, 1997). Following the DDP

110 procedure,  $D_e$  plateaux include all values that are within the range of uncertainty of a local minimum  $D_e$  value.  
111 The final  $D_e$  value is then derived from the mean of all  $D_e$  values within the plateau including an error which  
112 is calculated from the individual uncertainties (Schellmann and Radtke, 2001).

### 113 *ESR dose rate evaluation and age calculations*

114 The external gamma dose rate was measured in the field using a portable *in situ* gamma spectrometer  
115 (Ortec NaI(Tl) Scintillation Probe), calculated with the “threshold” technique (Duval and Arnold, 2013).  
116 Samples SEC 4-2 and SEC 4-2a were selected from the mollusc-rich layer at section S4, where shell fragments  
117 dominate the surrounding of the samples (Fig. 1). For these samples, matrix material has been extracted from  
118 the interior of the bivalve of sample SEC 4-2 and radionuclide contents ( $^{238}\text{U}$ ,  $^{234}\text{Th}$  and  $^{40}\text{K}$ ) were measured  
119 using the  $\mu\text{Dose}$ -system at the Justus-Liebig-University Gießen (Institute of Geography, Germany). For sample  
120 VIR 2-1, laboratory gamma spectrometry analyses were carried out to derive  $^{238}\text{U}$ ,  $^{234}\text{Th}$ , and  $^{40}\text{K}$  contents from  
121 the sediment surrounding the shell. The following parameters were used for dose rate calculations: an alpha  
122 efficiency of  $0.07 \pm 0.01$  (Grün and Katzenberger-Apel, 1994), Monte-Carlo beta attenuation factors from  
123 Marsh (1999), dose-rate conversion factors from Guérin et al. (2011), and an estimated long-term water content  
124 of  $13 \pm 7\%$  in the sediment of the VIR section, based on the previous evaluation by Bartz et al. (2020). Due to  
125 complex moisture conditions for the two SEC shells with initial water-saturated conditions and fast post-  
126 depositional drying, we simulated the water content between 1 and 30% covering hyper-arid to water-saturated  
127 conditions, respectively. Cosmic dose rate was calculated using Prescott and Hutton (1994). Age calculations  
128 were performed with USESR, a Matlab-based program (Shao et al., 2014) using the US and AU models defined  
129 by Grün et al. (1988) and Shao et al. (2012), respectively, which was originally developed for ESR dating of  
130 tooth enamel.

## 131 **Results and Interpretation**

### 132 *ESR fitting results*

133 The SSE function (EW) provides moderate to good goodness-of-fit with adjusted  $r^2$  values of 0.985-0.993.  
134 However, the high dose region is not well fitted with the SSE function. In contrast, the DSE function describes  
135 well the whole data set of each sample and provides an excellent goodness-of-fit with adjusted  $r^2$  values of  
136  $\sim 0.999$ , which is independent from the data weighting option ( $1/I^2$ , and EW) (Table S8).

137 Using the SSE function, all three samples show  $D_e$  values that clearly increase along with increasing  $D_{\text{max}}$  (Fig.  
138 S4), which caused a difficult determination of a local minimum  $D_e$  value and a corresponding  $D_e$  plateau as  
139 per the original DDP approach (Schellmann and Radtke, 2001). Nevertheless, taking into account  $D_e$  specific  
140 uncertainties, sample VIR 2-1 shows a small local minimum  $D_e$  at aliquot #12, building an indistinct plateau  
141 for aliquots #12-15 ( $D = 530\text{-}800\text{ Gy}$ ; Fig. S4). In contrast, both SEC samples do not show plateaux (Fig. S4).  
142 Thus, a final  $D_e$  value has only been calculated for sample VIR 2-1 using the SSE function (Fitting #1),  
143 resulting in  $77 \pm 8\text{ Gy}$  (Table S8).

144 The effect of  $D_{\text{max}}$  on the final  $D_e$  has also been studied with the DSE function. In contrast to the SSE function,  
145 DSE fitting reaches plateaux from  $D_{\text{max}} \geq 270\text{ Gy}$  for all three samples (Fig. S4). The larger scatter locally

146 observed for lower  $D_{\max}$  values with higher individual uncertainties is simply the result of a smaller number of  
147 experimental points to be fitted in combination with a large number of fitted parameters ( $n=5$ ) with this  
148 function (e.g., Duval et al., 2009; Duval and Grün, 2016). Due to recommendations by Lyons et al. (1992) we  
149 used at least 15 data points with the DSE function (i.e., 3 data points per fitted parameter, Lyons et al., 1992)  
150 for  $D_e$  calculation. Thus, using  $D_{\max} \geq 800$  Gy, samples VIR 2-1, SEC 4-2, and SEC 4-2a show consistent DSE  
151 results at  $1\sigma$  for the two weighting options (Fitting #2-3) resulting in  $D_e$  values of  $\sim 39$  Gy,  $\sim 80$  Gy, and  $\sim 84$   
152 Gy, respectively (Fig. S4, Table S8). These results show the robustness of the ESR data set: the  $D_e$  values do  
153 not depend on the selected  $D_{\max}$  or data weighting option.

#### 154 *Comparison of ESR $D_e$ values derived from the SSE and DSE functions*

155 Sample VIR 2-1 shows lower  $D_e$  values with the DSE function of  $\sim 50$  % compared to the  $D_e$  value derived  
156 from the SSE function (Table S8), which has been classically used so far for shells (e.g., Barabas et al., 1992;  
157 Molodkov, 2020, 1988; Radtke, 1989; Schellmann et al., 2020; Schellmann and Radtke, 2003, 2001, 1997).  
158 The overestimating behaviour of the SSE function has also been observed by Duval et al. (2009) in ESR dating  
159 of tooth enamel. Similarly, ESR dating of aragonitic molluscs might be affected by a multi-component dating  
160 signal that influences the dose response (Barabas, 1989; Barabas et al., 1992). Although Schellmann and  
161 Radtke (1997) proposed the DDP procedure together with the SSE function to account for interfering ESR  
162 signal components, this approach seems to have limited usefulness for our samples due to (1) inadequate fitting  
163 results, (2) increasing  $D_e$  values with increasing  $D_{\max}$ , and (3) no clear DDPs. In general, the existing correlation  
164 between  $D_e$  and  $D_{\max}$  values indicates that the fitting function is inappropriate to describe the ESR data (e.g.,  
165 Duval et al., 2009). Our results show that the behaviour of the ESR signal measured in these samples does not  
166 follow a SSE but rather a DSE function, which is consistent with the existing knowledge about the nature and  
167 composition of the radiation-induced ESR signal in mollusc shells. This is supported by the higher goodness-  
168 of-fit achieved by the DSE function, and the  $D_e$  plateaux observed over the data points  $\geq 270$  Gy (Fig. S4). This  
169 evidence highlights the high potential of the DSE function to describe well the ESR data of the three samples.  
170 Thus, due to the agreement of the DSE function using EW and  $1/I^2$ , we assume the DSE with EW as best  
171 estimate to calculate the true ESR ages of the three mollusc samples (Table S9).

#### 172 *ESR environmental dose rate*

173 The environmental dose rate was evaluated from the sediment in the surrounding of sample VIR 2-1 and  
174 sediment from the interior of the bivalve of sample SEC 4-2. Radionuclide concentrations derived from the  
175 latter are also representative for sample SEC 4-2a to calculate the beta dose rate as both shells originate from  
176 the same shell horizon. *In-situ* gamma measurements were performed at all three locations and individual  
177 gamma dose rates are included in the environmental dose rate calculation. Both SEC samples show gamma  
178 dose rates that vary in a narrow range with  $1.15 \pm 0.07$  Gy/ka (SEC 4-2) and  $0.99 \pm 0.07$  Gy/ka (SEC 4-2a),  
179 indicating an overall spatially homogenous radioactivity in the mollusc-rich layer at section S4. The *in-situ*  
180 gamma dose rate of sample VIR 2-1 ( $0.32 \pm 0.06$  Gy/ka) match within confidence interval with the values  
181 obtained for the IRSL samples from the same sand horizon previously dated by Bartz et al. (2020).

182 For the three samples the gamma dose rate represents  $>70\%$  of the total dose rate, while the weight of the  
183 internal dose rate is much lower ( $<20\%$ ). This indicates that the assumption around the long-term water content  
184 may have a significant impact on the calculated ESR age results. While a water content of  $\sim 13\%$  for section  
185 VIR already includes short- and long-term variations due to tectonic uplift and sea-level changes (Bartz et al.,  
186 2020), the situation is different at the SEC section. Although the molluscs have lived in a moist and water-  
187 saturated environment, they have likely been transported towards inland by a high-energetic event. Due to the  
188 hyper-arid conditions in the Atacama Desert, it can thus be assumed that the two SEC samples have  
189 experienced fast drying after deposition. Age simulations performed using water content values ranging from  
190  $1\%$  to  $30\%$  (i.e. hyper-arid to saturated, Bartz et al., 2020) are graphically displayed in Fig. S5. The large  
191 associated error ( $30\%$  relative  $1-\sigma$  uncertainty) was assumed to encompass short- and long-term variations in  
192 the water content. If considering  $30\%$  water content compared to  $1\%$ , the resulting ESR age estimates increase  
193 by  $\sim 27\%$ , but nevertheless remain within  $1-\sigma$  uncertainty. In order to encompass for both wet and dry  
194 conditions after deposition, we consider a water content of  $5\%$  as best estimate to calculate final ESR ages for  
195 samples SEC4-2 and SEC4-2a.

196

197

198

199 **Table S7.** U-series dating results obtained from solution MC-ICPMS analyses performed at the University of Cologne (Institute of Geology and  
 200 Mineralogy, Germany). All errors are at  $1\sigma$ , while the confidence intervals of the U-series age estimates and initial  $^{234}\text{U}/^{238}\text{U}$  ratios are at  $2\sigma$ .

Sample ID	U (ppm)	$^{232}\text{Th}$ (ppb)	$^{230}\text{Th}/^{232}\text{Th}$	$^{230}\text{Th}/^{238}\text{U}$	$^{234}\text{U}/^{238}\text{U}$	U-series Age (ka)	Init. $^{234}\text{U}/^{238}\text{U}$
VIR 2-1	C109	$0.342 \pm 0.001$	$0.055 \pm 0.005$	$15915 \pm 1791$	$0.838 \pm 0.051$	$127.2 \pm 28.4$	$1.269 \pm 0.023$
	C110	$0.339 \pm 0.001$	$0.0003 \pm 0.001$	$2985710 \pm 8767540$	$0.818 \pm 0.026$	$123.5 \pm 13.8$	$1.255 \pm 0.012$
	C111	$0.318 \pm 0.001$	$0.014 \pm 0.002$	$60855 \pm 10321$	$0.866 \pm 0.043$	$133.0 \pm 24.6$	$1.287 \pm 0.021$
	Mean ( $\pm 1$ s.d.)	<b><math>0.333 \pm 0.013</math> (3.9 %)</b>	<b><math>0.023 \pm 0.029</math></b>	<b><math>1020827 \pm 1701787</math></b>	<b><math>0.841 \pm 0.024</math></b>	<b><math>127.9 \pm 4.8</math> (3.7 %)</b>	<b><math>1.270 \pm 0.016</math></b>
SEC 4-2	C49	$0.666 \pm 0.002$	$0.008 \pm 0.0001$	$268571 \pm 4478$	$1.068 \pm 0.010$	$200.2 \pm 9.6$	$1.386 \pm 0.011$
	C65	$0.765 \pm 0.002$	$0.013 \pm 0.0001$	$182230 \pm 2210$	$1.037 \pm 0.008$	$197.3 \pm 8.3$	$1.340 \pm 0.009$
	C112	$0.648 \pm 0.002$	$0.003 \pm 0.001$	$651228 \pm 112162$	$1.088 \pm 0.017$	$199.6 \pm 16.6$	$1.422 \pm 0.020$
	Mean ( $\pm 1$ s.d.)	<b><math>0.693 \pm 0.063</math> (9.1 %)</b>	<b><math>0.008 \pm 0.005</math></b>	<b><math>367343 \pm 249613</math></b>	<b><math>1.064 \pm 0.026</math></b>	<b><math>199.0 \pm 1.5</math> (0.8 %)</b>	<b><math>1.383 \pm 0.041</math></b>
SEC 4-2a	C66	$0.421 \pm 0.001$	$0.001 \pm 0.0001$	$1975972 \pm 791046$	$1.034 \pm 0.036$	$210.9 \pm 56.7$	$1.304 \pm 0.071$
	C67	$0.408 \pm 0.001$	$0.038 \pm 0.002$	$35766 \pm 1868$	$1.085 \pm 0.005$	$223.8 \pm 35.2$	$1.367 \pm 0.057$
	C113	$0.424 \pm 0.001$	$0.006 \pm 0.001$	$221008 \pm 19849$	$1.013 \pm 0.017$	$192.6 \pm 17.1$	$1.311 \pm 0.016$
	C114	$0.491 \pm 0.001$	$0.008 \pm 0.0001$	$208488 \pm 10443$	$1.131 \pm 0.008$	$220.3 \pm 10.0$	$1.452 \pm 0.013$
	C115	$0.401 \pm 0.001$	$0.001 \pm 0.0001$	$1731791 \pm 883269$	$1.018 \pm 0.019$	$193.1 \pm 19.0$	$1.319 \pm 0.018$
	Mean ( $\pm 1$ s.d.)	<b><math>0.429 \pm 0.036</math> (8.3 %)</b>	<b><math>0.011 \pm 0.016</math></b>	<b><math>834605 \pm 937327</math></b>	<b><math>1.056 \pm 0.051</math></b>	<b><math>208.1 \pm 14.7</math> (7.1%)</b>	<b><math>1.361 \pm 0.079</math></b>

202 **Table S8.** ESR fitting results using the single saturating exponential (SSE) and double saturating  
203 exponential (DSE) functions. Weighting was performed by the inverse of the squared ESR intensity  
204 ( $1/I^2$ ), and equal weights (EW). The  $D_e$ - $D_{max}$  plot procedure was used following Schellmann and  
205 Radtke (1997).

Sample	VIR2-1	SEC4-2	SEC4-2
Average weight per aliquot (mg)	200	200	150
Nr. of repeated measurements	2	2	2
Measurement precision (%)	1.8	0.5	0.9
$D_E$ precision (%)	9.2	0.3	5.0
<b>Fitting #1 SSE function (data weighting by EW)</b>			
$D_{e1}$ (Gy)	$77.0 \pm 7.9$ (10.2%)	-	-
$D_{max}$ (Gy)	530-800	-	-
Adj. $r^2$	0.985	-	-
<b>Fitting #2 DSE function (data weighting by EW)</b>			
$D_{e2}$ (Gy)	$40.9 \pm 8.2$ (20.0%)	$79.5 \pm 13.3$ (16.7%)	$76.1 \pm 18.3$ (24.0%)
$D_{max}$ (Gy)	800-900	800-1250	530-1250
Adj. $r^2$	0.998	0.999	0.998
<b>Fitting #3 DSE function (data weighting by <math>1/I^2</math>)</b>			
$D_{e3}$ (Gy)	$37.9 \pm 4.6$ (12.0%)	$80.2 \pm 10.1$ (12.6%)	$72.8 \pm 13.9$ (19.1%)
$D_{max}$ (Gy)	800-900	800-1250	530-1250
Adj. $r^2$	0.999	0.999	0.999
$D_{e2}/D_{e1}$ ratio	0.53	-	-
$D_{e2}/D_{e3}$ ratio	1.08	0.99	1.05

206

207

208 **Table S9.** Data inputs and outputs for the combined US-ESR age calculation. All errors are given at  
 209 a 1 $\sigma$  confidence level.

	Sample	VIR 2-1	SEC 4-2	SEC 4-2a
Shell	Dose (Gy) <sup>(1)</sup>	40.9±8.2	79.5±13.3	76.1±18.3
	U (ppm)	0.33±0.01	0.69±0.06	0.43±0.04
	<sup>234</sup> U/ <sup>238</sup> U	1.19±0.01	1.22±0.02	1.19±0.03
	<sup>230</sup> Th/ <sup>234</sup> U	0.71±0.02	0.87±0.005	0.88±0.03
	Initial shell thickness (µm) <sup>(2)</sup>	3800	5100	4800
	Total removed thickness (µm) <sup>(2)</sup>	1000	1000	1000
Sediment	U (ppm)	0.75±0.05 <sup>(3)</sup>	1.47±0.15 <sup>(4)</sup>	1.47±0.15 <sup>(4)</sup>
	Th (ppm)	1.70±0.12 <sup>(3)</sup>	6.60±0.50 <sup>(4)</sup>	6.60±0.50 <sup>(4)</sup>
	K (%)	0.51±0.01 <sup>(3)</sup>	1.69±0.07 <sup>(4)</sup>	1.69±0.07 <sup>(4)</sup>
	Water content (%)	11.7±5.9 <sup>(5)</sup>	5.0±1.5	5.0±1.5
Age calculations	Internal dose rate (µGy a <sup>-1</sup> )	70±6	169±4	105±5
	Beta dose rate, shell (µGy a <sup>-1</sup> )	10±1	22±2	22±2
	Gamma dose rate (µGy a <sup>-1</sup> )	322±58	1147±72	989±70
	Cosmic dose rate (µGy a <sup>-1</sup> )	62±6	80±8	80±8
	Total dose rate (µGy a <sup>-1</sup> ) <sup>(5)</sup>	464±58	1418±73	1196±70
	<b>Combined AU/US-ESR age (ka)</b>	<b>88±19</b>	<b>56±10</b>	<b>64±16</b>
	<b>U-series age (ka)</b>	<b>128±5</b>	<b>199±2</b>	<b>208±15</b>

210 <sup>(1)</sup> Final D<sub>e</sub> values are derived from the double saturating exponential (DSE) function using equal weights (EW).  
 211 <sup>(2)</sup> 10 % uncertainty was assumed.  
 212 <sup>(3)</sup> Radionuclide concentrations are measured in the laboratory using high-resolution gamma-spectrometry.  
 213 <sup>(4)</sup> The two shells were collected from the same horizon. Radionuclide concentrations are measured with the µDose-system using the  
 214 sediment from the interior of sample SEC 4-2 and thus assumed to be similar for sample SEC 4-2a.  
 215 <sup>(5)</sup> the water content was measured to be 13±7 % (dry weight %; Bartz et al., 2020), and converted to wet weight % for US-ESR age  
 216 calculation.



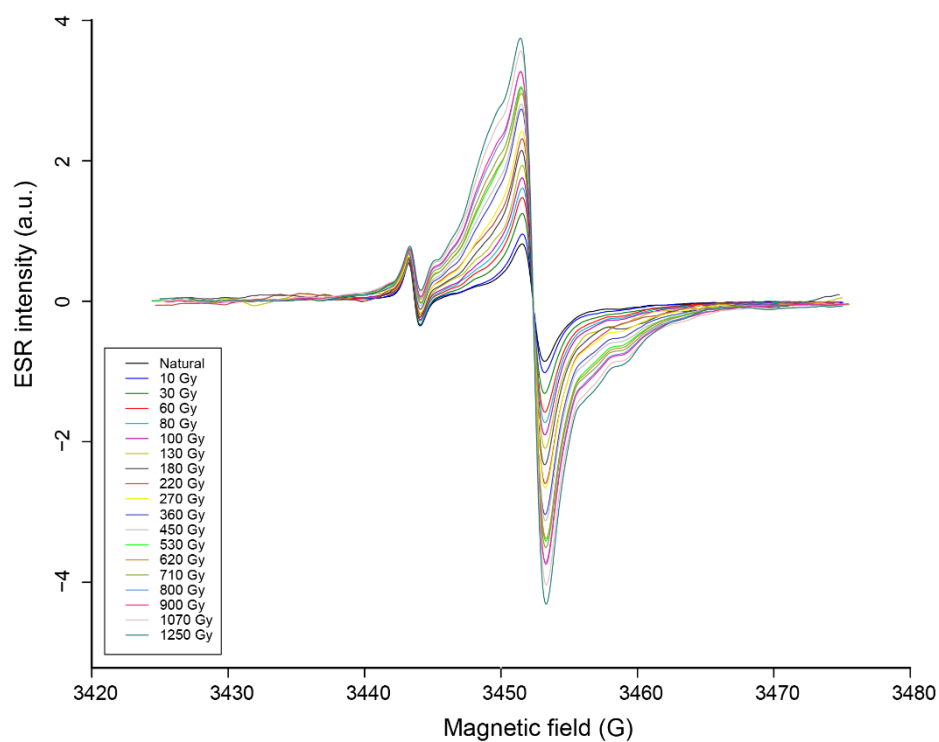


**Figure S3.** ESR spectra of mollusc shell sample VIR 2-1 showing the natural and gamma-irradiated aliquots. ESR intensities were extracted from peak-to-peak amplitude from the ESR signal at  $g=2.0006$ .

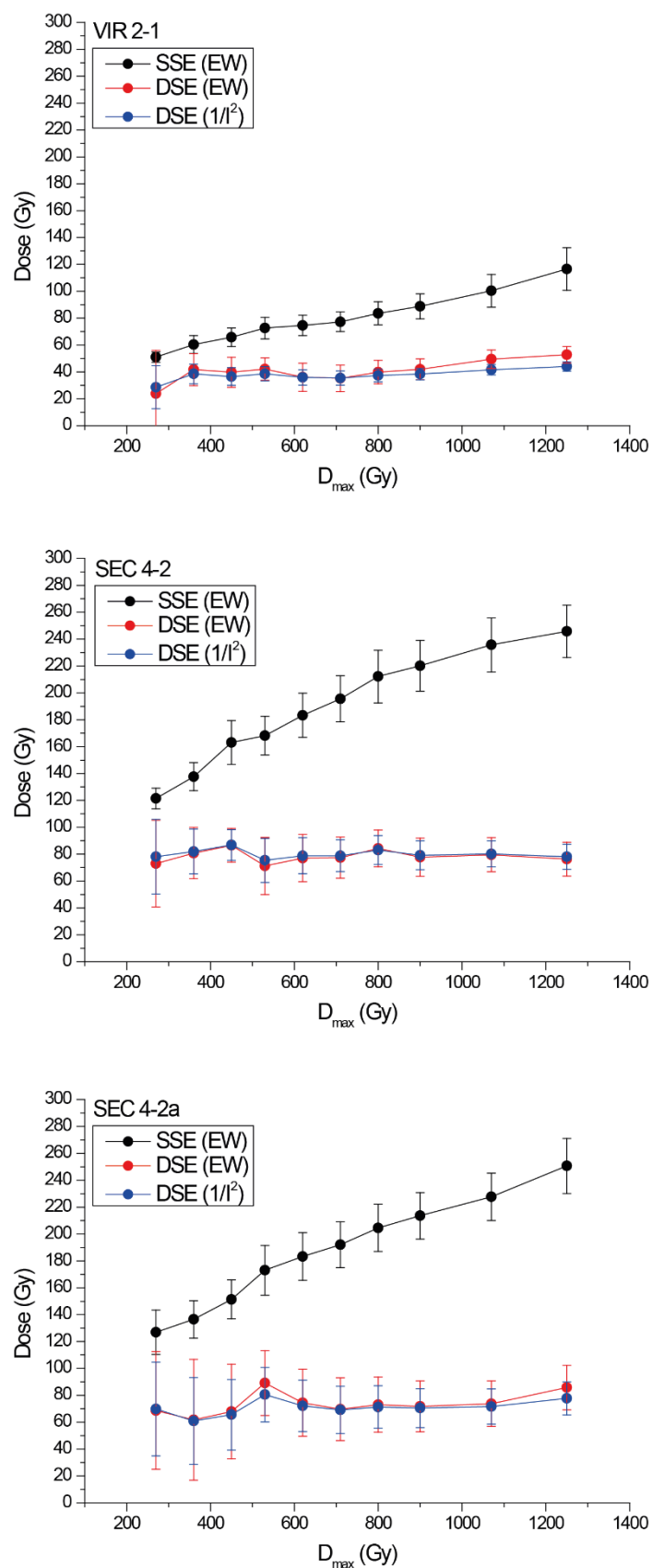


**Figure S4.**  $D_e$ - $D_{max}$  plot (DDP) data illustrated for samples VIR 2-1, SEC 4-2, and SEC 4-2a. Data are based on fitting using a single saturating exponential (SSE) function without data weighting (EW), a double saturating exponential (DSE) function with EW, and a DSE function with weighting by the inverse of the squared ESR intensity ( $1/I^2$ ).

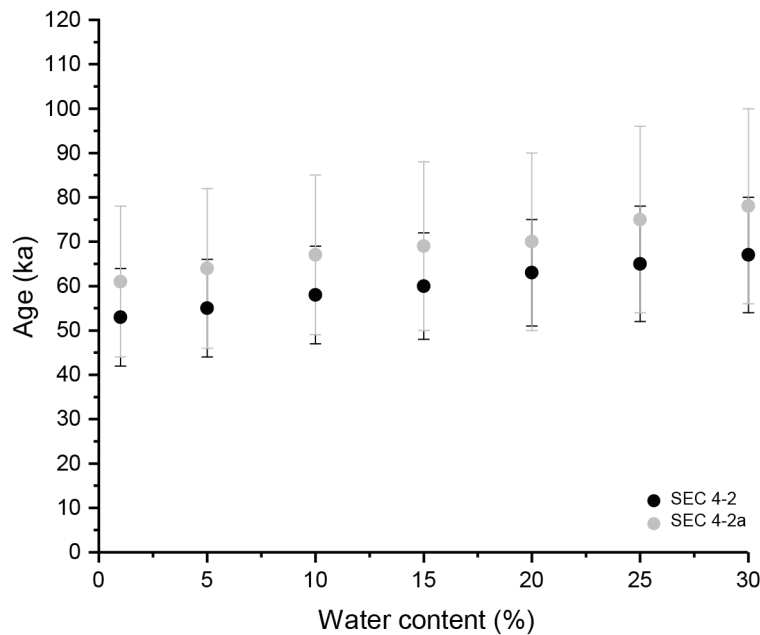


**Figure S5.** Simulated ESR ages of samples SEC 4-2 and SEC 4-2a as a function of the water content between 1 and 30 %.

## References

- Bahain, J.-J., Yokoyama, Y., Masaoudi, H., Falguères, C., Laurent, M., 1994. Thermal behaviour of ESR signals observed in various natural carbonates. *Quat. Sci. Rev.* 13, 671–674. [https://doi.org/10.1016/0277-3791\(94\)90096-5](https://doi.org/10.1016/0277-3791(94)90096-5)
- Barabas, M., 1989. ESR-Datierung von Karbonaten: Grundlagen, Systematik, Anwendung. Ph.D. thesis. Heidelberg.
- Barabas, M., Mudelsee, M., Walther, R., Mangini, A., 1992. Dose-response and thermal behaviour of the esr signal at  $g = 2.0006$  in carbonates. *Quat. Sci. Rev.* 11, 173–179. [https://doi.org/https://doi.org/10.1016/0277-3791\(92\)90060-L](https://doi.org/https://doi.org/10.1016/0277-3791(92)90060-L)
- Bartz, M., Duval, M., Brill, D., Zander, A., King, G.E., Rhein, A., Walk, J., Stauch, G., Lehmkuhl, F., Brückner, H., 2020. Testing the potential of K-feldspar pIR-IRSL and quartz ESR for dating coastal alluvial fan complexes in arid environments. *Quat. Int.* <https://doi.org/10.1016/J.QUAINT.2020.03.037>
- Cheng, H., Edwards, R.L., Shen, C.C., Polyak, V.J., Asmerom, Y., Woodhead, J., Hellstrom, J., Wang, Y., Kong, X., Spötl, C., Wang, X., 2013. Improvements in  $^{230}\text{Th}$  dating,  $^{230}\text{Th}$  and  $^{234}\text{U}$  half-life values, and U–Th isotopic measurements by multi-collector inductively coupled plasma mass spectrometry. *Earth and Planetary Science Letters* 371, 82–91.
- Duval, M., Arnold, L.J., 2013. Field gamma dose-rate assessment in natural sedimentary contexts using  $\text{LaBr}_3(\text{Ce})$  and  $\text{NaI}(\text{Tl})$  probes: A comparison between the “threshold” and “windows” techniques. *Appl.*

- Radiat. Isot. 74, 36–45. <https://doi.org/10.1016/j.apradiso.2012.12.006>
- Duval, M., Grün, R., 2016. Are published ESR dose assessments on fossil tooth enamel reliable? Quat. Geochronol. 31, 19–27. <https://doi.org/https://doi.org/10.1016/j.quageo.2015.09.007>
- Duval, M., Grün, R., Falguères, C., Bahain, J.J., Dolo, J.M., 2009. ESR dating of Lower Pleistocene fossil teeth: Limits of the single saturating exponential (SSE) function for the equivalent dose determination. Radiat. Meas. <https://doi.org/10.1016/j.radmeas.2009.03.017>
- Grün, R., 1989. Electron spin resonance (ESR) dating. Quat. Int. 1, 65–109.
- Grün, R., Katzenberger-Apel, O., 1994. An alpha irradiator for ESR dating. Anc. TL 12.
- Grün, R., Schwarcz, H.P., Chadam, J., 1988. ESR dating of tooth enamel: Coupled correction for U-uptake and U-series disequilibrium. Int. J. Radiat. Appl. Instrumentation. Part D. Nucl. Tracks Radiat. Meas. 14, 237–241. [https://doi.org/https://doi.org/10.1016/1359-0189\(88\)90071-4](https://doi.org/https://doi.org/10.1016/1359-0189(88)90071-4)
- Guérin, G., Mericier, N., Adamiec, G., 2011. Dose-rate conversion factors: update. Anc. TL 29, 5–8.
- Jaffey, A. H., Flynn, K.F., Glendenin, L.E., Bentley, W.T., Essling, A.M., 1971. Precision measurement of half-lives and specific activities of U 235 and U 238. *Physical review C* 4, no. 5, 1889.
- Lyons, R.G., Brennan, B.J., Hosking, P.L., 1992. Estimation of accumulated dose and its uncertainties: potential pitfalls in curve fitting. Anc. TL 10.
- Marsh, R.E., 1999. Beta-gradient Isochrons Using Electron Paramagnetic Resonance: Towards a New Dating Method in Archaeology.
- Molodkov, A., 2020. The Late Pleistocene palaeoenvironmental evolution in Northern Eurasia through the prism of the mollusc shell-based ESR dating evidence. Quat. Int. 556, 180–197. <https://doi.org/https://doi.org/10.1016/j.quaint.2019.05.031>
- Molodkov, A., 1988. ESR dating of quaternary shells: Recent advances. Quat. Sci. Rev. 7, 477–484. [https://doi.org/https://doi.org/10.1016/0277-3791\(88\)90049-2](https://doi.org/https://doi.org/10.1016/0277-3791(88)90049-2)
- Prescott, J.R., Hutton, J.T., 1994. Cosmic ray contributions to dose rates for luminescence and ESR dating: Large depths and long-term time variations. Radiat. Meas. 23, 497–500. [https://doi.org/10.1016/1350-4487\(94\)90086-8](https://doi.org/10.1016/1350-4487(94)90086-8)
- Radtke, U., 1989. Marine Terrassen und Korallenriffe – das Problem der quartären Meeresspiegelschwankungen erläutert an Fallstudien aus Chile, Argentinien und Barbados. Dusseld. Geogr. Schr. 27.
- Schellmann, G., Radtke, U., 2003. Coastal Terraces and Holocene Sea-level Changes Along the Patagonian Atlantic Coast. J. Coast. Res. 19, 983–996.
- Schellmann, G., Radtke, U., 2001. Progress in ESR dating of Pleistocene corals — a new approach for DE determination. Quat. Sci. Rev. 20, 1015–1020. [https://doi.org/https://doi.org/10.1016/S0277-3791\(00\)00060-3](https://doi.org/https://doi.org/10.1016/S0277-3791(00)00060-3)
- Schellmann, G., Radtke, U., 1999. Problems encountered in the determination of dose and dose rate in ESR dating of mollusc shells. Quat. Sci. Rev. 18, 1515–1527. <https://doi.org/https://doi.org/10.1016/S0277->

- Schellmann, G., Radtke, U., 1997. Electron spin resonance (ESR) techniques applied to mollusc shells from South America (Chile, Argentina) and implications for palaeo sea-level curve. *Quat. Sci. Rev.* 16, 465–475. [https://doi.org/https://doi.org/10.1016/S0277-3791\(96\)00104-7](https://doi.org/https://doi.org/10.1016/S0277-3791(96)00104-7)
- Schellmann, G., Schielein, P., Burow, C., Radtke, U., 2020. Accuracy of ESR dating of small gastropods from loess and fluvial deposits in the Bavarian Alpine Foreland. *Quat. Int.* 556, 198–215. <https://doi.org/https://doi.org/10.1016/j.quaint.2019.07.026>
- Shao, Q., Bahain, J.-J., Dolo, J.-M., Falguères, C., 2014. Monte Carlo approach to calculate US-ESR age and age uncertainty for tooth enamel. *Quat. Geochronol.* 22, 99–106. <https://doi.org/https://doi.org/10.1016/j.quageo.2014.03.003>
- Shao, Q., Bahain, J.-J., Falguères, C., Dolo, J.-M., Garcia, T., 2012. A new U-uptake model for combined ESR/U-series dating of tooth enamel. *Quat. Geochronol.* 10, 406–411. <https://doi.org/https://doi.org/10.1016/j.quageo.2012.02.009>

## Appendix E

# Paper contribution

1. **Ageby, L.**, Angelucci, D. E., Brill, D., Carrer, F., Rades, E. F., Rethemeyer, J., Brückner H., & Klasen, N. (2021). Rock surface IRSL dating of buried cobbles from an alpine dry-stone structure in Val di Sole, Italy. *Quaternary Geochronology*, 66. doi:10.1016/j.quageo.2021.101212.

*Fieldwork: 50 %*

*Data collection: 90 %*

*Analysis and interpretation: 70 %*

*Preparation for publication: 80 %*

2. Brill, D., **Ageby, L.**, Obert, C., Hollerbach, R., Duval, M., Kolb, T., & Bartz, M. (2022). Investigating the resetting of IRSL signals in beach cobbles and their potential for rock surface dating of marine terraces in Northern Chile. *Marine Geology*, 443. doi:10.1016/j.margeo.2021.106692.

*Fieldwork: 0 %*

*Data collection: 0 %*

*Analysis and interpretation: 50 %*

*Preparation for publication: 20 %*

3. **Ageby, L.**, Angelucci, D. E., Brill, D., Carrer, F., Brückner, H., & Klasen, N. (2022). Dating dry-stone walls with rock surface luminescence: A case study from the Italian Alps. *Journal of Archaeological Science*, 144. doi:10.1016/j.jas.2022.105625.

*Fieldwork: 60 %*

*Data collection: 100 %*

*Analysis and interpretation: 80 %*

*Preparation for publication: 80 %*

4. **Ageby, L.**, Brill, D., Angelucci, D. E., Brückner, H., & Klasen, N. (2023). Investigating optical dating of carbonate-rich cobbles from a river terrace: A pilot study from the Mula Valley, Spain. *Radiation Measurements* 166. doi:10.1016/j.radmeas.2023.106962.

*Fieldwork: 60 %*

*Data collection: 100 %*

*Analysis and interpretation: 80 %*

*Preparation for publication: 80 %*

## Appendix F

# Curriculum Vitae



# Lucas Mats Fredrik Ageby

lucas.ageby@hotmail.com

51503 Rösrath

Germany

## EDUCATION

---

- **Doctoral studies in Physical Geography**, University of Cologne 2018-2023
- **M.Sc. in Quaternary Sciences**, Stockholm University 2014-2017
- **B.Sc. in Earth Sciences**, Stockholm University 2011-2014

## EXPERIENCE

---

- **Postdoc**, Technical University of Denmark, Department of Environmental and Resource Engineering 2022-2023
- **Scientific Associate**, University of Cologne, Institute for Geography 2018-2021
- **Research Assistant**, Stockholm University, Department of Physical Geography 2017

## PUBLICATIONS

---

- *Towards the optically stimulated luminescence dating of unheated flint* **Ageby, L.**, Shanmugavel, J., Jain, M., Murray, A.S., & Rades, E.F. (2024). *Quaternary Geochronology*, 79. <https://doi.org/10.1016/j.quageo.2023.101471>. (peer-reviewed journal article)
- *Investigating optical dating of carbonate-rich cobbles from a river terrace: A pilot study from the Mula Valley, Spain.* **Ageby, L.**, Brill, D., Angelucci, D. E., Brückner, H., & Klasen, N. (2023). *Radiation Measurements* 166. <https://doi.org/10.1016/j.radmeas.2023.106962>. (peer-reviewed journal article)
- *Dating dry-stone walls with rock surface luminescence: A case study from the Italian Alps.* **Ageby, L.**, Angelucci, D. E., Brill, D., Carrer, F., Brückner, H., & Klasen, N. (2022). *Journal of Archaeological Science*, 144. <https://doi.org/10.1016/j.jas.2022.105625>. (peer-reviewed journal article)
- *Investigating the resetting of IRSL signals in beach cobbles and their potential for rock surface dating of marine terraces in Northern Chile.* Brill, D., **Ageby, L.**, Obert, C., Hollerbach, R., Duval, M., Kolb, T., & Bartz, M. (2022). *Marine Geology*, 443. <https://doi.org/10.1016/j.margeo.2021.106692>. (peer-reviewed journal article)

- *Luminescence dating*. **Ageby, L.**, Brill, D., Brückner, H., & Klasen, N. (2021). in: *The journey of modern humans from Africa to Europe: culture-environmental interaction and mobility*. Schweizerbart, Stuttgart, Germany, pp. 329–332. (book chapter)
- *Occupazione pastorale delle alte quote alpine nell'età del Bronzo: primi dati dal sito MZ051S (Camp da Ortisé, Val di Sole, Trento)*. Angelucci, D. E., Carrer, F., **Ageby, L.**, Castiglioni, E., Cavulli, F., Dell'Amore, F., Rethemeyer, J., Rottoli, M., Vezzoni, & L., Pedrotti, A., (2021). *Rivista di Scienze Preistoriche*, 71. <https://doi.org/10.32097/1143>. (peer-reviewed journal article)
- *Rock surface IRSL dating of buried cobbles from an alpine dry-stone structure in Val di Sole, Italy*. **Ageby, L.**, Angelucci, D. E., Brill, D., Carrer, F., Rades, E. F., Rethemeyer, J., Brückner H., & Klasen, N. (2021). *Quaternary Geochronology*, 66. <https://doi.org/10.1016/j.quageo.2021.101212>. (peer-reviewed journal article)

## SELECTED CONFERENCE PRESENTATIONS

---

- **International Luminescence and Electron Spin Resonance Dating conference**, Copenhagen, Denmark. 2023. Abstract: *Towards rock surface OSL dating of flint*. (oral presentation)
- **German Luminescence Meeting**, Cologne, Germany. 2022. Abstract: *Towards rock surface OSL dating of unheated stone tools: luminescence characteristics and signal bleaching in Danish flints*. (oral presentation)
- **UK Luminescence Meeting**, London, UK. 2022. Abstract: *Towards optical dating of stone artefacts: rock surface luminescence dating of Danish flints*. (poster presentation)
- **German Luminescence Meeting**, online. 2020. Abstract: *Rock surface luminescence dating of carbonate-rich cobbles compared with multi-grain luminescence dating from alluvial deposits in the Mula basin, southeastern Spain*. (poster presentation)
- **EGU**, online. 2020. Abstract: *Exploring the application of IRSL rock surface exposure dating of archaeological stone structures in Val di Sole, Italy*. (online presentation)
- **German Luminescence Meeting**, Bingen, Germany. 2019. Abstract: *IRSL rock surface dating of stone structures related to pastoralism in Val di Sole, Italy*. (oral presentation)
- **UK Luminescence Meeting**, Roskilde, Denmark. 2019. Abstract: *IRSL rock surface dating of pastoral dry stone structures in Val di Sole, Italy*. (oral presentation)
- **INQUA**, Dublin, Ireland. 2019. Abstract: *Luminescence dating of quartzite and granite cobbles from wadi terraces in the Eastern Desert, Egypt*. (oral presentation)
- **German Luminescence Meeting**, Beatenberg, Switzerland. 2018. Abstract: *Luminescence characteristics from cobbles from alluvial terraces near palaeolithic sites in the Mula basin, Spain*. (poster presentation)
- **UK Luminescence Meeting**, Sheffield, UK. 2018. Abstract: *Luminescence characteristics of quartzite and granite cobbles from terrace surfaces in Wadi Sodmein, Egypt*. (poster presentation)



Appendix G

Erklärung

**Erklärung zur Dissertation**  
gemäß der Promotionsordnung vom 12. März 2020

„Hiermit versichere ich an Eides statt, dass ich die vorliegende Dissertation selbstständig und ohne die Benutzung anderer als der angegebenen Hilfsmittel und Literatur angefertigt habe. Alle Stellen, die wörtlich oder sinngemäß aus veröffentlichten und nicht veröffentlichten Werken dem Wortlaut oder dem Sinn nach entnommen wurden, sind als solche kenntlich gemacht. Ich versichere an Eides statt, dass diese Dissertation noch keiner anderen Fakultät oder Universität zur Prüfung vorgelegen hat; dass sie - abgesehen von unten angegebenen Teilpublikationen und eingebundenen Artikeln und Manuskripten - noch nicht veröffentlicht worden ist sowie, dass ich eine Veröffentlichung der Dissertation vor Abschluss der Promotion nicht ohne Genehmigung des Promotionsausschusses vornehmen werde. Die Bestimmungen dieser Ordnung sind mir bekannt. Darüber hinaus erkläre ich hiermit, dass ich die Ordnung zur Sicherung guter wissenschaftlicher Praxis und zum Umgang mit wissenschaftlichem Fehlverhalten der Universität zu Köln gelesen und sie bei der Durchführung der Dissertation zugrundeliegenden Arbeiten und der schriftlich verfassten Dissertation beachtet habe und verpflichte mich hiermit, die dort genannten Vorgaben bei allen wissenschaftlichen Tätigkeiten zu beachten und umzusetzen. Ich versichere, dass die eingereichte elektronische Fassung der eingereichten Druckfassung vollständig entspricht.“

**Teilpublikationen:**

- *Rock surface IRSL dating of buried cobbles from an alpine dry-stone structure in Val di Sole, Italy.* Quaternary Geochronology, 66. 2021
- *Investigating the resetting of IRSL signals in beach cobbles and their potential for rock surface dating of marine terraces in Northern Chile.* Marine Geology, 443
- *Dating dry-stone walls with rock surface luminescence: A case study from the Italian Alps.* Journal of Archaeological Science, 144. 2022
- *Investigating optical dating of carbonate-rich cobbles from a river terrace: A pilot study from the Mula Valley, Spain.* Radiation Measurements, 166. 2023

**Datum, Name und Unterschrift**

23.06.2023, Lucas Ageby

